

SPIN STRUCTURE OF THE DEUTERON

by

Nevzat Guler

M.S. June 2002, University of Texas at Arlington

A Dissertation Submitted to the Faculty of
Old Dominion University in Partial Fulfillment of the
Requirement for the Degree of

DOCTOR OF PHILOSOPHY

PHYSICS

OLD DOMINION UNIVERSITY

December 2009

Approved by:

Sebastian E. Kuhn (Director)

Gail Dodge

Ian Balitsky

Charles I. Sukenik

John Adam

ABSTRACT

SPIN STRUCTURE OF THE DEUTERON

Nevzat Guler

Old Dominion University, 2009

Director: Dr. Sebastian E. Kuhn

Double spin asymmetries for the proton and the deuteron have been measured in the EG1b experiment using the CLAS detector at Jefferson Lab. Longitudinally polarized electrons at energies 1.6, 2.5, 4.2 and 5.7 GeV were scattered from longitudinally polarized NH_3 and ND_3 targets. The double spin asymmetry A_{\parallel} for the proton and the deuteron has been extracted from these data as a function of W and Q^2 with unprecedented precision. The virtual photon asymmetry A_1 and the spin structure function g_1 can be calculated from these measurements by using parametrization to the world data for the virtual photon asymmetry A_2 and the unpolarized structure functions F_1 and R . The large kinematic coverage of the experiment ($0.05 \text{ GeV}^2 < Q^2 < 5.0 \text{ GeV}^2$ and $1.08 \text{ GeV} < W < 3.0 \text{ GeV}$) helps us to better understand the spin structure of the nucleon, especially in the transition region between hadronic and quark-gluon degrees of freedom. The results on A_1 , g_1 and the first moment Γ_1^1 , as well as the higher moments Γ_1^3 and Γ_1^5 , using the entire data set for the deuteron, are presented in this thesis. The moments are compared to theoretical and phenomenological calculations. In addition, parameterizations of the world data on the asymmetries and the spin structure functions are studied to create and refine the models on these quantities that can be used in various applications. Finally, the neutron asymmetries are extracted from the combined proton and deuteron data and the preliminary results are demonstrated.

©Copyright, 2010, by Nevzat Guler, All Rights Reserved

ACKNOWLEDGMENTS

I would like to thank my advisor Sebastian Kuhn for his support, encouragement and patience throughout this work. His directions and dedication made the completion of this thesis possible. Also special thanks goes to Gail Dodge for her continued support from the very beginning. In addition, I have a great appreciation for Peter Bosted, who played a very important part in this analysis and saved the day many times. Ralph Mineheart was always there for us in every meeting and his dedication gave me a driving force. Many thanks goes to Keith Griffioen for his continuous support. Being a student under the care of all these people was a great pleasure and valuable experience. I want to thank them for giving me the opportunity to work on the EG1b experiment.

I would also like to thank Ian Balitsky, Charles Sukenik and John Adam for being in my thesis committee. Moreover, the other ODU professors Mark Havey, Larry Weinstein and Moskov Amarian, Lepsha Vuskovic, and many others, made the experience worthwhile with their help and teachings.

My fellow students, Robert Fersch, Josh Pierce and Sharon Careccia made this journey possible with their great work and support. I would like to thank Harut Avagyan, Alexander Deur and Stepan Stepanyan for being there whenever we need their help and for their valuable contributions. Many thanks to Volker Burkert for supporting us all the way. Moreover, thanks to Tony Forest, Angela Biselli, Mark Ito for their contributions on this experiment as well as on our analysis. I would also like to express my appreciation to Alexander Deur, Karl Slifer, Oscar Rondon and Patricia Solvignon for their help in collecting the world data for our fits and sharing their data with us.

I want to thank Stephan Bueltmann for his continuous support. He was always there as a friend and a humble mentor whenever he is needed. I also want to thank Yelena Prok and Vipuli Dharmawardane for defining a solid path for us with their earlier work on this experiment. Thank you very much Yelena also for the delicious food and dinner invitations.

I would like to thank my ODU fellows, Jixie Zhang, Svyatoslav Tkachenko, Hovanes Bagdasaryan, Khrishna Adhikari and Mike Mayer, Serkan Golge, Mustafa Canan and many others for their friendship and support. Special thanks to Jixie for being there whenever I need to discuss various programming issues.

Finally, I would also like to thank my parents and my wife for their patience during this work. Without their continuous support and love, none of these would be possible. Also, I appreciate many of my friends that came into my life, bring their love and provide me with their support and encouragement to continue on my path.

There are also many nameless heroes that I cannot thank enough because of their work on this experiment, which made this work possible. This research was supported by the US Department of Energy, thus, I would like to thank the taxpayers and the US Government for creating research opportunities for curious minds.

TABLE OF CONTENTS

| | Page |
|--|------|
| LIST OF TABLES | xi |
| LIST OF FIGURES | xv |
| CHAPTERS | |
| I Introduction | 1 |
| I.1 Lepton Hadron Scattering | 5 |
| II Theoretical Background | 14 |
| II.1 The Structure Functions | 14 |
| II.1.1 Polarized Inclusive Deep-Inelastic Scattering | 15 |
| II.1.2 Photo-Absorption Cross Sections | 19 |
| II.1.3 Asymmetries | 22 |
| II.1.4 Extension to Spin 1 Target | 24 |
| II.2 Interpretation in the Quark-Parton Model | 25 |
| II.3 Q^2 Evolution of the Structure Functions | 28 |
| II.3.1 QCD corrections to the probability distribution functions | 30 |
| II.3.2 Q^2 dependence of $g_1(x, Q^2)$ in the DIS region | 32 |
| II.3.3 The operator product expansion and moments of $g_1(x, Q^2)$ | 33 |
| II.3.4 Nucleon resonance region | 37 |
| II.3.5 Quark-hadron duality | 40 |
| II.4 Sum Rules and Theoretical Models | 42 |
| II.4.1 Vector and Axial Vector Coupling Constants | 44 |
| II.4.2 pQCD Corrections | 47 |
| II.4.3 The Ellis-Jaffe Sum Rule | 48 |
| II.4.4 The Bjorken Sum Rule | 50 |
| II.4.5 The Gerasimov-Drell-Hearn (GDH) Sum Rule | 51 |
| II.4.6 Generalized Forward Spin Polarizabilities | 59 |
| II.4.7 Phenomenological Models | 61 |
| II.5 The Deuteron, A Closer Look | 63 |
| II.5.1 Extraction of Neutron Information from A Deuteron Target | 67 |
| II.6 Summary | 69 |
| III Experimental Setup | 71 |
| III.1 Continuous Electron Beam Accelerator Facility | 71 |
| III.2 Hall B Beam-Line | 72 |
| III.3 CEBAF Large Acceptance Spectrometer | 75 |
| III.3.1 Torus Magnet | 76 |
| III.3.2 Drift Chambers | 78 |
| III.3.3 Time of Flight System | 81 |
| III.3.4 Cherenkov Counters | 83 |
| III.3.5 Electromagnetic Calorimeter | 85 |
| III.4 The Trigger And The Data Acquisition System | 89 |

| | | |
|-------|---|-----|
| III.5 | EG1b Targets | 91 |
| IV | Data Analysis | 94 |
| IV.1 | Eg1b Runs | 95 |
| IV.2 | Data reconstruction and calibration | 96 |
| | IV.2.1 Event reconstruction | 99 |
| | IV.2.2 Calibrations | 100 |
| IV.3 | DST Files | 108 |
| IV.4 | Helicity pairing | 109 |
| IV.5 | Quality checks and pre-analysis corrections | 111 |
| | IV.5.1 Event rates | 112 |
| | IV.5.2 Beam charge quality | 113 |
| | IV.5.3 Effects of beam charge asymmetry | 113 |
| | IV.5.4 Polarizations and asymmetry check | 115 |
| | IV.5.5 Faraday cup corrections | 115 |
| | IV.5.6 Additional comments | 116 |
| IV.6 | Data Binning | 118 |
| IV.7 | Electron Identification | 120 |
| | IV.7.1 Status Flag | 121 |
| | IV.7.2 Trigger Bit | 121 |
| | IV.7.3 Vertex Cuts | 122 |
| | IV.7.4 Cherenkov Counter Cuts | 122 |
| | IV.7.5 Electromagnetic Calorimeter Cuts | 124 |
| | IV.7.6 Additional kinematic cuts | 127 |
| IV.8 | Geometric and Timing Cuts on the CC | 128 |
| | IV.8.1 Geometric cuts | 130 |
| | IV.8.2 Timing cuts | 132 |
| | IV.8.3 Left-Right PMT cut | 134 |
| | IV.8.4 Final Comments | 134 |
| IV.9 | Fiducial Cuts | 136 |
| IV.10 | Kinematic Corrections | 141 |
| | IV.10.1 Raster Correction | 143 |
| | IV.10.2 Average Vertex Position | 146 |
| | IV.10.3 Torus Current Scaling Correction | 148 |
| | IV.10.4 Beam Energy Correction | 149 |
| | IV.10.5 Multiple Scattering and Magnetic Field Corrections | 153 |
| | IV.10.6 Energy Loss Correction | 155 |
| | IV.10.7 Momentum Correction | 158 |
| | IV.10.8 Patch Correction | 171 |
| | IV.10.9 Overall Results of the Kinematic Corrections | 174 |
| IV.11 | Dilution Factor | 185 |
| | IV.11.1 Calculation of Total Target Length L | 190 |
| | IV.11.2 Modeling ^{15}N from ^{12}C Data and Calculation of l_N | 195 |
| | IV.11.3 Calculation of Ammonia Target Length l_A | 202 |
| | IV.11.4 Dilution Factor Results | 211 |

| | | |
|---------|---|-----|
| IV.12 | Background Analysis | 215 |
| IV.12.1 | Pion Contamination | 216 |
| IV.12.2 | Pair Symmetric Electron Contamination | 225 |
| IV.13 | Beam and Target Polarization | 235 |
| IV.13.1 | Theoretical Asymmetry For Quasi-Elastic Scattering from the Deuteron | 236 |
| IV.13.2 | Extraction of Quasi-Elastic Asymmetry from the Data | 237 |
| IV.13.3 | Final $P_b P_t$ Values | 242 |
| IV.13.4 | $P_b P_t$ for Weighting Data from Different Helicity Configurations | 246 |
| IV.14 | Polarized Background Corrections | 254 |
| IV.15 | Radiative corrections | 258 |
| IV.16 | Model Input | 259 |
| IV.16.1 | Models of the unpolarized structure functions for the deuteron | 260 |
| IV.16.2 | Models of A_1 and A_2 in the DIS region | 262 |
| IV.17 | Combining Data from Different Configurations | 265 |
| IV.17.1 | Combining runs | 265 |
| IV.17.2 | Weighting of Asymmetries | 267 |
| IV.17.3 | t-Test | 267 |
| IV.17.4 | Combining opposite target polarizations | 268 |
| IV.17.5 | Combining data with slightly different beam energies | 270 |
| IV.17.6 | Combining data sets with opposite torus polarities | 271 |
| IV.17.7 | Combining data sets with different beam energies | 272 |
| IV.17.8 | Combining W bins for plotting | 273 |
| IV.18 | Physics Quantities and Propagation of the Statistical Errors | 274 |
| IV.19 | Systematic Error Calculations | 277 |
| IV.19.1 | Pion and pair-symmetric backgrounds | 279 |
| IV.19.2 | Dilution factor | 280 |
| IV.19.3 | Beam and target polarizations | 280 |
| IV.19.4 | Polarized background | 281 |
| IV.19.5 | Radiative corrections | 281 |
| IV.19.6 | Systematic errors due to models | 282 |
| V | Physics Results | 283 |
| VI | Modeling the World Data | 301 |
| VI.1 | Parametrization of A_1^p | 302 |
| VI.2 | Parametrization of A_2^p | 305 |
| VI.3 | Parametrization of A_2^n | 309 |
| VI.4 | Parametrization of A_1^n by using the deuteron data | 312 |
| VI.5 | Additional Comments | 315 |
| VII | Conclusion | 319 |

APPENDICES

| | | |
|---|-------------------------|-----|
| A | DST Variables | 321 |
| B | Fiducial Cuts | 325 |

| | | |
|-----|---|-----|
| B.1 | Inbending Fiducial Cuts | 325 |
| B.2 | Outbending Fiducial Cuts | 325 |
| C | Additional Tables | 328 |
| C.1 | Pion and pair symmetric contamination parameters | 328 |
| C.2 | Systematic Errors | 328 |
| C.3 | Kinematic Regions for Model usage in Γ_1^1 integration | 328 |
| | BIBLIOGRAPHY | 342 |
| | VITA | 352 |

LIST OF TABLES

| | | Page |
|----|--|------|
| 1 | Quark flavors | 5 |
| 2 | Contribution of various channels to the GDH integral. | 56 |
| 3 | CLAS Parameters | 92 |
| 4 | EG1b run sets by beam energy and torus current. | 96 |
| 5 | Run Summary Table. | 97 |
| 6 | Helicity error codes. | 111 |
| 7 | Helicity pairing table example | 112 |
| 8 | Faraday Cup normalization factors for beam divergence | 117 |
| 9 | Q^2 bins for the EG1b experiment | 119 |
| 10 | Parameters to translate the raster ADC to the beam position in transverse coordinate system. | 144 |
| 11 | The “nominal” (from MCC) and “true” (from Hall-A) beam energies for the EG1b | 152 |
| 12 | Parameter definitions in Bethe-Bloch Formula | 156 |
| 13 | Electron cuts applied for the momentum correction data sample. | 163 |
| 14 | Proton cuts applied for the momentum correction data sample. | 164 |
| 15 | Elastic event cuts applied for the momentum correction data sample. | 165 |
| 16 | Second iteration cuts for the elastic events. | 166 |
| 17 | Pion cuts applied for the momentum correction data sample. | 168 |
| 18 | First iteration $ep\pi^+\pi^-$ cuts for the momentum correction data sample. | 169 |
| 19 | Second iteration cuts for the $ep\pi^+\pi^-$ events. | 169 |
| 20 | Number of events in each data sample for the momentum correction fit. | 170 |
| 21 | Sector-dependent momentum correction parameters in EG1b. | 170 |
| 22 | Beam energy and torus current dependent parameters, T_{set} , for outbending data sets. | 171 |
| 23 | Forward angle momentum correction parameters for the EG1b experiment. | 173 |
| 24 | Polar angle θ bins for the kinematic correction plots. | 175 |
| 25 | Azimuthal angle ϕ bins for the kinematic correction plots. | 175 |
| 26 | Target parameter definitions. | 187 |
| 27 | The EG1b target material properties | 189 |
| 28 | The EG1b target material properties | 190 |
| 29 | Target parameter values | 191 |
| 30 | Calculated total target length L for different data sets in the EG1b experiment | 196 |
| 31 | Parameters a and b for $^{15}\text{N}/^{12}\text{C}$ cross-section ratios | 199 |
| 32 | The ^{15}N target length l_N for different data sets. | 203 |
| 33 | Frozen ammonia effective target lengths l_A for each data configuration. | 211 |
| 34 | Momentum bins used for the pion contamination analysis. | 218 |
| 35 | Polar angle bins used for the pion contamination analysis. | 219 |
| 36 | Pion selection cuts for the pion contamination analysis. | 219 |

| | | |
|----|--|-----|
| 37 | Cuts on Positron | 226 |
| 38 | Form factor $G_E(Q^2)$ and $G_M(Q^2)$ fit parameters | 236 |
| 39 | W limits for elastic event selection. | 238 |
| 40 | Electron cuts for $P_b P_t$ calculation with the inclusive method. | 238 |
| 41 | Electron cuts for $P_b P_t$ calculation with the exclusive method. | 243 |
| 42 | Cuts for the selection of quasi-elastic events for $P_b P_t$ calculation. | 243 |
| 43 | Q^2 limits in GeV for the $P_b P_t$ average. | 246 |
| 44 | $P_b P_t$ values from different methods for all data sets with ND ₃ target. | 252 |
| 45 | $P_b P_t$ values averaged over opposite target polarizations. | 255 |
| 46 | t-Test results for combining sets with opposite target polarizations. | 269 |
| 47 | z-Test results for combining data with slightly different beam energies. | 271 |
| 48 | z-Test results for combining sets of opposite torus polarity. | 272 |
| 49 | z-Test results for combining data sets with different beam energies. | 273 |
| 50 | Systematic error index | 279 |
| 51 | Final parameters for the first step A_1^p fit. | 305 |
| 52 | Final parameters for the second step A_1^p fit. | 307 |
| 53 | Final parameters for the A_2^p fit. | 309 |
| 54 | Final parameters for the A_2^p fit. | 312 |
| 55 | DST variables: particle ID. SEB is the standard particle ID used in RECSIS, whereas p_id(DST) is the DST equivalent. | 321 |
| 56 | DST event headers | 321 |
| 57 | DST scaler variables and run information | 322 |
| 58 | DST particle variables | 323 |
| 59 | DST particle variables (added later to use the geometric and timing cuts). | 324 |
| 60 | DST variables: helicity flag | 324 |
| 61 | Fiducial cuts parameters for the inbending data | 326 |
| 62 | Loose fiducial cut parameters for the inbending data | 326 |
| 63 | Fiducial cuts parameters for the outbending data | 327 |
| 64 | Standard π^-/e^- ratio parameters a and b. | 329 |
| 65 | Standard π^-/e^- ratio parameters c and d. | 330 |
| 66 | Total π^-/e^- ratio parameters a and b. | 331 |
| 67 | Total π^-/e^- ratio parameters c and d. | 332 |
| 68 | e^+/e^- ratio parameters a and b. | 333 |
| 69 | e^+/e^- ratio parameters c and d | 334 |
| 70 | Systematic errors on $A_1 + \eta A_2$ 1 GeV data. | 335 |
| 71 | Systematic errors on $A_1 + \eta A_2$ for 2 GeV data. | 336 |
| 72 | Systematic errors on $A_1 + \eta A_2$ for 4 GeV data. | 337 |
| 73 | Systematic errors on $A_1 + \eta A_2$ for 5 GeV data. | 338 |
| 74 | Systematic errors on A_1 | 339 |
| 75 | Systematic errors on A_1 for different W regions. | 340 |
| 76 | W regions (in GeV) used for Γ_1 calculation. Model was used where data is not available. | 341 |

LIST OF FIGURES

| | | Page |
|----|---|------|
| 1 | Electron scattering from nucleon. | 6 |
| 2 | Polarized electron-nucleon scattering. | 15 |
| 3 | Electron-nucleon scattering in QPM. | 26 |
| 4 | Scaling behavior of spin-flip transitions | 27 |
| 5 | Dependence of the resolution of nucleon's internal structure on Q^2 | 29 |
| 6 | Vertices that are used in the calculation of splitting functions. | 31 |
| 7 | Higher Twist contributions to the first moment of g_1 for the neutron. | 36 |
| 8 | Resonance states appearing in the total cross section. | 37 |
| 9 | Path of integration for Cauchy's integral formula. | 52 |
| 10 | Phenomenological models for the Q^2 evolution of $\Gamma_1^{1(p)}$ and $\Gamma_1^{1(p)}$ | 64 |
| 11 | Deuteron spin states as a combination of the proton and the neutron spins. | 65 |
| 12 | A schematic view of the CEBAF accelerator | 72 |
| 13 | A schematic view of Hall B and beam line monitoring devices. | 73 |
| 14 | Schematic of Moller polarimeter | 74 |
| 15 | Comparison of the beam charge asymmetry measurements from the Faraday Cup and the Synchrotron Light Monitor | 76 |
| 16 | Three dimensional view of CLAS | 77 |
| 17 | Configuration of the torus coils | 78 |
| 18 | CLAS magnetic field | 79 |
| 19 | Schematic of a section of drift chambers showing two super-layers | 80 |
| 20 | CLAS drift chamber for one sector. | 80 |
| 21 | The four panels of TOF scintillator counters for one of the sectors | 82 |
| 22 | Array of CC optical modules in one sector | 84 |
| 23 | One optical module of the CLAS Cherenkov detector | 85 |
| 24 | View of one of the six CLAS electromagnetic calorimeter modules | 87 |
| 25 | Schematic side view of the fiber-optic readout unit of the calorimeter module | 88 |
| 26 | Electron signal in the Electromagnetic Calorimeter | 90 |
| 27 | Data flowchart of the CLAS DAQ | 91 |
| 28 | A schematic of the target insert strip | 93 |
| 29 | Kinematic coverage of the EG1b experiment. | 97 |
| 30 | RF offset from run 28405. | 102 |
| 31 | RF bunch timing offsets. | 102 |
| 32 | Time-of-flight reconstructed mass spectrum. | 104 |
| 33 | Electromagnetic Calorimeter timing calibration | 105 |
| 34 | Time-based tracking in the CLAS drift chamber. | 107 |
| 35 | Residual average of the time based tracking (TBT). | 107 |
| 36 | Helicity pulses in the EG1b. | 110 |
| 37 | Quality check plot for beam charge asymmetry. | 114 |
| 38 | Quality check plot for polarizations and asymmetry check. | 114 |

| | | |
|----|---|-----|
| 39 | Vertex positions before and after raster corrections. | 123 |
| 40 | Cherenkov Counter signal. | 123 |
| 41 | EC_{in} vs. EC_{tot} for negative charged particles. | 125 |
| 42 | EC_{in} for negative charged particles. | 125 |
| 43 | Particle identification by energy deposited to the EC | 126 |
| 44 | EC_{tot}/p vs. p plots for negative charged particles. | 126 |
| 45 | Cut on Sector 5 polar angle | 128 |
| 46 | The CC projective plane | 129 |
| 47 | Polar angle cut on the CC signal. | 131 |
| 48 | Timing cut on the CC signal. | 133 |
| 49 | Left-right PMT cut on the CC signal. | 135 |
| 50 | Results of the geometric and timing cuts on the CC | 136 |
| 51 | Pion to electron ratio plots before and after geometric and time cuts. | 137 |
| 52 | Effects of the magnetic field of the polarized target on the scattering angle measurements for all 6 sectors. | 139 |
| 53 | The fiducial cuts for inbending data at low and high momentum bins. | 140 |
| 54 | The fiducial cuts for outbending data. | 141 |
| 55 | Loose fiducial cuts on inbending data for asymmetry measurement | 142 |
| 56 | Front view schematic of raster correction geometry. | 145 |
| 57 | Side view schematic of raster correction geometry. | 145 |
| 58 | Azimuthal angle vs. vertex position before and after raster corrections | 147 |
| 59 | Raster pattern for run 28110 | 148 |
| 60 | Elastic peak positions before correction | 150 |
| 61 | Elastic peak positions before correction | 151 |
| 62 | Artistic visualization of the effect of multiple scattering | 154 |
| 63 | Δt proton | 164 |
| 64 | Distribution in θ_{el} and ϕ_{el} of elastic ep events | 166 |
| 65 | Missing energy and momentum distributions for the elastic events. | 167 |
| 66 | Difference between electron and proton azimuthal angles for elastic scattering. | 167 |
| 67 | Δt proton | 169 |
| 68 | Low θ elastic peak positions prior to final corrections. | 173 |
| 69 | Missing energy for different sectors. | 176 |
| 70 | ϕ vs. $\Delta E'/E'$ before and after the kinematic corrections for the 1.606 and 1.723 GeV data sets. | 177 |
| 71 | ϕ vs. $\Delta E'/E'$ before and after the kinematic corrections for the 2.561 and 4.238 GeV data sets. | 178 |
| 72 | Elastic W peak for various ϕ bins before and after the kinematic cor- rections for 1.606 and 2.286 GeV data sets. | 179 |
| 73 | Elastic W peak for various ϕ bins before and after the kinematic cor- rections for 2.561 and 4.238 GeV data sets. | 180 |
| 74 | Elastic W peak improvement by the kinematic corrections. | 181 |
| 75 | Elastic W peak improvement by the kinematic corrections | 182 |
| 76 | Elastic W peak improvement by the kinematic corrections | 183 |

| | | |
|-----|--|-----|
| 77 | Elastic W peak improvement by the kinematic corrections | 184 |
| 78 | Target length L measurement from data | 193 |
| 79 | Target length L measurement from model | 195 |
| 80 | $^{15}\text{N}/^{12}\text{C}$ count rate ratios for the 2.3 GeV data set | 201 |
| 81 | Measurement of ^{15}N target length by using the radiated cross section model. | 203 |
| 82 | Measurement of the effective ammonia target length l_A from data. . . | 207 |
| 83 | Measurement of the effective ammonia target length l_A for different helicity states. | 208 |
| 84 | Measurement of ammonia target length l_A from the radiated cross section model. | 210 |
| 85 | Dilution factors plotted vs. W | 213 |
| 86 | Dilution factors (from data) plotted vs. Q^2 | 214 |
| 87 | Cherenkov spectrum for electrons and pions. | 217 |
| 88 | Cherenkov spectrum for electrons and pions. | 221 |
| 89 | Pion to electron ratio as a function of momentum for two polar angle bins. | 222 |
| 90 | Dependence of the exponential parameters on the polar angle. | 223 |
| 91 | Total and standard contaminations as a function of momentum for a single polar angle bin before the geometric and timing cuts. | 225 |
| 92 | π^+ contamination on positrons. | 228 |
| 93 | π^+ to positron ratio as a function of momentum for two θ bins. . . . | 229 |
| 94 | π^+ contamination of positron. | 229 |
| 95 | positron to electron ratio for a single polar angle bin. | 230 |
| 96 | exponential fit parameter | 231 |
| 97 | Positron asymmetry as a function of momentum for a single θ bin in various data sets. | 233 |
| 98 | e^+/e^- ratio for two opposite torus polarity data. | 234 |
| 99 | The exponential fit parameters for the e^+/e^- ratio as a function of θ . . | 234 |
| 100 | W distributions from inclusive events for the background removal pro- cedure in the ND_3 target. | 240 |
| 101 | W distributions from inclusive events for the background removal pro- cedure in the NH_3 target. | 241 |
| 102 | Distributions of azimuthal angle difference between the electron and the proton in exclusive quasi-elastic events for different data sets with the ND_3 target. | 244 |
| 103 | W distributions for exclusive ep quasi-elastic events for different data sets, showing the background removal for the ND_3 target. | 245 |
| 104 | $P_b P_t$ values for different data sets for ND_3 target. | 247 |
| 105 | $P_b P_t$ values for different data sets for ND_3 target. | 248 |
| 106 | $P_b P_t$ values for different data sets for ND_3 target. | 249 |
| 107 | $P_b P_t$ values for different data sets for ND_3 target. | 250 |
| 108 | $P_b P_t$ values for different data sets for ND_3 target. | 251 |
| 109 | Models of R and F_1 for the deuteron. | 263 |

| | | |
|-----|--|-----|
| 110 | The A_1 fits in the DIS region for the proton and neutron. | 264 |
| 111 | t-Test between data sets with opposite target polarizations. | 268 |
| 112 | $A_1 + \eta A_2$ versus final invariant mass W for different beam energy settings. | 286 |
| 113 | $A_1 + \eta A_2$ versus final invariant mass W for different beam energy settings. | 287 |
| 114 | $A_1 + \eta A_2$ versus W together with different sources of systematic error. | 288 |
| 115 | Virtual photon asymmetry A_1 versus W for a few Q^2 bins. | 289 |
| 116 | A_1 for the deuteron versus the final state invariant mass W for various Q^2 bins. | 290 |
| 117 | A_1 of the deuteron versus the final state invariant mass W for various Q^2 bins. | 291 |
| 118 | g_1 for the deuteron versus the final state invariant mass W for various Q^2 bins. | 292 |
| 119 | g_1 for the deuteron versus the final state invariant mass W for various Q^2 bins. | 293 |
| 120 | g_1 for the deuteron versus the Bjorken variable x for various Q^2 bins. | 294 |
| 121 | g_1 for the deuteron versus the Bjorken variable x for various Q^2 bins. | 295 |
| 122 | Γ_1^1 for the deuteron versus Q^2 from data and data+model. | 296 |
| 123 | Γ_1^1 for the deuteron versus Q^2 from data and data+model. | 297 |
| 124 | Γ_1^1 versus Q^2 , EG1b current and previous analysis. | 298 |
| 125 | Γ_1^3 and Γ_1^5 versus Q^2 | 299 |
| 126 | Forward Spin Polarizability (γ_0) versus Q^2 | 300 |
| 127 | A_1^p parametrization. | 306 |
| 128 | A_1^p parametrization for various Q^2 bins. | 307 |
| 129 | The A_2^p parametrization. | 310 |
| 130 | The A_2^n parametrization. | 313 |
| 131 | The A_2^n parametrization. | 314 |
| 132 | The model and data for g_1/F_1 for the deuteron. | 316 |
| 133 | The parametrized A_1^n | 317 |
| 134 | g_1/F_1 for the neutron and its parametrized calculation. | 318 |

CHAPTER I

INTRODUCTION

Understanding the fundamental structure of matter is a longstanding quest of science. Since the discovery of the atom, human beings have traveled a long distance toward a deeper understanding of the universe. Mass, spin and charge have been determined to be the three most basic properties of matter. However, we still don't know the source of these properties or how they are carried on to the higher level structures of matter. Different theories like Quantum Electrodynamics, Quantum Chromodynamics or String Theory dedicate themselves to investigate and explain these properties. But their foundation and continuation require experimental confirmation.

Scattering of charged particles has been used as a tool to study the structure of matter for a long time. In the years 1909–1911, Ernest Rutherford and his students, Hans Geiger and Ernest Marsden, conducted an experiment in which a thin gold foil was bombarded with α -particles. Rutherford showed that the angular distribution of the scattered α -particles was evidence for a sub-structure of the atom. Rutherford interpreted the atom as a positively charged nucleus with negatively charged electron cloud around it creating electrically neutral atoms. In 1918 Rutherford noticed that when alpha particles were shot into nitrogen gas, his scintillation detectors showed the signatures of hydrogen nuclei. Rutherford determined that this hydrogen could only have come from the nitrogen. He suggested that the hydrogen nucleus, which was known to have an atomic number of 1, was an elementary particle that makes up the nucleus of other atoms. Gradually, this concept of a fundamental particle that makes up the nucleus was accepted widely and later these particles were called protons.

On the other hand, the atomic mass of most elements was greater than the atomic number, the number of protons inside the nucleus. Contribution of the electrons to the atomic weight was negligibly small. For a neutral atom, the number of protons in the nucleus and the number of electrons should be equal. In order to account for the discrepancy between the atomic number and the atomic mass, Rutherford suggested that there were electrons as well as protons in the nucleus, canceling out some of the positive charge. However, this model had many problems. According to

This dissertation follows the style of *Physical Review D*.

the uncertainty principle formulated by Heisenberg in 1926, it would require a huge amount of energy to confine electrons inside a nucleus and that kind of energy has never been observed in any nuclear process. An even more striking puzzle involved the spin of the nitrogen-14 nucleus, which had been experimentally measured to be 1 in basic units of angular momentum. According to Rutherford's model, nitrogen-14 nucleus would be composed of 14 protons and 7 electrons to give it a charge of +7 but a mass of 14 atomic mass units. However, it was also known that both protons and electrons carried an intrinsic spin of $1/2$ unit of angular momentum, and there was no way to arrange 21 particles in one group, or in groups of 7 and 14, to give a spin of 1. All possible pairings gave a net spin of $1/2$.

Later in 1930, Bothe and Becker observed that bombardment of beryllium with alpha particles from a radioactive source produced neutral radiation which was penetrating but non-ionizing. At first this radiation was thought to be gamma radiation, although it was more penetrating than any gamma rays known. Then in 1932, an experiment by Irene Joliot-Curie and Frederic Joliot showed that if this unknown radiation fell on paraffin or any other hydrogen-containing compound it ejected protons of very high energy. This was not in itself inconsistent with the assumed gamma ray nature of the new radiation, but detailed quantitative analysis of the data became increasingly difficult to reconcile with such a hypothesis. Finally, in 1932 the physicist James Chadwick performed a series of experiments showing that the gamma ray hypothesis was untenable. He suggested that in fact the new radiation consisted of uncharged particles of approximately the mass of the proton, and he performed a series of experiments verifying his suggestion. These uncharged particles were called neutrons.

The discovery of the neutron immediately explained the nitrogen-14 spin puzzle. When nitrogen-14 was proposed to consist of 3 pairs of protons and 3 pairs of neutrons, with an additional unpaired proton and neutron each contributing a spin of $1/2$ in the same direction for a total spin of 1, the model became viable. Soon, nuclear neutrons were used to naturally explain spin differences in many different nuclides in the same way, and the neutron as a basic structural unit of atomic nuclei was accepted. Later, protons and neutrons were called under a common name, nucleon. The force that keeps the nucleons together in the nucleus is called the strong force. It turned out that apart from nucleons, there were many other strongly interacting particles called baryons, which are fermions with half-integer spin, and

mesons, which are bosons with integer spin. Baryons and mesons together are called hadrons.

History repeatedly proved that scattering of charged particles from nuclei is a strong tool to study the structure of matter. After the development of accelerators, the same approach was used to study the nucleon. In the 1960s high energy electron beams were used at the Stanford Linear Accelerator Center (SLAC) to probe the hadronic structure of proton and deuterium targets. In the experiment, 20 GeV electrons scattered on protons showed evidence for substructure of the proton. Similar experiments at CERN confirmed that the nucleon (proton or neutron) is not an elementary particle but made of so-called partons.

In 1964, the quarks were introduced by M. Gell-Mann and G. Zweig as the constituents of the hadrons. Quarks are fractionally charged fermions with spin 1/2. They come in six flavors, which are described in Table 1, in terms of their electrical charge Q , strangeness quantum number S and isospin (I, I_3) . The non-relativistic Constituent Quark Model (CQM) has been developed to describe the internal structure of the nucleon in terms of the quarks. In the naive approach of the CQM, a nucleon contains three spin 1/2 valence quarks. The proton is formed by two u quarks and one d quark. The neutron, on the other hand, has two d quarks and one u quark. The CQM became very successful in explaining the hadronic states as well as predicting the anomalous magnetic moment of the nucleon. Relativistic quantum mechanics predicts the magnetic moment of a pointlike particle with charge Z , spin S and mass M_N to be $\mu = Z\mu_N 2\mathbf{S}$, where $\mu_N = e/2M_N$ is the nuclear magneton. Experiments, on the other hand, indicate that the nucleon has a magnetic moment $\mu = (Z + \kappa_N)\mu_N 2\mathbf{S}$, where $Z = 1$ for the proton and $Z = 0$ for the neutron. The quantity κ_N is called the anomalous magnetic moment of the nucleon. Experiments measured the anomalous magnetic moment of the proton $\kappa_p = 1.79$ and that of the neutron $\kappa_n = -1.91$. This was a strong indication of the composite structure of the nucleon. The CQM predicts that $\mu_p = 2.85\mu_N$, yielding $\kappa_p = 1.85$, and $\mu_n = -1.90\mu_N$, giving a perfectly good agreement with the measured κ_n .

The CQM can also calculate the ratio of the axial vector coupling constant and the vector coupling constant $g_A/g_V = 5/3$. However, the experiment gives $g_A/g_V = 1.2695 \pm 0.0029$. There is a 25% disagreement between the experimental value and the prediction of the CQM. In this prediction, however, the CQM assumes that the valence quarks inside the nucleon have no orbital angular momenta, being in

the $L = 0$ state. According to relativistic quantum mechanics, non-zero orbital angular momentum contributions will reduce the value of the axial vector coupling and provide a better agreement with the measurements. These considerations led to the development of the relativistic CQM, which, in general, does a better job of explaining the static properties of the nucleon. However, it was obvious that a more rigorous theory was needed. We encourage the reader to look into [1] and [2] for the successes and failures of the CQM.

Later in 1972, Quantum Chromodynamics (QCD) was postulated as a way to explain the interactions between quarks. Today, the CQM is historically considered as a possible bridge between QCD and the experimental data. In the more rigorous approach by QCD, the valence quarks in either nucleon are surrounded by a sea of quark-antiquark pairs of $u\bar{u}$, $d\bar{d}$ and $s\bar{s}$ as well as gluons that act as the force carriers between the quarks. The other quarks listed in Table 1, which are generally referred to as heavy quarks, do not play an important part in the nucleon. In addition to flavor, spin and electrical charge, quarks also possess another quantum number called color charge. The color charge can take different values: red (r), green (g) and blue (b). The antiquarks carry the corresponding anti-colors, namely anti-red, anti-green and anti-blue. All bound states of quarks, hadrons or mesons, are colorless, which means they either carry all three color charges together or possess both color and anti-color. Gluons are electrically neutral particles with spin 1 but they also carry color. Gluons are mixtures of two colors, such as red and antigreen, which constitutes their color charge. According to Quantum Chromodynamics, the gluons are the gauge bosons of the strong interaction. Therefore, the quarks are bound together by the gluons. In addition, gluons can interact with each other since they also carry color charge. In field theories, the strength of the interaction is represented by a dimensionless quantity called the coupling constant. In QED, the fine structure constant α serves as the coupling constant of the electromagnetic interactions. In QCD, on the other hand, the coupling constant strongly depends on the energy scale of the interaction and increases with the distance between the quarks. As a result, the strong force diminishes at small distances so that the quarks are able to move freely within the hadron. This phenomenon is called Asymptotic Freedom. On the other hand, as the distance between the quarks increases, the strong coupling constant gets bigger, confining the quarks inside the hadron. This phenomenon is called Confinement, which is the basic reason why we cannot observe quarks outside

the hadrons. As a result of Asymptotic Freedom (a small coupling constant at small scales), QCD can be solved using perturbative calculations in the domain where the distances probed are small. In this domain, quarks can be observed as almost free particles. As the scale increases, however, the strong interaction increases and all quarks begin to react coherently so that what we observe is the collective response of all quarks and gluons inside the hadron. When the energy of the probe is increased, a quark can be knocked out of the hadron by means of deep inelastic scattering. Part of the energy is converted into quark-antiquark pairs as a result of Confinement and a “jet” of hadrons is formed.

TABLE 1: Known quark flavors (F) with their electrical charge Q , strangeness quantum number S and isospin (I, I_3).

| F | Q | S | I | I_3 |
|-----|--------|------|-------|--------|
| u | $2/3$ | 0 | $1/2$ | $1/2$ |
| d | $-1/3$ | 0 | $1/2$ | $-1/2$ |
| s | $-1/3$ | -1 | 0 | 0 |
| c | $2/3$ | 0 | 0 | 0 |
| t | $2/3$ | 0 | 0 | 0 |
| b | $-1/3$ | 0 | 0 | 0 |

I.1 LEPTON HADRON SCATTERING

According to Quantum Electrodynamics (QED), the electromagnetic force between the electron and the proton is mediated via a virtual photon. In order to observe the internal structure of hadrons, a probe which has a wavelength smaller than the size of the hadron is required. In scattering high energy electrons, the four-momentum transfer to the proton is generally large. This provides a virtual photon with a small enough wavelength to probe the internal structure of the proton. In addition to the energy transfer, there is an additional degree of freedom in this interaction, that is spin.

A typical electron-nucleon interaction $e + N \rightarrow e' + X$ is shown in Fig. 1, where an incoming electron emits a virtual photon which is then absorbed by a nucleon. In inclusive measurements only the scattered lepton is detected, whereas additional final state particles are detected for exclusive measurements.

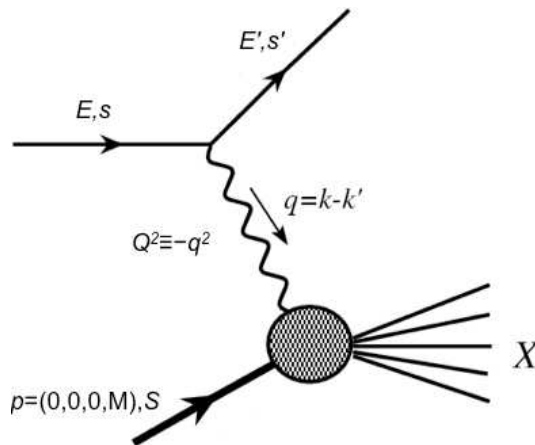


FIG. 1: Electron scattering from a nucleon.

A typical lepton-nucleon scattering can be analyzed in three different regimes according to the energy transferred, ν , during the interaction. If the transferred energy from lepton to nucleon is small during the interaction, the process can be described as an elastic collision. The energy transfer (recoil energy) is uniquely determined by the three-momentum \vec{q} transferred. The wavelength of the exchange particle during the interaction, the virtual photon, provides the resolution of the nucleon's interior but do not cause any internal excitation. In this way, we can resolve the electric and magnetic form factors of the nucleon, which contribute to the differential cross section. The form factors depend on the wavelength of the virtual photon, which is inversely proportional to the four momentum transferred, $Q^2 = \vec{q}^2 - \nu^2$, and this reflects that nucleon is not a point like particle but it has a finite spatial extent¹.

If the transferred energy is increased, the energy of the virtual photon increases and begins to create excitations in the inner state of the nucleon. These excited states of the nucleon (the so-called resonances) have more mass since the changes in the inner structure of the nucleon require energy, which is absorbed from the virtual photon. Therefore, the mass, W , of a resonance can be found by calculating the square of the total four-momentum of the final state after the electron scattering,

$$W^2 = M^2 + 2M\nu - Q^2, \quad (1)$$

where M is the nucleon mass. These resonance states are not stable. Therefore

¹See for example *Particles and Nuclei* by B. Povh and K. Rith

they will break down and decay after a short time. In some experiments, we observe the decay particles and reconstruct their vertex and total mass to learn more about the resonance state that has been formed during the scattering. By plotting the cross section versus the transferred energy or the final state mass W , different resonances can be observed. These resonances will show themselves as preferred final states, in other words as peaks in the spectrum, in the differential cross section versus W distributions. Standard notation for naming resonances is l_{2I2J} , where $l = 0(S), 1(P), 2(D), 3(F)$ is the orbital angular momentum, $I = 1/2$ or $3/2$ is the isospin and $J = |l \pm 1/2|$ is the total angular momentum of the final state. The $P_{33}(1232)$, commonly known as the Δ resonance, the $P_{11}(1440)$, $D_{13}(1520)$, $S_{11}(1535)$ and the $F_{15}(1680)$ are just a few examples.

At high energies, elastic scattering becomes relatively unlikely. Elastic form factors fall rapidly with the total four-momentum transferred, Q^2 , revealing the internal structure of the nucleon. As the transferred energy increases, the resonance states disappear from the cross section distributions versus final-state invariant mass W . The virtual photon interacts with a single parton and breaks the nucleon into different hadronic states. This region is called deep inelastic region (DIS).

Lepton-nucleon scattering experiments yield a lot of information about the internal structure of the nucleon depending on the resolution of the probe, the virtual photon. Apart from obtaining information about the momentum distribution of quarks inside the nucleon, it also reveals information on the spin polarizations of the quarks and their contribution to the overall spin of the nucleon. The virtual photon absorption cross section is sensitive to the quark spin polarization because the spin of the quark must be anti-parallel to the spin of the virtual photon for the quark to absorb the virtual photon and still remain in a spin $1/2$ state. Therefore, by measuring the virtual photon absorption cross sections for different helicities, we can measure the spin contributions of different quark flavors.

When the nucleon is probed at high Q^2 , the wavelength of the virtual photon is small enough to interact with individual quarks. At these energies, quark-quark and quark-gluon interactions can be neglected on the basis of Asymptotic Freedom. Bjorken predicted that the structure functions, which describe the momentum and spin distributions of the nucleon, show a scaling behavior in the region of high momentum transfer. This behavior actually reveals the existence of point like constituents inside the nucleon because scaling is expected when an electron scatters off a point

like particle. The total cross section can be written as a coherent sum of elastic scattering on point-like scattering centers and it becomes independent of Q^2 . As Q^2 decreases, on the other hand, the resolution of the virtual photon also decreases. The virtual photon begins to interact with a collection of quarks and gluon. The structure functions begin to show scaling violations; they begin to vary strongly with respect to Q^2 . Eventually, as $Q^2 \rightarrow 0$, the virtual photon is only sensitive to the static properties of the nucleon.

While the CQM was being developed, Richard Feynman [3] also proposed a parton model in 1969 as a way to analyze high-energy hadron collisions. The parton model was immediately applied to electron-proton deep inelastic scattering by Bjorken and Paschos [4]. Bjorken [5] suggested a scaling behavior in the DIS regime when the scattering cross sections are determined in terms of a dimensionless kinematic quantity such as $x = Q^2/2M\nu$, where ν is the energy of the virtual photon and M is the nucleon mass. The quantity x is often referred to as the Bjorken scaling variable. In this picture, the Deep Inelastic regime, or the Bjorken limit, is defined as:

$$-q^2 = Q^2 \rightarrow \infty \quad ; \quad \nu = E - E' \rightarrow \infty \quad ; \quad x \text{ fixed.} \quad (2)$$

As the four momentum of the virtual photon increases, its wavelength decreases, which implies an improved spatial resolution. Scaling behavior suggests the cross sections to be independent of the transferred energy, hence, the resolution scale. This means that the scattering centers are effectively point-like particles. In the simple parton model, the scattering cross sections scale exactly; in QCD, however, scaling is not exact and their Q^2 evolution can be calculated perturbatively.

After the validation of the quark model and the confirmation of asymptotic freedom in QCD, partons were matched to quarks and gluons, leading to the Quark Parton Model (QPM) description of the nucleon. It has been a successful tool in understanding many hadronic processes explained above. Today, the QPM still remains a justifiable approximation of QCD at high energies. It has been extended over the years and is often used to describe the deep inelastic electron-nucleon scattering as well as many properties of the nucleon such as spin.

On the other hand, the spin structure function of the nucleon turns out to be much more complicated than the QPM predicts. We shall briefly explain how the QPM approaches the spin of the nucleon and eventually see where it fails. In the QPM, the longitudinal spin structure function of the nucleon, g_1 , is related the quark

spin distributions by:

$$g_1(x) = \frac{1}{2} \sum_i e_i^2 (\Delta q_i(x) + \Delta \bar{q}_i(x)) \quad (3)$$

where e_i is the charge of the quark of flavor i and

$$\Delta q(x) = q^+(x) - q^-(x) \quad (4)$$

where $q^\pm(x)$ are the number densities of quarks with their spins parallel or antiparallel to the longitudinal spin of the nucleon. Considering the valence quarks u , d and s that form the nucleon, we can utilize particular groups of $SU(3)$ flavor transformations:

$$\Delta\Sigma = (\Delta u + \Delta\bar{u}) + (\Delta d + \Delta\bar{d}) + (\Delta s + \Delta\bar{s}) \quad (5)$$

$$\Delta q_3 = (\Delta u + \Delta\bar{u}) - (\Delta d + \Delta\bar{d}) \quad (6)$$

$$\Delta q_8 = (\Delta u + \Delta\bar{u}) + (\Delta d + \Delta\bar{d}) - 2(\Delta s + \Delta\bar{s}) \quad (7)$$

and we can rewrite the spin structure function g_1 in terms of these groups:

$$g_1(x) = \frac{1}{9} \left[\frac{3}{4} \Delta q_3 + \frac{1}{4} \Delta q_8 + \Delta\Sigma \right]. \quad (8)$$

Taking the first moment of the structure function yields:

$$\Gamma_1^{1(p)} = \int_0^1 g_1(x) dx = \frac{1}{9} \left[\frac{3}{4} a_3 + \frac{1}{4} a_8 + a_0 \right], \quad (9)$$

where

$$a_0 = \int_0^1 dx \Delta\Sigma(x) = \Delta\Sigma \quad (10)$$

$$a_3 = \int_0^1 dx \Delta q_3(x) \quad (11)$$

$$a_8 = \int_0^1 dx \Delta q_8(x). \quad (12)$$

The values of a_3 and a_8 are already known from neutron and hyperon β -decay measurements:

$$a_3 = g_A = 1.2670 \pm 0.0035 \quad \text{and} \quad a_8 = 0.585 \pm 0.025, \quad (13)$$

where g_A is the axial vector coupling constant. Therefore, one can determine a_0 by measuring the first moment of g_1 . Now, if we go back to the spin of the nucleon, it

can be written as the sum of the quark spins S_q , the gluon spins ΔG and the orbital angular momenta of the sea quarks and the gluons L_z :

$$\frac{1}{2} = S_q + \Delta G + L_z \quad (14)$$

where the quark spin contribution S_q can be written as the sum of individual flavors each carrying momentum fraction x with spin components $\pm\frac{1}{2}$ along the direction of motion of the nucleon:

$$S_q = \int_0^1 dx \sum_i \left[\frac{1}{2} q_i^+(x) - \frac{1}{2} q_i^-(x) + \frac{1}{2} \bar{q}_i^+(x) + \frac{1}{2} \bar{q}_i^-(x) \right] \quad (15)$$

$$= \frac{1}{2} \int_0^1 dx \sum_i (\Delta q_i(x) + \Delta \bar{q}_i(x)) \quad (16)$$

$$= \frac{1}{2} \int_0^1 dx \Delta \Sigma(x) = \frac{1}{2} \Delta \Sigma = \frac{1}{2} a_0. \quad (17)$$

In the simple QPM, ΔG and L_z are expected to vanish, therefore $\Delta \Sigma = a_0$ alone should be responsible for the total spin of the nucleon and be equal to 1. Relativistic corrections require some of the spin of the nucleon to be carried by the orbital angular momentum of the quarks since the quarks should have relativistic speeds in the confined space of the nucleon because of Heisenberg's uncertainty principle. As a result 60% of the nucleon spin should be carried by the spins of the quarks. In this approach, strange sea quark and gluon contributions are still not taken into account. Therefore the model fails to explain the spin content correctly. Indeed, that is exactly the outcome of the EMC experiment at CERN [6]. According to the experimental results of the EMC $\Delta \Sigma = a_0 = 0.12 \pm 0.17$ was reported, which means only a very small fraction of the proton's spin is carried by its constituent quarks. Moreover, by using Eqs. (10 - 12), we can evaluate that:

$$a_0 = \Delta \Sigma = a_8 + 3(\Delta s + \Delta \bar{s}) \quad (18)$$

If one could ignore the contribution from the strange quarks as Ellis and Jaffe suggested in 1974, a_0 should be close to $a_8 = 0.585$. The result of the EMC experiment contradicts this prediction of the QPM. This failure of the QPM is often referred to as the *spin crisis*.

As briefly mentioned, in the DIS region, the interaction cross section displays a phenomena called scaling, scattering centers are pointlike and free particles. If scaling is correct, the measured quantities should be independent of Q^2 , which determines the resolution of the probe, a virtual photon. The predictions of the QPM

do not depend on the resolution of the probe in the DIS region and hence it exhibits scaling. However, there are many experimental observations on scaling violations as the resolution of the scattering probe is increased. Therefore, the QPM also fails to explain these scaling violations: the Q^2 dependence of the measured quantities such as cross sections and structure functions of the nucleon. The spin structure function g_1 of the nucleon given in Eq. (3) also exhibits scaling violation, hence, it becomes also a function of Q^2 as well as the momentum fraction x .

Later, it was realized that the situation can be explained in the framework of QCD, in which the structure of the nucleon becomes much more complicated than the QPM anticipated. The scaling violations are actually predicted by perturbative QCD (pQCD). What appears to be quarks at a particular resolution turns out to be a collection of quarks, antiquarks and gluons at a higher resolution. Therefore pQCD can describe the change of the apparent distributions when the nucleon is probed at a different resolution. In the QCD framework, the ultra-violet divergences are taken care of by renormalization. Other divergences, which are called collinear divergences, arise because of small quark masses and are attended by using a scheme called factorization [7]. In this scheme, the interaction of virtual photons with a nucleon is broken up into long (soft) and short (hard) distance interactions. The point at which this separation is made is called factorization scale μ^2 . The long distance interactions cannot be calculated analytically. They can only be parametrized and studied experimentally. Therefore, the infinite terms can be absorbed into the long distance part of the interaction. As an example to explain this procedure, we can use a common term that arises in QCD calculations for parton densities such as $\alpha_s \ln \frac{Q^2}{m_q^2}$ where m_q represents the quark mass. Such a term can be split into two parts,

$$\alpha_s \ln \frac{Q^2}{m_q^2} = \alpha_s \ln \frac{Q^2}{\mu^2} + \alpha_s \ln \frac{\mu^2}{m_q^2}, \quad (19)$$

and the first term of the right hand side is absorbed into the short distance part of the equation while the second term is included in the long distance part. Here, the factorization scale μ^2 is an arbitrary number and physical results cannot depend on it. However, only a finite number of terms enters into the perturbative calculation; therefore our solution depends on the scale we choose. As a result, the solution should carry the factorization scale μ^2 as a label. It is generally agreed that an optimal choice for this scale is $\mu^2 = Q^2$, so the parton densities become also a function of Q^2 as well as the momentum fraction x : $q(x) \rightarrow q(x, Q^2)$, which means Bjorken scaling

is broken. Therefore, QCD is able to handle the scaling violations observed in the unpolarized and polarized structure functions. The QPM turns out to be a zero order approximation to pQCD. The parton densities $q(x)$ and $\Delta q(x)$ become just the zeroth order members of QCD calculations. However, the momentum distributions of quarks, antiquarks and gluons cannot be fully calculated from first principles of QCD and they have to be measured experimentally.

The predictions of QCD and the progress in theoretical work triggered many experimental efforts. The spin structure functions became the center of interest. Especially the longitudinal spin structure function of the nucleon g_1 and its moments are strong tests and complements of the QCD calculations. The Bjorken sum rule, which is explained in section II.4.4, is considered to be an important test for QCD in the DIS region at high Q^2 . At the opposite end of the kinematic region, the Gerasimov-Drell-Hearn (GDH) sum rule, which is explained in section II.4.5, plays an important role to understand the non-perturbative QCD region. The GDH sum rule is valid at the real photon point ($Q^2 = 0$) and connects spin observables to the static properties of the nucleon. Additional theoretical work, for example by Ji and Osborn (see section II.4.5), provided an extension of the GDH sum rule into the resonance and DIS regions. This work unified the two fundamental sum rules: The Bjorken sum rule in the DIS regime and the GDH sum rule at the real photon point. The connection between the two kinematic end points provides a theoretical tool to explore the transition region between the perturbative and non-perturbative QCD regimes. This is very important to understand the structure of the nucleon. However, this goal requires precise measurement of the spin observables in a large kinematic region.

The EG1b experiment, carried out at Jefferson Lab, measured the virtual photon asymmetry A_1 and the longitudinal spin structure function g_1 of the proton and the deuteron in an unprecedented kinematical range. As well as exploring the resonance contributions to A_1 and g_1 , the data will enable us to test different theoretical and phenomenological calculations of the Q^2 evolution of Γ_1 for both targets. Experimental verification of chiral perturbation theory and future Lattice QCD calculations, which are valid in the intermediate Q^2 regions, will also be possible by using the EG1b results. In addition, higher twist effects, which reveal information on quark-gluon interactions, can be explored and the validity of the quark-hadron duality in the spin sector can be tested by using this data. In this thesis, we present the results

on the deuteron. In addition, the deuteron, apart from being intrinsically interesting, can also be used as an effective source of information for the neutron spin structure functions when combined with proton measurements. Therefore, the methodology to extract the neutron spin structure function is also explained and preliminary results are presented in this thesis.

Chapter II introduces the theoretical background and explains the formalism of the nucleon spin structure functions. Chapter III describes the experimental apparatus. Chapter IV covers the data analysis and chapter V presents the final results. Chapter VI explains the parameterizations of the physics quantities and concluding remarks are presented in chapter VII.

CHAPTER II

THEORETICAL BACKGROUND

In this chapter, the nucleon structure functions will be introduced as an effective description of deep-inelastic scattering (DIS) between an electron and a nucleon or a nuclear target. The cross sections for such interactions will be evaluated. These cross sections can be expressed in terms of the structure functions and thus will give us a better understanding of the internal structure of the nucleon. Later, the interpretation of the structure functions in the QPM will be provided and it will be compared to the QCD interpretation, which explains the kinematical evolutions of the structure functions in a more rigorous way. Later, the moments of the spin dependent structure functions will be introduced and the resulting sum rules that play an important role for the test of QCD and many theoretical frameworks will be analyzed. Finally, the methods that can be used to obtain the neutron spin structure functions from the combined proton and deuteron spin structure functions will be explained together with required corrections.

II.1 THE STRUCTURE FUNCTIONS

The structure functions naturally rise from the formulation of deep-inelastic scattering (DIS) between a lepton and a nucleon in QED. In this section, the cross section for DIS will be calculated and expressed in terms of the structure functions. Emphasis will be given to the case of longitudinal polarization where the incoming electron and the target nucleon are both polarized parallel or anti-parallel to the direction of the electron beam. The cross section differences for certain polarization states during the interaction lead to experimentally observable asymmetries. These asymmetries can be used to isolate certain spin dependent and independent structure functions. The connection between the experimental asymmetries and the actual physical processes that take place during the polarized lepton-nucleon scattering will be established by introducing virtual photon asymmetries, that are evaluated from photo-absorption cross sections and give direct insight for the internal structure of the nucleon. This will give us a deeper understanding of the structure functions in terms of the virtual photon asymmetries.

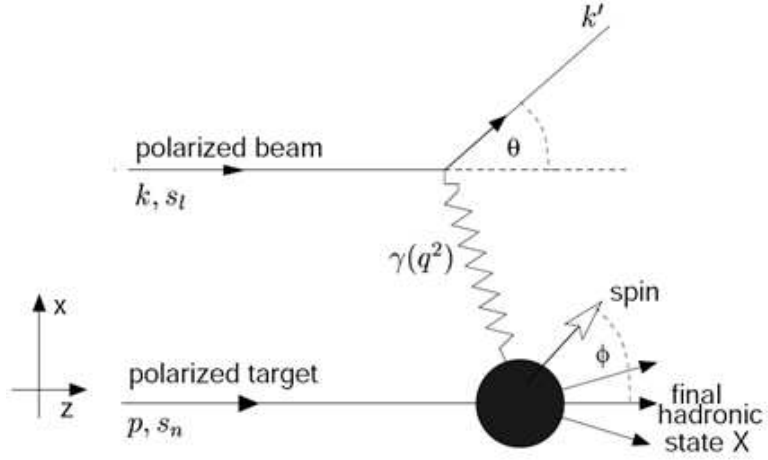


FIG. 2: Polarized electron-nucleon scattering.

II.1.1 Polarized Inclusive Deep-Inelastic Scattering

The electromagnetic interaction of an electron with a nucleon takes place by an exchange of a virtual photon. Fig. 2 shows polarized electron-nucleon scattering with one photon exchange. In this thesis, we will consider the inclusive case, in which only the scattered electron is observed experimentally. All kinematic variables are defined in the lab frame, where $k = (E, k_x, k_y, k_z)$ and $k' = (E', k'_x, k'_y, k'_z)$ are the four-momenta of the incoming and scattered electrons respectively, $p = (M, 0, 0, 0)$ is the four-momentum of the target nucleon and $q = (\nu, q_x, q_y, q_z)$ is the four-momentum of the virtual photon so that $q = k - k'$. M represents the target nucleon mass while s_l is the spin of the incident electron and s_n is the spin of the nucleon. The final spin states are not observed and therefore summed over.

A list of common variables often used for the description of an electron-nucleon scattering event is given in the following equations. It should be noted that the beam axis is defined in the \hat{z} -direction and the polar scattering angle is labeled as θ while the azimuthal angle is represented by ϕ .

$$Q^2 = -q^2 = 4EE' \sin^2 \frac{\theta}{2} = 2EE'(1 - \cos \theta) \quad (20)$$

$$\nu = E - E' = \frac{p \cdot q}{M} \quad (21)$$

$$W = \sqrt{(p + q)^2} = \sqrt{M^2 + 2M\nu - Q^2} \quad (22)$$

$$x = \frac{Q^2}{2p \cdot q} = \frac{Q^2}{2M\nu} \quad (23)$$

$$y = \frac{p \cdot (k - k')}{p \cdot k} = \frac{E - E'}{E} = \frac{\nu}{E} \quad (24)$$

$$\gamma = \frac{2Mx}{\sqrt{Q^2}} = \frac{\sqrt{Q^2}}{\nu} \quad (25)$$

$$\tau = \frac{\nu^2}{Q^2} = \frac{1}{\gamma^2} \quad (26)$$

$$\epsilon = (1 + 2(1 + \tau) \tan^2(\theta/2))^{-1} \quad (27)$$

$$\eta = \frac{\epsilon \sqrt{Q^2}}{E - \epsilon E'} \quad (28)$$

$$D = \frac{1 - \epsilon \frac{E'}{E}}{1 + \epsilon R} \quad (29)$$

where Q^2 is the squared four-momentum and ν is the energy of the virtual photon, W is the mass of final hadronic state, x is the Bjorken scaling variable and ϵ is the relative flux of the two polarization states of the virtual photon (ratio of longitudinal polarization to the transverse polarization). D is the depolarization factor that represents how much of the incoming lepton's polarization is transferred to the virtual photon. R is the ratio of longitudinal to transverse virtual photo absorbtion. More information is given on these factors in section II.1.3.

Assuming one photon exchange, the differential cross section for detecting the scattered electron in the solid angle $d\Omega$ and energy range $(E', E' + dE')$ is given by:

$$\frac{d^2\sigma}{d\Omega dE'} = \frac{\alpha^2}{2Mq^4} \frac{E'}{E} L_{\mu\nu} W^{\mu\nu} \quad (30)$$

where α is the fine structure constant, $L_{\mu\nu}$ is the leptonic tensor and $W^{\mu\nu}$ is the hadronic tensor. The leptonic tensor, which describes the emission of the virtual photon by the electron, can be calculated from QED. It is written in terms of Dirac spinors (u) and the gamma matrix (γ^μ) as:

$$L_{\mu\nu}(k, s_l; k') = \sum_{s'_l} \left[\bar{u}(k', s'_l) \gamma_\mu u(k, s_l) \right] * \left[\bar{u}(k', s'_l) \gamma_\nu u(k, s_l) \right] \quad (31)$$

where we summed over the final spin states s'_l of the electron. It has symmetric (S) and anti-symmetric (A) parts under μ, ν interchange:

$$L_{\mu\nu}(k, s_l; k') = 2L_{\mu\nu}^{(S)}(k; k') + 2iL_{\mu\nu}^{(A)}(k, s_l; k') \quad (32)$$

where

$$L_{\mu\nu}^{(S)}(k; k') = k_\mu k'_\nu + k'_\mu k_\nu - g_{\mu\nu}(k \cdot k' - m^2) \quad (33)$$

and

$$L_{\mu\nu}^{(A)}(k, s_l; k') = \epsilon_{\mu\nu\alpha\beta} s_l^\alpha (k - k')^\beta \quad (34)$$

where m is the electron mass, $\epsilon_{\mu\nu\alpha\beta}$ is the Levi-Civita antisymmetric tensor and $g_{\mu\nu} = \text{diag}(1, -1, -1, -1)$ is the metric tensor.

The hadronic tensor describes the interaction between the virtual photon and the nucleon. Since we don't know the internal structure of the nucleon, it is not possible to calculate it analytically. For the nucleon with spin 1/2, the hadronic tensor can be written in terms of symmetric and anti-symmetric parts just like the leptonic tensor.

$$W_{\mu\nu}^{(A)}(k, s_l; k') = W_{\mu\nu}^{(S)}(q; p) + iW_{\mu\nu}^{(A)}(q; p, s_n) \quad (35)$$

with

$$\begin{aligned} W_{\mu\nu}^{(S)}(q; p) &= \left[\frac{q_\mu q_\nu}{q^2} - g_{\mu\nu} \right] 2F_1(x, Q^2) \\ &+ \left[p_\mu - \frac{p \cdot q}{q^2} q_\mu \right] \left[p_\nu - \frac{p \cdot q}{q^2} q_\nu \right] \frac{2}{M\nu} F_2(x, Q^2) \end{aligned} \quad (36)$$

and

$$W_{\mu\nu}^{(A)}(q; p, s_n) = \epsilon_{\mu\nu\alpha\beta} q_\alpha \frac{2M}{p \cdot q} \left[s_n^\beta g_1(x, Q^2) + \left(s_n^\beta - \frac{s_n \cdot q}{p \cdot q} p^\beta \right) g_2(x, Q^2) \right] \quad (37)$$

The coefficients F_1 and F_2 are unpolarized structure functions and g_1 and g_2 are polarized structure functions. The differential cross section in Eq. (30) can be written in the following form separating the symmetric and antisymmetric parts

$$\frac{d^2\sigma}{d\Omega dE'} = \frac{\alpha^2}{2MQ^4} \frac{E'}{E} \left[L_{\mu\nu}^{(S)} W^{\mu\nu(S)} - L_{\mu\nu}^{(A)} W^{\mu\nu(A)} \right] \quad (38)$$

When we consider the spin averaged cross section (summing over all possible spin orientations where electron and nucleon spins are either parallel or anti-parallel), only the symmetric part of the hadronic tensor, $W^{\mu\nu(S)}$ contribute yielding:

$$\frac{d^2\sigma^{\uparrow\uparrow}}{d\Omega dE'} + \frac{d^2\sigma^{\uparrow\downarrow}}{d\Omega dE'} = \frac{4\alpha^2 E'^2}{Q^4} \cos^2\left(\frac{\theta}{2}\right) \left[\frac{2}{M} \tan^2\left(\frac{\theta}{2}\right) F_1(x, Q^2) + \frac{1}{\nu} F_2(x, Q^2) \right] \quad (39)$$

The first and the second arrows indicate the electron and the nucleon spin orientations respectively. If we consider the difference between the cross sections with the two

possible spin orientations of the longitudinally polarized electron and the nucleon being parallel or anti-parallel, then only the anti-symmetric part of the hadronic tensor, $W^{\mu\nu(A)}$ contribute:

$$\frac{d^2\sigma^{\uparrow\uparrow}}{d\Omega dE'} - \frac{d^2\sigma^{\uparrow\downarrow}}{d\Omega dE'} = \frac{4\alpha^2 E'}{Q^2} \frac{1}{E} \frac{1}{M\nu} \left[(E + E' \cos \theta) g_1(x, Q^2) - 2Mx g_2(x, Q^2) \right] \quad (40)$$

Since we have the structure functions as a function of (x, Q^2) , it is desirable to express the differential cross sections also in terms of these variables. By using $d\Omega = 2\pi \sin \theta d\theta$ where we assumed azimuthal symmetry, which is usually the case in the inclusive scattering experiments, and the kinematical relations

$$Q^2 = 2EE'(1 - \cos \theta) = 4EE' \sin^2 \frac{\theta}{2}, \quad (41)$$

$$\nu = E - E' = Q^2/2Mx, \quad (42)$$

the conversion factor between the two different sets of the kinematical variables can be obtained,

$$\frac{d^2\sigma}{d\Omega dE'} = \frac{\pi}{EE'} \frac{\nu}{x} \frac{d^2\sigma}{dQ^2 dx} \quad (43)$$

and the differential cross section equations can be written in a more convenient way in terms of x and Q^2 ,

$$\sigma = \frac{4\pi\alpha^2}{Q^4 x} \left[\frac{Q^4}{4M^2 E^2 x} F_1(x, Q^2) + \left(1 - \frac{Q^2}{2MEx} - \frac{Q^2}{4E^2} \right) F_2(x, Q^2) \right], \quad (44)$$

$$\Delta\sigma_{\parallel} = \frac{4\pi\alpha^2}{Q^2 x} \frac{1}{ME} \left[\left(2 - \frac{Q^2}{2MEx} - \frac{Q^2}{2E^2} \right) g_1(x, Q^2) - \frac{2Mx}{E} g_2(x, Q^2) \right] \quad (45)$$

where we used notations:

$$2\sigma = \frac{d^2\sigma^{\uparrow\uparrow}}{dQ^2 dx} + \frac{d^2\sigma^{\uparrow\downarrow}}{dQ^2 dx}, \quad (46)$$

$$\Delta\sigma_{\parallel} = \frac{d^2\sigma^{\uparrow\uparrow}}{dQ^2 dx} - \frac{d^2\sigma^{\uparrow\downarrow}}{dQ^2 dx}. \quad (47)$$

These cross section differences are useful for isolating specific structure functions or their combinations. Since they are experimentally accessible quantities, the above relations form the basis of most experiments trying to measure the unpolarized and polarized structure functions of the nucleon. In the following sections, we will define experimental asymmetries in terms of these cross section differences and establish their connections to a deeper understanding of physical processes that take place during the lepton-nucleon scattering events.

The limit $Q^2 \rightarrow \infty$ and $\nu \rightarrow \infty$, where x is fixed, determines the Bjorken regime. In this region, the structure functions $F_{1,2}$ and $g_{1,2}$ are observed to approximately scale, i.e., they almost become independent of Q^2 . This behavior of the structure functions in the DIS region actually reveal the existence of point like constituents inside the nucleon because scaling is expected when electrons scatter off point like particles. As explained in chapter 1, the simple QPM predicts exact scaling for these functions. On the other hand, as the wavelength of the exchanged virtual photon increases, hence, the resolution of the probe decreases, the structure functions begin to show scaling violations and begin to vary strongly with respect to Q^2 . These scaling violations are handled in pQCD. However, QCD cannot predict any value for the structure functions, which makes them basic subjects of experimental measurements and models.

II.1.2 Photo-Absorption Cross Sections

As explained in the previous section, the interaction of the the electron with the nucleon can be viewed as a two step process described separately by leptonic and hadronic tensors. Eventually, the contraction of these tensors yields the differential cross sections which can be defined in terms of the polarized and unpolarized structure functions. When we concentrate on the photon-nucleon vertex of this interaction, the process can be viewed as forward Compton scattering of a virtual photon off a nucleon. The optical theorem states that the total cross section of an incident plane wave (the rate at which flux is removed from the incident plane wave by the processes of scattering and absorption) is proportional to the imaginary part of the forward scattering amplitude.

$$\sigma_{tot} = \frac{4\pi}{K} \text{Im}[\mathcal{M}(\theta = 0)] \quad (48)$$

where θ is the scattering angle and $1/K$ is a factor associated with the incoming photon flux. For a real photon beam ($Q^2 \rightarrow 0$), the flux is inversely proportional to the energy of the photon (represented by ν , given in Eq. (21)), therefore the flux factor is $1/\nu$. If we consider the invariant mass of the final state (given in Eq. (22)) and apply it for real photon case where $Q^2 = 0$ and $K = \nu$ we get:

$$W^2 = M^2 + 2M\nu = M^2 + 2MK \quad (49)$$

For a virtual photon ($Q^2 > 0$), flux is somewhat arbitrary. By using the so-called Hand convention, Eq. (49), evaluated for a real photon, could also be used for a

virtual photon, which yields for K [8]

$$K = \frac{W^2 - M^2}{2M} = \nu - \frac{Q^2}{2M} \quad (50)$$

\mathcal{M} in Eq. (48) represents the forward Compton scattering amplitude, which depends on the helicity states of the virtual photon and the nucleon before and after the scattering process. The scattering amplitudes for different helicity combinations of the virtual photon and the nucleon can be referred as helicity amplitudes. The forward scattering amplitude can be decomposed into different forward helicity amplitudes. We can write these helicity amplitudes with defining indices for corresponding helicity states as $\mathcal{M}_{i,j;i',j'}$, where i, j are the spin projections of the incident photon and nucleon and i', j' are that of the scattered photon and nucleon respectively. The nucleon, being a spin 1/2 particle, has two possible helicity states, $m = 1/2, -1/2$. The virtual photon, being a spin 1 particle and which may attain mass unlike a real photon, can have 3 possible polarization states, namely $m = 1, 0, -1$. If the virtual photon is polarized in the $m = \pm 1$ states, it is called transversely (or circularly) polarized. If it is polarized in the $m = 0$ state, it is called longitudinally (or linearly) polarized. As a result, there are 10 possible helicity combinations for the scattering amplitude. By employing the parity conservation $\mathcal{M}_{i,j;i',j'} = \mathcal{M}_{-i,-j;-i',-j'}$ and invariance of time reversal $\mathcal{M}_{i,j;i',j'} = \mathcal{M}_{i',j';i,j}$, these 10 combinations can be reduced to 4 independent forward helicity amplitudes: $\mathcal{M}_{1,-\frac{1}{2};1,-\frac{1}{2}}$, $\mathcal{M}_{1,\frac{1}{2};1,\frac{1}{2}}$, $\mathcal{M}_{0,\frac{1}{2};0,\frac{1}{2}}$, $\mathcal{M}_{0,\frac{1}{2};0,-\frac{1}{2}}$. These helicity amplitudes can be computed in terms of the hadronic tensor $W_{\mu\nu}$.

$$\mathcal{M}_{i,j;i',j'} = \epsilon_i^{\mu\dagger} \epsilon_{i'}^\nu W_{\mu\nu} \quad (51)$$

where ϵ^μ is the polarization vector of the virtual photon, which can either be transverse or longitudinal [9]. Indeed, the parameter introduced in Eq. (27) corresponds to the relative strength of these two polarization states and solely depends on the kinematics of the scattered lepton (that emitted the virtual photon being discussed). At this point, we can formulate the virtual photon-nucleon interaction by using the optical theorem and calculate the total photo-absorption cross sections for different helicity states in terms of the forward helicity amplitudes, which are indeed expressible in terms of the polarized and unpolarized structure functions introduced earlier.

As a result, the four independent virtual photon-nucleon cross sections can be expressed as [9][10]:

$$\sigma_{\frac{1}{2}}^T = \frac{4\pi\alpha}{K} \mathcal{M}_{1, \frac{1}{2}; 1, \frac{1}{2}} = \frac{4\pi^2\alpha}{KM} (F_1 + g_1 - \gamma^2 g_2) \quad (52)$$

$$\sigma_{\frac{3}{2}}^T = \frac{4\pi\alpha}{K} \mathcal{M}_{1, -\frac{1}{2}; 1, -\frac{1}{2}} = \frac{4\pi^2\alpha}{KM} (F_1 - g_1 + \gamma^2 g_2) \quad (53)$$

$$\sigma_{\frac{1}{2}}^L = \frac{4\pi\alpha}{K} \mathcal{M}_{0, \frac{1}{2}; 0, \frac{1}{2}} = \frac{4\pi^2\alpha}{KM} \left(-F_1 + \frac{1 + \gamma^2}{2x} F_2 \right) \quad (54)$$

$$\sigma_{\frac{1}{2}}^{TL} = \frac{4\pi\alpha}{K} \mathcal{M}_{0, \frac{1}{2}; 0, -\frac{1}{2}} = \frac{4\pi^2\alpha}{KM} \gamma (g_1 + g_2) \quad (55)$$

The cross sections, σ_J^P , are labeled by the total initial helicity of the virtual photon-nucleon system, J and the polarization of the virtual photon, P . The polarization states include transverse (T) and longitudinal (L) polarizations as well as the interference term (TL).

It is clear that certain combinations of the photo-absorption cross sections given above lead to specific structure functions or their combinations. We can define total absorption cross sections for transverse and longitudinal virtual photon polarization as

$$\sigma^T = \frac{1}{2} \left(\sigma_{\frac{1}{2}}^T + \sigma_{\frac{3}{2}}^T \right) \quad (56)$$

and

$$\sigma^L = \sigma_{\frac{1}{2}}^L \quad (57)$$

The unpolarized structure functions can be written in terms of these cross sections,

$$F_1 = \frac{KM}{8\pi^2\alpha} \sigma^T \quad (58)$$

$$F_2 = \frac{KM}{8\pi^2\alpha} \frac{x}{1 + \gamma^2} (\sigma^L + \sigma^T) \quad (59)$$

The ratio of the two cross sections give rise to the unpolarized structure function R , that was used earlier in Eq. (29),

$$R = \frac{\sigma^L}{\sigma^T} = (1 + \gamma^2) \frac{F_2}{2xF_1} - 1 \quad (60)$$

Also, the spin structure function g_1 can be calculated from these cross sections:

$$g_1 = \frac{MK}{8\pi^2\alpha(1 + \gamma^2)} (\sigma_{1/2}^T - \sigma_{3/2}^T + 2\gamma\sigma_{1/2}^{TL}) \quad (61)$$

II.1.3 Asymmetries

Now we can define the virtual photon asymmetries A_1 and A_2 in terms of the virtual photon absorption cross sections given above

$$A_1(x, Q^2) = \frac{\sigma_{\frac{1}{2}}^T - \sigma_{\frac{3}{2}}^T}{\sigma_{\frac{1}{2}}^T + \sigma_{\frac{3}{2}}^T} = \frac{g_1(x, Q^2) - \gamma^2 g_2(x, Q^2)}{F_1(x, Q^2)} \quad (62)$$

$$A_2(x, Q^2) = \frac{2\sigma_{\frac{1}{2}}^{TL}}{\sigma_{\frac{1}{2}}^T + \sigma_{\frac{3}{2}}^T} = \frac{\gamma[g_1(x, Q^2) + g_2(x, Q^2)]}{F_1(x, Q^2)} \quad (63)$$

By using these equations, we can express the spin dependent structure functions in terms of the virtual photon asymmetries:

$$g_1(x, Q^2) = \frac{F_1(x, Q^2)}{1 + \gamma^2} (A_1 + \gamma A_2) \quad (64)$$

$$g_2(x, Q^2) = \frac{F_1(x, Q^2)}{1 + \gamma^2} \left(-A_1 + \frac{A_2}{\gamma} \right) \quad (65)$$

The asymmetries A_1 and A_2 have straight forward physical meanings but they are not experimentally accessible quantities except that A_1 can be measured with real photons in principle. Therefore, we define an experimental asymmetry A_{\parallel} by using the differential lepton-nucleon cross sections defined in the Eqs. (44) and (45).

$$A_{\parallel}(x, Q^2) = \frac{\Delta\sigma_{\parallel}}{2\sigma} \quad (66)$$

Working in terms of asymmetries instead of cross sections allows us to disregard the geometric acceptance of the detector since the acceptance from the numerator and the denominator cancels out. By substituting the Eqs. (64) and (65) for g_1 and g_2 into (66), A_{\parallel} can be expressed in terms of A_1 and A_2

$$A_{\parallel} = D(A_1 + \eta A_2) \quad (67)$$

where ϵ , η and D are defined in Eqs. (27), (28) and (29), respectively. In polarized deep inelastic scattering experiments with longitudinally polarized leptons and nucleons, the spins of the incoming lepton and the nucleon are aligned in the direction of the lepton's propagation axis. When the virtual photon is emitted, its propagation axis can be different than the propagation axis of the incoming lepton. The spin of the virtual photon is either parallel or perpendicular to its own propagation axis.

Therefore, the polarization of the lepton is not fully transferred to the virtual photon. The depolarization factor takes this loss into account.

We can analyze the the expressions for A_1 and A_2 a little bit to estimate their boundaries. The photo-absorption cross sections $\sigma_{1/2}^T$ and $\sigma_{3/2}^T$ are always positive, therefore, the absolute value of the ratio defining A_1 is bound to be less than or equal to 1. For elastic scattering $A_1 = 1$. The cross section term σ^{TL} is an interference term between σ^L and σ^T , therefore we can deduce an orthogonality relation

$$|\sigma^{TL}| \leq \sqrt{\sigma^L \sigma^T} \quad (68)$$

which yields

$$|A_2| = \left| \frac{\sigma^{TL}}{\sigma^T} \right| \leq \sqrt{\frac{\sigma^L}{\sigma^T}} = \sqrt{R} \quad (69)$$

In elastic scattering, $\sigma^{TL} \propto \tau G_E G_M$ and $\sigma^T \propto \tau G_M^2$, where $\tau = 1/\gamma$ and G_E and G_M are electric and magnetic form factors of the nucleon [1], so that $A_2 = \gamma G_E / G_M = \sqrt{R}$. There is even a more specific boundary requirement, that is often used, on A_2 , which states that

$$|A_2| \leq \sqrt{R(1 + A_1)/2} \quad (70)$$

This requirement is called Soffer limit [11]. It follows directly from Eqs. (62) and (63), together with the fact the $|\sigma^{TL}| \leq \sqrt{\sigma^L \sigma_{1/2}^T}$ and $R = \sigma^L / (\sigma_{1/2}^T + \sigma_{3/2}^T)$.

Let's focus on the virtual photon asymmetry A_1 and the spin structure function g_1 . A_1 can be evaluated as:

$$A_1 = \frac{A_{\parallel}}{D} - \eta A_2 \quad (71)$$

and by putting this into Eq. (64), g_1 can be evaluated as:

$$g_1 = \frac{F_1}{1 + \gamma^2} \left[\frac{A_{\parallel}}{D} + (\gamma - \eta) A_2 \right] \quad (72)$$

The kinematical factors η and γ in front of A_2 are typically small in high energy experiments. In the Bjorken limit, where x is fixed, they both go to 0. According to the kinematical range of the experiment, one can measure A_1 and g_1 by either assuming the second term on the right hand side of the Eqs. (71) and (72) is negligibly small and can be treated as a systematic error or using measured results or models of A_2 in the corresponding kinematics. In any case, we need to know the structure functions F_1 and R , which have been measured by several experiments [12][13].

II.1.4 Extension to Spin 1 Target

In this thesis, our analysis is focused on the deuteron target, which is a spin 1 nuclear object. So far, our derivations for the relationships between the photo-absorption cross sections and the structure functions assumed a spin 1/2 nucleon target. In case of the deuteron, there are three different helicity states, $m = \pm 1$, when the third component of the deuteron's spin is aligned or anti-aligned in the direction (z) of the incoming lepton, and $m = 0$, when the spin component along z is zero. As a result, the number of independent helicity amplitudes, hence the photo-absorption cross sections become 8 instead of 4. This requires four additional structure functions, usually referred to as b_{1-4} ; for a complete definition of the process see [14][15]. These additional structure functions are called tensor structure functions and all arise because of the binding effects between the proton and the neutron that form the deuteron. When we approximate the deuteron as a combination of a proton and a neutron in a relative S-state, hence, with no interaction between them, the helicity amplitudes for the deuteron can be expressed as a sum of the individual helicity amplitudes from the proton and the neutron such that

$$\mathcal{M}_{1,0;1,0} = \frac{1}{2}(\mathcal{M}_{1,\frac{1}{2};1,\frac{1}{2}} + \mathcal{M}_{1,-\frac{1}{2};1,-\frac{1}{2}}) \quad (73)$$

and therefore the additional independent helicity amplitudes vanish, leaving us with the same definitions for the asymmetries and structure functions for the spin 1 deuteron as we obtained for a spin 1/2 nucleon target.

In case we need to take the nuclear binding effects and D-state of the deuteron into account, we need to consider the additional structure functions. In the DIS limit, however, the the kinematical factors in front of b_{2-4} structure function become essentially zero, therefore their effects can be neglected, but b_1 can make a small contribution. The structure function b_1 describes the difference in the cross sections between the helicity-0 and the averaged non-zero helicity contributions. In case of the deuteron, we can define two types of polarizations: a vector polarization $P_z = (n^+ - n^-)/(n^+ + n^- + n^0)$ and a tensor polarization $P_{zz} = (n^+ + n^- - 2n^0)/(n^+ + n^- + n^0)$. Here n^+, n^-, n^0 are the atomic populations with positive, negative and zero spin projections on the beam direction, respectively. For a spin 1/2 target the vector polarization is defined as $P_z = (n^+ - n^-)/(n^+ + n^-)$ while tensor polarization vanishes. Existence of the tensor polarization for spin 1 target leads to the structure function b_1 .

It should be pointed out that the probability of finding the deuteron in a D-state is already small, on the order of 5%, which makes the the structure function b_1 a small quantity in general. Indeed, the results of HERMES [15] experiment on the measurement of the b_1 structure function of the deuteron confirms that. Especially in the kinematic range of the EG1b experiment it is consistent with zero. Moreover, in the EG1b experiment, the tensor polarization is small, on the order of 10%, making the contribution of the b_1 structure function even smaller. In addition to these, since we take the difference of the cross sections, the tensor polarization, hence, the b_1 contribution cancels out in the numerator of the expression (40), only contributing to the denominator. As a result, the contribution of the b_1 structure function is three-fold small in the EG1b experiment, therefore, we can safely neglect its effect on the other structure functions measured in the experiment. This leaves us with the same definitions for the structure functions of the deuteron that we previously obtained for the nucleon.

II.2 INTERPRETATION IN THE QUARK-PARTON MODEL

The Quark-Parton Model (QPM) [8][16] describes the nucleon as a composition of partons, pointlike objects, which are later identified as elementary quarks. The structure we observe by probing the nucleon with a virtual photon depends on the resolution of the probe, that is the four-momentum transferred Q^2 . This is also called virtuality of the photon since $Q^2 \rightarrow 0$ for real photons. The partonic structure is observed if the virtuality of the photon is high. In a so-called infinite momentum frame, where the the energy and the four-momentum of the virtual photon are large, the virtual photon scatters off the pontlike partons, i.e., elementary quarks. This provides us with the structure of the nucleon described in the Bjorken limit and the Bjorken variable x becomes the fraction of the nuclear momentum carried by the struck quark. The scattering cross section of the nucleon can then be computed from the incoherent sum over the quark contributions. In the Bjorken limit, quarks are essentially non-interacting free particles because the strong coupling constant goes to 0 as $Q^2 \rightarrow \infty$, which leads to asymptotic freedom. Fig. 3 shows a simple image of the scattering process in the QPM.

In this regime, the unpolarized structure functions can be evaluated by using the impulse approximation [17], where the nucleon matrix element in the hadronic tensor $W_{\mu\nu}$ can be replaced by a sum of quark matrix elements weighted by their

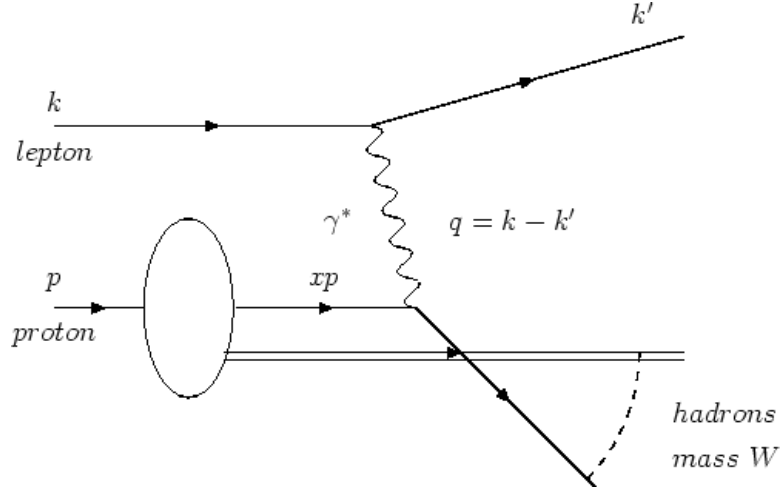


FIG. 3: Electron-nucleon scattering in QPM.

distribution functions. The result for the unpolarized structure functions yields

$$F_1(x) = \frac{1}{2} \sum_i e_i^2 [q_i(x) + \bar{q}_i(x)] \quad (74)$$

and

$$F_2(x) = 2xF_1 \quad (75)$$

where e_i is the charge of the quark i and $q_i(x)$ is the probability density for the quark i to carry a fraction x of the nucleon's momentum. $\bar{q}_i(x)$ corresponds to the probability density for the anti-quark i . Therefore, $F_1(x)$ at a given x can be interpreted as the sum of the distribution of quark (and anti-quark) flavors carrying a momentum fraction x of the nucleon, weighted by their squared charges. F_2 , integrated over all x , indicates the total four-momentum fraction carried by all the quarks (and anti-quarks), weighted by squares of their charges. It can be understood as a spatial current density of the nucleon. Similarly, the polarized structure functions in the QPM can be written as:

$$g_1(x) = \frac{1}{2} \sum_i e_i^2 [\Delta q_i(x) + \Delta \bar{q}_i(x)] \quad (76)$$

$$g_2(x) = 0 \quad (77)$$

with

$$\Delta q(x) = q^+(x) - q^-(x) \quad (78)$$

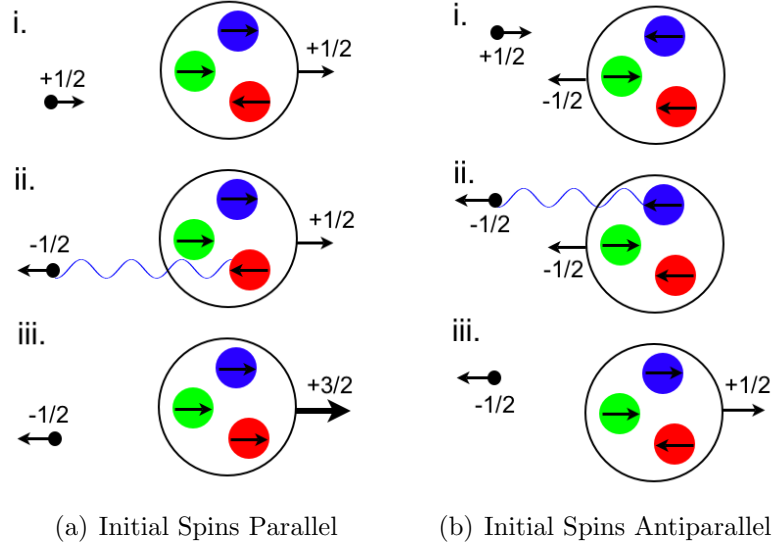


FIG. 4: Interpretation of the spin-transitions in the scaling region for a longitudinally polarized electron scattering off a longitudinally polarized nucleon. Valence quarks with their spin directions are shown inside the nucleon. (i) Incoming electron and target nucleon are shown. (ii) The electron emits a virtual photon and flips its spin. The virtual photon can only interact with the quarks that carries an opposite spin with respect to the photon. (iii) The quark flips its spin and the resulting final state has either spin $3/2$ or $1/2$ depending on the initial spin configurations.

where $q^\pm(x)$ are the number densities of quarks with their spin parallel or antiparallel to the longitudinal spin of the nucleon. When we put these expressions for the structure functions into Eqs. (52) and (53), we find that $\sigma_{1/2}^T \sim \sum(q^+ + \bar{q}^+)$ and $\sigma_{3/2}^T \sim \sum(q^- + \bar{q}^-)$. The virtual photon absorption cross sections are, therefore, sensitive to the quark spin polarizations because the quark with spin $1/2$ can only absorb the virtual photon if its spin is anti-parallel to the spin of the photon. Therefore, in the QPM, which actually holds in the Bjorken limit, one can get the spin contributions of different quark flavors to the overall spin of the nucleon by measuring the virtual photon absorption cross sections for different nucleon helicities. Therefore, A_1 defined as $(\sigma_{1/2}^T - \sigma_{3/2}^T)/2\sigma^T$ can be interpreted as the asymmetry in quark distributions with their spins aligned and anti-aligned with that of the nucleon (see Fig. 4).

Another implication of the QPM is that the structure function R goes to zero in the Bjorken limit. In this frame, the transverse components of the quark momenta can be neglected because the nucleon momentum is large. In this limit, longitudinally

polarized quarks can only absorb transversely polarized virtual photons, so that σ^L in Eq. (54) becomes essentially 0 making $R = 0$. The same argument leads to the conclusion that the virtual photon asymmetry A_2 is also 0 in this regime. Then we can approximate $g_1 \approx A_1 F_1$. Therefore, the structure function g_1 can be interpreted as the distribution of quarks inside the nucleon multiplied by their spin asymmetries with respect to the absorbed virtual photon. So, it reveals the polarization distribution of the quarks inside the nucleon.

Finally, the most important implication of this picture is that the polarized and unpolarized structure functions are independent of Q^2 . This is called scaling invariance, which was initially observed in SLAC experiments performed in the DIS region, but ruled out by later experiments performed over larger Q^2 ranges. This shows that in the kinematic regions where the four-momentum transfer is finite, the simple partonic interpretation is not valid anymore. The scaling violations can be explained by perturbative QCD (pQCD). What appears to be quarks at a particular resolution turns out to be a collection of quarks, antiquarks and gluons at a different resolution.

II.3 Q^2 EVOLUTION OF THE STRUCTURE FUNCTIONS

There are various different calculation methods to express the Q^2 dependence of the structure functions. At high Q^2 regions, perturbative QCD (pQCD) gives a rigorous approach by adding higher order correction terms to the parton distribution functions defined in the simple QPM. The zeroth order approximation of pQCD is equivalent to the QPM definitions. However, pQCD expansions require small coupling constant, therefore, the expansions break down in the region where $Q^2 < 1 \text{ GeV}^2$. There are also resonance contributions that begin to strongly affect the structure functions in the intermediate Q^2 regions (Q^2 a few GeV^2) and cannot be incorporated into the pQCD methods. Therefore pQCD is only efficient for the DIS region where Q^2 is large and $W > 2 \text{ GeV}$. In the medium Q^2 regions, a method called Operator Product Expansion is generally used to express the Q^2 dependence of the structure functions. At even lower Q^2 regions lattice QCD and effective theories like Chiral Perturbation Theories come into play.

As we mentioned in the previous section, probing the nucleon with photons at different energies results in different pictures of the nucleon. At low Q^2 what appears to be a valence quark with momentum fraction x begins to look like combination

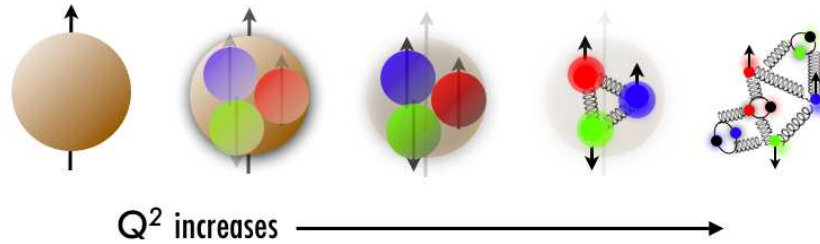


FIG. 5: Dependence of the resolution of nucleon's internal structure on Q^2 due to a finer resolution of the nucleon's internal structure with increasing Q^2 .

of quarks, antiquarks and gluons at higher Q^2 . Or, we can say, each quark itself is surrounded by a cloud of partons and as we increase our resolution, we begin to see inside the cloud. Therefore, the probability distribution functions that describe the probability of finding a quark with flavor i and momentum fraction x , varies with Q^2 . We can make a simple analogy to explain this behavior by considering appearance of an image on a computer screen. If the pixel size of the screen is smaller or at least equal to the pixel size of the image, we see the net image. If the pixel size of the image is smaller than that of the screen, which means screen resolution is not high enough, the image begins to appear blurry because a few pixel in the image are blended together. As the resolution of the screen decreases, which corresponds to the Q^2 in our definition, more and more pixels of the image will be combined on the screen. By zooming out the image, eventually the whole image can be fit into a single pixel on the screen. Then, only the average color of whole image will be visible to us. Of course, the dynamic properties of the nucleon makes this analogy too simple to describe the whole situation.

In the range of $Q^2 \ll 1 \text{ GeV}^2$, the resolved distance is compatible with the nucleon size. As Q^2 increases, the internal quark-gluon and gluon-gluon substructures begin to effect the scattering cross section. These interactions reduce the observed momentum of the valence quarks because the nucleon's momentum is distributed between many partons (number of resolved partons that share the nucleon's momentum increases with Q^2). Therefore, the valence quark probability distribution functions (PDF), $q_i(x)$, decrease with increasing Q^2 in the high x region while they increase with increasing Q^2 in the low x region. As a result, the probability distribution functions, thus, the structure functions become functions of both x and Q^2 .

II.3.1 QCD corrections to the probability distribution functions

QCD is able to give a rigorous approach to explain the Q^2 dependencies of the structure functions. The evolution of the probability distribution functions with respect to Q^2 is formalized by Dokshitzer-Gribov-Lipatov-Altarelli-Parisi (DGLAP) equations [18][19]. A pedagogical introduction to the derivation of these equations can be found in [8]. The main mechanisms that can change the momentum distribution of the quarks and gluons are categorized in three basic interactions: Quarks can lose momentum by radiating gluons, gluons can generate quark-antiquark pairs and gluons can decompose into gluon-gluon pairs. The amplitude for these processes are given in terms of so-called splitting functions $P_{ij}(x/y)$, which describes the probability to find a parton i carrying a momentum fraction y to split into two partons, one of which (j), that later interacts with the virtual photon, carries a momentum fraction x . The partons can either be quarks or gluons and there are no flavor dependencies. There are 4 splitting functions, two of which, P_{qq} and P_{qG} , contribute only to the evolution of the quark distribution functions $q_i(x, Q^2)$ and the other two, P_{Gq} and P_{GG} , contribute only to the gluon distribution function $G(x, Q^2)$.

The Q^2 evolution of the distribution function for a quark or a gluon with momentum fraction x can be written as a sum of the distribution functions of possible parent partons with momentum fraction y weighted by corresponding probabilities of the processes required for the creation of the quark or gluon at hand. Finally this sum is integrated over the full range of momentum fraction y ($> x$). The integration covers the whole range of possible momentum fractions for the parent partons above x (For a parent parton with momentum fraction y to be able to create a quark with momentum fraction x , $y \geq x$ should be satisfied). The resulting equations show a logarithmic dependence on Q^2 . The final DGLAG evolution equations for spin averaged quark and gluon distributions are written as:

$$\frac{dq_i(x, Q^2)}{d \ln Q^2} = \frac{\alpha_s}{2\pi} \int_x^1 \frac{dy}{y} \left[q_i(y, Q^2) P_{qq} \left(\frac{x}{y} \right) + G(y, Q^2) P_{qG} \left(\frac{x}{y} \right) \right] \quad (79)$$

$$\frac{dG(x, Q^2)}{d \ln Q^2} = \frac{\alpha_s}{2\pi} \int_x^1 \frac{dy}{y} \left[\sum_i q_i(y, Q^2) P_{Gq} \left(\frac{x}{y} \right) + G(y, Q^2) P_{GG} \left(\frac{x}{y} \right) \right] \quad (80)$$

Therefore, Eq. (79) mathematically expresses the fact that the quark with momentum fraction x , the one that interacts with the virtual photon, $[q_i(x, Q^2)]$ on the

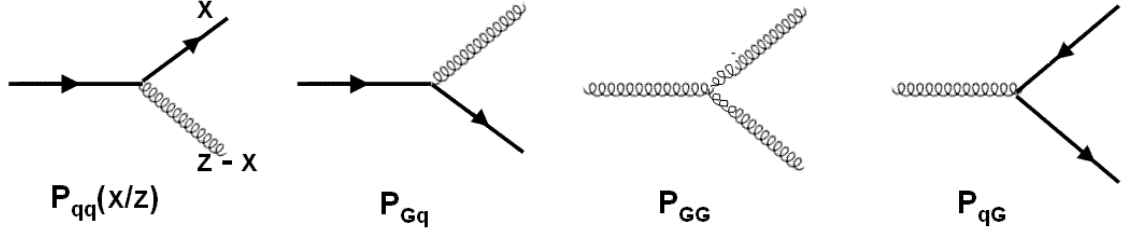


FIG. 6: The processes related to the lowest order QCD splitting functions. Each splitting function $P_{ij}(x/z)$ gives the probability that a parton of type i converts into a parton of type j , carrying a fraction x/z of the momentum of parton i .

left hand side] could have come from a parent quark $q_i(y, Q^2)$, which has radiated a gluon or could also have come from a parent gluon $G(y, Q^2)$ that created a quark-antiquark pair. The probabilities for each of these processes are described by the splitting kernels $P_{ij}(x/y)$.

Similarly, the spin dependent case can be written [20],

$$\frac{d\Delta q_i(x, Q^2)}{d \ln Q^2} = \frac{\alpha_s}{2\pi} \int_x^1 \frac{dy}{y} \left[\Delta q_i(y, Q^2) \Delta P_{qq} \left(\frac{x}{y} \right) + \Delta G(y, Q^2) \Delta P_{qG} \left(\frac{x}{y} \right) \right] \quad (81)$$

$$\frac{d\Delta G(x, Q^2)}{d \ln Q^2} = \frac{\alpha_s}{2\pi} \int_x^1 \frac{dy}{y} \left[\sum_i \Delta q_i(y, Q^2) \Delta P_{Gq} \left(\frac{x}{y} \right) + \Delta G(y, Q^2) \Delta P_{GG} \left(\frac{x}{y} \right) \right] \quad (82)$$

with

$$\Delta G(x) = \Delta G^+(x) - \Delta G^-(x) \quad (83)$$

where $G^\pm(x)$ are the number densities of gluons with their spin parallel or antiparallel to the longitudinal spin of the nucleon. Also, $\Delta P_{ij} \equiv P_{i+j+} - P_{i+j-}$ where $+$ and $-$ representing the corresponding parton helicities. Parity conservation requires $P_{i-j\pm} = P_{i+j\mp}$. It is customary to separate the polarized quark distribution function in Eq. (81) for singlet $\Delta\Sigma$ and non-singlet q^{NS} quark distributions since they evolve independently from each other. The second term in Eq. (81) does not contribute to evolution of q^{NS} .

P_{ij} Functions

The splitting functions used in Eqs. (81-82) also depend on the strong coupling constant $\alpha_s(Q^2)$. In pQCD, the polarized splitting function $\Delta P_{ij}(x)$ can be expanded in a power series of $\alpha_s(Q^2)$,

$$\Delta P_{ij}(x, \alpha_s) = \Delta P_{ij}^{(0)}(x) + \frac{\alpha_s(Q^2)}{2\pi} \Delta P_{ij}^{(1)}(x) + \dots \quad (84)$$

where the subscripts (0) and (1) refer to leading order (LO) and next to leading order (NLO) contributions. The splitting function that appear in Eqs. (81-82) correspond to the LO term. The crucial point is that the strong coupling constant $\alpha_s(Q^2)$ enters as a coefficient for each term, therefore, this procedure works only in the kinematic regions where the strong coupling constant is small enough for perturbative expansion, i.e. in the regime where pQCD is applicable.

Q^2 evolution of the probability distribution functions imply that the structure functions defined in Eqs. (74-76) now become functions of Q^2 as well. In the next section we will focus on the structure function g_1 and explain its dependence on Q^2 .

II.3.2 Q^2 dependence of $g_1(x, Q^2)$ in the DIS region

In perturbative QCD the Q^2 dependence of the g_1 structure function is given by [19]:

$$g_1(x, Q^2) = \frac{1}{2} \sum_i^{n_f} e_i^2 [C_q(x, \alpha_s) \otimes \Delta q(x, Q^2) + C_G(x, \alpha_s) \otimes \Delta G(x, Q^2)] \quad (85)$$

where sum over all quark flavors n_f is taken. The convolution \otimes is defined as

$$C_q(x, \alpha_s) \otimes \Delta q(x, Q^2) = \int_x^1 \frac{dy}{y} C_q\left(\frac{x}{y}, \alpha_s\right) q(y, Q^2) \quad (86)$$

The coefficients $C_q(x, \alpha_s)$ and $C_G(x, \alpha_s)$ are called Wilson coefficients and correspond to photon-quark and photon-gluon hard scattering cross sections respectively. The Wilson coefficients can be expanded perturbatively in powers of α_s ,

$$C_i(x, \alpha_s) = C_i^{(0)}(x) + \frac{\alpha_s(Q^2)}{2\pi} C_i^{(1)}(x) + \dots \quad (87)$$

The LO terms are given as $C_q(x) = \delta(1-x)$ and $C_q G(x) = 0$, therefore, we can write the g_1 structure function up to the NLO term as

$$\begin{aligned}
g_1(x, Q^2) &= \frac{1}{2} \sum_i^{n_f} e_i^2 [\Delta q(x, Q^2) + \Delta \bar{q}(x, Q^2)] \\
&+ \frac{1}{2} \sum_i^{n_f} e_i^2 \frac{\alpha_s(Q^2)}{2\pi} \int_x^1 \frac{dy}{y} C_q \left(\frac{x}{y} \right) [\Delta q(y, Q^2) + \Delta \bar{q}(y, Q^2)] \\
&+ \frac{1}{2} \sum_i^{n_f} e_i^2 \frac{\alpha_s(Q^2)}{2\pi} \int_x^1 \frac{dy}{y} C_G \left(\frac{x}{y} \right) \Delta G(y, Q^2)
\end{aligned} \tag{88}$$

The spin dependent probability distribution functions $\Delta q(x, Q^2)$ and $\Delta G(x, Q^2)$ can be calculated by using DGLAP equations given in the previous section. Calculation of the Wilson coefficients and the probability distribution functions beyond leading order (LO) depends on the renormalization scheme used. For information on the different schemes commonly used, the reader is referred to [7].

II.3.3 The operator product expansion and moments of $g_1(x, Q^2)$

In order to understand the quark confinement in QCD, one needs to understand the dynamics of quark-gluon interactions at large distances. This requires the study of structure functions at intermediate and low Q^2 values. This is a transition region between the DIS and the resonance regions. In these kinematics, pQCD corrections break down while contributions from the resonance states of the nucleon and multi-parton correlations, known as higher twists, come into play. The Operator Product Expansion (OPE) [21][22][23] method is used in this regime to express the structure functions in terms of short distance effects that are calculable by pQCD, and long distance effects that can only be measured experimentally.

The OPE analysis of the spin structure function g_1 expresses the n^{th} moment of g_1 as a power series expansion of the nucleon matrix elements M_τ^n by using the Wilson coefficients $E_\tau^n(Q^2/\mu^2, \alpha_s)$ as expansion parameters:

$$\Gamma_1^n(Q^2) = \int_0^1 dx x^{n-1} g_1(x, Q^2) = \sum_{\tau=2,4,\dots}^{\infty} M_\tau^n(\mu^2) E_\tau^n \left(\frac{Q^2}{\mu^2}, \alpha_s \right) \tag{89}$$

for $n = 1, 3, 5, \dots$ and μ is the factorization scale. The explanations that follow are made by considering the first moment, $n = 1$. The sum in (89) is ordered according to the twist $\tau = (\text{dimension} - \text{spin})$ of the current operators, beginning with the

lowest twist $\tau = 2$. The lowest twist corresponds to the largest contribution to the expansion. Each additional unit of τ produces a factor of order Λ_{QCD}/Q , which makes their contribution less important at high Q^2 region.

The Wilson coefficients E_τ^n are calculable by pQCD. The nucleon matrix elements $M_\tau^n(\mu^2)$ are local operators which describe the quark-gluon structure of the nucleon. The term $\tau = 2$ (twist-2) in Eq. (89) is known as the leading twist and can be decomposed into flavor triplet ($a_3 \equiv g_A$), octet (a_8) and singlet ($a_0 \equiv \Delta\Sigma$) axial charges [24][25]:

$$\mu_2^{p,n}(Q^2) = C_{NS}(Q^2) \left[\pm \frac{1}{12} g_A + \frac{1}{36} a_8 \right] + C_S(Q^2) \frac{1}{9} \Delta\Sigma \quad (90)$$

where C_{NS} and C_S are the non-singlet and singlet Wilson coefficients. The flavor triplet axial charge can be obtained from neutron β -decay, $g_A = 1.2670 \pm 0.0035$ while the octet axial charge is determined from hyperon decay, $a_8 = 0.579 \pm 0.025$. The singlet axial charge, $\Delta\Sigma$, is defined in the Bjorken limit ($Q^2 \rightarrow \infty$) as,

$$\Delta\Sigma = \sum_{i=1}^{n_f} [\Delta q_i(x, Q^2) + \Delta \bar{q}_i(x, Q^2)] \quad (91)$$

and contains information about the contribution of quarks to the total spin of the nucleon or nuclei. More information is given on the axial charges in section II.4.2. The other terms ($\tau > 2$) in Eq. (89) are known as the higher twist corrections.

Higher twist corrections to the first moment of $g_1(x, Q^2)$

According to OPE, Γ_1^1 , the first moment of g_1 , can be expressed in powers of $1/Q^2$:

$$\Gamma_1^1(Q^2) \equiv \int_0^1 dx g_1(x, Q^2) = \sum_{\tau=2,4,\dots} \frac{\mu_\tau(Q^2)}{Q^{\tau-2}} = \mu_2(Q^2) + \frac{\mu_4(Q^2)}{Q^2} + \frac{\mu_6(Q^2)}{Q^4} + \dots \quad (92)$$

where μ_τ contains specific nucleon matrix elements. The lowest order term, known as twist-2, is a direct measure of the single parton behavior while the higher order terms come from quark-quark and quark-gluon correlations. The higher twist contribution to the first moment of g_1 is obtained by subtracting the leading twist term from the total:

$$\Delta\Gamma_1^1(Q^2) \equiv \Gamma_1^1(Q^2) - \mu_2(Q^2) = \frac{\mu_4(Q^2)}{Q^2} + \frac{\mu_6(Q^2)}{Q^4} + O\left(\frac{1}{Q^6}\right) \quad (93)$$

We can write the coefficient of the $1/Q^2$ term as:

$$\mu_4(Q^2) = \frac{M^2}{9} [a_2(\ln Q^2) + 4d_2(\ln Q^2) + 4f_2(\ln Q^2)] \quad (94)$$

where a_2 is a twist-2 operator (also called kinematical higher twist), entering here due to target mass correction [27], which can be calculated as [1]:

$$a_2 = 2 \int_0^1 dx x^2 g_1(x, Q^2) \quad (95)$$

The coefficient d_2 , which is a twist-3 operator, can be calculated by:

$$d_2 = 3 \int_0^1 dx x^2 [g_2(x, Q^2) - g_2^{WW}(x, Q^2)] \quad (96)$$

where

$$g_2^{WW}(x, Q^2) = -g_1(x, Q^2) + \int_x^1 \frac{dy}{y} g_1(y, Q^2) \quad (97)$$

is the Wandzura-Wilczek form of the spin structure function g_2 . Therefore, d_2 shows the deviation of g_2 from the Wandzura-Wilczek form.

The coefficient f_2 is a twist-4 operator. It cannot be measured directly but it can be extracted from data as a fit parameter. The analysis performed on the neutron in [24] can be studied as an example for f_2 extraction. Data from all available experiments were analyzed to determine the total higher twist effects, $\Delta\Gamma_1^n$, on the first moment of g_1^n for the neutron. Fig. 7 shows $\Delta\Gamma_1^n$ versus $1/Q^2$ for various experiments. Known values for g_A , a_8 together with $\Delta\Sigma = 0.35$ are used to calculate μ_2^n according to Eq. (90). Also, the values for $a_2^n = -0.0031 \pm 0.0020$ and $d_2^n = 0.0079 \pm 0.0048$, evaluated from world data at $Q^2 = 5 \text{ GeV}^2$, are used in the analysis. A two parameter fit, using f_2^n and μ_6^n as parameters, in the range of $Q^2 > 0.5 \text{ GeV}^2$, and a one parameter fit, using only f_2^n as parameter, in the range of $Q^2 > 1 \text{ GeV}^2$, were performed on the data. Any possible Q^2 dependence of μ_6^n is neglected. The solid curve shows the result of the two parameter fit while the dashed curve shows the result of the one parameter fit. The values of f_2^n and μ_6^n determined from this fit are:

$$f_2^n = 0.034 \pm 0.043 \quad \mu_6^n = M^4(-0.019 \pm 0.017) \quad (98)$$

where M is the nucleon mass. By using this value of f_2^n , it is obtained that $\mu_4^n = M^2(0.019 \pm 0.024)$. Combining this with μ_6^n obtained from the fit, $\Delta\Gamma_1^n$ becomes exactly 0 at $Q^2 = 1 \text{ GeV}^2$.

The twist-3 and twist-4 operators, d_2 and f_2 , are thought to be related to the color electric χ_E and color magnetic χ_B polarizabilities of the nucleon:

$$\chi_E = \frac{2}{3}(2d_2 + f_2) \quad (99)$$

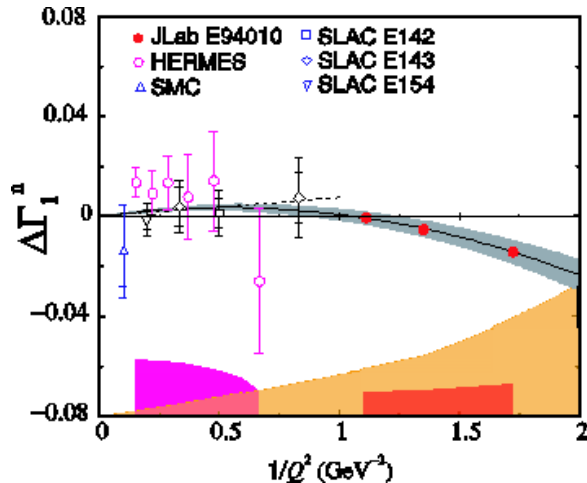


FIG. 7: Higher Twist contributions to the first moment of g_1 for the neutron [24]. Total higher twist effects, $\Delta\Gamma_1^n$, calculated from various experiments and plotted versus $1/Q^2$. Two parameter χ^2 minimization fit to the $\Delta\Gamma_1^n$ used to extract f_2 . More information is given in the text.

$$\chi_B = \frac{1}{3}(4d_2 - f_2) \quad (100)$$

Different models for the nucleon give different values for these color polarizabilities, which makes the determination of higher twist contributions to the first moment of g_1 important to distinguish between those nucleon models. Two groups performed higher twist analysis on the neutron [24] and the proton [25][26] g_1 structure functions and calculated the color magnetic and color electric polarizabilities from higher twist contributions and found consistent values within statistical and systematic errors. Both results seem to favor the MIT bag model [27]. Unfortunately, the lack of available data, especially on the neutron, makes this analysis more difficult at low and intermediate Q^2 regions where the higher twist effects become relatively important. Hopefully the data from EG1b experiment will contribute to the solution of this problem. Moreover, the current world data show that higher twist contributions to the first moment of g_1 are almost zero for $Q^2 = 1 \text{ GeV}^2$, which is a strong indication of quark-hadron duality in this kinematic region. We will cover this topic in the following sections.

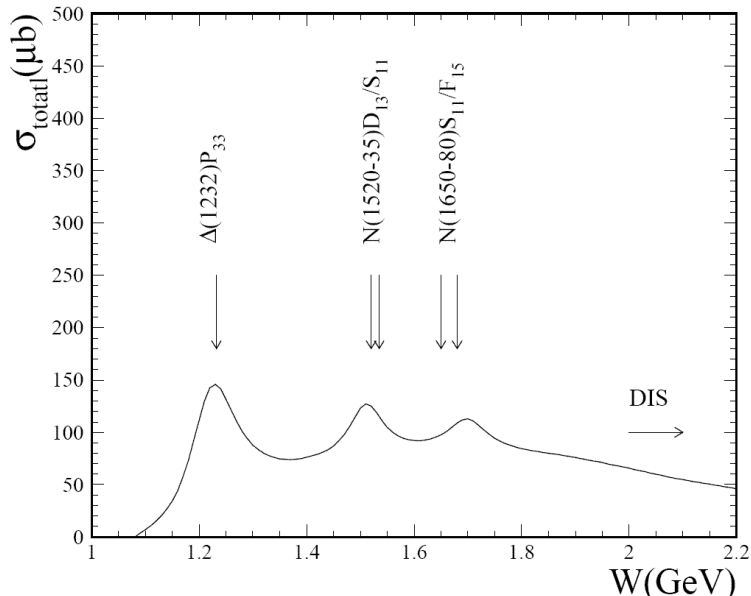


FIG. 8: Resonance states appearing in the total cross section of inclusive reaction $ep \rightarrow e'X$ at $Q^2 = 1.4 \text{ GeV}^2$.

II.3.4 Nucleon resonance region

Nucleon resonances are excited states of the nucleon. They have short life-time and decay mainly by emitting mesons. The kinematic region $W < 2 \text{ GeV}$ and $Q^2 < 10 \text{ GeV}^2$ is known as resonance region because the inclusive cross section shows clear resonance structure in this region. Standard notation for identifying resonances is l_{2I2J} , where $l = 0(S), 1(P), 2(D), 3(F)$ is the orbital angular momentum, $I = 1/2$ or $3/2$ is the isospin and $J = |l \pm 1/2|$ is the total angular momentum of the final baryonic state NM , where N is nucleon and M stands for a pseudo-scalar meson. Some of the well known resonances are P_{33} , commonly referred as the $\Delta(1232)$ resonance, D_{13} , S_{11} and F_{15} .

There are ongoing theoretical efforts to quantify the contribution of the resonances to the kinematic evolution of the structure functions [28][29]. The EG1b experiment covers the resonance region well, therefore, it provides important experimental results for the test of these theoretical models. The nucleon resonances are described in terms of virtual photon helicity amplitudes. The formalism is actually the same as introduced in section II.1.2. The virtual photon can be polarized in either transverse or longitudinal directions. The polarization four-vectors for these two states are

written respectively as:

$$\epsilon_{\pm}^{\mu} = \frac{1}{\sqrt{2}}(0, \pm 1, -i, 0) \quad (101)$$

$$\epsilon_0^{\mu} = \frac{1}{Q}(|q|, 0, 0, \nu) \quad (102)$$

The corresponding components for the electromagnetic current $J_{\mu\nu}$ are

$$J_{\pm} = \epsilon_{\pm}^{\mu} J_{\mu\nu} = \pm \frac{1}{\sqrt{2}}(J_x + iJ_y) \quad (103)$$

$$J_0 = \epsilon_0^{\mu} J_{\mu\nu} = \frac{Q}{\nu} J_z \quad (104)$$

Conventionally, three transition amplitudes, connecting a nucleon $N_{\frac{1}{2}, m_s}$ with a spin projection m_s , with any nucleon resonance N_{j, m_j}^* with spin j and projection m_j , are written as follows [30]:

$$A_{\frac{1}{2}} = \frac{e}{2M} \sqrt{\frac{M}{W^2 - M^2}} \langle N_{j, +\frac{1}{2}}^* | J_+ | N_{\frac{1}{2}, -\frac{1}{2}} \rangle \quad (105)$$

$$A_{\frac{3}{2}} = \frac{e}{2M} \sqrt{\frac{M}{W^2 - M^2}} \langle N_{j, +\frac{3}{2}}^* | J_+ | N_{\frac{1}{2}, +\frac{1}{2}} \rangle \quad (106)$$

$$S_{\frac{1}{2}} = \frac{e}{2M} \sqrt{\frac{M}{W^2 - M^2}} \langle N_{j, \frac{1}{2}}^* | J_0 | N_{\frac{1}{2}, \frac{1}{2}} \rangle \quad (107)$$

The transition amplitudes $A_{1/2}$ and $A_{3/2}$ correspond to transversely polarized photons leading to final state helicities 1/2 and 3/2 respectively while $S_{1/2}$ corresponds to longitudinally polarized photons. The transverse and longitudinal virtual photon cross sections can be written in terms of these amplitudes,

$$\sigma_{1/2}^T(\nu_R, Q^2) = \frac{4M}{\Gamma_R M_R} (|A_{\frac{1}{2}}|^2) \quad (108)$$

$$\sigma_{3/2}^T(\nu_R, Q^2) = \frac{4M}{\Gamma_R M_R} (|A_{\frac{3}{2}}|^2) \quad (109)$$

$$\sigma_{1/2}^L(\nu_R, Q^2) = \frac{2M}{\Gamma_R M_R} (|S_{\frac{1}{2}}|^2) \quad (110)$$

while the interference term is

$$\sigma^{TL}(\nu_R, Q^2) = \frac{2M}{\Gamma_R M_R} (|A_{\frac{1}{2}}|^2 + |S_{\frac{1}{2}}|^2) \quad (111)$$

where M_R is the invariant mass of the resonance state, Γ_R is the decay width and $\nu_R = (M_R^2 - M^2 + Q^2)/2M$.

The total transverse cross section, $\sigma^T = (\sigma_{1/2}^T + \sigma_{3/2}^T)/2$, and the interference cross section, σ^{TL} , can be written in terms of the structure functions:

$$\sigma_{1/2}^T(\nu_R, Q^2) = \frac{4\pi^2\alpha}{MK} \left(F_1 + g_1 - \frac{2Mx}{\nu} g_2 \right) \quad (112)$$

$$\sigma_{3/2}^T(\nu_R, Q^2) = \frac{4\pi^2\alpha}{MK} \left(F_1 - g_1 + \frac{2Mx}{\nu} g_2 \right) \quad (113)$$

$$\sigma^{TL}(\nu_R, Q^2) = \frac{4\pi^2\alpha Q}{MK \nu} (g_1 + g_2). \quad (114)$$

The transition amplitudes in Eqs. (105–107) are related to photon asymmetry A_1 ,

$$A_1 = \frac{|A_{1/2}|^2 - |A_{3/2}|^2}{|A_{1/2}|^2 + |A_{3/2}|^2} \quad (115)$$

When we consider the $\Delta(1232)$ resonance (with spin-3/2), calculation of the transition amplitudes in terms of multipoles (see Ref. [30]) reveals that $A_{3/2} \approx \sqrt{3}A_{1/2}$ at small Q^2 . Therefore, $A_1 \approx -0.5$ is expected for the electromagnetic excitation of the $\Delta(1232)$ resonance. At large Q^2 , on the other hand, $A_{3/2}$ amplitude tends to vanish and $A_{1/2}$ transition dominates, hence, A_1 approaches to +1. In case of the $D_{13}(1520)$ resonance, $A_{1/2}$ amplitude becomes zero at $Q^2 = 0$ [30], which yields $A_1 = -1$ at the real photon point. At large Q^2 , however, $A_{1/2}$ is expected to dominate over $A_{3/2}$ as $Q^2 \rightarrow \infty$, yielding $A_1 = +1$. In addition, electromagnetic excitation of spin-1/2 resonances, such as $S_{11}(1535)$, will have an asymmetry $A_1 = 1$ since the amplitude $A_{3/2}$ cannot contribute. By studying the Q^2 variation of the photon asymmetries for different mass ranges, one can understand the relative strength of the transition amplitudes contributing to different resonance states.

Electron-nucleon scattering in the DIS and resonance regions follow two seemingly different mechanisms. In the DIS region, electrons scatter from quarks in relative isolation (asymptotically free) and the cross section is given by the incoherent sum over the individual quark contributions. Interpretations utilize quark-gluon degrees of freedom in these kinematics. In the resonance region, on the other hand, the entire nucleon responds to the probe coherently, and the interaction is best described by utilizing hadronic degrees of freedom. An intriguing observation, first made by Elliot Bloom and Fred Gilman [31], is that there is a similarity between the data from the two different kinematic regions. In fact, the structure functions measured in the resonance region are found to be approximately equivalent to the deep inelastic structure functions if a proper scaling variable that connects the two kinematic regions is used. This phenomena is known as quark-hadron duality, which will be described next.

II.3.5 Quark-hadron duality

Quark hadron duality explores the connection between the hadronic and partonic descriptions of the nucleon. It states that the smooth scaling curve seen at high momentum transfer should be an accurate average of resonance bumps seen at low momentum transfer for the same values of Bjorken x variable. If duality holds after averaging over all kinematical regions (a concept known as global duality), single quark interactions should successfully describe lepton-nucleon interactions even for low energy and small Q^2 values. Then, perturbative calculations by QCD should approximately yield the average of hadronic observables over a large kinematical region. Moreover, the same concept can also be tested for a limited kinematic range within the resonance region to understand the contribution of different resonance states to the global duality. Duality limited to certain resonances is known as local duality. The data from EG1b for 4.2 and 2.4 GeV will clarify the situation for resonance states around the P_{33} region, where preliminary results show a breakdown of local duality. A more detailed study of duality for polarized structure functions at low and intermediate Q^2 regions is definitely required to understand the spin of the nucleon in terms of quarks and gluons. It is arguable that manifestation of the strong force might be hidden under the aspects of duality because it creates a relationship between single quark interactions, which govern the short distance dynamics, and resonance electro-production, where the long distance dynamics of the nucleon become important. A detailed review about the current standing of duality can be found in [7][32][33].

For kinematic regions where $Q^2 \gg M^2$, the Bjorken x variable can be interpreted as the momentum fraction carried by the struck quark. But at low Q^2 regions, a kinematic correction that arises due to the non-zero target mass is needed. Introduction of the Nachtmann scaling variable $\xi = 2x/(1 + \sqrt{1 + 4M^2x^2/Q^2})$ partly takes care of the target mass effects. Explicit target mass corrections have also been derived under the QCD framework [34].

There are experimental confirmations for duality in the structure function F_2 of the proton [35]. It has been shown that duality holds for the unpolarized structure functions integrated over the entire resonance region (global duality) for $Q^2 > 1.5 \text{ GeV}^2$. A more careful investigation for the intermediate and low Q^2 regions is important in the sense that breakdown of duality might be observed.

Duality also needs to be studied for the polarized structure functions, which are

given by the differences of cross sections, rather than the sum, therefore, they are not positive-definite like the unpolarized structure functions. This brings up a question if duality still holds for the asymmetries or is it only good for the cross sections? Recent results [36][37] confirmed that global duality for the g_1 structure function is indicated by the data for Q^2 values larger than 1.7 GeV^2 for the proton and 2 GeV^2 for the deuteron. Hence, a general preliminary conclusion can be made that the description of the spin asymmetry of the nucleon in terms of quark degrees of freedom is also valid in the resonance region. However, an exception is the spin structure function g_1 in the region of $\Delta P_{33}(1232)$ resonance, where (local) duality seems to break down [37].

According to OPE, a partonic description of the moments of the structure functions at intermediate Q^2 should be always possible if one accounts for the contribution of higher twist corrections at sufficient level. Indeed, Ref. [38] showed how duality can be understood under the OPE framework. In this framework, global duality implies suppression of the higher twist effects, leaving mainly the leading twist contribution dominant. Therefore, experimental observation of higher twist effects in the resonance region is an important tool to study global duality. On the other hand, understanding local duality in the QCD framework is more subtle since there is no clear understanding how the cancellations of the higher twist effects can take place in limited kinematic regions.

There is also an interpretation of duality in the constituent quark model in [39]. The authors argue that duality may be explained in terms of the cancellations of resonance contributions with opposite parities. Ref. [39] also suggests that global duality must fail at Q^2 where electric and magnetic multipoles have comparable strengths. Calculations with simplistic models predicted that this would be $Q^2 \sim 0.5 \text{ GeV}^2$. Indeed, duality is expected to eventually break down as $Q^2 \rightarrow 0$.

In addition to local vs. global and polarized vs. unpolarized aspects of duality, it is also important to investigate proton vs. neutron cases. The unpolarized structure function in DIS region is proportional to the sum of the squares of the constituent quark charges $\sim \sum e_q^2$. Coherent excitation of the resonances, on the other hand, is driven by the square of the sum of the constituent quark charges $\sim (\sum e_q)^2$ [39]. In the constituent quark model, these two quantities are the same for the proton but not for the neutron, which creates a curiosity if there are different aspects of duality for the proton and the neutron.

II.4 SUM RULES AND THEORETICAL MODELS

Since QCD cannot be solved analytically, we don't have a complete description of the spin structure functions in order to understand the behavior of the quarks inside the nucleon. However, integrals over the spin structure functions can be compared to rigorous theoretical results, like sum rules, lattice QCD calculations and chiral perturbation theory, providing a powerful tool to study the spin structure of the nucleon. Sum rules are precise predictions of the behavior of the spin structure functions in certain kinematic limits. Experimental data can be used to test these predictions and extract information.

In this section, we will explain some of the sum rules that are specifically related to the first moment of $g_1(x, Q^2)$,

$$\Gamma_1^1(Q^2) = \int_0^1 dx g_1(x, Q^2), \quad (116)$$

which can be expressed in terms of the nucleon matrix elements of current operators via the Operator Product Expansion (OPE) as shown in Eq. (92). It should be noted that, the OPE is valid only if the moments include the elastic contribution at $x = 1$. However, in the DIS region, the elastic contribution is completely negligible. For that reason, the experimentally measured moments at high Q^2 often excludes the elastic term from the upper limit of the integral. On the other hand, at low Q^2 , especially in the resonance region, elastic contribution becomes large, hence, cannot be neglected for a complete description of the moments in terms of the nucleon matrix elements. Therefore, moments in these kinematics are distinguished according to their inclusion or exclusion of the elastic contribution. This distinction becomes important for the sum rules that specifically apply to the low Q^2 regions.

Before defining the sum rules related to the first moment of g_1 , let's visit the QPM that preserves its validity in the limit $Q^2 \rightarrow \infty$. In the QPM, the spin structure function g_1 can be written as in Eq. (76). Therefore, the first moment of g_1 simplifies in the case of free quark fields to:

$$\Gamma_1^1 = \int_0^1 dx g_1 = \frac{1}{2} \int_0^1 \sum_i e_i^2 (\Delta q_i(x) + \Delta \bar{q}_i(x)) dx \quad (117)$$

Assuming three quark flavors (u, d, s), we get for the proton

$$\Gamma_1^{1(p)} = \frac{1}{2} \left(\frac{4}{9} \Delta u + \frac{1}{9} \Delta d + \frac{1}{9} \Delta s \right) \quad (118)$$

and for the neutron

$$\Gamma_1^{1(n)} = \frac{1}{2} \left(\frac{1}{9} \Delta u + \frac{4}{9} \Delta d + \frac{1}{9} \Delta s \right) \quad (119)$$

where Δq_i represents the integrated quark distributions defined by

$$\Delta q_i = \int_0^1 (\Delta q_i(x) + \Delta \bar{q}_i(x)) dx, \quad (120)$$

which is the fraction of the nucleon spin carried by the quark flavor q_i .

The transition currents between baryons made out of three quark types are described in terms of the octet axial vector currents,

$$J_k^\mu = \bar{\psi} \gamma^\mu \gamma^5 \left(\frac{\lambda_k}{2} \right) \psi \quad (k = 1, \dots, 8) \quad (121)$$

where λ_k are the SU(3) Gell-Mann flavor matrices and ψ is a column vector for three quark fields (u, d, s):

$$\psi = \begin{pmatrix} \psi_u \\ \psi_d \\ \psi_s \end{pmatrix} \quad (122)$$

At this point, it is convenient to introduce the nucleon axial charge a_k defined in terms of the matrix elements of the nucleon state vector [30][20]:

$$2Ma_k S^\mu = \langle P, S | J_k^\mu | P, S \rangle \quad (123)$$

where M is the nucleon mass and $|P, S\rangle$ is the state vector of the nucleon with spin S . Assuming SU(3) symmetry holds exact, the non-singlet vector currents are conserved. This leads to the a_k ($k = 1, \dots, 8$) to be independent of Q^2 and conserved to any order in α_s . The singlet current is not conserved because it requires factorization to deal with divergences that arise and it is convenient to choose Q^2 as the factorization scale. Its exact value depends on the factorization scheme utilized. In commonly used factorization schemes [7], a_0 depends on Q^2 when we go beyond the Leading Order calculations.

The relevant matrix elements to this analysis are a_0 , a_3 and a_8 . The singlet element, a_0 , represents the net spin carried by the quarks, $\Delta\Sigma$, in the DIS measurements. Based on the assumption that SU(3) is a good symmetry, the other two matrix elements of the axial vector currents can be expressed in terms of the weak decay constants F and D [40], which are constrained by the neutron and hyperon

β -decay measurements. As a result, the three matrix elements can be written as:

$$a_0 = \Delta u + \Delta d + \Delta s = \Delta\Sigma \quad (124)$$

$$a_3 = \Delta u - \Delta d = F + D = 1.26 \quad (125)$$

$$a_8 = \Delta u + \Delta d - 2\Delta s = 3F - D = 0.58 \quad (126)$$

Finally, by combining Eqs. (118) and (119) with (124-126), we can write the first moment of g_1 in terms of the axial charges for the proton,

$$\Gamma_1^{1(p)} = \int_0^1 g_1(x) dx = \frac{1}{9} \left[\frac{3}{4} a_3 + \frac{1}{4} a_8 + a_0 \right] = \frac{1}{18} [9F - D + 6\Delta s] \quad (127)$$

and for the neutron

$$\Gamma_1^{1(n)} = \int_0^1 g_1(x) dx = \frac{1}{9} \left[-\frac{3}{4} a_3 + \frac{1}{4} a_8 + a_0 \right] = \frac{1}{18} [6F - 4D + 6\Delta s] \quad (128)$$

It should be noted that the above relations between the quark spin distributions and the weak decay constants are only valid in the limit that $Q^2 \rightarrow \infty$. For finite Q^2 , corrections provided by pQCD, should be utilized

II.4.1 Vector and Axial Vector Coupling Constants

In order to understand the relations between the quark spin distributions and the weak decay constants mentioned above, let's look at weak charged current transitions, such as neutron β -decay, in the framework of the Constituent Quark Model (CQM) [1], in which we assume that nucleon contains three constituent quarks, UUD for the proton and UDD for the neutron. The constituent quarks are labeled with capitol letters to distinguish them from the current quarks u and d used in the QPM earlier. The neutron β -decay can be visualized as electron capture by a proton under the assumption of time reversal invariance in physical processes. The weak charged current transitions contain vector (V) and axial vector (A) parts.

At low energies, as in the case of nuclear β -decay, the vector part of the hadronic current can be written as $V = g_V \langle n | \tau^- | p \rangle$, where $|n\rangle$ and $|p\rangle$ represents the neutron and proton states while τ^- is the isospin lowering operator, which turns the proton into a neutron. The matrix element $\langle n | \tau^- | p \rangle$ is simply equal to 1. The vector coupling constant g_V accounts for the fact that the weak interaction acts on the individual quarks, not the whole nucleon. In the case of electron capture by the proton, one of the U quarks is converted into a D quark, with simultaneous emission of an electron

neutrino. As a result, we can write the vector part as $V = \langle n | \sum_q \tau_q^- | p \rangle$, in which sum goes over all quarks in the nucleon and $\tau_q^- | U \rangle = | D \rangle$ and $\tau_q^- | D \rangle = 0$. By utilizing SU(2) symmetry we can write [1],

$$\langle n | \sum_q \tau_q^- | p \rangle = \langle p | \sum_q \tau_q^3 | p \rangle, \quad (129)$$

which simply states that matrix element of any isospin lowering operator τ^- between two members of iso-doublet (e.g., the proton and the neutron or the U and D quarks) is the same as the matrix element of the operator τ^3 between two $I_3 = +1/2$ states. The operator τ^3 behaves as $\tau^3 | U \rangle = +1$, $\tau^3 | D \rangle = -1$, which means the right hand side of the above equation is equal to 1. Therefore, $g_V \langle n | \tau^- | p \rangle = 1$, indicating that $g_V = 1$. The experimentally measured [41] value is $g_V = 1.000 \pm 0.003$. Hence, the vector weak charge is conserved. So, it can be said that just like the electric charge, the vector charge is also protected by conservation laws. This is often referred to as Conserved Vector Current (CVC).

In the case of the axial vector, we can write the three spatial components as $A_i = g_A \langle n, s | \tau^- \sigma^i | p, s \rangle$, where σ^i are the Pauli spin matrices that act on the spin wave function in the same way the τ 's act on isospin. $|p, s\rangle$ and $|n, s\rangle$ are the proton and neutron states with spin $s = \uparrow$ or \downarrow . The axial vector coupling constant g_A accounts for the quark level interaction. At the quark level, the matrix elements can be written as $A_i = \langle n, s | \sum_q \tau_q^- \sigma_q^i | p, s \rangle$. Again by utilizing the SU(2) group symmetry, the z component of the axial vector current A_z can be written as:

$$g_A \langle n, s | \tau^- \sigma^3 | p, s \rangle = \langle p, s | \sum_q \tau_q^3 \sigma_q^3 | p, s \rangle \quad (130)$$

The left hand side gives g_A . The operator combination $\tau_q^3 \sigma_q^3$ at the right hand side behaves on the individual quarks as:

$$\tau_q^3 \sigma_q^3 | U \uparrow \rangle = + | U \uparrow \rangle, \quad \tau_q^3 \sigma_q^3 | U \downarrow \rangle = - | U \downarrow \rangle \quad (131)$$

$$\tau_q^3 \sigma_q^3 | D \uparrow \rangle = - | D \uparrow \rangle, \quad \tau_q^3 \sigma_q^3 | D \downarrow \rangle = + | D \downarrow \rangle \quad (132)$$

Summing over all possible flavor and spin states, the Eq. (130) eventually yields,

$$g_A = \Delta U - \Delta D \quad (133)$$

where $\Delta U = |U \uparrow\rangle - |U \downarrow\rangle$ and $\Delta D = |D \uparrow\rangle - |D \downarrow\rangle$. This relation derived by using the CQM also holds for the QPM once we apply the same idea to the current

quarks instead of the constituent quarks and take also the anti-quark polarizations into account. Therefore, $g_A = \Delta u - \Delta d$, in which the definition of Δq is now changed to Eq. (120). This relation holds its validity at the limit $Q^2 \rightarrow \infty$, where quarks are asymptotically free. However, in this approach, the orbital angular momentum of the quarks are assumed to be zero, which is not exactly true. Therefore, relativistic corrections are required. This simple calculation gives an idea for the connection between the quark spin distributions and the g_A coupling constant.

The axial vector coupling constant was measured from neutron β -decay. It can be written in terms of the weak decay constants F and D , which describe the anti-symmetric and symmetric $SU(3)$ couplings respectively. This, however, is based on the assumption that $SU(3)$ symmetry of baryon octet is exact and the strange quarks in the nucleon are unpolarized. The most up to date value of g_A is [7]:

$$g_A = F + D = 1.2670 \pm 0.0035 \quad (134)$$

Hence, the axial vector charge, unlike the vector charge, is not exactly conserved by the strong interactions.

Another weak decay we need to consider is the β -decay of a Λ -hyperon into a proton by emitting electron and electron anti-neutrino [1]. In this process, the s quark changes into a u quark. Again, one can define vector and axial vector parts of this transition. By utilizing $SU(3)$ group symmetry of isospin and strangeness, the axial vector coupling constant of the transition, g_A^Λ can be related to the quark spin distributions in the framework of the QPM: $g_A^\Lambda = \Delta u + \Delta d - 2\Delta s$. Under the assumption that $SU(3)$ symmetry is exact, this quantity is often written in terms of the weak decay constants as:

$$g_A^\Lambda = 3F - D = 0.585 \pm 0.025 \quad (135)$$

The experimental value is obtained by a global fit to the world data [7]. In the CQM, in which there is no strange quark inside the nucleon, g_A^Λ must be equal to 1. Therefore, the experimental result indicates that the s quark polarization is non-negligible or $SU(3)$ symmetry is not exact. pQCD corrections address some of the issues and provide an extension of these definitions, that are only valid in the $Q^2 \rightarrow \infty$ limit, for a finite Q^2 .

II.4.2 pQCD Corrections

Following the prescriptions given in section II.3, the structure functions can be evolved to finite Q^2 . By using DGLAP equations to take radiative effects into account and utilizing the OPE for higher twist corrections, the Q^2 dependency of the Γ_1^1 can be evaluated. However, divergences arise in pQCD corrections. The ultra-violet divergences are taken care of by renormalization. Collinear divergences that arise because of masslessness of quarks are attended by using a scheme called factorization. The interaction of the virtual photon with a nucleon is visualized as a combination of long (soft) and short (hard) distance interactions. The point this separation is made is called factorization scale μ^2 . The long distance interactions cannot be calculated analytically. They can only be parametrized and studied experimentally. Therefore, the infinite terms can be absorbed into the long distance part of the interaction. For instance, we can use a common term that arises in pQCD calculations for parton densities such as $\alpha_s \ln \frac{Q^2}{m_q^2}$ where m_q represents quark mass. Such a term can be split into two parts as:

$$\alpha_s \ln \frac{Q^2}{m_q^2} = \alpha_s \ln \frac{Q^2}{\mu^2} + \alpha_s \ln \frac{\mu^2}{m_q^2} \quad (136)$$

then the first term of the right hand side is absorbed into the short distance part of the equation and the second term is into the long distance part. Here, the factorization scale μ^2 is an arbitrary number and physical results cannot depend on it. However, only a finite number of terms enters into the analytic calculation, therefore, our solution depends on the scale we choose. As a result, the solution should carry the factorization scale μ^2 as a label. It is generally agreed that an optimal choice for this scale is $\mu^2 = Q^2$, so the parton densities become also a function of Q^2 as well as the momentum fraction x : $q(x) \rightarrow q(x, Q^2)$. There are different factorization schemes in use. In the Modified-Minimal-Subtraction (\overline{MS}) scheme, a_3 and a_8 are independent of Q^2 and $a_0 = \Delta\Sigma$. The correction term C_G in Eq. (88) vanishes, so that ΔG does not contribute to Γ_1 . By utilizing Eqs. (89), (90) and (92), the expression for the Γ_1 up to twist-4 correction can be written as:

$$\Gamma_1^{1(p,n)}(Q^2) = \frac{1}{12} \left[\left(\pm a_3 + \frac{1}{3} a_8 \right) C_{NS}(Q^2) + \frac{4}{3} a_0(Q^2) C_S(Q^2) \right] + \frac{\mu_4(Q^2)}{Q^2} \quad (137)$$

where $\mu_4(Q^2)$ is given in (94) and the non-singlet (NS) and singlet (S) Wilson coefficients are given by:

$$C_{NS}(Q^2) = 1 - \left(\frac{\alpha_s}{\pi} \right) - 3.58 \left(\frac{\alpha_s}{\pi} \right)^2 - 20.22 \left(\frac{\alpha_s}{\pi} \right)^3 \dots \quad (138)$$

$$C_S(Q^2) = 1 - \left(\frac{\alpha_s}{\pi}\right) - 1.096 \left(\frac{\alpha_s}{\pi}\right)^2 \dots \quad (139)$$

The QPM turns out to be a zero order approximation to pQCD. The parton densities $q(x)$ and $\Delta q(x)$ becomes just the leading order members of QCD calculations. These perturbative corrections are small for DIS experiments such as the EMC experiment that triggered the so called spin crises. Next, we will define a few sum rules that are initially based on the quark parton model, compare their results with experiments and analyze their implications after the pQCD corrections are applied.

II.4.3 The Ellis-Jaffe Sum Rule

By using the SU(3) flavor symmetry and assuming the strange sea quark is unpolarized, $\Delta s = 0$, Ellis and Jaffe predicted a value for the first moment of g_1^p in the framework of the QPM. Starting from Eq. (127) and using measured values of the weak decay constants, they found $\Gamma_1^{1(p)} = 0.186$ and $\Gamma_1^{1(n)} = -0.024$. It should be stated that this prediction also assumes net gluon polarization $\Delta G = 0$. Later, in the EMC experiment, however, $\Gamma_1^{1(p)} = 0.128 \pm 0.013 \pm 0.019$ was measured at $Q^2 = 10.7$ GeV². The experimental value is much lower than the prediction made by Ellis-Jaffe. This discrepancy is what triggered the so-called spin crisis. This low value of the $\Gamma_1^{1(p)}$ was also confirmed by later experiments.

The assumption $\Delta s = 0$ made in the Ellis-Jaffe sum rule implies that $a_0 = a_8$. Therefore, in the regime of the QPM, $a_0 = 3F - D = 0.585$, as known from the hyperon decay. Remember that in the QPM (at the limit $Q^2 \rightarrow \infty$), a_0 corresponds to the total spin carried by the quarks. In a non-relativistic model, it is expected that all of the proton's spin is carried by the valence quarks, which means $a_0 = 1$. Relativistic corrections consider the orbital angular momentums of the quarks and decrease this value to $a_0 \sim 0.6$. Ellis-Jaffe prediction is in good agreement with the relativistic model. However, if one tries to extract the value of a_0 by using Eq. (127) and the measured value of the $\Gamma_1^{1(p)}$,

$$a_0 = 9\Gamma_1^{1(p)} - \frac{3}{4}a_3 - \frac{1}{4}a_8 = 0.05 \pm 0.12 \pm 0.17, \quad (140)$$

which is much smaller than the Ellis-Jaffe prediction. Indication of the EMC experiment is that the contribution of the quark spins to the overall spin of the proton is very small.

One can argue that the EMC regime, $Q^2 = 10.7$ GeV², is not high enough for the QPM equations to be valid, therefore, one must apply the pQCD corrections. This

is done by using the Eq. (137). However, the perturbative corrections turn out to be small for the EMC data. The corrected value becomes [42] $a_0 = 0.17 \pm 0.12 \pm 0.17$ evaluated at $Q^2 = 10 \text{ GeV}^2$. Hence, the QCD-improved corrections do not resolve the question why the value of a_0 is much smaller than the expected. Later, several more precise experiments were performed in order to measure $\Gamma_1^{1(p)}$, $\Gamma_1^{1(n)}$ and $\Gamma_1^{1(d)}$ [43][44][45][46][47][48][49]. It should be noted that the experimental verification of the sum rule requires inclusion of the elastic peak at $x = 1$. However, for the DIS experiments, the elastic peak contribution is very small. Hence, most experimental results in the DIS regime do not include the elastic peak. But, the importance of the elastic peak increases as we get to lower Q^2 regions, where the results should be handled carefully. In addition, low x extrapolation while calculating the Γ_1^1 integral is an important factor. The HERMES and COMPASS experiments used different and more precise low x extrapolation than the previous experiments did. By using the recent measurements on the deuteron, these experiments estimated the most precise singlet axial charge a_0 , yielding $a_0 = 0.33 \pm 0.04$ for HERMES evaluated at $Q^2 = 5 \text{ GeV}^2$ and $a_0 = 0.35 \pm 0.06$ for COMPASS at $Q^2 = 3 \text{ GeV}^2$.

Gluon Polarization and Axial Anomaly

Several schemes have been developed to incorporate a non-zero gluon polarization in order to explain the low a_0 measured in the experiments. It has been shown in [51] that there is an anomalous contribution to the axial current, which breaks the axial current conservation and causes a gluonic contribution to a_0 such that [52]

$$a_0 = \Delta\Sigma - \frac{3}{2\pi}\alpha_s(Q^2)\Delta G(Q^2), \quad (141)$$

where $\Delta\Sigma$ represents the net spin carried by the quarks. However, this actually depends on the factorization scheme. In the \overline{MS} scheme, the gluonic contribution turns out to be zero, thus $\Delta\Sigma = a_0(Q^2)$, which means $\Delta\Sigma$ becomes Q^2 dependent thus cannot be directly interpreted as the net spin carried by the quarks. In the other factorization schemes, AB and JET, $\Delta\Sigma$ is Q^2 independent and therefore, corresponds to the net spin carried by the quarks. However, in these factorization schemes the gluonic contribution to a_0 is non-zero. As a result, a small a_0 does not necessarily mean that the quarks carry a small fraction of the total spin as long as there is also a gluon polarization contributing. In order to explain the small a_0 , a gluon polarization as large as $\Delta G \approx 1.7$ is required at $Q^2 = 1 \text{ GeV}^2$. Unfortunately,

the recent experimental results pretty much ruled out such a large gluon polarization [7], which brings us back to the question why a_0 is small.

As a conclusion, the Ellis-Jaffe sum rule is important because its violation implies that the strange quark polarization and the gluonic contributions should be taken into account seriously. The reader is strongly encouraged to look into Ref. [7] for these ongoing efforts and recent experimental results on this subject. In addition, determining the orbital angular momentum contributions from both quarks and the gluon is also an important ingredient to understand the spin content of the nucleon.

II.4.4 The Bjorken Sum Rule

By using Eqs. (118) and (119), we obtain:

$$\Gamma_1^{1(p)} - \Gamma_1^{1(n)} = \frac{1}{6}(\Delta u - \Delta d) \quad (142)$$

According to Eq. (133), the right hand side of (142) is directly related to the axial vector coupling constant g_A . This is, however, only valid in the QPM frame. Therefore, we can write in the QPM that

$$\Gamma_1^{1(p)} - \Gamma_1^{1(n)} = \frac{1}{6} g_A \quad (143)$$

This is the celebrated Bjorken sum rule, which was derived before QCD was invented. Its validity can be extended into a finite Q^2 region by applying the QCD corrections to the structure functions as prescribed earlier. By using Eq. (137), the most general form of the Bjorken sum rule can be written as

$$\Gamma_1^{1(p)} - \Gamma_1^{1(n)} = C_{NS} \frac{g_A}{6} + \text{higher twist}, \quad (144)$$

where C_{NS} is the non-singlet Wilson coefficient as given in Eq. (138).

The strength of the Bjorken sum rule comes from the fact that all additional spin contributions from the gluon and the strange sea quarks are canceled in the difference, leaving only the contributions from the up and the down quarks. There is no model dependency or any underlying assumption in the Bjorken sum rule, other than QCD and isospin symmetry. It completely relies on QCD assumptions. Therefore it is considered as one of the most important tests of QCD. In the region $2 < Q^2 < 10$ GeV², the Bjorken sum rule has been verified at the level of 10% accuracy [30]. Taking $\alpha_s(M_z^2) = 0.119 \pm 0.002$, which yields $\alpha_s(5 \text{ GeV}^2) = 0.29 \pm 0.02$, gives,

$$\Gamma_1^{1(p)} - \Gamma_1^{1(n)} = 0.182 \pm 0.005 \quad \text{at } Q^2 = 5 \text{ GeV}^2. \quad (145)$$

The E155 experiment measured [7][47]

$$\Gamma_1^{1(p)} - \Gamma_1^{1(n)} = 0.176 \pm 0.008 \quad \text{at } Q^2 = 5 \text{ GeV}^2. \quad (146)$$

At this point, we can also look at the sum of the first moments for the proton and the neutron. In the first approximation (by neglecting nuclear effects as well as the higher twist contributions), the first moment for the deuteron can be expressed by summing the proton and neutron such that $\Gamma_1^{1(d)} = \frac{1}{2}(\Gamma_1^{1(p)} + \Gamma_1^{1(n)})(1 - 1.5w_D)$ where w_D is a probability that deuteron is in a D state and the factor $1/2$ is introduced to express the value “per nucleon” (see section II.5 for details). From Eq. (137), we can immediately conclude that the a_3 term has no effect on $\Gamma_1^{1(d)}$ and the a_0 term will dominate. Therefore, $\Gamma_1^{1(d)}$ is especially sensitive to $\Delta\Sigma$ (without the interference of a_3), and via its Q^2 evolution, to gluons.

II.4.5 The Gerasimov-Drell-Hearn (GDH) Sum Rule

When the momentum transfer of the photon becomes smaller, at low Q^2 , perturbative QCD cannot be utilized because the strong coupling constant approaches 1. There are phenomenological models that incorporate the photo-absorption cross sections in order to predict the low Q^2 evolution of the structure functions.

As explained in section II.3.4, the photo-absorption cross sections can be related to the helicity transition amplitudes and expressed in terms of the structure functions. The Gerasimov-Drell-Hearn (GDH) sum rule relates the difference between the two real photo-absorption cross sections $\sigma_{1/2}^T$ and $\sigma_{3/2}^T$ to the anomalous magnetic moment of the nucleon κ [53][54],

$$I(0) = \int_{\nu_0}^{\infty} \frac{d\nu}{\nu} [\sigma_{1/2}^T(\nu) - \sigma_{3/2}^T(\nu)] = -\frac{4\pi^2\alpha}{M^2} S\kappa^2 = -\frac{2\pi^2\alpha}{M^2} \kappa^2 \quad (147)$$

where ν_0 marks the inelastic (pion production) threshold, $S = 1/2$ is the spin of the nucleon, M is the nucleon mass and α is the fine structure constant. The anomalous magnetic moment for the proton is $\kappa_p = +1.79$ and for the neutron it is $\kappa_n = -1.91$. Therefore, the numerical results for the GDH sum rule for the proton $I_p(0) = -205 \mu b$ and the neutron $I_n(0) = -233 \mu b$.

The GDH integral was originally derived for real photons at $Q^2 = 0$. Derivation of the sum rule exclusively relies on very general principles such as Lorentz invariance, Gauge invariance, crossing symmetry and the low energy theorem. The details on the derivation can be found in [55] and [56]. Here, we can briefly outline the steps

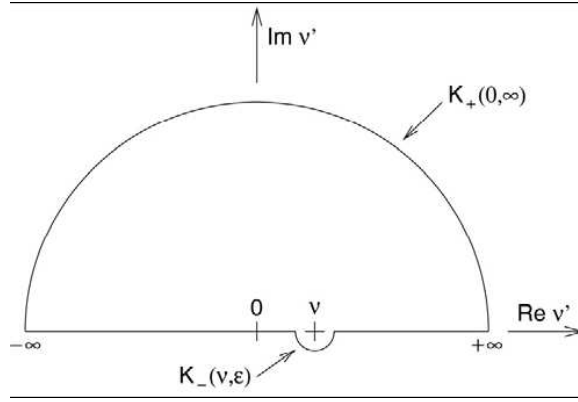


FIG. 9: Path of integration for Cauchy's integral formula.

involved. The spin dependent Compton forward scattering amplitude for real photons with energy ν can be written as,

$$T(\nu, \theta = 0) = \vec{\epsilon}_f^* \cdot \vec{\epsilon}_i f_T(\nu) + i\vec{\sigma} \cdot (\vec{\epsilon}_f^* \times \vec{\epsilon}_i) g_{TT}(\nu) \quad (148)$$

where f_T and g_{TT} are scalar functions, ¹ $\vec{\sigma}$ is the vector of Pauli spin matrices and $\vec{\epsilon}_{i,f}$ label the initial and final polarization of the photon. The above scattering amplitude is a simplified case of the full scattering amplitude by fulfilling the transversity condition for real photons, $\vec{\epsilon} \cdot \vec{k} = 0$, where \vec{k} represents the nucleon momentum.

The Compton scattering is symmetric under the exchange of in and outgoing photons ($\vec{\epsilon}_i \leftrightarrow \vec{\epsilon}_f^*$). This symmetry is called crossing symmetry and is exact for all orders of electromagnetic coupling. As a result of this symmetry we have:

$$T(-\nu, \theta = 0) = T^*(\nu, \theta = 0), \quad f_T(-\nu) = f_1^*(\nu), \quad g_{TT}(-\nu) = -f_2^*(\nu) \quad (149)$$

We can compute the Compton amplitude for different spin orientations of the photon and the nucleon. For this analysis, we only need to focus our attention to two cases where the spins are either aligned, which yields an amplitude $f_{3/2}$, or anti-aligned, which yields $f_{1/2}$:

$$f_{3/2}(\nu) = f_T(\nu) - g_{TT}(\nu), \quad f_{1/2}(\nu) = f_T(\nu) + g_{TT}(\nu) \quad (150)$$

$f_{3/2}$ and $f_{1/2}$ are associated to the helicity amplitudes described in section II.1.2. By using the optical theorem, the forward scattering amplitudes for different helicity

¹ $f_T(\nu)$ represents the spin independent amplitude while $g_{TT}(\nu)$ is the spin-flip amplitude. Sometimes $f_T(\nu)$ and $g_{TT}(\nu)$ may be referred to as $f_1(\nu)$ and $f_2(\nu)$ respectively.

combinations can be related to the total cross sections,

$$\text{Im } f(\nu) = \frac{\nu}{4\pi} \sigma(\nu). \quad (151)$$

Then, we can write the amplitudes f_T and g_{TT} as:

$$\text{Im } f_T(\nu) = \frac{\nu}{8\pi} (\sigma_{1/2}(\nu) + \sigma_{3/2}(\nu)) = \frac{\nu}{4\pi} \sigma^T(\nu) \quad (152)$$

$$\text{Im } g_{TT}(\nu) = \frac{\nu}{8\pi} (\sigma_{1/2}(\nu) - \sigma_{3/2}(\nu)) = \frac{\nu}{4\pi} \sigma^{TT}(\nu) \quad (153)$$

At this point, we are ready to use the Cauchy's integral formula to evaluate the scattering amplitudes. The Cauchy's integral is written as:

$$f(\nu) = \frac{1}{2\pi i} \oint_C d\nu' \frac{f(\nu')}{(\nu' - \nu)} \quad (154)$$

The path of integration is shown in Fig. 9. In terms of different segments of the integration, we can rewrite the Cauchy's integral:

$$\begin{aligned} f(\nu) &= \frac{1}{2\pi i} \mathcal{P} \int_{-\infty}^{\infty} d\nu' \frac{f(\nu')}{(\nu' - \nu)} \\ &+ \frac{1}{2\pi i} \int_{K_+(0, \infty)} d\nu' \frac{f(\nu')}{(\nu' - \nu)} + \lim_{\delta \rightarrow 0} \frac{1}{2\pi i} \int_{K_-(\nu, \delta)} d\nu' \frac{f(\nu')}{(\nu' - \nu)} \end{aligned} \quad (155)$$

where \mathcal{P} denotes the principal value integral. The important point here is that the integral along the path $K_+(0, \infty)$ vanishes according to the No-subtraction hypothesis. It should be noted that there is no strong reason why the No-subtraction hypothesis should hold. This remains as one of the assumptions that the GDH sum rule just relies on. The No-subtraction itself relies on other fundamental assumptions like Lorentz and gauge invariance and causality. The integral above is reduced to:

$$f(\nu) = \frac{1}{\pi i} \mathcal{P} \int_{-\infty}^{\infty} d\nu' \frac{f(\nu')}{(\nu' - \nu)} \quad (156)$$

Recalling the crossing symmetry properties of the scattering amplitudes, we can write the above integral as:

$$f(\nu) = \frac{1}{\pi i} \mathcal{P} \int_0^{\infty} d\nu' \left(\frac{f(\nu')}{(\nu' - \nu)} + \frac{f^*(\nu')}{(-\nu' - \nu)} \right) \quad (157)$$

Considering only the real part, this integral simplifies to Kramers-Kronig dispersion relation:

$$\text{Re } f(\nu) = \frac{2}{\pi} \mathcal{P} \int_0^{\infty} d\nu' \text{Im } f(\nu') \left(\frac{\nu'}{\nu'^2 - \nu^2} \right) \quad (158)$$

By incorporating the results of the optical theorem for the scattering amplitudes $f_T(\nu)$ and $g_{TT}(\nu)/\nu$ given in Eqs. (152 - 153) into the Kramers-Kronig dispersion relation we get,

$$\begin{aligned} \text{Re } f_T(\nu) &= \frac{1}{2\pi^2} \int_0^\infty d\nu' \sigma^T(\nu') \left(\frac{\nu'^2}{\nu'^2 - \nu^2} \right) \\ &= \frac{1}{2\pi^2} \int_0^\infty d\nu' \sigma^T(\nu') \sum_{n=0}^\infty \left(\frac{\nu}{\nu'} \right)^{2n} \\ &= \frac{1}{2\pi^2} \sum_{n=0}^\infty \left[\int_0^\infty d\nu' \sigma^T(\nu') \left(\frac{\nu}{\nu'} \right)^{2n} \right] \end{aligned} \quad (159)$$

where we used Binomial expansion for the terms in ν in the integration. Similarly, for g_{TT}/ν we have,

$$\text{Re } \frac{g_{TT}(\nu)}{\nu} = \frac{1}{4\pi^2} \sum_{n=0}^\infty \left[\int_0^\infty \frac{d\nu'}{\nu'} [\sigma_{1/2}(\nu') - \sigma_{3/2}(\nu')] \left(\frac{\nu}{\nu'} \right)^{2n} \right] \quad (160)$$

Now, we will compare these equations for f_T and g_{TT}/ν with their expansion based on the low energy theorems and deduce the GDH sum rule.

The Low energy theorem

The Low energy theorem in Compton scattering, first suggested by Thirring and then generalized by Low, Gell-Mann and Goldberger, provides an expansion of the Compton scattering amplitudes in terms of the photon energy ν up to the the lowest non-trivial order in electromagnetic coupling. The expansion yields:

$$f_T(\nu) = -\frac{\alpha}{M} + (\alpha_E + \beta_M)\nu^2 + \mathcal{O}(\nu^4) \quad (161)$$

$$\frac{g_{TT}(\nu)}{\nu} = -\frac{\alpha}{2M^2}\kappa^2 + \gamma_0\nu^2 + \mathcal{O}(\nu^4) \quad (162)$$

where M is the nucleon mass. Note that f_T is even and g_{TT} is an odd function of ν as a result of the crossing symmetry. α_E is the electric and β_M is the magnetic dipole polarizabilities. The leading term in the spin-flip amplitude g_{TT}/ν is determined by the anomalous magnetic moment κ of the nucleon while the quadratic terms in ν is governed by the forward spin polarizability γ_0 .

By comparing the dispersion relations with the low energy theorem expansions for the scattering amplitudes, we obtain our basic sum rules. The Baldin's sum rule for the electric and magnetic polarizabilities,

$$\frac{1}{2\pi^2} \int_0^\infty \frac{d\nu'}{\nu'^2} \sigma^T(\nu') = \alpha_E + \beta_M \quad (163)$$

the GDH sum rule,

$$\frac{1}{4\pi^2} \int_0^\infty \frac{d\nu'}{\nu'} [\sigma_{1/2}(\nu') - \sigma_{3/2}(\nu')] = -\frac{\alpha}{2M^2} \kappa^2, \quad (164)$$

and the forward spin polarizability,

$$\frac{1}{4\pi^2} \int_0^\infty \frac{d\nu'}{\nu'^3} [\sigma_{1/2}(\nu') - \sigma_{3/2}(\nu')] = \gamma_0 \quad (165)$$

In the Eq. (164), the lower limit of integration is often replaced with pion production threshold ν_0 because the cross-sections for real photon are zero below this threshold, which means the GDH sum rule has no elastic contribution due to kinematic constraint. This convention brings us the original GDH sum rule written in Eq. (147) at the beginning of this section.

The GDH Sum Rule for the Deuteron

The GDH sum rule can also be established for the deuteron because the low energy theorem holds its validity for composite systems such as the deuteron. The deuteron anomalous magnetic moment $\kappa_d = -0.143$ is relatively small, which yields a small value for the GDH sum rule $I_d(0) = -0.65 \mu b$. Because of its small binding energy, the deuteron has a quite extended spatial structure. Its anomalous magnetic moment is small because of an almost complete cancellation of proton and neutron anomalous magnetic moments in the deuteron. When we consider the small GDH sum for the deuteron, we expect some cancellations to occur in the deuteron GDH integral as well. Different production channels contributing to the integral must be analyzed separately to understand the overall value of the sum. For example, there is a photo-disintegration process $\gamma + d \rightarrow n + p$ as well as some meson production channels that contribute to the GDH sum of the deuteron. The same meson production channels also contribute to the GDH sum of the nucleon. Table 2 shows the estimated contributions of various production channels to the deuteron (d) and the neutron + proton (n+p) GDH integrals. If one considers only the meson production channels, $I_{n+p} \approx -476.74 \mu b$ is relatively close to $I_d \approx -408.83 \mu b$. However, if we include the photo-disintegration channel contribution for the deuteron, we get $I_d \approx -27.31 \mu b$. The remaining discrepancy can be attributed to additional final state channels that were neglected in these calculations. Nevertheless, a strong anti-correlation between the low energy photo-disintegration process and the high energy meson production channels is the main reason of the small GDH integral for the deuteron.

TABLE 2: Estimated contributions of various channels to the GDH integral (in μb) for the neutron+proton I_{n+p} and for the deuteron I_d . The photo-disintegration channel $\gamma + d \rightarrow n + p$ is integrated up to $\nu = 0.8$ GeV, the single pion and eta production channels are integrated up to $\nu = 1.5$ GeV and the double pion channel is integrated up to $\nu = 2.2$ GeV [57].

| Channel | I_{n+p} | I_d |
|----------|-----------|---------|
| np | 0 | 381.52 |
| π | -315.33 | -263.44 |
| $\pi\pi$ | -175.95 | -159.34 |
| η | 14.54 | 13.95 |
| Sum | -476.74 | -27.31 |
| GDH Sum | -437.94 | -0.65 |

At high energies, especially above pion production threshold, the contribution from the photo-disintegration channel completely vanishes. In that case, the deuteron GDH integral can be approximated by the sum of the proton and neutron integrals plus nuclear corrections. This is the situation in the kinematic regime of the EG1b experiment. One straightforward correction comes from the D-state. In the DIS experiments, a valid approximation for the deuteron GDH integral can be written as $I_d = (I_p + I_n)(1 - 1.5w_D)$ with $w_D \approx 0.056$. However, higher order nuclear corrections are required for better comparison between the GDH integral of the deuteron and the sum of the integrals of the nucleons, see section II.5 for those details.

Generalization of the GDH integral for virtual photons

As explained earlier, for the low Q^2 regions, it is important to distinguish between the moments with elastic contribution at $x = 1$ either included or excluded. The relations between the moments of the structure functions and the matrix elements of operators are only valid if the moments include the elastic contribution. In the DIS region, the elastic contribution is negligible and generally excluded. But, at low Q^2 , the contribution becomes important. Therefore, we will label the moments with elastic contribution included as Γ_1^1 , while we will use $\bar{\Gamma}_1^1$ for the moments with no elastic contribution. Experimentally tabulated moments generally exclude the elastic contribution. From now on, we will use the same labeling convention for the integrals as well.

The GDH integral can be generalized for virtual photons, hence, for $Q^2 > 0$. The most straightforward method is to assume that real photon cross sections connect smoothly to the virtual photon cross sections. Therefore, we can simply replace the real photo-absorption cross sections with the corresponding virtual photo-absorption cross sections and write the generalized integral with no elastic contribution as:

$$\bar{I}(Q^2) = \int_{\nu_0}^{\infty} \frac{d\nu}{\nu} [\sigma_{1/2}^T(\nu, Q^2) - \sigma_{3/2}^T(\nu, Q^2)] \quad (166)$$

By using Eqs. (52) and (53), the integral is often written in terms of the spin structure functions:

$$\bar{I}(Q^2) = \frac{8\pi^2\alpha}{M} \int_0^{x_0} \frac{dx}{x} \frac{1}{K} [g_1(x, Q^2) - \gamma^2 g_2(x, Q^2)] \quad (167)$$

where $\gamma = Q/\nu$, x is the Bjorken variable and K is the flux factor. In the commonly used Hand's convention $K = \nu(1-x)$. Another convention is that of Gilman's, in which $K = \nu\sqrt{1+\gamma^2}$. The upper limit of the integration is determined by:

$$x_0 = \frac{Q^2}{Q^2 + m_\pi(2M + m_\pi)} \quad (168)$$

where $m_\pi = 0.137$ GeV is the lightest pion mass. In the high energy limit, when $\gamma \ll 1$, the integral becomes

$$\bar{I}(Q^2) = \frac{16\pi^2\alpha}{Q^2} \int_0^{x_0} g_1(x, Q^2) dx = \frac{16\pi^2\alpha}{Q^2} \bar{\Gamma}_1^1(Q^2) \quad (169)$$

The above equation provides a connection between the GDH integral and experimental observables. This connection can be established in a more rigorous way by introducing an integral related to the moment $\bar{\Gamma}_1^1$,

$$\bar{I}_1(Q^2) = \frac{2M^2}{Q^2} \bar{\Gamma}_1^1(Q^2) = \frac{2M^2}{Q^2} \int_0^{x_0} g_1(x, Q^2) dx \quad (170)$$

using Eqs. (52), (53) and Hand's convention for the flux factor K , this integral can be expressed in terms of the cross sections,

$$\begin{aligned} \bar{I}_1(Q^2) = \frac{M^2}{8\pi^2\alpha} \int_{\nu_0}^{\infty} \frac{1 - Q^2/2M\nu}{1 + Q^2/\nu^2} [\sigma_{1/2}(\nu, Q^2) \\ - \sigma_{3/2}(\nu, Q^2) + \frac{2Q}{\nu} \sigma^{TL}(\nu, Q^2)] \frac{d\nu}{\nu} \end{aligned} \quad (171)$$

It is clear that the integral $\bar{I}_1(Q^2)$ is only an approximation to the GDH integral $\bar{I}(Q^2)$ because of the interference cross section $\sigma^{TL}(\nu, Q^2)$. However, when we take the limit as $Q^2 \rightarrow 0$ on the $\bar{I}_1(Q^2)$, we recover the generalized GDH integral:

$$\lim_{Q^2 \rightarrow 0} \bar{I}_1(Q^2) = \frac{M^2}{8\pi^2\alpha} \int_{\nu_0}^{\infty} [\sigma_{1/2}^T(\nu, Q^2) - \sigma_{3/2}^T(\nu, Q^2)] \frac{d\nu}{\nu} = \frac{M^2}{8\pi^2\alpha} \bar{I}(Q^2) \quad (172)$$

Hence, we can write the GDH sum rule in terms of the first moment:

$$\lim_{Q^2 \rightarrow 0} \bar{I}_1(Q^2) = -\frac{\kappa^2}{4}, \quad \lim_{Q^2 \rightarrow 0} \bar{\Gamma}_1^1(Q^2) = -\frac{Q^2}{8M^2} \kappa^2 \quad (173)$$

The anomalous magnetic moment of nucleon is a precisely measured quantity. Therefore, the generalized GDH sum rule becomes a strong argument to constrain the first moment of g_1 as Q^2 approaches to 0. The form of Eq. (173) is interesting in the sense that $\bar{\Gamma}_1^1$ approaches 0 from negative value as $Q^2 \rightarrow 0$. But, $\bar{\Gamma}_1^1$ is expected to be positive in the DIS region. This means it must change its sign in the resonance region and converge to 0 at $Q^2 = 0$ with a slope of $-\kappa^2/8M^2$.

Another method to generalize the GDH sum rule was developed by Ji and Osborne [58] by generalizing the Compton scattering amplitude in Eq. (148), which was given for real photons, to a virtual photon case by introducing an additional longitudinal polarization vector. They begin by defining a time-ordered forward virtual-photon Compton scattering tensor and express its spin dependent (antisymmetric) part in terms of two new scalar functions $S_1(\nu, Q^2)$ and $S_2(\nu, Q^2)$, which are spin-dependent Compton amplitudes. These amplitudes satisfy crossing relations:

$$S_1(\nu, Q^2) = S_1(-\nu, Q^2), \quad S_2(\nu, Q^2) = -S_2(-\nu, Q^2) \quad (174)$$

By optical theorem, these Compton amplitudes are connected to the spin structure functions,

$$S_i(\nu, Q^2) = 2\pi G_i(\nu, Q^2) \quad (175)$$

with $M^2\nu G_1(\nu, Q^2) = g_1(x, Q^2)$ and $M\nu^2 G_2(\nu, Q^2) = g_2(x, Q^2)$. The dispersion relation for S_1 is given by:

$$S_1(\nu, Q^2) = 4 \int_{\nu_0(Q^2)}^{\infty} \frac{\nu' d\nu' G_1(\nu', Q^2)}{(\nu'^2 - \nu^2)} \quad (176)$$

Here, G_1 is difficult to calculate analytically but it can be measured while S_1 is hard to measure but it can be calculated. At least in principle, by taking $\nu = 0$ in Eq. (176), Ref. [58] arrives at a possible candidate for a generalized Q^2 -dependent sum rule:

$$\begin{aligned} S_1(0, Q^2) &= 4 \int_{\nu_0(Q^2)}^{\infty} \frac{d\nu'}{\nu'} G_1(\nu', Q^2) \\ &= \frac{8}{MQ^2} \bar{\Gamma}_1^1(Q^2) \\ &= \frac{4}{M^3} \bar{I}_1(Q^2) \end{aligned} \quad (177)$$

where $\bar{\Gamma}_1^1(Q^2)$ is the inelastic portion of the first moment $\Gamma_1^1(Q^2)$ and we have Eq. (173) for the integral $\bar{I}_1(Q^2)$. It should be noted that, when $Q^2 \neq 0$, the Compton amplitude receives a contribution $S_1^{el}(0, Q^2)$ from elastic scattering. This contribution can be calculated by using Dirac and Pauli elastic form factors $F_{1,2}^{el}(Q^2)$ [58][7]:

$$S_1^{el}(0, Q^2) = \frac{4}{Q^2} F_1^{el}(Q^2) [F_1^{el}(Q^2) + F_2^{el}(Q^2)] \quad (178)$$

then, by using Eq. (177), the full moment with elastic contribution, yields,

$$\lim_{Q^2 \rightarrow 0} I_1(Q^2) = \frac{M^2}{Q^2} F_1^{el}(Q^2) [F_1^{el}(Q^2) + F_2^{el}(Q^2)] - \frac{\kappa^2}{4} \quad (179)$$

Theoretical predictions can be made for the Compton amplitude $S_1(0, Q^2)$. For $Q^2 > 1 \text{ GeV}^2$, the operator product expansion can be utilized by expanding the first moment in powers of $1/Q^2$ using the twist coefficients. In this approach, including the elastic contribution to the first moment is vital. For $Q^2 < 0.1 \text{ GeV}^2$, on the other hand, chiral perturbation (χ PT) theories can be used. The details on χ PT calculations can be found in [58][59][60]. In the region $0.1 < Q^2 < 0.5 \text{ GeV}^2$, Lattice QCD has been suggested in [58]. There are several different schemes each yielding slightly different generalized GDH integrals. A nice review for these various definitions of integrals and their comparisons to each other can be found in [61].

II.4.6 Generalized Forward Spin Polarizabilities

In the previous section, we mentioned the forward spin polarizability γ_0 for real photons, deduced from the comparison of the dispersion relations with the low energy theorem. Several different methods have been used to generalize the dispersion relations to the virtual photon case [61]. Generalization of all amplitudes in virtual Compton scattering is given in [56]. As mentioned in the previous section, one can generalize the Compton scattering amplitude for real photons in Eq. (148) to doubly virtual Compton scattering (VVCS) by introducing an additional longitudinal polarization vector \hat{q} :

$$\begin{aligned} T(\nu, Q^2, \theta = 0) &= \vec{\epsilon}_f^* \cdot \vec{\epsilon}_i f_T(\nu, Q^2) + i\vec{\sigma} \cdot (\vec{\epsilon}_f^* \times \vec{\epsilon}_i) g_{TT}(\nu, Q^2) \\ &+ f_L(\nu, Q^2) + i\vec{\sigma} \cdot [(\vec{\epsilon}_f^* - \vec{\epsilon}_i) \times \hat{q}] g_{TL}(\nu, Q^2) \end{aligned} \quad (180)$$

f_T and g_{TT} are now functions of ν and Q^2 . $f_L(\nu, Q^2)$ is the amplitude for the longitudinal polarization of the virtual photon while $g_{TL}(\nu, Q^2)$ is the amplitude for

the interference between the transverse and the longitudinal polarizations. In the limit $Q^2 = 0$, f_T and g_{TT} coincide with those in Eq. (148) while f_L and g_{TL} vanish.

While taking the limit $Q^2 \rightarrow 0$, it is important to send $\nu \rightarrow 0$ limit first so that elastic contributions can be accounted for. In case of elastic scattering, We need to preserve the virtuality of the photon in order not to loose the elastic contribution to the virtual Compton scattering off a nucleon. The inelastic contributions, on the other hand, are independent of the order of the limits.

These amplitudes are related to the cross sections via the optical theorem.

$$\text{Im } f_L(\nu) = \frac{K}{4\pi} \sigma^L(\nu, Q^2), \quad \text{Im } f_{TL}(\nu) = \frac{K}{4\pi} \sigma^{TL}(\nu, Q^2) \quad (181)$$

Note that, we are now using the flux factor K while incorporating the optical theorem for virtual photons. These Compton amplitudes minus their corresponding Born terms (subtracting the elastic contribution) can be expanded in powers of ν^2 according to the low energy theorem. The leading term in the expansion of g_{TT} yields the generalized GDH integral:

$$I_A(Q^2) = \frac{2M^2}{Q^2} \int_0^{x_0} dx [g_1(x, Q^2) - \gamma^2 g_2(x, Q^2)] \quad (182)$$

with

$$I_A(0) = -\frac{\kappa^2}{4} \quad (183)$$

The advantage of this definitions is that the factor K for the photon flux, which depends on the choice of convention, hence, arbitrary, disappears.

The next-to-leading term in the expansion of g_{TT} yields the generalized forward spin polarizability γ_0 :

$$\gamma_0(Q^2) = \frac{16\alpha M^2}{Q^6} \int_0^{x_0} x^2 \left[g_1(x, Q^2) - \frac{4M^2 x^2}{Q^2} g_2(x, Q^2) \right] dx \quad (184)$$

Similarly, the expansion of the amplitude g_{TL} yields yet another generalized forward spin polarizability δ_{TL} :

$$\delta_{TL}(Q^2) = \frac{16\alpha M^2}{Q^6} \int_0^{x_0} x^2 [g_1(x, Q^2) + g_2(x, Q^2)] dx \quad (185)$$

Note the factor Q^{-6} in the definitions. This means, unlike some of the other generalized integrals, γ_0 and δ_{TL} still manage to preserve quantifiable values at very small Q^2 . The forward spin polarizabilities exploit soft, non-perturbative aspects of the nucleon structure. Therefore, they provide an excellent ground for testing χ PT theories, which are only valid at $Q^2 < 0.1 \text{ GeV}^2$.

II.4.7 Phenomenological Models

In the kinematic region below $Q^2 \approx 0.1 \text{ GeV}^2$ the generalized GDH Sum Rule and χ PT theory should be applicable. Above $Q^2 = 1 \text{ GeV}^2$, one can utilize OPE, pQCD and the modified Bjorken Sum Rule. Constraints enforced by the sum rules govern the Q^2 evolution of Γ_1^1 in these regions. In the low Q^2 region, Γ_1^1 is expected to be negative and approach to 0 as $Q^2 \rightarrow 0$. In the high Q^2 region, on the other hand, Γ_1^1 should asymptotically approach a constant positive value. This indicates that Γ_1^1 should cross zero somewhere in the range of $0.2 < Q^2 < 1.0 \text{ GeV}^2$. This region is known to be dominated by the nucleon resonances, where we don't have a good theoretical understanding of the Q^2 dependence of the structure functions. For that reason, experimental data in the resonance region are very important. This is one of the main goals of the EG1b experiment. There are Lattice QCD calculations and some phenomenological models that try to describe the Q^2 behavior of the structure functions in this kinematic region. In this section, we will discuss two models, with which we compare our results.

The Q^2 evolution of the GDH integral was parametrized by Anselmino [62] and later refined by Burkert and Ioffe [63] by splitting the quantity into resonant and non-resonant parts:

$$I_{GDH}(Q^2) = \frac{2M^2}{Q^2} \bar{\Gamma}_1^1(Q^2) = I^{res}(Q^2) + I'(Q^2) \quad (186)$$

where I^{res} is the contribution from the resonant states and decreases rapidly with increasing Q^2 . This contribution is of course also unknown a priori, but can be approximated by the amplitudes for $\gamma^*N \rightarrow N^* \rightarrow N\pi$, which are reasonably well known from phase shift analysis of π (virtual) photo-production. The integral I_{GDH} in this equation satisfies $I_{GDH}(Q^2 = 0) = -\kappa^2/4$. The term I' has the following form, inspired by vector meson dominance models [64] of photon-nucleon interaction,

$$I'(Q^2) = 2M^2\Gamma^{as} \left[\frac{1}{Q^2 + \mu^2} - \frac{c\mu^2}{(Q^2 + \mu^2)^2} \right] \quad (187)$$

where Γ^{as} is the asymptotic value of $\Gamma_1^1(Q^2 \rightarrow \infty)$, used as a constraining parameter, and μ is a mass parameter that characterizes the scale of the Q^2 variation and is taken at the ρ or ω mass. The variable c is determined by using the GDH sum rule at the real photon point,

$$I_{GDH}(Q^2 = 0) = I^{res}(0) + I'(0) = -\frac{1}{4}\kappa^2, \quad (188)$$

yielding

$$c = 1 + \frac{1}{2} \frac{\mu^2}{M^2} \frac{1}{\Gamma_{as}} \left[\frac{1}{4} \kappa^2 + I^{res}(0) \right] \quad (189)$$

This parametrization predicts a change of sign for $\Gamma_1^1(Q^2)$ at $Q^2 \sim 0.3 \text{ GeV}^2$. This occurs due to the contribution of the $\Delta(1232)$ resonance, which has a large negative contribution to Γ_1^1 at small Q^2 .

Another parametrization of Γ_1^1 is provided by Soffer and Teryaev [65]. They considered the sum,

$$\Gamma_{1+2}^1(Q^2) = \Gamma_1^1(Q^2) + \Gamma_2^1(Q^2) \quad (190)$$

where

$$\Gamma_2^1(Q^2) = \int_0^1 g_2(x, Q^2) dx \quad (191)$$

is the first moment of the spin structure function g_2 . Therefore, the GDH integral can be calculated as

$$I_{GDH}(Q^2) = \frac{2M^2}{Q^2} \bar{\Gamma}_1^1(Q^2) = \frac{2M^2}{Q^2} [\bar{\Gamma}_{1+2}^1(Q^2) - \bar{\Gamma}_2^1(Q^2)] \quad (192)$$

with $I_{GDH}(Q^2 = 0) = -\kappa^2/4$. For all Q^2 , Γ_2^1 is constrained by the Burkhardt-Cottingham sum rule (BCSR) [66],

$$\Gamma_2^1 = \int_0^{1+\epsilon} g_2(x, Q^2) dx = 0, \quad (193)$$

where the integral includes the elastic contribution. At large $Q^2 \rightarrow \infty$, $\bar{\Gamma}_2^1 \approx \Gamma_2^1 = 0$, which means at large Q^2 , the main contribution to $\bar{\Gamma}_{1+2}^1(Q^2)$ comes from the asymptotic value of $\bar{\Gamma}_1^1(Q^2)$, thus $\bar{\Gamma}_{1+2}^1(Q^2)$ is known for large Q^2 . On the other hand, at the real photon point, $Q^2 = 0$, it follows from the BCSR that [65]

$$\bar{\Gamma}_2^1(0) = \Gamma_2^1(0) - \text{elastic contribution} = \frac{Q^2}{8M^2} (\kappa^2 + e\kappa) \quad (194)$$

$$\Gamma_1^1(0) = -\frac{Q^2}{8M^2} \kappa^2 \quad (\text{GDH sum rule}) \quad (195)$$

where e is the nucleon charge and κ is the anomalous magnetic moment of the nucleon. Therefore we have,

$$\bar{\Gamma}_{1+2}^1(0) = \frac{Q^2}{8M^2} e\kappa \quad (196)$$

Therefore, since $\bar{\Gamma}_{1+2}^1(Q^2)$ is known for both large Q^2 and at $Q^2 = 0$, and it is positive at both limits, a smooth parametrization can be performed between the two limits. Parameterizing the positive $\bar{\Gamma}_{1+2}^1(Q^2)$ is an advantage over parameterizing $\bar{\Gamma}_1^1(Q^2)$

because it avoids a sign change. Unfortunately, this approach will not work for the neutron since its charge is 0, implying $\Gamma_{1+2}^{1(n)}(0) = 0$. For the proton case, on the other hand, [65] suggests the following parametrization:

$$\bar{\Gamma}_{1+2}^1(Q^2) = \theta(Q_0^2 - Q^2) \left[\frac{e}{4} \kappa_p - \frac{Q^4}{Q_0^2} \bar{\Gamma}_1^1(Q^2) \right] + \theta(Q_0^2 - Q^2) \bar{\Gamma}_1^1(Q^2) \quad (197)$$

with

$$Q_0^2 = \frac{16M^2}{e\kappa_p} \bar{\Gamma}_1^{1(p)} \sim 1 \text{ GeV}^2 \quad (198)$$

The value of $\Gamma_1^{1(p)} = 0.128$ was initially taken from the EMC experiment. This choice of Q_0^2 ensures the continuity of the function and its derivative. Once $\Gamma_{1+2}^1(Q^2)$ is parametrized, $\Gamma_1^1(Q^2)$ can be deduced from $\Gamma_1^1(Q^2) = \Gamma_{1+2}^1(Q^2) - \Gamma_2^1(Q^2)$. This, however, requires the Q^2 dependence of $\Gamma_2^1(Q^2)$, which is provided by the Schwinger sum rule,

$$\bar{\Gamma}_2^1(Q^2) = \frac{Q^2}{8M^2 + 2Q^2} \mu G_M(Q^2) [\mu G_M(Q^2) - G_E(Q^2)] \quad (199)$$

where G_E and G_M are the electric and magnetic form factors of the nucleon and μ is the nucleon magnetic moment. In the latest model from Soffer and Teryaev, $\Gamma_1^{1(p)}$ crosses zero is at $Q^2 \sim 0.25 \text{ GeV}^2$.

Experimental verification of all these models and calculations is crucial in order to understand the dynamics of the spin variables inside the nucleon or nuclei. Fig. 10 shows the expected Q^2 evolution of Γ_1^1 for the proton and the deuteron from different calculation methods and previous experiments. Filling the missing kinematic regions and mapping the entire Q^2 range in the resonance region and beyond is one of the biggest motivations of the EG1b experiment.

II.5 THE DEUTERON, A CLOSER LOOK

In previous sections, we explained how the asymmetries, the GDH integral and some other quantities that are related to nucleon structure can also be applied to a deuteron with modifications that arise from nuclear effects. In this section, we will take a closer look at the deuteron.

The deuteron is a stable nucleus, composed of a proton and a neutron with a binding energy of $\sim 2.2 \text{ MeV}$. It has a mass of 1875.6 MeV . It is the only bound system of two nucleons found in nature. Since they are both fermions, the total wave function of both the proton and neutron must be antisymmetric. The deuteron

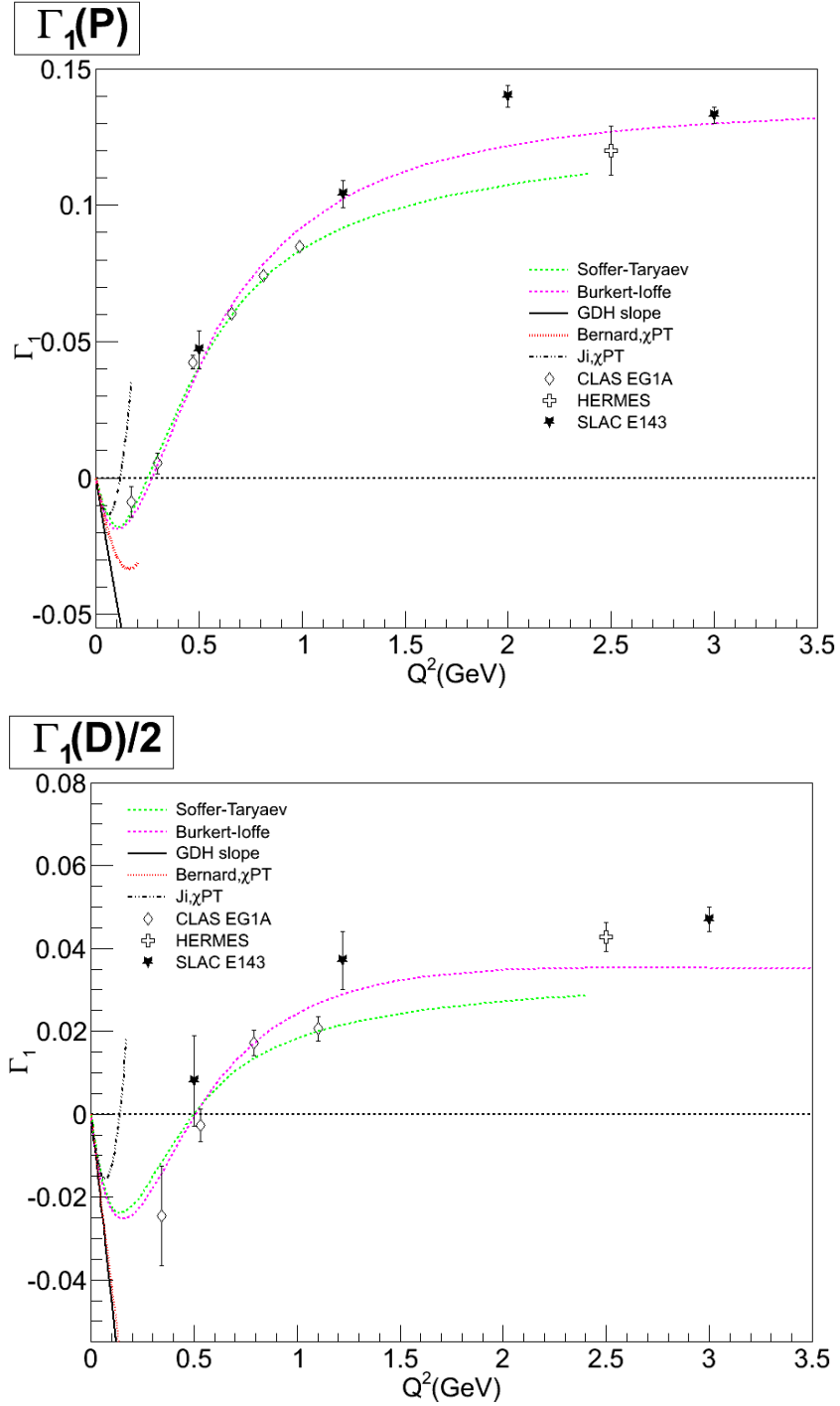


FIG. 10: Predictions from phenomenological models [59][60][63][65] for the Q^2 evolution of $\Gamma_1^{1(p)}$ (top) and $\Gamma_1^{1(d)}$ per nucleon (bottom). SLAC E143 [45], HERMES [48] and the previous CLAS EG1a [67][68] data are also shown.

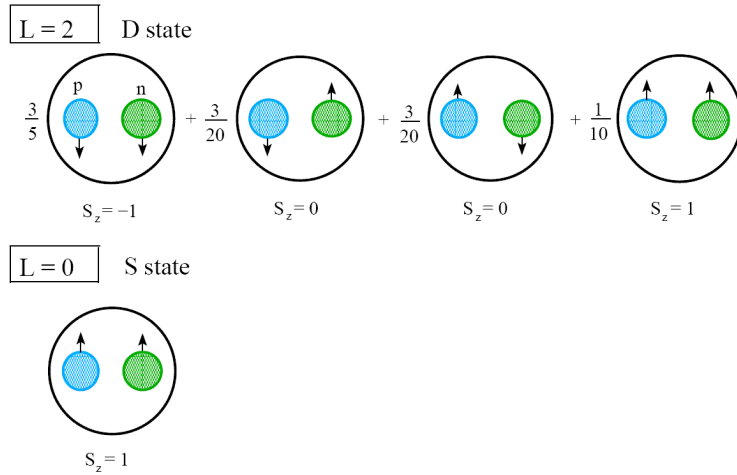


FIG. 11: Deuteron spin states as a combination of the proton and neutron spins. Two possible angular momentum states are shown: $L = 0$ (S-state) and $L = 2$ (D-state).

is an isospin singlet state (antisymmetric under the exchange of the proton and the neutron). Apart from their isospin, the two nucleons have also their spins and spatial distributions (locations). The symmetry for the exchange of the locations of the member nucleons is called parity, often denoted by P . If the exchange is symmetric, the parity is said to be even or positive. If it is antisymmetric, the parity is odd or negative. The parity is determined by the total orbital angular momentum L of the two nucleons by $P = (-1)^L$. Being an isospin singlet state, the deuteron must be symmetric under the double exchange of the spins and the locations of the member nucleons. Therefore, the deuteron can either be in a symmetric spin and even parity or an antisymmetric spin and odd parity states. The former case forms a spin triplet state with total spin $S = 1$. The even parity requires the total orbital angular momentum $L = 0, 2, \dots$. The ground state prefers the lowest possible orbital angular momentum. The latter case forms a spin singlet state with total spin $S = 0$. However, the spin singlet state does not lead to a bound state for the deuteron. Somehow, the nuclear force prefers the spin triplet state while the singlet state is just (barely) unbound. Therefore, at first approximation, the deuteron ground state has $S = 1$, $L = 0$ (even parity), which means the total angular momentum $J = 1$. This is called the S-state of the deuteron. However, the $L = 2$ state is also possible, which is called the D-state. Indeed, the sum of the magnetic moments for the member nucleons,

$\mu(\text{proton}) + \mu(\text{neutron}) = 0.8797$, is slightly different than the precisely measured magnetic moment of the deuteron, $\mu(\text{deuteron}) = 0.8574$. This deviation indicates that the higher orbital angular momentum states are contributing to the deuteron wave function. The deuteron also has a non-zero electric quadrupole moment, which means the electric charge inside the deuteron is not spherically distributed. That is another indication that the deuteron is not a simple spherically symmetric S-state with $L = 0$ but it is a mixture of the S and D states. The S-state can be written as:

$$|J = 1, J_z = 1\rangle = |L = 0, L_z = 0\rangle|S = 1, S_z = 1\rangle. \quad (200)$$

Therefore, the spins of the proton and the neutron are both aligned with the spin of the deuteron. In the D-state, however, the z projection of the nucleon spins is not always aligned with the total angular momentum. Both nucleons can have their spins oriented in opposite direction to the spin of the deuteron (see Fig. 11). The D-state is written as:

$$\begin{aligned} |J = 1, J_z = 1\rangle &= \sqrt{\frac{1}{10}} |L = 2, L_z = 0\rangle|S = 1, S_z = 1\rangle \\ &- \sqrt{\frac{3}{10}} |L = 2, L_z = 1\rangle|S = 1, S_z = 0\rangle \\ &+ \sqrt{\frac{3}{5}} |L = 2, L_z = 2\rangle|S = 1, S_z = -1\rangle. \end{aligned} \quad (201)$$

The probability of finding the deuteron in the D-state is $w_D \approx 0.056$. Therefore, the likelihood of finding a nucleon with spin down is $\frac{3}{4}w_D$ (see Fig. 11). If we ignore nuclear effects, which will be explained later, the following relations between the deuteron and nucleon cross sections can be derived:

$$\sigma_d^{\uparrow\downarrow} = \left(1 - \frac{3}{4}w_D\right) \sigma_N^{\uparrow\downarrow} + \frac{3}{4}w_D \sigma_N^{\uparrow\uparrow} \quad (202)$$

$$\sigma_d^{\uparrow\uparrow} = \left(1 - \frac{3}{4}w_D\right) \sigma_N^{\uparrow\uparrow} + \frac{3}{4}w_D \sigma_N^{\uparrow\downarrow} \quad (203)$$

where the first arrow indicates the electron beam helicity while the second arrow is the spin direction of the target with respect to the electron. If we normalize the deuteron cross section σ_d as ‘‘per nucleon’’, the nucleon cross section above is given by $\sigma_N = (\sigma_p + \sigma_n)/2$. By substituting these into Eq. (62), we obtain,

$$A_1^d = \left(1 - \frac{3}{2}w_D\right) \left[\frac{\sigma_p^T A_1^p + \sigma_n^T A_1^n}{\sigma_p^T + \sigma_n^T} \right]. \quad (204)$$

By using Eqs. (52 - 53), the cross sections can be replaced by the structure functions so that g_1^d can be written as

$$g_1^d(x, Q^2) = \left(1 - \frac{3}{2}w_D\right) \left[\frac{g_1^p(x, Q^2) + g_1^n(x, Q^2)}{2}\right], \quad (205)$$

where the factor $1/2$ is introduced by convention because the deuteron structure functions are typically given “per nucleon”. The correction factor represents the ratio of the polarization P_N of the member nucleon to the polarization of the deuteron, P_D [69] (see Eqs. (202 - 203)).

II.5.1 Extraction of Neutron Information from A Deuteron Target

One of our purposes is to extract neutron information from the deuteron and proton data. In order to extract the nucleon structure function from a measurement on a nucleus, we need to understand the effects of the nuclear medium on the nucleon structure. Once we understand these effects, we can make the necessary corrections on the deuteron structure function and extract the neutron information by using deuteron and proton data. Moreover, by comparing our results to the available neutron data from ^3He targets [70], for example, we can justify our understanding of the nuclear medium and its effects on the nucleon structure. The EG1b data will make an important contribution to the neutron spin structure and reduce the uncertainties substantially over a good kinematic range of x and Q^2 .

In the resonance region, for spin structure functions, the most important nuclear effects are considered to be the Fermi motion and the depolarizing effect of the D-wave [71]. The correction for the depolarizing effect of the D-wave is described in the previous section in Eqs. (204) and (205). Although this is the most important correction for $x < 0.7$, the additional corrections are required, especially for larger x [72], the most important of which being the Fermi motion. There are additional effects such as off-shell mass effect and the EMC effect that should be considered. However, those are found to be relatively small corrections [71]. In the following sections, we summarize the corrections required to extract neutron information from deuteron and proton data.

Fermi Motion

Bound nucleons are moving inside the nucleus, causing kinematic shifts and Doppler broadening of peaks in the cross section. If we assume that the proton and neutron

spin structure functions have similar behavior in the resonance region, the positions of the nucleon resonances should be the same for both nucleons. However, in case of the deuteron, the resonance peaks may be smeared and shifted because of the Fermi motion of the nucleons. If one tries to extract the neutron structure functions by subtracting the proton from the deuteron, the maximum of the proton structure function may become the minimum of the neutron structure function. This turns the Fermi smearing into an important effect to consider while extracting neutron information from the deuteron and proton data.

Recently it was suggested by [73] that a convolution method can be used iteratively to take these effects into account and extract the neutron structure functions from nuclear data. The method uses convoluted proton and neutron structure functions (SFs) to model the deuteron and relies on the knowledge of the proton and deuteron to iteratively extract the neutron SFs. A predefined input function for the neutron is evolved iteratively until the function becomes stable. Currently, the convolution only corrects for the Fermi motion and the D-state of the deuteron and disregards other nuclear effects. Still, the method is suitable to incorporate other corrections as they are modeled. It has been successfully tried on the unpolarized structure functions. However, the convolution method is only well proven for functions with no sign change. On the other hand, the spin structure function g_1 has several sign changes in the resonance region. This causes the iterative method to fail in some kinematic regions. This mainly happens if one uses data with errors for the proton and deuteron. Using parameterizations of the structure functions, instead, makes the method more reliable. The results of the EG1b experiment, with both the proton and the deuteron data, provides a perfect environment to test this method. More information on this together with parameterizations of the world asymmetry data are given in chapter VI.

Off-Mass Shell Effects

The deuteron is made up of a proton and a neutron. But because of the negative contribution coming from the binding energy to the overall mass of deuterium, $M_d = M_p + M_n - 2.2 \text{ MeV}$, both nucleons cannot be on the mass shell at the same time. Moreover, the nucleons will also have relativistic motion and their total energy should be calculated by $\sqrt{M_p^2 + p_p^2} + \sqrt{M_n^2 + p_n^2} \gg M_d$, therefore, the mass of a bound nucleon is much smaller than that of a free one in this picture. Various corrections

for this off-shell effect have been proposed.

EMC Effect

This effect can be summarized as the observed dependence of the cross section per nucleon on the nuclear medium. It was first observed by the EMC Collaboration [42]. It is due to the distortion of the free-nucleon structure function by the nuclear medium. The effect has a strong kinematical dependence being most pronounced at large $x > 0.5$. However, currently we don't have a reliable model of the EMC effect in the deuteron, thus, this effect is not included into our method to extract the neutron SF from the deuteron data. More information on the EMC effect can be found in [6][74][75].

Effects of non-nucleonic states

Effects of nucleonic resonance states and pions (meson exchange currents) as part of the structure of the deuteron should also be considered. According to the six quark bag model of the deuteron, one should include direct correlations between quarks and gluons in the proton and neutron. Finally, one could consider nuclear shadowing, which is re-scattering of the lepton from both nucleons in the deuteron or from the meson cloud within the nucleus. However, there is no universally accepted quantitative model for the deuteron which corrects for these effects.

II.6 SUMMARY

We described the theoretical background and purpose of the EG1b experiment. Since the "spin crisis", many experimental data have been collected to explain the spin of the nucleon. More data are still needed to understand the full picture. The EG1b experiment covered a very important kinematic range that has not been explored by previous experiments. The data generated by the experiment will help to put further constraints on the contribution of different quark flavors to the total spin of the nucleon. EG1b is one of the very few experiments with high statistics and very large kinematic coverage. The data will map the dependence of the spin structure functions on the four-momentum transferred and the momentum fraction carried by the struck quark. Moreover, the results will provide new information on resonance

excitations, duality, higher twist coefficients and the approach to $Q^2 = 0$, especially for the neutron.

The analysis presented in this thesis is mainly focused on the deuteron data for all beam energies. The proton data are also analyzed in parallel with the deuteron data. The combined analysis will utilize the large statistics of the experiment at full extend. This will be very useful to extract the neutron information by using the fact that a deuteron is a bound state of a proton and a neutron. Since they have no electric charge, manipulating and polarizing free neutrons is very difficult with the technology at hand. Moreover, a neutron is radioactive and decays into a proton when it is not in a bound state. As a result, we have a very limited information on the neutron spin structure. The EG1b experiment will be one of the major contributors to the scientific information on the spin structure function of the neutron.

CHAPTER III

EXPERIMENTAL SETUP

III.1 CONTINUOUS ELECTRON BEAM ACCELERATOR FACILITY

The EG1b experiment has been carried out using the electron beam provided by the Continuous Electron Beam Accelerator Facility (CEBAF) at the Thomas Jefferson National Accelerator Facility (TJNAF). A schematic of the machine is shown in Fig. 12. CEBAF is composed of two linear accelerators joined by two 180° arcs with a radius of 80 meters. Each recirculating arc is composed of five separate beam line sections. There is also a 45 MeV injector delivering polarized electrons obtained from a strained GaAs photocathode source by inducing excitations using a circularly polarized laser beam. Another component that should be mentioned at this point is the half wave plate (HWP) that can be inserted in the laser beam to change the polarization phase of the produced electron beam by 180°. The status of the HWP (in or out) was changed periodically during the experiment to make sure no polarity dependent bias was created on the asymmetry. If the HWP is in, the beam helicity requires an extra negative sign.

The accelerator is based on 338 superconducting radio-frequency (SRF) cavities that boost the beam with radio-frequency waves. Eight SRF cavities are grouped together to make a cryomodule. In each linear accelerator, there are twenty cryomodules. In order to maintain the superconductivity, all cryomodules are cooled to 2 Kelvin by liquid helium, produced at the Lab's Central Helium Liquefier.

The beam has a 1.497 GHz micro bunch structure. Connected by two recirculating arcs, the two parallel linacs can accelerate the beam up to five times boosting the beam energy up to 1.2 GeV for each turn. The accelerator can provide a high luminosity continuous electron beam with energies ranging between 800 MeV and 5.8 GeV. There are quadrupole and dipole magnets in the tunnel to steer and focus the beam as it passes through each arc. More than 2,200 magnets are necessary to keep the beam on a precise path and tightly focused. The energy spread of the beam is around $\Delta E/E < 10^{-4}$.

CEBAF is designed to deliver polarized or unpolarized electron beam to three experimental areas simultaneously. These experimental areas are called Hall-A, B and C. Beam is directed into each experimental hall's transport channel using

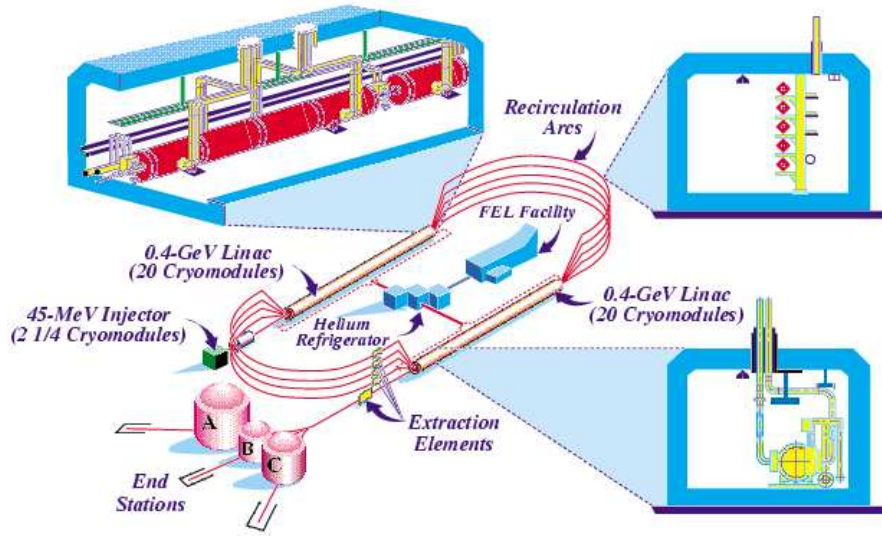


FIG. 12: A schematic view of the CEBAF accelerator. One of the cryomodules is shown in the upper left corner. A vertical cross section of a cryomodule is shown in the lower right corner. A cross section of the five recirculation arcs is shown in the upper right corner.

magnetic or RF extraction. The RF scheme uses 499 MHz cavities, which kick every third bunch out of the machine. A typical bunch length is 1.7 ps. The EG1b experiment took place in Hall B, which is shown in Fig. 13.

The orientation of the electron spin can be selected at the injector by using a Wien filter [17], consisting of perpendicular electric and magnetic fields transverse to the electron momentum. The Wien filter can rotate the polarization of the beam without disturbing the momentum. The electric field is adjusted for a desired spin rotation and the magnetic field is used to make the net Lorentz force on the electron zero. The total precession angle depends on the number of passes and the beam energy.

III.2 HALL B BEAM-LINE

Hall B houses the CEBAF Large Acceptance Spectrometer (CLAS). The electron beam delivered to Hall B is monitored by several devices. Beam position monitors (BPMs) measure the intensity and the position of the beam in real-time with resolution better than $100 \mu\text{m}$. There are three BPMs located at 36.0 m, 24.6 m and 8.2 m upstream of CLAS, which read the intensity of the beam at a rate of 1 Hz.

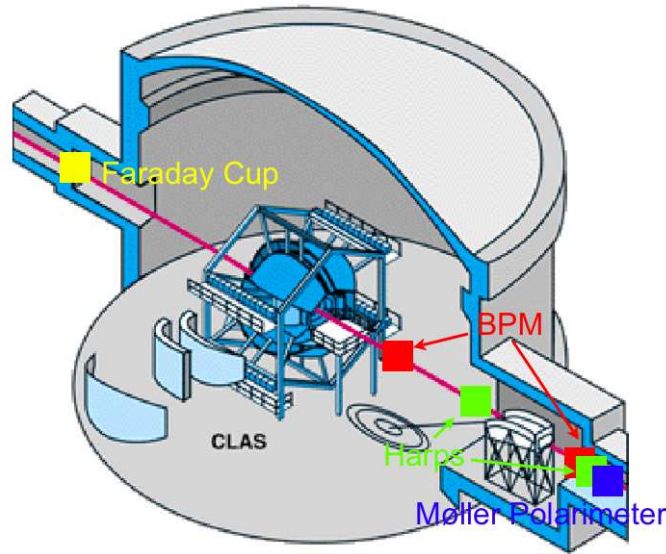


FIG. 13: A schematic view of Hall B and the beam line monitoring devices: Beam position monitors (BPM), harps and the Moller polarimeter. The Faraday cup is also shown downstream. These components are explained throughout the text.

A “Harp” is located upstream from the center of the CLAS detector to measure the beam profile. The Harp is a system of thin wires. The beam position in the x and y direction is measured by moving the wires through the beam by using stepper motors while no physics data are taken. Cerenkov light produced by scattered electrons is measured in photomultiplier tubes to obtain x and y distributions of the beam. The acceptable width of the beam distribution is typically less than $200 \mu\text{m}$.

The EG1b experiment used longitudinally polarized beam. The polarization of the beam was monitored by a Moller polarimeter at the entrance of Hall B. Separate Moller runs had to be taken periodically in order to measure the beam polarization. A typical Moller measurement carries a statistical uncertainty of about 1% and takes around 30 minutes. Fig. 14 shows the diagram of the Moller polarimeter as viewed from above. It consists of a target chamber, two quadrupole magnets and two detectors. The target chamber encapsulates a permendur foil (alloy of 49% cobalt, 49% iron and 2% vanadium), oriented at ± 20 degrees with respect to the beam line and magnetized by a coil system. The two quadrupoles are used to separate the scattered electrons from the unscattered beam. These electrons are later detected and the number of coincidences for each helicity state are recorded to calculate the asymmetry. The interaction between the electron beam and the polarized permendur

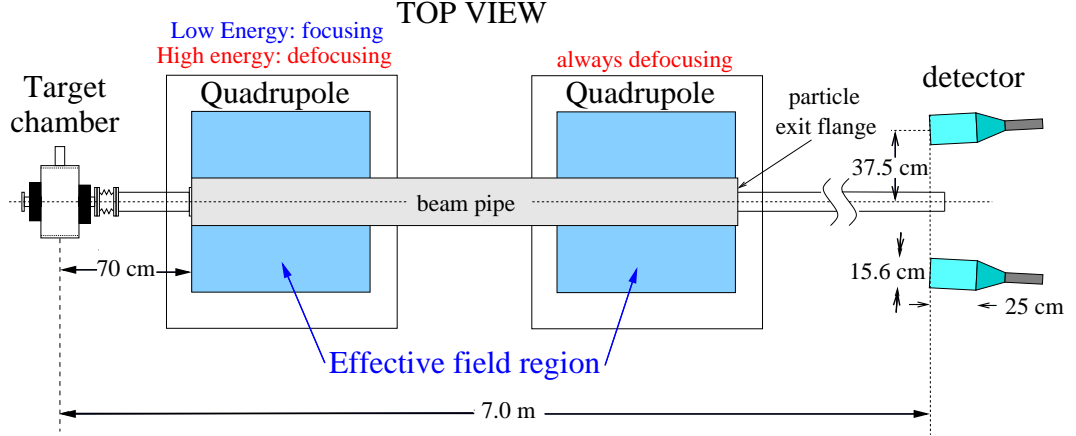


FIG. 14: Top view schematic diagram of the Hall B Moller polarimeter [76].

target can be expressed in terms of the beam (P^b) and the target (P^t) polarizations as [77]:

$$\frac{d\sigma}{d\Omega} \propto \left(1 + \sum_{i,j=x,y,z} P_i^t A_{ij} P_j^b \right) \quad (206)$$

where, the parameters A_{ij} are defined as:

$$-A_{xx} = A_{yy} = \frac{\sin^4 \theta_{CM}}{(3 + \cos^2 \theta_{CM})^2} \quad (207)$$

$$-A_{zz} = \frac{(7 + \cos^2 \theta_{CM}) \sin^2 \theta_{CM}}{(3 + \cos^2 \theta_{CM})^2} \quad (208)$$

$$A_{ij} \approx 0 \quad \text{for } i \neq j \quad (209)$$

The electron beam is in the z direction, θ_{CM} represents the scattering angle in the center of mass frame. Therefore, knowing the differential cross section, the target polarization and the scattering parameters, one can calculate the beam polarization. In the EG1b experiment, the beam polarization was around 70%. Although the beam polarization was monitored during the experiment, the results of Moller measurements were only used for a consistency check. In the EG1b experiment, the beam times the target polarization is deduced from the elastic scattering events, which is explained in section IV.13.

At the very end of the beam line, the Faraday cup (FC) measures and records the accumulated beam charge. This is used to determine the flux of the beam, which is later used for normalization purposes while calculating the cross sections. The Faraday cup signal is gated with respect to the beam helicity so that it is recorded

separately for each beam helicity (+ or -) and used to measure the beam charge asymmetry defined by,

$$A_{beam} = \frac{FC^+ - FC^-}{FC^+ + FC^-}. \quad (210)$$

The FC is the final stop for the electron beam. It is made of 4 tons of lead and is 70 radiation lengths deep. During the experiment, the FC reading was halted when the readout electronics were busy. This is known as the live-time gated FC. Ungated FC readings, which measure the total accumulated beam charge, were also taken for both helicities. By using the ungated FC readings, the beam charge asymmetry was calculated for all data files and monitored for data quality (see section IV.5). Another way of measuring the beam charge asymmetry is by using the readings from the Synchrotron Light Monitor (SLM), which is located at the beam injector. SLM ungated and live-time gated readings are also available in the EG1b data for each beam helicity. Comparing the beam charge asymmetry at the SLM (at the start of the beam) and the FC (at the stop of the beam) can be an interesting way of deducing the beam quality. Fig. 15 shows the comparison of the beam charge asymmetry from both sources.

III.3 CEBAF LARGE ACCEPTANCE SPECTROMETER

CLAS is a unique detector, with almost 4π coverage, that can be used to investigate reaction mechanisms of electron scattering because it allows detection of almost all charged particles as well as neutrons and photons emitted after the absorption of a virtual photon during the scattering. Superconducting coils separate the detector into six equivalent sectors.

Each sector in CLAS acts as an independent spectrometer. In each sector there are three units of Drift Chamber (DC) assemblies to determine the trajectories and momenta of charged particles, Cherenkov Counters (CC) for electron identification, Scintillation Counters (SC) for time-of-flight (TOF) measurements, and an Electromagnetic Shower Calorimeter (EC) to identify showering particles such as electrons and photons and to detect neutral particles such as neutrons (see Fig. 16). Combinations of any of these detectors may be used to build a desired trigger configuration for the reaction of interest. The polar angle coverage in CLAS varies from 8° to 140° for the DC, 8° to 142° for the SC, and 8° to 45° for the CC and EC detectors. In the following sections, brief descriptions will be given for each of these components

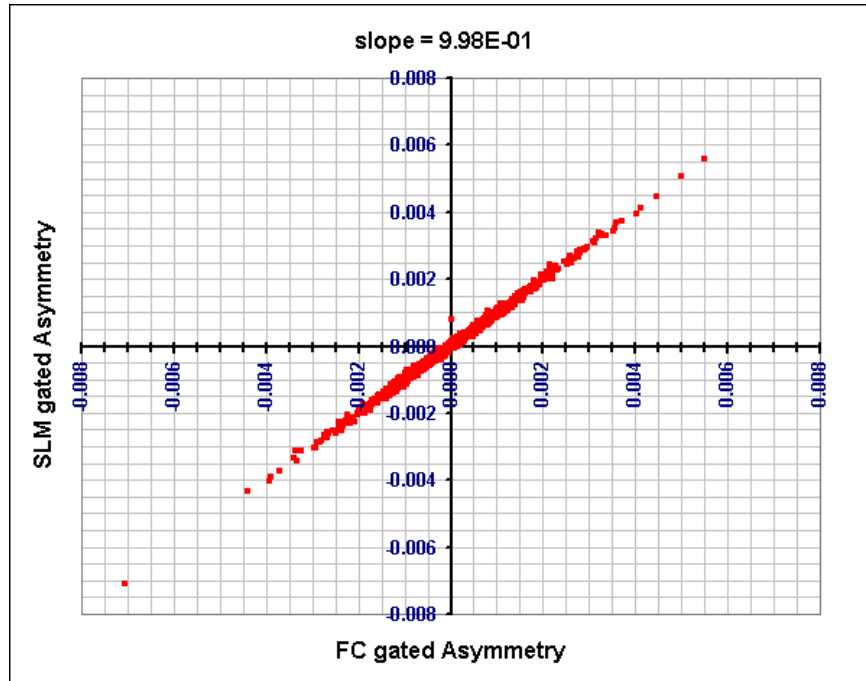


FIG. 15: Comparing the beam charge asymmetry measurements from the Faraday Cup and the Synchrotron Light Monitor. The linear relationship is a sign of good beam quality.

of the CLAS detector .

III.3.1 Torus Magnet

The torus magnet consists of six superconducting coils as shown in Fig. 17. The purpose of the coils is to produce a magnetic field, which is generally referred to as the torus field, inside the detector system. The coils are arranged around the beam line to produce a magnetic field of up to 2 Tesla primarily in the azimuthal direction about the beam axis. This magnetic field enables us to measure the momentum of a charged particle by inducing a curvature in its path. In addition the coils serve as a support structure for the rest of the detector assemblies. The toroidal magnetic field configuration has a few advantages for the CLAS detector:

- Allows homogeneous geometrical coverage of charged particles at large angles.
- Provides good momentum and angle resolution and low background from electromagnetic interactions.

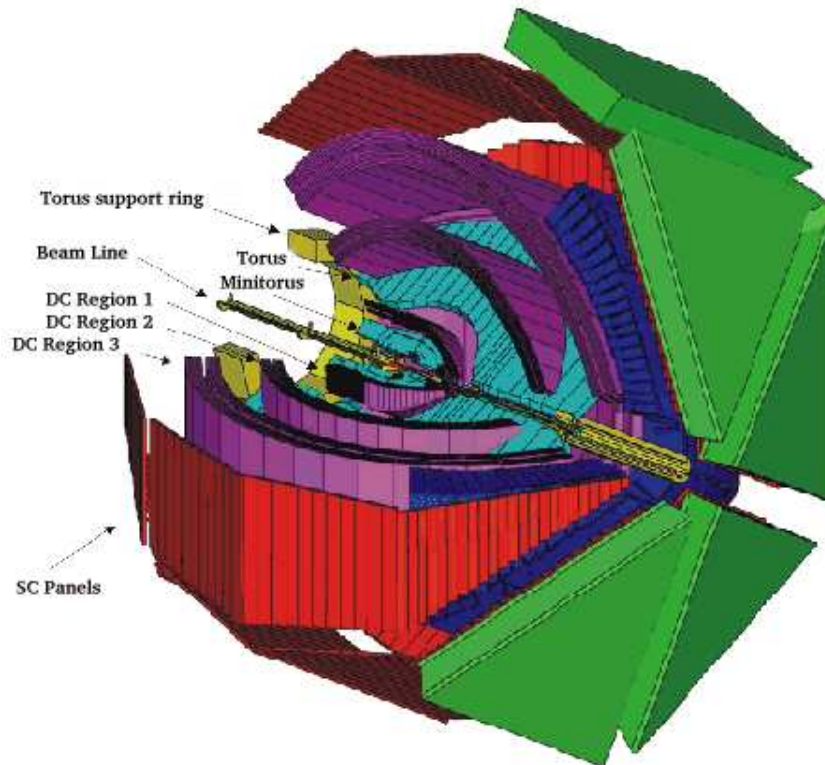


FIG. 16: Three dimensional view of CLAS. Three layers of DC are shown in purple, CC in dark blue, SC in red and EC in green.

- Leaves a field free region at the center of the detector around the target, which is a very useful feature for implementing polarized targets there.

The direction of the beam line defines the z coordinate of the detector system. Then the horizontal and vertical directions are the x and y coordinates respectively. The polar angle θ is the angle between a scattered particle and the z coordinate. The azimuthal angle ϕ is the angle of scattering projected on the x - y plane. The reference angle for ϕ is taken as the center of sector 1. Each coil consists of 4 layers of 54 turns of aluminum-stabilized NbTi/Cu conductor. The coils are surrounded by cooling tubes that constantly circulate liquid helium so that the coils are kept at superconducting temperature of 4.5 K. The maximum design current of the coil is 3860 A, which creates a magnetic field of 2.5 Tesla-meters integrated along the forward direction and the field drops to 0.6 Tesla-meters at a polar angle of 90 degrees. Operation of the torus, on the other hand, has been limited to 3375 A to avoid any failure. A

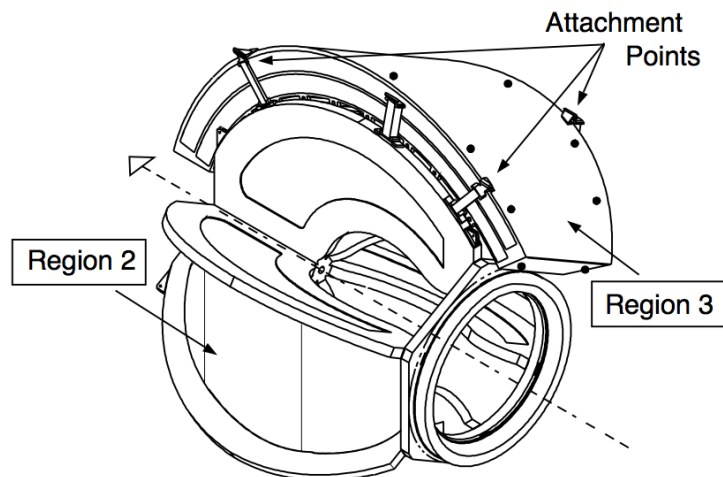


FIG. 17: Configuration of the torus coils is shown. This configuration effects the placement of the drift chambers creating three different regions.

contour plot of the magnetic field of CLAS in the mid-plane between two coils is shown in Fig. 18. The direction of the current can be changed in the coils, thus creating different configurations for the magnetic field. In one configuration, called inbending, the negative particles are curved toward the beam-line. In the outbending configuration, negative particles are curved away from the beam-line.

III.3.2 Drift Chambers

In the EG1b experiment, the trajectories and momenta of the charged particles are measured by the drift chambers (DC) [78]. A drift chamber is a detector for particles of ionizing radiation. It operates on the principle that a charged particle traveling through a carefully chosen gas will ionize surrounding atoms/molecules. If one introduces wires with positive electric potential into such an environment, the resulting electrons from ionization will be accelerated toward the nearest wires by the electric field created between the wires. If the electric field is high enough, the electrons will reach a point where they have enough kinetic energy to liberate other electrons and ions in collisions with surrounding atoms/molecules in the gas. The resulting cascade of ionization is eventually collected on the wire and creates a flow of current. This current is later detected by electronic sensors. The location of the wire gives an idea about the path of the ionizing particle. If one also precisely measures the timing of the signal on the wire and takes into account that the electrons need

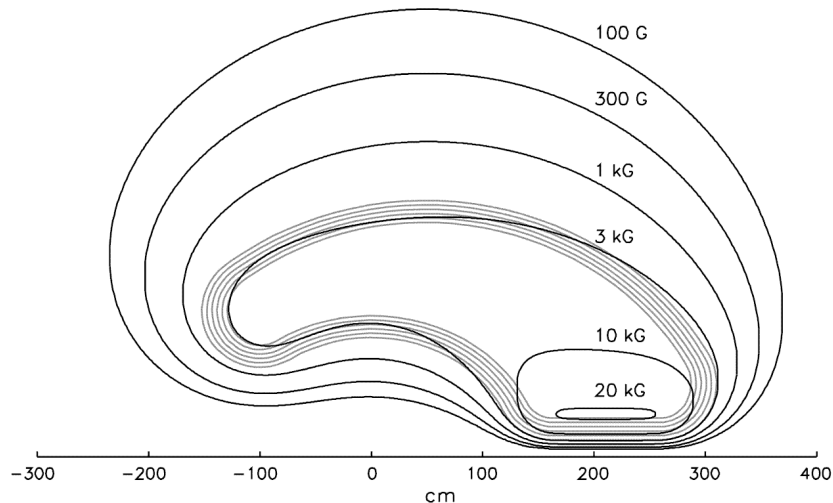


FIG. 18: A contour magnetic field of the CLAS torus magnet in the mid-plane between two coils.

some time to drift to the nearest wire, one can infer the distance at which the particle passed the wire. This greatly increases the accuracy of the path reconstruction. The electric signal passes through a preamplifier, an amplifier, a discriminator and 2:1 multiplexer and then starts a TDC. The TDCs are stopped by the event trigger. More details on the DC and their calibration are given in section IV.2.2.

The CLAS has multi-layers of drift chamber assemblies in each sector that can be grouped into three main regions. Region 1 is the closest one to the target and it resides in a low magnetic field region inside the torus bore. It is used to determine the initial direction of charged particle tracks. Region 2 is located between the coils, where there is a high magnetic field up to 2 Tesla. Region 3 is the outermost layer, located outside the coils (see Figs. 16 and 17).

Each region of drift chamber has two super-layers. In each super-layer, there are 6 layers of hexagonal cells, except for the first super-layer of the region 1 drift chamber, which has 4 layer of cells. Each hexagonal cell has six field wires at the corners of the hexagon, which work as cathode. At the center, there is the sense wire which is the anode (see Fig. 19). The hexagonal shape is the most cost-effective shape to minimize the error in drift time to drift distance conversion. In each region of drift chambers, there is one axial and one stereo super-layer. Axial wires follow the direction of the torus magnetic field (perpendicular to the direction of the beam). Stereo wires, on the other hand, are oriented at an angle of 6 degrees relative to the

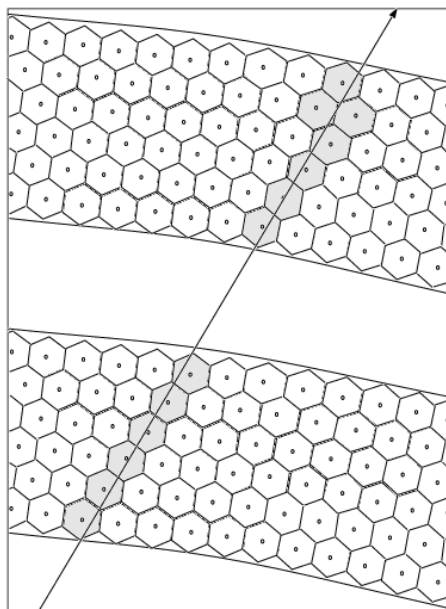


FIG. 19: Cross-sectional picture of a drift chamber with two super-layers. The sense wires (anode) are located at the center of hexagonal cells created by the surrounding field wires (cathode). The arrow shows a charged particle passing through the drift chamber and the shadowed hexagons represent the cells that give a signal.

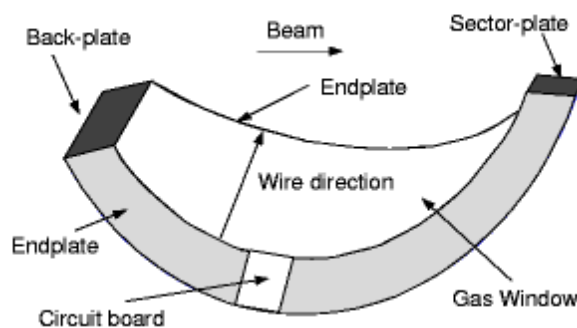


FIG. 20: CLAS drift chamber for one sector.

axial wires. This combination in each region allows one to determine the azimuthal angle ϕ of the particle. Fig. 20 shows a single sector drift chamber box in the shape of an onion slice. Wires extend from end plate to end plate, on which the circuit boards are mounted. The beam direction is also shown in the picture. The box is filled with a gas mixture of 88% argon and 12% carbon dioxide. This mixture provides a drift velocity of typically 4 cm/ μ sec. The radius of the hexagonal cells increases semi-uniformly from region 1 to region 3. It is 0.7 cm in region 1, 1.5 cm in region 2 and 2 cm in region 3. Each of the sense wires, made from gold plated tungsten, has a diameter of 20 μ m, while the field wires, which are aluminium, are 140 μ m in diameter. The drift chambers can detect charged particles with momenta greater than 200 MeV/c over the polar angle range from 8° to 140° with a spatial resolution of \approx 400 μ m [79]. The resulting momentum resolution is \approx 0.5–1.5%. More about the CLAS drift chambers will be explained in section IV.2.2.

III.3.3 Time of Flight System

In addition to the tracking information and momentum determined by the DC, we also need to determine the velocity of the particle in order to find its mass. The Time-of-Flight (TOF) system of CLAS is designed to precisely measure the time of flight of charged particles [80], which allows us to determine the velocity of the particle. Therefore, its mass, which explicitly identifies the particle, can be calculated according to:

$$m = \frac{p\sqrt{1 - \beta^2}}{\beta}. \quad (211)$$

The TOF detectors are made from scintillator material. In general, we can describe a scintillator as a material that emits fluorescence photons when struck by a high-energy charged particle. Scintillators have characteristic values for their light output (absorbed energy vs. number of emitted photons) and decay times (how long the photon emission lasts). The shorter the decay time of a scintillator, the less dead time the detector will have, and therefore the more ionizing events per unit of time it will be able to detect. Because of their relatively short decay time, scintillators are used for high resolution timing information. Moreover, the light output enables us to determine the amount of energy deposited into the scintillator, which later becomes useful for particle identification. The fluorescence light emitted by the scintillator is collected by photomultiplier tubes (PMTs), which are extremely sensitive

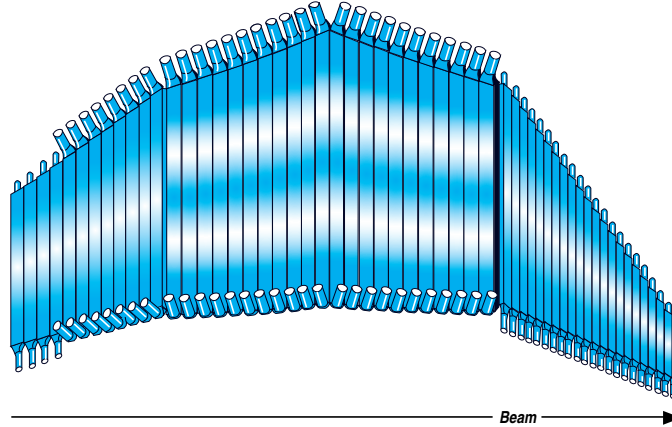


FIG. 21: Time of flight scintillator counters for one of the sectors. It is built in 4 panels to accommodate the CLAS geometry.

light detectors. These detectors multiply the signal produced by incident light by as much as 10^8 . Therefore, even a single photon can be detected. Incident photons induce emission of photo-electrons on the surface of the cathode of the tube, which is coated with a material that has a low work function. Emitted photo-electrons from the photo cathode are directed toward an electron multiplier. In the electron multiplier, electrons are multiplied by the process of secondary emission. Basically, the multiplier consists of several electrodes with increasing positive voltage. Each time an electron hits the electrode, more electrons are released and accelerated toward the next electrode. This creates an avalanche effect and produces more electrons, amplifying the signal. Then this signal is transferred to electronic circuits and can be used as timing and trigger information. Their high frequency response makes PMTs a natural choice for timing measurements.

The TOF counter unit for one sector includes 57 scintillator strips (BC-408) mounted as four panels combined together (see Fig. 21). The width and length of the scintillators vary according to their location. Forward angle scintillators, which cover up to 45 degrees, are 15 cm wide while the rest are 22 cm. The length of the strips vary from 30 to 450 cm. All scintillator strips have a thickness of 5.08 cm. They are perpendicular to the beam direction with angular coverage of 2 degrees each. They are positioned within a sector in such a way that particles will always pass through the strips along the normal line. The total geometric coverage of a TOF unit is 8 to 142 degrees of the polar angle and 100% of the azimuthal angle,

except the angles occupied by the torus coils.

The signals from the scintillators are collected in PMTs and transferred to time-to-digital converters (TDC) and analog-to-digital converters (ADC) to convert the signal into a digital information and stored. The TDC keeps track of timing information while the ADC stores the amplitude of the signal, which is proportional to the energy released by the incident particle. The last 18 scintillators in the back angles are grouped into 9 pairs and each pair is connected to a single TDC and ADC channel to reduce the number of converters used. Therefore 48 channels of scintillator strip are being read out for each sector. The timing resolution of the scintillator counters varies with the length and width of the strip. The CLAS TOF detector is designed such that pions and kaons can be separated and identified up to 2 GeV/c. As a result, the time resolution is ≈ 120 ps for the forward counters, which are shorter, and ≈ 250 ps for polar angles above 90 degrees. The average time resolution is about 140 ps.

III.3.4 Cherenkov Counters

Between the Drift Chambers and the Time Of Flight Counters, a Cherenkov detector is positioned within each sector. These detectors are called the Cherenkov counters (CC). They are designed to discriminate between electrons and hadrons, specifically negative pions [81]. The Cherenkov detector uses the fact that a charged particle traveling through the medium with a speed exceeding the local phase velocity of light in that medium emits electromagnetic radiation called Cherenkov light. This light is emitted in a cone about the direction in which the particle is moving. In the Ring Imaging Cherenkov detectors, the angle of the cone can be used as a direct measure of the particle's velocity by utilizing the relation:

$$\cos \Theta_c = \frac{c}{nv}. \quad (212)$$

In the EG1b experiment, however, the Cherenkov counters are used as a threshold detector, which only tells if a particle is detected or not. The primary purpose of the CC is to identify electrons and discriminate negative pions. Therefore, a medium was chosen such that only electrons should be able to travel above the speed of light in that medium. The velocity threshold for Cherenkov light emission is $\beta=1/n$ where n is the refraction index of the medium. The Cherenkov material that was chosen for this purpose is perfluorobutane C_4F_{10} , which has $n=1.00153$. That corresponds

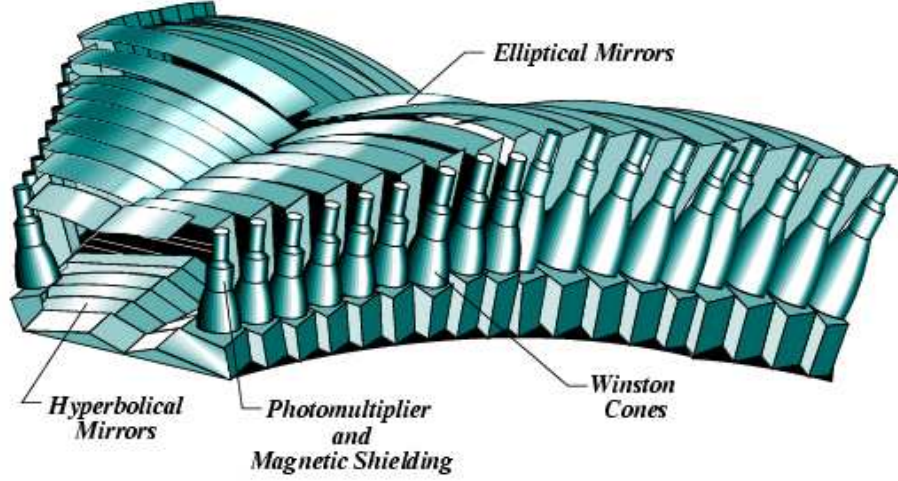


FIG. 22: Array of CC optical modules in one sector.

to a threshold in energy of the particle:

$$E = \frac{m}{\sqrt{1 - \beta^2}} = \sqrt{\frac{n}{n - 1}} m = 18.1 m, \quad (213)$$

where m is a mass of the particle. This provides an acceptably high pion momentum threshold ($p_\pi > 2.5 \text{ GeV}/c$).

The Cherenkov Counter of CLAS consists of six independent identical Cherenkov optical units (one unit per sector). One of these units is shown in Fig. 22. One Cherenkov unit contains 18 segments each covering a different region of polar angle. The whole unit with 18 segments extends from 8° to 45° in the polar direction. Each segment is divided into two optical modules along the symmetry plane of each sector. These modules, which look like wings, are named left and right modules. Therefore, each Cherenkov unit in each sector consists of 36 optical modules (see Fig. 22). Each optical module has three mirrors - elliptical, hyperbolic and cylindrical - to direct the light into a light collecting Winston cone (see Fig. 23). One PMT is connected to the end of each module. The mirrors are aligned to optimize the light collection by the PMTs.

The amount of light collected in the PMTs is measured and stored for each particle in the event. The Cherenkov counter is one of the detectors that is generally used in the event trigger for electron scattering experiments with CLAS. Typically, a Cherenkov threshold for the acceptance of the particle as an electron or not is

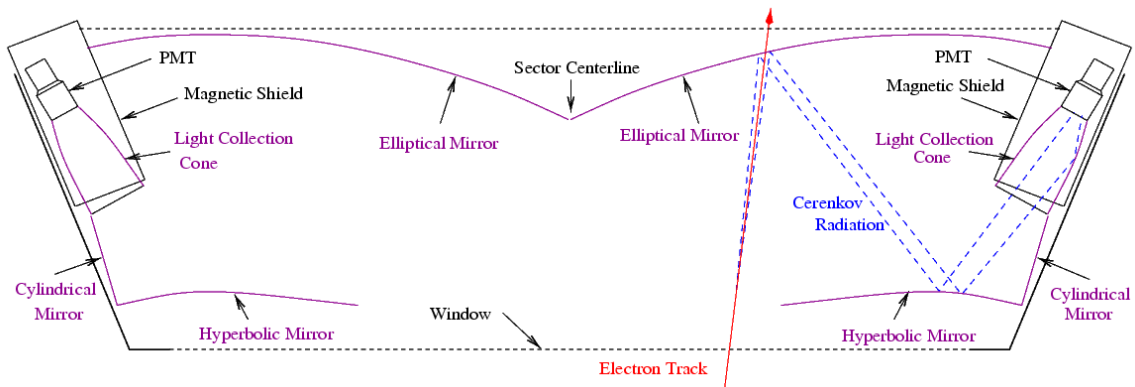


FIG. 23: A schematic of one optical segment of the CLAS Cherenkov detector. Cherenkov light is reflected from the hyperbolic and elliptical mirrors into the Winston Cone (WC), which is surrounded by a Magnetic Shield. The light is then collected by the Photomultiplier Tubes (PMTs).

determined later in the analysis software (see section IV.7.4). As mentioned above, the Cherenkov counters are useful to discriminate pions from electrons up to the pion momentum of $2.5 \text{ GeV}/c$. Pions that exceed this momentum can emit Cherenkov radiation that is comparable to the radiation produced by the electrons. In order to identify these more energetic pions, the other detectors are used. In addition, it should be noted that pions below $2.5 \text{ GeV}/c$ are also able to create some Cherenkov radiation through primary and secondary ionization of atomic electrons in the gas and surrounding environment. This, however, occurs for around 1% of the pions. The electron efficiency within the fiducial acceptance of the CC from the measured photo-electron yield exceeds 99% (see [81]). Outside of the fiducial region the efficiency drops rapidly and varies strongly. Therefore the non-fiducial region is usually excluded from the data analysis. The limiting factor in the acceptance of CLAS measurements mainly comes from the Cherenkov Counter efficiency, which is discussed extensively in section IV.9.

III.3.5 Electromagnetic Calorimeter

The last component of the CLAS detector system is the Electromagnetic Calorimeter (EC). A Calorimeter is a detector used to identify particles by measuring their energy deposition in matter and determining the method of deposition. An incident

particle deposits energy in the absorber material of the calorimeter, which is generally a high density material (with a high electric charge Z in its nucleus) like lead or steel, and the deposited energy is measured by a collector material layered with the absorber material¹. The collector material is generally some kind of scintillator material connected to photomultiplier tubes. Based on the pattern of energy deposition, the calorimeters are used to distinguish between electrons and hadrons and to detect neutral particles.

At energies up to a few MeV, the dominant interaction of photons with matter is through Compton scattering and the photoelectric effect. Above the 10 MeV range, pair-production becomes the dominant method of interaction for photons within material with high- Z nuclei. Low energy electrons interact with matter by creating excitations within atoms. High energy electrons, on the other hand, lose their energy mostly by bremsstrahlung. The electron is deflected by the Coulomb field of the nucleus, because it has a very small mass, and emits a photon. These high energy photons interact with matter and create high energy electron-positron pairs. The resulting electrons again create photons via bremsstrahlung. The sequence of these processes result in an electromagnetic shower. The sequence continues until the e^+e^- pairs are not energetic enough to produce bremsstrahlung radiation. The energy of the shower is converted into light by the scintillator strips, which is finally collected by PMTs.

On the other hand, massive particles, for example hadrons, have very small bremsstrahlung cross-sections at energies at which CLAS operates. The main energy loss mechanism for these particles is ionization. Ionization and radiation produce different signals in the EC. The Coulomb field of an atom extends over regions far larger in radius than the nucleus of the atom. As a result, the probability of an electron being deflected by the Coulomb field of an atom is much larger than the probability that a hadron creates ionization within an atom. Therefore, electromagnetic showers begin within a much shorter distance into the calorimeter than the hadronic showers. Electrons deposit a constant fraction of their total energy mostly in the first half of the EC. Energy deposition of hadrons, on the other hand, is independent of beam energy and peaks around the minimum ionizing energy of the particle in that material. In CLAS, the EC signal produced by electrons is much stronger than, and

¹There are also calorimeters made from one type of material, which is both high density and scintillating, such as lead-glass calorimeters.

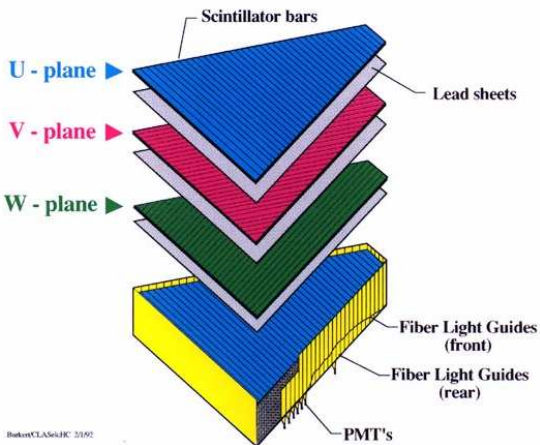


FIG. 24: View of one of the six CLAS electromagnetic calorimeter modules.

distinguishable from, the signal produced by hadrons. Separating pions from electrons becomes particularly important when the pion momentum exceeds $2.5 \text{ GeV}/c$ because they too begin to create a signal in the CC. Hence, the EC becomes vital to identify electrons correctly at high energies. For this reason, the EC is a part of the trigger scheme of the CLAS detector. The Electromagnetic Calorimeter of CLAS has the following basic functionalities [82]:

- Detection of electrons above 0.5 GeV .
- Detection of photons above 0.2 GeV .
- Reconstruction of π^0 and η by measuring their 2γ decays.
- Detection of neutrons and separation of neutrons from photons based on their time-of-flight.

In the CLAS detector, there are 6 modules, one for each sector, of Electromagnetic Calorimeters, which are commonly known as the Forward Angle Calorimeter (EC) and cover polar angles from 8 to 45 degrees. There are also two extra modules in the first and second sectors to cover angles from 50 to 75 degrees. These two are called the Large Angle Calorimeter (LAC). Even if they are based on the same principles, the design specifications of the EC and the LAC are slightly different from each other. Here, only the design specifications of the EC are explained because the LAC is not actively used in our experiment. However, full specifications for the LAC can

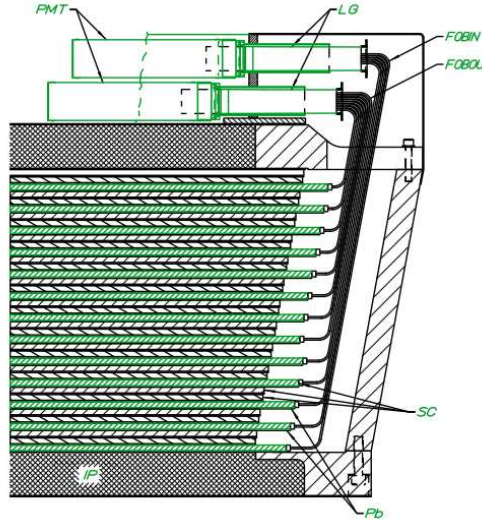


FIG. 25: Schematic side view of the fiber-optic readout unit of the calorimeter module. The scintillators sandwiched between the lead sheets are shown together with the fiber optic readout system.

be found in [76]. Each of the EC modules consists of alternating layers of scintillator strips and lead sheets. There are 39 layers of lead-scintillator pairs, each consisting of a 10 mm BC-412 scintillator followed by a 2.2 mm thick lead sheet. Therefore each module has 39 cm of scintillator material and 8.6 cm of lead. That results in approximately 1/3 of the energy of the shower deposited in the scintillator. The total energy deposited in the scintillators, expressed as a fraction on the incident particle energy, is called the EC sampling fraction. From GEANT simulations, the expected sampling fraction for the CLAS EC is about 0.27 after energy calibrations are performed. In the EG1b experiment, the sampling fraction ranged between 0.27 and 0.29 (see Fig. 26, for example). The whole package has a total thickness of 16 radiation lengths. The shape of each EC detector module is designed to be an equilateral triangle in order to match the hexagonal geometry of the CLAS (see Fig. 24). In addition, the calorimeter utilizes a “projective” geometry, which means that the area of each successive layer increases by a certain amount. This special geometry minimizes shower leakage at the edges of the active volume and minimizes the dispersion in arrival times of signals originating in different scintillator layers.

Each scintillator layer is made of 36 strips parallel to one side of the triangle, with the orientation of the strips rotated by 120° in each successive layer (see Fig.

24). This creates three orientations or views, which are labeled as U, V and W. Each of these specific orientations contain 13 layers of the 39 layers in one detector module. This arrangement provides stereo information on the location of energy deposition. The first 5 layers of each view, the first 15 layers of the module, are grouped together to form an inner stack, referred to as the inner calorimeter. The inner calorimeter has total of 36×3 strips. The remaining 8 layers are also grouped to form an outer stack in the module, referred to as the outer calorimeter, which also has total of 36×3 strips. This separation enhances longitudinal sampling of the shower for improved hadron identification. Therefore, the whole module has $36(\text{strips}) \times 3(\text{views}) \times 2(\text{stacks}) = 216$ strips. One PMT module is connected to each strip via a fiber-optic light readout system that transmits the scintillator light to the PMTs. Fig. 25 displays a schematic side view of the fiber-optic readout unit of the calorimeter module. These fibers were bent in a controlled way to form semi-rigid bundles originating at the ends of the scintillator strips and terminating at a plastic mixing light-guide adapter coupled to a PMT.

The EC is the main detector to separate electrons from pions above 2.5 GeV/c. The total energy deposited in the calorimeter is readily available at the trigger level to reject minimum ionizing particles or to select a particular range of scattered electron energy. Triggering on the correct particle is very important for timing information of all particles detected. Pion events are largely suppressed by setting the EC total energy threshold E_{total} in the CLAS hardware trigger. From the detector performance under running conditions, it is determined that the overall position resolution is $\sigma = 2.3$ cm. The time resolution is about $\tau = 3$ ns. Neutral hits, photon and neutron, in the EC are determined by the absence of a corresponding DC track. The neutrons and photons can further be discriminated by their time-of-flight information. The π^0 and η are identified by requiring two neutral hits whose reconstructed energies combine to the mass of π^0 or η .

III.4 THE TRIGGER AND THE DATA ACQUISITION SYSTEM

The event trigger is formed by a combination of the signals from different components of the CLAS detector. The CLAS detector has several trigger levels. For the EG1b experiment, the level-1 trigger was used, which is based on a coincidence between the EC and the CC detectors. The level-2 trigger also includes information from the DC as well, but it was not used in the EG1b experiment. During the experiment, the

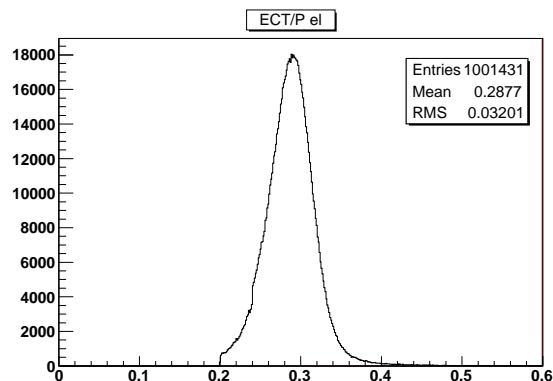


FIG. 26: The plot shows the total energy deposited in the EC (inner and outer combined) divided by the momentum for the electrons. 29% of the energy deposited is observed by the scintillators of the EC. This quantity is usually called the EC sampling fraction.

thresholds of the detectors used for the trigger were adjusted to specifically accommodate each beam/torus configuration. The signals from the detector subsystems are sent to a pre-trigger logic module, where the bit patterns from the subsystems are compared against patterns preloaded in memory tables. If the pre-trigger conditions are satisfied, the signal is submitted to the level-1 trigger. If there is a trigger in the event, the signal is passed to the Trigger Supervisor (TS), which communicates with the Readout Controllers (ROCs). TS has 12 trigger inputs, 8 of which are used by the level-1 trigger. It also has a level-2 trigger confirmation input so that the TS can be configured only to require level-1 input or to require level-1 input and level-2 confirmation. Level-2 confirmation was not required in the EG1b experiment. If the level-1 trigger is satisfied, then the data are read out, digitized and transferred to the Event Builder (EB). Finally the Event Recorder (ER) receives the information from the Event Builder through the Data Distribution (DD) shared memory. The data are written to the disk and later transferred to the tape SILO for permanent storage. The data flowchart of the CLAS DAQ system is shown in Fig. 27.

The DAQ system was initially designed for an event rate of 2 kHz. During the EG1b experiment, the event rate was about 4 kHz and the data rate was 25 MB/s. Nowadays, the DAQ can reach up to 5 kHz in event rate. The live time was about 90%. The DAQ system for CLAS uses software called CODA (CEBAF Online Data Acquisition). CODA provides specific configurations of the DAQ components for

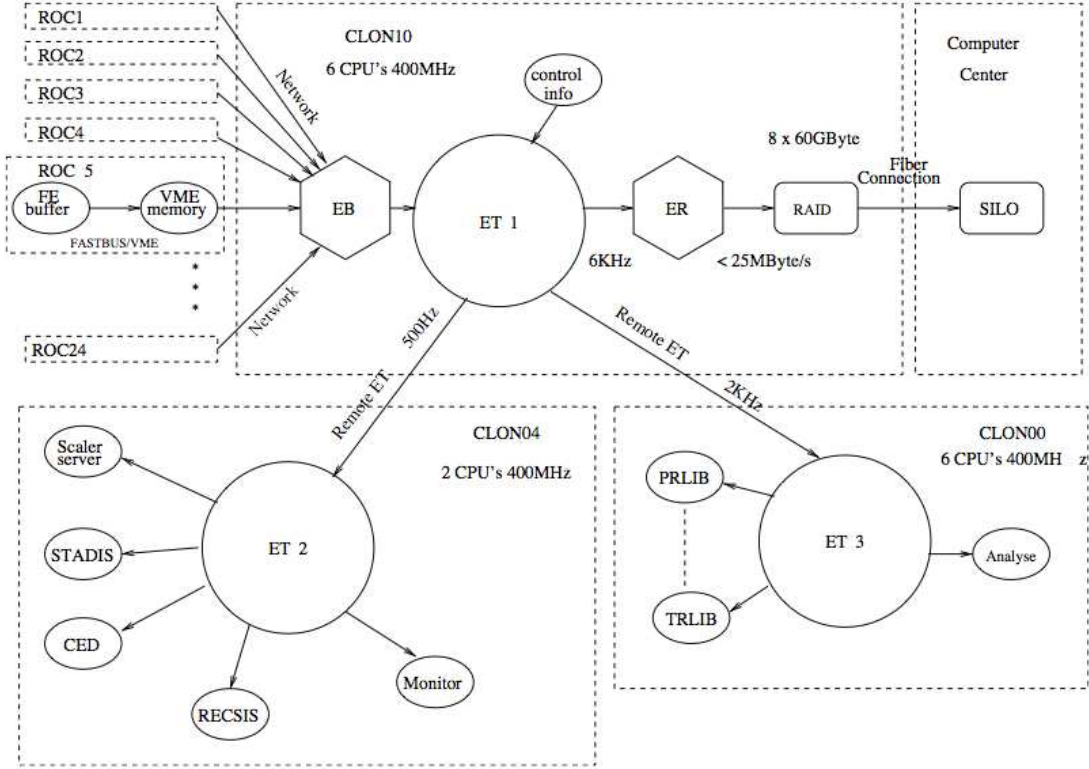


FIG. 27: Data flowchart of the CLAS DAQ system

different experiments. During the experiment, the data was stored in continuous segments and each segment was assigned a specific run number, one of the configuration parameters in the CODA. The CODA software internally divides each run into files of 2 GB in size for storage. More detailed information on the trigger system and data acquisition system (DAQ) of the CLAS detector can be found in [76]. Table 3 gives brief information about some general parameters of the CLAS detector.

III.5 EG1B TARGETS

NH_3 and ND_3 are the polarized targets used in the EG1b experiment. In addition, unpolarized targets ^{12}C , ^4He and ^{15}N were also used. In order to polarize the proton and the deuteron targets, a technique called Dynamic Nuclear Polarization (DNP) [17][83] was used. The resulting polarizations were constantly monitored by the Nuclear Magnetic Resonance (NMR) system [83]. Although NMR results are not used for the final analysis, they served as a consistency check and data quality monitor.

TABLE 3: Some useful CLAS Parameters

| Capability | Quantity | Range |
|-------------|--|---|
| Coverage | polar angle momentum | $8^\circ \leq \theta \leq 140^\circ$ $p \geq 0.2 \text{ GeV}/c$ |
| Resolution | momentum ($\theta \leq 30^\circ$) momentum ($\theta \geq 30^\circ$) polar angle azimuthal angle time | $\sigma_p/p \approx 0.5\%$ $\sigma_p/p \approx 1\text{-}2\%$ $\sigma_\theta \approx 1 \text{ mrad}$ $\sigma_\phi \approx 4 \text{ mrad}$ $\sigma_t \approx 100\text{-}250 \text{ ps}$ |
| Particle ID | π/K separation π/p separation | $p \leq 2 \text{ GeV}/c$ $p \leq 3.5 \text{ GeV}/c$ |
| Luminosity | electron beam | $L \approx 10^{34} \text{ nucleon cm}^{-2}\text{sec}^{-1}$ |
| DAQ | event rate data rate | 4 kHz 25 MB/s |

In this section, we will describe the target system of the EG1b experiment.

The EG1b targets are located on the symmetry axis of CLAS and are surrounded by a pair of superconducting Helmholtz coils. The coils produce a 5 Tesla magnetic field around the target cell. The magnet was kept at 4.2 K through a liquid Helium reservoir located outside the CLAS. The target itself was kept at 1 K by a refrigeration system. The target cells were attached to a target insert as shown in Fig. 28. Each cell is 1 cm in length and 1.5 cm in diameter. The entrance window of each cell is sealed by a thin aluminum foil of $71\mu\text{m}$ thickness (aluminum was chosen for its strength) while the exit window is sealed by a thin kapton foil. A stepping motor connected to the insert moves the insert in the vertical direction so that targets can be switched mechanically. The ND_3 and NH_3 target cells are surrounded by NMR coils for polarization measurements. Part of the target stick remained immersed in a mini-cup filled by liquid Helium in order to keep the targets at low (1 K) temperature. This was necessary to maintain the polarization of the target materials. Another target insert very similar to the one shown in Fig. 28 was also used for ^{15}N runs and contained only two target cells, ^{12}C and frozen ^{15}N .

$^{15}\text{NH}_3$ and $^{15}\text{ND}_3$ were chosen as polarized target materials in the EG1b experiment because of their high content of polarizable nucleons: 16.7% for the $^{15}\text{NH}_3$ and 28.6% for the $^{15}\text{ND}_3$. They also have high resistance to radiation damage. Moreover,

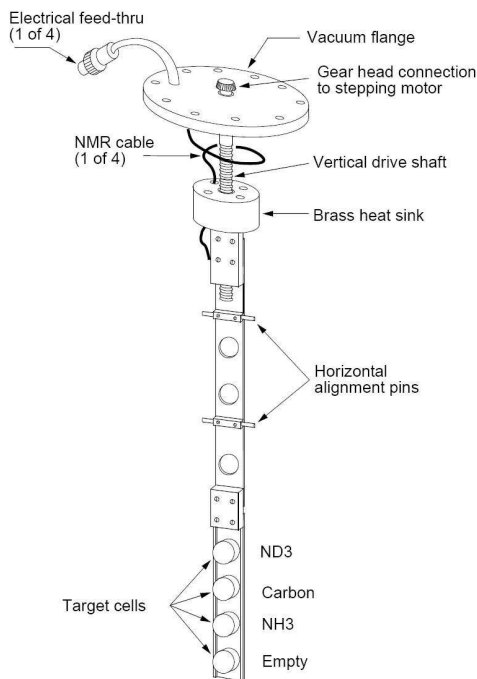


FIG. 28: A schematic of the target insert strip showing the four target cells used for the EG1b experiment: ND_3 , ^{12}C , NH_3 and Empty. NMR coils surround the ND_3 and NH_3 target cells.

it is easy to correct the measured asymmetry of the proton or the deuteron for the ^{15}N polarization contribution. The spin of the ^{15}N is carried by a single valence proton and the required corrections to the measured asymmetries due to the ^{15}N polarization are well understood. More information about the target materials is given in section IV.11.

CHAPTER IV

DATA ANALYSIS

Handling data from complex experiments like EG1b requires certain precautions and corrections. In this chapter, we are going to focus on the analysis techniques we used to extract physics results from the EG1b data. The raw data from the experiment includes a wide range of events representing many different physical processes. The events relevant to a specific analysis goal must be determined. The data should be calibrated and corrected according to the detector behavior and experimental conditions. We followed certain procedures to convert the raw data into descriptions of physical properties that can be interpreted and compared to theoretical calculations. The following list summarizes the most important procedures in a chronological order:

- Data calibration and reconstruction
- Creating Data Summary Tape (DST) files
- Helicity pairing
- Quality checks and data selection
- Particle identification
- Precision (geometric and timing) cuts
- Fiducial cuts
- Kinematic corrections
- Dilution factors
- Pion and pair symmetric background corrections
- Extraction of the beam \times target polarization
- Polarized background correction
- Radiative corrections
- Combining data

- Models
- Systematic errors
- Extraction of the neutron structure functions from the combined proton and deuteron data

Some of these procedures include many sub-steps. Throughout this chapter, we will give detailed descriptions of these procedures and provide a layout for the analysis of the EG1b data.

The double spin asymmetry A_{\parallel} is obtained from the measured experimental asymmetry A_{raw} via,

$$A_{\parallel} = \frac{C_1}{f_{RC}} \left(\frac{A_{raw}}{F_D P_b P_t} C_{back} - C_2 \right) + A_{RC} \quad (214)$$

where $P_b P_t$ is the product of beam and target polarizations, F_D is the dilution factor, which accounts for the scattering from the unpolarized components of the target, C_{back} represents the pion and pair symmetric background corrections, f_{RC} and A_{RC} take care of the radiative effects while C_1 and C_2 corrects for the contributions from the polarized background. The experimental asymmetry A_{raw} is defined by:

$$A_{raw} = \frac{n^- - n^+}{n^- + n^+} \quad (215)$$

where n^- and n^+ are determined by counting the inclusive scattering events for each helicity state and normalizing with the accumulated (live-time gated) beam charge (N_e) for that helicity state:

$$n^- = \frac{N^{\uparrow\downarrow}}{N_e^{\uparrow\downarrow}} \quad ; \quad n^+ = \frac{N^{\uparrow\uparrow}}{N_e^{\uparrow\uparrow}} \quad (216)$$

with arrows indicating the relative spin orientations of the electron and the target nucleus (or nucleon). The quantity A_{raw} is extracted for certain kinematic bins in Q^2 and W in the resonance region and above, for each beam energy and detector setting separately.

IV.1 EG1B RUNS

During the experiment, a longitudinally polarized electron beam of various energies ranging from 1.6 GeV to 5.7 GeV was incident on longitudinally polarized proton (NH_3) and deuteron (ND_3) targets. This ensures a good coverage of the entire resonance region and above: $1.08 \text{ GeV} < W < 3.0 \text{ GeV}$; $0.05 \text{ GeV}^2 < Q^2 < 5.0 \text{ GeV}^2$.

In order to increase the kinematic coverage, the torus current was also switched between inbending and outbending settings for some beam energies. In addition to the NH_3 and ND_3 targets, data on the ^{12}C target and the empty target (with only liquid Helium) were also collected for each beam energy and torus setting. These runs were used to estimate the unpolarized background contribution to the data. Occasional runs were also taken on pure ^{15}N target and used to monitor the effectiveness of the background removal procedure using the ^{12}C runs. Table 4 provides a simple summary of all runs taken together with corresponding target, beam and torus settings. Fig. 29 shows the kinematic coverage of the entire experiment. Coverage of different beam energies are shown in different colors. Based on Table 4, we separated the data into different configurations and analyzed each set separately. We analyzed 11 different data sets for both ND_3 and NH_3 targets, which are listed in Table 5. At the end, the results from these sets were combined with specific guidelines.

TABLE 4: EG1b run sets by beam energy and torus current.

| Run Numbers | Beam Energy(GeV) | Torus Current(A) |
|---------------------------------------|------------------|------------------|
| 25488-25559; 25669-26221 | 1.606 | +1500 |
| 26222-26359 | 1.606 | -1500 |
| 28512-28526 | 1.723 | +1500 |
| 27644-27798; 28527-28532 | 1.723 | -1500 |
| 27205-27351 | 2.286 | +1500 |
| 28001-28069 | 2.561 | +1500 |
| 27799-27924; 27942-27995 | 2.561 | -1500 |
| 27936-27941 | 2.792 | -1500 |
| 28074-28277; 28482-28494; 28506-28510 | 4.238 | +2250 |
| 28280-28479; 28500-28505 | 4.238 | -2250 |
| 27356-27364; 27386-27499 | 5.615 | +2250 |
| 27366-27380 | 5.615 | -2250 |
| 27069-27198 | 5.725 | +2250 |
| 26874-27068 | 5.725 | -2250 |
| 26468-26722; 26776-26851 | 5.743 | -2250 |

IV.2 DATA RECONSTRUCTION AND CALIBRATION

During the experiment, the data was stored in segments and each segment was assigned a specific run number. The DAQ software internally divides each run into files

TABLE 5: Analyzed data sets by target, listing the beam energy E_B and the torus current I_T . Throughout each data set, there are also occasional ^{12}C and empty target runs, used for background analysis.

| ND ₃ [$E_B(\text{GeV}), I_T(\text{A})$] | NH ₃ [$E_B(\text{GeV}), I_T(\text{A})$] |
|--|--|
| 1.606, +1500 | 1.606, +1500 |
| 1.606, -1500 | 1.606, -1500 |
| 1.723, -1500 | 1.723, -1500 |
| 2.561, +1500 | 2.386, +1500 |
| 2.561, -1500 | 2.561, -1500 |
| 4.238, +2250 | 4.238, +2250 |
| 4.238, -2250 | 4.238, -2250 |
| 5.615, +2250 | 5.615, +2250 |
| 5.725, +2250 | 5.725, +2250 |
| 5.725, -2250 | 5.725, -2250 |
| 5.743, -2250 | 5.743, -2250 |

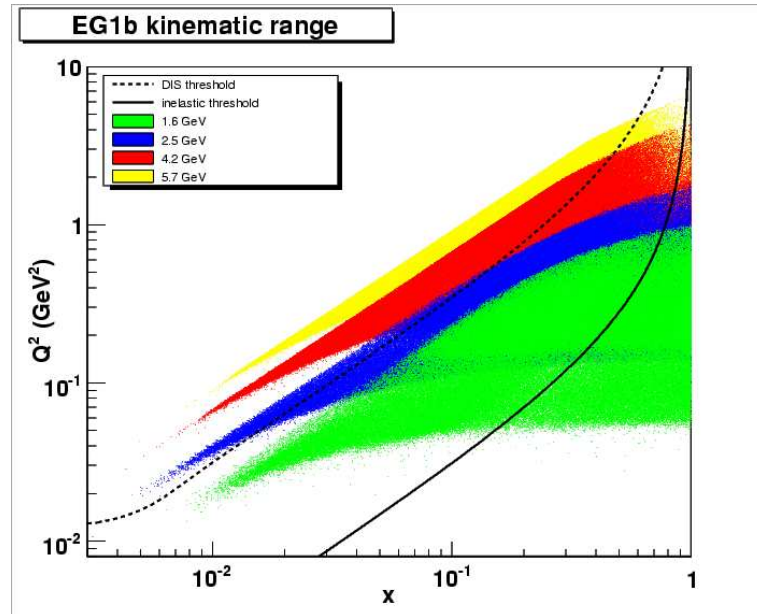


FIG. 29: Kinematic coverage of the EG1b experiment for all beam energies. The solid and dotted lines mark the inelastic threshold at $W = 1.08$ GeV and the DIS threshold at $W = 2.0$ GeV, respectively.

of 2G B for storage. Each run took approximately 2 hours and consists of 20-30 files. These files were stored on tapes for further processing. The data were written in a special format based on the BOS bank system. The BOS banks are logical records for the data file that consist of a four word header (1 word = 4 bytes) followed by various data words. This system allows programs reading the tapes to skip unknown or uninteresting headers altogether. The format also provides a robust error handling system. If the reading software encounters faulty parts in the file, it can parse the file for the next valid BOS header and continue reading. Information in the raw data files consist of TDC and ADC values from detector components as well as beam related information. The next step is data reconstruction. During the reconstruction process, the simple event builder (SEB) [84] is used. The SEB incorporates geometric parameters and calibration constants for the CLAS detector and converts the raw data into physics quantities like particle IDs, positions, energies and momenta, etc.

The standard package for the reconstruction of the CLAS data is called RECSIS, which communicates via log messages that appear both on the screen and in a log file. RECSIS executes a set of programs called *ana* and *user_ana*, FORTRAN based reconstruction software for the CLAS detector. The libraries for this software can be checked out from CVS repository and executables can be created from the libraries. One also needs to set environmental parameters to choose a specific calibration database for the experiment as well as to set other CLAS parameters. The *user_ana* program is configured by using a tcl script, i.e., *rec_eg1sql.tcl*. The tcl script sets the names for input and output files, torus magnet current values and the number of events to process for each file. It basically determines a small subset of a large number of run control parameters required for the process of reconstruction. It also manages which BOS banks should be used for the output file so that one would be able to choose only the interesting BOS banks for the analysis. Once everything is set, the reconstruction can be initiated by using a command line: *user_ana -t rec_eg1sql.tcl*, which reconstructs a specified raw data file in the tcl script for the specified BOS banks.

There are more than 40,000 files in the EG1b experiment. The reconstruction procedure is semi-automated by using other sets of scripts, *run_a_run.pl* and *run_a_file.pl*. The template form of these scripts can be found under jlab cue “/u/home/claseg1/eg1b/scripts/”. They must be modified for each data set with different beam energy and torus current. These scripts launch the reconstruction of

each file as a batch job to make use of the computing power of the Jefferson Lab batch farm [85].

IV.2.1 Event reconstruction

Event reconstruction consists of identification of particles in the event together with calculation of their momenta in the CLAS coordinate system. In this coordinate system, the z -component points along the beam axis while the x and y -components are in the horizontal and vertical directions, respectively. Charged particles are expected to give signals in all detector components while neutral particles give signals only in the Scintillator Counter (SC) and the Electromagnetic Calorimeter (EC). Tracks are reconstructed in a two-step process. Hit-based tracking is used for preliminary identification. After the trigger start time is determined, calibrations on the DC are performed to establish time-based tracking, which is explained in the last part of section IV.2.2.

Charged particles

Track reconstruction begins by identifying hit-based tracks in the DC. In this stage, only the sense wires at the center of each DC cell that had a signal are used to create a preliminary trajectory for the particle. The momentum and the charge of the particle is determined from the curvature of the trajectory obtained from the DC. This is called hit-based tracking, which provides a preliminary production angle and momentum for the particle. The code cycles through each particle in the event to verify coinciding signals in the CC and EC for electron identification. The signals must agree with the trajectory of the particle within the time of flight window. If all signals register for a negative charged particle, the particle is accepted as an electron candidate. If there are more than one electron candidates, the one with the highest momentum is selected as an electron.

After the electron is identified, its time of flight information is obtained from the SC signal. Then, the trigger start time can be determined by tracing the electron back to the vertex along its geometrical path and assuming the electron travels with the speed of light. In case there is no negative particle track in the event, the positive particle with the highest momentum is used to establish the start time. This is generally a positron that comes from pair production.¹ The reconstruction

¹Positive trigger events are only used for pair symmetric contamination analysis.

of the start time requires calibration of the SC for time delays and synchronization of individual scintillators. These calibrations are described in section IV.2.2 in more detail.

Once the start time is established from the trigger particle, usually an electron, the time of flight for the other particles in the event can be determined from their signals in the SC by subtracting the start time. If the SC signal is not available for a particle, the EC signal is used instead. Then, the velocity of the particles in the event, other than the electron, can be calculated by using their path lengths from the vertex to the hit location in the SC. The mass of the particle is calculated from its velocity and momentum by $m = p/\beta\gamma$.²

Neutral particles

Neutral particles are identified by energy clusters in the EC that do not match any of the tracks. The photons create electromagnetic showers and deposit all their energy in the EC. The signal amplitude from the EC ADC is used to calculate the energy of the photons. Neutrons may deposit energy in the EC, mostly by proton recoil followed by ionization. The energy deposition clusters from neutrons usually appear in the outer parts of the EC. Neutrons can be identified from a hit in the calorimeter that does not satisfy any of the requirements for a charged particle. Neutrons are distinguished from photons by their time of flight to the EC. Neutral particles are not affected by the toroidal magnetic field, so they follow a straight path to the location they are first observed. The angle of their trajectory is determined from the position of the energy cluster at the surface of the calorimeter. Particles like π^0 and η mesons can be identified from their decay products [82]. A π^0 decays into two photons with 98.8% probability while η mesons have additional decay channels. Nevertheless, by applying kinematic requirements to the decay products, one can establish a missing mass spectrum and identify some of these neutral mesons.

IV.2.2 Calibrations

For the correct reconstruction of the events in the detector, the response of each detector component should be parametrized according to experimental conditions. This procedure is called calibration. The reconstruction and calibration procedures

²Natural units with $c = 1$ were chosen.

go together in an iterative manner. During the data acquisition, once a trigger is detected, the TDCs in each detector component start measuring the time until a signal is received to stop them, at which point the data is recorded. Calibration of the detectors is required to synchronize their timing with the beam radio frequency (RF) time. An energy calibration is also required for the EC. The calibration procedure produces certain parameters, ADC and TDC offsets, for different detector components. These parameters are often referenced as calibration constants. Afterward, these constants are written into the CLAS calibration database [86] allocated to the EG1b experiment. The reconstruction code reads this database and reconfigures the response of the detector components to each event according to the parameters provided.

Time of flight calibration and reconstruction of the start time

The time of flight information is obtained from the SC with 48 paddles for each sector and two PMTs on each paddle. During the reconstruction, TDC and ADC values from the PMTs are converted into time and energy. The leading edge discriminator registers the signal pulse when the amplitude passes a certain threshold. However, the timing of this threshold depends on the amplitude of the pulse, which affects the steepness of the rising edge of the pulse. This creates a dependence of the TDC signal on the ADC amplitude, a known phenomena called time-walk. The PMTs are calibrated to take the time-walk corrections into account. The ADC vs. TDC (pulse height vs. time) signal is fitted for each PMT and the time-walk correction parameters are obtained to calibrate the PMTs.

Each scintillator paddle has two PMTs attached, one at either end, referred to as the left (L) and right (R) PMTs. The signal generated at any location in the scintillator paddle takes different times, t_L and t_R , to travel to each of these PMTs. The crucial point is that for a signal generated at the center of the paddle, $t_L = t_R$ must always be true. For some paddles, this requirement necessitates the introduction of a left-right calibration offset. The offset is determined by using cosmic ray runs or data runs. More information about these calibrations can be found in [87] and [88].

After the above calibrations are performed on the SC, the trigger start time can be calculated by using,

$$t_{start} = t_{SC} - \frac{l_{path}}{\beta c}, \quad (217)$$

where t_{SC} is the time recorded at the SC when an electron is registered. $\beta = 1$ for

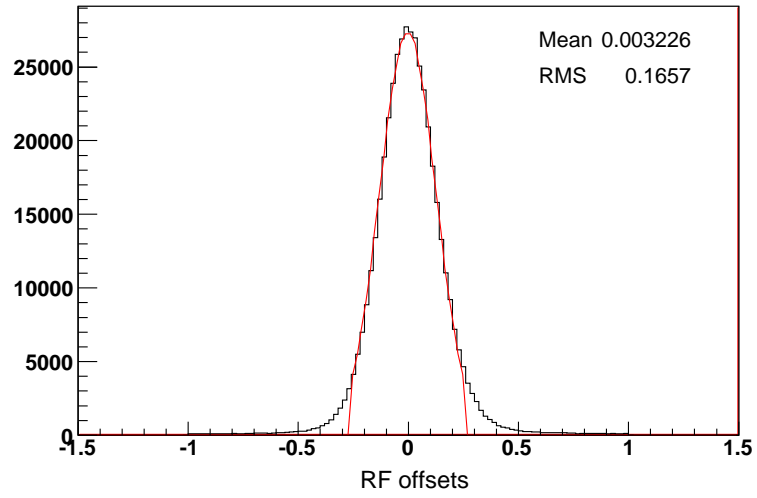


FIG. 30: RF offset from run 28405. The sigma of the distribution is 0.16 ns.

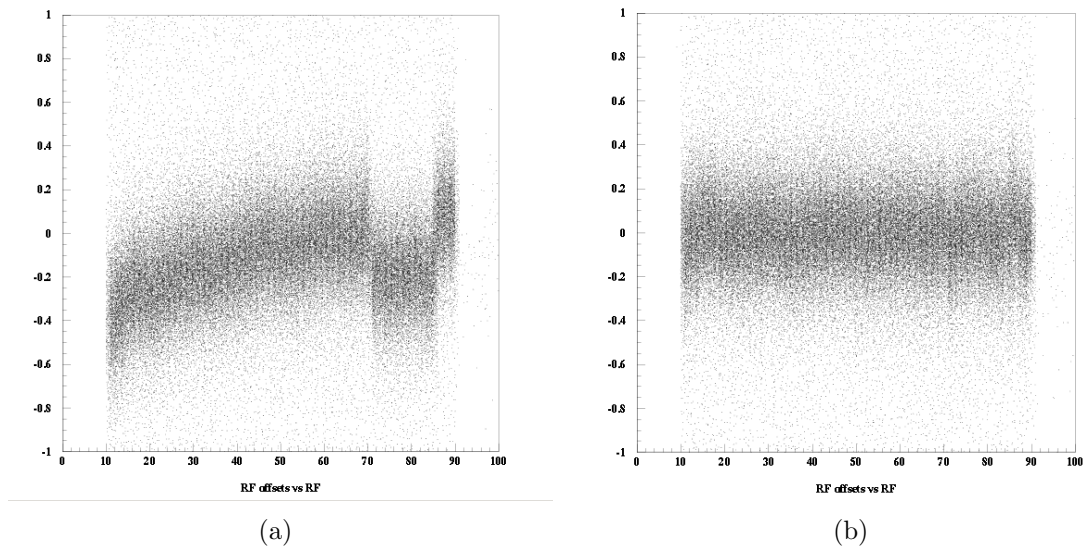


FIG. 31: RF offset vs. RF time before (a) and after (b) the TOF calibration. RF offset should not show any RF dependence after the calibration. A polynomial offset function is fitted in segments to center the offset at zero.

the electrons and l_{path} is the path length obtained by tracing the electron back to the vertex along its track. As shown in Fig. 30, the reconstructed start time shows a Gaussian distribution around the RF time provided by the accelerator. The electron beam is delivered to the experimental hall in bunches with a 499 MHz frequency. The bunch period is $\Delta t = 2.0039$ ns. Ideally, the reconstructed start time should coincide with the arrival of one of the bunches. However, the finite resolution of the reconstructed start time creates a Gaussian distribution centered around the RF time (see Fig. 30). The width of the distribution corresponds to the time resolution, which is generally around 0.16 - 0.20 ns. If the mean of the start time distribution is different than the RF time of the beam, the start time should be corrected for the offset,

$$t_{RFoff} = t_{start} - t_{RF}. \quad (218)$$

The start time with the RF correction, therefore, is written as,

$$t_{start} = t_{SC} - \frac{l_{path}}{\beta c} + t_{RFoff}. \quad (219)$$

The phase of the RF signal may sometimes change after a long run period. Therefore, each run period might require a calibration of the RF offset. Normally, the RF offset distribution vs. RF time should not show any dependence on the RF time. If it is not the case, the RF offset is fitted by a third degree polynomial in four different regions of the RF time. The resulting parameters readjust the RF offset distribution to make it independent of the RF time in all regions. These parameters are written into the calibration database and applied to the other runs within the same run period. Fig. 31 shows the RF offset vs. RF time before and after the RF calibration. In some part of the EG1b experiment, however, the RF signal was not available and this calibration was not performed.

The final step is a paddle to paddle delay calibration of all SC units. The idea is to synchronize the timing of all scintillators to the same RF signal so that they behave as a coherent unit. The paddle to paddle delay effects show themselves in the reconstructed time of flight (TOF) mass of the secondary particles plotted against the paddle ID. In addition, if certain paddles have their timing off with respect to the others, expected minus measured TOF of the secondary particles, which should be around zero, is disturbed for those paddles. TOF Mass vs. paddle ID and Δt vs. paddle ID plots are monitored during the calibration to make sure there are no bad paddles which give a wrong mass or TOF information for protons and pions.

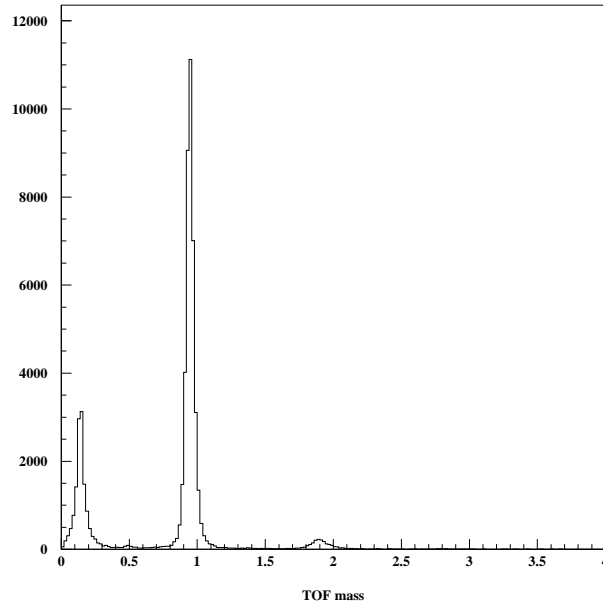


FIG. 32: TOF mass spectrum for secondary particles for an EG1b data run. Mass is given in GeV. The pion and proton peaks are clearly visible. The deuteron peak can also be resolved at 1.876 GeV.

In case there is no RF signal available from the accelerator, the reconstructed start time is used as a reference to determine the TOF information for the secondary particles. Fig. 32 shows the reconstructed time of flight mass spectrum after proper calibrations are made.

Electromagnetic calorimeter calibration

Once the SC calibrations are done, the EC timing signal is calibrated to the SC signal. The average difference between the EC and SC timing is minimized by using a 5-parameter fit. A sample plot of the overall time resolution is shown in Fig. 33.

In addition, the PMTs in the EC require calibration of the ADC pedestals [82][89]. The EC sampling fraction, the energy from the electromagnetic shower detected by the scintillator material in the EC and divided by the energy of the incident particle, should normally be a distribution around 0.27-0.29 with $\sigma \sim 0.03$. This quantity is monitored during the calibration procedure. File to file variation of the EC sampling fraction should be minimal for the same run period if the calibration is successful.

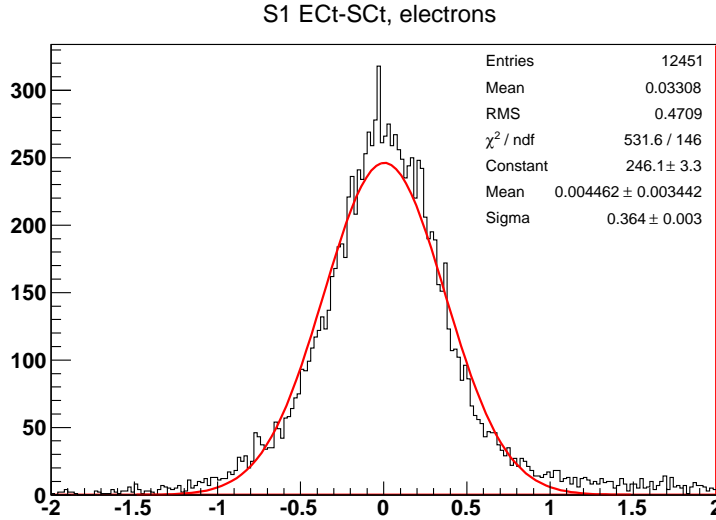


FIG. 33: Difference between EC and SC times (in ns) for reconstructed electron events after EC timing calibrations. The plot is from run 28079 sector 1.

Drift chamber calibration

Initially, the track reconstruction is performed by using only the location of the sense wires in the DC (hit-based tracking). If one precisely measures the timing of the current pulses of the wire and takes into account that the induced ions/electrons need some time to drift to the nearest wire, one can infer the distance at which the particle passed the wire. This greatly increases the accuracy of the path reconstruction. Therefore, after the start time is determined, a more accurate path for the particle can be calculated by taking the drift time in each DC cell into account. The drift time is converted to the drift distance, which is called the distance of closest approach (DOCA). By using the calculated DOCA, a more accurate track of the particle is obtained as shown in Fig. 34. This is called time-based tracking (TBT) [76][78][90]. During the DC calibration, first the drift time, t_{drift} , needs to be determined,

$$t_{drift} = t_{start} + t_{cable} + t_{TDC} - t_{flight} - t_{prop} - t_{walk}, \quad (220)$$

where t_{start} is the event start time, t_{cable} is the time-delay from the cable, t_{TDC} is the time measured by the TDC, t_{flight} is the flight time of the particle from the event vertex to the sense wire and t_{walk} is the time-walk correction (see section IV.2.2). The next step is to parametrize the drift distance as a function of the drift time.

This parametrization may have different forms for different drift chamber regions. For example, the Region 3, was parametrized by the following functional form [78],

$$x(param) = v_0 t + \eta \left(\frac{t}{t_{max}} \right)^p + \kappa \left(\frac{t}{t_{max}} \right)^q, \quad (221)$$

where v_0 is the drift velocity (at $t = 0$), $t = t_{drift}$, t_{max} is the maximum drift time for the ions created at the edge of the drift cell and η , κ , p and q are the fit parameters. Then the parametrized DOCA, $x(param)$, is used to minimize the difference

$$\chi^2 = \sum_i \frac{|x_i(param) - x_i(trial)|^2}{\sigma_i^2(trial)}, \quad (222)$$

where $x_i(trial)$ is the DOCA from a global trial track, often referred as fitted DOCA, including all superlayers and initially obtained from the hit based track (HBT), and $\sigma_i(trial)$ is the corresponding error for the fitted DOCA. The parameters are determined for each superlayer for a best fit to a global track with all superlayers. The difference between the calculated DOCA and the fitted DOCA is called the residual and should be around zero after going from HBT to TBT. This quantity is monitored separately for each superlayer and sector to ensure the quality of the DC calibration. The residual for superlayer 3 for all sectors combined is shown in Fig. 35. The sigma of the residual is monitored for all files and kept around 0.05 to ensure the quality of the DC calibration. It should never exceed 0.06 for any file.

The drift distance is the radial distance of the track from the wire but does not predict which side of the wire the track is. This ambiguity is resolved by a separate fit within each superlayer. A straight line fit is made to various choices within each superlayer, trying all possible left-right combinations and selecting the one with the highest probability. A more detailed explanation on the time based track reconstruction can be found in [76].

Final comments on data reconstruction

The reconstruction code produces ntuple files and monitoring histograms as well as BOS files. The monitoring histograms are used to determine the success of the calibration procedure. The calibration is normally performed on a sample data set, which is often referred to as the pass0 calibration. Sometimes a few iterations are required to establish a good calibration. Then the calibration constants are applied to the entire data set and the resulting monitoring histograms are investigated to

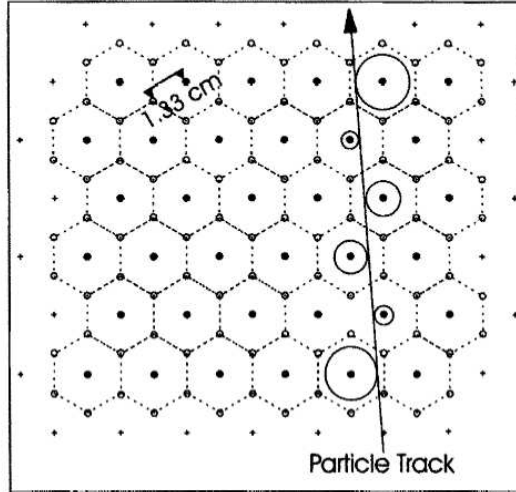


FIG. 34: A track through one DC superlayer showing the the calculated distance of closest approach (DOCA) for each sense wire. The accuracy of the particle track can be increased by using the DOCA, which is called time-based tracking [76][90].

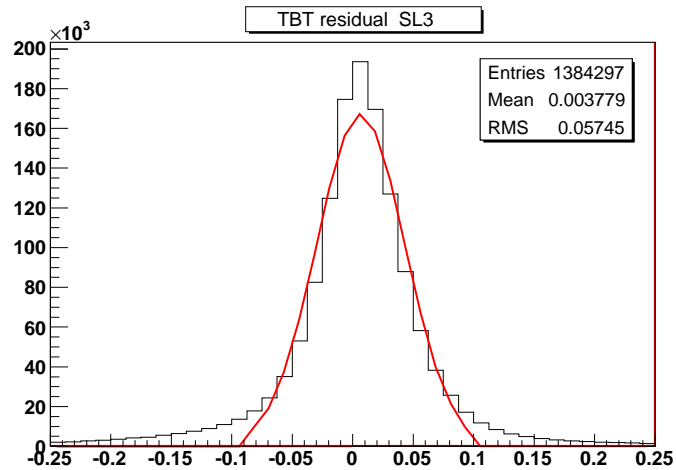


FIG. 35: Residual average of the time based tracking (TBT) from run 28079 for superlayer 3, all sectors combined. The sigma of the residual is monitored for all files and kept around 0.05 to ensure the quality of the DC calibrations.

make sure that the calibration is successful on the entire set. The final stage is referred to as the pass1 calibration. The data sets for different beam energy and torus current configurations are calibrated independently.

Normally, the ntuple files produced by the reconstruction code are used for the analysis of the data. Only the events that pass a set of basic criteria (e.g. one good electron in the event) are written into these files in a simpler format, so, they are already well compressed compared to the original BOS files. However, the EG1b experiment was one of the largest experiments at the time with an unprecedented amount of data. Limited disk space at the time of the experiment required further compression of the data. This led to data summary tapes (DST).

IV.3 DST FILES

The DST files reduced the amount of stored data for the analysis by changing the data format. For the main analysis of the EG1b experiment, we used the DST files. The ntuple files were briefly used for a few data sets for comparison purposes. Only certain variables were written into the DST files with certain precision. Detailed information on the variables and their precision in the DST files can be found in Tables 55-60 under Appendix A.

After the reconstruction code created the calibrated data in BOS format [91], another code called “HelP.cc” [92] was used to read the BOS files and create the DST files. “HelP” was executed by a script called “makeDST.pl”, which is located under the “/u/home/nguler/eg1b/upg_eg1_dst/HelP/” directory in the Jefferson Lab CUE³ system. Another program called “DSTMaker_byRun.pl”, located under “/u/home/nguler/eg1b/upg_eg1_dst/makeDST/”, was written in order to automate the DST file creation procedure. It automatically finds the files for a specific beam energy and torus configuration, pulls them from the silo tapes, checks if the file is copied fully without error⁴, executes “HelP” to create the DST files and puts the created files back into the silo for storage. All the DST files are stored under “/mss/home/nguler/dst/” for electron triggered events and “/mss/home/nguler/dstp/” for positron triggered events (with no negative track

³CUE is the Common User Environment, which encompasses all of the managed systems by the Jefferson Lab Computer Center and various other hosts at the lab

⁴The script compares the crc32 (Cyclic Redundancy Check with 32 bits) checksum of the file in the silo and the file copied into the work disk and proceeds only if the comparison is successful and creates a list of failed files for a second trial.

found), which are called DSTp files. The DSTp files are used later only for pair symmetric contamination analysis.

Another useful program called “LinkDATA.pl” organizes all the DST (and DSTp) files that belong to different beam energy and torus current configurations and creates an easy to manage database. The script caches the DST files (and/or the DSTp files based on the options given to the code) and creates links into a directory specified by the user (or the default directory, DATA). Since it uses soft links to the cache directory, the file storage database created by the “LinkDATA.pl” does not use any disk space, and it can be created anywhere that can access the cache disks of the Jefferson Lab farm machines. The user can also tell the script to re-cache certain files, create a list of missing files, link files of specific criteria based on the quality checks and link the DST files only if the corresponding DSTp file also exists. This script can be found under the “/u/home/nguler/eg1b/eg1_dst/makeDST/” directory in the Jefferson Lab CUE system.

IV.4 HELICITY PAIRING

In order to determine the experimental asymmetry A_{raw} , given in Eq. (215), it is important to distinguish between different helicity states. The helicity of the beam is pseudo-randomly alternated at the injector with a frequency of 30 Hz. This is called the original state. The original state is always followed by a complement state. The information about the helicity state and the total integrated charge for that helicity state are stored in the data stream after each helicity flip (sometimes the information was injected after 2 helicity flips depending on the DAQ throughput). A sync pulse, with twice the frequency of the helicity pulse, is also delivered to the experimental hall and stored in the data stream. The sync pulse is used to identify the helicity flips and detect missing helicity bits. The original helicity state is always labeled with 1 or 2, while the complement state is labeled with 3 or 4. The original helicity pulse labeled with 1 should always be followed by a complement helicity pulse labeled with 4. Similarly, 2 should always be followed by 3. The flip should always coincide with the rising edge of every other sync pulse. Fig. 36 shows the flow of helicity states together with corresponding helicity bits labeled with + or -.

Knowing the order of helicity labels, one can identify if any helicity state was missed due to dead time problems in the DAQ system. A broken sequence leads to unpaired helicity states, which would introduce a false asymmetry. It was determined

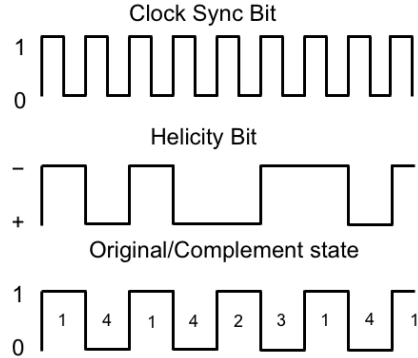


FIG. 36: The sync pulse is used to identify helicity flips and arrange the helicity buckets into pairs of original (labeled 1 or 2) and complement (labeled 3 or 4) states. State 1 is always followed by 4, and state 2 is always followed by 3. This helps to identify bad helicity states in the data stream.

that the helicity label stored in each physics event sometimes failed to latch leading to a broken sequence. Fortunately, the Faraday Cup scaler had its own helicity label latch which did not fail. The information from the FC scalers was used to recover the correct sequence.

An algorithm, as a part of the “HelP.cc” [92] program, was designed to track down the helicity states and determine the problematic helicity buckets. The algorithm was incorporated as a part of the DST library and the necessary flags to identify correct helicity sequencing were written into the DST files. The code extracts the helicity in terms of 1 or 0 or a number less than 0, which indicates that the helicity state is suspect.⁵ The negative values are encoded according to the list in Table 6.

While processing the DST files for analysis, a program called PATCH was used to produce tables for each DST data file to monitor the helicity sequence and throw away bad helicity buckets. The tables produced by PATCH include minimum and maximum event numbers for each helicity bucket together with the labels of original or complement states and the corresponding helicity bits determined by the HelP algorithm. The table also includes the minimum and maximum event numbers from scaler BANKS in the DST and finally a flag for the helicity bucket indicating whether it is good (flag = 1) or bad (flag = 10, -1000). The PATCH program labels any helicity state smaller than 1 or larger than 4 with -10. These states will be disregarded from

⁵The ultimate correlation between true beam helicity and the helicity label depends on many factors, e.g. beam energy and the status of the half wave plate (see section III.1).

TABLE 6: Helicity error codes.

| Err Code | Reason |
|----------|---------------------------------------|
| -1 | ROC out of sync |
| -2 | Helicity mismatch |
| -3 | Sync mismatch |
| -5 | Scaler physics helicity mismatch |
| -10 | Skip in TGBI helicity scaler |
| -20 | Skip in HLS scaler |
| -50 | Other pair failed helicity test |
| -100 | Smaller than usual number of triggers |
| -200 | No beam current in FC |

further analysis. The program also examines the order of the helicity states and determines the buckets that are out of sequence. It also compares minimum and maximum event numbers from the trigger banks with the output of the scaler banks and labels unmatched helicity buckets. The label for these two latter cases is -1000. In addition, PATCH takes care of suspicious helicity states at the end of some DST files that occur during file closing. Whenever a bad helicity bucket is found, the original and the complement states are always thrown away together until the correct sequence is recovered. This ensures that the removal of problematic buckets will not bias any particular helicity state. During the analysis process, the PATCH program is executed first and its output table is used by the DST reader to determine problematic helicity buckets. A segment from its output is shown in Table 7.

IV.5 QUALITY CHECKS AND PRE-ANALYSIS CORRECTIONS

First level quality checks were performed during data reconstruction. The time of flight information from SC, EC sampling fractions, DC residuals and EC-SC time differences were monitored for each file after full reconstruction of each data set. This ensures the applied calibration constants, determined by using sample runs, are successfully calibrating the full data set. After the reconstruction, there are about 40,000 DST files. Some of these files are not usable for physics analysis due to experimental conditions or DAQ errors during the data taking process. Therefore, a second level quality check is required to determine corrupted or bad files. The quality checks are performed on a file by file basis and separately executed for each

TABLE 7: A short segment from tables produced by the PATCH program. The table is from file dst28237_00.B00. Columns show minimum and maximum events in the helicity bucket, the corresponding helicity state and the resulting helicity bit. Event numbers from a different BOS bank, SCLR, are also listed for error check. The last column is the final flag, 1 meaning an acceptable bucket. The fraction of problematic buckets that show up in one file is less than 1%.

| evmin | evmax | state | bit | evmin_SCLR | evmax_SCLR | flag |
|-------|-------|-------|-------|------------|------------|-------|
| 73779 | 73889 | 2 | 0 | 73779 | 73889 | 1 |
| 73893 | 73994 | 3 | 1 | 73893 | 73994 | 1 |
| 73996 | 74164 | 1 | 1 | 73996 | 74164 | 1 |
| 74169 | 74261 | 4 | 0 | 74169 | 74261 | 1 |
| 74269 | 74351 | 2 | 0 | 74269 | 74351 | -1000 |
| 75023 | 75196 | -1000 | -1000 | 75023 | 75196 | -10 |
| 75197 | 75305 | 2 | 0 | 75197 | 75305 | 1 |
| 75306 | 75402 | 3 | 1 | 75306 | 75402 | 1 |
| 75406 | 75559 | 2 | 0 | 75406 | 75559 | 1 |
| 75562 | 75663 | 3 | 1 | 75562 | 75663 | 1 |
| 75665 | 75764 | 2 | 0 | 75665 | 75764 | 1 |

data set (Target, Beam Energy, Torus Current). In this section, the general outline for these quality checks will be described.

IV.5.1 Event rates

Count rates, normalized by the integrated beam charge, for inclusive events were monitored. The normalization was done by using the gated Faraday cup information. The event selection procedure includes standard electron cuts, which are used for the analysis of the data. As well as the inclusive count rates, we also monitored proton and pion count rates by using the standard ID cuts in the DST files. The count rates are monitored separately for each sector. The files with different count rates from the average were identified for all sectors. We checked the entries in the logbook while monitoring the count rates, especially the inclusive rates. If the count rate fell within 8% (sometimes 5% according to the sigma of the distribution) of the average count rate, the file was accepted as a good file. In order to do this correctly, the rates were monitored separately for each sector as well so that quality checks would not give a wrong decision because of a specific sector failure which effects the total

count rate. A group of files that fail the 8% requirement for three or more sectors are reported in the bad file list. On the other hand, if the group of files show lower count rates for only one or two sectors, they are reported in the warning file list. A single file that fails, even for a single sector, is directly eliminated. If the files fail the 8% percent requirement for all sectors, a sector independent failure, we look for reasons in the logbook entries and report them if there is an obvious reason. This practice helps to find out if any mistake has been made in labeling the files for their target. Rates for proton counts as well as for π^+ and π^- counts were also monitored for each sector. If these exclusive counts fail for any file or segment of files while their inclusive rates look good, we report them in the warning file list. The final fate of a file with a warning label is determined after a group discussion. In addition, we require the helicity bit, from PATCH, in the DST to be either 1 or 0.

IV.5.2 Beam charge quality

When measuring asymmetry, it is important to eliminate false asymmetries caused by experimental conditions. For example, we checked to make sure that the same amount of beam charge was delivered to the target in both helicity states. The integrated beam charge asymmetry was determined by using un-gated Faraday cup values,

$$A_{beam} = \frac{FC^+ - FC^-}{FC^+ + FC^-}, \quad (223)$$

where, + and - represent the corresponding helicity states. The distribution of beam charge asymmetry for all DST files was monitored to determine files with unusually high beam charge asymmetry. A Gaussian fit to its distribution was used in order to make a proper cut (see Fig. 37). The files that remain outside the cut are eliminated. Our final beam charge asymmetry cut was ± 0.005 , using the ungated Faraday cup asymmetry value.

IV.5.3 Effects of beam charge asymmetry

During the quality checks we also looked at the effect of the beam charge asymmetry on the inclusive asymmetry. This study led to a more detailed investigation on the dependence of the inclusive asymmetry on the beam charge asymmetry. The overall conclusion was that the data behave as expected and our normalization scheme (normalizing the counts with the gated Faraday cup values) works well to remove

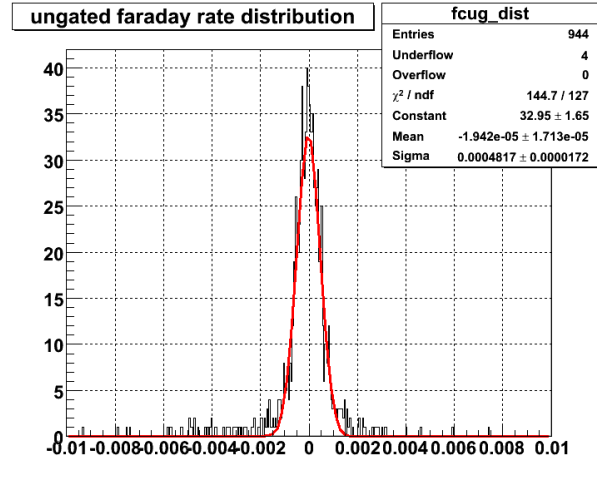


FIG. 37: Beam charge asymmetry is determined by using ungated Faraday cup counts from two helicity states. It should be a narrow distribution around zero. Each contribution to the histogram represents one DST file. A cut at 0.005 is generally applied to exclude files with large beam charge asymmetry.

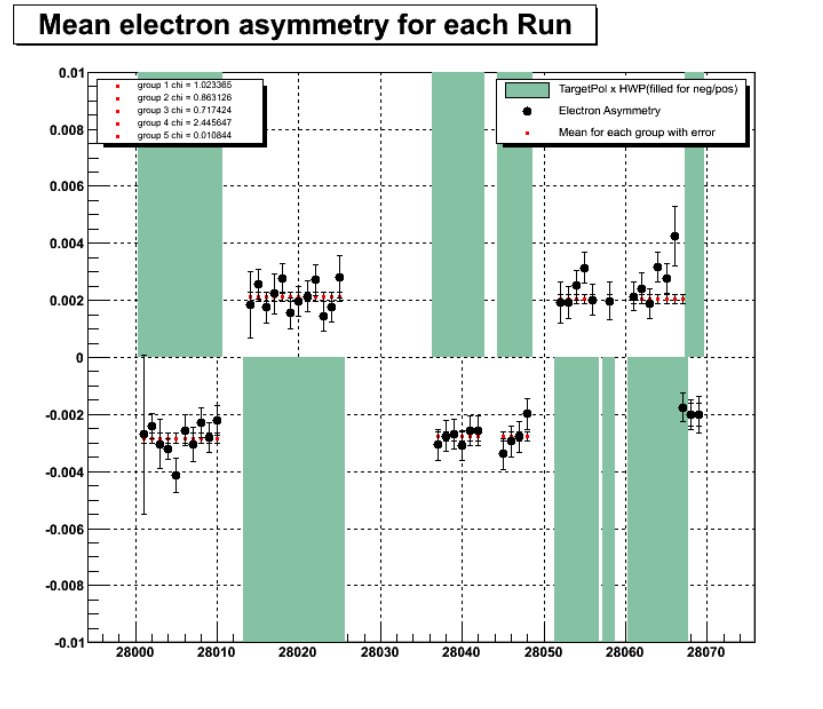


FIG. 38: Asymmetry versus run number for the ND_3 target and the 2.5 GeV data set with positive torus current. The shaded areas show the sign of the target polarization times HWP status (see section III.1). For this beam energy, there is an overall sign change that comes from the accelerator setup⁷, so, the asymmetry for each run must be in the unshaded part of the vertical axis. This plot reveals that run 28067 has the wrong asymmetry, which comes from the fact that its target polarization in the database was wrong.

unphysical asymmetry from the data. More detailed information on this specific study can be found among the CLAS notes archive [93].

IV.5.4 Polarizations and asymmetry check

It is important to determine the correct sign for the product of beam and target polarization since a wrong sign would dilute the asymmetry. Electron asymmetry plots were generated for groups of runs from the same data set. These are plots of electron asymmetry versus the run number. An example of such a plot is shown in Fig. 38. The products of the half wave plate (HWP) sign (1 for in, -1 for out) and the target polarization sign for each run are also shown in this plot. There are various ways to show the overall polarization state properly. We decided to show only the multiplication of the HWP sign and the target polarization sign by creating a shaded area on the positive or negative side of the plot according to the result. The primary purpose is to understand if there were any runs with the wrong sign of the electron asymmetry. In case it should occur, we examined these specific runs more carefully to find out if any mistake was made in recording the HWP state or the target polarization during the data taking. In the plot shown, for example, run 28067 was determined to have the wrong target polarization in the database. Logbook investigation reveals that its target polarization should be the same as the subsequent runs. The runs determined to have the wrong sign for the HWP or the target polarization were corrected during the data analysis process.

IV.5.5 Faraday cup corrections

The Faraday cup is located 29.5 m downstream from the CLAS target cell. Its diameter is 15 cm. We get the integrated beam charge information from the Faraday cup. However, while the beam passes through the target, multiple scattering causes an overall spread of the beam. If the spread angle of the beam is larger than 0.146° , some of the beam charge will be lost outside the Faraday cup, leading to an unaccounted beam charge. The beam divergence can be calculated by the Molière distribution [95][94] but the target magnet complicates the situation, causing an additional divergence. Therefore, a detailed study was conducted by R. Minehart *et al.* measuring the current at the upstream Beam Position Monitors (BPMs) and comparing it to the Faraday cup values for different targets and beam energies. It was assumed that no correction was needed for 5.7 GeV beam, which has a small divergence. This

energy was used to establish the exact correspondence between the BPMs and the Faraday cup. Then, for each beam energy and target, the ratio of the BPM value to the Faraday cup value was recorded. It was determined that no correction was required for any target from the 4.X and 5.X GeV data sets. However, correction factors for other data sets were determined as given in Table 8. The Faraday Cup value should be divided by the normalization factor to get the true integrated beam charge to normalize the counts. These factors are recorded in a run information table that is used by the DST reader during the analysis. Note that the correction is largest for the lowest beam energy, as expected.

Another correction for the Faraday cup information comes from the fact that for Empty target runs, the Faraday cup recorded at half the rate it did for other targets. This was intentionally done by removing one bit from FC response rate to be able to accommodate a higher beam current during the experiment. Since the empty target has a much shorter radiation length, it could accommodate a higher beam current without increasing the dead time for the DAQ. However, this results in only half the FC count for the empty target runs. Therefore, a factor of 2 must be multiplied with the FC counts for empty targets. The quality checks revealed that there are also a few other runs with missing FC bit, so their FC values must also be multiplied by 2. The FC multiplicative factor is also incorporated into the run information table and used by the DST reader during the analysis process. The run information table can be consulted for detailed information and correction factors for each run.

It should be noted that the Faraday Cup corrections above do not affect the raw asymmetry calculations but become important only for background analysis where we need to divide normalized counts from different targets, with differing radiation lengths. Therefore, these corrections are applied for cases like dilution factor studies only but they are not applied while calculating the raw asymmetries, where FC corrections cancel out. In this way, we avoid possible type conversion and precision loss problems that may arise when dividing a large integer number, like Faraday cup values, by a normalization factor.

IV.5.6 Additional comments

During the quality checks, some of the runs were determined to have the wrong torus current encoded (with value -1 A) in the DST file. In particular runs 26256-26276 from the 1.6 GeV data set, 27248-27256, 27270-27275 from the 2.3 GeV data set and

TABLE 8: Faraday Cup normalization factors correcting for angular beam divergence.

| E_{beam} (GeV) | NH ₃ | ND ₃ | ¹² C | Empty(LHe) |
|------------------|-----------------|-----------------|-----------------|------------|
| 1.606 | 0.846 | 0.828 | 0.850 | 0.965 |
| 1.723 | 0.856 | 0.840 | 0.860 | 0.967 |
| 2.286 | 0.951 | 0.951 | 0.962 | 1.000 |
| 2.561 | 0.986 | 0.986 | 0.986 | 1.000 |

26591-26598, 26723-26775 from the 5.8 GeV data set had the wrong torus current of -1 A in the database. We made sure that the torus currents for these runs were set manually in the tcl script during the data reconstruction. The torus currents are also corrected during data analysis by replacing the encoded torus current with the corrected torus current in the DST file.

There are also files which crash the DST reader program or give empty or unusual outputs. These files are flagged and removed from the final list. Finally, we always checked the logbook for specific runs we labeled as bad. We briefly went over the logbook entries for each run and marked the bad or problematic runs. In summary, we compared the logbook entries with our results as a consistency check.

In addition, detailed investigations were made on the raster patterns for each run. Some runs show elevated count rates in certain parts of the target material, which usually means that the beam is scraping the target edge or there may be an interfering material in front of the target. More information about this study as well as some additional concerns about the quality checks can be found in [95].

At the end of the quality check procedure, a list of bad files and a complete run information table are produced. The table includes a flag for each run together with corresponding target, energy, torus and polarization information as well as the Faraday Cup correction factors. The script LinkDATA.pl, described in section IV.3, is used to organize the files and exclude the bad files from the final list. Missing files from storage or cache disks are determined and recovered if they are good files. The DST reader consults with the bad file list and the run information table while processing each file for analysis. More information and detailed monitoring plots for quality checks can be found in [96] and [97]. At this point, we begin to describe the higher level analysis.

IV.6 DATA BINNING

The goal of our experiment is to determine asymmetries as a function of at least two kinematic variables. The kinematic variables have been defined and explained in earlier sections. Among these variables, we choose to use the squared four-momentum transfer Q^2 and invariant mass W as our official variables. Once we have the cross section distributions for different helicities with respect to these variables, $d\sigma(\Delta Q^2, \Delta W)$, we can express them as a function of any other pair of kinematic variables as well. Another common pair is (Q^2, x) , where x is the Bjorken scaling variable. While converting the (Q^2, W) pair into (Q^2, x) , we used kinematic values directly obtained from data, which are averaged over the amount of data observed for that specific kinematic bin. In order to go into details, we first need to explain our data binning method. We divided the Q^2 and W range of the data into finite bins. The W bins are simply generated as 10 MeV bins. Binning in Q^2 is logarithmically calculated by using the formula:

$$\text{Bin Number} = n = \text{int} \left(13 \log_{10} \left(\frac{Q^2}{C} 10^{27/13} \right) \right), \quad (224)$$

where,

$$C = \frac{(1 + 10^{-1/13})}{2}. \quad (225)$$

From these equations, we can calculate Q_{min}^2 and Q_{max}^2 for each bin by using the following definitions:

$$Q_{min}^2 = C \times 10^{(n-27)/13} \quad (226)$$

$$Q_{max}^2 = C \times 10^{(n+1-27)/13} \quad (227)$$

Table 9 show the Q^2 bins of the EG1b data together with the minimum and maximum value for each bin. The table also shows the arithmetic and geometric average of each bin. For our analysis, we did not use a simple average for the bin centers but determined the central values directly from the data itself. This was done by calculating the Q^2 and W values of each data point in the bin and then averaging all data for a single bin by using the corresponding counts in each bin. The kinematic centers of the bins do not always peak at the arithmetic or geometric bin centers.

TABLE 9: Q^2 bins for EG1b experiment

| Bin | Q2min | Q2max | geoAve | ariAve |
|-----|-------------|--------------|--------|--------|
| 1 | 0.009188388 | 0.010968883 | 0.0100 | 0.0101 |
| 2 | 0.010968883 | 0.013094397 | 0.0120 | 0.0120 |
| 3 | 0.013094397 | 0.015631785 | 0.0143 | 0.0144 |
| 4 | 0.015631785 | 0.018660860 | 0.0171 | 0.0171 |
| 5 | 0.01866086 | 0.022276898 | 0.0204 | 0.0205 |
| 6 | 0.022276898 | 0.026593641 | 0.0243 | 0.0244 |
| 7 | 0.026593641 | 0.031746867 | 0.0291 | 0.0292 |
| 8 | 0.031746867 | 0.037898668 | 0.0347 | 0.0348 |
| 9 | 0.037898668 | 0.045242545 | 0.0414 | 0.0416 |
| 10 | 0.045242545 | 0.054009494 | 0.0494 | 0.0496 |
| 11 | 0.054009494 | 0.064475272 | 0.0590 | 0.0592 |
| 12 | 0.064475272 | 0.076969073 | 0.0704 | 0.0707 |
| 13 | 0.076969073 | 0.091883882 | 0.0841 | 0.0844 |
| 14 | 0.091883882 | 0.109688832 | 0.100 | 0.101 |
| 15 | 0.109688832 | 0.130943966 | 0.120 | 0.120 |
| 16 | 0.130943966 | 0.156317848 | 0.143 | 0.144 |
| 17 | 0.156317848 | 0.186608595 | 0.171 | 0.171 |
| 18 | 0.186608595 | 0.222768982 | 0.204 | 0.205 |
| 19 | 0.222768982 | 0.265936407 | 0.243 | 0.244 |
| 20 | 0.265936407 | 0.317468671 | 0.291 | 0.292 |
| 21 | 0.317468671 | 0.378986684 | 0.347 | 0.348 |
| 22 | 0.378986684 | 0.452425451 | 0.414 | 0.416 |
| 23 | 0.452425451 | 0.540094935 | 0.494 | 0.496 |
| 24 | 0.540094935 | 0.644752718 | 0.590 | 0.592 |
| 25 | 0.644752718 | 0.769690734 | 0.704 | 0.707 |
| 26 | 0.769690734 | 0.918838820 | 0.841 | 0.844 |
| 27 | 0.91883882 | 1.096888321 | 1.00 | 1.01 |
| 28 | 1.096888321 | 1.309439656 | 1.20 | 1.20 |
| 29 | 1.309439656 | 1.563178475 | 1.43 | 1.44 |
| 30 | 1.563178475 | 1.866085950 | 1.71 | 1.71 |
| 31 | 1.86608595 | 2.227689819 | 2.04 | 2.05 |
| 32 | 2.227689819 | 2.659364071 | 2.43 | 2.44 |
| 33 | 2.659364071 | 3.174686710 | 2.91 | 2.92 |
| 34 | 3.17468671 | 3.789866839 | 3.47 | 3.48 |
| 35 | 3.789866839 | 4.524254507 | 4.14 | 4.16 |
| 36 | 4.524254507 | 5.400949352 | 4.94 | 4.96 |
| 37 | 5.400949352 | 6.447527179 | 5.90 | 5.92 |
| 38 | 6.447527179 | 7.696907344 | 7.04 | 7.07 |
| 39 | 7.696907344 | 9.188388200 | 8.41 | 8.44 |
| 40 | 9.1883882 | 10.968883209 | 10.0 | 10.1 |

IV.7 ELECTRON IDENTIFICATION

During the EG1b experiment, the event trigger used a combination of the Electromagnetic Calorimeter and the Cherenkov counter signals and accepted all events above the threshold, which was determined specifically for each electron beam configuration. The off-line reconstruction code (RECSIS) creates a second filter of events by requiring more strict particle definitions and uses the Simple Event Builder (SEB) to identify particles. The RECSIS identification of particles is primarily based on the time of flight information from Scintillator Counters (SC) and the track reconstruction by the Drift Chamber (DC). More detailed information on the off-line data reconstruction can be found in section IV.2. At high energies, as in the case of the EG1b experiment, the SEB method is not reliable because all particles are very fast and the time of flight (TOF) information does not reliably distinguish electrons from pions. The inclusive analysis requires a very careful selection of electrons, which was accomplished by requiring a negative track with matching signals in the TOF scintillators, the Cherenkov Counters (CC), and the Electromagnetic Calorimeter (EC). If more than one track was found satisfying this condition, the track with the shortest flight time was selected as the electron candidate. The primary contamination for electrons comes from negatively charged pions. The EC and the CC detectors were specifically used to separate pions and other negatively charged particles from electrons. After the completion of the reconstruction by the RECSIS code, the list of cuts below were applied for the inclusive analysis to identify electrons:

1. Charge = -1
2. Status Flag selection
3. Trigger Bit selection
4. Helicity selection
5. Vertex cut
6. Cherenkov photo-electron cut
7. Electromagnetic Calorimeter cut
8. First electron candidate (with shortest flight time)

9. Additional kinematic cuts

- Momentum cut
- Polar angle cut
- Energy transfer cut
- Polar angle cut for sector 5

10. Geometric and Timing cuts on the Cherenkov Counter

11. Fiducial cut

The following sections will provide more detailed information on some of these cuts.

IV.7.1 Status Flag

Each identified particle in the DST carries a status flag. If the particle status flag is in the $[0,5]$ range, the reconstruction is time-based and the event is acceptable. Particles with status flag > 5 are reconstructed from hit-based tracking only and should be eliminated. In addition, if a particle is detected in all 3 superlayers of the DC and its trajectory is reconstructed accurately, 10 is added to the status flag variable, which carries some of the time based tracks into a range of $[10,15]$. Therefore, the status flag selection criteria is:

$$0 \leq \text{status flag} \leq 5 \quad \text{OR} \quad 10 \leq \text{status flag} \leq 15$$

IV.7.2 Trigger Bit

Each event in the DST carries a trigger bit information. It is an integer value that represents a 16 digit binary number. We call this value a trigger word. Each bit corresponds to a specific trigger response. We will call these bits as trigger bits and they can either be on or off (1 or 0). The very first bit (the least significant bit) is trigger bit 1. Trigger bits 1 to 6 correspond to our standard triggers, one for each sector, based on CC and EC signals. Trigger bit 7 requires a hit in EC and CC anywhere, while trigger bit 8 requires a hit only in the EC with a lower threshold (no CC hit). Trigger bit 8 is mainly used for minimally biased pion selection. Trigger bits 9 to 14 are not used for any purpose. Trigger bits 15 and 16 record the value of the helicity bucket (redundantly). The trigger bits are combined to yield trigger

words. If only trigger bit 1 is fired, the trigger word would be 1, which corresponds to an event in sector 1. If trigger bit 3 is fired (event in sector 3), the trigger word is 4. For an event observed in sector 1 and 3, the trigger bit configuration (only considering the first 6 digits) would be 000101, giving a trigger word of 5. Our event selection criteria is based on signals in trigger bits 1 through 6. If none of these bits were on for the event, it is discarded. If any of the bits from 1 to 6 were signaled, we accept the event regardless of the higher bit values.

IV.7.3 Vertex Cuts

It is important that the scattered electrons come from the target, not the surrounding material. Therefore, the interaction vertex should be within certain boundaries. By looking at the vertex distribution of the electron, we determined global values for the minimum and maximum position of the interaction vertex in the z coordinate (along the beam direction). In CLAS coordinates, the target center is at $z = -55.0$ cm. The minimum z position was chosen to be -58.0 cm while the maximum z position is -52.0 cm,

$$-58 \leq v_z \leq -52.$$

Interactions that come from outside of this region are rejected for all particles. Of course, before applying the vertex cut, proper vertex corrections are applied (see Fig. 39). These corrections are described in section IV.10.1 in detail. It should be noted that the target configuration makes it impossible to cut out the target window material with a vertex cut since the resolution of the event vertex reconstruction is not fine enough to resolve distinct scattering peaks within the ~ 2.3 cm distance of the target banjo length. In order to eliminate contributions from the aluminum, Kapton and liquid helium on either side of the target material, other background subtraction methods, such as dilution factor calculations, are used.

IV.7.4 Cherenkov Counter Cuts

The Cherenkov counter (CC) is designed primarily to separate electrons from pions. The threshold for the electrons is 9 MeV while for pions it is 2.5 GeV^8 . Identification of pions in the CC is quite successful as long as the pion energy is below the threshold value, in which case the pion peak can easily be distinguished from the electron

⁸These are momentum thresholds and natural units are used with $c = 1$.

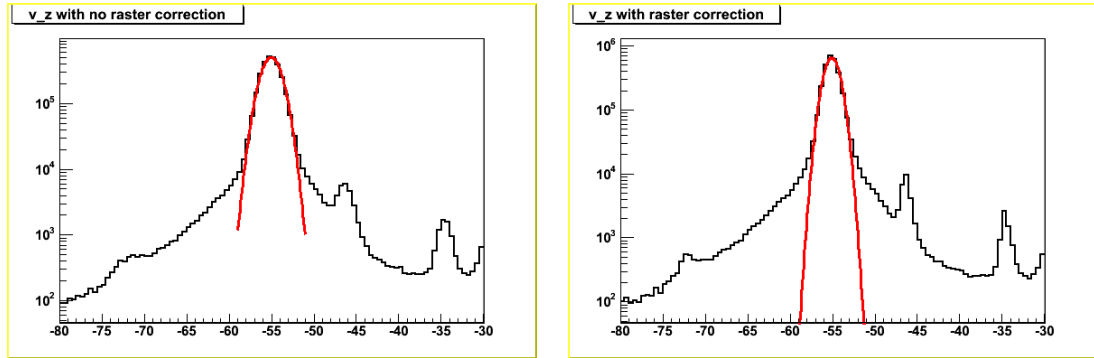


FIG. 39: Vertex positions for the electrons are shown before (left) and after (right) the raster correction (see section IV.10.1). No other kinematic corrections are applied at this point. After the correction, a vertex cut of $(-58 \leq v_z \leq -52)$ is applied for each particle. Note that the vertical scale is logarithmic.

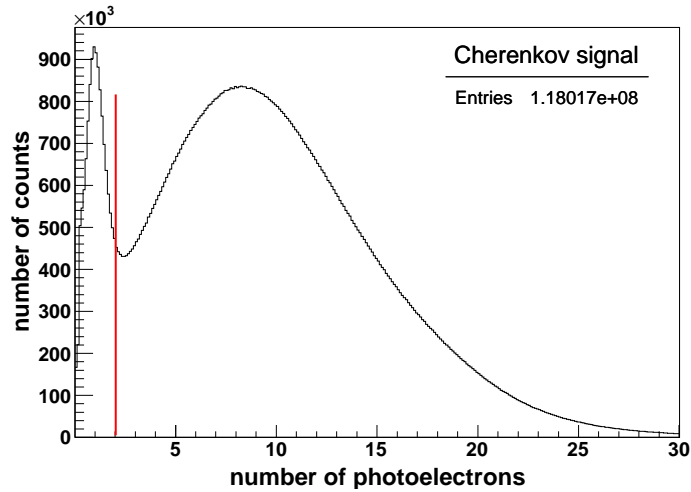


FIG. 40: Sample Cherenkov Counter signal showing the pion peak with a low CC photoelectron signal and the cut applied at 2 photoelectrons for electron selection.

signal. However, the signal from high energy pions above the threshold becomes indistinguishable from the electron signal, making the Cherenkov detectors inefficient to separate high energy pions from electrons. Fig. 40 shows a sample signal from CC together with the applied cut at 2 photoelectrons to identify the electrons. This cut is applied for momenta less than 3.0 GeV. Since the CC efficiency is relatively low at higher momenta, a cut requiring that the number of photoelectrons exceed 0.5 for momenta above 3.0 GeV is used. Any remaining pion contamination is taken care of by other cuts that will be defined in the following sections.

IV.7.5 Electromagnetic Calorimeter Cuts

When we plot the energy deposition in the inner calorimeter (EC_{in}) versus the total energy deposition in the EC (EC_{tot}), we see a clear separation between the electron and pion signals. The total energy deposited by an electron in the EC is proportional to its momentum (p). This ratio is called a sampling fraction, which is ~ 0.29 for this experiment (see Fig. 44). The pions, on the other hand, are minimum ionizing particles, hence, their energy deposition mechanism is different than that of the electrons. Details about this are given in section III.3.5. The energy loss for a pion in the calorimeter is mostly independent of its momentum. The localized events in the bottom left corner of each plot in Figs. 41 and 43 represent the pions detected by the EC. As the momentum of the particles increase, the distinction between the electrons and the pions in the calorimeter become more evident because EC_{in}/p and EC_{tot}/p for the pions decrease rapidly while EC_{tot}/p for the electrons remains as a Gaussian distribution around the sampling fraction as shown in Fig. 44. In order to select the electrons, we applied the following cuts:

- $EC_{tot}/p > 0.20$ for $p \leq 3$ GeV
- $EC_{tot}/p > 0.24$ for $p > 3$ GeV
- $EC_{in} > 0.06$

EC sum correction

The Electromagnetic Calorimeter records three different signals for the energy deposited by an incident particle. These signals correspond to the inner calorimeter (EC_{in}), outer calorimeter (EC_{out}) and total energy deposited (EC_{tot}) in both layers.

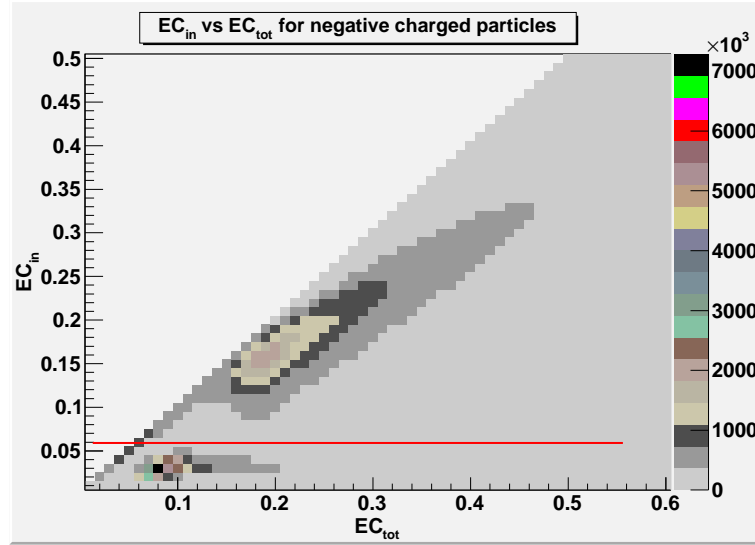


FIG. 41: EC_{in} vs. EC_{tot} for negative charged particles. $EC_{in} > 0.06$ is required to select the electrons. These events are from the 4.2 GeV outbending data.

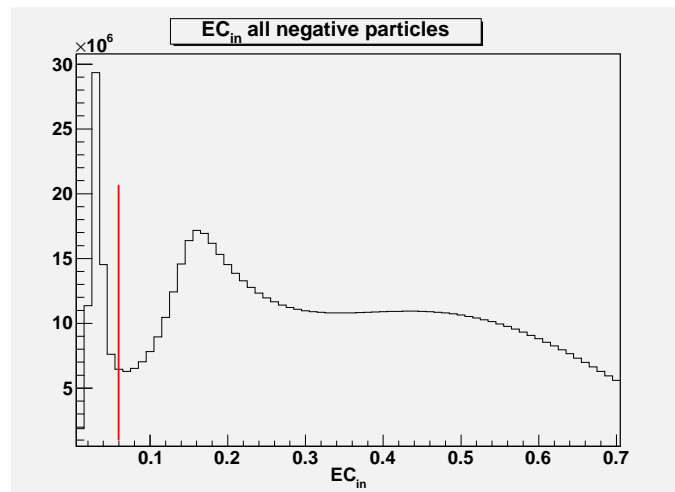


FIG. 42: The energy deposition of negative charged particles in the inner layer of the EC (energy spectrum of the EC_{in}). $EC_{in} > 0.06$ is required to select the electrons and separate them from negative pions. These events are from the 4.2 GeV outbending data.

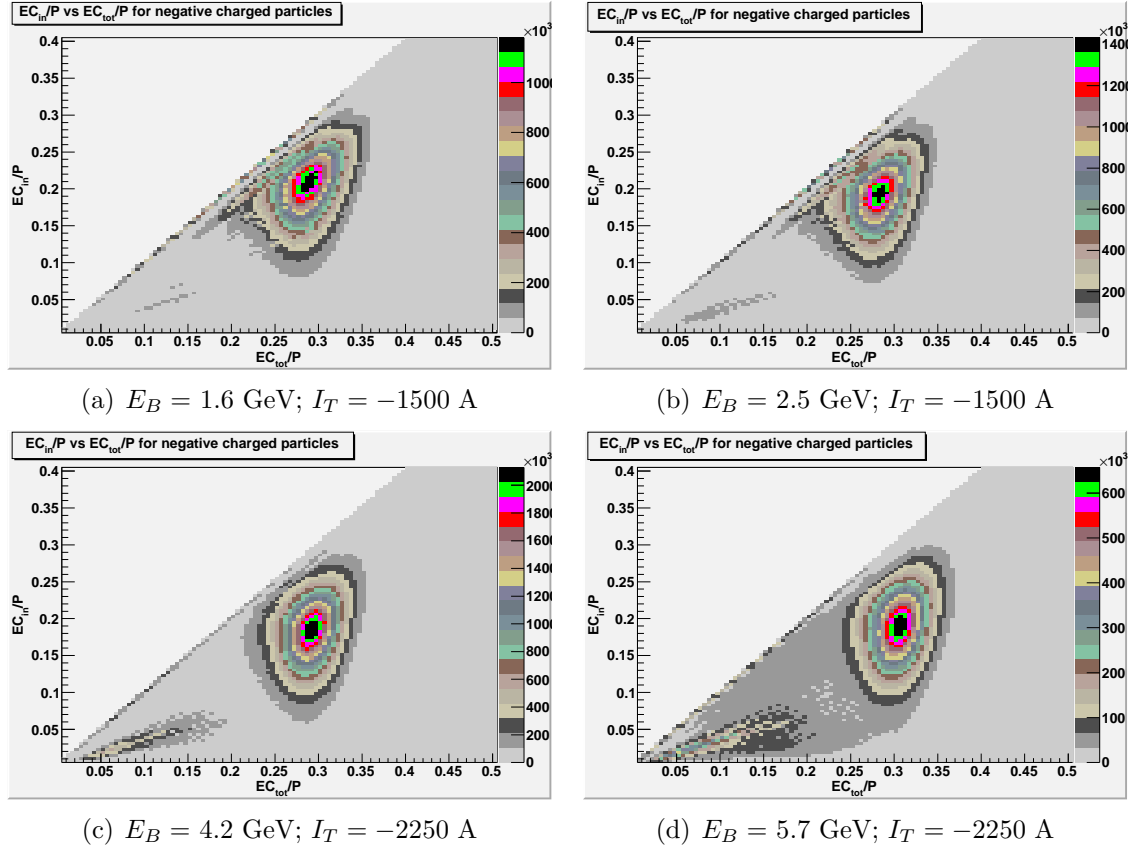


FIG. 43: EC_{in}/p vs. EC_{tot}/p for 4 different beam energies (E_B) with outbending torus currents (I_T). The beam energies increase from the top left to the bottom right plot. The events concentrated in the left bottom corner of each picture are pions, which become more visible with increasing beam energy.

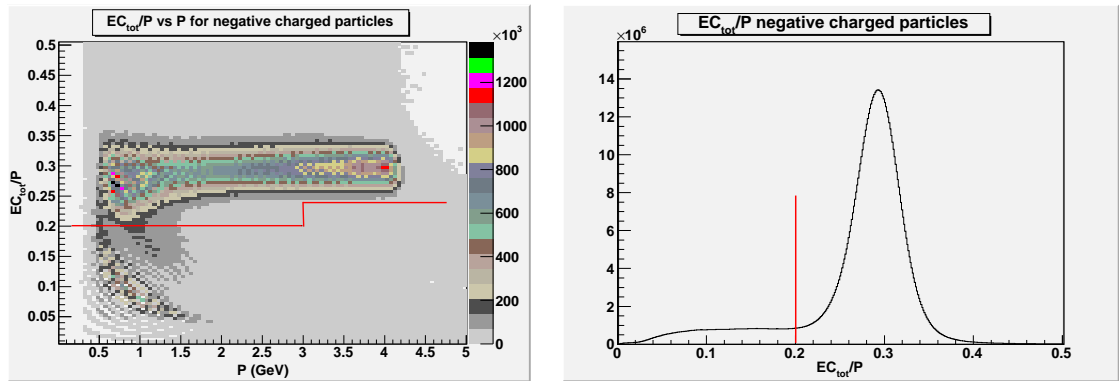


FIG. 44: EC_{tot}/p vs. p distribution (left) and EC_{tot}/p spectrum for negative charged particles (right). The applied cut is shown with the straight lines and explained in the text.

Normally, $EC_{tot} = EC_{in} + EC_{out}$ should always be true. However, the readout for these three signals did not always fulfill this condition. Even if the event is good, sometimes a few channels in the EC failed to record the deposited energy leading to a mismatch. These occasional failures required an additional correction for the energy deposited in the EC such that:

$$EC_{tot} = \text{MAX}(EC_{tot}, (EC_{in} + EC_{out})). \quad (228)$$

This correction makes sure that the total measured energy in the EC was employed in the PID cuts described above.

IV.7.6 Additional kinematic cuts

The event reconstruction becomes unreliable when scattered particles get too close to the edge of the geometric acceptance of the detector. Also, the detector efficiency becomes unpredictable in case of very low momentum particles. Therefore, we employed the following additional cuts on the data:

$$y \equiv 1 - \frac{E'}{E} < 0.80;$$

$$7.5^\circ < \theta_{DC} < 49^\circ,$$

where θ_{DC} is the polar angle measured at Drift Chamber region 1. The upper angle limit comes from the interference of the target magnet coils with the detector. The lower angle limit is employed to make sure the data is within the acceptance of the CLAS detector. It is also smaller than the usual DC coverage because the target was shifted back during the experiment. In addition, we also applied a cautionary requirement on the transferred energy such that:

$$\nu \equiv E - E' > 0. \quad (229)$$

Sector 5 Cut

Sector by sector inspection of the data revealed a problematic kinematic region in sector 5, where the event reconstruction failed for unknown reasons resulting in a discrepancy between the calculated and measured polar angles. This was observed in the DST files as well as the original ntuple files, which means the reconstruction failed at the SEB level. The problem becomes more obvious if one plots the reconstructed

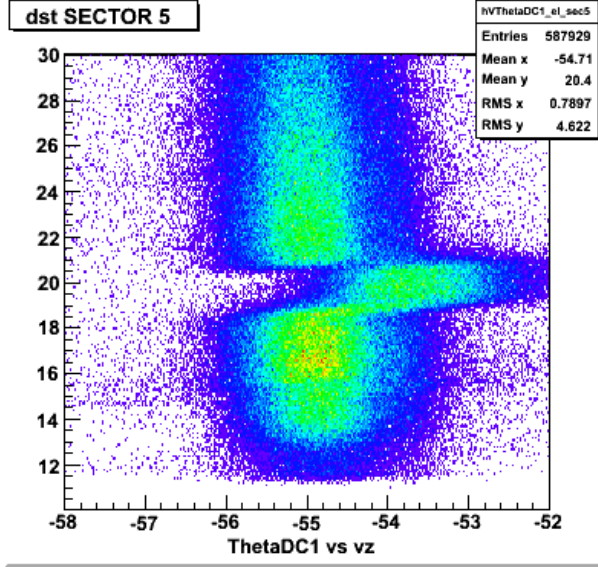


FIG. 45: Reconstructed vertex position versus θ_{DC} for electrons in sector 5. A polar angle cut in sector 5 was necessary to remove the part of data with bad vertex definition. The kinematic region $18 < \theta_{DC} < 21$ for this sector was excluded from analysis.

z -vertex position vs. θ_{DC} , as shown in Fig. 45. This kinematic region is excluded from further analysis by applying the following cut on the data:

$$\theta_{DC} \leq 18^\circ \text{ and } \theta_{DC} \geq 21^\circ \text{ (Sector 5 only)} \quad (230)$$

There are other cuts we used on the data to identify the electrons even more precisely. Since these additional cuts require a thorough analysis of the data and detailed explanations, we prefer to dedicate an entire section to them. The following sections describe the additional cuts for precise electron identification and minimization of pion contamination.

IV.8 GEOMETRIC AND TIMING CUTS ON THE CC

Geometrical and timing cuts on Cherenkov Counter signals, first developed by M.Osipenko *et al.* [98], were applied to the EG1b data for the first time. The original set of parameters determined by Osipenko did not work very efficiently for our data because they greatly reduced the electron sample while clearing up the pions. We extensively studied the data to develop a new set of parameters that worked better for us. This section provides some explanations of these cuts.

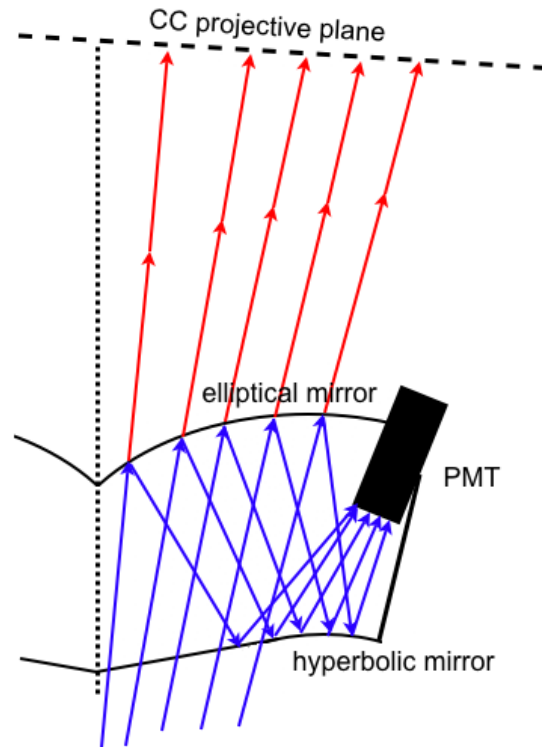


FIG. 46: The projective plane is shown for a CC segment. Incoming light normally travels on the path shown by the blue lines and is reflected by the elliptical and hyperbolic mirrors. The CC projective plane is constructed by assuming that the light continues on a straight path along the initial direction and travels the same distance it would normally take to reach the PMT. This means the sum of the blue lines after the first reflection is equal to the total length of the red line, which is called a projected path. The plane is formed by such a projection of many possible paths. The angle between the projected path and the normal of the projective plane (dotted line) is the projected polar angle, θ_p . The angle between the projected path of the segment center and the normal of the plane is the polar angle of the segment center, θ_p^c .

Each sector in the CLAS detector contains 18 CC segments. Each of these segments has two photomultiplier tubes (PMT), one at right and one at left. These PMTs have a certain rate of noise that has been measured to be around 42 kHz and each noise pulse may have an amplitude around one photo-electron. The main purpose of the CC is to distinguish between the electron and pion tracks. It has been determined that if a noise pulse in the CC and a negative pion track measured in the DC coincides within the same trigger time window of the CLAS detector, which is 150 ns, the pion can be registered as an electron by the analysis code. This is apparently the biggest source of pion contamination for the inclusive data. In order to eliminate the coincidences between the CC noise and a pion track, the geometric and time matching requirements between the CC signal and a measured track were implemented into our data selection criteria.

IV.8.1 Geometric cuts

An imaginary CC projective plane is constructed behind the CC detector at a distance traveled by the CC radiation from the emission point to the PMT but without doing any reflections in the mirror system. The resulting CC projective plane is shown in Fig. 46 and is given in terms of the CLAS coordinate system as:

$$1 - 7.840784063 \times 10^{-4} x - 1.681461571 \times 10^{-3} z = 0 \quad (231)$$

where x is the radial distance along the sector center and z is the direction along the beam line. Then, for each CC segment, the polar angle of the segment is constructed by connecting the points from the center of CLAS to the center of the image of the CC segment at the projective plane. The polar angle of each electron candidate is also determined by using the SC impact point of the track and projecting it to the CC projective plane. This quantity will be referred as the projected polar angle. Fig. 46 shows the construction of this polar angle.

Distributions of the particles' polar angles, θ_p , are monitored for each segment. They should show a Gaussian distribution around the polar angle of the segment center, θ_p^c . For some segments, however, slight offsets have been observed. After correcting the distribution for these offsets, we can apply a cut to remove the tails of the distribution. In order to determine where to apply the cuts exactly, we plotted the electron and pion (π^-) distributions together on a logarithmic scale, as shown in Fig. 47. It is clear that the tails of the electron polar angle distributions are actually

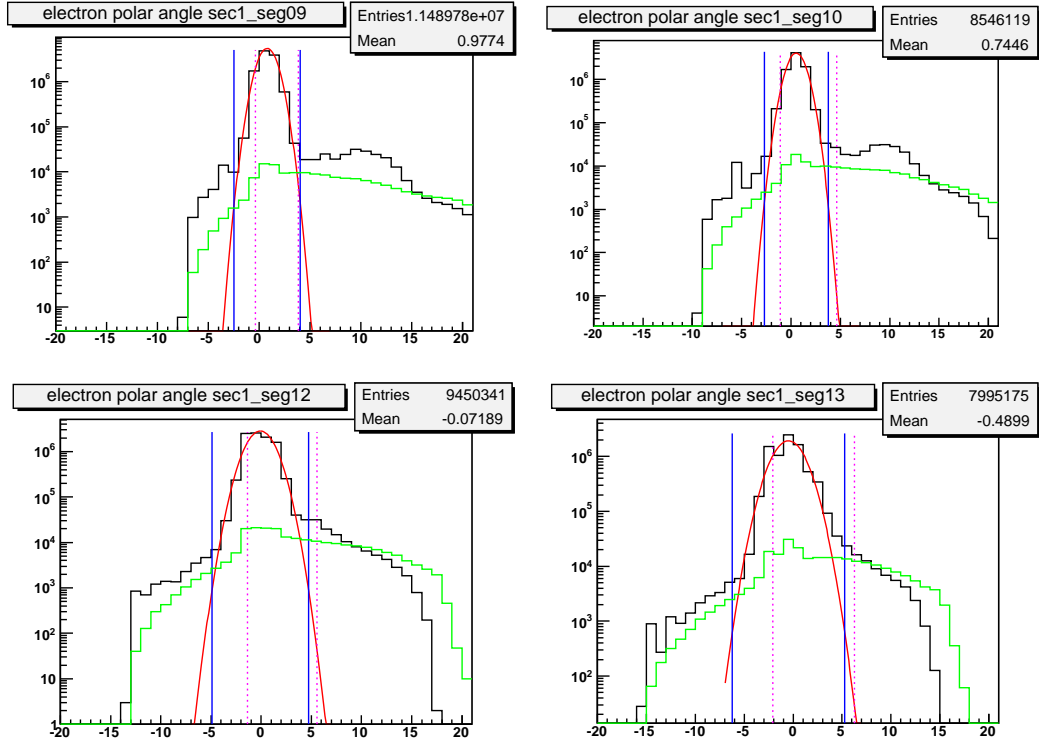


FIG. 47: Distribution of the projected polar angles of the electrons (black lines) and the pions (green lines) for a few segments in sector 1. There are 6 sectors and each sector contains 18 segments. Similar plots are produced for each segment and fitted by a Gaussian function to determine the mean value of the distribution. Comparison of the electron distribution to the pion distribution proves that most of the particles that “pretend” to be electrons and stay 3σ away from the mean value of the electron distribution are actually pions. These particles are eliminated from the electron sample by applying the cuts shown by the blue lines. Note that the y scale is logarithmic.

mislabeled pions. By looking at the distributions for each segment, we determined an appropriate polar angle cut for each segment in all sectors.

IV.8.2 Timing cuts

After the geometrical cuts applied on polar angles, we still need to apply time matching between the CC signal and the passage of the particle. To determine the timing of the electron candidate, we use the SC signal. If the particle is a real electron, the SC and CC signals should be produced by the same particle. We assume the electron travels with the speed of light. Therefore, the time difference between the SC and CC signals should be given by:

$$\Delta t^{SC-CC} = \frac{r^{SC} - r^{CC}}{c\beta} \quad (232)$$

where $r^{SC} - r^{CC}$ is the track distance between the SC paddle and the CC projective plane. These variables exist in the DST files as “sc_r” and “cc_r”. The time of hits also recorded as “sc_time” and “cc_time”.

It should be pointed out that the original DST files, produced during the calibration and reconstruction process, did not have these variables, although they existed in the original BOS files. We had to change the DST structure to implement the variables into the DST libraries and *reproduce* all the DST files again in order to complete this analysis. This procedure took a substantial amount of time. After completing the new DST production, we compared the old DST results with the new ones to ensure the success of the implemented changes. Finally, by using the recorded times and the track distances from the SC and CC detectors, it is possible to determine the difference between the expected time and the observed time, Δt , as:

$$\Delta t = t^{SC} - t^{CC} - \left(\frac{r^{SC} - r^{CC}}{c\beta} \right) \quad (233)$$

The Δt distribution should normally peak around zero. Again, we plotted the electron and pion Δt distributions together in a logarithmic scale, as shown in Fig. 48. The tails of the electron distributions are clearly mostly pions. However, if one looks at the positive side of the electron peak, around the 60 ns region, there is another peak that begins to appear for the electron candidates in some segments. Pion candidates do not have any peak in that region. This shows that this strange peak actually represents true electrons and should not be cut out. Because of that, we

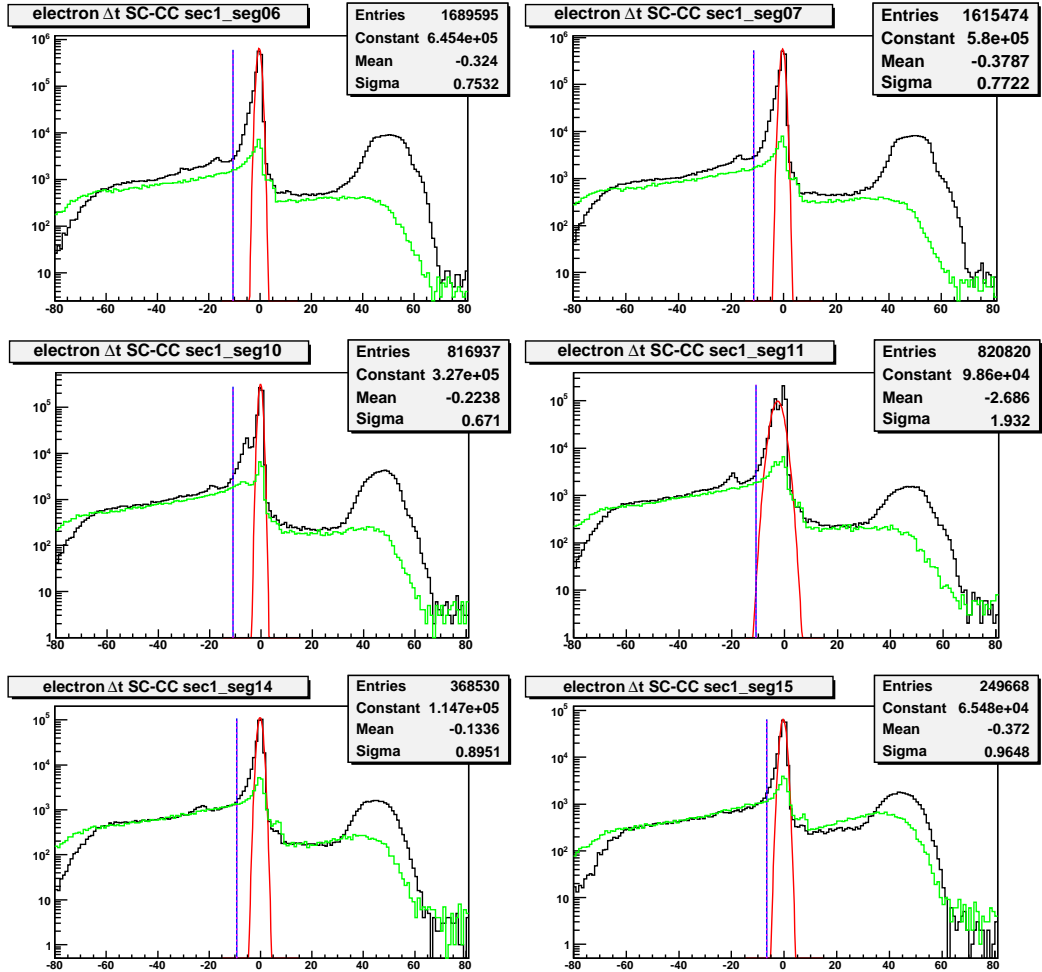


FIG. 48: Distribution of the Δt given in Eq. (233) for electrons (black lines) and pions (green lines) for some segments in sector 1. Similar plots are produced for all sectors and segments and electron distributions are fitted by a Gaussian function to determine the mean value of the distribution. Comparison of the electron distribution to the pion distribution proves that most of the particles that “pretend” to be electrons but stay at the tails of the electron distributions are actually pions. These particles are eliminated from the electron sample by applying the cuts shown by the blue lines. Note that the y scale is logarithmic. The cut is applied only on the left side since there are electron peaks that appear around the 60 ns region. Those extra peaks are clearly not pions so they were kept.

applied the timing cut only to the left side of the distribution. In rare cases, especially for outbending runs, a similar peak appears also on the negative side of the electron distribution, around the -60 ns region. In those cases, we moved the cut even below the range of that peak in order not to lose those electrons. Each segment was carefully examined to determine the best location of the cut to eliminate most of the pions but still keep the electron sample intact. Finally, a table of cut parameters was produced for the main analysis program.

IV.8.3 Left-Right PMT cut

One last geometrical cut we applied on the electron candidates was the left-right PMT cut. For this cut, we observed the projected azimuthal angle distribution for each segment and kept track of the source PMT for the CC signal. If the azimuthal angle is negative, the left PMT should give a signal and if the azimuthal angle is positive, the right PMT should give the signal. If the track is close to the sector center, both PMTs may give signal for the same track. By plotting the azimuthal angle distributions separately for left and right PMTs, we can see in Fig. 49 that sometimes the wrong PMT is being fired, which we interpret as an accidental coincidence and we eliminate that particle from the final electron sample. See Fig. 49 for details.

IV.8.4 Final Comments

The impact of the geometric and timing cuts on the analysis is explained in section IV.12 in more detail. Fig. 50 shows how these cuts greatly eliminate the pions from the electron sample. In these plots, all electron cuts, except the CC cuts, were applied. Using these cuts, on the other hand, causes the loss of some electrons, around 5 to 10% at most, from our analysis sample, especially for the outbending data. However, the amount of electrons we lose will not increase our statistical errors considerably while the pions we clear up by these cuts will reduce our systematic error substantially. This can be seen from Fig. 51, which shows pion to electron ratios as a function of momentum for various polar angle bins before and after the cuts were applied. This ratio directly enters into our systematic error, which only becomes small after the cleanup procedure. Similar plots for various momentum and polar angle bins are also shown in section IV.12 as well as in [99].

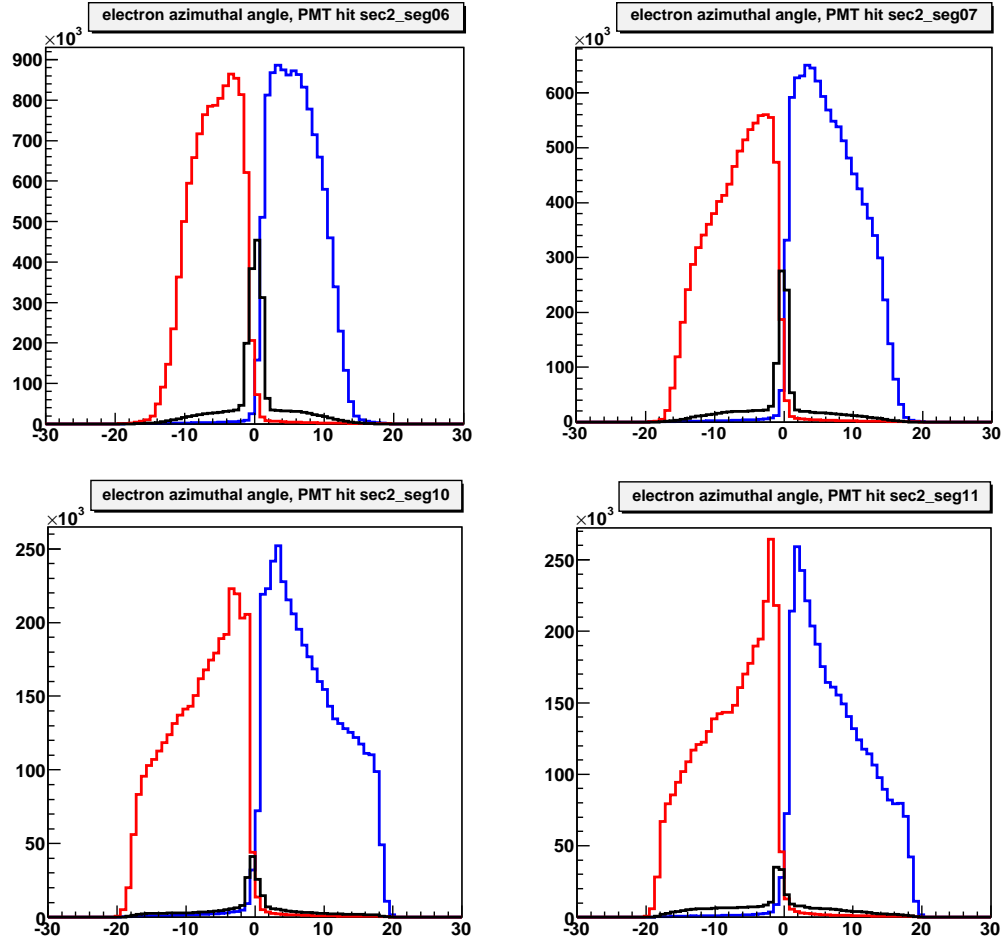


FIG. 49: Azimuthal angle (ϕ) distributions of electron candidates for a few segments in sector 2. The azimuthal angles of the electrons coming from the left PMT of the CC segment are plotted in red. The ones coming from the right PMT are plotted in blue. If both PMTs have a signal, the distribution is plotted in black. Electrons that have a signal in both PMTs should be coming from the region around the segment center, at $\phi = 0$. The left PMT should fire for electrons with $\phi < 0$, while the right PMT should fire for electrons with $\phi > 0$. Particles with positive ϕ angle that had a signal only in the left PMT and vice versa cannot be true electrons. They are assumed to be accidental coincidences and eliminated from the inclusive sample.

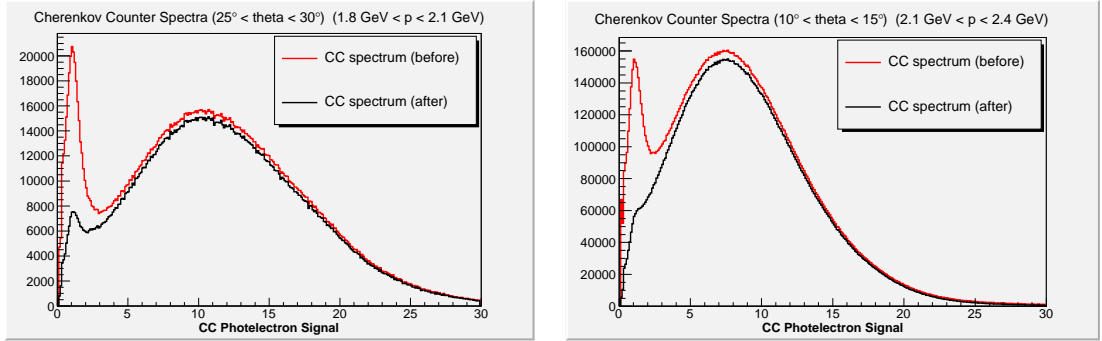


FIG. 50: The overall effect of the geometric and timing cuts on the CC signal for electron tracks for two different θ and momentum bins. The red line shows the situation before the cuts are applied. A large pion peak with a low photoelectron signal is clearly visible. The black line shows the situation after the cut; the pion peak is greatly reduced.

IV.9 FIDUCIAL CUTS

While calculating the asymmetry described in Eq. (66), the detector efficiencies cancel out in the ratio. However, the carbon and helium runs are used to estimate the unpolarized background. The data used to calculate the asymmetry should have the same acceptance as the data used to estimate the background. Although the carbon and helium runs were taken in the middle of ND_3 runs to minimize the acceptance fluctuations among different targets, inefficiencies in some detector channels can create rapid fluctuations of the kinematic acceptance. This can introduce systematic errors into the background subtraction in certain kinematic regions. Therefore, fiducial cuts are required to remove inefficient regions of detectors where acceptance is poorly understood. This is especially important for the background calculations, in which data from different targets are compared.

The most prominent efficiency fluctuations in CLAS come from the Cherenkov detector. The Cherenkov PMTs do not receive light for a certain range of azimuthal and polar angles. These geometric regions where the Cherenkov detector becomes highly inefficient were determined by requiring certain criteria for the expected number of photoelectrons in each region of the Cherenkov Counter. Alexander Vlassov [100] did the initial study of Cherenkov efficiency by using the 1.6 GeV inbending data set from EG1b. In the procedure, elastic electron scattering events were used to determine the expected number of photoelectrons as a function of detector geometry.

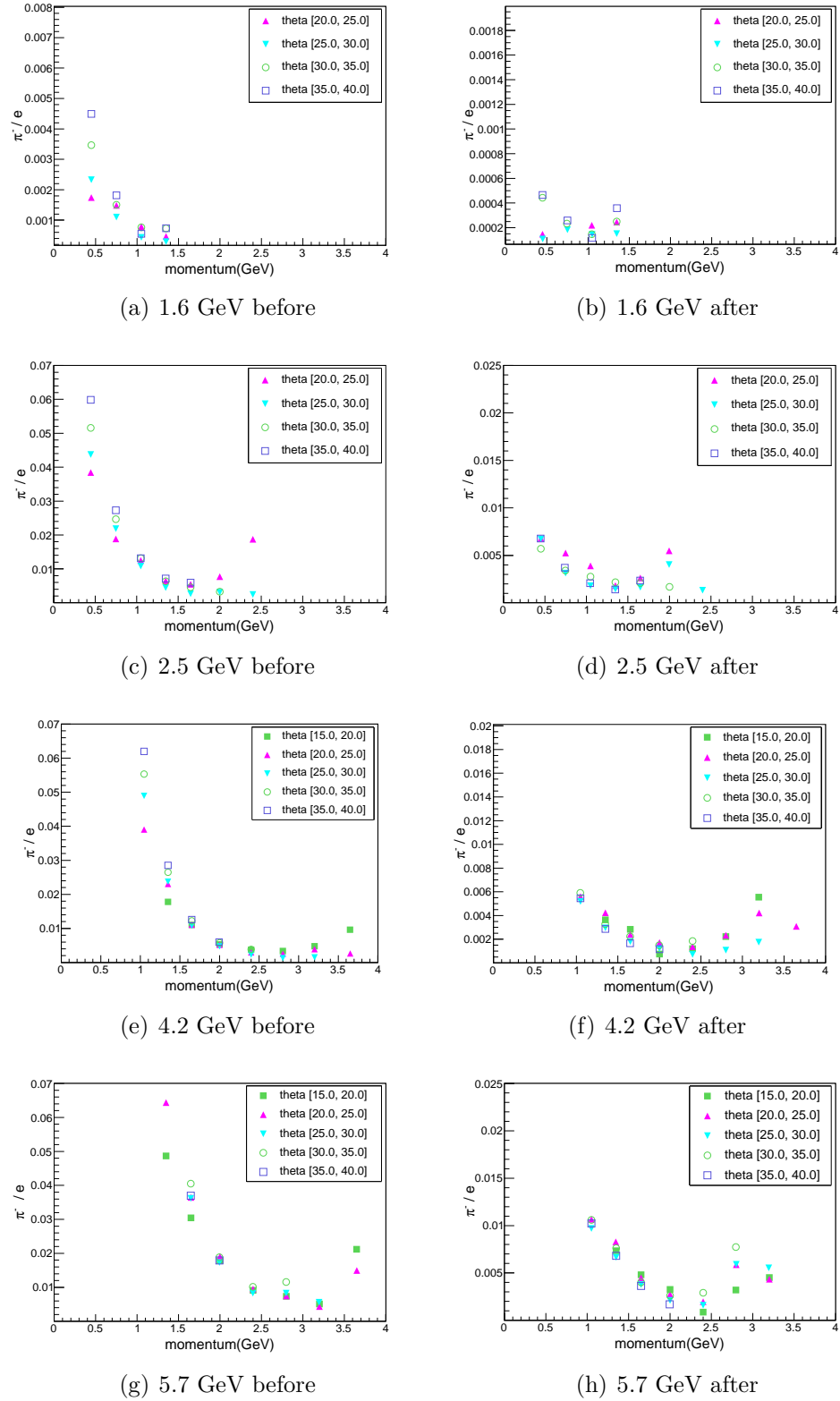


FIG. 51: π^-/e ratio versus momentum for various polar angle bins, before and after the CC geometric and timing cuts. ND₃ inbending data are shown. Note that the vertical scale of the after-cut plots is smaller.

The event selection criteria include cuts on the missing mass (W), vertex and the energy deposited in the EC. In addition, geometrical matching of the track's x and y coordinates from the EC and CC detectors were also required by putting a reasonable limit on the deviation. The Cherenkov efficiency function is assumed to obey Poisson distribution. The main idea behind Vlassov's work was to determine the mean number of photoelectrons as a function of projective angles θ and ϕ measured at the SC/EC plane. Once the expected number of photoelectrons is known, the Poisson distribution can be used to calculate the Cherenkov efficiency for each θ and ϕ bin. Therefore, the efficiency of a specific detector location can be written as:

$$\text{efficiency} = \sum_{n > c} \frac{\mu^n e^{-\mu}}{n!} \quad (234)$$

where μ is the expected number of photoelectrons and c is the minimum cutoff. In order to eliminate pions from the electron sample, a lower limit of 2.0 photoelectrons was used as the minimum electron detection threshold. In order to determine inefficient CC regions, an 80% efficiency requirement was employed. Then events were collected for each θ and ϕ bin that satisfies this efficiency threshold. When the distribution of these events were plotted with respect to each geometric region of the detector (different sectors and θ and ϕ bins), certain geometric regions of the detector showed no events. These were determined as inefficient regions.

For fiducial cuts, the polar angle is reconstructed from the momentum of the particle by using $\theta = \arctan(p_z/p_r)$. The azimuthal angle is measured at the drift chamber layer 1. Due to the magnetic field around the polarized target, which is along the \hat{z} direction, the trajectory of the scattered particle experiences a ϕ -kick, which causes the angle at the vertex and the angle reconstructed by the drift chambers to be slightly different. As a result, the azimuthal angle shows some distortions with respect to the polar angle θ if it is calculated at the vertex. The distortion can be seen in Fig. 52. Therefore, the more symmetric ϕ_{DC} values are used to determine the fiducial geometry.

The study to determine the geometric values of the fiducial cut was made by R. Fersch [95]. After carefully studying the efficiency map of θ vs. ϕ for different electron momenta (0.15 GeV bins used), parametrized functions of ϕ , θ and p_e with 6 parameters (inbending) and 10 parameters (outbending) were produced. The values for the parameters were determined empirically as a function of momentum and kept constant for momenta larger than 4.0 GeV. Curves drawn on top of inclusive data

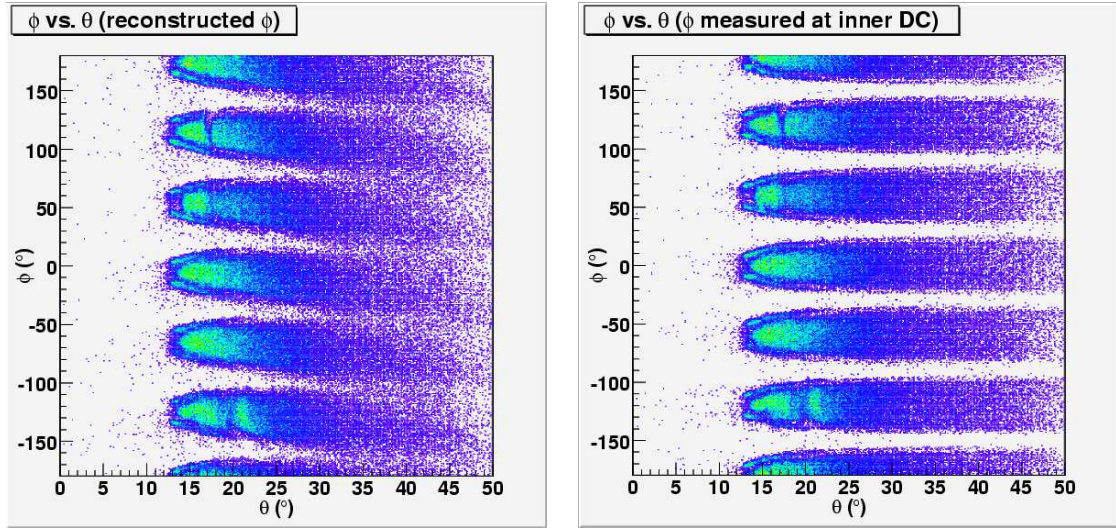


FIG. 52: Distribution of the scattered electrons in the θ vs. ϕ plane. The samples are taken from the 2.3 GeV data set. The left plot shows the ϕ angle reconstructed at the vertex. The plot at the right shows the angle measured by the layer 1 drift chamber. The azimuthal angle reconstructed at the vertex shows some distortion with respect to the azimuthal angle. The drift chamber measurement is more reliable for fiducial cut determination. The plot is courtesy of Robert Fersch [95].

using the final equations are shown in Figs. 53 and 54. Data remaining outside of these curves are eliminated by the fiducial cuts. Fig. 53 shows inbending data for low and high momentum bins. The inbending data are relatively easier to handle since fiducial regions don't show much dependence on sectors. Therefore, the same fiducial cuts were used for all sectors in the case of inbending data. For the outbending data, however, the sector by sector variation is too much. Parameters were produced independently for each sector. Fig. 54 shows the situation for outbending data for sectors 1 and 3. In this figure, only electron events that meet the 80% requirement are shown. The fiducial region at the sector center is clearly different for sector 1 and 3. It should also be noted that the empty vertical strip on the sector 3 plot is because of an inactive SC paddle. Also, the “eyebrow” structures observed in the inbending data in Fig. 53 do not appear for outbending data because of different electron projection angles.

The fiducial cuts are a set of “restrictive” cuts that remove the part of data coming from the inefficient regions of the CC. Acceptance in these regions of the detector is not well understood so it may vary between different data configurations and targets.

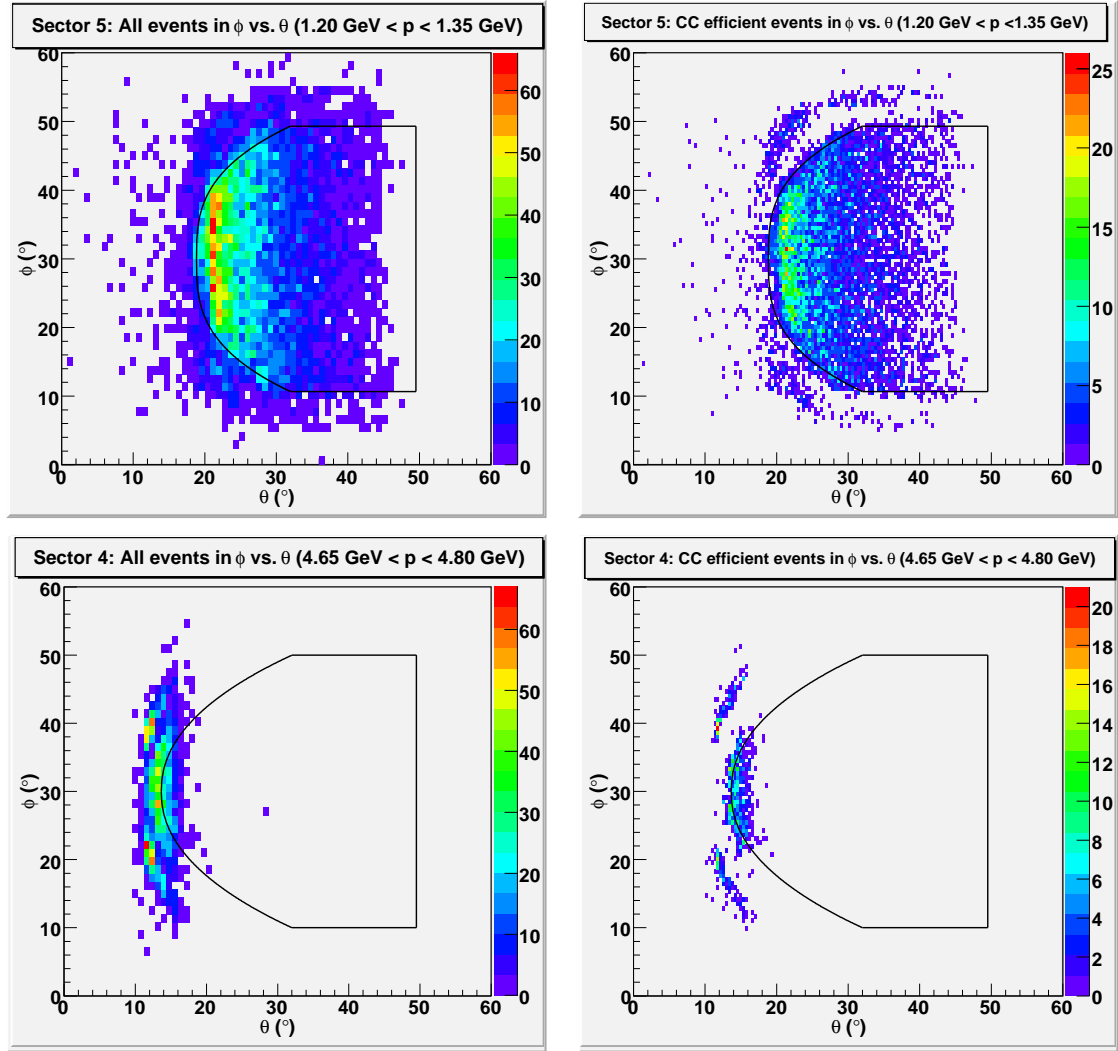


FIG. 53: ϕ vs. θ for inclusive inbending data (torus current 2250) at low (top) and high (bottom) momentum bins. The fiducial cuts are shown as black lines. The top row is for the momentum bin $1.20 \text{ GeV} < p < 1.35 \text{ GeV}$ and sector 5. The bottom row is for a the momentum bin $4.65 \text{ GeV} < p < 4.80 \text{ GeV}$ and sector 4. The figures on the left column show all electron events. The right column figures show electrons that meet the 80% efficiency criteria. The two are shown together to create an idea on the effect of the fiducial cuts on the data statistics. In the second plot, the so called “eyebrow” structures represent direct impacts on the CC PMT. The fiducial cut excludes those data from further analysis. The plots are courtesy of Robert Fersch [95].

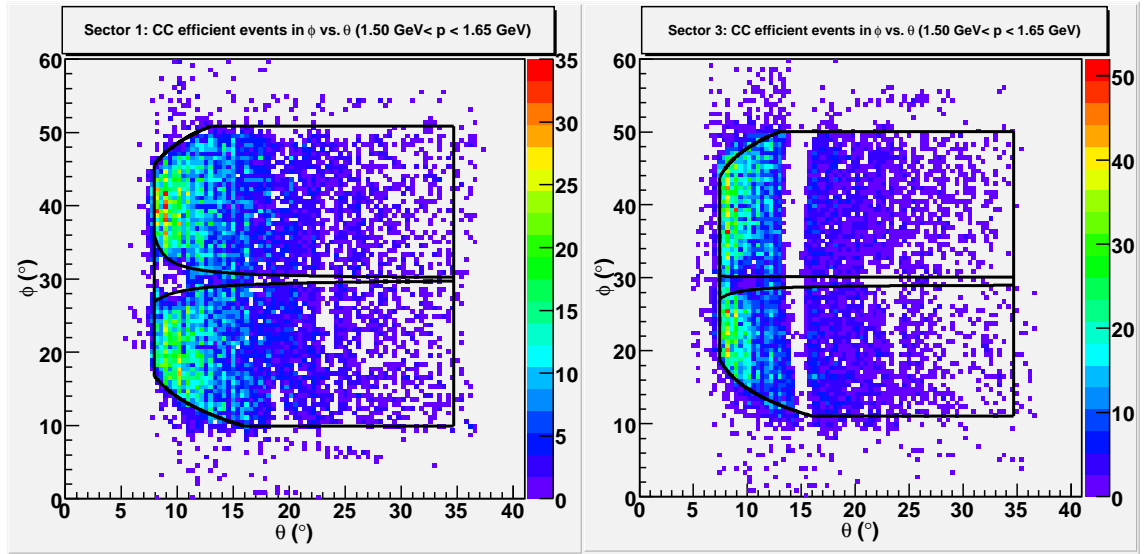


FIG. 54: Fiducial cuts for outbending data from two different sectors (1 and 3) in the same momentum bin ($1.50 \text{ GeV} < p < 1.65 \text{ GeV}$) are shown. Detailed explanations are in the text.

This requires the use of the fiducial cuts for the background calculations, in which data from different targets are compared to estimate the background contribution to the total count. So, the restrictive fiducial cuts are mainly used for the dilution factor and the pion and pair symmetric contamination calculations. The raw asymmetry, on the other hand, was measured without applying these restrictive cuts in order to gain more statistics. However, in Fig. 53, the “eyebrow” structure, which represents particles directly impacting the Cherenkov PMT, still presents an obvious concern. A set of loose fiducial cuts were created just to exclude these events, the direct PMT hits. These events only show up for the inbending data. Therefore, loose fiducial cuts were used for inbending data and no fiducial cuts were used for the outbending data in order to measure the asymmetry. An example of a loose fiducial cut is shown for momentum bin $3.45 \text{ GeV} < p < 3.60 \text{ GeV}$ in Fig. 55. The parameterizations for the fiducial cuts together with the final parameters can be found in Appendix B.

IV.10 KINEMATIC CORRECTIONS

In all CLAS experiments, it is necessary to correct the measured momenta and scattering angles of all identified final state particles. The 4-momentum of the particle

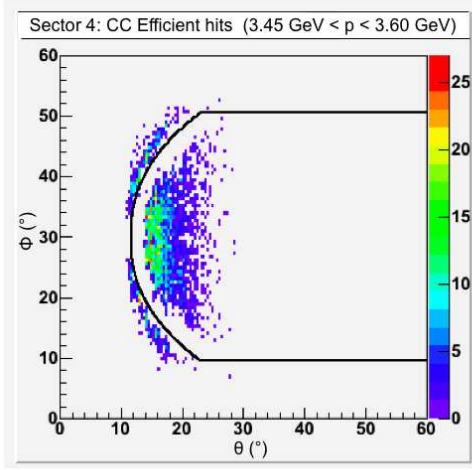


FIG. 55: Loose fiducial cut for a single momentum bin and sector on inbending data used for the asymmetry measurement. The loose cuts specifically target the direct PMT hits in the CC.

is assumed to be influenced by different factors that arise from the experimental setup. These factors distort the reconstructed path of the particle giving rise to miscalculation of its 4-momentum by the reconstruction code. The distortions can be monitored by looking at certain distributions of data. One of the most important ones is the position of the missing mass W peak for the elastic events. For inclusive data, the centroid for the W distribution of the elastic peak should be at the proton mass $M_p = 0.9382$ GeV. Moreover, the width of the distribution should be small enough to be compatible with the momentum resolution of the CLAS detector. In our data, we saw a clear dependence of the W peak position on azimuthal angle ϕ . In order to show the ϕ dependence, we plotted the difference between expected and observed electron momenta of the elastic events. The plot shows a strong ϕ dependence of this difference. We also observed broader distributions than expected. The peak position, integrated over all kinematics, was also significantly shifted from its expected value.

The main idea behind the kinematic corrections lies in the minimization of missing 4-momentum for events with well understood kinematics. These mainly include

elastic $ep \rightarrow ep$ and inelastic $ep \rightarrow ep\pi^+\pi^-$ events. In order to correct the kinematics of all final state particles, it is necessary to apply various corrections in a certain order. These corrections include: raster correction, torus scaling, beam energy correction, multiple scattering correction, stray magnetic field correction, energy loss correction and finally momentum correction. Since the momentum correction is performed by fitting elastic and inelastic events and minimizing the missing energy and momentum, all other corrections need to be applied first in order to correct for all known and calculable effects. After that, the momentum correction will take care of the remaining unquantifiable effects. We developed a kinematic correction package for the EG1b experiment. This stand-alone package includes all various types of correction functions and it applies the individual corrections in the correct order. In the following parts, we will describe each of these functions in detail in the order of application.

IV.10.1 Raster Correction

The electron beam does not always pass through the center of the target. Indeed, the beam position is constantly changed by raster magnets so that the radiation damage on the target material (because of constant beam exposure) can be minimized. This procedure is called rastering of the beam. Generally a spiral pattern is followed. Two pairs of magnets, one for the horizontal (X) and the other for the vertical (Y) movement of the beam position, are used for this purpose. The current that goes into the raster magnets are recorded by analog-to-digital converters (ADCs). The exact (r_x, r_y) coordinates of the beam position can be determined by using these ADC values. The procedure to translate the ADC values (X_{ADC} and Y_{ADC}) into beam position coordinates (r_x, r_y) was developed by Peter Bosted [101]. The calibration procedure assumes a linear relationship between ADC values and the beam position, therefore expressing the beam coordinates (r_x, r_y) as:

$$r_x = (X_{ADC} - X_0)c_x \quad (235)$$

$$r_y = (Y_{ADC} - Y_0)c_y \quad (236)$$

We define the corrected vertex position z_{corr} as:

$$z_{corr} = z_{meas} + x'/\tan(\theta) \quad (237)$$

where z_{meas} is the vertex position determined by the tracking code assuming $x=y=0$, θ is the polar angle of the particle, as measured at the vertex, and x' is transverse

displacement of the vertex position along the particle track from the center of the target, defined as:

$$x' = [r_x \cos(\phi_s) + r_y \sin(\phi_s)] / \cos(\phi - \phi_s) \quad (238)$$

where ϕ is the particle's azimuthal angle (in degrees), calculated via $\phi = \tan^{-1}(p_x, p_y)$, where p_x and p_y are the momentum components in the x and y directions in the detector coordinate system and ϕ_s is the sector angle given by $\phi_s = (S - 1) * 60$, where S is the sector number from 1 to 6. Fig. 56 shows the geometry of these variables. The values X_0 , Y_0 , c_x and c_y are determined for each beam energy by minimizing the χ^2 defined by:

$$\chi^2 = \sum_{i=0}^N (z_{corr} - z_0)^2 \quad (239)$$

where z_0 is another fit parameter which defines the center of the target and the sum is taken over all tracks. The final values of the parameters are listed in Table 10. Vertex and azimuthal angle corrections for each particle in the event can be performed once the final parameters are obtained. The vertex is corrected by using Eq. (237). The typical geometry can be seen in Fig. 57.

TABLE 10: Parameters to translate the raster ADC to the beam position in the transverse coordinate system. Data sets are given in energy (GeV) and torus sign (+/-).

| Data Set | X_0 | c_x | Y_0 | c_y |
|---------------------|-------|-----------|-------|----------|
| 1.6+; 1.6- | 3800 | -0.000175 | 5600 | -0.00018 |
| 1.7+; 1.7- | 3900 | -0.00060 | 4000 | -0.00060 |
| 2.3+ | 3900 | -0.00048 | 4000 | -0.00048 |
| 2.5+; 2.5- | 3900 | -0.00041 | 4000 | -0.00041 |
| 4.2+; 4.2- | 3900 | -0.00026 | 4000 | -0.00026 |
| 5.6+; 5.6- | 3900 | -0.00019 | 4000 | -0.00019 |
| 5.73+; 5.73-; 5.76- | 4250 | -0.000195 | 6360 | -0.00019 |

The transverse displacement x' of the vertex position also requires azimuthal angle correction. The raster correction changes the calculated distance that a particle travels in the magnetic field of the target. Since the magnetic field creates an additional ϕ deflection, the RECSIS code automatically corrects for this deflection assuming the original (uncorrected) vertex position. Once the true vertex is determined, the

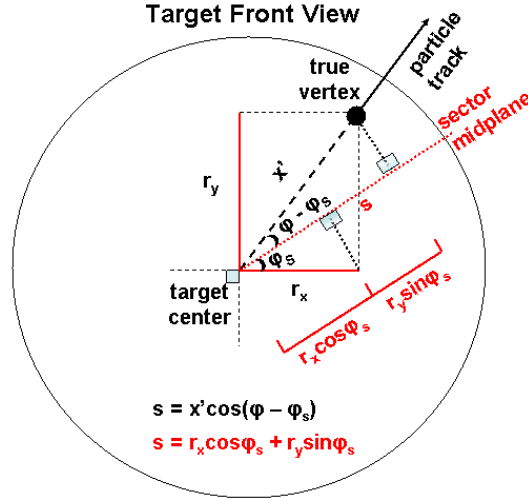


FIG. 56: Raster correction geometry, as viewed from the upstream of the beam. The dotted red line (s) is the mid-plane of the triggered sector, which is defined at an angle ϕ_s from the horizontal axis. The raster coordinates (r_x , r_y , the solid red lines) are projected onto the sector mid-plane. This projection is used to express the vertex displacement x' along the particle track in radial direction.

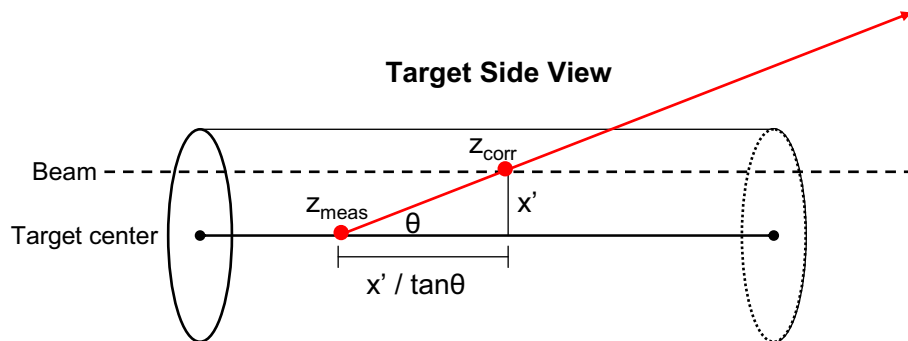


FIG. 57: Raster correction geometry, as viewed from the side of the target. Longitudinal displacement of the vertex position is determined by using its transverse displacement and the polar angle from DC1. The RECSIS code assumes all events come from the central line (solid black line). We first apply the transverse displacement correction x' . Then the longitudinal displacement correction $x'/\tan\theta$ brings the vertex position to its true place.

azimuthal angle is corrected by:

$$\phi_c = \phi_0 - (q \times 50) \left(\frac{x'}{100} \right) \left(\frac{c}{p_t} \right) \quad (240)$$

where p_t stands for the transverse component of the particle's momentum, q is the charge (± 1), 50 is the strength of the 5 Tesla magnetic field in kGauss, c is the speed of light and x' is the radial displacement of the vertex. The final correction in the subroutine after appropriate unit conversions is:

$$\phi_c = \phi_0 - (q \times 50) \left(\frac{x'}{100} \right) \left(\frac{1}{33.356} \right) \left(\frac{1}{p_t} \right) \quad (241)$$

Fig. 58 shows the azimuthal angle vs. the vertex position before and after applying the raster corrections. It can be seen that the correction provided a better vertex resolution and mostly removed the phi dependence of the vertex position.

Having the proper values for raster coordinates r_x and r_y , a target image can be constructed by plotting the number of events as a function of r_x and r_y . Fig. 59 shows such a plot from run number 28110. These raster patterns are useful to understand what went on during that run. If the density of events is low, it might indicate a hole in the target material in that region, or if too many scattering events are coming from a certain region of the target, it might indicate strange material or a wire shadowing the target. These raster patterns are generated and carefully monitored for each run during the quality check procedure.

IV.10.2 Average Vertex Position

After applying the raster correction to each particle in the event, the average vertex position is calculated by using the vertex position of charged particles that come from the interaction. At this point, we also apply reasonable cuts to eliminate particles that come from the target windows (see Fig. 39). By using the GEANT simulation package for the CLAS detector (GSIM) [102], it was shown that using the weighted average of vertex positions from all charged particles in the event improves the accuracy of the determination of the event vertex [103]. From the GSIM studies, which will be explained more in the next section, a vertex resolution, σ_z , is assigned to each particle as $\sigma_z = 0.1/(\beta p_t)$ where p_t is the transverse momentum of the scattered particle and $\beta = p/E$, where p is the total momentum and E is the total energy of the particle. The vertex position of the event is determined by summing over the

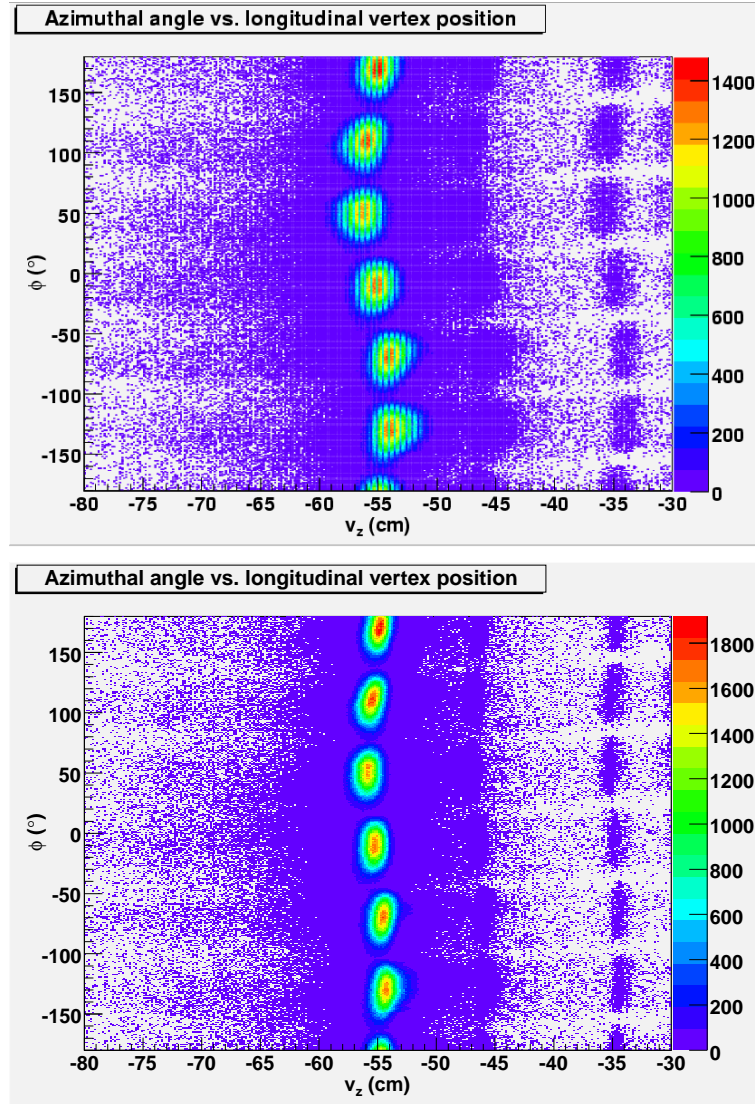


FIG. 58: Azimuthal angle (in degrees) vs. vertex position (in cm) before (top plot) and after (bottom plot) raster corrections. The plot is from 1.6 GeV inbending data set. No other kinematic corrections are applied at this point. After the correction, a vertex cut of $(-58 \leq v_z \leq -52)$ is applied for each particle.

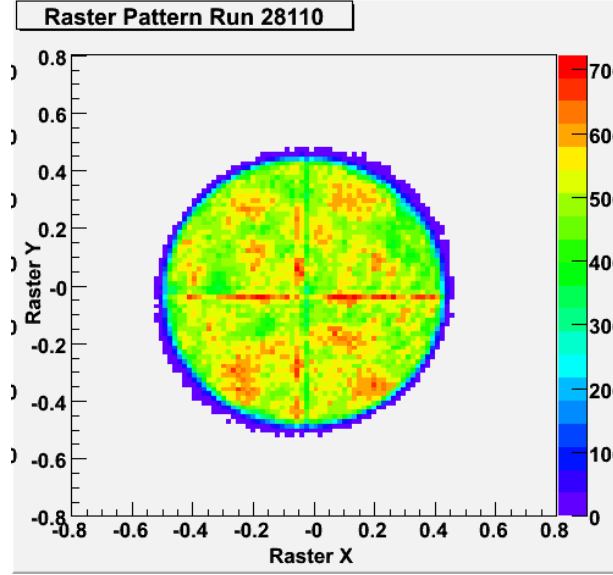


FIG. 59: Raster pattern for run 28110. The circular shape of the target is clearly distinguishable. A homogeneous distribution of scattered events is an indication of good run. The “cross shaped” pattern is an artifact of the ADC readout.

vertex positions of all particles, weighted by the vertex resolution:

$$z_{ave} = \frac{\sum_i z_i / \sigma_{z_i}^2}{\sum_i 1 / \sigma_{z_i}^2}. \quad (242)$$

IV.10.3 Torus Current Scaling Correction

Data reconstruction of the EG1b experiment for 2.3, 2.5 and 4.2 GeV beam energies was done using the values for the torus current from the EG2000 database. These values fluctuate up to 0.5 percent while the true current is constant. The fluctuations may affect the reconstructed momentum of the particles. Indeed, the position of the elastic peak from the data clearly revealed that data reconstruction was affected by the wrong values of the torus current provided from the EG2000 database.

The data reconstruction routine actually checks the value of the torus current for each run and corrects it if the fluctuation is within 0.2 percent of the correct value [104] by replacing the torus current with the default value. However, the program does not correct larger fluctuations. In order to correct for fluctuations larger than 0.2 percent we multiplied each component of a particle’s momentum by a scaling

factor. The scaling factor is equal to the ratio of the database torus current value to the correct torus current value.

$$p_{true} = \frac{I_{true}}{I_{meas}} p_{meas} \quad (243)$$

We monitored the changes in the position of the elastic peak before and after the correction for each run. The top plot in Fig. 60 shows the position of the elastic peak for several runs from the 4.2 GeV data before any correction. The bottom plot in the figure shows the same data after the torus scaling correction is applied.

We also calculated a grand average of elastic peak positions for all runs with the same torus current value. The top plot in Fig. 61 shows these grand averages with respect to the corresponding torus currents before the scaling correction is applied. The data are from the 4.2 GeV inbending set. As can be seen in the top figure, there is a clear correlation between the torus current deviation from its nominal value and the elastic peak position. The main purpose of this correction is to remove this correlation. The bottom plot shows the situation after the correction is applied. By comparing the two figures before and after the correction, we concluded that the dependency of the elastic peak position on the value of the torus current fluctuations is removed by the scaling correction. It should be noted that no other kinematic corrections have been applied yet on these plots. The offset of the elastic peak position from its expected value even after the scaling correction is clearly a problem but may come from other sources or even from a poor fitting function to find the elastic peak. The main point of this correction is to scale all elastic peak positions and make them independent of the torus current value. The other kinematic corrections will take care of the offset. The effect for the 2.3 GeV data is much smaller compared to the 4.2 GeV data set simply because the fluctuations are smaller. This correction is applied only to the 2.3, 2.5 and 4.2 GeV data sets. The other data sets were reconstructed with the correct torus value.

IV.10.4 Beam Energy Correction

The electron beam comes with a predefined energy from the accelerator and hits the target nucleus or nuclei after it traverses some matter in the target material. Knowing the energy of the electron just before the interaction occurs is critical to determine the kinematic observables accurately. During the experiment, nominal beam energy measurements were supplied from the MCC (Machine Control Center) based on

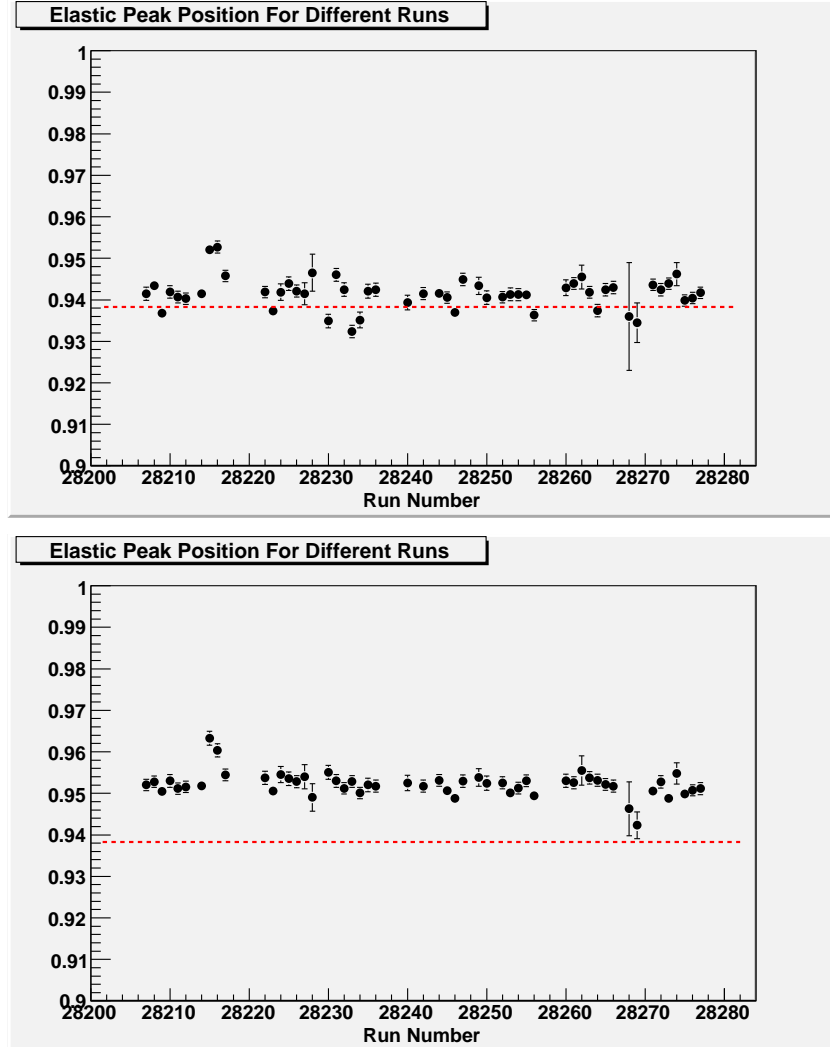


FIG. 60: Elastic peak positions for different runs before (top) and after (bottom) torus current scaling correction. The dotted red line represents the expected location of the elastic peak at 0.938 GeV.

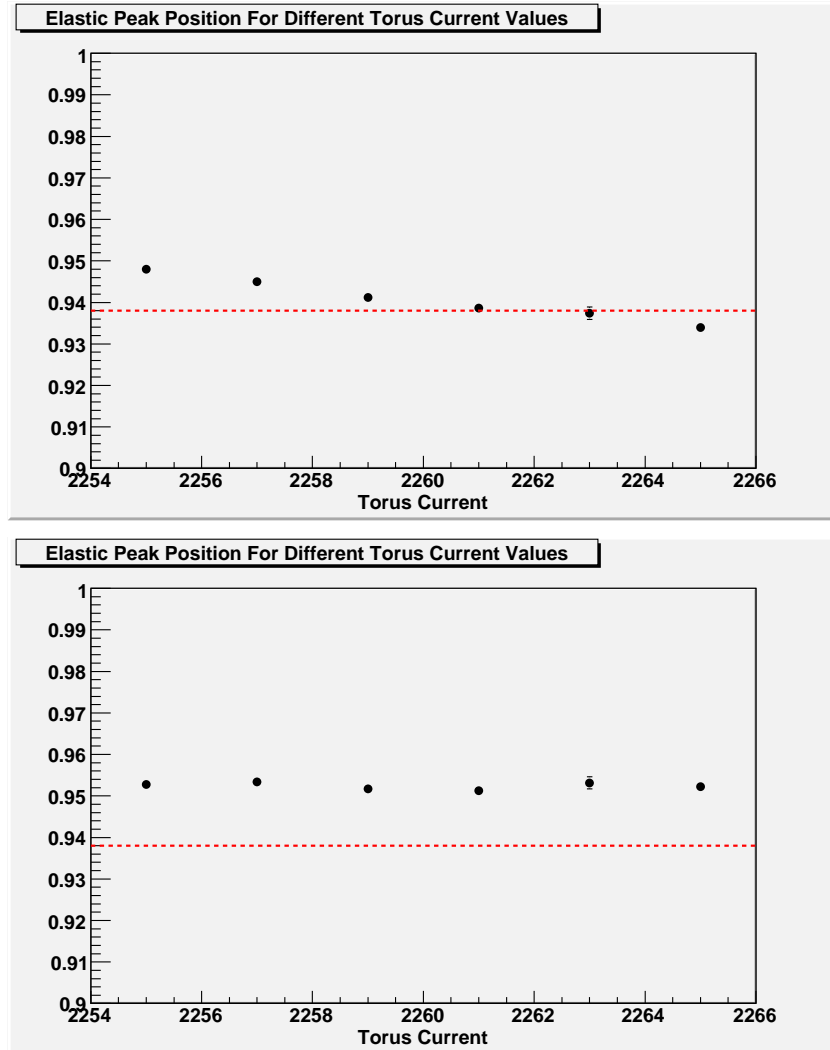


FIG. 61: Average elastic peak positions for group of runs with respect to their torus current value before (top) and after (bottom) torus current scaling correction. The dotted red line represents the expected location of the elastic peak at 0.938 GeV. The scatter of these positions with run number is clearly reduced. The overall shift is later corrected by the remaining kinematic corrections.

the number of passes through the accelerator. However, these nominal values are known to be limited in accuracy. Therefore, more accurate energy measurements were performed by Hall-A during the same time period [105]. The Hall-B energies are found from those measurements by accounting for the number of accelerator passes delivered. Table 11 lists the nominal (by MCC) and “true” beam energies (from Hall-A) for each data set.

TABLE 11: The “nominal” (from MCC) and “true” (from Hall-A) beam energies for the EG1b

| Data Set | Nominal Beam Energy(GeV) | Actual Beam Energy(GeV) |
|----------|--------------------------|-------------------------|
| 1.6± | 1.606 | 1.606 |
| 1.7± | 1.724 | 1.723 |
| 2.3+ | 2.288 | 2.286 |
| 2.5± | 2.562 | 2.561 |
| 4.2± | 4.239 | 4.238 |
| 5.6± | 5.627 | 5.615 |
| 5.7± | 5.735 | 5.723 |
| 5.76− | 5.764 | 5.743 |

The kinematic corrections package sets the true beam energies for each configuration by using the values determined from Hall-A. In addition to accurately determining the beam energy, the energy loss of the beam within the target material before the interaction should also be taken into account. Therefore, we corrected the initial energy of the scattered electron based on the location of the interaction vertex within the target material. At the EG1b energies, the electron energy loss due to radiation dominates the energy loss due to ionization [106]. The effects of energy loss because of radiation (by Bremsstrahlung) are accounted for by the radiative corrections applied later. The energy loss because of ionization (dE/dx), on the other hand, is handled in the kinematic corrections package. The effect of this correction is small and the intention is to get a reasonable estimate of the electron energy just before the interaction occurs.

Once we determine the interaction point within the target as described in section IV.10.2, we assume the electron loses its energy at a constant rate within the target material until it reaches that interaction point. For a typical EG1b target the energy loss rate of the electron through ionization is approximately 2.8 MeV cm²/g [107]. At the EG1b energies, this value remains fairly constant as a function of electron

momentum. Moreover, the dE/dx corrections can safely be generalized for all targets in the experiment because it basically depends of the ratio of the atomic number over the mass number (Z/A), which is roughly the same for all the EG1b targets. Energy loss is calculated by:

$$\frac{\Delta E}{\Delta x} = 2.8 \rho. \quad (244)$$

Therefore,

$$\Delta E[\text{MeV}] = 2.8 [\rho_{foil} l_{foil} + \rho_{He} l_{He} + \rho_A l_A \delta z] \quad (245)$$

where $\rho_{foil} l_{foil}$, $\rho_{He} l_{He}$ and $\rho_A l_A$ represent the mass thickness for the window foils, the liquid Helium and the ammonia target respectively while δz is the fraction of the target length the electron traveled within the ammonia target. In this correction, we used typical values (estimated from the previous analysis of 1.6 and 5.7 GeV data sets [17][77]) for these parameters: $\rho_{foil} l_{foil} = 0.1 \text{ g/cm}^2$; $\rho_{He} l_{He} = 0.3 \text{ g/cm}^2$; $\rho_A l_A = 0.6 \text{ g/cm}^2$; $\delta z = (z_{ave} - z_c + 0.5)/L_A$ where $L_A = 1 \text{ cm}$ (physical length of the ammonia target) and $z_c = -55.1$ (the target center position). It should also be noted that vertex positions z_{ave} and z_c are negative numbers. The average energy loss of the electron because of ionization varies around 2-3 MeV depending on the vertex position z_{ave} . The energy loss determined from Eq. (245) is subtracted from the true beam energy, listed in Table 11, for each event.

IV.10.5 Multiple Scattering and Magnetic Field Corrections

Two additional effects that are known to affect the momentum reconstruction are:

- The possible angular distortions that may come from multiple scattering experienced by the detected particles.
- The effects of the target magnetic field that extend into the far regions of the detector.

While the scattered particles travel through the material in their path, they experience multiple scattering within that material. The net result of these multiple scatterings can distort the angular distribution of the particles when they are detected because the reconstruction code (RECSIS) does not account for these effects. Moreover, the angular distortion can cause the reconstructed vertex position for each particle to shift from its true place. Fig. 62 shows an artistic visualisation of this

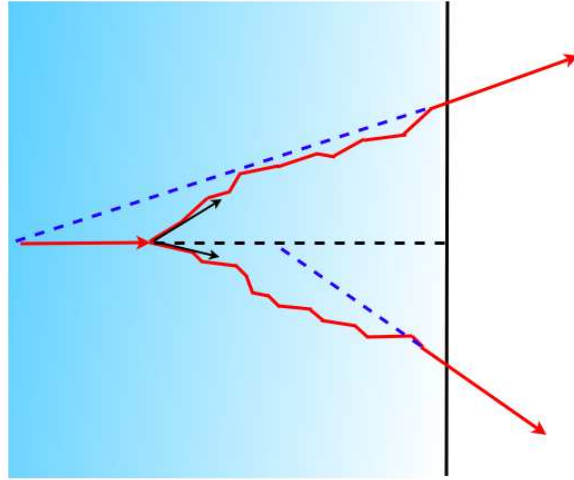


FIG. 62: Artistic visualization of the effect of multiple scattering on the angular distributions and the vertex positions of each scattered particles (by R. Fersch). The black arrows show the true angles while the blue dotted lines show the apparent angles that the reconstruction code would supply.

situation for two scattered particles. In addition to the multiple scattering, the effect of the target magnetic field beyond Region 1, which will be referred to as stray magnetic field, was not incorporated into the RECSIS code during the EG1b data reconstruction. The reconstruction code only accounted for the target magnetic field in the vicinity of the target.

The GEANT simulation package for the CLAS detector (GSIM) [102] was used in order to understand the overall results of these effects on the kinematics of the detected particles and determine the necessary corrections. The GSIM package was updated to incorporate a reasonably accurate model of the EG1b target. A large random sample of particles was generated by using the GSIM package and reconstructed with the same version of the RECSIS code that was used for the EG1b data reconstruction. The original and the reconstructed quantities were compared to isolate the effects of the multiple scattering and the stray magnetic field on the kinematics of some detected particles, mainly electrons and protons. It was realized that the required corrections could be parametrized by simple formulas and eventually applied to all charged particles. The details of this study can be found in [103].

The final corrections to the polar angle θ and the azimuthal angle ϕ because of the multiple scattering effects are:

$$\theta_c = \theta - \delta z \left(0.018\theta + \frac{0.002}{p} \right), \quad (246)$$

$$\phi_c = \phi + 0.015q \left(\frac{\delta z}{p} \right), \quad (247)$$

where p is the total momentum of the particle measured in GeV and δz is given by:

$$\delta z = z_{par} - z_{ave}, \quad (248)$$

where θ and ϕ are expressed in radians, q is the particle's charge (± 1), z_{par} is the vertex position of the particle, and z_{ave} is found by using Eq. (242).

The corrections because of the stray magnetic field are:⁹

$$\theta_c = \theta + 0.005 \left(\frac{\theta - 0.26}{p} \right) \quad (249)$$

$$\phi_c = \phi - 0.0015q \left(\frac{\sqrt{2.2\theta}}{p} \right). \quad (250)$$

Again, θ and ϕ are expressed in radians. After determining the corrected angles θ_c and ϕ_c , the total energy and the momentum components of the particle are updated for the corrected kinematics:

$$\begin{aligned} p'_z &= p \cos \theta_c \\ p'_t &= \sqrt{p^2 - p_z'^2} \\ p'_x &= p'_t \cos \phi_c \\ p'_y &= p'_t \sin \phi_c \\ E' &= \sqrt{E^2 + (p_x'^2 - p_x^2) + (p_y'^2 - p_y^2) + (p_z'^2 - p_z^2)}. \end{aligned} \quad (251)$$

IV.10.6 Energy Loss Correction

After an electron is scattered from a nucleon or nucleus, the scattered particles lose energy as they travel within the target and through CLAS. The scattered electrons or positrons lose their energy due to electromagnetic radiation (Bremsstrahlung) and ionization while scattered hadrons, which are moderately relativistic, lose their

⁹These equations are not exactly the same as those listed in Ref. [103] because of an update in the parametrization since Ref. [103] was written.

energy primarily due to ionization and atomic excitations. The energy loss of the electron due to radiation is handled by the radiative corrections, which are applied later in the analysis. The mean rate of energy loss due to ionization (also called stopping power) is best described by the Bethe-Bloch formula [108]:

TABLE 12: Parameter definitions in Bethe-Bloch Formula

| Symbol | Definition | Unit or Value |
|-----------|--------------------------------|---|
| c | Speed of light | 299 792 458 m/s |
| β | v/c of the incident particle | |
| γ | $1/\sqrt{1-\beta^2}$ | |
| $m_e c^2$ | Electron mass $\times c^2$ | 0.510 998 918(44) MeV |
| r_e | Classical electron radius | $e^2/4\pi\epsilon_0 m_e c^2 = 2.817 940 325(28)$ fm |
| N_A | Avogadro's number | $6.022 1415(10) \times 10^{23}$ mol $^{-1}$ |
| W_{max} | Maximum energy transfer | MeV |
| K | $4\pi N_A r_e^2 m_e c^2$ | 0.307 075 MeV g $^{-1}$ cm 2 |
| ρ | Density of absorbing material | gr/mol |
| z | Charge of incident particle | electron charge (e) |
| Z | Atomic number of absorber | |
| A | Atomic mass of absorber | g/mol |
| I | Mean excitation energy | MeV |

$$-\frac{dE}{dx} = \rho \left[K \frac{Z z^2}{A \beta^2} \left[\frac{1}{2} \ln \left(\frac{2m_e c^2 \beta^2 \gamma^2 W_{max}}{I^2} \right) - \beta^2 \right] \right] \quad (252)$$

The definitions and values of the variables in the Bethe-Bloch formula are given in Table 12. In the equation we used the following approximations:

$$\begin{aligned} W_{max} &= 2m_e c^2 \beta^2 \gamma^2, \\ Z/A &= 0.5, \\ I &= 90 \times 10^{-6} \text{ MeV}. \end{aligned} \quad (253)$$

Therefore, we can write Eq. (252) in its final form that we used in the kinematic corrections package:

$$-\frac{dE}{dx} = \rho \left[0.307 \times \frac{0.5}{\beta^2} \times \left[\ln \left(\frac{2 \times 0.511 \beta^2 \gamma^2}{90 \times 10^{-6}} \right) - \beta^2 \right] \right]. \quad (254)$$

Since the correction is applied only to charged particles of $q = \pm 1$, we used $z = 1$. The energy loss ΔE can be calculated by approximating $dE/dx = \Delta E/\Delta x$, which is

a safe approximation for high energies and thin target. Therefore, we can write Eq. (254) as:

$$-\Delta E[\text{MeV}] = \rho \Delta x R_E \quad (255)$$

where R_E represents the rate of collisional energy loss and is given by the β dependent factor in square bracket in Eq. (254) while $\rho \Delta x$ is given by:

$$\rho \Delta x[\text{g/cm}^2] = [\rho_{foil} l_{foil} + \rho_{He} l_{He} + \rho_A l_A \delta z] / \cos \theta \quad (256)$$

where $\rho_{foil} l_{foil} = 0.1 \text{ g/cm}^2$ is the mass thickness of the window foils, $\rho_{He} l_{He} = 0.3 \text{ g/cm}^2$ is the mass thickness of the liquid Helium and $\rho_A l_A = 0.6 \text{ g/cm}^{210}$ represents the mass thickness of the ammonia target while δz , the fraction of a distance the electron traveled within the ammonia target, is $\delta z = (z_{ave} - z_c + 0.5)/L_A$ where $L_A = 1 \text{ cm}$ (physical length of the ammonia target), $z_c = -55.1$ (the target center position) and z_{ave} is calculated by Eq. (242).¹¹ All the lengths should be divided by $\cos \theta$ because the scattered particle traverses the target material with an angle of θ , which increases the effective length by a factor of $1/\cos \theta$. For electrons and positrons we assumed a constant rate of energy loss at $R_E = 2.8 \text{ MeV cm}^2/\text{g}$. For hadrons, R_E is calculated by using the expression in Eq. (254). Once $-\Delta E$ is calculated, the absolute value of the energy loss needs to be added to the measured energy so that the true scattering energy can be determined. Therefore, we determined the final corrected kinematics (E', p'_x, p'_y, p'_z) of the scattered particle at the scattering point in terms of the uncorrected kinematics (E, p_x, p_y, p_z) as:

$$\begin{aligned} E' &= E + |-\Delta E| \\ p'^2 &= E'^2 - E^2 + p_x^2 + p_y^2 + p_z^2 \\ p'_x &= p_x \times p'/p \\ p'_y &= p_y \times p'/p \\ p'_z &= p_z \times p'/p \end{aligned} \quad (257)$$

where p represents the measured total vector momentum of the particle. At this point, the kinematics of the scattered charged particles are corrected for all quantifiable effects at the first order. Now we are ready to apply the minimization of missing energy and momentum to determine the final part of the kinematic corrections.

¹⁰The average density of $^{15}\text{NH}_3$ and $^{15}\text{ND}_3$ targets is $\rho_A \sim 1 \text{ g/cm}^3$ and the average effective length for the ammonia targets is $\sim 0.6 \text{ cm}$

¹¹Because of resolution limits, the average vertex occasionally ended up outside the target window. In that case, the vertex was assumed to be on the target edge for purposes of the dE/dx calculations.

IV.10.7 Momentum Correction

The purpose of the corrections described in the previous sub-sections is to obtain the best possible information for the kinematics of the scattered particles. After these corrections are applied, there are still unaccounted effects that will change the reconstructed kinematics of the detected particles from their true values. These effects include:

1. Misalignment of the drift chamber wires or drift chambers themselves relative to their nominal positions, or wire sag.
2. Incomplete map of all drift chamber wires passed to the tracking code
3. Wrong or incomplete magnetic field map used by the reconstruction code.

Unfortunately, there is no exact way to account for such effects. Therefore, we need to rely on the data to understand the cumulative results of the unknown effects and correct them based on available information.

There are many different momentum correction schemes for the CLAS detector. For the EG1b experiment we used the technique developed by Sebastian Kuhn and Alexei Klimenko [109]. This technique is based on the selection of well-identified elastic $ep \rightarrow ep$ events as well as at least one channel of multi-particle final states and utilizes four-momentum conservation. Having multi-particle final states in the data sample helps to cover lower hadron momenta and avoids strong kinematic correlation between angle and momentum in the elastic events. We chose $ep\pi^+\pi^-$ as our multi-particle final state. Once the data were obtained and corrected for all the effects described earlier, we went over all events one by one to determine the four-momentum of each particle in the event and applied a parametrized correction to it. By summing over all particles in the event, we determined the total final four-momentum of the event. We also calculated the total initial four-momentum of each scattering event by using the corrected beam energy and the target mass, for which, we used the proton mass because our data for the fit was obtained from NH_3 runs. By taking the difference between the total initial and final four-momentum of the scattering event, we determined the total missing four-momentum of the event. Ideally the missing four-momentum for each event should exactly be zero. However, for each component of the missing four-momentum $(E_{[miss]}, p_{x[miss]}, p_{y[miss]}, p_{z[miss]})$, we get a Gaussian distribution. These distributions can be minimized by optimizing the value

of each parameter in the parametrized correction. Our parametrized correction of momentum and polar angle had 16 parameters per sector. Eight of them ($A-H$) were used to minimize the effect of drift chamber displacements. These displacements can be categorized as shifts along the beam direction (in z), radial shifts (away from the beam line), phi-dependent z displacements and phi-dependent radial displacements. The radial shift terms are proportional to $\cos \theta$, where θ is the polar angle, because the offset in momentum and polar angle becomes largest at forward direction (small θ) and the effect diminishes as we approach $\theta = 90$ degrees. On the other hand, the displacements in the z direction are proportional to $\sin \theta$ because the effect becomes maximum for $\theta = 90$ degrees. The displacements are all relative to the Region 1 drift chamber, which is kept fixed in this scheme. The azimuthal angle ϕ is also untouched since it has larger intrinsic uncertainty and seems to be correct according to the elastic events because the difference $\phi_e - \phi_p$ is usually well centered on the correct value of 180 degrees. The overall effect of the drift chamber displacements on the reconstructed track can be written as a change in the polar scattering angle at the vertex ($\Delta\theta$),¹²

$$\Delta\theta = (A + B\phi)\frac{\cos\theta}{\cos\phi} + (C + D\phi)\sin\theta. \quad (258)$$

Once determined, the vertex angle θ was corrected by adding $\Delta\theta$ and the corrected angle was used for the subsequent corrections. The next correction is on the momentum of the particle:

$$\frac{\Delta p}{p} = \left((E + F\phi)\frac{\cos\theta}{\cos\phi} + (G + H\phi)\sin\theta \right) \frac{p}{qB_{torus}}. \quad (259)$$

The quantity $B_{torus} \equiv \int B_{\perp} dl$ along the track path is approximated by (θ given in radians) [110]:

$$B_{torus} = 0.76 \frac{I_{torus} \sin^2 4\theta}{3375 \theta} \quad (\theta < \pi/8) \quad (260)$$

$$B_{torus} = 0.76 \frac{I_{torus}}{3375 \theta} \quad (\theta \geq \pi/8)$$

The parameters A and E are for radial displacement of the Region 2 and Region 3 drift chambers while B and F are the terms for the phi-dependent radial displacement

¹² ϕ is written in sector coordinates: $\phi = (\phi_{calc} - \phi_s)$, where ϕ_s marks the center baseline of the sector and $\phi_{calc} = \tan^{-1}(p_y/p_x)$. The $1/\cos\phi$ factor arises because of the flatness of the drift chambers and because the particle track in ϕ is only perpendicular to the DC surface at the sector center.

(a rotation around the beam axis). Similarly, C and G are the parameters to describe displacement along the beam axis and D and H correspond to the phi dependent displacement (yaw).

Another source of kinematic miscalculations in the reconstruction code arises from the incomplete magnetic field map used by the code. In order to correct the momentum of the particles for the unknown effects of the magnetic field from the torus magnet, we introduced a new function $f(\theta, \phi)$ that only depends on the path geometry:

$$f(\theta, \phi) = J \cos \theta + K \sin \theta + L/\theta^3 + (M \cos \theta + N \sin \theta + O/\theta^3)\phi. \quad (261)$$

Therefore, the cumulative correction for the momentum can be written as (p stands for the uncorrected momentum while p_c represents the corrected momentum):

$$p_c = p \left(1 + \frac{\Delta p}{p} + f(\theta, \phi) \right) + Q + R\phi + pT_{set} \quad (262)$$

where we also introduced some extra correction parameters. The parameters Q and R are specifically for low momentum particles. These correction terms are added directly to the momentum itself so that their effect increases as the momentum decreases. The last parameter, called T_{set} is applied only to outbending (torus current < 0) configurations. T_{set} stands for 7 distinct parameters, each being effective only for one beam energy. Having at least one independent parameter for each beam energy for outbending data sets improved the location and resolution of the elastic missing mass peak. In this way, the independent parameter can be adjusted to compensate the specific characteristics of the individual data set while all other parameters are constrained by all data sets together. It should be noted that the parameters A through R are for each sector. Therefore, we have 16 parameters per sector to optimize, for a total of 96 parameters. With the addition of T_{set} parameters, the total number of parameters is 103.

The optimization of parameters is based on the fact that the components of the missing four-momentum of these well identified events should be narrow distributions around zero. The missing energy and the components of the missing momentum were

calculated for the elastic events,

$$\begin{aligned}
p_{x[miss]} &= -p_{x[e]} - p_{x[p]} \\
p_{y[miss]} &= -p_{y[e]} - p_{y[p]} \\
p_{z[miss]} &= E_B - p_{z[e]} - p_{z[p]} \\
E_{[miss]} &= E_B + M_p - E'_e - E'_p
\end{aligned} \tag{263}$$

where E_B is the beam energy, M_p is proton mass, $E'_{e(p)}$ is the energy of the scattered electron (proton) and $p_{x[e(p)]}$, $p_{y[e(p)]}$, $p_{z[e(p)]}$ are the x , y and z components of the momentum of the electron (proton). Similarly for the $ep\pi^+\pi^-$ events, the components of the missing four-momentum were calculated by:

$$\begin{aligned}
p_{x[miss]} &= -p_{x[e]} - p_{x[p]} - p_{x[\pi^-]} - p_{x[\pi^+]} \\
p_{y[miss]} &= -p_{y[e]} - p_{y[p]} - p_{y[\pi^-]} - p_{y[\pi^+]} \\
p_{z[miss]} &= E_B - p_{z[e]} - p_{z[p]} - p_{z[\pi^-]} - p_{z[\pi^+]} \\
E_{[miss]} &= E_B + M_p - E'_e - E'_p - E'_{\pi^-} - E'_{\pi^+}.
\end{aligned} \tag{264}$$

Then the χ^2 of the fit was evaluated by adding the squares of each component, normalized to the expected resolution of that component,

$$\Delta\chi^2 = \sum_{\text{events}} \left(\frac{p_{x[miss]}^2}{\sigma_{p_x}^2} + \frac{p_{y[miss]}^2}{\sigma_{p_y}^2} + \frac{p_{z[miss]}^2}{\sigma_{p_z}^2} + \frac{E_{[miss]}^2}{\sigma_E^2} \right). \tag{265}$$

The expected resolutions for the missing four-momentum components were set to $\sigma_{p_x} = \sigma_{p_y} = 0.014$ GeV and $\sigma_{p_z} = \sigma_E = 0.020$ GeV. We used MINUIT [111] to minimize the χ^2 and optimize all the parameters in the correction formula. For each elastic event, we also added another term to the total χ^2 :

$$\Delta\chi^2 = \sum_{\text{elas-events}} \left(\frac{(W_{calc} - M_p)^2}{(0.020 \text{ GeV})^2} \right) \tag{266}$$

where M_p is proton mass and W_{calc} is the missing mass of the inclusive elastic event. After looping over all events (elastic and multi-particle final states for both inbending and outbending configurations), an additional term was added to the total χ^2 for each parameter:

$$\Delta\chi^2 = \sum_{\text{parm}=0}^{102} \frac{\text{parm}^2}{\sigma_{\text{parm}}^2}. \tag{267}$$

The reason of the last addition is to limit the parameters to reasonable ranges and avoid run-away solutions in some corner of the parameter space. An intrinsic uncertainty of 0.01 was used for parameters F and H . For parameters Q and R , the uncertainty was set to 0.003. For the rest of the parameters, the intrinsic uncertainty was set to 0.001.

It should be noted that the momentum correction fit is an iterative procedure. Initially we began with all parameters set to zero and ran the minimization routine. We determined the parameter values that minimized the χ^2 . Then we used those parameters as initial parameters and ran the minimization again. We continued the iteration until the parameter values were stabilized. During the iteration, we also tightened the data sample by applying the intermediate correction. Once we determined the optimal values of all parameters that minimized the overall χ^2 , the parameters were frozen together with all applied corrections. Since this data driven correction absorbs all unknown effects that previous corrections missed, the parameters really belong not only to the momentum correction part of the kinematic corrections package but also to all previous corrections applied before this stage.

Data selection for the momentum correction fit

The data selection is very important for the success of the momentum correction scheme. As we mentioned earlier, we used elastic $ep \rightarrow ep$ and inelastic $ep \rightarrow ep\pi^+\pi^-$ events. Of course, the elastic events are the most reliable events in terms of correctly identifying the final state and they do a good job of fixing the kinematics around the elastic peak. However, we also needed to incorporate some inelastic events into the data sample in order to ensure a reasonable fit for all kinematics including the resonance and the DIS regions. The next final state we have in the EG1b data with enough statistics that can be used for this purpose is $ep \rightarrow ep\pi^+\pi^-$ events. While determining these events, particle identifications should be made carefully.

For electrons, we applied the cuts listed in Table 13. The cuts for proton identification can be found in Table 14. One element in the table, the proton ID cut, is a cut specially applied only for hadrons based on the time of flight information of the particle. When the particle is found in the event and if it is not an electron, its expected time of flight (TOF_{calc}) is calculated by using the start time, the path

TABLE 13: Electron cuts applied for the momentum correction data sample.

| |
|--|
| particle charge = -1 |
| good helicity selection |
| one electron per event |
| $p \geq 0.01E_B$ |
| $p \leq E_B$ |
| $0 \leq flag \leq 5$ or $10 \leq flag \leq 15$ |
| triggerbit cut (see section IV.7.2) |
| $CC_{nphe} > 2.0$ |
| $EC_{tot}/p > 0.21$ |
| $EC_{in} > 0.06$ |
| $-58.0 \leq z_{vertex} \leq -52.0$ |
| $5^\circ < \theta < 49^\circ$ |

length and the momentum of the particle:

$$TOF_{calc} = StartTime + \frac{PathLength}{c\sqrt{p^2/(p^2 + M^2)}}. \quad (268)$$

The TOF_{calc} is calculated by assuming the hadron is a proton, pion, kaon or deuteron and using the corresponding mass values. Then the calculated TOF for each particle is compared to the time of flight registered by the TDC during the experiment. The hadron type that gives the smallest difference between the calculated TOF and the measured value is tagged to that particle. This is a preliminary method to determine the hadron type.

After the preliminary cuts that include charge, helicity and ID cuts, the initial kinematic corrections were applied to the particle and more precise cuts were applied afterward. The difference between the measured and calculated TOF (see Eq. (268)) is calculated again for the particle and a cut is applied on Δt . The Δt distribution for the proton can be seen in Fig. 63.

The cuts applied to select the elastic $ep \rightarrow ep$ events are listed in Table 15. In the table, $\phi_p - \phi_e$ represents the difference between the azimuthal angles of the electron and proton while $\theta_p - \theta_Q$ is the difference between the polar angles of the proton and the virtual photon, where θ_Q was calculated by:

$$\theta_Q = \tan^{-1} \left(\frac{E'_e \sin \theta_e}{E - E'_e \cos \theta_e} \right). \quad (269)$$

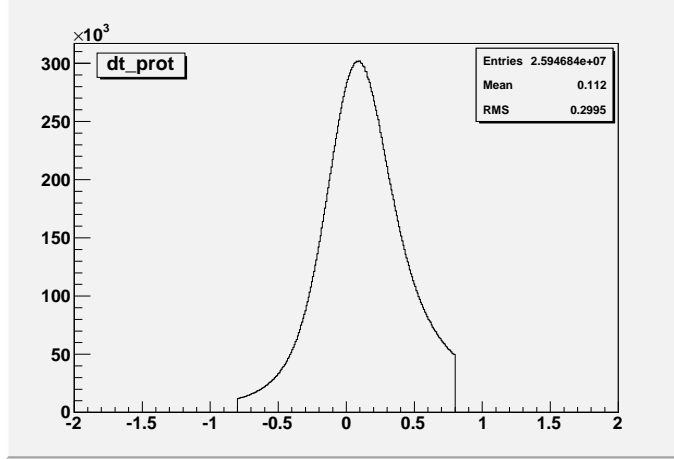


FIG. 63: Difference between measured and expected time of flight (in ns) for protons in EG1b. The plot shown has cuts for regular proton selections (see section IV.13). For the momentum correction data sample, a slightly tighter cut on the positive side, $\Delta t < 0.6$ ns, was applied.

TABLE 14: Proton cuts applied for the momentum correction data sample.

| |
|-------------------------------------|
| particle charge = +1 |
| good helicity selection |
| electron found in the event |
| one proton per event |
| proton ID cut (see text) |
| not the first particle in the event |
| $-0.8 < \Delta t < 0.6$ |
| $\theta < 49^\circ$ |
| $-58.0 \leq v_z \leq -52.0$ |

TABLE 15: Elastic event cuts applied for the momentum correction data sample.

| |
|--|
| good helicity selection |
| number of particles in the event = 2 |
| electron found in the event |
| proton found in the event |
| $ E_{[miss]} < 0.10 \text{ GeV}$ |
| $ p_{z[miss]} < 0.10 \text{ GeV}$ |
| $-2^\circ < \phi_p - \phi_e - 180^\circ < 2^\circ$ |
| $ \theta_p - \theta_Q < 2^\circ$ |
| $\theta_Q < 49^\circ$ |
| $\nu > 0$ |
| $0.75 \text{ GeV} \leq W \leq 1.05 \text{ GeV}$ |

The events should be taken smoothly over a full range of available kinematics so that final parameter values can be optimized for and represent the whole kinematic region. If the number of events is much larger for certain kinematic regions (or certain parts of the detector geometry), those regions will bias the final parameter values in their favor. This might decrease the quality of the correction for the other regions with less influence on the data sample. Therefore, the data sample needs to be as homogeneous as possible over the detector geometry. It is known that scattering events have non-homogeneous distribution with respect to the polar angle. Fig. 64 shows a typical distribution of elastically scattered electrons with respect to polar angle θ . Therefore, while selecting the elastic events, we randomly rejected a certain percentage of events from regions of θ with a high event rate and accepted all events from the regions with less events. However, the number of exclusive events from very forward angles is simply not enough, which results in a poorer correction for low angles $\theta < 10$ or 11 degrees. A separate correction routine was developed specifically for low angles, which will be explained later in this section.

The missing energy and momentum cuts for the elastic events were tightened after the first iteration (see Table 16). The plots for these can be seen in Fig. 65. In the figure, the red plot represents the distribution before the correction while the black is after the corrections are applied. The improvement is significant. The azimuthal angle distribution is also shown in Fig. 66.

For the multi-particle channel, we applied the same electron and proton cuts

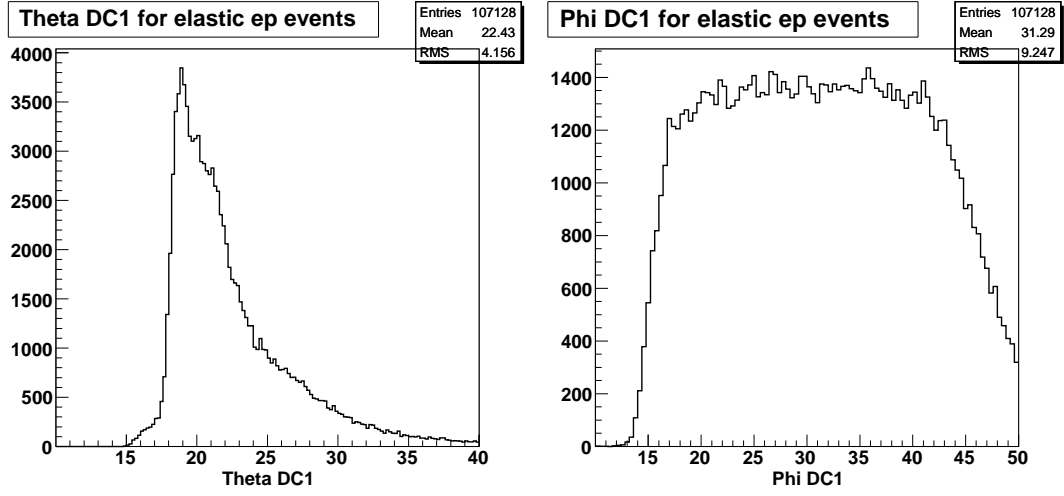


FIG. 64: Distribution in θ (left) and ϕ (right) of elastic ep events for the 4.2 GeV outbending data. The θ distribution has a strong kinematic dependence while the ϕ distribution is flat.

TABLE 16: Second iteration cuts for the elastic events.

| |
|--|
| $ p_{x[miss]} \leq 0.055 \text{ GeV}$ |
| $ p_{y[miss]} \leq 0.055 \text{ GeV}$ |
| $ p_{z[miss]} \leq 0.060 \text{ GeV}$ |
| $ E_{[miss]} \leq 0.060 \text{ GeV}$ |
| $-1^\circ < \phi_p - \phi_e - 180^\circ < 1^\circ$ |

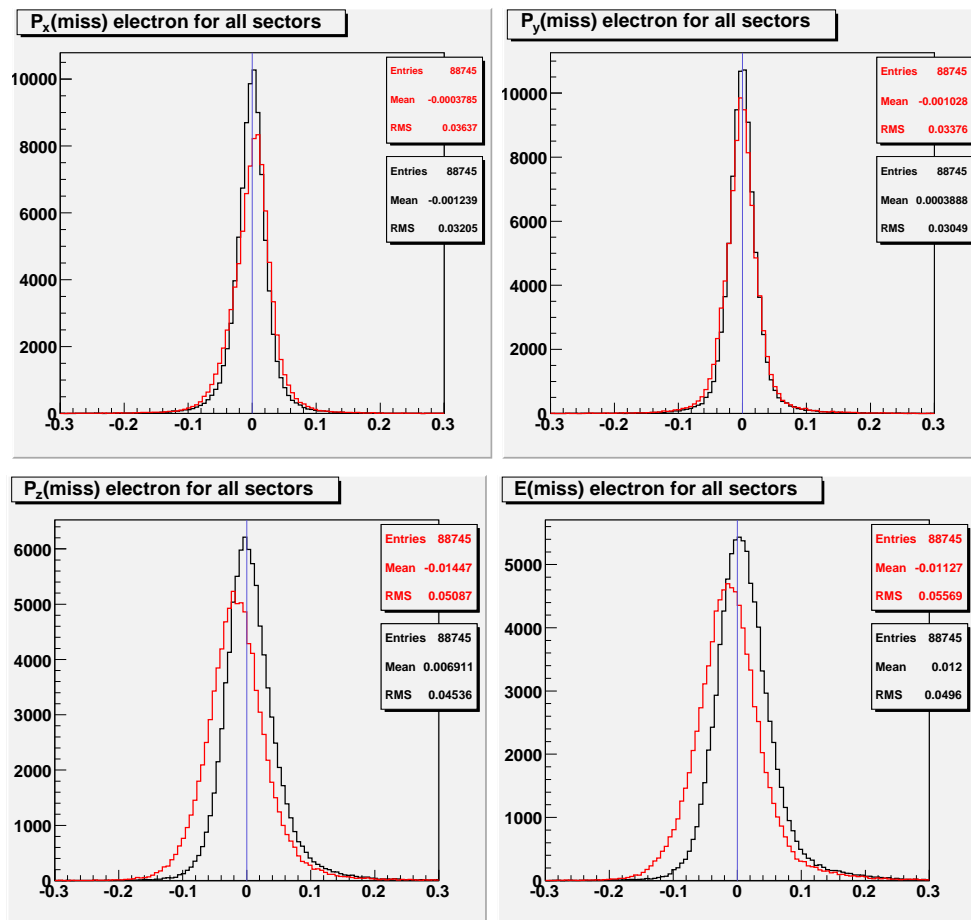


FIG. 65: Missing energy and momentum distributions from elastic events in the EG1b data. Beam energy = 4.2 GeV; Torus = -2250 A; Target is NH_3 . The red line is before and the black line is after the correction.

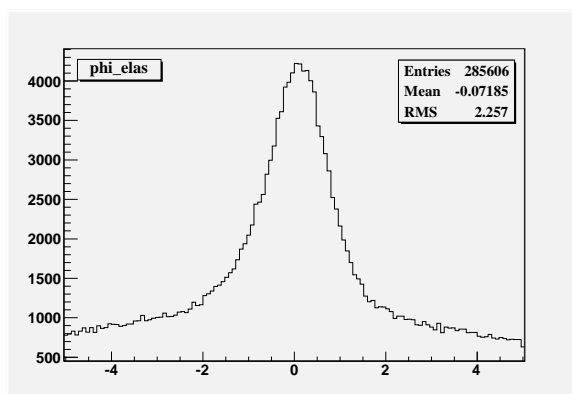


FIG. 66: The difference between electron and proton azimuthal angles for elastic scatterings after subtracting 180 degrees. (Beam energy = 4.2 GeV; Torus = -2250 A; Target is NH_3).

listed in Tables 13 and 14. The cuts applied for pions are listed in Table 17. In the table,

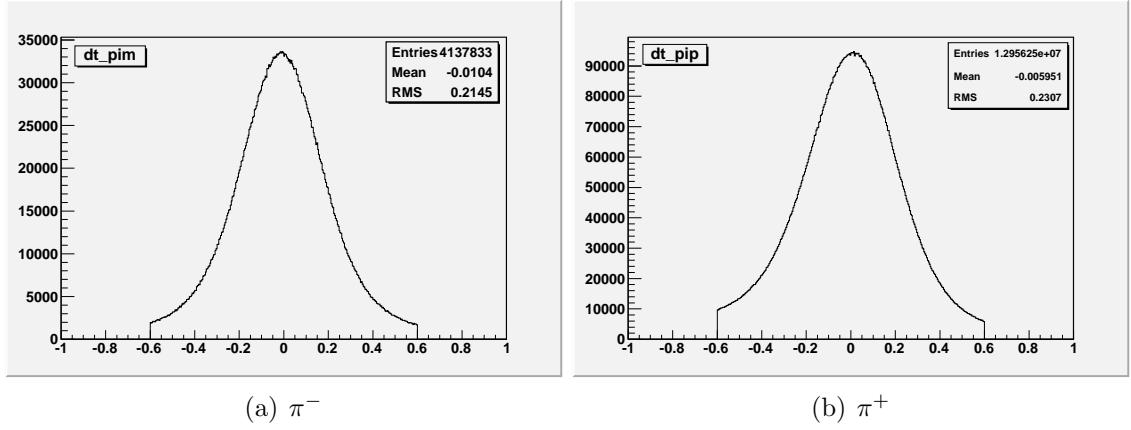
$$p_{t[miss]} = \sqrt{p_{x[miss]}^2 + p_{y[miss]}^2} \quad (270)$$

is the transverse missing momentum. Finally for the selection of $ep\pi^+\pi^-$ events we used the cuts listed in Table 18. The number of particles required for this final state was kept between 4 and 6 in order not to lose events with accidental signals in any of the detectors, such as cosmic ray or stray photons. Once all four particles were found in the event and the missing energy and momentum cuts were applied, the limit on the number of particles become only be a precautionary cut. After the first iteration corrections, the cuts on the data were tightened even more as listed in Table 19.

TABLE 17: Pion cuts applied for the momentum correction data sample.

| |
|--|
| charge = +1 for π^+ and -1 for π^- |
| good helicity selection |
| electron found in the event |
| pion ID cut (see text) |
| not the first particle in the event |
| $ \Delta t < 0.6$ |
| $\theta < 49^\circ$ |
| $-58.0 \leq z_{vertex} \leq -52.0$ |
| $p > 0.01E_B$ |
| $0 \leq flag \leq 5$ or $10 \leq flag \leq 15$ |
| $CC_{nphe} < 3.5$ |
| $EC_{tot}/p < 0.20$ |
| $EC_{in} \leq 0.06$ |
| $EC_{in}/p \leq 0.08$ |

We tried to keep the number of ep events and $ep\pi^+\pi^-$ events close to each other for all data sets. We also tried to gather the same amount of data from all different beam energy and torus configurations. Table 20 shows the number of events from different data sets for both final states. The final parameters are also listed in Tables 21 and 22.

FIG. 67: Difference between the measured and expected time of flight for π^- and π^+ TABLE 18: First iteration $ep\pi^+\pi^-$ cuts for the momentum correction data sample.

| |
|--|
| good helicity selection |
| $4 \leq \text{number of particles} \leq 6$ |
| electron found |
| proton found |
| π^+ found |
| π^- found |
| $ E_{[miss]} < 0.12 \text{ GeV}$ |
| $ p_{z[miss]} < 0.12 \text{ GeV}$ |
| $ p_{t[miss]} < 0.10 \text{ GeV}$ |

TABLE 19: Second iteration cuts for the $ep\pi^+\pi^-$ events.

| |
|--|
| $ p_{t[miss]} \leq 0.055 \text{ GeV}$ |
| $ p_{z[miss]} \leq 0.060 \text{ GeV}$ |
| $ E_{[miss]} \leq 0.060 \text{ GeV}$ |

TABLE 20: Number of events in each data sample for the momentum correction fit.

| Data Set | ep events | $ep\pi^+\pi^-$ events |
|----------|-------------|-----------------------|
| 1.6+ | 10000 | 10000 |
| 1.6- | 6258 | 451 |
| 1.7- | 10000 | 6009 |
| 2.3+ | 10000 | 10000 |
| 2.5- | 10000 | 10000 |
| 4.2+ | 10000 | 10000 |
| 4.2- | 10000 | 10000 |
| 5.6+ | 7028 | 6441 |
| 5.7+ | 9316 | 8781 |
| 5.7- | 8667 | 10000 |
| 5.8- | 10000 | 10000 |
| Total | 101269 | 90615 |

TABLE 21: Sector-dependent momentum correction parameters in EG1b.

| Par | Sector 1 | Sector 2 | Sector 3 | Sector 4 | Sector 5 | Sector 6 |
|-----|------------|------------|-----------|-----------|------------|------------|
| A | 0.00091 | 0.00085 | -0.00005 | -0.00084 | -0.00152 | -0.00162 |
| B | -0.00265 | -0.00112 | -0.00425 | 0.00269 | -0.00052 | 0.000145 |
| C | -0.00369 | -0.00465 | -0.00130 | 0.00103 | 0.00147 | 0.00091 |
| D | 0.00236 | 0.00266 | -0.00156 | -0.00363 | -0.00355 | -0.00534 |
| E | 0.00003 | -0.00063 | -0.00423 | 0.00239 | 0.00041 | 0.00072 |
| F | 0.02302 | 0.01214 | 0.01677 | -0.01380 | 0.00404 | -0.02218 |
| G | 0.00261 | 0.00715 | 0.00510 | -0.00439 | -0.00065 | -0.00552 |
| H | -0.03800 | -0.01755 | -0.01946 | 0.02098 | -0.00409 | 0.04574 |
| J | 0.00117 | -0.00593 | -0.00277 | 0.00258 | 0.00273 | 0.000992 |
| K | -0.00348 | 0.00304 | -0.01295 | -0.01154 | -0.780 | -0.00584 |
| L | -0.0000098 | -0.000009 | 0.0000016 | -0.000016 | -0.000018 | -0.0000088 |
| M | -0.00200 | -0.00393 | 0.00 | -0.00400 | -0.00678 | 0.00319 |
| N | -0.00778 | -0.01507 | -0.01295 | -0.01491 | -0.00755 | -0.00623 |
| O | -0.0001340 | -0.0000603 | 0.0000082 | 0.0000144 | -0.0000485 | 0.0000755 |
| Q | 0.00196 | 0.00183 | 0.00120 | 0.00117 | 0.00080 | 0.00139 |
| R | -0.00094 | -0.00463 | -0.00486 | -0.00523 | -0.00120 | -0.00437 |

TABLE 22: Beam energy and torus current dependent parameters, T_{set} , for outbending data sets.

| Data set | T_{set} |
|----------|-------------------------|
| 1.6– | -0.000159 |
| 1.7– | 0.000705 |
| 2.5– | 0.000308 |
| 4.2– | 0.003203 |
| 5.6– | -1.64×10^{-12} |
| 5.73– | 0.000854 |
| 5.76– | -0.000589 |

IV.10.8 Patch Correction

The momentum correction relies on the elastic and inelastic events in the data for minimization of missing four-momentum. The amount of those events at extremely small angles is rather limited. Moreover, there is a complex magnetic field around the target that mainly affects scattered particles at small angles. Therefore, even after the momentum corrections were applied, we still saw a deviation of the elastic peak in the W spectrum from its true value and also a strong dependence of the elastic peak position on the azimuthal angle in this angular range. This means that because of the lack of sample events at these small angles, the momentum correction has failed to account for the complex magnetic field which is especially important at small angles. Even if there are not many ep and $ep\pi^+\pi^-$ events at these forward angles (this is mainly an acceptance problem for protons), there are many inclusive e^- events that can be used for our analysis.

A patch correction that can be applied on top of the momentum correction was developed by Peter Bosted to correct specifically the scattering events at small angles. The correction simply utilizes the linear dependence of the elastic peak position on the azimuthal angle and uses a fit function to minimize that dependence over selected events in the range of small polar angles. The fit function also includes a θ dependent term to smoothly merge the small angle correction and large angle correction. The functional form of the correction is:

$$\Delta p = 0.02 \left[U + \left(V + X \frac{1}{30^\circ} (\phi - 30^\circ) \right) \left(\frac{10^\circ}{\theta} \right)^3 \right], \quad (271)$$

where U , V and X are the fit parameters that should be determined separately for each sector and torus current configuration. The latter depends on the sign of the product of the torus polarity and particle's charge. If $\text{torus} \times \text{charge}$ is positive, the particle's configuration is outbending (particle's trajectory is bent away from the beam line), otherwise it is inbending (toward the beam line). The polar (θ) and the azimuthal (ϕ) angles were taken from the Region 1 drift chamber. In order to determine the parameter values, the data were separated into θ and ϕ bins for each sector. For θ , 1° bins and for ϕ 10° bins were used during the fit procedure. The elastic peak W position was determined for each bin. The correction requires the elastic peak position to be calculated as precisely as possible with all background contributions removed. Since we have NH_3 and ND_3 data together for all beam energies (except 2.3 GeV data¹³), the ratio of NH_3 to ND_3 scattering events were used to obtain a more precise elastic peak distribution. In the ratio, the ^{15}N background cancels out leaving the ratio of the free proton elastic peak to the deuteron quasi-elastic peak. The resulting elastic peak is narrower and the position is more precise. Fig. 68 shows an example of this peak ratio for 6 ϕ bins in sector 1 before the corrections were made.

Once the elastic peak position was determined for each sector, θ and ϕ bin, the MINUIT minimization package was used to minimize the difference between the elastic peak position and the proton mass and determine the fit parameters in Eq. (271). The fit was made separately for each sector and for inbending and outbending torus configurations. The patch correction is designed to be only effective in the forward angle region; its effect quickly diminishes as we go to higher angles and the standard momentum correction takes over there. The effectiveness of this correction depends on the abundance of inclusive NH_3 and ND_3 data at small polar angles. Therefore, the correction was good for outbending data and low beam energies. The patch correction was applied only to the 1.6 GeV inbending and outbending data sets and the 1.7, 2.5 and 4.2 GeV outbending data sets. The final values of these parameters are listed in Table 23.

¹³Since ND_3 data is not available for 2.3 GeV beam energy, ^{12}C was used to remove the background contribution. However, in the end, the patch correction was not applied to this data set.

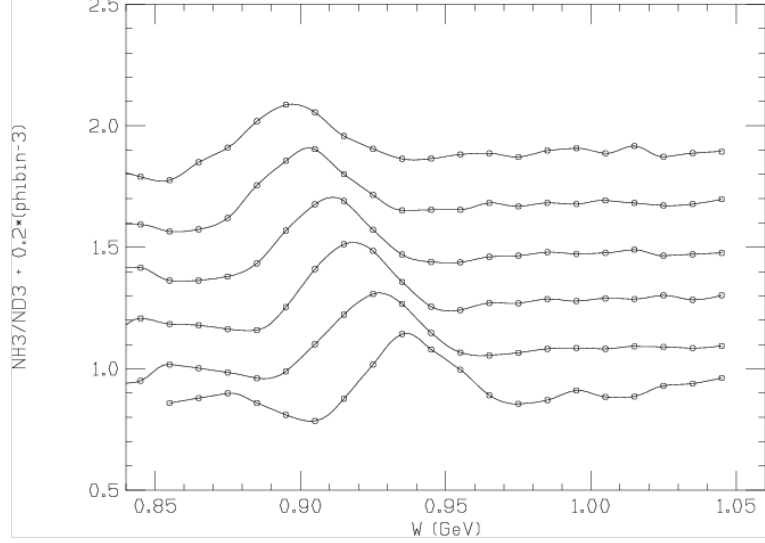


FIG. 68: Ratios of NH_3/ND_3 spectra for six different ϕ bins in Sector 1 for $\theta < 13^\circ$, separated by an arbitrary offset for visibility. Corrections are needed in this angular range to remove the dependence of the peak position on the azimuthal angle and center the peak at the proper elastic value of $W = 0.938$ GeV. Plot courtesy P. Bosted.

TABLE 23: Forward angle momentum correction parameters for the EG1b experiment. The sign of $\text{torus} \times \text{charge}$ determines which set (inbending or outbending) should be applied for the particle.

| Parameter | Sector 1 | Sector 2 | Sector 3 | Sector 4 | Sector 5 | Sector 6 |
|------------|----------|----------|----------|----------|----------|----------|
| Outbending | | | | | | |
| U | -0.0472 | -0.0378 | -0.2485 | -0.0066 | 0.0257 | -0.5182 |
| V | -0.2235 | -0.1650 | -0.0532 | -0.2370 | -0.2588 | 0.1406 |
| X | -0.2730 | -0.1789 | -0.4687 | -0.1929 | -0.1733 | -0.2743 |
| Inbending | | | | | | |
| U | -0.2238 | -0.2621 | -0.0024 | -0.1918 | -0.1217 | -0.1203 |
| V | 0.2786 | 0.3348 | -0.4065 | 0.3624 | 0.2378 | 0.1846 |
| X | -0.963 | -0.748 | 0.713 | 0.591 | -0.032 | -1.070 |

IV.10.9 Overall Results of the Kinematic Corrections

In order to evaluate the overall effect of the kinematic correction package, we monitored various different dependencies. The missing energy and momentum distributions for each sector before and after each correction were monitored. In addition, the $\Delta E'/E'$ vs. ϕ and W versus ϕ behaviors of the elastic peak from the inclusive events were examined in different θ bins. Tables 24 and 25 list the polar and azimuthal angle bins used to generate these plots. $\Delta E'/E'$ is the difference between the expected and measured energy of the scattered electron,

$$\frac{\Delta E'}{E'} = \frac{E'_{theo} - E'_{meas}}{E'_{theo}}. \quad (272)$$

The expected energy E'_{theo} for the electron in elastic scattering was calculated by

$$E'_{theo} = \frac{ME_B}{M + E_B(1 - \cos \theta)} \quad (273)$$

where we used Eqs. (20), (21) and (22), with $W = M$ for the elastic events. Finally $\Delta E'/E'$ was plotted with respect to ϕ .

In the remainder of this section, we will present these monitored distributions before and after the kinematic corrections were applied. Fig. 69 shows the change in the missing energy distribution of the elastic events separately for different sectors. Similar plots were also shown in Fig. 65 for missing momentums and energy integrated over all sectors. The results also show a clear improvement of the elastic peak location and width for most data sets. The dependence of the elastic peak on the azimuthal angle is shown in Figs. 72 and 73. In addition, Figs. 74 through 77 show the distributions of the invariant mass W for inclusive counts after the proper background subtractions were made by using the ^{12}C data. In these plots, the elastic (or the quasi-elastic) peak before and after the kinematic corrections are shown together, for both NH_3 and ND_3 targets and various data sets.

TABLE 24: Polar angle θ bins used to plot the monitoring histograms for the kinematic corrections.

| bin | min $^{\circ}$ | max $^{\circ}$ |
|-----|----------------|----------------|
| 1 | 7.0 | 8.0 |
| 2 | 8.0 | 9.0 |
| 3 | 9.0 | 10.0 |
| 4 | 10.0 | 11.0 |
| 5 | 11.0 | 12.0 |
| 6 | 12.0 | 14.0 |
| 7 | 14.0 | 16.0 |
| 8 | 16.0 | 18.0 |
| 9 | 18.0 | 22.0 |
| 10 | 22.0 | 26.0 |
| 11 | 26.0 | 32.0 |
| 12 | 32.0 | 49.0 |

TABLE 25: Azimuthal angle ϕ bins used to plot the monitoring histograms for the kinematic corrections. The bins are selected to maximize and equally distribute events in each bin.

| bin | min $^{\circ}$ | max $^{\circ}$ |
|-----|----------------|----------------|
| 1 | 1.0 | 15.0 |
| 2 | 15.0 | 20.0 |
| 3 | 20.0 | 25.0 |
| 4 | 25.0 | 30.0 |
| 5 | 30.0 | 35.0 |
| 6 | 35.0 | 40.0 |
| 7 | 40.0 | 50.0 |

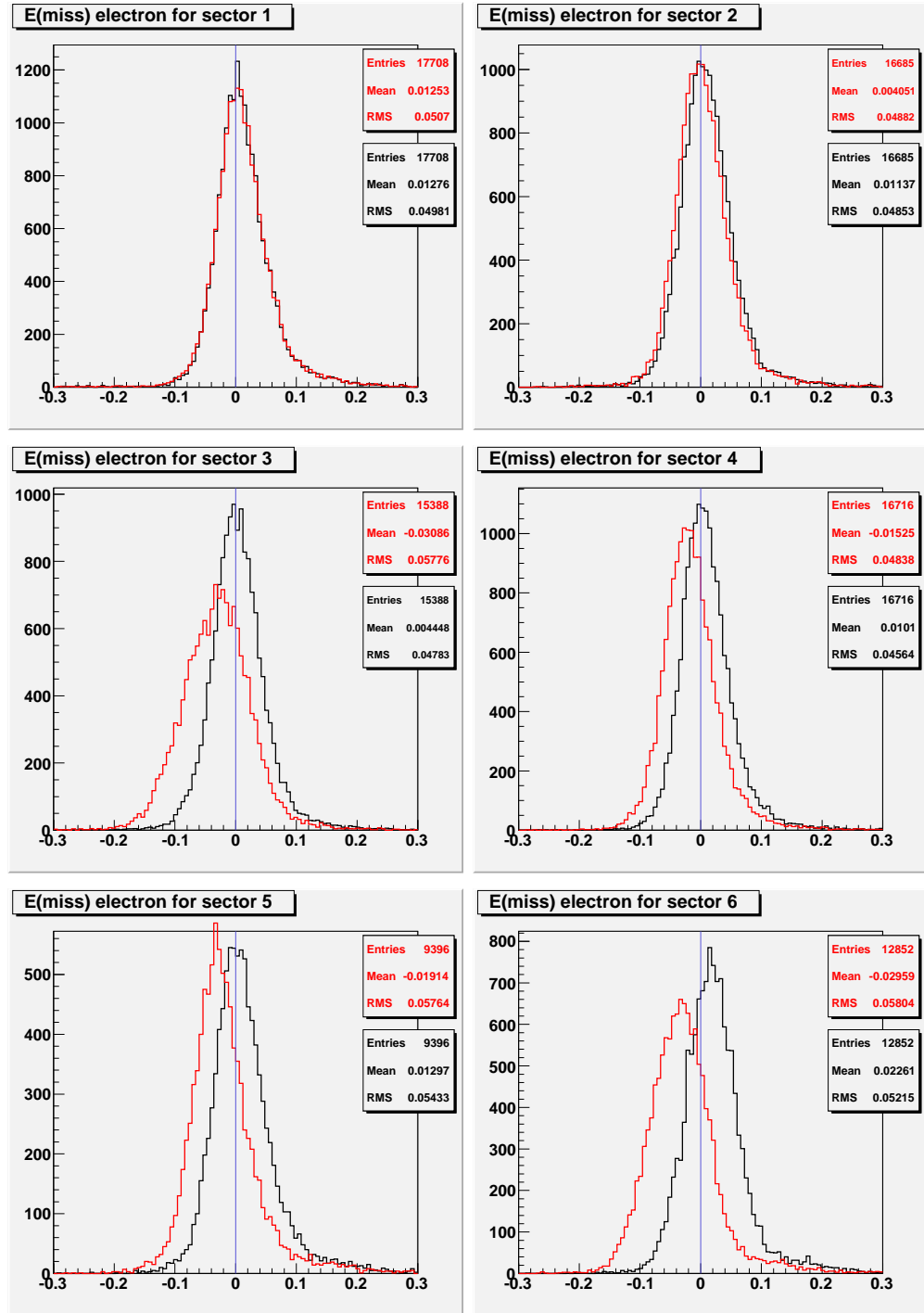


FIG. 69: Missing energy $E_{[miss]}$ for elastic events in different sectors. The red line is before the kinematic corrections are applied while the black line represents the final situation. The plots shown are from the 4.2 GeV outbending data set.

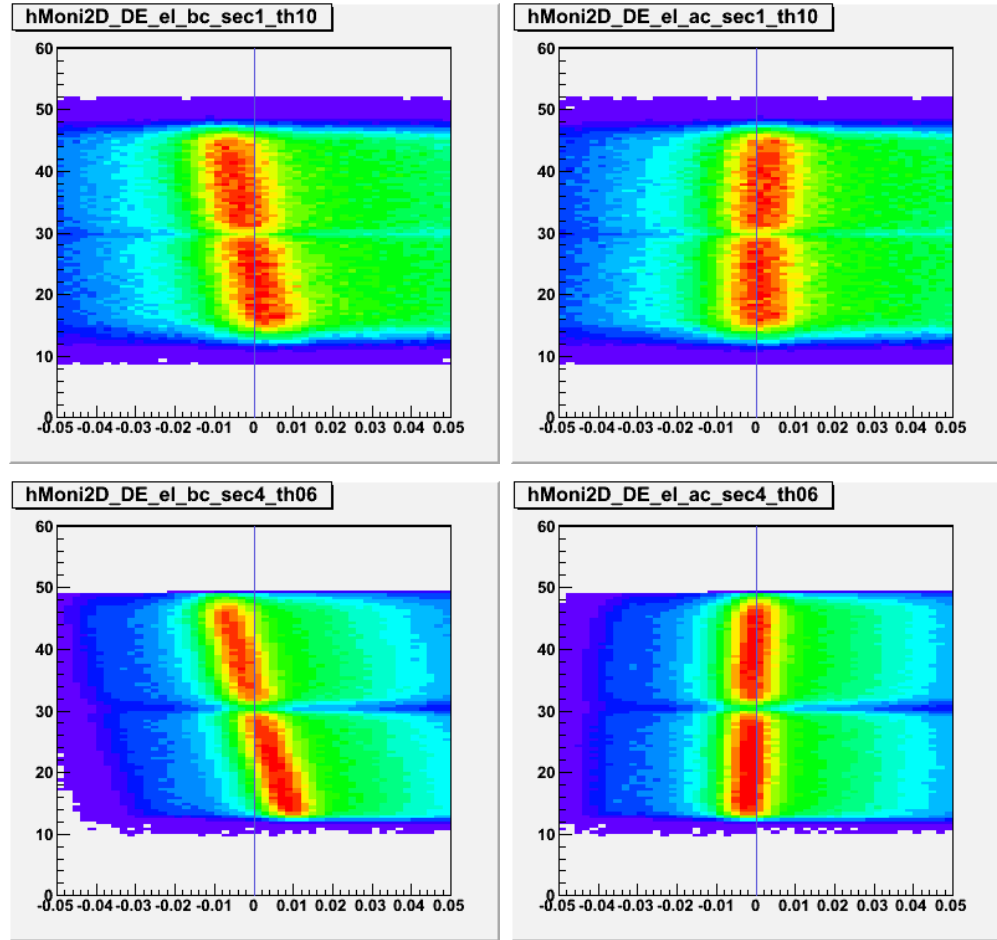


FIG. 70: ϕ vs. $\Delta E'/E'$ before (the left panel) and after (right panel) the kinematic corrections (see Eq. (272)). The pictures are randomly selected among more than thousand plots for different beam energy, torus, sector and polar angle θ . The top row is from the 1.606 GeV inbending data set while the bottom row is from the 1.723 GeV outbending set. The dependency of $\Delta E'/E'$ on the azimuthal angle is removed successfully for most kinematic regions.

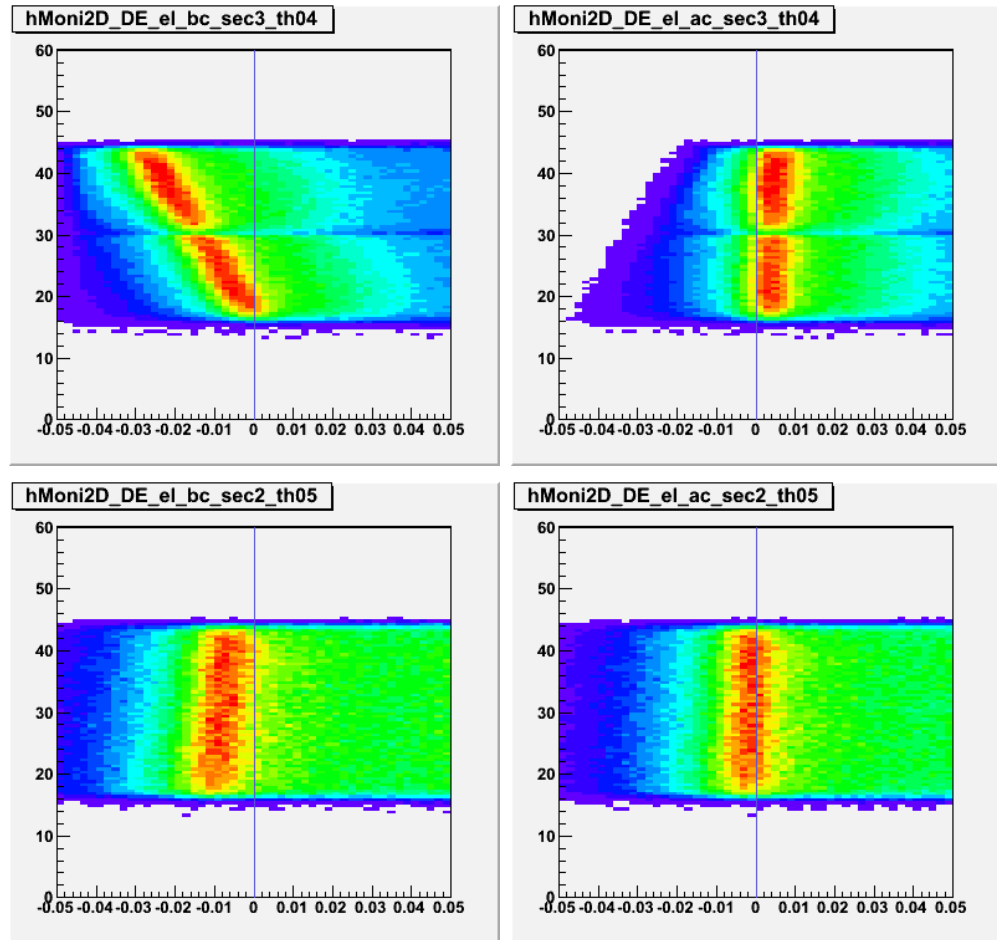


FIG. 71: Same as Fig. 70 except the top row is for the 2.561 GeV data and the bottom row is for the 4.238 GeV outbending data sets.

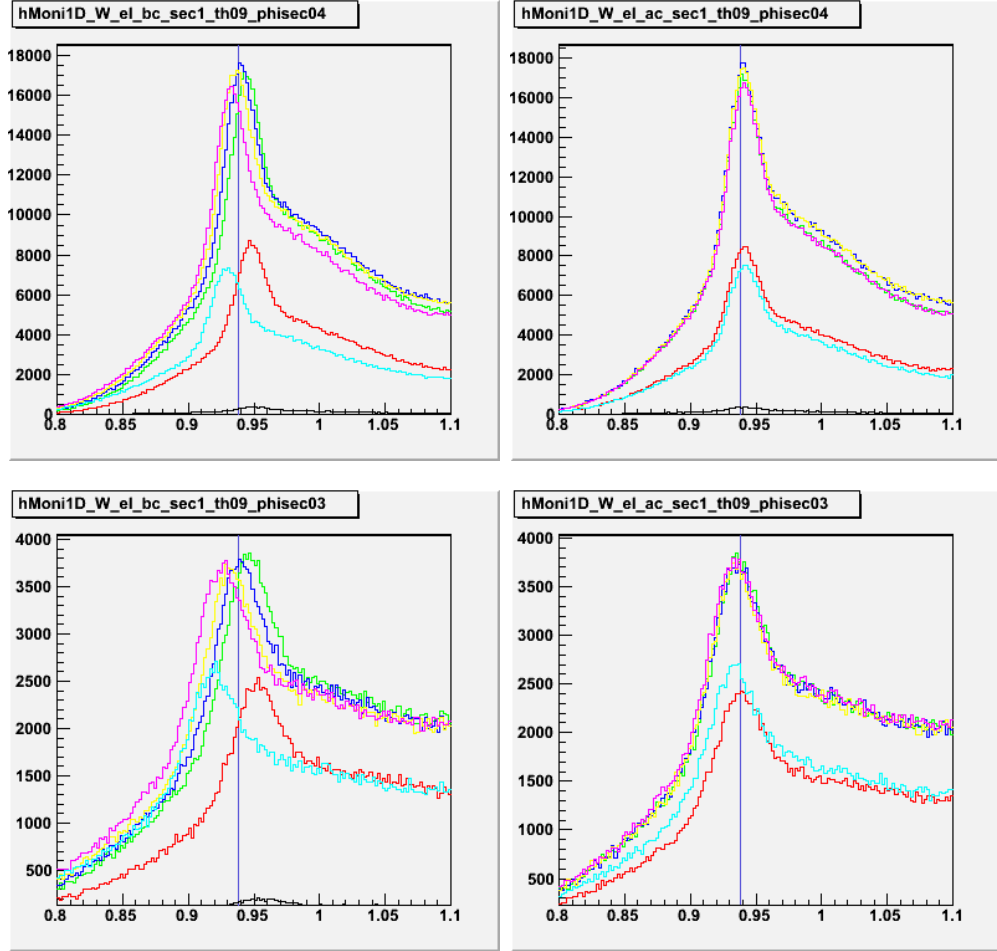


FIG. 72: Elastic W peak for various ϕ bins shown in different colors before (left) and after (right) the kinematic corrections for 1.606 (top) and 2.286 (bottom) GeV data sets. The plots represent a selected beam energy, torus, sector and polar angle bin. The ϕ dependence of the elastic W peak is a concern for the kinematic corrections and is successfully managed.

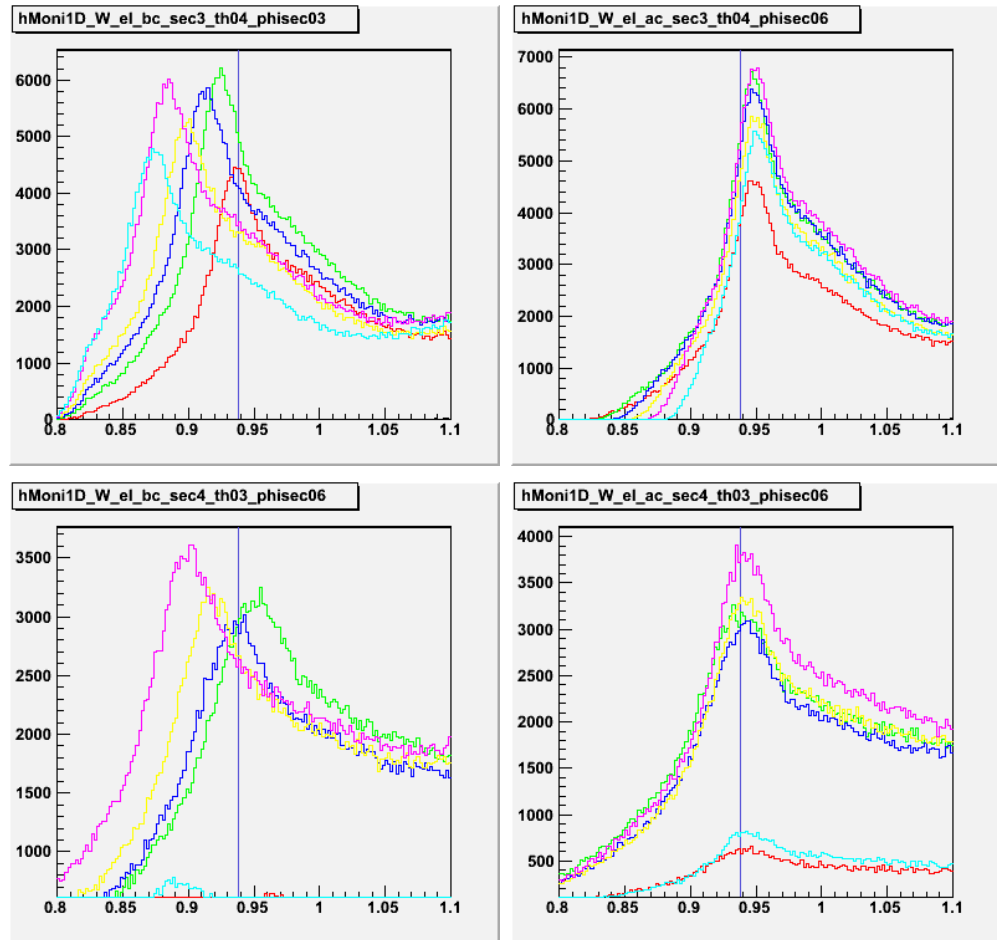


FIG. 73: Same as Fig. 72 except the top row is for the 2.561 GeV and the bottom row is for the 4.238 GeV outbending data sets.

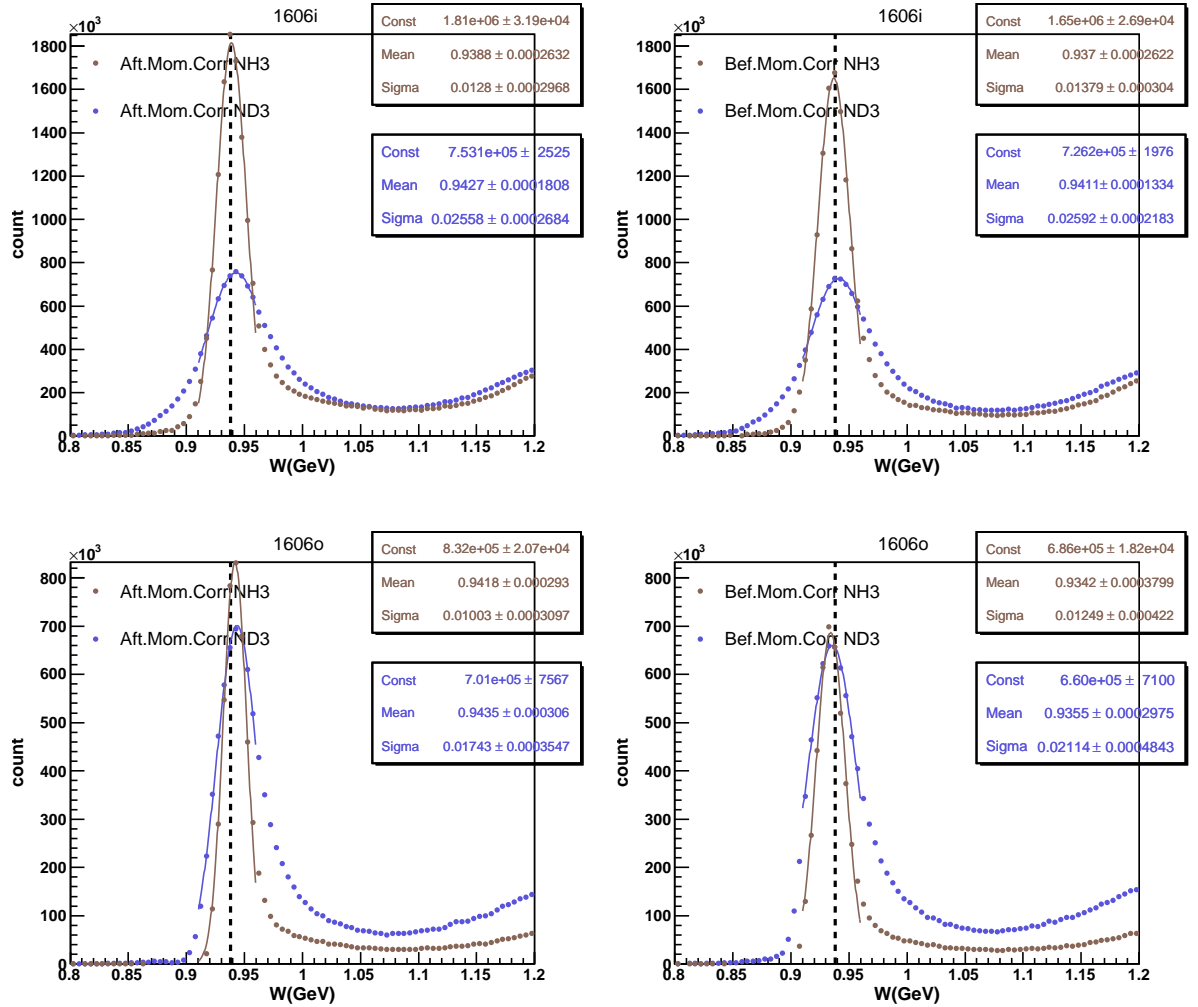


FIG. 74: Inclusive number of counts versus invariant mass W distributions after proper background subtractions are made by using the ^{12}C data. Each row represents a different data set. The left plot is after all kinematic corrections are applied while the right plot is before the corrections, except the raster correction. The brown curves (with the higher peak) are for NH_3 and the blue curves are for ND_3 targets. Each plot representing a different data set is labeled with the beam energy in MeV and the torus configuration i (inbending) or o (outbending). After the kinematic corrections, the invariant mass peak for the elastic events should be centered around the proton mass (0.938 GeV) and the sigma of the distribution should be smaller.

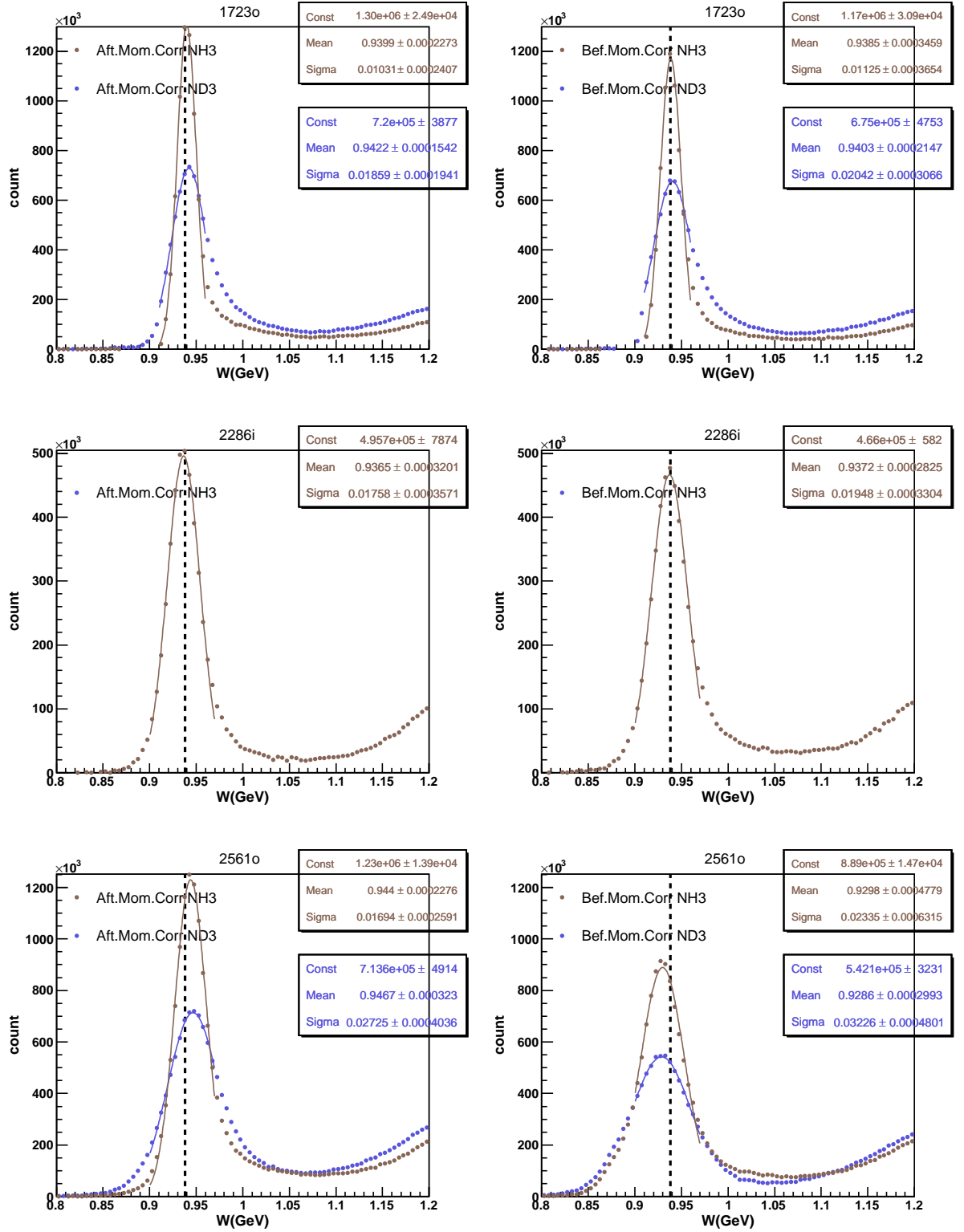


FIG. 75: Continuation of Fig. 74 for other data sets.

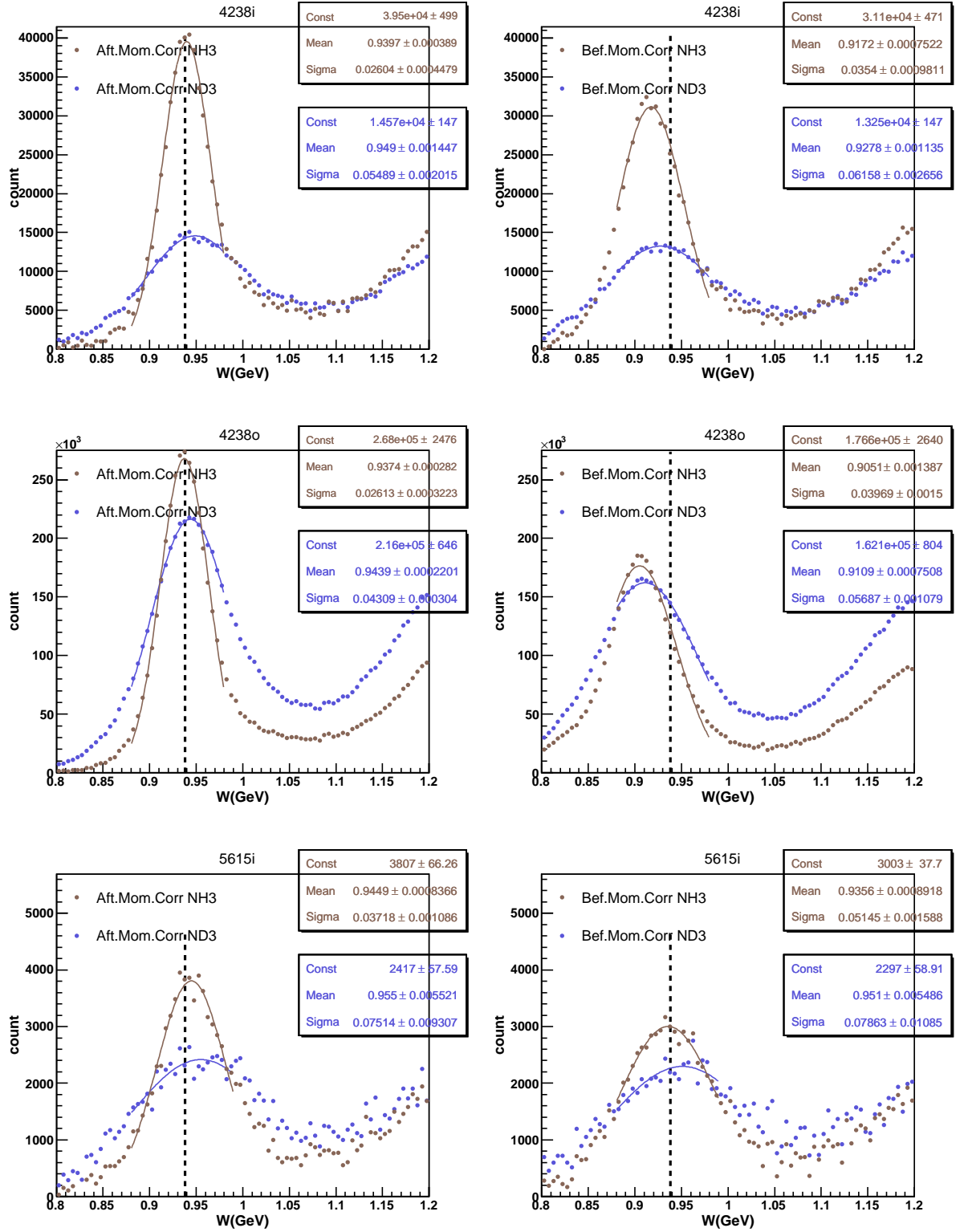


FIG. 76: Continuation of Fig. 75 for other data sets.

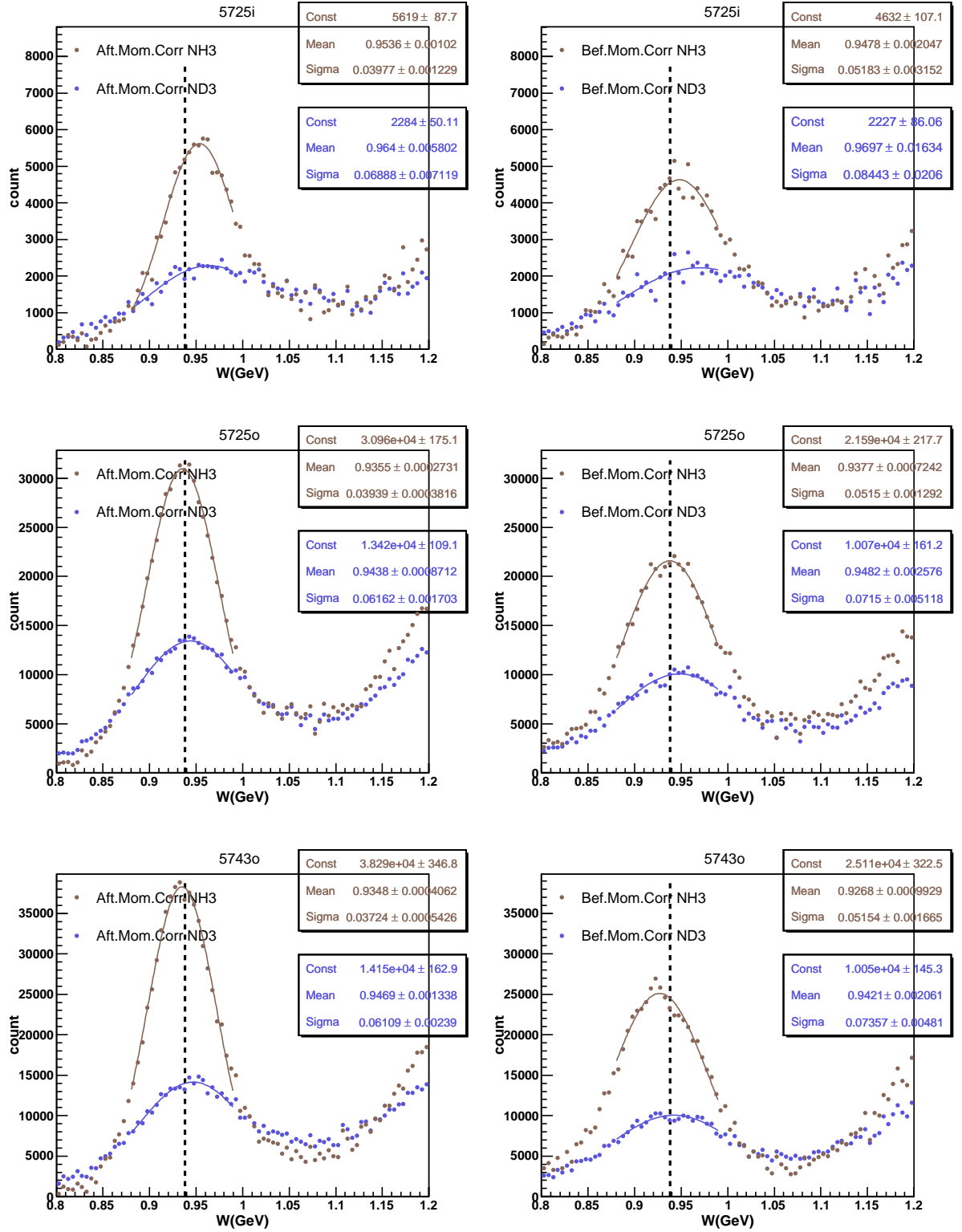


FIG. 77: Continuation of Fig. 76 for the remaining data sets.

IV.11 DILUTION FACTOR

Since we are interested in scattering events from polarized nucleons, the asymmetries must be corrected for the contributions from unpolarized background. These contributions mainly come from the nearly unpolarized ^{15}N nucleus in the target material (ND_3), the liquid helium bath that surrounds it for cooling and the target windows that keep the whole apparatus together. For this purpose, we define a quantity called dilution factor, which is the fraction of events scattered from the polarized deuteron target. First we define the raw asymmetry as:

$$A_{raw} = \frac{n^- - n^+}{n^- + n^+} \quad (274)$$

In this equation, n^- and n^+ are determined by counting the inclusive scattering events for each helicity and normalizing with the accumulated beam charge. During the counting procedure, we have no way to know if the event is coming from the polarized target or from the unpolarized background. However, since the unpolarized contribution is the same for both helicities, it cancels out in the numerator. The denominator, on the other hand, is heavily diluted by the background contribution. Therefore, we need to correct the denominator such that:

$$A_{undil} = \frac{n^- - n^+}{n^- + n^+ - n_B} \quad (275)$$

where n_B stands for the count of the background events. Based on this approach, we can define a dilution factor (F_D) to correct the asymmetry for the background contribution:

$$F_D = \frac{n^- + n^+ - n_B}{n^- + n^+} = \frac{n_A - n_B}{n_A} = 1 - \frac{n_B}{n_A}, \quad (276)$$

where n_A represents the total count of events from all sources in the beam path. Then we can write the undiluted asymmetry in terms of the diluted asymmetry and the dilution factor defined in Eq. (276) as:

$$A_{undil} = \frac{A_{raw}}{F_D}. \quad (277)$$

In a naive approach, when we consider the $^{15}\text{ND}_3$ target, we see that there are 3 polarized deuterons (6 polarized nucleons) for every 21 nucleons. Therefore, the dilution factor, which was defined as the fraction of events scattered from polarized target nucleons, would be 6/21. For a more precise approach, this number would be slightly modified by the difference in cross section for scattering off proton versus scattering

off neutron, and nuclear effects. However, the additional material in the beam path, mainly the target windows and the liquid helium bath, makes the determination of the dilution factor more complicated. The ideal way to determine the dilution factor would be to take ^{15}N runs under the exact same conditions as the $^{15}\text{ND}_3$ runs and subtract the scattering events of the former case from the latter after scaling them with appropriate normalization to make them comparable. However, due to technical difficulties with ^{15}N targets [112], taking frequent ^{15}N runs in between $^{15}\text{ND}_3$ runs was not an option. Another way would be to simulate the ^{15}N contribution by taking data on a material with a structure close to ^{15}N . One possible choice for that is a ^{12}C target. However, scattering from ^{12}C is not exactly the same as scattering from ^{15}N because of the different number of nucleons in these targets and the extra neutron in the ^{15}N . In order to overcome this obstacle, limited ^{15}N runs were taken at some beam energies together with ^{12}C runs taken regularly for all beam conditions and ^{15}N runs were simulated by using the cross section ratio of ^{12}C to ^{15}N targets. In addition, empty target runs, in which the target slot was filled only with the liquid helium, were also taken regularly for each beam condition. By using these runs, the liquid helium contribution to the scattering events was determined. From now on, we will refer to these liquid helium runs as the empty target (E) runs. The required quantities¹⁴ that will be used throughout this section are defined in Table 26.

Two different methods were used to calculate the dilution factor and their results were compared. In a chronological order, the first method was developed by Sebastian Kuhn and is based on the parametrization of data and the neutron-to-deuterium cross section ratios to simulate the ^{15}N background in terms of ^{12}C . The second method was developed by Peter Bosted and Robert Fersch and is based on the radiated cross section model described in Ref. [112].

Method 1: dilution factors from parametrization of data

In order to calculate F_D by using the first method, we need to determine the amount of background events n_B in Eq. (276). In terms of the quantities described in Table 26, we can define n_B as:

$$n_B = n_E + \frac{\rho_A l_A}{\rho_C l_C} \frac{\sigma_N}{\sigma_C} n'_C - l_A n'_{He}, \quad (278)$$

¹⁴Note that cross sections are in terms of cm^2 per nucleus.

TABLE 26: Target parameter definitions. The subscript \mathcal{X} represents different target types used during the experiment. The following acronyms are used for different target types throughout this section: N for nitrogen; A for ammonia; T (or D) for deuteron; C for carbon and He for liquid helium. In addition, Al is aluminum, K is kapton and F represents all kapton and aluminum foils. All counts (represented by $n_{\mathcal{X}}$) are normalized to the corresponding total integrated beam charge for each target. The quantity f is introduced for convenience. It assumes $\sigma_F \approx \sigma_C$ so that the foil mass thickness can be expressed as a fraction of carbon mass thickness. This quantity is used in later sections while calculating the target lengths.

| Parameter | Definition |
|--|--|
| L | Total length of the target cell |
| $l_{\mathcal{X}}$ | Length of target \mathcal{X} |
| $\rho_{\mathcal{X}}$ | Density of target \mathcal{X} |
| $\sigma_{\mathcal{X}}$ | Cross section of target \mathcal{X} |
| $n_{\mathcal{X}}$ | Measured counts from target \mathcal{X} |
| $n'_C = \rho_C l_C \sigma_C$ | Expected counts scattered only from ^{12}C |
| $n'_{He} = \rho_{He} l_{He} \sigma_{He}$ | Expected counts per 1 cm length of liquid ^4He |
| $n'_N = \rho_N l_N \sigma_N$ | Expected counts scattered only from ^{15}N |
| $n'_A = \rho_A l_A \sigma_A$ | Expected counts scattered from ammonia |
| $f = \rho_F l_F / \rho_C l_C$ | Contribution to count rate from all Aluminium (Al) and Kapton (K) foils combined, expressed as a fixed fraction of the contribution from ^{12}C |

which states that the total normalized count from background materials in the beam path is equal to the number of scattered events from the empty target plus the ^{15}N contribution in the ammonia target minus the contribution from the liquid Helium replaced by the solid ammonia. In the equation, the ^{15}N contribution in the ammonia target is expressed in terms of the carbon material scattering rate multiplied by the nitrogen to carbon ratio. The second element in this equation is the key part that requires the simulation of ^{15}N background in terms of the ^{12}C counts. By using this definition for the normalized background counts, we can write the dilution factor as:

$$F_D = 1 - \frac{1}{n_A} \left(n_E - l_A n'_{He} + \frac{\rho_A l_A \sigma_N}{\rho_C l_C \sigma_C} n'_C \right). \quad (279)$$

Method 2: dilution factors from radiated cross section model

Another way of calculating F_D is to express the numerator and the denominator of Eq. (276) individually in terms of the radiated cross section model. The numerator $n_A - n_B$ represents the normalized counts from the polarized target material only. We will use $n_A - n_B = n_T$, where T stands for the polarized target (deuteron in our case). The denominator n_A in (276) represents the total normalized count of events from all sources in the beam path. In terms of the radiated cross section model, n_T and n_A can be expressed,

$$n_T = \frac{6}{21} \rho_A l_A \sigma_T \quad (280)$$

$$n_A = F + \rho_A l_A \left(\frac{6}{21} \sigma_T + \frac{15}{21} \sigma_N \right) + \rho_{He} (L - l_A) \sigma_{He} \quad (281)$$

where F represents the contribution from the Aluminium (Al) and Kapton (K) foils in the target window. We define $F = \rho_{Al} l_{Al} \sigma_{Al} + \rho_K l_K \sigma_C$ where we approximated $\sigma_K \approx \sigma_C$. With the cross section values at hand from the radiated cross section model [112] as a function of Q^2 and W , F_D can be calculated as a smooth function of our kinematical variables:

$$F_D = \frac{n_T}{n_A} = \frac{\frac{6}{21} \rho_A l_A \sigma_T}{F + \rho_A l_A \left(\frac{6}{21} \sigma_T + \frac{15}{21} \sigma_N \right) + \rho_{He} (L - l_A) \sigma_{He}}. \quad (282)$$

General comments and preparation

The advantage of the first method is that it is based on a parametrization of data and does not require any cross section models. However, it is statistical in nature and gives poor results where there is not enough data for parametrization. This causes

TABLE 27: Densities of the target materials in the EG1b experiment. Values are from Refs. [113] and [114].

| Target Material | Density (g/cm ³) | Density (mol/cm ³) |
|--------------------------------|------------------------------|--------------------------------|
| ammonia (NH ₃) | 0.917 | 0.0508 |
| ammonia (ND ₃) | 1.056 | 0.0502 |
| carbon (¹² C) | 2.17 | 0.180 |
| nitrogen-15 (¹⁵ N) | 1.1 | 0.073 |
| liquid helium (He) | 0.145 | 0.0362 |
| kapton (K) | 1.42 | 0.00371 |
| aluminum (Al) | 2.69 | 0.0997 |

artificially large bin by bin statistical fluctuations, which causes large errors on F_D and therefore on the undiluted asymmetry. The advantage of the second method is that F_D is obtained as a smooth function of Q^2 and W . Therefore, the results can easily be extrapolated into regions where there is not enough data for the first method. F_D was calculated by both methods and it was confirmed that the second method behaves exactly as the parametrization of the first method. In the end, the first method was only used for the calculation of systematic errors and in the quasi-elastic region. The second method was used to determine the dilution factors for asymmetry measurements.

After defining the dilution factor and the methods to calculate it, we can now determine what we need to carry out the necessary calculations in both methods. When we examine Eq. (279) closely, we see that we need to determine the densities and the lengths for the ammonia and the carbon targets to carry out the method 1 calculation. We also need the nitrogen cross section, which we will simulate by using the carbon data. That will require the knowledge of the target length for the carbon as well as the nitrogen. From the Eq. (282), we see that we need the target density and the length for the ammonia as well as the total target length L . For the cross sections we will use the radiated cross section model. The target densities are already known and they are written in Table 27.

Approximate target lengths from physical measurements are given in Table 28. The value for the window foil material changes after the run 27997 because of the addition of a Kapton (K) piece after this run. The true length of the ammonia

TABLE 28: Lengths of the target materials in the EG1b experiment. Values are from Refs. [113] and [114].

| Target Material | Approximate Length (cm) |
|---------------------------------|--|
| total (L) | 1.9 |
| ammonia (NH_3) | 0.6 |
| ammonia (ND_3) | 0.6 |
| carbon (^{12}C) | 0.23 |
| carbon (^{12}C) | 0.22 (for ^{15}N target runs) |
| nitrogen-15 (^{15}N) | 0.5 |
| liquid helium (He) | L minus solid target material |
| kapton (K) | 0.0304(0.0384 after 27997) |
| kapton (K) | 0.0354 (for ^{15}N target runs) |
| aluminum (Al) | 0.0167 |

targets ($^{15}\text{NH}_3$ or $^{15}\text{ND}_3$), which is represented by l_A , depends on the packing fraction (the percentage of volume occupied by ammonia beads in the total target volume). Therefore, it should be studied explicitly. The same situation is also valid for the ^{15}N target. The liquid Helium exists in all target types since it is used to keep the target at low temperature. Its length depends on how much of the liquid Helium was displaced by the other target material that it is hosting. The length of the Kapton (K) and the Aluminum (Al) targets are known from physical measurements during the experiment. Since the dilution factor is very sensitive to these values, the target lengths for the ammonia and the nitrogen targets were studied explicitly to determine the correct F_D . Next we will describe how the target lengths are determined. Table 29 shows the values of some target parameters defined earlier in Table 26. These values will be used for the calculations of other quantities.

IV.11.1 Calculation of Total Target Length L

The total target length L includes the length of the mini-cup that includes the target cell itself and the liquid Helium around it as well as the foil materials for the windows. The nominal value for L is 1.9 cm. However, this length may change slightly according to experimental conditions because of varying pressure that causes the window material to change its shape, liquid Helium overflow or the beam position

TABLE 29: Target parameter values

| Quantity | Value | Comment |
|--------------------|---|---------------------------------|
| $\rho_C l_C$ | 0.498 g/cm ² = 0.0415 mol/cm ² | mass thickness of carbon |
| $\rho_C l_C$ | 0.476 g/cm ² = 0.0397 mol/cm ² | for ¹⁵ N target runs |
| $\rho_K l_K$ | 0.0432 g/cm ² (0.055 g/cm ² after 27997) | mass thickness of Kapton |
| $\rho_K l_K$ | 0.0503 g/cm ² | for ¹⁵ N target runs |
| $\rho_{Al} l_{Al}$ | 0.0450 g/cm ² | mass thickness of Al |
| $\rho_F l_F$ | 0.0882 g/cm ² (0.0996 g/cm ² after 27997) | mass thickness of Al + K foils |
| $\rho_F l_F$ | 0.0952 g/cm ² | for ¹⁵ N target runs |
| f | 0.177(0.200 after 27997) | $\rho_F l_F / \rho_C l_C$ |
| f | 0.235 | for ¹⁵ N target runs |

with respect to the curvatures of the target window. Therefore, it is desirable to determine L separately for different data sets because its value affects the F_D calculation directly. Two different methods, the data driven method and the radiated cross section model method, mentioned previously, are used for the calculation of L . We will go over these methods separately and provide their comparison.

Calculation of L from data

The normalized counts for each target can be expressed in terms of the contributions from the liquid Helium, the window foil material and the target material itself. So we can write the normalized count for the empty target as the counts from the foil (F) and the liquid Helium (that fills the whole mini-cup therefore the total length L is used as the target length):

$$n_E = \rho_F l_F \sigma_F + \rho_{He} L \sigma_{He}. \quad (283)$$

Similarly, we can write the carbon counts in terms of the foil material, the carbon and the liquid Helium contributions:

$$n_C = \rho_F l_F \sigma_F + \rho_C l_C \sigma_C + \rho_{He} l_{He} \sigma_{He}. \quad (284)$$

In this equation, we can replace the He target length l_{He} with the total target length L minus the carbon target length l_C since the carbon displaced the He in the mini-cup.

$$n_C = \rho_F l_F \sigma_F + \rho_C l_C \sigma_C + \rho_{He} (L - l_C) \sigma_{He}. \quad (285)$$

However, an extra correction is needed for the liquid Helium target because of its larger radiation length ($X_o(\text{g/cm}^2)$) compared to the other targets. All solid targets in the experiment were designed to be around the same mass thickness $t = \rho_{\mathcal{X}}l_{\mathcal{X}}(\text{g/cm}^2)$. However, the count rate from a target is affected by its radiation thickness, defined by t/X_o . Since the radiation thickness of He is smaller compared to carbon, its count rate should be corrected by adding an extra length to it. Then fully radiated cross sections for the He are calculated by using two different target lengths. The ratio of these cross sections was determined for each kinematical bin of the experiment and used as a multiplication factor for any liquid He count whenever the counts were obtained from the data. In addition, an extra raster cut was applied to the empty target counts. More detailed information on the corrections on the empty target can be found in [95].

At this point, we can use the convenience factor f introduced in the previous section to simplify Eqs. (283) and (285) as:

$$n_E = f\rho_C l_C \sigma_C + \rho_{He} L \sigma_{He} \quad (286)$$

$$n_C = (1 + f)\rho_C l_C \sigma_C + \rho_{He}(L - l_C)\sigma_{He} \quad (287)$$

The ratio $r_{EC} = n_E/n_C$ is employed and $\sigma_C = 3\sigma_{He}$ is assumed to determine the total target length for each kinematical bin L_{bin} :

$$L_{bin} = \left(\frac{3\rho_C l_C [(1 + f)r_{EC} - f]}{\rho_{He}} - r_{EC} l_C \right) / (1 - r_{EC}). \quad (288)$$

Then the error weighted average of L_{bin} is taken to determine the average total target length L for each data set. For this purpose, we also need to calculate the statistical error on L_{bin} . This statistical error is calculated with respect to r_{EC} as:

$$\sigma_{L_{bin}} = \frac{\partial L}{\partial r_{EC}} \sigma_{r_{EC}} = \left[\frac{N(1 + f) - l_C}{1 - r_{EC}} + \frac{N[(1 + f)r_{EC} - f] - r_{EC} l_C}{(1 - r_{EC})^2} \right] \sigma_{r_{EC}}, \quad (289)$$

where

$$N = 3\rho_C l_C / \rho_{He}, \quad (290)$$

and

$$\sigma_{r_{EC}} = \sqrt{\left(\frac{\partial r_{EC}}{\partial n_E} \right)^2 n_E + \left(\frac{\partial r_{EC}}{\partial n_C} \right)^2 n_C}, \quad (291)$$

which yields

$$\frac{\sigma_{r_{EC}}}{r_{EC}} = \sqrt{n_E^{-1} + n_C^{-1}}. \quad (292)$$

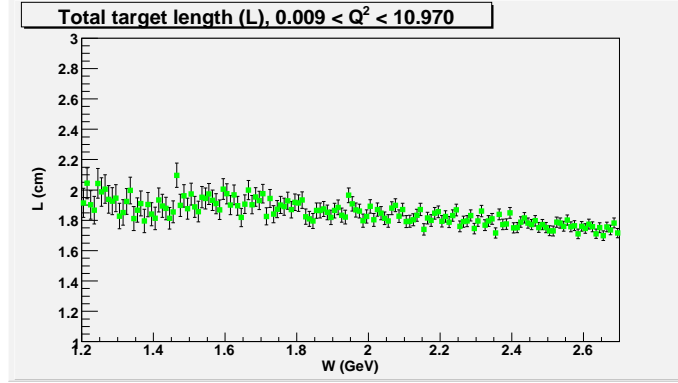


FIG. 78: Total target length, L , calculated using the EG1b data, shown as a function of W averaged over Q^2 bins. A W cut of 1.40 GeV is incorporated for the final value of L to remove the effects of the Δ -resonance. Plot is courtesy of R. Fersch.

Therefore, the error weighted average of the total target length is calculated as:

$$L = \frac{\sum_{Q^2} \sum_W L_{bin} / \sigma_{L_{bin}}^2}{\sum_{Q^2} \sum_W 1 / \sigma_{L_{bin}}^2} \quad (293)$$

The statistical error on L is not used anywhere else since it underestimates the real error on the target length. Instead, we used the systematic errors which are explained in [95]. In averaging L , specific W and Q^2 ranges were used for the validity of the model. In order to remove the $\Delta(1232)$ region, where L_{bin} does not show a flat behavior, only the $W > 1.40$ GeV was used for average L . There are also upper W cuts that change for different Q^2 bins and can be found in [95]. The final results of L from this method are listed in Table 30 under “Method 1”. The plot of L as a function of W (without the W cut incorporated for the final value), with error-weighted average taken over Q^2 bins, is also shown in Fig. 78 for the 5.76 GeV outbending data set.

Calculation of L from models

The second method of calculation of L incorporates the radiated cross section model. Detailed explanation of this model can be found in [112]. The measured ^{12}C count rate can be expressed in terms of the radiated cross section model (derived by using the carbon data, which is expressed by the square brackets after the cross section

terms) of the individual contributions from the foils, the liquid helium and the nitrogen target itself as:

$$n_C = \rho_{Al} l_{Al} \sigma_{Al[C]} + \rho_K l_K \sigma_{C[C]} + \rho_C l_C \sigma_{C[C]} + \rho_{He} (L - l_C) \sigma_{He[C]}, \quad (294)$$

with $\sigma_K \sim \sigma_C$. Similarly, the measured count rate for the empty target is:

$$n_E = \rho_{Al} l_{Al} \sigma_{Al[E]} + \rho_K l_K \sigma_{C[E]} + \rho_{He} L \sigma_{He[E]}. \quad (295)$$

The model ratio of the count rates of the carbon and empty targets is given by:

$$r_{EC}^{model} = \frac{n_E}{n_C} \quad (296)$$

Solving this equation for the target length L gives us:

$$L_{bin} = \frac{r_{EC} F_{[C]} - F_{[E]} + r_{EC} \rho_C l_C \sigma_{C[C]} - r_{EC} \rho_{He} l_C \sigma_{He[C]}}{\rho_{He} \sigma_{He[E]} - r_{EC} \rho_{He} \sigma_{He[C]}}, \quad (297)$$

where the foil contribution from Al and Kapton are combined under the term $F = \rho_{Al} l_{Al} \sigma_{Al} + \rho_K l_K \sigma_C$. The error on L_{bin} can be estimated (assuming the foil contributions are small ($F \rightarrow 0$) and $\sigma_{He[C]} \sim \sigma_{He[E]}$) by its variation with respect to the ratio r_{EC} :

$$\sigma_{L_{bin}} = \frac{\partial L_{bin}}{\partial r_{EC}} \sigma_{r_{EC}} = \frac{\rho_C l_C \sigma_{C[C]} - \rho_{He} l_C \sigma_{He[C]}}{\rho_{He} \sigma_{He[C]} (1 - r_{EC})^2}, \quad (298)$$

with $\sigma_{r_{EC}}$ given in Eq. (292). The error weighted average of the total target length is calculated by summing over all Q^2 and W bins as described in the previous section. Since the model cross sections already have the corrections for nuclear EMC effects, the W cut can be reduced to $W > 1.10$ GeV for this calculation. Also, Q^2 dependent upper W cuts are used, which are described in [95] in detail. This is a direct calculation of L from models, in which the cross sections, unlike the previous method, are determined by a fit to the world data. However, for the radiated cross section model, the total target length must be known first. Therefore, an iterative method is used by beginning from an initial value of $L = 1.90$ cm. Radiated cross sections are calculated from initial value and L is recalculated with the method described. Then the cross sections are recalculated from the new L . The iteration is continued until L stabilizes, which is usually after 2 iterations for most data sets. An additional iteration was always performed to make sure the length was absolutely stable. Fig. 79 shows the final L from method 2 as a function of W , averaged over Q^2 bins ($0.317 < Q^2 < 0.645$) for the 4.2 GeV inbending data set.

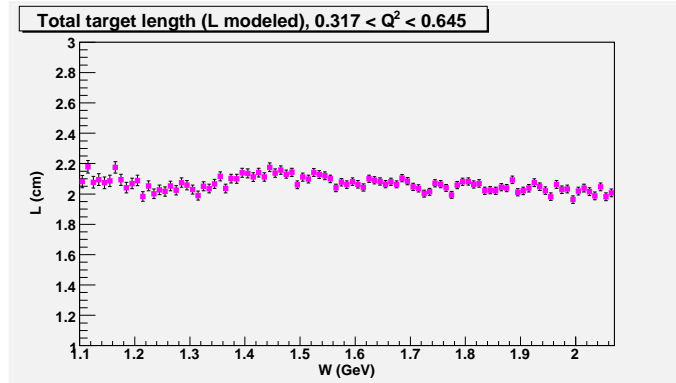


FIG. 79: Total target length, L , calculated using the radiated cross-section models, shown as a function of W , averaged over Q^2 bins ($0.317 < Q^2 < 0.645$) for the 4.2 GeV inbending data set. Plot is courtesy of R. Fersch.

The two methods are compared carefully and their results agree very well. The final results of both methods can be seen in Table 30. For the final analysis, the results from the radiated cross section model (method 2) was used. The method just described for the calculation of L stands as a general outline for all target length calculations, which we will describe in the following sections. Even though the calculation methods are similar or the same, there are still slight differences that should be explained.

IV.11.2 Modeling ^{15}N from ^{12}C Data and Calculation of l_N

As already mentioned, the best way to remove the ^{15}N contribution from the ammonia ($^{15}\text{NH}_3$ and $^{15}\text{ND}_3$) target counts is to take data on the ^{15}N with the same beam conditions. Since it was not possible because of technical difficulties, instead we took data on a ^{12}C target as the closest possible approximation of ^{15}N . However, scattering from ^{12}C is not identical to scattering from ^{15}N because of a different number of nucleons. Even if this can be taken care of by parametrization and scaling of the ^{12}C data, there is also an extra neutron in the ^{15}N target, which has to be accounted for. There are, fortunately, some ^{15}N target runs during the EG1b experiment, at least for some of the beam configurations. These data were used to express the ^{15}N cross section in terms of the ^{12}C cross section. Two different methods, explained in the previous section, were used to create a good fit for the ^{15}N cross section. The first method used a parametrized definition of the ^{15}N cross section in terms of the

TABLE 30: Calculated total target length L for different data sets in the EG1b experiment are shown for both methods. Method 2 results were used for the final analysis. L_{avg} is used only for $^{12}\text{C}/^{15}\text{N}$ analysis [112].

| Beam Energy (GeV) | Torus Setting | $L(\text{cm})$ -Method 1 | $L(\text{cm})$ -Method 2 |
|-------------------|-------------------------------|--------------------------|--------------------------|
| 1.606 | + | 1.93 | 1.90 |
| 1.606 | - | 1.82 | 1.85 |
| 1.723 | - | 1.87 | 1.87 |
| 2.286 | + | 1.76 | 1.77 |
| 2.561 | + | 1.93 | 1.92 |
| 2.561 | - | 1.84 | 1.86 |
| 4.238 | + | 2.01 | 2.00 |
| 4.238 | - | 2.04 | 2.05 |
| 5.615 | + | 1.77 | 1.78 |
| 5.725 | - | 1.79 | 1.83 |
| 5.743 | + | 1.93 | 1.95 |
| 5.743 | - | 1.82 | 1.87 |
| L_{avg} | $^{12}\text{C}/^{15}\text{N}$ | 1.89 | 1.90 |

^{12}C cross section and utilized the available EG1b data on ^{15}N to determine the best values for the parameters. Later, the parametrized definition of the ^{15}N cross section was used for all data sets. The second method uses the radiated cross section model for ^{15}N , so no fit is required. Next, we will explain both of these methods.

Parametrization of ^{15}N cross section

The first method makes the assumption that in the high W region ($W > 1.5$ GeV), the ratio of cross sections for different target materials can be approximated in terms of the composite number of protons and neutrons in the material (this assumption obviously neglects the EMC effect, which is one of the reason that the second method was developed later). On this basis, since ^{15}N contains 7 protons and 8 neutrons while ^{12}C contains 6 protons and 6 neutrons, we can write the following relations for ^{15}N and ^{12}C cross sections:

$$\sigma_C \approx 6\sigma_D \quad (299)$$

$$\sigma_N \approx 7\sigma_D + 1\sigma_n \quad (300)$$

$$\sigma_N \approx \left(\frac{7}{6} + \frac{1}{6} \frac{\sigma_n}{\sigma_D} \right) \sigma_C, \quad (301)$$

where σ_n and σ_D are the neutron and the deuteron cross sections respectively, given in cm^2 per nucleus. The nominal values $7/6$ and $1/6$ can be turned into parameters a and b , respectively, and fit to the the nitrogen data for the beam energies where they are available, so that small deviations from these nominal values can be determined. Therefore, we can write the above equation as:

$$\sigma_N = \left(a + b \frac{\sigma_n}{\sigma_D} \right) \sigma_C \quad (302)$$

The world data parametrization by S. Kuhn [113] is used for the neutron to deuteron cross section ratio σ_n/σ_D . Following the same prescription given in the previous sections, we can express the count rates for the carbon and the empty targets as:

$$n_C = (1 + f)n'_C + (L - l_C)n'_{He} \quad (303)$$

$$n_E = fn'_C + Ln'_{He}, \quad (304)$$

where n'_C and n'_{He} are the expected count rates for the carbon and helium targets as given in Table 26. The expected count rates can be expressed in terms of the measured count rates by using the above equations:

$$n'_C = \frac{L}{L + fl_C} n_C + \frac{L - l_C}{L + fl_C} n_E \quad (305)$$

and

$$n'_{He} = \frac{1 + f}{L + fl_C} n_E + \frac{f}{L + fl_C} n_C \quad (306)$$

By using a similar approach, the measured nitrogen count rate can be expressed in terms of the foils, the liquid helium and the ^{15}N contribution:

$$n_N = f\rho_C l_C \sigma_C + \rho_{He}(L - l_N)\sigma_{He} + \rho_N l_N \sigma_N \quad (307)$$

And again using the definitions given in Table 26:

$$n_N = fn'_C + (L - l_N)n'_{He} + n'_N \quad (308)$$

By using the defined parametrization of the nitrogen cross section in terms of the carbon cross section, we can write:

$$n_N = fn'_C + (L - l_N)n'_{He} + \frac{\rho_N l_N}{\rho_C l_C} \left(a + b \frac{\sigma_n}{\sigma_D} \right) n'_C. \quad (309)$$

Inserting back Eq. (304) for the measured empty target count rate, the parametrized nitrogen count rate is expressed in its final form as:

$$n_N = n_E - l_N n'_{He} + \frac{\rho_N l_N}{\rho_C l_C} \left(a + b \frac{\sigma_n}{\sigma_D} \right) n'_C. \quad (310)$$

The next step is to fit this parametrized definition to the available nitrogen data in order to determine the parameters. However, the carbon/nitrogen data were taken by using a different target insert and therefore may not be directly comparable to the empty target runs, which also enter into the parametrized definition above. The best way to resolve this problem was to normalize all counts to the carbon and to use the parametrized definition of the nitrogen to carbon count ratio instead. So, dividing all terms in Eq. (310) by the carbon count rate n_C and using Eq. (305) to express n'_C/n_C and Eq. (306) to express n'_{He}/n_C , we can write¹⁵:

$$\frac{n_N}{n_C} = \frac{n_E}{n_C} - l_N n''_{He} + \frac{\rho_N l_N}{\rho_C l_C} \left(a + b \frac{\sigma_n}{\sigma_D} \right) n''_C \quad (311)$$

where

$$n''_C = \frac{L}{L + fl_C} + \frac{L - l_C}{L + fl_C} \frac{n_E}{n_C} \quad (312)$$

and

$$n''_{He} = \frac{1 + f}{L + fl_C} \frac{n_E}{n_C} + \frac{f}{L + fl_C}. \quad (313)$$

The ratio for the nitrogen to carbon count rates expressed in Eq. (311) (abbreviated as *calc* below) was fit to the ratio obtained from the data to minimize the χ^2 of the fit defined as:

$$\chi^2 = \sum_{W, Q^2} \left(\left(\frac{n_N}{n_C} \right)^{data} - \left(\frac{n_N}{n_C} \right)^{calc} \right)^2. \quad (314)$$

Ideally, a , b and l_N could all be used as parameters. Unfortunately, the limited amount of nitrogen data made it difficult for MINUIT to deal with all three parameters together. In the old analysis procedure, the quantity l_N was taken as a known quantity. However, the precision of l_N was about 0.1 cm, which created large uncertainties in the resulting parameters a and b . In order to reduce these uncertainties, it was decided that l_N could be determined with better precision by using the available radiated cross section model for the nitrogen to carbon cross section ratios. Therefore, the model for σ_N/σ_C was substituted in Eq. (311) instead of $a + b \sigma_n/\sigma_D$. This

¹⁵Because of the 0.1 mm difference in thicknesses of the 2 carbon targets used, a multiplicative factor of 1.047 was used on the n_E/n_C count ratio. See [95].

leaves us with a single parameter l_N to determine from the fit in Eq. (314). The χ^2 minimization was performed separately for each data set. Then the final values of l_N were used in the original form of Eq. (311) to determine the parameters a and b . The resulting values for these parameters are listed in Table 31 together with their uncertainties. The average values of the parameters are very close to their nominal values $a = 7/6$ and $b = 1/6$. It should be pointed out that these values for a and b are only used in systematic error calculations. The final values for the target length l_N are also listed in Table 32 under “Method 1”.

TABLE 31: Values of the parameters a and b for different data sets for which there is available nitrogen data. These parameters are used to express the nitrogen cross section in terms of the carbon cross section.

| Data Beam (GeV) Torus | a | b |
|-----------------------|-------------------|--------------------|
| 1.723 + | 1.12 ± 0.0030 | 0.27 ± 0.0073 |
| 1.723 - | 1.08 ± 0.0019 | 0.37 ± 0.0047 |
| 2.286 + | 1.18 ± 0.0015 | 0.12 ± 0.0036 |
| 4.238 + | 1.12 ± 0.0187 | 0.28 ± 0.0452 |
| 4.238 - | 1.20 ± 0.0014 | 0.07 ± 0.0031 |
| 5.615 + | 1.04 ± 0.0186 | 0.47 ± 0.0461 |
| 5.615 - | 1.24 ± 0.0070 | -0.01 ± 0.0155 |
| average | 1.16 ± 0.0008 | 0.15 ± 0.0019 |

Modeling the ^{15}N from radiated cross sections to determine l_N

There are 7 carbon-nitrogen data sets taken with different beam energy and torus configurations as part of the EG1b experiment. Among these data sets, the 2.286 GeV inbending set is used to create a reliable model for the cross section ratios of $^{15}\text{N}/^{12}\text{C}$ and $^4\text{He}/^{12}\text{C}$ targets. Detailed explanations of this analysis can be seen in [112] and it is beyond the content of this thesis. Once the model was generated, it was successfully tested by using the other available data sets on the nitrogen and carbon.

The ^{15}N count rate can be expressed in terms of radiated cross sections (derived by using the nitrogen data, which is expressed by the square brackets after the cross section terms) of the individual contributions from the foils, the liquid helium and

the nitrogen target itself as:

$$n_N = \rho_{Al} l_{Al} \sigma_{Al[N]} + \rho_K l_K \sigma_{C[N]} + \rho_N l_N \sigma_{N[N]} + \rho_{He} (L - l_N) \sigma_{He[N]} \quad (315)$$

In the same way, the ^{12}C count rate can also be written in terms of radiated cross sections (derived by using the carbon data):

$$n_C = \rho_{Al} l_{Al} \sigma_{Al[C]} + \rho_K l_K \sigma_{C[C]} + \rho_C l_C \sigma_{C[C]} + \rho_{He} (L - l_C) \sigma_{He[C]}. \quad (316)$$

The model for the count rate ratio of the nitrogen and carbon is written as:

$$r_{NC}^{model} = \frac{n_N}{n_C} \quad (317)$$

and this count rate ratio (abbreviated as model) is fit to the real data count rate ratio (abbreviated as data) to minimize the χ^2 of the fit:

$$\chi^2 = \sum_{W, Q^2} (r_{NC}^{data} - r_{NC}^{model})^2 / \sigma_{r_{NC}}^2, \quad (318)$$

where $\sigma_{r_{NC}}$ is given by

$$\sigma_{r_{NC}} = \sqrt{\left(\frac{\partial r_{NC}}{\partial n_N}\right)^2 n_N + \left(\frac{\partial r_{NC}}{\partial n_C}\right)^2 n_C} \quad (319)$$

which yields

$$\frac{\sigma_{r_{NC}}}{r_{NC}} = \sqrt{n_N^{-1} + n_C^{-1}}. \quad (320)$$

This fit uses an iterative method to determine the total target length L for these run sets, which used a different target insert. After getting the fit results from 2.286 GeV data, the model is extrapolated to other kinematic regions by using the available data from other beam energies. Some additional corrections are also needed to account for the beam charge normalization of the count rates because of the discrepancy between the true beam charge and the measured beam charge due to the spread of the beam aperture, through multiple scattering, that exceeded the faraday cup radius. In addition, the model for the 4.2 GeV data needed an additional scaling. More information about these additional corrections for this analysis, as well as the description of the systematic errors applied, can be found in [95]. Fig. 80 shows the count rate ratios $^{15}\text{N}/^{12}\text{C}$ and the resulting fit for the 2.286 GeV data set. The model represents the data very well in most kinematic regions.

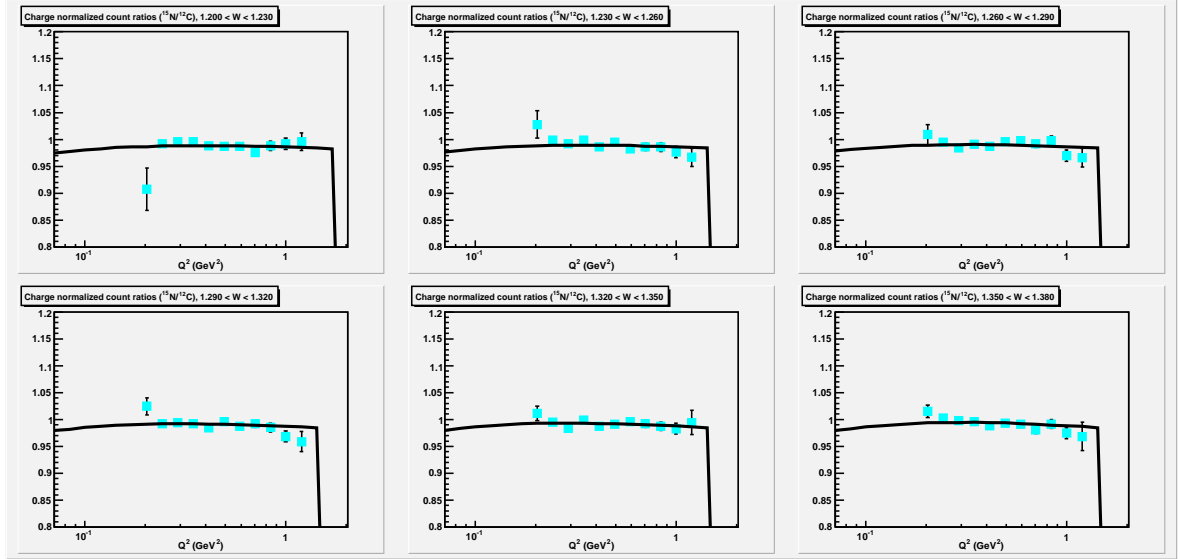
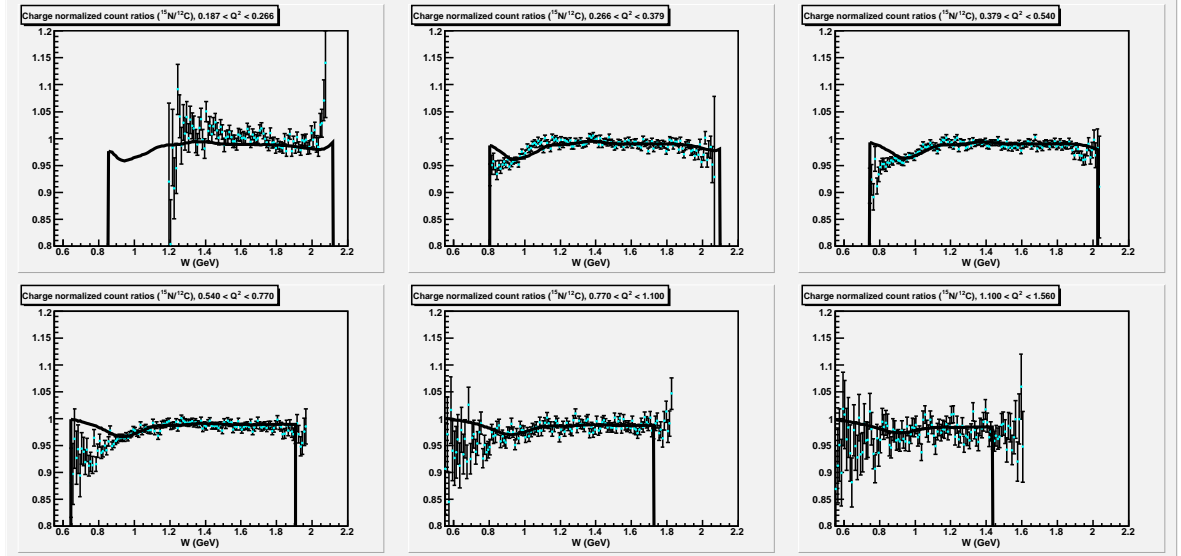
(a) $^{15}\text{N}/^{12}\text{C}$ count rate ratios vs. Q^2 for various W bins.(b) $^{15}\text{N}/^{12}\text{C}$ count rate ratios vs. W for various Q^2 bins.

FIG. 80: $^{15}\text{N}/^{12}\text{C}$ count rate ratios for the 2.3 GeV data set are shown together with the final model for different kinematic regions. Plots are courtesy of R. Fersch.

The second method of determining the target length l_N utilizes the radiative cross section model. Solving Eq. (317) for l_N yields:

$$l_N(bin) = \frac{r_{NC}F_{[C]} - F_{[N]} + r_{NC}\rho_C l_C \sigma_{C[C]} - \rho_{He} L \sigma_{He[N]} + r_{NC}\rho_{He}(L - l_C)\sigma_{He[C]}}{\rho_N \sigma_{N[N]} - \rho_{He} \sigma_{He[N]}}, \quad (321)$$

where the foil contribution from Al and Kapton are combined under the term $F = \rho_{Al} l_{Al} \sigma_{Al} + \rho_K l_K \sigma_C$. This is a direct calculation of l_N for each kinematic bin by using only the cross section model derived for each bin of the experiment. The error on the $l_N(bin)$ can also be estimated (assuming the foil contributions are small ($F \rightarrow 0$) and $\sigma_{He[N]} \approx \sigma_{He[C]}$) by its variation with respect to the ratio r_{NC} :

$$\sigma_{l_N(bin)} = \frac{\partial l_N(bin)}{\partial r_{NC}} \sigma_{r_{NC}} = \frac{\rho_C l_C \sigma_{C[C]} + \rho_{He}(L - l_C)\sigma_{He[C]}}{\rho_N \sigma_{N[N]} - \rho_{He} \sigma_{He[N]}} \sigma_{r_{NC}} \quad (322)$$

with $\sigma_{r_{NC}}$ given in Eq. (319). The error weighted average of the target length is calculated by summing over all Q^2 and W bins:

$$l_N = \frac{\sum_{Q^2} \sum_W l_N(bin) / \sigma_{l_N(bin)}^2}{\sum_{Q^2} \sum_W 1 / \sigma_{l_N(bin)}^2} \quad (323)$$

$$\sigma_{l_N} = \frac{1}{\sqrt{\sum_{Q^2} \sum_W 1 / \sigma_{l_N(bin)}^2}} \quad (324)$$

While taking the average over Q^2 and W bins, the same cuts, applied for the calculation of total target length L , are also used here. Fig. 81 shows the model calculated l_N with respect to W , averaged over Q^2 bins, for one data set. Unpredictable behavior is observed in the quasi elastic region and below, where the models are extrapolated. However, l_N is quite constant in the inelastic region. Therefore, specifically the inelastic region ($W > 1.10$) is used for the calculation of the average value. For more details on the Q^2 and W cuts applied, you can look at [95]. Results from this method (method 2) are compared with the results of method 1 in Table 32. The method 2 results were used for the final analysis.

IV.11.3 Calculation of Ammonia Target Length l_A

One more ingredient to the F_D calculation is the effective ammonia target length. The EG1b experiment used $^{15}\text{ND}_3$ and $^{15}\text{NH}_3$ target beads immersed in liquid Helium. There are gaps in between these target granules, reducing the effective length

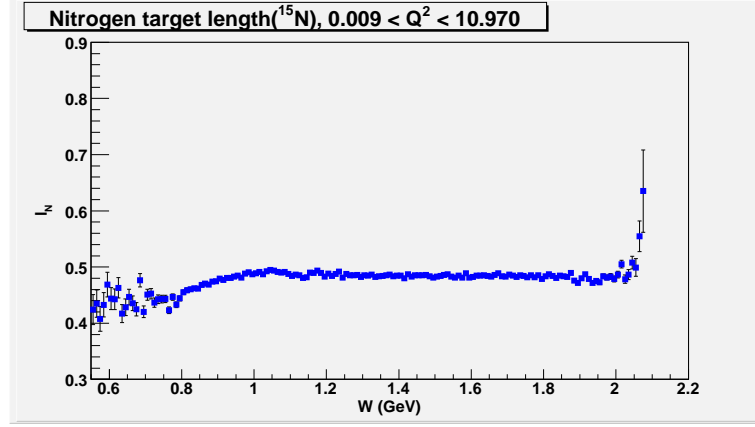


FIG. 81: The ^{15}N target length l_N , calculated from the radiated cross section model is shown for different W bins. The value in each W bin is averaged over Q^2 bins. For the final value, lower ($W > 1.10$) and upper [95] W cuts are applied as in the case of the L calculation. The plot is for the 2.286 GeV data set.

TABLE 32: Values of the ^{15}N target length l_N for different data sets from two methods. There are 7 data sets with nitrogen data. More explanations on the methods are in the text.

| Data set | $l_N(\text{cm})$ -Method 1 | $l_N(\text{cm})$ -Method 2 |
|----------|----------------------------|----------------------------|
| 1.723 + | 0.44 ± 0.00039 | 0.45 ± 0.00057 |
| 1.723 - | 0.45 ± 0.00033 | 0.45 ± 0.00056 |
| 2.286 + | 0.45 ± 0.00015 | 0.46 ± 0.00023 |
| 4.238 + | 0.47 ± 0.00086 | 0.48 ± 0.00103 |
| 4.238 - | 0.47 ± 0.00008 | 0.47 ± 0.00022 |
| 5.615 + | 0.43 ± 0.00066 | 0.44 ± 0.00119 |
| 5.615 - | 0.45 ± 0.00028 | 0.46 ± 0.00043 |
| average | 0.46 ± 0.00007 | 0.46 ± 0.00014 |

of the target. The design length of the ammonia target cell is about 1 cm. The fraction of this length that contains only the target material (ammonia) is called the packing fraction and is approximately 60%, which gives an effective length of 0.6 cm. Accurate calculation of F_D requires a precise value for the packing fraction. The packing fraction can vary according to the beam configuration as well as the geometric location within the target cell. An overall effective value of the packing fraction will be determined for each beam configuration. In this section, we will introduce two methods, the same ones used for the other quantities, for the calculation of the packing fraction.

Calculation of l_A from data

Following the same prescription developed for the nitrogen target length calculation, we begin by parameterizing the ammonia cross section in terms of the carbon cross section by using the number of protons and neutrons in each material. The same procedure is used for both $^{15}\text{ND}_3$ and $^{15}\text{NH}_3$ targets, but in this analysis, we will go over the $^{15}\text{ND}_3$ calculations, so, the abbreviation A will refer to $^{15}\text{ND}_3$.

$$\sigma_C \approx 6\sigma_D \quad (325)$$

$$\sigma_N \approx 7\sigma_D + 1\sigma_n \quad (326)$$

$$\sigma_A \approx \sigma_N + 3\sigma_D \quad (327)$$

It should be pointed out that the above equations are only approximate for large W . Also, the EMC effect is neglected with these approximation, which is one of the basic disadvantages of this method. By using the previous parametrization for the nitrogen cross section given in Eq. (302), we can parametrize the ammonia cross section in terms of carbon:

$$\sigma_A = \left(a + b \frac{\sigma_n}{\sigma_D} + 3 \frac{\sigma_D}{\sigma_C} \right) \sigma_C \quad (328)$$

Also using the initial assumption given in Eq. (325) that $\sigma_C = 6\sigma_D$, we have:

$$\sigma_A = \left(a + b \frac{\sigma_n}{\sigma_D} + 0.5 \right) \sigma_C \quad (329)$$

For the neutron to deuteron cross section ratio σ_n/σ_D , the parametrization by S. Kuhn [113] is used, which is given as a function of beam energy, Q^2 and W . Now

we can express the ammonia target count in terms of the contributions from the foil material, the liquid Helium and the ammonia itself:

$$n_A = f\rho_C l_C \sigma_C + \rho_{He}(L - l_A)\sigma_{He} + \rho_A l_A \sigma_A, \quad (330)$$

using the same expressions for the carbon and helium counts as given in Eqs. (305) and (306) as well as the definitions given in Table 26:

$$n_A = fn'_C + (L - l_A)n'_{He} + n'_A, \quad (331)$$

where

$$n'_A = \rho_A l_A \sigma_A \quad (332)$$

is normalized counts scattered only from ammonia. Inserting the ammonia cross section parametrization into Eq. (329):

$$n_A = fn'_C + (L - l_A)n'_{He} + \frac{\rho_A l_A}{\rho_C l_C} \left(a + b \frac{\sigma_n}{\sigma_D} + 0.5 \right) n'_C \quad (333)$$

and using Eq. (304) for the measured empty target count, we obtain the final parametrized form of the ammonia target count as:

$$n_A = n_E - l_A n'_{He} + \frac{\rho_A l_A}{\rho_C l_C} \left(a + b \frac{\sigma_n}{\sigma_D} + 0.5 \right) n'_C. \quad (334)$$

From Eq. (334), the ammonia target length $l_A(bin)$ can be expressed for each kinematic bin as:

$$l_A(bin) = (n_A - n_E) / \left(\frac{\rho_A}{\rho_C l_C} \left[a + b \frac{\sigma_n}{\sigma_D} + 0.5 \right] n'_C - n'_{He} \right). \quad (335)$$

Figs. 82 and 83 show the final distribution of the effective ammonia target length (in cm) over different kinematic bins. The latter figure shows the results for individual helicity states separately in different colors for various Q^2 bins. The error on this quantity can be estimated by taking its variation with respect to each measured count rate.

$$\sigma_{l_A(bin)} = \sqrt{\left(\frac{\partial l_A}{\partial n_A} \right)^2 n_A + \left(\frac{\partial l_A}{\partial n_C} \right)^2 n_C + \left(\frac{\partial l_A}{\partial n_E} \right)^2 n_E} \quad (336)$$

Partial derivatives are calculated with the help of Eqs. (305) and (306) that relate the expected carbon and helium count rates to the measured carbon and empty target count rates. We define the quantities:

$$P = a + b \frac{\sigma_n}{\sigma_D} + 0.5 \quad (337)$$

$$R = \frac{\rho_A}{\rho_C l_C} R n'_C - n'_{He} \quad (338)$$

Therefore:

$$\frac{\partial l_A}{\partial n_A} = 1/R \quad (339)$$

$$\frac{\partial l_C}{\partial n_C} = - \frac{(n_A - n_E) \left(P \frac{L}{L+fl_C} - \frac{f}{L+fl_C} \right)}{R^2} \quad (340)$$

$$\frac{\partial l_E}{\partial n_E} = - \frac{(R + (n_A - n_E) \left(\frac{\sigma_A}{\sigma_C} \frac{L-l_C}{L+fl_C} + \frac{1+f}{L+fl_C} \right))}{R^2} \quad (341)$$

While determining the final l_A for each data set, the error weighted average of $l_A(bin)$ is taken and the same Q^2 and W cuts are used as before, i.e., $W > 1.4$ GeV (to exclude the $\Delta(1232)$ resonance) up to a maximum value that differs for each Q^2 bin. These upper W cuts can be found in [95]. The high W regions are avoided because systematic errors (i.e. pion contamination, radiative corrections) dominate. The average l_A for each data set and the errors are calculated as:

$$l_A = \frac{\sum_{Q^2} \sum_W l_A(bin) / \sigma_{l_A}^2(bin)}{\sum_{Q^2} \sum_W 1 / \sigma_{l_A}^2(bin)} \quad (342)$$

$$\sigma_{l_A} = \frac{1}{\sqrt{\sum_{Q^2} \sum_W 1 / \sigma_{l_A}^2(bin)}} \quad (343)$$

Table 33 shows the final values of the ammonia target length calculated with this method (method 1).

Calculation of l_A from radiated cross-section models

Calculating the packing fraction from the parametrization as described above has certain drawbacks. In this method, the main assumption is that the cross sections for different target materials can be expressed in terms of the composite number of protons and neutrons in the material. This assumption obviously neglects the EMC effect. Therefore, the parametrization method requires W cuts in order to exclude regions where the EMC effect can have a big impact as well as to exclude regions where systematic errors can dominate the result. This issue becomes important especially for the data sets taken with low beam energies since it leaves a narrow W region to average over. These issues required the development of the second method, in which the radiated cross section model can be used safely in all W regions. In this section, we will present the results of the calculation of l_A from the cross section

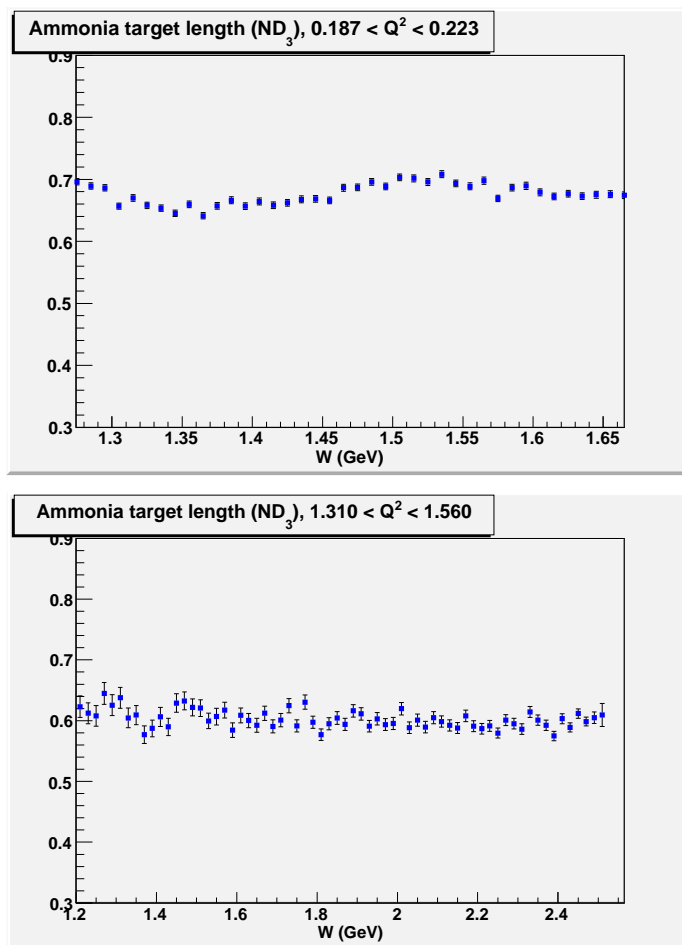


FIG. 82: ND₃ effective target length in cm (calculated from method 1) as a function of W for the 1.6 GeV inbending (top) and 4.2 GeV inbending (bottom) data sets are shown.

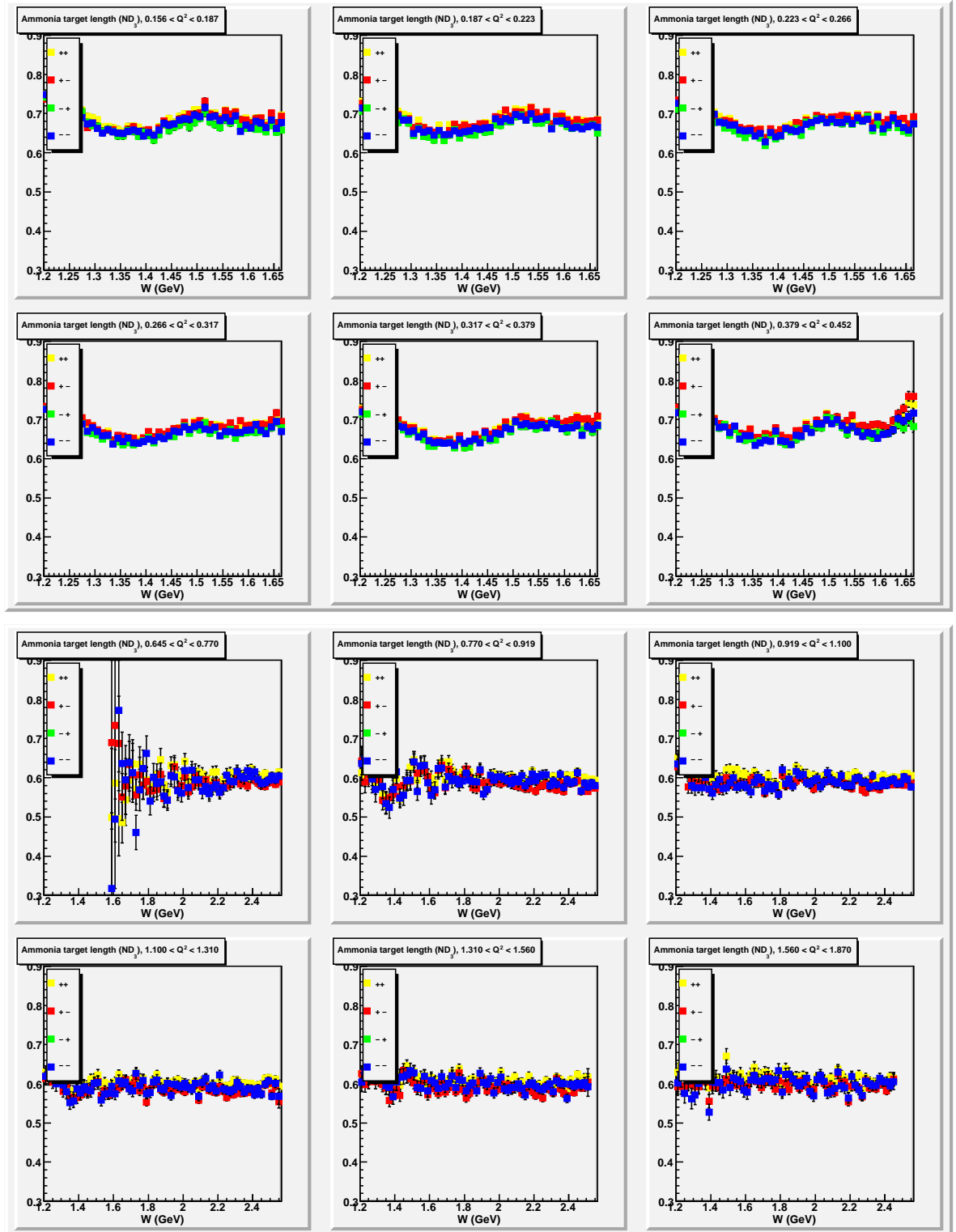


FIG. 83: ND₃ effective target length (in cm) as a function of W for the 1.6 GeV (top) and 4.2 GeV (bottom) inbending data sets. Different colors represent different helicity configurations. The calculations were made by using method 1.

model. The same prescription, already described above for the calculation of the nitrogen target length, can also be applied to this case. First we write

$$n_A = \rho_{Al} l_{Al} \sigma_{Al[A]} + \rho_K l_K \sigma_{C[A]} + \rho_N l_N \sigma_{A[A]} + \rho_{He} (L - l_A) \sigma_{He[A]}. \quad (344)$$

In the same way, the ^{12}C count rate can also be written in terms of radiated cross sections (derived by using the carbon data) as:

$$n_C = \rho_{Al} l_{Al} \sigma_{Al[C]} + \rho_K l_K \sigma_{C[C]} + \rho_C l_C \sigma_{C[C]} + \rho_{He} (L - l_C) \sigma_{He[C]} \quad (345)$$

The model for the count rate ratio of the nitrogen and carbon is written as:

$$r_{AC}^{model} = \frac{n_A}{n_C} \quad (346)$$

Solving for l_A and describing the foil terms by $F = \rho_{Al} l_{Al} \sigma_{Al} + \rho_K l_K \sigma_C$ yields:

$$l_A(bin) = \frac{r_{AC} F_{[C]} - F_{[A]} + r_{AC} \rho_C l_C \sigma_{C[C]} - \rho_{He} L \sigma_{He[A]} + r_{AC} \rho_{He} (L - l_C) \sigma_{He[C]}}{\rho_A \sigma_{A[A]} - \rho_{He} \sigma_{He[A]}} \quad (347)$$

where the square brackets are inserted after the cross section terms to indicate which targets are used to generate the radiated cross section model. At this point, we can describe the ammonia cross section in terms of individual parts as:

$$\sigma_A = \frac{15}{21} \sigma_N + \frac{6}{21} \sigma_D \quad (348)$$

where the constant multiplication factors $15/21$ and $6/21$ are the ratios of the atomic masses of ^{15}N and D_3 to that of $^{15}\text{ND}_3$, respectively. They account for the molar masses of the constituents in the ammonia target. This weighting is necessary because the unit of the mass thickness in the radiated cross section model is g/cm^2 , not moles/cm^2 . Therefore, we can rewrite Eq. (347):

$$l_A(bin) = \frac{r_{AC} F_{[C]} - F_{[A]} + r_{AC} \rho_C l_C \sigma_{C[C]} - \rho_{He} L \sigma_{He[A]} + r_{AC} \rho_{He} (L - l_C) \sigma_{He[C]}}{\rho_A \left(\frac{15}{21} \sigma_{N[A]} + \frac{6}{21} \sigma_{D[A]} \right) - \rho_{He} \sigma_{He[A]}}. \quad (349)$$

The error on the target length is:

$$\sigma_{l_A(bin)} = \frac{\partial l_A(bin)}{\partial r_{AC}} \sigma_{r_{AC}} = \frac{\rho_C l_C \sigma_{C[C]} + \rho_{He} (L - l_C) \sigma_{He[C]}}{\rho_A \left(\frac{15}{21} \sigma_{N[A]} + \frac{6}{21} \sigma_{D[A]} \right) - \rho_{He} \sigma_{He[A]}} \sqrt{n_C^{-1} + n_A^{-1} r_{AC}}. \quad (350)$$

The average value for l_A is calculated the same way as described in the case of method 1. However, since the radiated cross section model was used for this method, which accounts internally for the EMC effect, the lower W cut is safely reduced to $W = 1.10$ GeV. The final results for l_A from this method are shown in Fig. 84. In addition, the final values of l_A from both methods are shown in Table 33 for each data set.

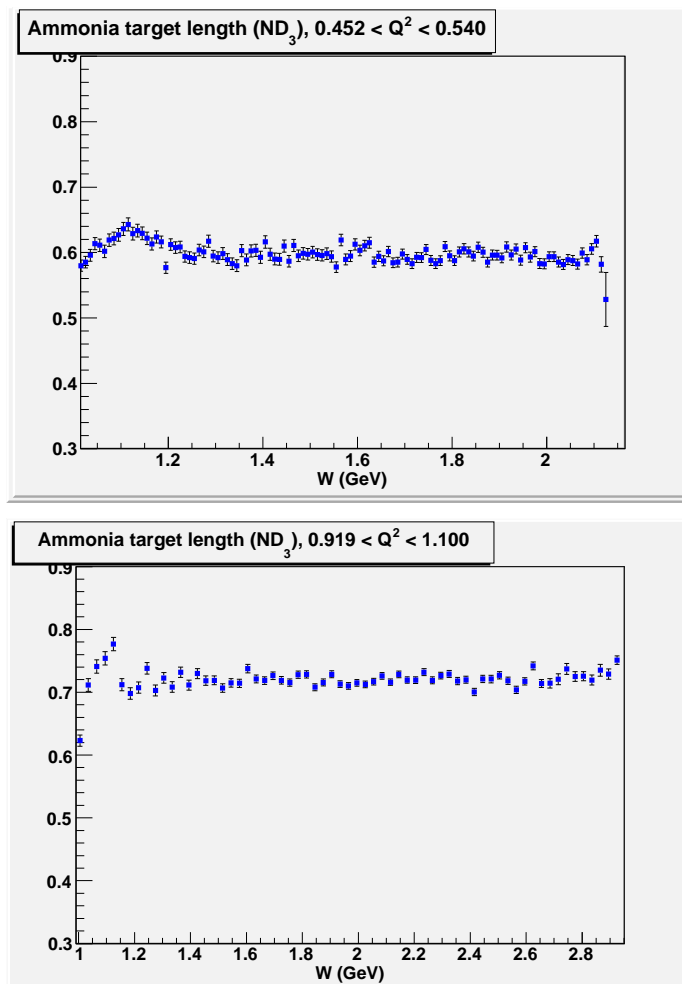


FIG. 84: ND₃ target length shown as a function of W for the 2.5 GeV inbending and the 5.8 GeV outbending data sets. These values are calculated using the radiated cross section model. Plot is courtesy of R. Fersch.

TABLE 33: Values of the effective ammonia target length (l_A), using the two different methods described in the text. The error bars reflect only the error on the statistical fit, not the true uncertainty on the value.

| Beam E | Torus | $l_A(\text{cm})$ -Method 1 | $l_A(\text{cm})$ -Method 2) |
|--------|-------|----------------------------|-----------------------------|
| 1.606 | + | 0.6611 ± 0.0005 | 0.6865 ± 0.0002 |
| 1.606 | - | 0.6394 ± 0.0022 | 0.6755 ± 0.0005 |
| 1.723 | - | 0.5926 ± 0.0008 | 0.6262 ± 0.0002 |
| 2.561 | + | 0.5887 ± 0.0009 | 0.5974 ± 0.0004 |
| 2.561 | - | 0.6179 ± 0.0003 | 0.6314 ± 0.0002 |
| 4.238 | + | 0.5977 ± 0.0009 | 0.5978 ± 0.0004 |
| 4.238 | - | 0.6084 ± 0.0003 | 0.6130 ± 0.0001 |
| 5.615 | + | 0.6045 ± 0.0011 | 0.6049 ± 0.0005 |
| 5.725 | + | 0.5947 ± 0.0013 | 0.5897 ± 0.0006 |
| 5.725 | - | 0.5719 ± 0.0005 | 0.5703 ± 0.0003 |
| 5.743 | - | 0.7226 ± 0.0006 | 0.7232 ± 0.0003 |

IV.11.4 Dilution Factor Results

As we have all the ingredients now, we can resume our original Eqs. (279) and (282) for the dilution factor calculation with method 1 and method 2, respectively. Fig. 85 shows the dilution factor with respect to W for different Q^2 bins as calculated from the first method by parametrization of the data. The F_D peaks at the quasi-elastic region as expected because most of the elastic scatterings come from the free polarized deuterons (or protons in case of the $^{15}\text{NH}_3$) in this region, reducing the background contributions. The results from method 2 are also shown in Fig. 85 as blue lines together with the method 1 results, shown as red points. The errors on the dilution factors for each kinematic bin were determined systematically by varying the contributions from each ingredient one at a time, obtaining the final result of F_D and summing over all variations. More details on the systematic errors on the dilution factor are given in section IV.19.2. In addition, Ref. [95] gives a full description of the method by which the systematic errors were calculated. None of the statistical errors in method 1 were used anywhere except for determining the error weighted F_D over all kinematic bins for each data set.

Comparison of the results from the two different approaches confirms the validity of our analysis method. While both methods have their advantages and drawbacks,

calculating F_D from the radiated cross section model has a certain advantage over the parametrization method. It creates a continuous function as well as an opportunity for extrapolation into kinematic bins where the data are not enough for a good parametrization. Moreover, the parametrization method creates statistical fluctuations in the final results, while the model method avoids these fluctuations creating much smoother F_D over different kinematic bins. For these reasons, the results from the method 2 were used for the final analysis of A_1 measurement. On the other hand, the drawback of the cross section model method comes in the elastic region, where it overestimates the dilution factor. Fig. 85 shows the inadequacy of this method at the elastic peak.

The only place where F_D for the quasi-elastic region was used was for the extraction of target times beam polarization (PbPt) from the elastic scattering data. Since the parametrization results in this kinematic range are quite precise, those results were used for the PbPt calculations. Moreover, as it is explained in section IV.13, PbPt was calculated by various methods. The PbPt results for which the dilution factors were used agrees statistically well with the results obtained from the other methods for most data sets (see section IV.13). In addition, the PbPt values obtained by using the dilution factors were only used for the 1.6 and 1.7 GeV outbending data sets. The F_D results for the elastic region were not used anywhere else throughout this analysis.

After full consideration of all advantages and drawbacks of both methods in calculating F_D , it was decided that the parametrization method will be used in the $W < 1.08$ GeV region while the radiated cross section method will be used for the $W \geq 1.08$ GeV. When an integration of F_D results over kinematic bins was needed, the two methods were averaged separately and kept separate across the W boundary.

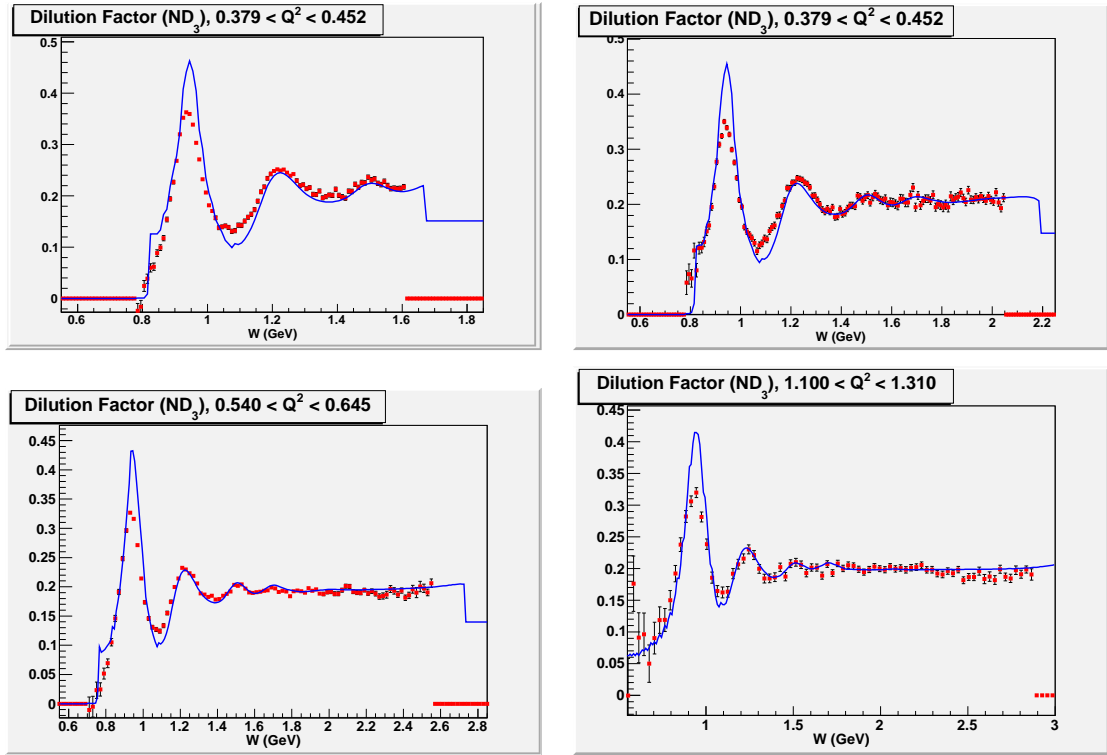


FIG. 85: Dilution factors as a function of W , shown at four different beam energies (1.6+ (top left), 2.5– (top right), 4.2– (bottom left) and 5.7– (bottom right)). The results from method 1 are shown as the red data points while the method 2 results are overlaid as blue lines.

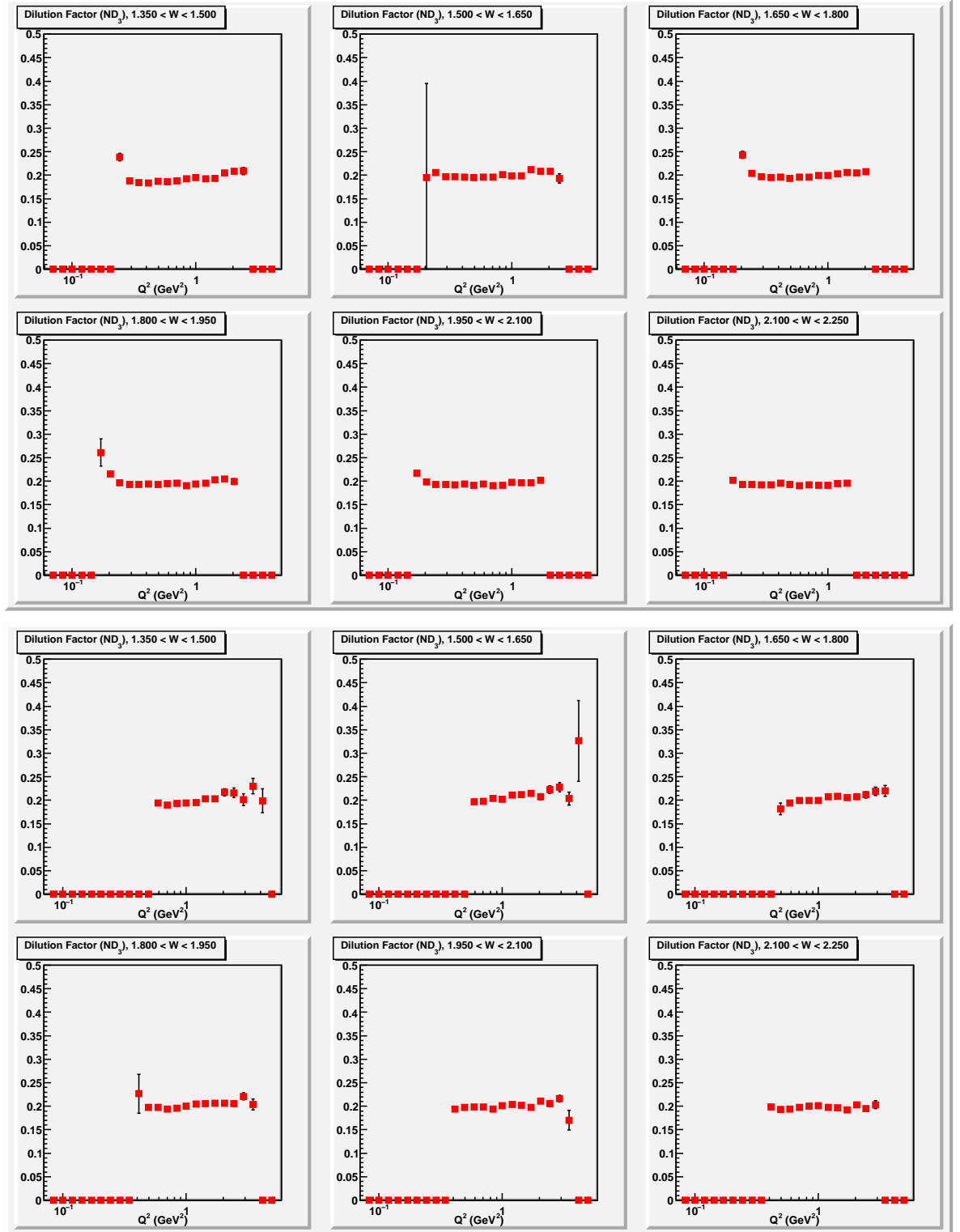


FIG. 86: Dilution factors as a function of Q^2 , shown for several W bins, for the 4.2– (top) and 5.7– (bottom) data sets. There is a slight Q^2 dependence of the dilution factor for some W regions.

IV.12 BACKGROUND ANALYSIS

Electron rates measured in the EG1b experiment are contaminated by misidentified pions and pair symmetric electrons. This contamination affects the measured asymmetry, and therefore an extra correction should be applied to account for this effect. The correction to the asymmetry comes from the fact that the count rates used to calculate the asymmetry are changed by the amount of misidentified particles. Therefore, when we calculate the raw asymmetry in terms of the electron count rates for positive (N^+) and negative (N^-) helicities,

$$A_{raw} = \frac{N^- - N^+}{N^- + N^+}, \quad (351)$$

the count rates should be corrected by the amount of corresponding contaminations N_c^+ and N_c^- for both helicities:

$$A_{corr} = \frac{(N^- - N_c^-) - (N^+ - N_c^+)}{(N^- - N_c^-) + (N^+ - N_c^+)} \quad (352)$$

where $(N^- - N_c^-)$ and $(N^+ - N_c^+)$ are the uncontaminated count rates for the two helicity states. Let's assign for total counts $N \equiv N^+ + N^-$ and $N_c \equiv N_c^+ + N_c^-$, and re-arrange the terms to isolate the contamination:

$$A_{corr} = \frac{(N^- - N^+) - (N_c^- - N_c^+)}{(N - N_c)}. \quad (353)$$

By dividing the numerator and the denominator by N , we can write

$$A_{corr} = \frac{\frac{N^- - N^+}{N} - \frac{N_c^- - N_c^+}{N}}{1 - N_c/N}. \quad (354)$$

With the ratio of the contaminant to the contaminated count $R \equiv N_c/N$, the above expression can be written as:

$$A_{corr} = \frac{A_{raw} - \frac{N_c^- - N_c^+}{N_c/R}}{1 - R}. \quad (355)$$

Defining $A_c \equiv (N_c^- - N_c^+)/N_c$, which is the raw asymmetry of the contaminant, yields

$$A_{corr} = \frac{A_{raw} - RA_c}{1 - R} \quad (356)$$

or we can write:

$$A_{corr} = C_{back} A_{raw} \quad (357)$$

where

$$C_{back} = \frac{1 - RA_c/A_{raw}}{1 - R}. \quad (358)$$

Therefore, in order to correct the raw asymmetry, we need to know the ratio R and also the asymmetry of the contaminating particle in the corresponding kinematics. In a more generalized form, the background correction to the asymmetry can be written as:

$$A_{corr} = A_{raw} \frac{1 - \sum_i R_i \frac{A_i}{A_{raw}}}{1 - \sum_i R_i} \quad (359)$$

where R_i are the fractions of events coming from a given background and A_i are the asymmetries of the contributing background processes.

There are mainly two distinct sources of such background in the EG1b analysis. The first one is pions misidentified as electrons and the second one is secondary electrons that mostly come from the pair production process. In the following subsections, we investigate these backgrounds separately and come up with a method of correction.

IV.12.1 Pion Contamination

In the EG1b experiment the main tool to separate pions from electrons is the Cherenkov counter (CC). The CC can separate pions from electrons up to 2.5 GeV. A pion in this energy range can have a CC signal around 0-1 photoelectrons. When we examine the signal from the CC, we see a huge pion peak around 1 photoelectrons. The tail of this peak contaminates the electron sample up to the 4 or 5 photoelectron range. Above 2.5 GeV, on the other hand, pions also begin to produce a Cherenkov signal in the detector material. It is not possible to separate these high energy pions from electrons at all using the CC alone. Therefore, we need to correct the resulting asymmetry for contamination. To remove pions up to 2.5 GeV from the electron sample, we apply a CC signal cut to the electrons. We need to optimize the place of this cut to remove most of the pions and not to reduce the electron statistics too much at the same time. If we increase the strictness of the Cherenkov cut too much to remove more pions, we lose too many electrons, hence causing a larger statistical uncertainty in our results. Therefore, we need to apply an optimum cut to remove the pion peak from our electron sample and deal with the rest of the pions by other methods.

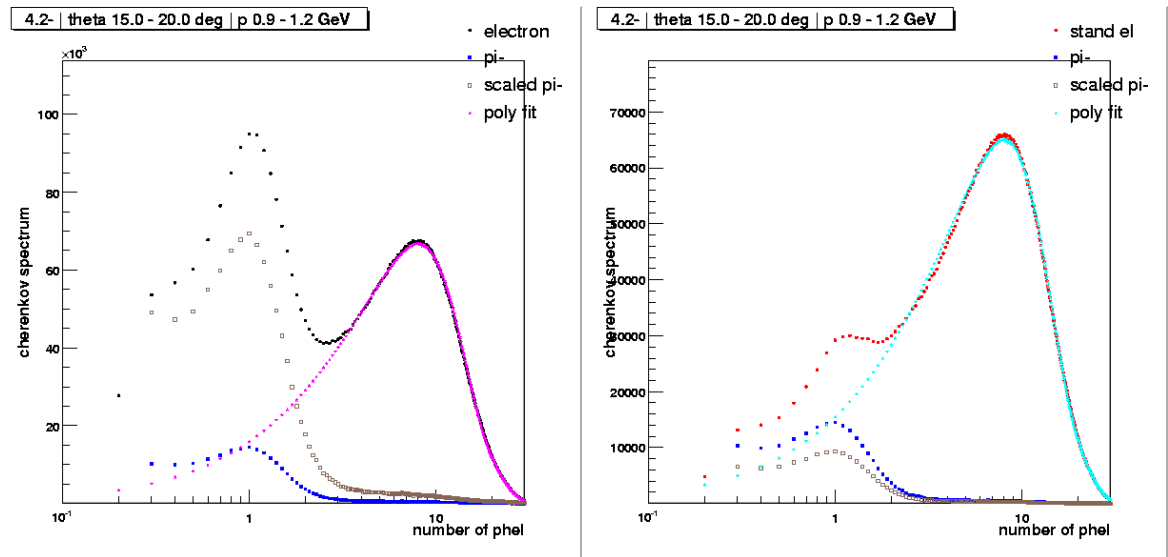


FIG. 87: Cherenkov spectrum for electrons and pions before (left) and after (right) the CC geometric and timing cuts. On the left plot, the electron signal before the cuts is shown in black dots together with the fit above 2 photoelectrons shown in magenta dots. On the right plot, the electron signal after the cuts is shown in red and the fit is shown in cyan. The fit to the electron signal represents our best estimate for the true electron signal in the CC. In both plots, the pion signal is shown in blue dots while the pion signal scaled to the difference between the observed and true electron signals is shown in brown squares. The huge pion peak at 1 photoelectron can be seen as reduced to a small bump by the cuts. The x axis is logarithmic.

TABLE 34: Momentum bins (in GeV) used for the pion contamination analysis.

| bin | min | max |
|-----|------|------|
| 1 | 0.03 | 0.30 |
| 2 | 0.30 | 0.60 |
| 3 | 0.60 | 0.90 |
| 4 | 0.90 | 1.20 |
| 5 | 1.20 | 1.50 |
| 6 | 1.50 | 1.80 |
| 7 | 1.80 | 2.20 |
| 8 | 2.20 | 2.60 |
| 9 | 2.60 | 3.00 |
| 10 | 3.00 | 3.40 |
| 11 | 3.40 | 3.90 |
| 12 | 3.90 | 4.40 |
| 13 | 4.40 | 4.90 |
| 14 | 4.90 | 5.40 |

Applying geometrical and temporal cuts to remove pion contamination from the electron sample was a breakthrough in our pion contamination analysis (see Fig. 51). The huge pion peak shown in the left plot of Fig. 87 is reduced by these cuts as shown on the right. The remaining contamination was carefully analyzed to determine the pion to electron ratio in the CC region above the photoelectron cut and in the full CC region. The ratio above the 2 photoelectrons cut is called standard contamination and the ratio in the full CC region is called total contamination. The standard contamination is used for pions below 2.5 GeV. The total contamination is used to determine contamination above 3.0 GeV. A linear combination of standard and total contamination is used between 2.5 and 3.0 GeV.

The main idea behind the pion contamination analysis lies with the assumption that the pion to electron ratio must be a smooth function of momentum and polar angle. Once we determine the form of this function, we can determine the ratio for any given kinematics. By using carefully determined momentum and polar angle bins shown in Tables 34 and 35, we examined the data bin by bin to determine pion to electron ratios and extract the functional dependence of the ratio R_π on momentum and θ . The ratio for a specific momentum and polar angle bin is determined by scaling a pion sample with small photoelectron signal to the pion peak in the electron

TABLE 35: Polar angle bins (in degrees) used for the pion contamination analysis.

| bin | min | max |
|-----|------|------|
| 1 | 2.0 | 5.0 |
| 2 | 5.0 | 10.0 |
| 3 | 10.0 | 15.0 |
| 4 | 15.0 | 20.0 |
| 5 | 20.0 | 25.0 |
| 6 | 25.0 | 30.0 |
| 7 | 30.0 | 35.0 |
| 8 | 35.0 | 40.0 |
| 9 | 40.0 | 45.0 |
| 10 | 45.0 | 49.0 |

TABLE 36: Pion selection cuts for the pion contamination analysis. Δt in the table was determined by calculating the difference between the measured and expected time of flight. More detailed explanations on these cuts can be found in sections IV.7 and IV.10.7.

| |
|--|
| $0 \leq flag \leq 5$ or $10 \leq flag \leq 15$ |
| $-58.0 \leq z_{vertex} \leq -52.0$ |
| $p > 0.1E_B$ |
| $CC_{nphe} > 0.01$ |
| $EC_{in} < 0.06$ |
| $EC_{in}/p < 0.07$ |
| $EC_{in}/p < 0.07EC_{tot}/p$ |
| $EC_{tot}/p < 0.15$ |
| $ \Delta t < 0.6$ ns |

sample. Electromagnetic calorimeter signals and timing cuts are used to extract the best pion selection for our purpose. Table 36 summarizes all major detector cuts we applied to select pions. For the 1.6 GeV data we also applied an additional trigger bit cut because this data set required a more precise selection of pions to get a clean sample. Trigger bits 1 to 6 correspond to our standard triggers based on the CC and EC signals and they are used for electrons. Trigger bit 7 requires a hit in EC and CC anywhere, while trigger bit 8 requires a hit only in EC with a lower threshold (no CC hit). Trigger bit 8 is mainly used for minimally biased pion selection (see IV.7.2) but since it is pre-scaled it also reduces the sample size a great deal. For the 1.6 GeV set it was very difficult to get a clean sample by just applying the EC and timing cuts, so, we used trigger bits 7 and 8 to select pions in addition to the regular cuts described in Table 36.

It is probably best to explain our method of finding the pion to electron ratio by using Fig. 88. The plot shows the Cherenkov spectrum after all cuts for electrons (red) and pions (blue). The horizontal axis is a logarithmic scale and represents the number of photoelectrons produced by the particle in the Cherenkov counter. The cyan points represent a fit to the electron spectrum and approximates the true electron sample without pion contamination. It is a simple combination of 3^{rd} and 7^{th} degree polynomial fits in the region of the spectrum above the pion peak. The fit can be thought as a simulation of electrons with the same kinematics in the Cherenkov counter. The difference between the red and cyan distributions is assumed to all come from pions that are misidentified as electrons by the detector. We can call these pions extracted pions. The “true” pions from our pion sample (blue points), are scaled to the extracted pions. The resulting spectrum is shown with the brown points (hollow squares) and represents our best guess for the pion contamination. By summing all pions and electrons above our photoelectron threshold, which is 2 photoelectrons, we determined their ratio. This ratio is called the standard contamination. We also took the pion to electron ratio in the full spectrum, above and below our photoelectron threshold, which gave us the total contamination. This procedure was repeated for each momentum and polar angle bin where enough data for a clean fit and extraction were available.

When we examine the distribution of pion to electron ratio with respect to momentum for a single polar angle bin, we see an exponential dependence. Fig. 89

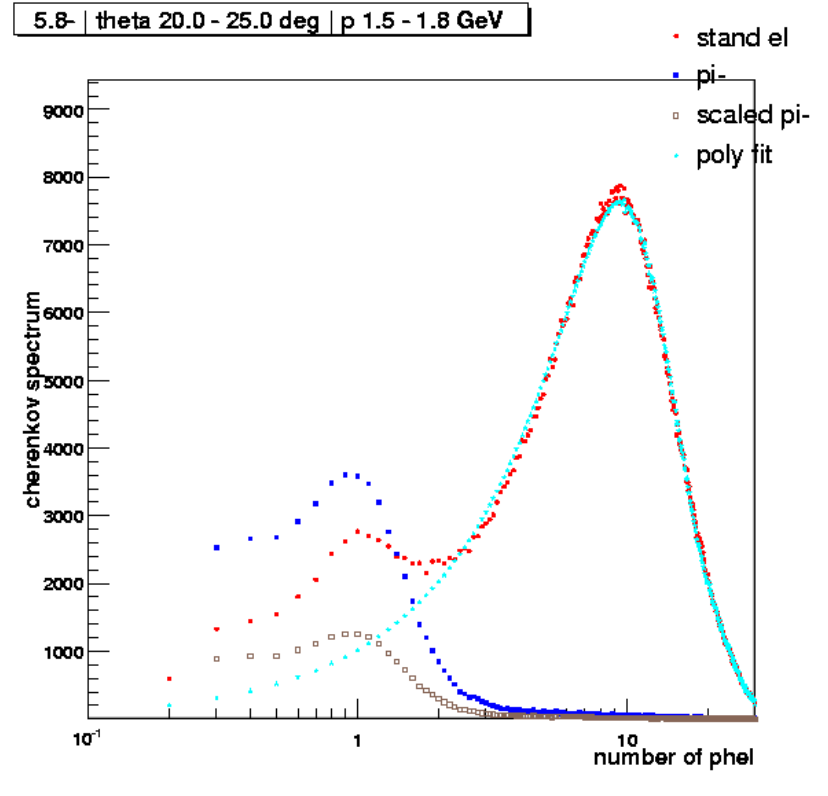


FIG. 88: Cherenkov spectrum for electrons and pions. The horizontal axis represents the number of photoelectrons produced by the particle in the Cherenkov counter. The red points represent electrons after all cuts except the Cherenkov cut. The blue points are pions. The cyan points represent a fit to the electron spectrum and are therefore the true electron sample without pion contamination. The difference between red and cyan signals are assumed to all come from misidentified pions. The true pion distribution in blue is scaled to the the distribution of the misidentified pions. The final distribution for the pions is shown by the hollow-brown squares.

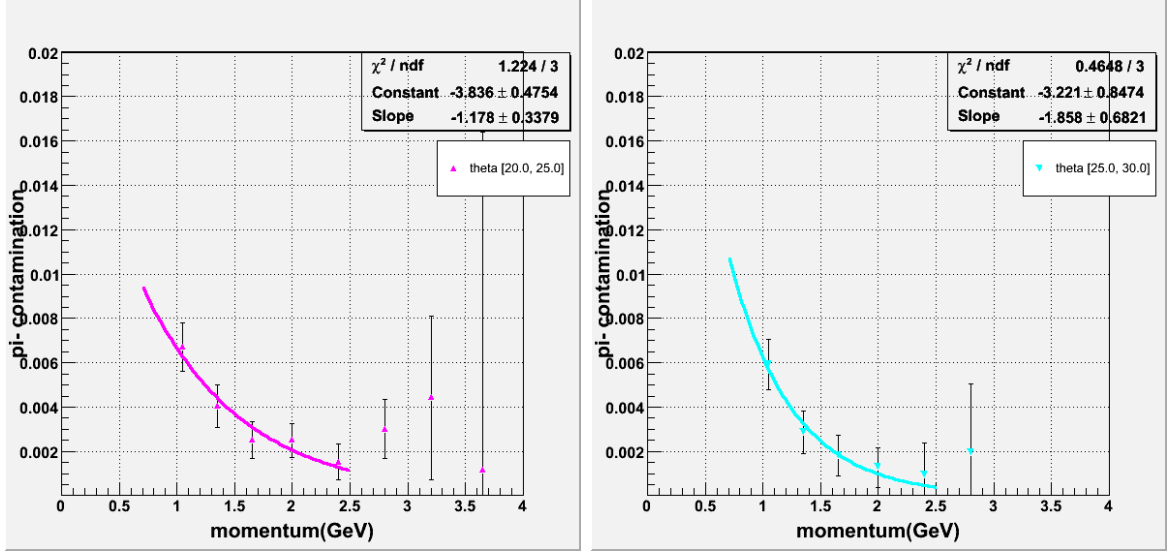


FIG. 89: Pion to electron ratio as a function of momentum for polar angle bins for 20-25 (left) and 25-30 (right) degrees.

shows the distribution of ratios for different momentum bins and the overall exponential fit to the points. The ratio follows a smooth function up to a momentum of 2.5 GeV, where the Cherenkov counter is no longer able to distinguish between electrons and pions. Below 2.5 GeV, we can write the pion to electron ratio as:

$$R_{\pi} = e^{C_{\pi} + S_{\pi}p} \quad (360)$$

where p is momentum of the particle (electron). In the above equation, C_{π} and S_{π} actually depend on θ . Therefore, we can write the equation in the form:

$$R_{\pi} = e^{C_{\pi}(\theta) + S_{\pi}(\theta)p} \quad (361)$$

We need to find the form of $C_{\pi}(\theta)$ and $S_{\pi}(\theta)$. When we examine the dependence of the parameters C_{π} and S_{π} on polar angle, we see, according to Fig. 90, that they are both linear functions of the polar angle. Therefore,

$$C_{\pi}(\theta) = a + b\theta \quad (362)$$

$$S_{\pi}(\theta) = c + d\theta \quad (363)$$

As a result, we can write the overall functional form of the pion to electron ratio in the following form:

$$R_{\pi} = e^{C_{\pi}(\theta) + S_{\pi}(\theta)p} = e^{a + b\theta + cp + d\theta p} \quad (364)$$

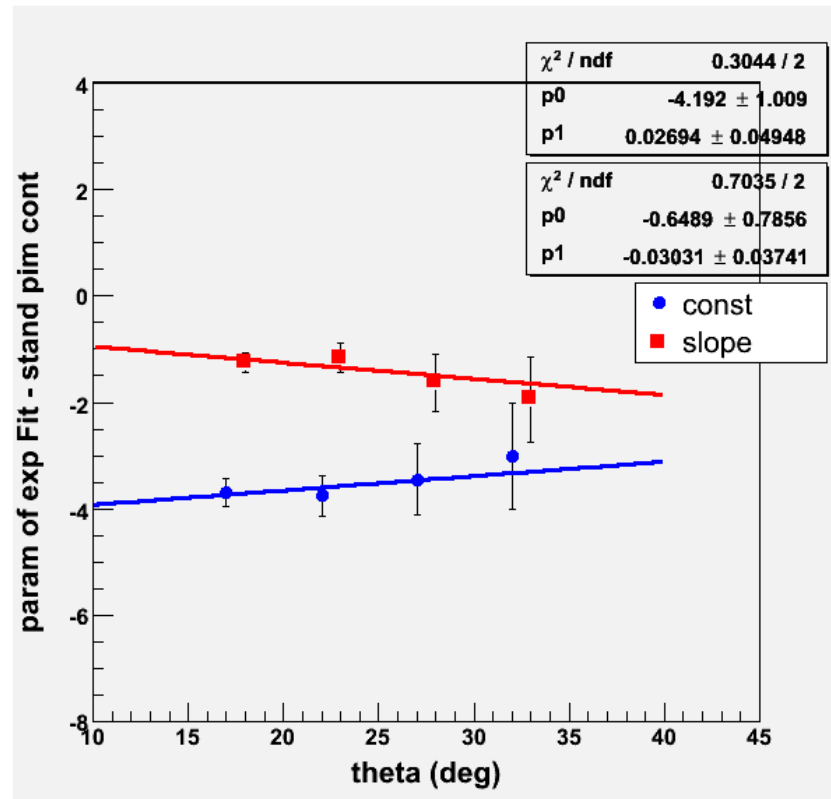


FIG. 90: Dependence of the exponential parameters on the polar angle. In the plot, the red data points represent $C_\pi(\theta)$ (the constant factor in the equation) and the blue points represent $S_\pi(\theta)$ (the slope factor of the equation). The resulting parameters from the fit to $C_\pi(\theta)$ give a and b (in the upper box), while the parameters from the fit to $S_\pi(\theta)$ give c and d (in the lower box) according to Eq. (364).

By using momentum and polar angle bins where data are available, we can determine all parameters a , b , c and d with good precision for each energy and torus current configuration. It should be noted that these parameters depend on the beam energy and the torus polarity, hence, a separate fit must be done for each data set. Once these parameters are determined, it is possible to calculate the ratio R_π for any momentum and polar angle value. Once we parametrized the ratio R_π , we can fix our raw asymmetry for pion contamination according to:

$$A_{el}^{corr} = A_{el} \frac{1 - R_\pi \frac{A_\pi}{A_{el}}}{1 - R_\pi} \quad \text{where} \quad R_\pi = \frac{\pi}{e} \quad (365)$$

However, since our pion contamination was reduced significantly after the geometric and timing cuts, mentioned in section IV.8, we decided to use the contamination itself as an estimate of the systematic error. Some final typical values for the ratio R_π can be seen in Fig. 89 for two different θ bins. In addition, more values of R_π for various data sets and kinematics are also shown at the right hand side of Fig. 51. The maximum value of the ratio is generally around 0.5% for low momentum range and it rapidly decreases with increasing momentum. Consequently, we do not need to determine the pion asymmetry at all. We can simply take it to be practically zero¹⁶ and correct the electron asymmetry according to

$$A_{el}^{corr} = \frac{A_{el}}{1 - R_\pi} \quad R_\pi = \frac{\pi}{e}. \quad (366)$$

The difference between the corrected asymmetry and the uncorrected asymmetry is then taken as a systematic error on the final asymmetry.

As we mentioned earlier, this whole procedure is valid for electrons up to 2.5 GeV. At higher energies, pions also begin to give a strong signal in the CC and those pions contaminate the electron sample in a different way. To determine the amount of contamination in the high energy region, we followed a similar approach but we used an electron sample which was not cleaned by the geometric and timing cuts. Moreover, we used the full CC spectrum to determine total pion contamination. Again this analysis was done as explained earlier for each momentum and polar angle bins and the functional form of the total pion contamination was determined. Of course, the functional form is the same as the standard contamination except that the parameters are different. Fig. 91 shows the standard and total contamination before the geometric and timing cuts were applied for a single θ bin. Extrapolation

¹⁶This corresponds to a limit $-1 \leq A_\pi/A_{el} \leq 1$.

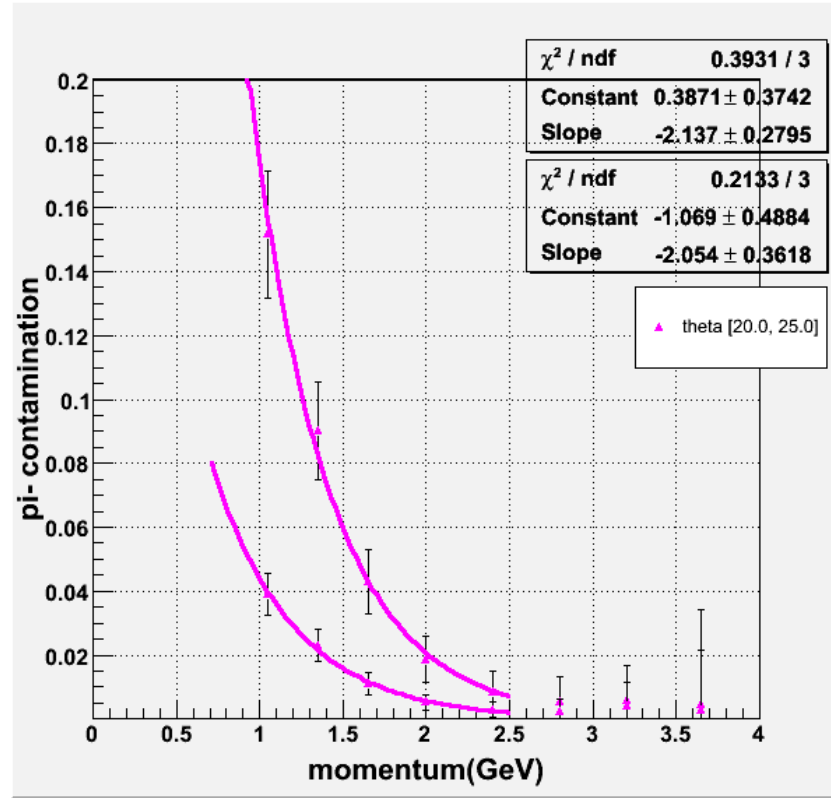


FIG. 91: Total and standard contaminations as a function of momentum for a single polar angle bin. This analysis was done by using an electron sample that was not cleaned by the geometric and timing cuts (see section IV.8). The total contamination on the full CC spectrum and the standard contamination above the photoelectron threshold are shown together. The total contamination is larger than the standard contamination.

of the total contamination was used to find the pion to electron ratio above 3.0 GeV. In between 2.5 and 3.0 GeV, a simple linear combination of standard contamination and total contamination was used.

IV.12.2 Pair Symmetric Electron Contamination

Another source of background contamination in the EG1b experiment is secondary electrons. The secondary electrons mainly come from electron-positron pair production inside the detector. There is no way to tell if the detected electron is a primary electron from the scattering off the target or a secondary electron from the pair production process. The system simply accepts the first electron as the trigger particle. The number of electrons that come from pair production is very small but we still

TABLE 37: Cuts on Positrons

| |
|--|
| $0 \leq flag \leq 5$ or $10 \leq flag \leq 15$ |
| $-58.0 \leq z_{vertex} \leq -52.0$ |
| triggerbit cut (see section IV.7.2) |
| $p > 0.15E_B$ |
| $CC_{nphe} > 0.01$ |
| $EC_{in} > 0.06$ |
| $EC_{tot}/p > 0.20$ for $p \leq 3.0$ |
| $EC_{tot}/p > 0.24$ for $p > 3.0$ |

need to correct the asymmetry for the contamination caused by these electron, which are referred to as the pair symmetric electrons.

Electron-positron pair production has two main sources inside the CLAS detector: The decay $\pi^0 \rightarrow e^+e^-\gamma$ (also known as the Dalitz decay) plays the leading role with a 1.2% branching ratio. The other possible source is $\pi^0 \rightarrow \gamma\gamma$ and $\gamma \rightarrow e^+e^-$. Other sources of e^+e^- pair creation such as Bremsstrahlung photons are all very small and hence negligible. More detailed information about pair production rates in the EG1b experiment can be found in CLAS note Ref. [115].

Since we cannot distinguish pair symmetric electrons from the original scattered electrons, the only way to estimate the contribution from electrons coming from pair creation is to monitor the corresponding positrons because every pair symmetric electron should be accompanied by a positron with the same kinematics. Normally, the positron to electron ratio would automatically give us the amount of pair symmetric contamination. However, there is a strong magnetic field inside the CLAS detector which bends the particle's trajectory according to its charge. This affects the acceptance of the detector depending on the charge of the particle. Therefore, the acceptance is not the same for electrons and positrons since they will be bent in opposite directions by the torus field. In order to get the same acceptance, we actually need to compare electrons to positrons from opposite torus polarity configurations.

In the EG1b experiment, we have DST files, where the electron is the trigger particle, and also DSTp files where no electron was found and therefore the trigger particle was a positron. The DSTp files are stored separately. There are a few positron counts in the DST files but most positrons are in the DSTp files. We

processed both file types to get the total count of positrons in each kinematic bin. The electron and positron cuts are the same except for the charge requirement. Table 37 lists the cuts applied to select positrons. In addition to those shown in the table, we also applied fiducial cuts as well as geometrical and timing cuts. We cleaned the positron and electron samples from pion contamination. We performed the π^+ contamination analysis on positrons exactly the same way we performed the π^- contamination analysis on the electrons.

Fig. 92 shows the CC spectra for positrons and π^+ for a single polar angle and momentum bin. The positron peak shown is already cleaned from most misidentified π^+ by applying the geometric and timing cuts. Still, a huge π^+ contamination distorts the shape of the positron spectrum. Our goal is to obtain the uncontaminated positron spectrum and find the difference between contaminated and uncontaminated spectra to determine the amount of π^+ in the positron rate. For this purpose, we used the fact that the positron and electron CC spectra should be exactly the same as long as we have the same acceptance. Therefore, we used a fit to the corresponding electron spectrum (with the reduced pion contamination, i.e., after geometric and timing cuts), with the same acceptance to estimate the true (uncontaminated) positron distribution. This was done by scaling the electron spectrum to the positron spectrum above 7 photoelectrons, and fitting the resulting electron spectrum, thus obtaining the estimated positron spectrum. The cyan colored fit in Fig. 92 shows our best estimate for the final true positrons in the CC. It should be noted that, while creating the true positron spectrum by using the electrons from the opposite torus current data, both of the samples should be normalized to the corresponding total beam charge before the scaling is done.

Afterward, the amount of π^+ contamination on positrons can be estimated by looking at the difference between the true and observed positron distributions (note that the observed positron distributions must have the geometric and timing cuts applied to them). Once the spectrum for this difference was generated, the true (or scaled) pion distribution, the brown-triangle data in Fig. 92, was obtained by scaling the observed pion distribution¹⁷ to this difference. Then we summed the number of pions in the true (scaled) pion distribution to determine the integrated pion rate. Similar summation was also made for the positrons by using the the observed positron distribution, in the same range of number of photoelectrons in the CC. The

¹⁷The observed π^+ peak is much too big to fit on the scale of that plot.

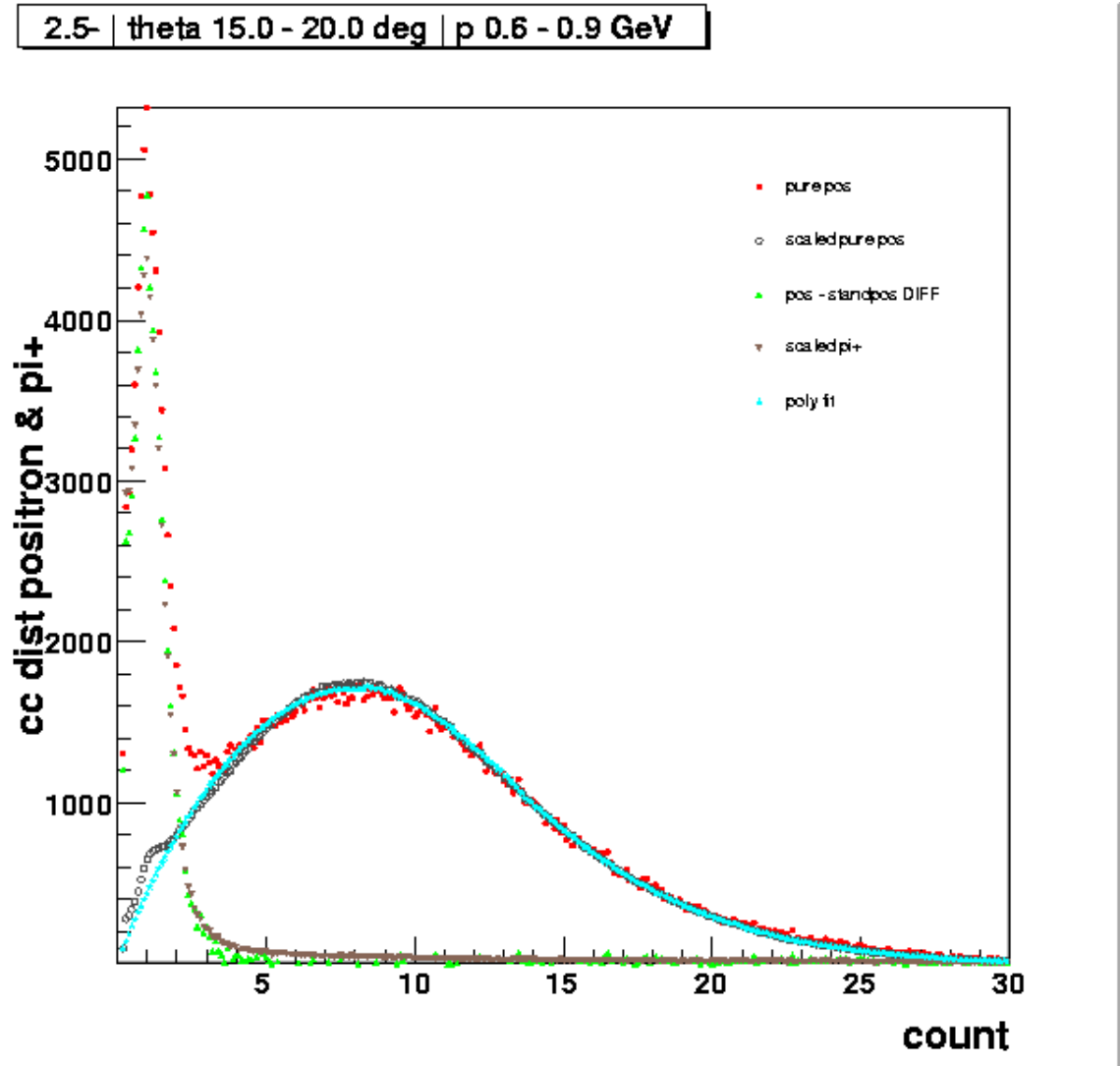


FIG. 92: π^+ contamination of positrons. The observed π^+ peak is too big to fit on the scale of the plot. First, the positron spectrum (red-square dots, *purepos*) was established after proper cuts described in the text (including the geometric-timing and tight fiducial cuts). The electron spectrum from the opposite torus current data is scaled to the positron spectrum above 7 photoelectrons (shown as black-hollow circles, *scaled purepos*). The fit to this spectrum (cyan-triangles, *polyfit*) is our best estimate of the true positrons without any pion contamination. The difference between the observed and true positron spectra (green-triangle, *pos-standpos DIFF*) is the estimate of the amount of pions in the positron sample. The observed pion spectrum is scaled to this difference below 6 photoelectrons. The resulting spectrum (brown-triangles, *scaled pi+*) is the final true pion distribution that contaminates the positron sample.

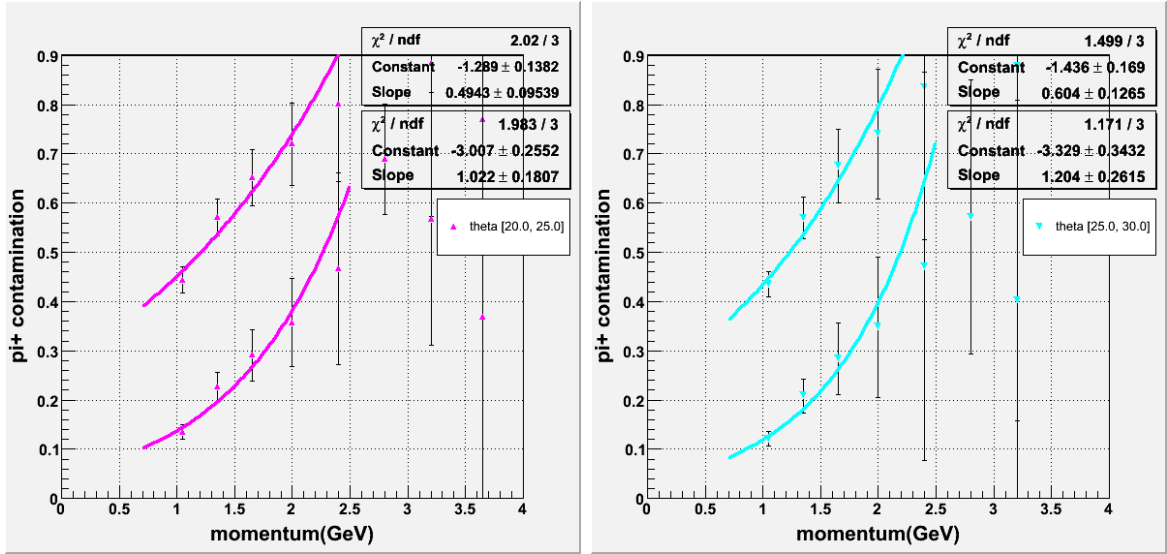


FIG. 93: π^+ to positron ratio as a function of momentum is shown for the θ bins $20^\circ < \theta < 25^\circ$ (left) and $25^\circ < \theta < 30^\circ$ (right). As in the case of electrons, this ratio follows an exponential form and can be considered as a smooth function of momentum.

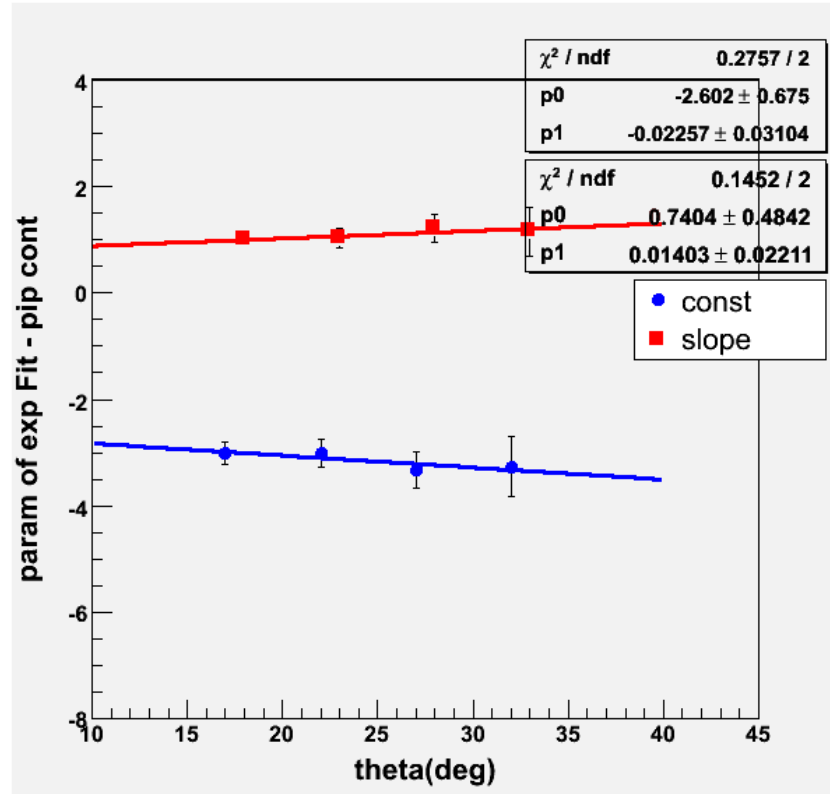


FIG. 94: π^+ contamination of positron. The points show the θ dependence of the exponential fit parameters, the slope $S_e(\theta)$ and the constant factor $C_e(\theta)$.

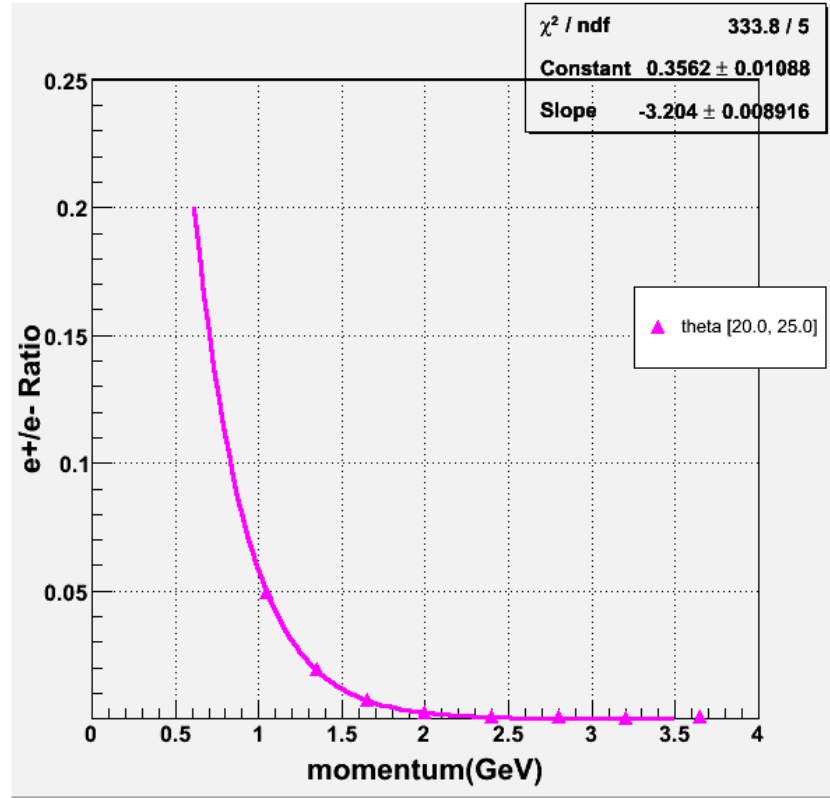


FIG. 95: e^+/e^- ratio as a function of momentum for a single polar angle bin. It follows an exponential function as in the previous cases.

ratio of the integrated pion and positron (from the observed positron distribution) rates for each kinematic bin determines the amount of pion contamination in the positron sample. The ratio of the integrated rates in the full CC range gives the total contamination, while the ratio above a CC threshold of 2 photoelectrons gives the standard contamination. Fig. 93 shows the pion to positron ratio as a function of momentum. It is fitted by an exponential function. In the figure, the total contamination (the larger ratio) and the standard contamination are shown together. It should be noted that this plot is for a single polar angle bin. The fit parameters should be a smooth function of polar angle as well. Fig. 94 shows the exponential fit parameters (C_e and S_e) for each θ bin as a function of θ . Therefore, Figs. 93 and 94 together actually confirms our basic assumption that the contamination should be a smooth function of momentum and polar angle.

The amount of pair symmetric electrons contaminating the true electron sample is estimated by using the true positron spectrum from opposite torus polarity data

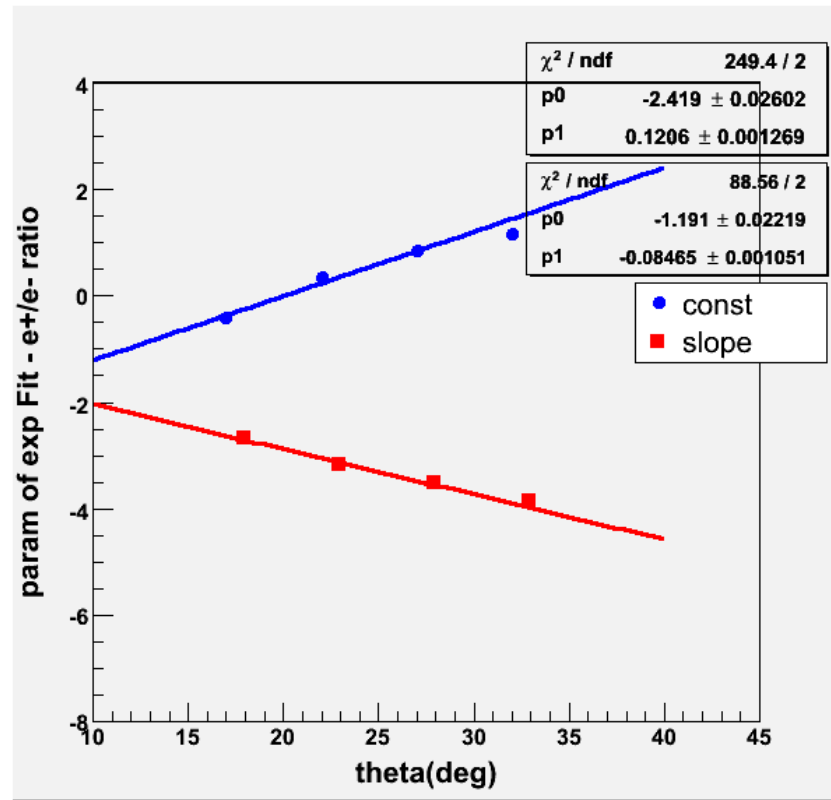


FIG. 96: The exponential fit parameters $C_e(\theta)$ (blue, labeled as *const*) and $S_e(\theta)$ (red, labeled as *slope*) for each θ bin are plotted as a function of θ . They follow a linear dependence as expected.

(after π^+ contamination is removed from the sample). Therefore, the ratio of the integrated true (uncontaminated) positron spectrum (from opposite torus polarity) over the integrated electron spectrum (after minimizing the π^- contamination by geometric and timing cuts) gives us the contamination caused by the pair symmetric electrons. The integrations for both spectra were done above 7 photoelectrons so that the remaining π^- contamination in the electron sample (that persists in the low photoelectron region but it is very small in general) does not propagate into the e^+/e^- ratio. Note that both data samples were first normalized to their corresponding beam charge before taking their ratio. Fig. 95 shows an example of such a ratio as a function of momentum for a single θ bin. As expected, it follows an exponential form:

$$R_e = e^{C_e(\theta)+S_e(\theta)p} \quad (367)$$

C_e and S_e are fit parameters that depend on the polar angle θ . Fig. 96 shows the dependence of these parameters on θ . In the end, the pair symmetric contamination is also a smooth function of momentum and polar angle in the form:

$$R_e = e^{C_e(\theta)+S_e(\theta)p} = e^{a+b\theta+cp+d\theta p} \quad (368)$$

Once we determine the parameters from available data, we can determine the ratio $R_e = e^+/e^-$ for any kinematics and correct the asymmetry by applying the correction formula:

$$A_{el}^{corr} = A_{el}^{raw} \frac{1 - R_e \frac{A_{pos}^{raw}}{A_{el}^{raw}}}{1 - R_e} = \frac{A_{el}^{raw} - R_e A_{pos}^{raw}}{1 - R_e} \quad (369)$$

$$\sigma_{A_{el}^{corr}} = \sqrt{\frac{\sigma_{A_{el}^{raw}}^2 + R_e^2 \sigma_{A_{pos}^{raw}}^2}{(1 - R_e)^2}} \quad (370)$$

In order to correct the asymmetry, we need the raw asymmetry of the contaminant electrons as well as the ratio. By definition, the asymmetry of pair symmetric electrons is the same as the asymmetry of positrons for the opposite torus polarity. Therefore, we determined the positron asymmetry from data for each of our momentum and polar angle bins and wrote the values into a table. The analysis program reads in this table to find the corresponding positron asymmetry for a given momentum and polar angle. Fig. 97 shows the positron asymmetries as a function of momentum for a single θ bin. A few data sets are shown to give a general idea. In most kinematics, the positron asymmetry is consistent with zero. This correction is, in general, very small, on the order of 0.2% of the statistical error in most bins, less

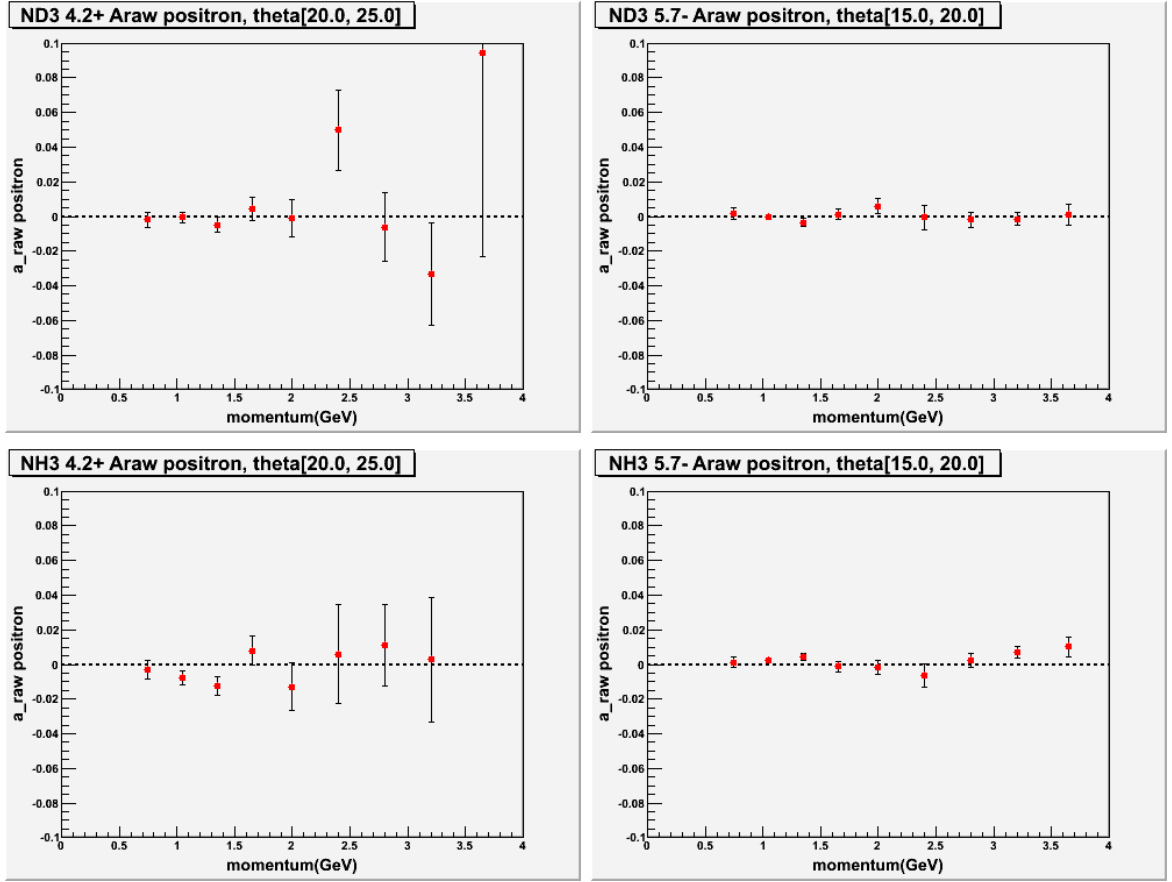


FIG. 97: Positron asymmetry as a function of momentum for a single θ bin. The top row is from the ND_3 target showing the 4.2 GeV inbending (left) and the 5.7 GeV outbending (right) data sets. The bottom row is from the NH_3 target showing again the 4.2 GeV inbending (left) and the 5.7 GeV outbending (right) data sets.

than 10% of the statistical error in more than 99% of the bins and it never exceeds 50% of the statistical error.

In order to determine the systematic error due to the pair symmetric correction, we compared the kinematic dependence of the correction function for data sets with opposite torus polarities. Fig. 98 shows the ratios as a function of momentum overlaid onto each other for opposite torus polarities. In general, the results from opposite torus polarities agree with each other very well. In addition, Fig. 99 shows the fit parameters $C_e(\theta)$ and $S_e(\theta)$ as a function of θ for the corresponding data sets with opposite torus currents.

The final parameters for the π^-/e^- and e^+/e^- ratios for all data sets (target, beam, torus) are listed in the Appendix section C.1.

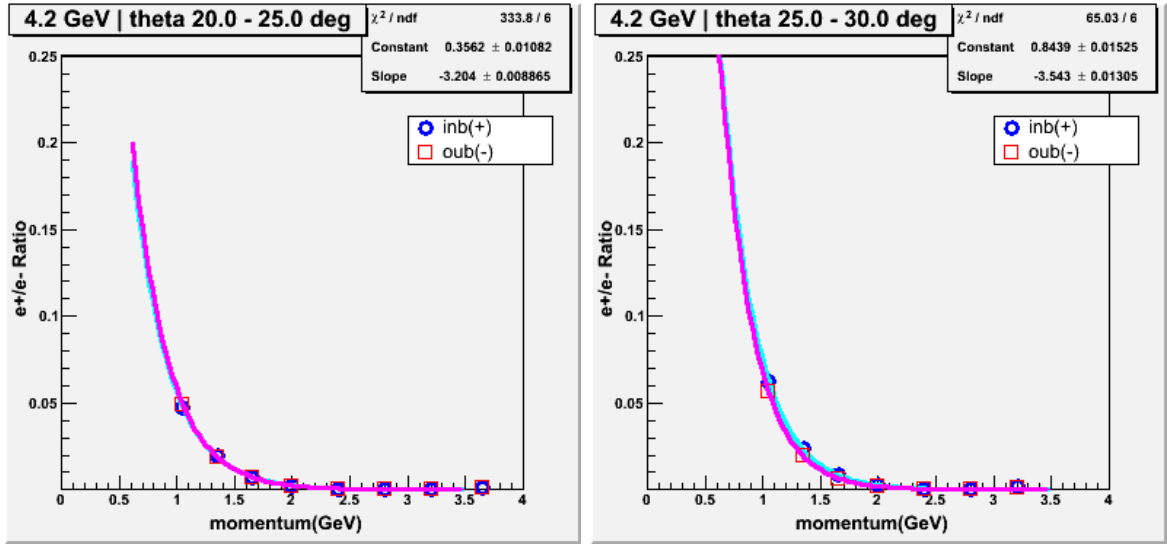


FIG. 98: e^+/e^- ratio for opposite torus polarity data for two θ bins.

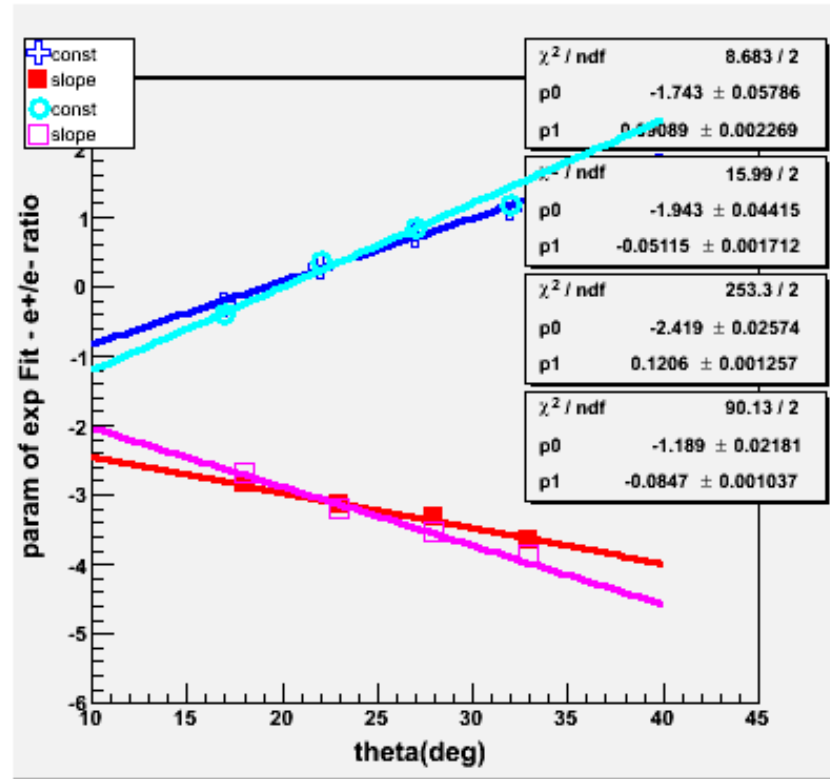


FIG. 99: The exponential fit parameters C_e (const) and S_e (slope) for 4.2 GeV inbending and outbending data sets are shown together as a function of θ .

IV.13 BEAM AND TARGET POLARIZATION

In order to determine the double spin asymmetry, the raw asymmetry from the count rates needs to be corrected for the net polarization. Therefore the product of the beam and target polarization is required. During the experiment, the beam polarization was measured by using the Moller Polarimeter and the target polarization was monitored by the Nuclear Magnetic Resonance (NMR) system. In the EG1b experiment, the electron beam polarization was very stable and the measurements from the Moller Polarimeter are dependable. On the other hand, the target polarization was not quite stable. Moreover, the NMR coils are located outside the target, and are therefore more sensitive to the outer layers of the target material. However, the polarization of the target can change within the target volume, especially since the regions of the target exposed to the beam are depolarized more quickly. To prevent quick and local depolarization of the target material, the beam is rastered over the target area in a spiral motion. However, the rastering is not always perfect and especially the outer layer of the target, to which the NMR is most sensitive, is not efficiently rastered. Therefore, it is generally expected that NMR values are superficially higher than the true polarization of the target. Moreover, there are other technical uncertainties on the NMR readings that are not well understood. As a result, we need a reliable method of determining the true beam \times target polarization.

The most reliable method to determine the polarization is to extract the information from the data itself. This extraction is based on the fact that the theoretical asymmetry for elastic and quasi-elastic events is well determined. Once the theoretical asymmetry is known, the beam and target polarization can be determined according to:

$$P_b P_t = \frac{A_{meas}^{quasi-el}}{F_D A_{theo}^{quasi-el}} \quad (371)$$

where F_D stands for the dilution factor to remove the effect of scattering from unpolarized nucleons in the target. Therefore, what we need to do is to extract the asymmetry by using quasi-elastic scattering from the deuteron, correct it for the background contributions and then divide it by the theoretical prediction. For the EG1b experiment, this was done separately for each Q^2 bin. Then, the $P_b P_t$ values from all Q^2 bins with reasonable statistical error were averaged to determine the final value.

IV.13.1 Theoretical Asymmetry For Quasi-Elastic Scattering from the Deuteron

The double-spin asymmetry A_{\parallel} can be calculated by using the electric and magnetic form factors G_E and G_M in the elastic region. The virtual photon asymmetries for elastic scattering are simply [1]:

$$A_1 = 1 \quad (372)$$

and

$$A_2 = \sqrt{R_{(el)}} = \frac{\sqrt{Q^2} G_E(Q^2)}{\nu G_M(Q^2)}. \quad (373)$$

$R_{(el)}$ represents the structure function R in the elastic region. It can be shown from Eqs. (20), (21) and (22) that $Q^2 = 2M\nu$ for the elastic events. Hence, the double spin asymmetry for elastic scattering can be calculated by using Eqs. (26-29) and (67) such that [17]:

$$A_{\parallel} = \frac{2\tau G[\frac{M}{E} + G(\tau \frac{M}{E} + (1 + \tau) \tan^2(\theta/2))]}{1 + G^2 \tau/\epsilon}, \quad (374)$$

where $\tau = Q^2/4M^2$, $G = G_M/G_E$, E is the beam energy, M is the mass of the nucleon and θ is the polar scattering angle of the electron. For the electromagnetic form factors we used the latest parametrization by J. Arrington [116]:

$$G_E(Q^2) = [1 + p_2 Q^2 + p_4 Q^4 + p_6 Q^6 + \dots + p_{12} Q^{12}]^{-1} \quad (375)$$

$$G_M(Q^2) = \mu_p [1 + p_2 Q^2 + p_4 Q^4 + p_6 Q^6 + \dots + p_{12} Q^{12}]^{-1} \quad (376)$$

where the coefficients p_2 - p_{12} are given in Table 38.

TABLE 38: Fit parameters for the Rosenbluth form factors G_E and G_M [116].

| Parameter | G_E | G_M |
|-----------|---------|------------------------|
| p_2 | 3.226 | 3.19 |
| p_4 | 1.508 | 1.355 |
| p_6 | -0.3773 | 0.151 |
| p_8 | 0.611 | -0.0114 |
| p_{10} | -0.1853 | 5.33×10^{-4} |
| p_{12} | 0.01596 | -9.00×10^{-6} |

The double spin asymmetries of the proton and the neutron were calculated according to Eq. (374) using the parameterization given by Arrington. After that,

the deuteron quasi-elastic asymmetry was determined from that of the proton and the neutron as the weighted average:

$$A_{||}^D = \frac{\sigma_p^{el} A_p^{el} + \sigma_n^{el} A_n^{el}}{\sigma_p^{el} + \sigma_n^{el}} \left(1 - \frac{3}{2} w_D \right) \quad (377)$$

where w_D is the probability of finding deuteron in D-state. However, this procedure was later replaced with a more advance calculations of the theoretical asymmetries by Sebastian Kuhn, which included the proper momentum distribution of the nucleons inside the deuteron as well as radiative effects. Not much difference was observed for the proton; however, for the deuteron we found that it is important to account for the nuclear and radiative effects. For the final results, the theoretical elastic asymmetries from S. Kuhn were used to calculate $P_b P_t$ for the deuteron.

IV.13.2 Extraction of Quasi-Elastic Asymmetry from the Data

There are two methods for the extraction of the quasi-elastic asymmetries from data. In the first method, quasi-elastic events are selected by detecting only the scattered electrons. This is called the inclusive method. The final state mass W is reconstructed and a specific cut on W depending on the data configuration (beam energy and torus settings) is applied to select the quasi-elastic events. Table 39 lists the applied cuts for each configuration. After subtracting the background contributions, the elastic asymmetry is evaluated in the elastic W region. In the second method, the scattered electron and a knock-out proton are both detected in the final state and their azimuthal angle correlation is used as an additional constraint to select the quasi-elastic events. This method is known as the exclusive method. Both methods have their own advantages and drawbacks. Below, we will explain both methods in more detail.

Inclusive Method

The first step is to identify the electrons. The set of cuts we used for this purpose is shown in Table 40. The advantage of the inclusive method is its statistical power. The amount of the quasi-elastic events determined from inclusive scattering is very high compared to the exclusive method. However, the higher statistics comes with a price: more background contribution. The main challenge of this method is to isolate the elastic peak by correctly removing the background. We developed two methods to remove the background from inclusive elastic events.

TABLE 39: W limits in GeV for (quasi-)elastic event selection in the inclusive (incl) and exclusive (excl) methods.

| E_{beam} | incl W_{min} | incl W_{max} | excl W_{min} | excl W_{max} |
|------------|----------------|----------------|----------------|----------------|
| 1.606 | 0.90 | 0.98 | 0.88 | 0.98 |
| 1.723 | 0.90 | 0.98 | 0.88 | 0.98 |
| 2.286 | 0.90 | 0.99 | 0.87 | 0.99 |
| 2.561 | 0.90 | 0.99 | 0.87 | 0.99 |
| 4.238 | 0.90 | 0.99 | 0.86 | 1.02 |
| 5.615 | 0.88 | 1.00 | 0.84 | 1.02 |
| 5.725 | 0.88 | 1.00 | 0.84 | 1.02 |
| 5.743 | 0.88 | 1.00 | 0.84 | 1.02 |

TABLE 40: Electron cuts for $P_b P_t$ calculation with the inclusive method.

| |
|---|
| particle charge = -1 |
| good helicity selection |
| one electron per event |
| $p \geq 0.01 E_B$ |
| $p \leq E_B$ |
| $0 \leq flag \leq 5$ or $10 \leq flag \leq 15$ |
| triggerbit cut (section IV.7.2) |
| $CC_{nphe} > 2.0$ if $p \leq 3.0$ GeV or $CC_{nphe} > 0.5$ if $p > 3.0$ GeV |
| $EC_{tot}/p > 0.20$ if $p \leq 3.0$ GeV or $EC_{tot}/p > 0.24$ if $p > 3.0$ GeV |
| $EC_{in} > 0.06$ |
| $-58.0 \leq z_{vertex} \leq -52.0$ |
| $7.5^\circ < \theta < 49^\circ$ |
| $\nu > 0$ GeV |
| sector 5 cut (section IV.7) |
| loose fiducial cuts |
| geometric-timing cuts on the CC (section IV.8) |
| W cut (see Table 39) |

The first one is based on the carbon data and referred to as the carbon subtraction method. In this method we assume that counts from the ^{12}C target can be used to simulate the ^{15}N counts in the elastic region. We also assume that the lower tail of the W distribution mainly comes from background. Therefore in the low W tail, beam charge normalized ND_3 counts and ^{12}C counts should be exactly the same apart from a scaling factor. The scaling factor accounts for the difference in the mass thickness of the nitrogen in the ammonia and the carbon targets. Therefore, the total background in the ND_3 counts is determined by normalizing the carbon counts to the ND_3 counts in the low W region to evaluate the scaling factor and then multiplying the carbon counts with this scaling factor in all W regions. The difference between the ND_3 and the scaled ^{12}C counts yields the true (quasi-)elastic events. The crucial point in this approach is to evaluate the scaling factor correctly, hence, to determine the low W region where only the background counts contribute. We systematically studied this W_{low} region and monitored the resulting scaling factor. At the end, we determined $0.50 \leq W \leq 0.65$ to be the optimal region. Below this region, we don't have enough events for a reliable calculation. Above this region the quasi-elastic tail begins to interfere. Figs. 100 and 101 show the background removal procedure by using the carbon data.

The second method for background subtraction is to simply use the previously determined dilution factor values. This method became superior to the carbon subtraction method especially after the radiated cross section models were developed for $^{15}\text{N}/^{12}\text{C}$ ratios, which enabled us to reliably determine the dilution factors in the elastic region. After this accomplishment, we abandoned the carbon subtraction method and used the dilution factors instead while determining $P_b P_t$ with the inclusive method. However, in the exclusive method, which is explained next, carbon subtraction remained as the main method to remove the background from elastic ep events.

Another crucial point was to define the quasi-elastic region. We varied the W cuts and monitored the resulting $P_b P_t$ values and their statistical errors. We began with a tight cut, which results in a large statistical error and then we loosened the cut step by step until the $P_b P_t$ value stabilized. Then we also moved the cut region by an offset and monitored the $P_b P_t$ values in order to choose the region where the values are most stable. We performed this procedure for each data configuration. Table 39 lists the final W cuts for different beam energies.

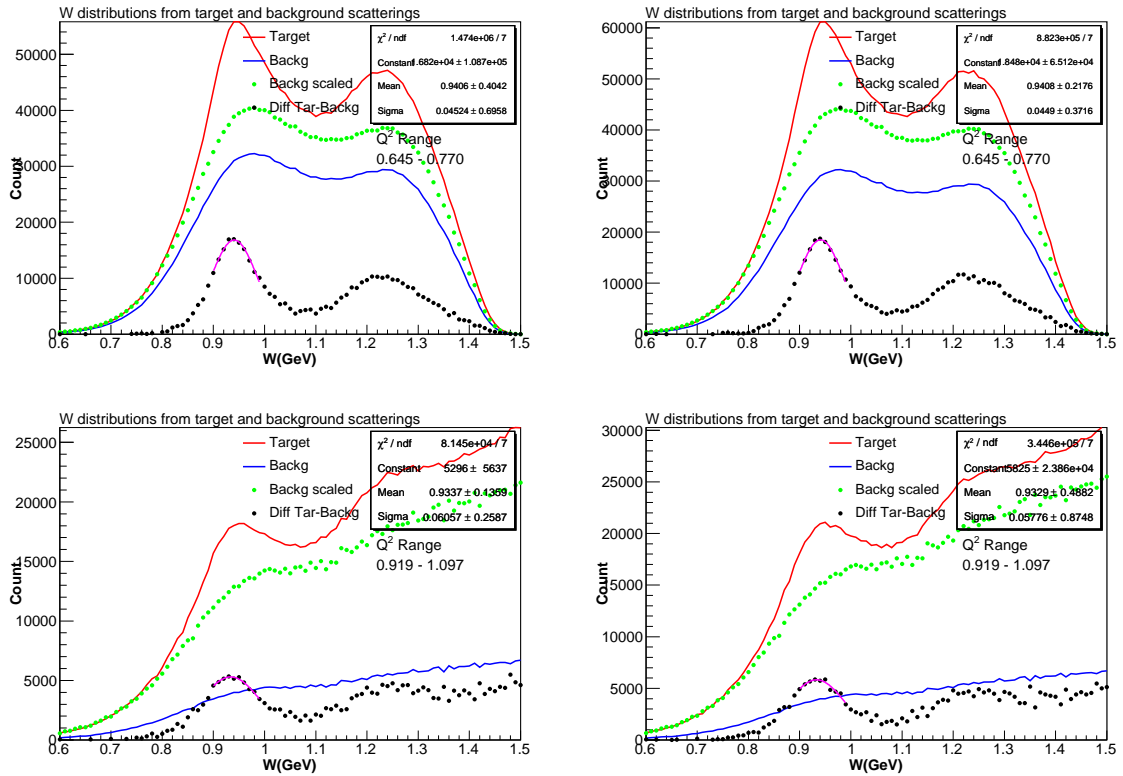


FIG. 100: W distributions from inclusive events are shown for the background removal procedure. The top row is from the 1.6 GeV ND_3 positive (left) and negative (right) target polarizations. The bottom row is the same for the 2.5 GeV ND_3 data set. The red solid line (*Target*) is the raw inclusive data from the ND_3 target. The blue solid line (*Backg*) represents the ^{12}C data, which is scaled to the ND_3 data (green dots) and subtracted from it. The final quasi-elastic distribution is shown with black dots (*Diff*).

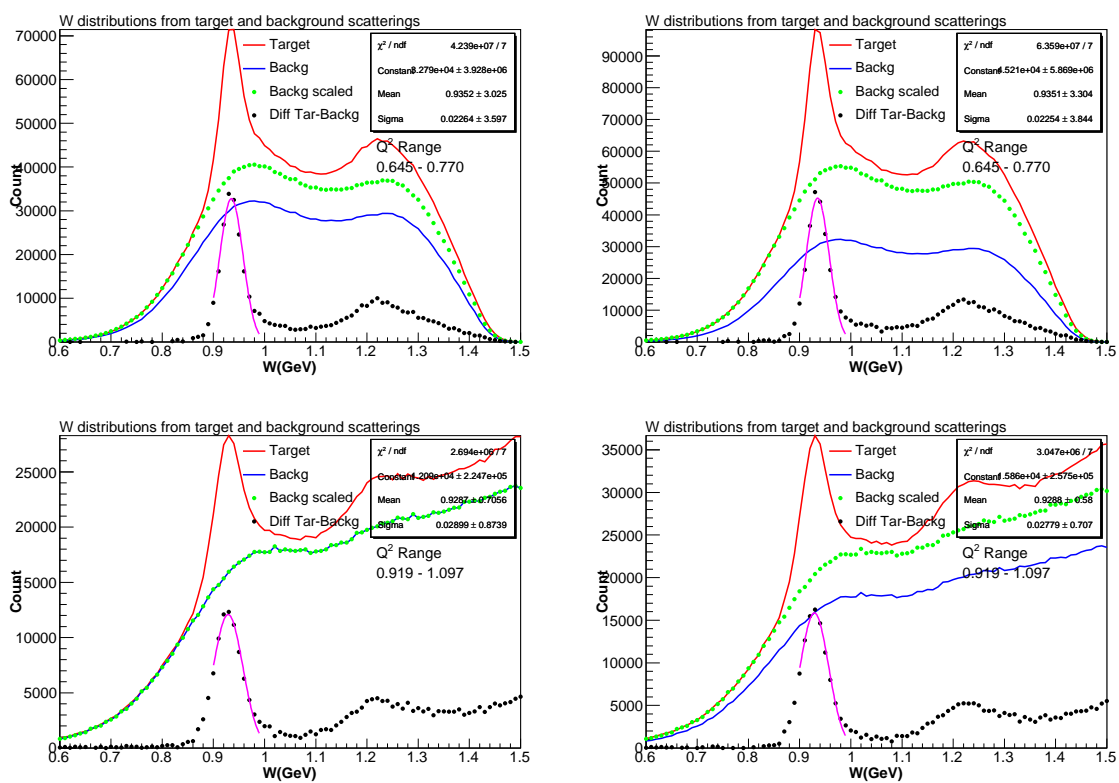


FIG. 101: Same as Fig. 100 for the NH_3 data sets. The top row is from the 1.6 and the bottom is from the 2.3 GeV data sets. Background removal for the NH_3 target is much cleaner than for the ND_3 target.

Exclusive Method

In the exclusive method, we determined the quasi-elastic $ed \rightarrow epn$ events by identifying the electron and recoil proton in coincidence. The electron cuts applied for this case are slightly different than the previous case. Especially, the cuts on the EC and CC can be loosened because the requirement for proton together with the collinearity (by using the azimuthal angle difference) and missing energy cuts already restricts our particle selection. The final electron cuts are listed in Table 41. For proton, we applied the cuts described in section IV.10.7 and listed in Table 14, except for the timing cut, which was changed to $-0.8 < \Delta t < 0.8$ to gain more events. In addition, the cuts applied for the selection of quasi-elastic events are listed in Table 42.

The advantage of the exclusive method is that the background contribution is small since we apply strict kinematic constraints on the data. However, because the proton is not always detected, this approach generally reduces the statistics, which results in a higher statistical error on the extracted $P_b P_t$ value in comparison to the inclusive method. In order to remove the background contribution from the ND₃ data, we used the carbon subtraction method, described in the previous section. Fig. 102 shows the distributions of the azimuthal angle differences between the protons and the electrons ($\Delta\phi = \phi_p - \phi_e$) in quasi-elastic events for a few data sets with the ND₃ target. Also, Fig. 103 shows the W distributions for the same events. In the exclusive case, the scaling factor (to scale the carbon data) was determined by using the ϕ distribution of the quasi-elastic events. The ϕ ranges used for this purpose were $160^\circ \leq \Delta\phi \leq 170^\circ$ and $190^\circ \leq \Delta\phi \leq 200^\circ$. The scaling factors calculated from the ϕ distributions of the exclusive events and from the W distributions of the inclusive events were very similar in general.

IV.13.3 Final $P_b P_t$ Values

For each target and beam polarization in the EG1b experiment, the $P_b P_t$ values from inclusive and exclusive methods were determined as described above for each Q^2 bin. Some sample plots can be seen in Figs. 104-108. In the end, the $P_b P_t$ values are averaged over Q^2 bins as:

$$P_b P_t = \sum_{Q^2} \frac{P_b P_t(Q^2)}{\sigma_{P_b P_t}^2(Q^2)} / \sum_{Q^2} \frac{1}{\sigma_{P_b P_t}^2(Q^2)} \quad (378)$$

TABLE 41: Electron cuts for P_bP_t calculation with the exclusive method.

| |
|---|
| particle charge = -1 |
| good helicity selection |
| one electron per event |
| $p \leq E_B$ |
| $0 \leq flag \leq 5$ or $10 \leq flag \leq 15$ |
| triggerbit cut (section IV.7.2) |
| $CC_{nphe} > 1.0$ |
| $EC_{tot}/p > 0.15$ if $p \leq 3.0$ GeV or $EC_{tot}/p > 0.20$ if $p > 3.0$ GeV |
| $-58.0 \leq z_{vertex} \leq -52.0$ |
| $8.5^\circ < \theta < 49^\circ$ |
| sector 5 cut (section IV.7) |
| $\nu > 0$ GeV |

TABLE 42: Cuts for the selection of quasi-elastic events for P_bP_t calculation. An electron and a proton were required with at most one neutral particle in the event in order not to lose events with accidental signals in any of the detectors (by a cosmic ray or a stray photon). $E_{[miss]}$ and θ_Q were calculated according to Eqs. (264) and (269), respectively.

| |
|---|
| good helicity selection |
| particles in the event = 2 (or 3 with one neutral particle) |
| electron found in the event |
| proton found in the event |
| $ E_{[miss]} \leq 0.08$ GeV |
| $ \theta_p - \theta_Q < 2^\circ$ |
| $\theta_Q < 49^\circ$ |
| $-3^\circ < \phi_p - \phi_e - 180^\circ < 3^\circ$ |
| W cut (see Table 39) |

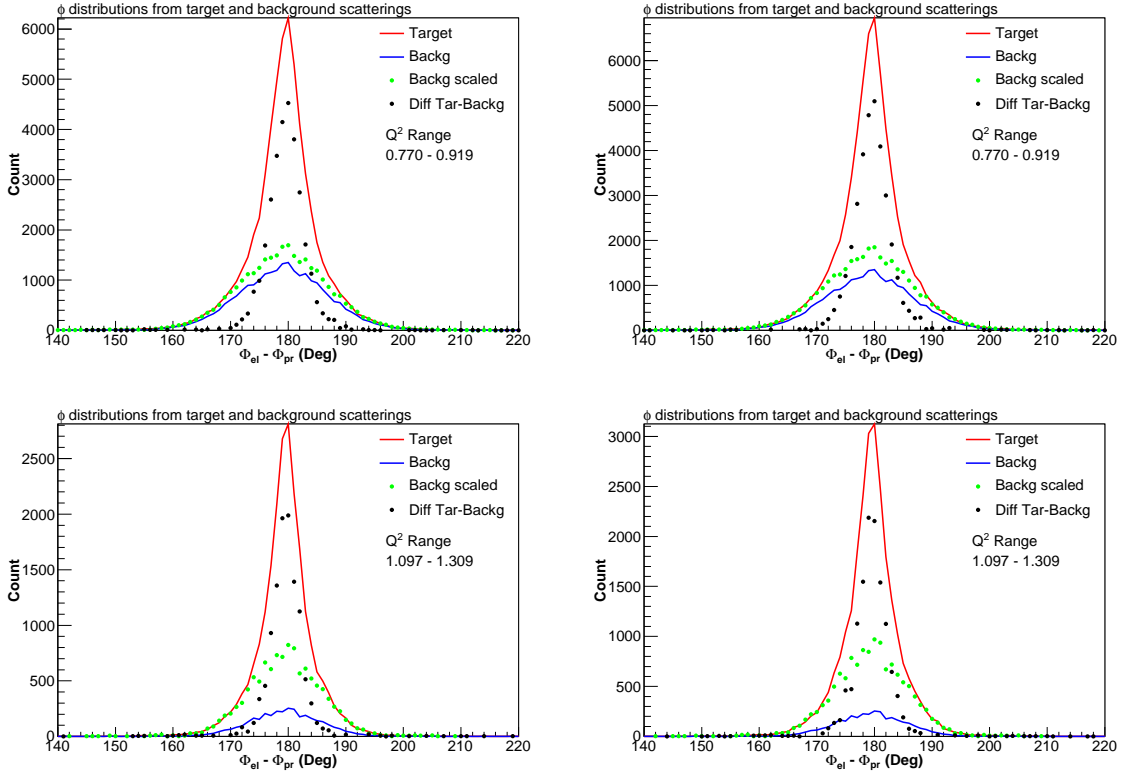


FIG. 102: Distribution of azimuthal angle difference between the electron and the proton ($\Delta\phi = \phi_p - \phi_e$) in exclusive quasi-elastic events for different data sets with the ND_3 target. The top row is from the 1.6 GeV positive (left) and negative (right) target polarizations. The bottom row is the same for the 2.5 GeV data set. The red solid line (*Target*) is the raw inclusive data from the ND_3 target. The blue solid line (*Backg*) represents the ^{12}C data, which is scaled to the ND_3 data (green dots) and subtracted from it. The final quasi-elastic distribution is shown with black dots (*Diff*). The range $-3^\circ < |\phi_p - \phi_e| - 180^\circ < 3^\circ$ was selected for the calculation of $P_b P_t$.

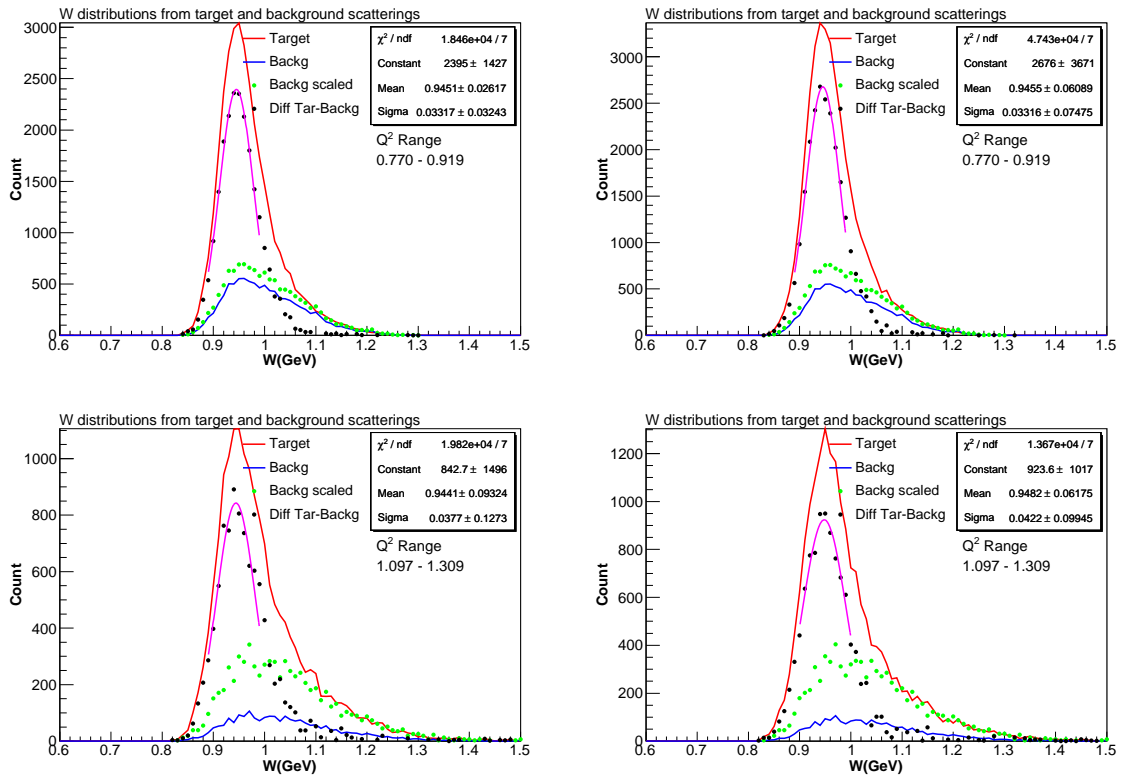


FIG. 103: W distributions for exclusive ep quasi-elastic events for different data sets, showing the background removal for the ND_3 target. The top row is from the 1.6 GeV positive (left) and negative (right) target polarizations. The W cut applied on this data set to calculate $P_b P_t$ was $0.88 \leq W \leq 0.98$. The bottom row is the same for the 2.5 GeV data. The W cut was $0.87 \leq W \leq 0.99$. The explanations for the curves and data points are provided in the caption of Fig. 102.

$$\sigma_{P_b P_t} = 1 / \sum_{Q^2} \frac{1}{\sigma_{P_b P_t}^2(Q^2)} \quad (379)$$

leaving out the Q^2 bins with high statistical errors (the ones with statistical error larger than 0.5). The Q^2 bin ranges for different data configurations can be seen in Table 43. The final values are listed in Table 44 for different data sets and target polarizations. Then the values were compared from four different independent studies of the $P_b P_t$ [117]. The values agree well within statistical fluctuations. After careful considerations, it was agreed that the exclusive method in general gave more reliable results. Therefore, for the final analysis, exclusive values were used except for the 1.6 and 1.7 GeV outbending data sets, for which we used the inclusive $P_b P_t$ values because the exclusive values had large statistical errors. The error on the inclusive method is rather small because of the statistical power of the method. Therefore, we did not use the statistical error for those data but instead “assigned” 10% error on the value, which is a reasonable estimate made by comparing the independent studies on $P_b P_t$.

TABLE 43: Q^2 limits in GeV for the $P_b P_t$ average.

| E_{beam} | Torus | incl Q_{min}^2 | incl Q_{max}^2 | excl Q_{min}^2 | excl Q_{max}^2 |
|------------|-------|------------------|------------------|------------------|------------------|
| 1.606 | + | 0.20 | 1.00 | 0.71 | 1.00 |
| 1.606 | − | 0.24 | 0.71 | 0.71 | 0.84 |
| 1.723 | − | 0.17 | 0.84 | 0.71 | 1.00 |
| 2.561 | + | 0.29 | 2.00 | 1.00 | 2.00 |
| 2.561 | − | 0.29 | 1.86 | 1.00 | 1.70 |
| 4.238 | + | 0.59 | 3.50 | 1.40 | 2.90 |
| 4.238 | − | 0.59 | 3.50 | 1.40 | 3.50 |
| 5.615 | + | 1.20 | 5.90 | 1.70 | 6.00 |
| 5.725 | + | 0.84 | 5.90 | 1.70 | 5.90 |
| 5.725 | − | 0.84 | 5.90 | 1.70 | 5.90 |
| 5.743 | − | 0.84 | 5.90 | 1.70 | 5.90 |

IV.13.4 $P_b P_t$ for Weighting Data from Different Helicity Configurations

We have various data sets with different beam energies, torus currents and target polarizations. In order to combine the asymmetries from these data sets, we would like to give them different weights according to their overall statistical precision. In particular, while combining the data sets with opposite target polarizations, we know

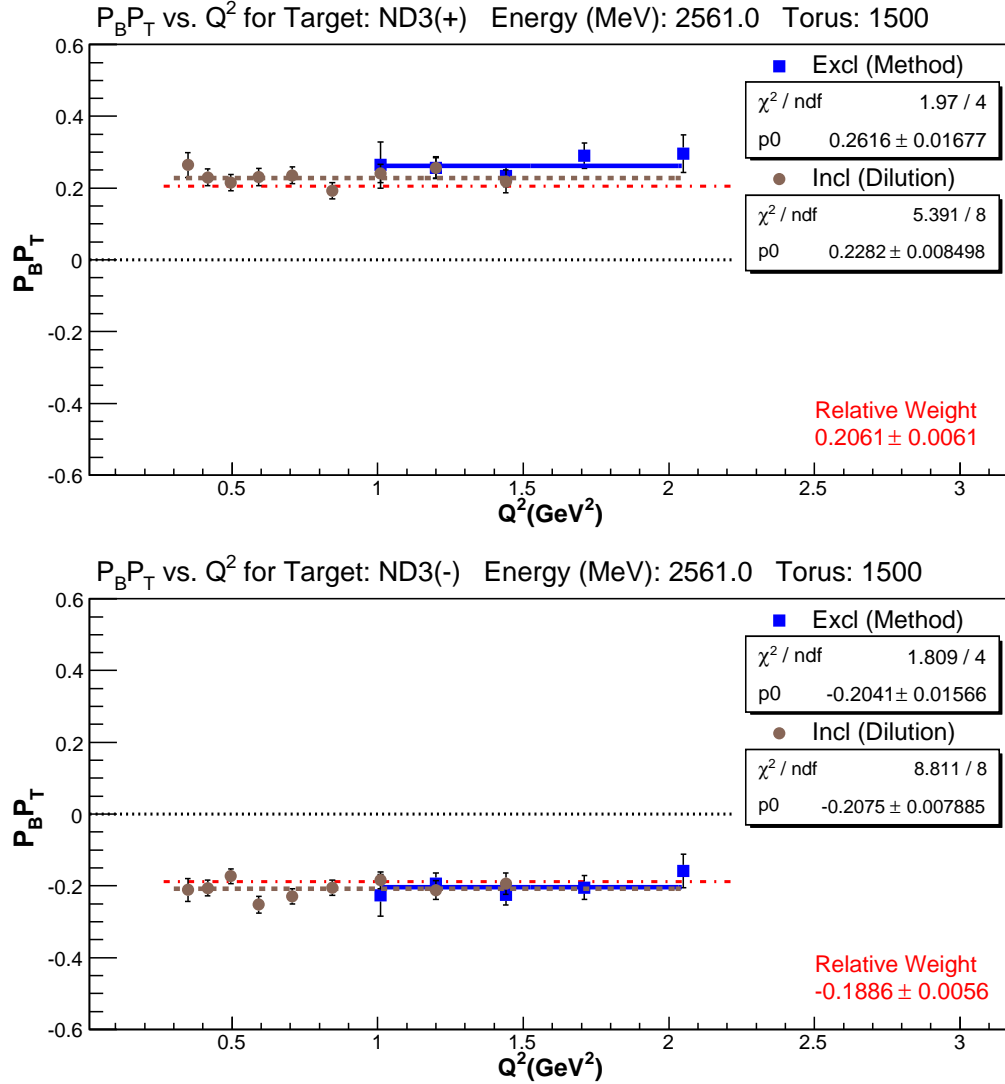


FIG. 104: $P_b P_t$ values for the 2.5 GeV inbending data sets for ND_3 target. The plot shows the resulting $P_b P_t$ values for the Q^2 bins with available data. The results from the exclusive (blue square) and the inclusive (brown circle) methods are shown. The corresponding linear fits to the data are also shown as lines: the solid blue line is for the exclusive and the dashed brown line is for the inclusive methods. The results of the linear fits are shown. Note that these results from the linear fits are not the actual $P_b P_t$ values but they are practically the same up to 3rd significant figure. In addition, the relative weighting factor described in section IV.13.4 is also written on each plot.

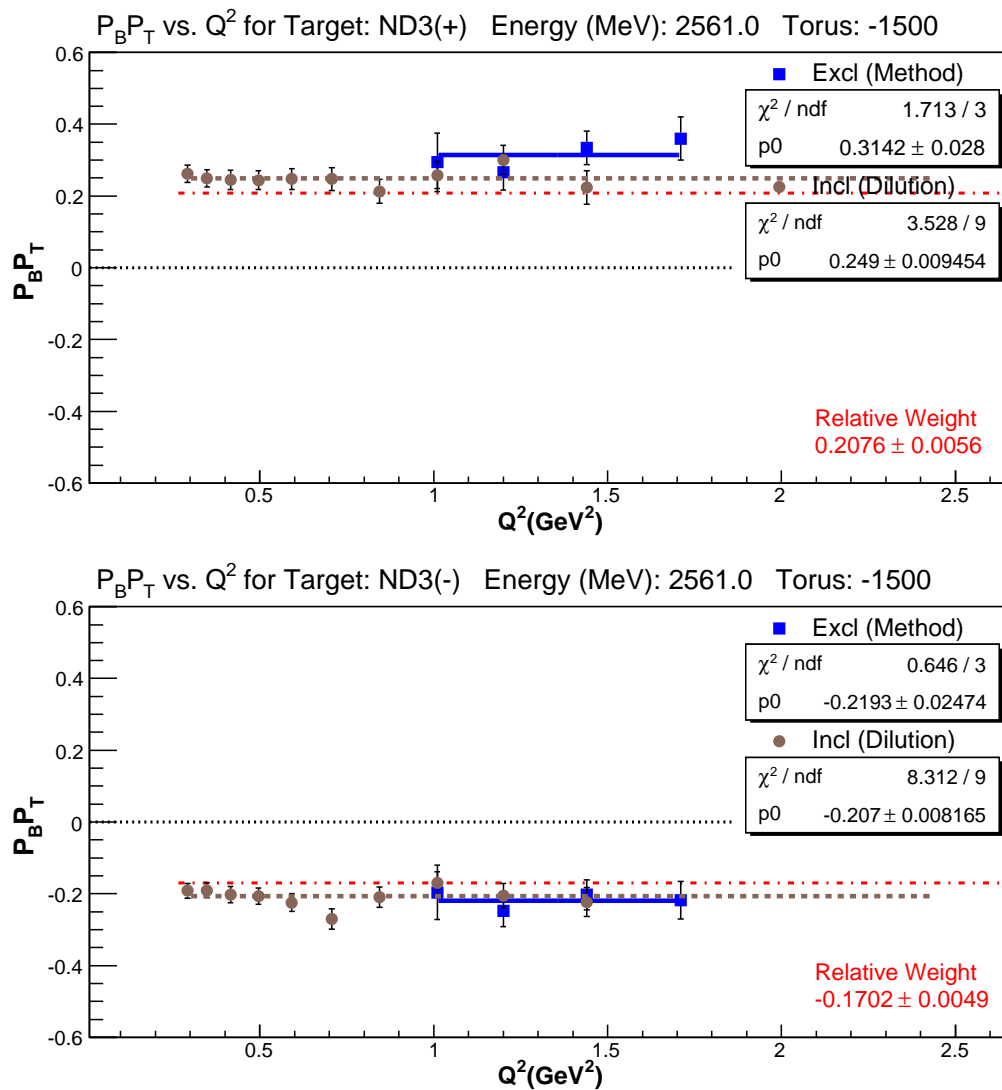
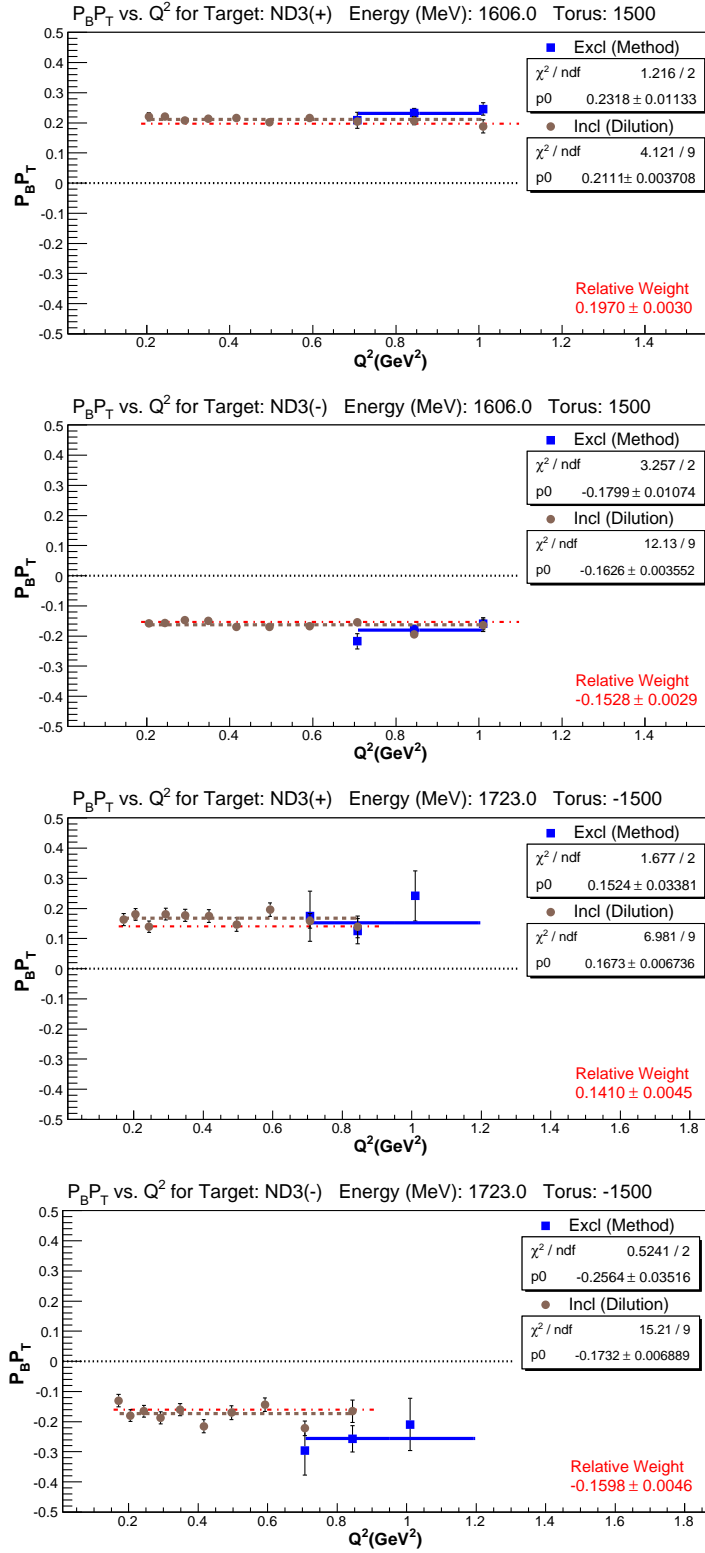


FIG. 105: $P_b P_t$ values for different data sets for ND₃ target.

FIG. 106: $P_b P_t$ values for different data sets for ND₃ target.

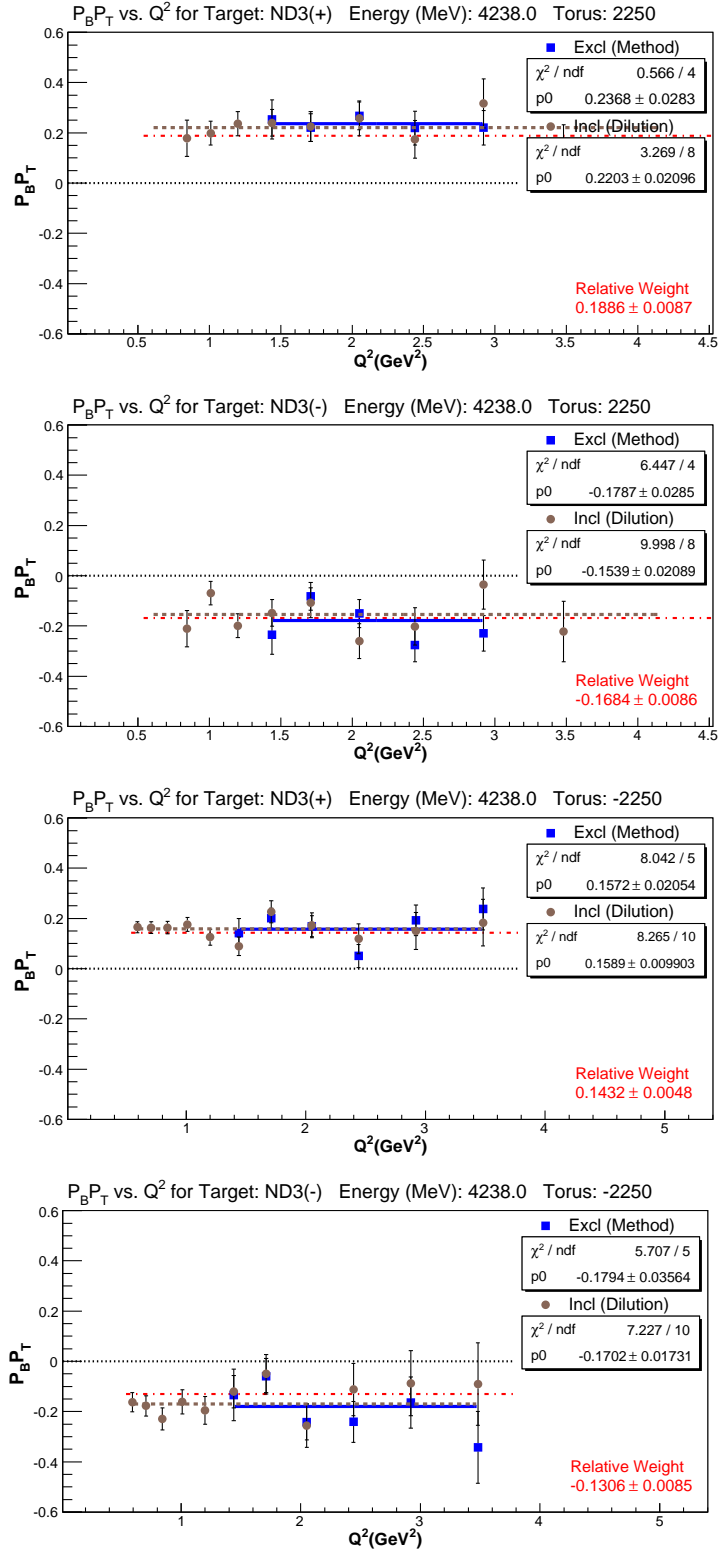


FIG. 107: $P_b P_t$ values for different data sets for ND₃ target.

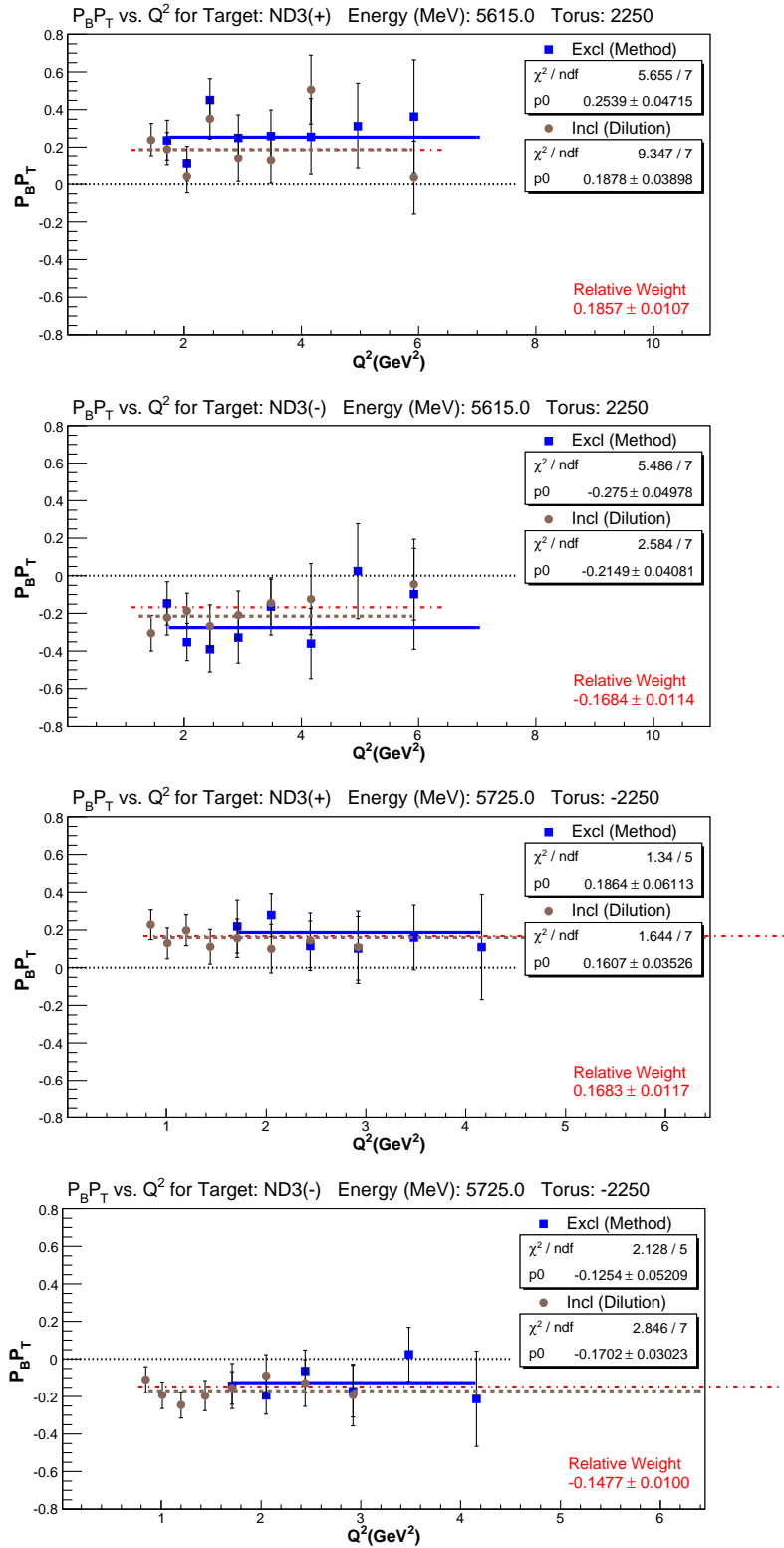


FIG. 108: $P_b P_t$ values for different data sets for ND₃ target.

TABLE 44: $P_b P_t$ values from different methods for all data sets with ND₃ target. E_B is the beam energy, I_T refers to torus polarity (inbending or outbending) and T.Pol is the target polarization sign. The results from the exclusive (*excl*) and the inclusive (*incl*) are listed together with the corresponding errors. The values given in the *rela* column are only used as statistical weighting factors for each set as described in section IV.13.4. For the 1.6 and 1.7 GeV outbending data, the inclusive method results were used with 10% error assigned. For the other data sets, the exclusive method results were used for the final analysis.

| E_B I_T | T.Pol | excl | excl Err | incl | incl Err | rela | rela Err |
|-------------|-------|----------|----------|----------|----------|----------|----------|
| 1606 i | + | 0.23178 | 0.01132 | 0.21105 | 0.00370 | 0.19703 | 0.00297 |
| 1606 i | - | -0.17988 | 0.01074 | -0.16261 | 0.00355 | -0.15276 | 0.00285 |
| 1606 o | + | 0.16393 | 0.04255 | 0.17576 | 0.00835 | 0.14743 | 0.00481 |
| 1723 o | + | 0.15237 | 0.03380 | 0.16729 | 0.00673 | 0.14103 | 0.00450 |
| 1723 o | - | -0.25638 | 0.03515 | -0.17316 | 0.00688 | -0.15980 | 0.00461 |
| 2561 i | + | 0.26164 | 0.01677 | 0.22823 | 0.00849 | 0.20608 | 0.00608 |
| 2561 i | - | -0.20413 | 0.01565 | -0.20754 | 0.00788 | -0.18859 | 0.00564 |
| 2561 o | + | 0.31421 | 0.02800 | 0.24898 | 0.00945 | 0.20761 | 0.00562 |
| 2561 o | - | -0.21925 | 0.02473 | -0.20697 | 0.00816 | -0.17016 | 0.00487 |
| 4238 i | + | 0.23679 | 0.02830 | 0.22025 | 0.02095 | 0.18858 | 0.00865 |
| 4238 i | - | -0.17867 | 0.02850 | -0.15393 | 0.02089 | -0.16836 | 0.00864 |
| 4238 o | + | 0.15718 | 0.02054 | 0.15887 | 0.00990 | 0.14322 | 0.00483 |
| 4238 o | - | -0.17944 | 0.03564 | -0.17019 | 0.01731 | -0.13058 | 0.00845 |
| 5615 i | + | 0.25389 | 0.04714 | 0.18794 | 0.03860 | 0.18574 | 0.01072 |
| 5615 i | - | -0.27504 | 0.04978 | -0.21475 | 0.04043 | -0.16840 | 0.01135 |
| 5725 i | + | 0.20472 | 0.04431 | 0.14481 | 0.04412 | 0.14373 | 0.00978 |
| 5725 i | - | -0.16837 | 0.06136 | -0.09890 | 0.06151 | -0.16245 | 0.01365 |
| 5725 o | + | 0.18639 | 0.06113 | 0.15285 | 0.03435 | 0.16828 | 0.01170 |
| 5725 o | - | -0.12537 | 0.05208 | -0.15797 | 0.02945 | -0.14766 | 0.01002 |
| 5743 o | + | 0.20225 | 0.04369 | 0.14955 | 0.02561 | 0.13693 | 0.00817 |
| 5743 o | - | -0.21154 | 0.06641 | -0.10261 | 0.03849 | -0.09903 | 0.01224 |

that the two sets can have a rather significant difference in the magnitude of their target polarizations. An optimal strategy requires us to include this information in our statistical weighting. However, our method of determining the product of beam and target polarization $P_b P_t$ (using elastic or quasi-elastic scattering) will not yield sufficient statistical accuracy over a single “group” to make this feasible. Therefore, we need a more precise method at least to estimate the *relative* magnitude of $P_b P_t$ for a given data set.

The main purpose is to extract an estimate of $P_b P_t$ using our model of the existing spin structure function data together with the already determined asymmetries for each bin for a given group. This does not have to be too precise (and of course may be off by an overall scale factor, since we don’t know whether our existing model has the correct overall scale). However, it is sufficient to give us a *relative* magnitude of $P_b P_t$, that we will call P_{rel} .

This requires to use the “models” to determine a “predicted” $A_{||}$ for each bin where the group under investigation has data. Above $W = 1.08$ GeV this was done with a simple code that uses the A_1 , A_2 and R from “models” and combines them into $A_{||}^{model} = D(A_1 + \eta A_2)$, using the correct beam energy and electron scattering angle for each bin to calculate the required kinematic quantities like ϵ , η and D , given in Eq. (29). For kinematic bins below $W = 1.08$ GeV, we used the (quasi-)elastic inclusive asymmetries instead. These were calculated according to Eqs. (374) and (377). It should be noted that, bins below $W = 0.9$ GeV are not used in this process since the data in these bins are largely unpolarized and/or have large random errors.

At this point, we can calculate an estimate for P_{rel} for each bin in $W > 0.9$ GeV and Q^2 for a given data set (G) as follows:

$$P_{rel}(W, Q^2) = \frac{A_{raw}^G(W, Q^2)}{F_D A_{||}^{model}}, \quad (380)$$

where A_{raw}^G represents the raw asymmetry of the data set (all runs combined) and F_D is the dilution factor for the bin in question. The error on this quantity, for just one kinematic bin, is

$$\sigma_{P_{rel}} = \frac{\sigma_{A_{raw}^G}}{F_D A_{||}^{model}}. \quad (381)$$

We can then combine the information from *all* $[Q^2, W]$ bins with $W > 0.90$ GeV by

the usual statistically weighted mean:

$$P_{rel}^G = \frac{\sum_{bins} P_{rel} / \sigma_{P_{rel}}^2}{\sum_{bins} 1 / \sigma_{P_{rel}}^2}, \quad (382)$$

with statistical error

$$\sigma_{P_{rel}^G}^2 = \frac{1}{\sum_{bins} 1 / \sigma_{P_{rel}}^2}. \quad (383)$$

From Eqs. (380) and (381), we can deduce that

$$\frac{P_{rel}}{\sigma_{P_{rel}}^2} = F_D A_{||}^{model} \frac{A_{raw}^G}{\sigma_{A_{raw}^G}^2}, \quad (384)$$

so, the last equation can also be written as

$$P_{rel}^G = \frac{\sum_{bins} F_D A_{||}^{model} A_{raw}^G / \sigma_{A_{raw}^G}^2}{\sum_{bins} (F_D)^2 (A_{||}^{model})^2 / \sigma_{A_{raw}^G}^2}, \quad (385)$$

which avoids any need to divide by (potentially) small (zero) numbers.

While combining the two different data sets with opposite target polarizations, we multiply the total count for each set with the square of its relative $P_b P_t$, given by P_{rel}^G , to determine its weight. Then this weight is divided by the sum from both data sets to determine the scaling factor associated with each set. Then, this scaling factor is used whenever we need to sum quantities from the two data sets. The raw asymmetries and the true $P_b P_t$ values are summed in this way while combining the data sets with opposite target polarizations. More detailed explanations on the data combining procedure is given in section IV.17.

IV.14 POLARIZED BACKGROUND CORRECTIONS

The dilution factor corrects for scattering off unpolarized “non-target” nucleons or nuclei in the target material. However, some of these might be polarized and, therefore, affect the observed asymmetry. This section explains the corrections required to account for the effects of the polarized background on the measured asymmetry.

The proton and deuteron targets are embedded in $^{15}\text{NH}_3/^{15}\text{ND}_3$ molecules. As the targets are polarized by the DNP process, surrounding nucleons from ^{15}N can

TABLE 45: $P_b P_t$ values for the ND₃ target averaged over opposite target polarizations, from three different methods. E_B is the beam energy, I_T refers to torus polarity (inbending or outbending).

| E_B I_T | excl 1 | Err | excl 2 | Err | incl | Err |
|-------------|--------|--------|--------|--------|--------|--------|
| 1606 i | 0.2112 | 0.0080 | 0.2236 | 0.0067 | 0.1918 | 0.0026 |
| 1606 o | 0.1639 | 0.0425 | 0.2244 | 0.0346 | 0.1757 | 0.0083 |
| 1723 o | 0.2096 | 0.0246 | 0.2241 | 0.0192 | 0.1705 | 0.0048 |
| 2561 i | 0.2332 | 0.0114 | 0.2439 | 0.0101 | 0.2180 | 0.0058 |
| 2561 o | 0.2694 | 0.0188 | 0.2616 | 0.0152 | 0.2291 | 0.0063 |
| 4238 i | 0.2109 | 0.0201 | 0.1852 | 0.0179 | 0.1907 | 0.0148 |
| 4238 o | 0.1619 | 0.0178 | 0.1608 | 0.0165 | 0.1613 | 0.0086 |
| 5615 i | 0.2628 | 0.0344 | 0.2383 | 0.0309 | 0.1992 | 0.0280 |
| 5725 i | 0.1903 | 0.0361 | 0.1802 | 0.0303 | 0.1266 | 0.0361 |
| 5725 o | 0.1551 | 0.0400 | 0.1814 | 0.0373 | 0.1554 | 0.0225 |
| 5743 o | 0.2040 | 0.0376 | 0.1775 | 0.0338 | 0.1407 | 0.0220 |

also become polarized. In addition, there is an approximately 2% contamination of ¹⁴N, which is also polarizable. Moreover, a small percentage of residual nuclei such as NH₃ and ND₂H₁ also introduce polarizable nucleons. Although the effect of the polarized background on the measured asymmetry is small, it should be considered as one of the correction factors. In order to correct for the polarized background, we followed the prescription developed by [118]. The general form of the correction can be written as:

$$A_{\parallel}^{corr} = C_1 (A_{\parallel} - C_2), \quad (386)$$

where A_{\parallel}^{corr} is the asymmetry due only to the polarized deuterons (or protons) in the target material. A_{\parallel} represents the asymmetry after the dilution factor and the beam \times target polarization corrections were applied. At this point, radiative corrections have not yet been applied to A_{\parallel} . The multiplicative factor C_1 stands as a weight factor for additional polarized nucleons of the same type as the intended target. The additive factor C_2 corrects for the asymmetry introduced by nucleons of a type other than the intended target.

Corrections on the deuteron target

In case of the deuteron, the correction factors in Eq. (386) can be written as [118]:

$$C_1^d = \frac{1}{1 - \eta_p + D_n/(1 - 1.5w_D)} \approx 1.02, \quad (387)$$

$$C_2^d = \frac{\sigma_p}{\sigma_d}(D_n - D_p)A_p \approx -0.03A_p, \quad (388)$$

where A_p is the proton asymmetry, $A_{||}(Q^2, W)$, with all corrections applied, except for the radiative correction. The term w_D corrects for the D-state contribution to the deuteron. The remaining terms are defined as:

$$\eta_p = \frac{\text{number of protons}}{\text{number of protons} + \text{number of deuterons}} \approx 0.015, \quad (389)$$

$$D_n = \eta_N \frac{P_N g_{EMC}}{P_d 9} \quad (390)$$

$$D_p = \eta_p \frac{P_p}{P_d} + (2\eta_N - 1) \frac{P_N g_{EMC}}{P_d 9} \quad (391)$$

$$\eta_N = \frac{\text{number of } ^{14}\text{N}}{\text{number of } ^{14}\text{N} + \text{number of } ^{15}\text{N}} \approx 0.02, \quad (392)$$

where the values of the η_p and η_N comes from general expectations for a typical target. The η_p , for example, assumes approximately 4.5% of the ND_3 molecules are actually ND_2H_1 , giving rise to proton impurities in the target. The factor g_{EMC} is the correction for the EMC effect,

$$g_{EMC}^{^{15}\text{N}} \approx g_{EMC}^{^{14}\text{N}} \equiv g_{EMC} \approx 1, \quad (393)$$

which is just a crude approximation but its uncertainty, together with the uncertainty of the other factors, is considered in the systematic error calculations. The factors P_d , P_p , P_N represent the corresponding polarizations of the deuteron, proton and nitrogen targets respectively. The nitrogen polarizations are given by,

$$P_{^{15}\text{N}} \approx -P_{^{14}\text{N}} \equiv P_N = -0.40P_d. \quad (394)$$

while the proton polarization is:

$$P_p = \begin{cases} 0.191 + 0.683P_d & \text{for } P_d > 0.16 \\ 1.875P_d & \text{for } P_d \leq 0.16 \end{cases}$$

Although the effect of the factor C_1^d is very minor, the factor C_2^d becomes important since it is multiplied by the proton asymmetry. The overall correction is

approximately 3 to 5% of the asymmetry. The uncertainties in the values of the correction factors, C_1^d and C_2^d , are considered as part of our systematic error calculations. For the proton asymmetries, initially the radiated asymmetries from the EG1b NH₃ target were used since for each beam energy for the deuteron, there is a corresponding data set on the proton and they are analyzed together in parallel. On the other hand, using the data has the disadvantage that the statistical error on the proton measurements directly propagate into the statistical error on the deuteron measurements. Even though this is a very small effect, instead of using data, we also tried using the model for the proton asymmetry. When using the model, the error on the proton asymmetry is set to zero, therefore the statistical error on the deuteron data is not affected by the statistical uncertainty of the proton measurements. Since the final model inputs agree with the proton data at a very good level, we eventually decided to use the model values for the proton asymmetry while applying the polarized background correction to the deuteron.

Corrections on the proton target

In the case of the NH₃ target, the main contribution to the measured proton asymmetry comes from the unpaired “quasi-free” protons in the ¹⁵N nuclei. Because of its negative magnetic moment, the ¹⁵N nucleus polarizes in the opposite direction of the target-protons. But the unpaired proton in the ¹⁵N is expected to be “anti-aligned” with the nuclear spin with a relative polarization of -1/3. Therefore, the polarization of the quasi-free proton in the ¹⁵N adds positively to the total polarization of the target-protons.

The correction factors in Eq. (386) can be written explicitly for the NH₃ target as¹⁸,

$$C_1^p = \left[1 - \frac{1}{3} \frac{P_N}{P_p} \right]^{-1}, \quad C_2^p \approx 0, \quad (395)$$

where P_N and P_p represent nitrogen and target-proton polarizations, respectively. The term $-1/3$ in the C_1^p is the Clebsch-Gordan coefficient, representing the relative polarization of the quasi-free proton in ¹⁵N. The second $1/3$ term is there because the ammonia target has three hydrogen atoms for each nitrogen molecule. Other polarized nucleons might enter from the small amount of ¹⁴N present in the target material. This would enter via a C_2^p term; however, in our case this contribution was

¹⁸The factor $g_{EMC}(x)$ for EMC effect is neglected, since its effect is negligible for this correction.

negligible and its estimated effect is considered as a systematic error.

In order to calculate C_1^p , we need to know the nitrogen polarization. A fit was developed by the E143 collaboration [118] to express the ^{15}N polarization, P_N , in terms of the proton polarization, P_p , in the NH_3 target:

$$P_{^{15}\text{N}} = -(0.136P_p - 0.183P_p^2 + 0.335P_p^3). \quad (396)$$

In order to obtain the quantitative form of the correction, we express A_{\parallel} in terms of the raw asymmetry divided by the dilution factor and the beam \times target polarization,

$$A_{\parallel} = \frac{A_{\text{raw}}}{F_D P_b P_p}. \quad (397)$$

Using this for the uncorrected asymmetry in Eq. (386), and expressing the C_1^p term as given in Eq. (395), the corrected proton asymmetry can be written as

$$A_p = \frac{A_{\text{raw}}}{F_D P_b (P_p - \frac{1}{3} \frac{1}{3} P_N)}, \quad (398)$$

which means that the effective target polarization is increased by the amount $|\frac{1}{3}\frac{1}{3}P_N|$. For the implementation of this corrections, we used $P_p = P_b P_t / P_b$, where $P_b P_t$ values were obtained as described in section IV.13 and P_b is the Møller polarization averaged over all runs within the same data set. In general, this correction is on the order of the statistical errors on the extracted $P_b P_t$ values. Detailed information on the polarized background corrections for the proton target is given in [95].

IV.15 RADIATIVE CORRECTIONS

In the experiment, our goal is to extract asymmetries for a single photon exchange process, which is also called Born scattering. However, there are higher order QED processes contributing to the measured asymmetries. These contributions are removed by the radiative corrections. The corrections can be examined in two main categories: internal and external radiative corrections.

The internal radiative corrections account for higher order QED processes that may occur during the interaction. These include internal Bremsstrahlung, where the incoming or the scattered electron emits a photon; vertex correction, in which a photon exchange occurs between the incoming and the scattered electron; and vacuum polarization of the virtual exchange photon. The correction for the internal

radiative effects can be calculated by adding the cross sections of each higher order process to the Born cross section [119].

The external radiative corrections [120] account for the energy loss of the electron while passing through the detector field and the target material mainly by the Bremsstrahlung process. As an electron traverses the target it can radiate a real photon, which changes the energy of the scattering process. The resulting energy loss may affect the kinematic calculations. The effect becomes especially important for elastic scattering because the elastic cross section grows rapidly as the beam energy decreases, which increases the probability for radiation of a high energy photon followed by elastic scattering. This creates a radiative elastic tail extending from the elastic peak into the inelastic region. The corrections depend on the experimental conditions.

For the radiative corrections in the EG1b experiment, an iterative, model dependent program called RCSLACPOL was used. For detailed information on the incorporation of the internal and external radiative effects into this software, the reader is referred to [119][120][121]. The program creates a multiplicative and an additive correction term, $1/f_{RC}$ and A_{RC} . These correction terms were generated for each beam energy in our standard (Q^2, W) bins. The correction is applied to the asymmetry A_{\parallel} , as the last correction before the calculation of the virtual photon asymmetries,

$$A_{\parallel}^{Born} = \frac{A_{\parallel}^{corr}}{f_{RC}} + A_{RC}. \quad (399)$$

The additive term, A_{RC} , corrects for the quasi-elastic radiative tail as well as the inelastic tail and is negative for the big majority of our kinematics. The multiplicative term, $1/f_{RC}$, which is always larger than 1, corrects for the radiative elastic tail underneath the inelastic region. Since $0 \leq f_{RC} \leq 1$, we can interpret the measured asymmetry consisting of a fraction f_{RC} of the true asymmetry and a fraction $1 - f_{RC}$ of the contaminating asymmetry. Therefore, this term takes into account the additional dilution caused by the internal and external radiations. Using a multiplicative factor also provides a way to properly propagate the statistical errors.

IV.16 MODEL INPUT

Knowledge of the structure functions F_1 and R as well as the virtual photon asymmetry A_2 is necessary to extract the physics quantities of interest, namely A_1 and

g_1 , from the EG1b data. Moreover, the deep inelastic contributions to the integral over g_1 are required for a full evaluation of the moments. Eqs. (447-452) provide a brief summary of these calculations and the usage of these quantities.

Parameterizations based on the existing world data were used for these quantities that are required but not measured in this experiment. A package program, developed by S. Kuhn *et al.*, generates models of all physics quantities of interest based on world data parameterizations and current theoretical knowledge. This program was used to generate the models for A_2 , F_1 and R as well as A_1 and g_1 , which are mainly used for comparisons to the our final experimental results. Then, the experimental results, in an iterative approach, can be used to refine these models.

The models are under continues development as new data come to exist on the asymmetries and the structure functions. Especially the models on A_1 and A_2 in the resonance region went through rigorous upgrade with the inclusion of many experiments, including EG1b. Studies on the parameterizations of the virtual photon asymmetries in the resonance region are provided in chapter VI. The first part of this section describes the models of the unpolarized structure functions. In the second part, we will give the current status of the virtual photon asymmetries in the DIS region.

IV.16.1 Models of the unpolarized structure functions for the deuteron

The F_1 model is used for the calculation of g_1 from the virtual photon asymmetries, according to Eq. (64). The model for $R = \sigma^L/\sigma^T$, the ratio of longitudinal to transverse cross-sections for unpolarized scattering (see Eqs. (60) and (70)), is used for calculation of the depolarization factor D , given in Eq. 29. Also, the same models are used, while processing the data, for the parametrization studies on the spin structure functions and asymmetries in chapter VI.

The most detailed information on the models for the unpolarized structure functions of the deuteron can be found in [122]. The calculations of R , F_1 and F_2 all follow from fits to the world data for the total transverse (σ^T) and longitudinal (σ^L) cross sections (see Eqs. (56 - 60)). Inelastic electron scattering on the deuteron can be divided into two distinct contributions: quasi-elastic and inelastic scattering. The unpolarized structure functions were modeled separately for these two regimes.

In the quasi-elastic region, PWIA Fermi smearing based on the pre-integrated Paris wave function was used by replacing the continuous inelastic cross-section with

a δ -function elastic cross section at $W = M_p$. The elastic cross-section was calculated using the nucleon form factors modified for off-shell effects and taking Pauli suppression into account.

In the inelastic region, a fit was performed by using the world data for the electro-production cross section measurements and minimizing χ^2 defined by [122]

$$\chi^2 = \sum_{i=1}^N [\sigma_i(W_i, Q_i^2) - \sigma_D^T(W, Q^2)]^2 / [\delta\sigma_i(W_i, Q_i^2)]^2 \quad (400)$$

where the sum is over all experimental points with transverse inelastic cross section $\sigma_i(W_i, Q_i^2)$ and total statistical and systematic error $\delta\sigma_i(W_i, Q_i^2)$. Since the fit was performed for inelastic scattering only, the quasi elastic contribution was subtracted from data prior to the fit. In addition, because of limited kinematics of the longitudinal cross section measurements on the deuteron, the fit was performed only to the transverse portion of the cross section. The transverse cross section was extracted from data by using

$$\sigma_D^T = \sigma_D^r / (1 + \epsilon R_D), \quad (401)$$

where ϵ is the relative polarization of the virtual photon and σ_D^r is reduced cross section defined as

$$\sigma^r = \sigma^T(W, Q^2) + \epsilon\sigma^L(W, Q^2). \quad (402)$$

An assumption was made that $R_p = R_n$ and R_D was evaluated by Fermi smearing σ_p^L and σ_p^t , which were obtained from proton model [123]. It was concluded that the effect of Fermi smearing is small for most kinematics of interest and $R_D = R_p$ to a good approximation. The model cross section $\sigma_D^T(W, Q^2)$ was defined in terms of the average free nucleon transverse cross section, $\sigma_N^T = (\sigma_p^T + \sigma_n^T)/2$, with Fermi motion taken into account in the Plane Wave Impulse Approximation [122]:

$$\sigma_D^T(W, Q^2) = \sigma_{dip}(W, Q^2) + \int \sigma_N^T(W', (Q^2)') \Phi^2(\vec{k}) d^3\vec{k} \quad (403)$$

where the integral is over the Fermi momentum \vec{k} and integrates the deuteron wave function $\Phi^2(\vec{k})$ times the average free nucleon transverse cross section $\sigma_N^T(W, Q^2)$. The term σ_{dip} is an additional parametrization for the dip region between the quasi-elastic peak and the $\Delta(1232)$ resonance. This dip region had to be treated with extra parameters to account for meson exchange currents and final state interactions.

In the DIS region, the parametrization from the NMC collaboration was used [124], which is a 15 parameter fit to F_2 , by using inclusive muon scattering in the

kinematic range $0.006 < x < 0.6$ and Q^2 from 0.5 to 75 GeV² together with existing world data at that time. As a reference, plots for R and F_1 models of the deuteron are shown for various Q^2 bins in Fig. 109.

IV.16.2 Models of A_1 and A_2 in the DIS region

The proton and neutron models for A_1 in the DIS region were produced by parameterizing the world data. The A_1^p parametrization included data from EMC [6], SMC [44], E143 [45], E155 [47], HERMES [48], EG1a [68] and EG1b [17]. The A_1^n parametrization included data from measurements on ³He targets (E142 [43], E154 [46], HERMES [48] and Hall-A [70]) as well as ND₃ targets (E143 [45], E155 [47], HERMES [48], SMC [44], COMPASS [49], EG1a [67] and EG1b [50]). We also used real photon data from ELSA [125][126] and MAMI [127] for both parameterizations to constrain the fit as $Q^2 \rightarrow 0$. The data on A_1^n were used as presented by the experiments with the ³He target. In order to extract neutron data from ND₃ measurements, we used the simplified assumption:

$$A_1^d = (1 - 1.5w_D) \left[\frac{F_1^p A_1^p + F_1^n A_1^n}{F_1^p + F_1^n} \right] \quad (404)$$

and solved the equation for A_1^n using models for A_1^p and the unpolarized structure functions $F_1^{p,n}$. In the end, the A_1^p fit utilized the following parametrization:

$$A_1^p = \xi^{P_1 + P_2 \tan^{-1}(P_3^2 Q^2)} [1 + (P_4 + P_5 \tan^{-1}(P_6^2 Q^2)) \sin(\pi \xi^{P_7})], \quad (405)$$

while the parametrization for A_1^n was

$$A_1^n = \xi^{P_1} [(P_2 + P_3 \tan^{-1}(P_4^2 Q^2)) \sin(\pi \xi^{P_5}) - \cos(\pi \xi^{P_6})], \quad (406)$$

where P_i represents parameter i . We also allowed the overall scale of each experiment to vary within the stated systematic error by employing additional parameters for each experiment. The kinematic variable ξ in the parameterizations was defined by

$$\xi = \frac{Q^2 + (M + M_\pi)^2 - M^2}{M(\nu + \sqrt{\nu^2 + Q^2})}, \quad (407)$$

where M is the nucleon mass and M_π is the mass of the $\pi^0 = 0.135$ GeV/ c^2 . The error on the fit was calculated by using the error matrix E_k^j determined by the minimization routine such that $\delta A_1 = \partial_j E_k^j \partial^k$, where $\partial_i = \partial A_1 / \partial P_i$ is the derivative of A_1 with respect to parameter P_i , and summation is implied over repeating indexes. Fig. 110

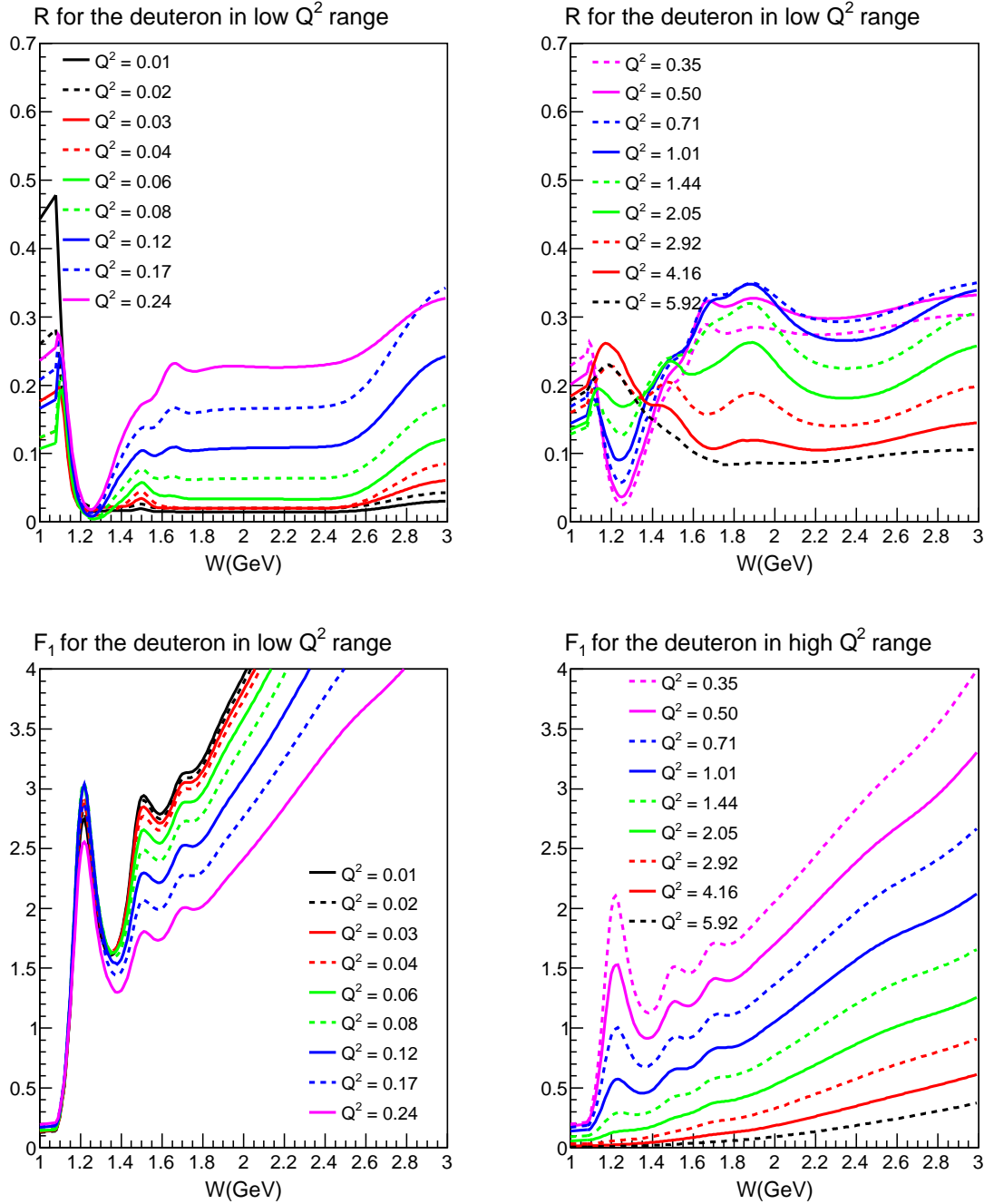


FIG. 109: The models for R (top) and F_1 (bottom) for the deuteron are shown for various Q^2 bins.

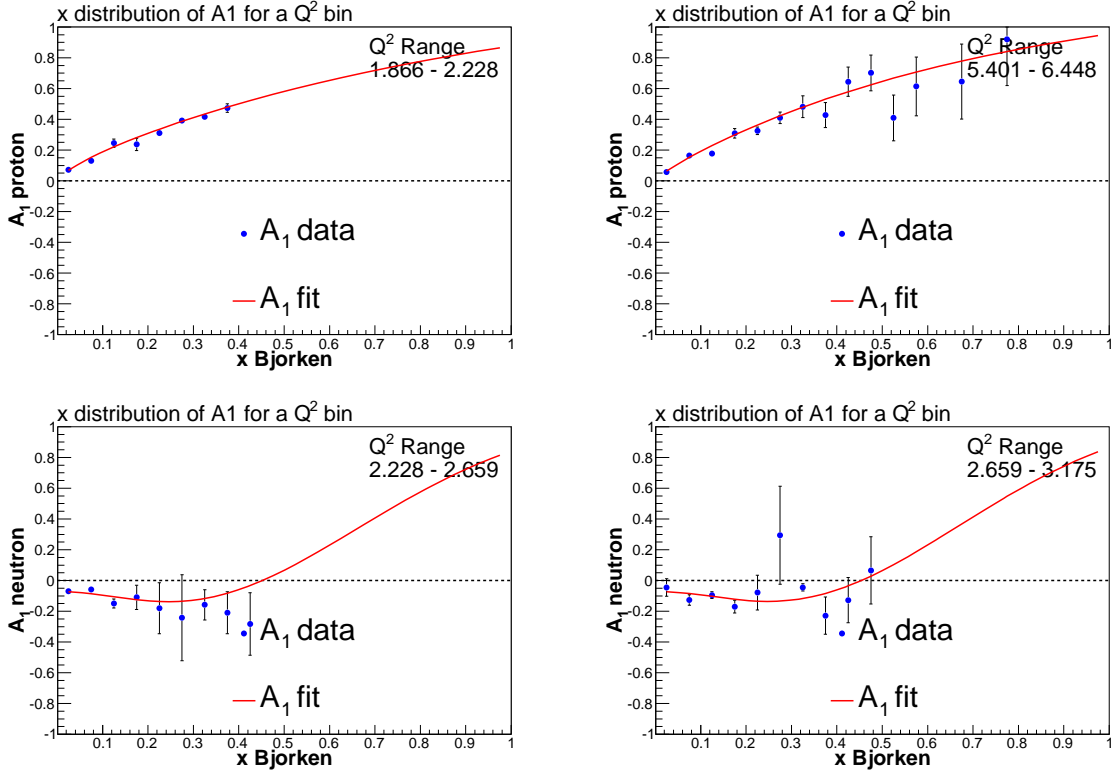


FIG. 110: The A_1 fits in the DIS region for the proton (top) and neutron (bottom).

shows some results for both A_1^p and A_1^n fits. Afterwards, the deuteron model was obtained by using Eq. (404), with the corresponding error calculated by

$$\delta A_1^d = \frac{1 - 1.5w_D}{F_1^p + F_1^n} [(F_1^p)^2(\delta A_1^p)^2 + (F_1^n)^2(\delta A_1^n)^2]^{1/2}. \quad (408)$$

A_2 in the DIS region was calculated by employing the Eq. (63) and using the the *Wandzura-Wilczek* [7] relation for g_2^{WW} , which yields

$$A_2 = \gamma \frac{g_T^{WW}}{F_1} \quad (409)$$

where F_1 comes from our model and g_T^{WW} was calculated by solving

$$g_T^{WW} = \int_x^1 \frac{g_1}{y} dy \quad (410)$$

iteratively in terms of our A_1 and F_1 models, without considering the higher twist contributions. The higher twist contributions were taken into account for the systematic error on the model by including twist-3 calculations. After the calculations

of both A_2^p and A_2^n , the asymmetry A_2^d for the deuteron was determined as a weighted sum of the two by using F_1 as a weight factor (similar to Eq. (404)).

In order to ensure a smooth transition between the resonance and the DIS regions, the parameterizations for A_1 and A_2 in the DIS region were later used for parameterizations in the resonance region by employing their extrapolation. This will be described in chapter VI in more detail.

IV.17 COMBINING DATA FROM DIFFERENT CONFIGURATIONS

Extraction of the most precise information on the asymmetries and the structure functions from a set of heterogeneous runs in the EG1b data requires a solid methodology to combine the data sets from different configurations. During the experiment, several runs of data were taken with each possible combination of a set of parameters that determine the kinematic reach and the overall scale of the measured asymmetries. We want to combine all this information into the quantities of interest (e.g., $A_1 + \eta A_2$) for each of our standard W and Q^2 bins, while minimizing the final statistical error. The parameters that can possibly vary from one run to the next are:

1. Beam energy
2. Torus polarity
3. Target material and polarization (including direction of polarization, along (+) or opposite (−) to the beam direction)
4. $\lambda/2$ -plate status (in = 1 or out = 0)

It should be noted that even a small change in the beam energy can correspond to a different setting of injector optics, resulting potentially in a reversal of beam polarization. After considering various possibilities on how to combine runs with different run parameters, the following scheme was selected for the *double-spin asymmetry* analysis of the EG1b data.

IV.17.1 Combining runs

All runs belonging to the same beam energy, torus current (including sign) and target polarization (including sign) should be combined to calculate the first set of raw asymmetries, $A_{raw}(W, Q^2)$, for each kinematic bin. This means summing

over several runs, *including* runs with opposite status of the “half-wavelength” ($\lambda/2$) plate. Such a set of runs is called a *group*, “ G ”. The advantage of summing over a relatively large set of runs is that the asymmetries for each bin will be distributed more like a Gaussian around the “true” values, with errors that are not excessively large in general. This makes combining such asymmetries more straightforward and less error-prone.

While performing this summation, we define, for each bin, the two quantities N_0 and N_1 , which are the total inclusive counts for the two helicities, as well as the quantities FC_0 and FC_1 , the corresponding accumulated beam charges for both counts. For each event passing all cuts, we increase the counter N_0 for two cases:

1. the helicity label is 0 and the status of the $\lambda/2$ plate is 0 (“out”)
2. the helicity label is 1 and the status of the $\lambda/2$ plate is 1 (“in”),

for the given run from which the event came. In the two remaining cases, the counter N_1 is increased. Similarly, for each run the counters FC_0 and FC_1 are increased according to the life-time gated Faraday Cup scalar sums for the two helicities, again after reversing the correspondence of helicity labels if the status of the $\lambda/2$ plate is 1. After summing over all runs within a group, the asymmetry in a given bin is then calculated as:

$$A_{raw}^G(W, Q^2) = \frac{N_0 - (FC_0/FC_1)N_1}{N_0 + (FC_0/FC_1)N_1}. \quad (411)$$

The error on the asymmetry is, to a very good approximation, given by

$$\sigma_{A_{raw}^G}(W, Q^2) = \sqrt{\frac{1}{N_0 + N_1}}. \quad (412)$$

At the same time, for future reference, we also need to determine the averaged values of several kinematic variables for each of the bins. Those variables are Q^2 , ν and

$$W = (M^2 + 2M\nu - Q^2)^{1/2} \quad (413)$$

$$E' = E - (W^2 - M^2 + Q^2)/2M \quad (414)$$

$$x = Q^2/2M\nu \quad (415)$$

$$\gamma = \sqrt{Q^2}/\nu \quad (416)$$

$$\theta = \tan^{-1} \left(\sqrt{p_x^2 + p_y^2}/p_z \right) \quad (417)$$

$$\epsilon = \frac{2EE' - Q^2/2}{E^2 + E'^2 + Q^2/2} \quad (418)$$

$$\eta = \frac{\epsilon\sqrt{Q^2}/E}{1 - \epsilon E'/E}. \quad (419)$$

The averages of these kinematic variables for a given bin in Q^2 and W are calculated by simply calculating the quantity in question for each event in the bin, summing over all events within a group, and then dividing by the number of events in the bin for the group.

IV.17.2 Weighting of Asymmetries

While combining the asymmetries from different groups, we must give them different weights according to their overall statistical precision. For the next step, we will combine asymmetries with opposite target polarizations, but with the same combination of beam energy and torus current. Since we know that the two opposite target polarizations can have rather significant differences in magnitude, we need to determine a proper weighting factor for each set so that the relative polarizations can be correctly propagated into the combined result. This was managed by using the P_{rel}^G defined in section IV.13.4.

IV.17.3 t-Test

Before combining two different groups with opposite target polarizations, we first want to ascertain whether their individual results are statistically compatible with each other. This allows us to discover previously unknown problems with particular groups (e.g., vastly different dilution factors), as well as showing us at what level *single spin* asymmetries might be present. The method for this comparison is a t-test. For each kinematic bin, we define

$$t(W, Q^2) = \frac{A_{raw}^{G1}/P_{rel}^{G1} - A_{raw}^{G2}/P_{rel}^{G2}}{\sqrt{\sigma_{A_{raw}^{G1}}^2/(P_{rel}^{G1})^2 + \sigma_{A_{raw}^{G2}}^2/(P_{rel}^{G2})^2}}. \quad (420)$$

If the fluctuations between group 1 and group 2 are purely statistical, we expect that the distribution of t for the different bins is Gaussian with a mean of zero and a standard deviation of 1. This can be tested by calculating the average t , averaged over all bins, and the standard deviation of the t 's, which is simply given by

$$\sigma(t) = \sqrt{\sum_{bins} t^2 / N_{bins}}. \quad (421)$$

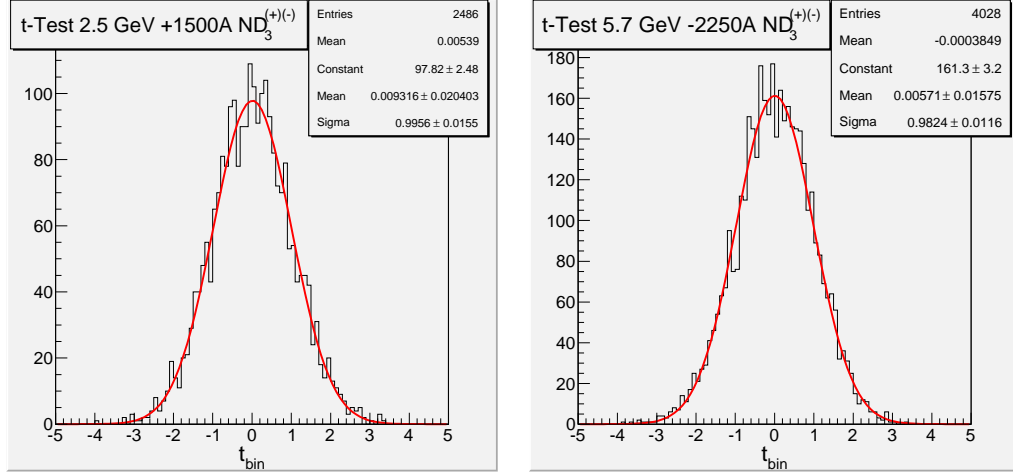


FIG. 111: Plots showing the distribution of $t(W, Q^2)$, in Eq. (420), for the t-Test between data sets with opposite target polarizations.

This latter quantity is equivalent to χ^2 and should not exceed 1 significantly. The mean t should be zero within the error on the mean, which is simply $1/\sqrt{N_{bins}}$. Large deviations from these expectations suggest that additional scrutiny of the two groups in question is warranted. Fig. 111 shows sample plots from the t-tests for 2.5 and 5.7 GeV data sets.

IV.17.4 Combining opposite target polarizations

Finally, we can combine the two groups with opposite target polarizations bin by bin by once again weighting the asymmetries with their statistical weight, including the preliminary approximate $P_b P_t$ of each group. In order to do this consistently, we define a relative weight as a single number for each of the two groups. The method we used here required us to simply add up the total number of counts (N_1 and N_0) for all bins of each group and call the sum N_{tot}^G :

$$N_{tot}^{G(1,2)} = \sum_{bins} \left[N_{0(bin)}^{G(1,2)} + N_{1(bin)}^{G(1,2)} \right]. \quad (422)$$

Then the relative weight for group 1 is

$$W_1 = \frac{N_{tot}^{G1} \times (P_{rel}^{G1})^2}{N_{tot}^{G1} \times (P_{rel}^{G1})^2 + N_{tot}^{G2} \times (P_{rel}^{G2})^2} \quad (423)$$

TABLE 46: t-Test results for combining sets with opposite target polarizations.

| Target | $E_{beam}(\text{GeV})(\text{Torus})$ | t_{ave} | σ_t | χ^2 | N_{bin} |
|-----------------|--------------------------------------|-----------|------------|----------|-----------|
| ND ₃ | 1606i | -0.0198 | 0.0238 | 1.01 | 1753 |
| ND ₃ | 1723o | 0.0128 | 0.0207 | 1.01 | 2314 |
| ND ₃ | 2561i | 0.0057 | 0.0200 | 1.01 | 2486 |
| ND ₃ | 2561o | 0.0023 | 0.0176 | 0.99 | 3213 |
| ND ₃ | 4238i | 0.0036 | 0.0185 | 0.99 | 2894 |
| ND ₃ | 4238o | 0.0364 | 0.0157 | 0.99 | 4047 |
| ND ₃ | 5615i | 0.0105 | 0.0179 | 1.00 | 3119 |
| ND ₃ | 5725i | 0.0001 | 0.0180 | 1.03 | 3056 |
| ND ₃ | 5725o | 0.0009 | 0.0157 | 0.99 | 4028 |
| ND ₃ | 5743o | 0.0168 | 0.0158 | 1.01 | 3990 |
| NH ₃ | 1606i | 0.0156 | 0.0238 | 1.02 | 1762 |
| NH ₃ | 1723o | -0.0099 | 0.0207 | 0.99 | 2328 |
| NH ₃ | 2286i | 0.0111 | 0.0206 | 0.99 | 2353 |
| NH ₃ | 2561o | -0.0159 | 0.0176 | 1.01 | 3202 |
| NH ₃ | 4238i | 0.0044 | 0.0184 | 0.98 | 2949 |
| NH ₃ | 4238o | 0.0074 | 0.0156 | 1.01 | 4079 |
| NH ₃ | 5615i | 0.0100 | 0.0181 | 1.00 | 3028 |
| NH ₃ | 5725i | 0.0001 | 0.0178 | 1.01 | 3152 |
| NH ₃ | 5725o | 0.0131 | 0.0156 | 1.01 | 4109 |
| NH ₃ | 5743o | -0.0094 | 0.0155 | 1.01 | 4151 |

and the weight of the second group, W_2 , is calculated the same way. Then, the average raw asymmetry of the two groups, for each bin, can be written as

$$A_{raw}^C(W, Q^2) = W_1 A_{raw}^{G1} - W_2 A_{raw}^{G2} \quad (424)$$

with a statistical error of

$$\sigma_{A_{raw}^C} = \sqrt{W_1^2 \sigma_{A_{raw}^{G1}}^2 + W_2^2 \sigma_{A_{raw}^{G2}}^2} \quad (425)$$

The difference instead of the sum in Eq. (424) takes into account the assumption that the target polarization for group 2 is negative, while it is positive for group 1. So, the overall result is actually a summation of the absolute values.

The result in Eq. (424) is the average raw asymmetry extracted from the 2 combined groups, with different statistical weights given to each of the groups. The average kinematic variables introduced earlier were also combined for each bin with the same statistical weights, but of course, one should be careful with the minus sign in Eq. (424) and replace it with a plus sign since kinematic values are always defined positive. The result for the 2 groups with opposite target polarizations combined is

referred to as a “set” in the following. The only difference between the sets is their beam energy and torus currents. Table 46 shows the results for the t-tests for all data sets.

Before continuing any further in combining runs, at this stage we converted the raw asymmetries by dividing out $P_b P_t$ and F_D for each set. In addition, the corrections for pion and pair-symmetric contaminations as well as the polarized background and the radiative corrections were all applied at this stage. Finally, the resulting values for $A_{||}^{Born}(W, Q^2)$ were converted to values for $A_1 + \eta A_2(W, Q^2)$ by dividing with the averaged D results (obtained from models) for each bin. All of these manipulations in principle depend on the beam energy and in case of contaminations, also on the torus polarity (see section IV.12). The values for $A_1 + \eta A_2$, for each bin, as well as the averaged kinematic variables and the count rates are propagated into the next step.

IV.17.5 Combining data with slightly different beam energies

At this stage we have 11 data sets for both targets. These sets are given in Table 5. Among these, there are sets with slightly different beam energies but the same torus current. These sets are:

- 1.606 GeV, $-1500A$; 1.723 GeV, $-1500A$
- 5.615 GeV, $+2250A$; 5.725 GeV, $+2250A$
- 5.725 GeV, $-2250A$; 5.743 GeV, $-2250A$

The values for $A_1 + \eta A_2 \equiv A_{12}$ are combined for these sets by taking their error weighted average for each kinematic bin,

$$A_{12}^{mean}(W, Q^2) = \frac{A_{12}^{G1}/\sigma_{A_{12}^{G1}}^2 + A_{12}^{G2}/\sigma_{A_{12}^{G2}}^2}{1/\sigma_{A_{12}^{G1}}^2 + 1/\sigma_{A_{12}^{G2}}^2}, \quad (426)$$

$$\sigma_{A_{12}^{mean}}(W, Q^2) = \left(\frac{1}{1/\sigma_{A_{12}^{G1}}^2 + 1/\sigma_{A_{12}^{G2}}^2} \right)^{1/2}. \quad (427)$$

The kinematic factor η does depend on the beam energy, however, it is very small for our kinematic region, which makes the combination of $A_1 + \eta A_2$ for slightly different beam energies possible. Moreover, we applied a z-test in order to make sure that

TABLE 47: z-Test results for combining data with slightly different beam energies.

| Target | E_{beam} (GeV) | z_{ave} | σ_z | χ^2 | N_{bin} |
|-----------------|------------------|-----------|------------|----------|-----------|
| ND ₃ | 1.606 - 1.723 | 0.0004 | 0.0230 | 0.98 | 1887 |
| ND ₃ | 5.615 - 5.725 | -0.0561 | 0.0197 | 0.99 | 2572 |
| ND ₃ | 5.725 - 5.743 | 0.0950 | 0.0169 | 0.98 | 3486 |
| NH ₃ | 1.606 - 1.723 | 0.0294 | 0.0234 | 1.02 | 1825 |
| NH ₃ | 5.615 - 5.725 | -0.0544 | 0.0201 | 0.98 | 2474 |
| NH ₃ | 5.725 - 5.743 | -0.0179 | 0.0172 | 1.00 | 3366 |

these data sets are compatible with each other for combining. The form of the z-test for this case is

$$z(w, Q^2) = \frac{A_{12}^{G1} - A_{12}^{G2}}{\sigma_{A_{12}^{G1}}^2 + \sigma_{A_{12}^{G2}}^2} \quad (428)$$

for each of the overlapping kinematic bin. The average z-score,

$$z_{ave} = \frac{\sum_{w, Q^2} z(w, Q^2)}{N} \quad \sigma_{z_{ave}} = \sqrt{\frac{1}{N}} \quad (429)$$

and the χ^2 values

$$\chi^2 = \left[\frac{\sum_{w, Q^2} z^2(w, Q^2)}{N} \right]^{1/2} \quad (430)$$

are monitored for each combination. Table 47 provides the overall result of this test.

We also propagated the kinematic variables and the count rates to the next step. The kinematic variables are averaged between the two data sets by using the total counts for each set as a weighting factor, e.g.,

$$\langle Q^2 \rangle = \frac{Q_{G1}^2 N_{G1} + Q_{G2}^2 N_{G2}}{N_{G1} + N_{G2}}. \quad (431)$$

IV.17.6 Combining data sets with opposite torus polarities

Opposite torus polarities for the same beam energy do not have any effect on the values of $A_1 + \eta A_2$. Therefore they can safely be combined in a straightforward way, taking error weighted averages. Therefore, we followed exactly the same prescription outlined in the previous section, using Eqs. (426) and (427). Again, we performed a z-test for each pair of data sets combined. Table 48 provides the results.

TABLE 48: z-Test results for combining sets of opposite torus polarity.

| Target | E_{beam} (GeV)(Torus) | z_{ave} | σ_z | χ^2 | N_{bin} |
|-----------------|-------------------------|-----------|------------|----------|-----------|
| ND ₃ | 1.6(+)-1.6(-) | -0.0468 | 0.0276 | 0.97 | 1310 |
| ND ₃ | 2.5(+)-2.5(-) | -0.0290 | 0.0237 | 0.98 | 1778 |
| ND ₃ | 4.2(+)-4.2(-) | -0.0256 | 0.0215 | 0.99 | 2162 |
| ND ₃ | 5.7(+)-5.7(-) | -0.0268 | 0.0193 | 0.98 | 2683 |
| NH ₃ | 1.6(+)-1.6(-) | 0.1492 | 0.0281 | 1.05 | 1258 |
| NH ₃ | 2.4(+)-2.5(-) | -0.0722 | 0.0237 | 1.04 | 1768 |
| NH ₃ | 4.2(+)-4.2(-) | -0.0143 | 0.0222 | 1.00 | 2028 |
| NH ₃ | 5.7(+)-5.7(-) | 0.1240 | 0.0196 | 1.02 | 2585 |

At this point, before combining data sets with different beam energies, we need to extract A_1 and g_1 by using models for A_2 and F_1 ,

$$A_1(W, Q^2) = [A_1 + \eta A_2](W, Q^2) - \langle \eta \rangle A_2^{model}(W, Q^2) \quad (432)$$

$$g_1(W, Q^2) = \frac{F_1^{model}(W, Q^2)}{1 + \langle Q^2 \rangle / \langle \nu \rangle^2} \left[A_1(W, Q^2) + \frac{\sqrt{\langle Q^2 \rangle}}{\langle \nu \rangle} A_2^{model}(W, Q^2) \right]. \quad (433)$$

These values, again, together with the kinematic variables, averaged according to Eq. (431), and the count rates for each bin are propagated to the next level of analysis.

IV.17.7 Combining data sets with different beam energies

At this point we have 4 independent data sets, which we can label E^1 , E^2 , E^4 and E^5 , corresponding to 1.x, 2.x, 4.x and 5.x GeV data sets. In each set, we have A_1 , g_1 , kinematic variables and the count rates for each bin. The A_1 and the g_1 values from different sets can be combined by taking their error weighted averages. The kinematic variables are, again, combined by weighting them with corresponding count rates in each bin. In this way, the data sets were combined, two at a time: first combining E^1 and E^2 , then combining $E^{(1:2)}$ with E^4 and finally combining $E^{(1:2:4)}$ with E^5 . We performed a z-test between each individual data set, as well as between the combined and the individual data sets. The results are given in Table 49.

As a result, all data are combined into a single set, consisting of A_1 and g_1 values, as well as the properly averaged kinematic variables and the count rates, for W and Q^2 bins. In the next section, we will summarize the corrections applied on the asymmetries and describe how we propagated the statistical errors after each

TABLE 49: z-Test results for combining data sets with different beam energies.

| Target | Beam Sets | z_{ave} | σ_z | χ^2 | N_{bin} |
|-----------------|-------------------|-----------|------------|----------|-----------|
| ND ₃ | E^1-E^2 | 0.126 | 0.024 | 1.01 | 1666 |
| ND ₃ | E^2-E^4 | -0.021 | 0.024 | 1.00 | 1727 |
| ND ₃ | E^4-E^5 | 0.093 | 0.019 | 0.99 | 2699 |
| ND ₃ | E^2-E^5 | 0.095 | 0.031 | 1.02 | 1033 |
| ND ₃ | E^1-E^4 | 0.104 | 0.035 | 1.03 | 788 |
| ND ₃ | $E^{(1:2)}-E^4$ | 0.003 | 0.024 | 1.00 | 1732 |
| ND ₃ | $E^{(1:2:4)}-E^5$ | 0.093 | 0.019 | 0.96 | 2719 |
| NH ₃ | E^1-E^2 | 0.105 | 0.024 | 1.10 | 1616 |
| NH ₃ | E^2-E^4 | -0.055 | 0.025 | 1.10 | 1519 |
| NH ₃ | E^4-E^5 | 0.161 | 0.019 | 1.03 | 2593 |
| NH ₃ | E^2-E^5 | 0.125 | 0.033 | 1.06 | 871 |
| NH ₃ | E^1-E^4 | 0.098 | 0.037 | 1.16 | 729 |
| NH ₃ | $E^{(1:2)}-E^4$ | -0.045 | 0.025 | 1.07 | 1524 |
| NH ₃ | $E^{(1:2:4)}-E^5$ | 0.151 | 0.019 | 1.01 | 2639 |

correction. Then we will outline the systematic errors and the final results for these quantities, as well as the other quantities of interest, are presented in chapter V.

IV.17.8 Combining W bins for plotting

Our final results are created as a function of Q^2 and W . Section IV.6 explains the kinematic values of our standard Q^2 and W bins. On the other hand, while demonstrating the results for various quantities, it is generally better to combine a few W bins and plot the average result in a larger kinematic range for better visibility. Therefore, we combined data in standard W bins within a $\Delta W = 40$ MeV range and plot the average results. For this purpose, the data from standard W bins were combined by taking their error weighted average:

$$\bar{x} = \frac{\sum_i x_i/\sigma_i^2}{\sum_i 1/\sigma_i^2} \quad (434)$$

$$\sigma_{\bar{x}}^2 = \frac{1}{\sum_i 1/\sigma_i^2} \quad (435)$$

where summation is performed within $\Delta W = 40$ MeV range. It should be pointed out that this kind of combination was only made for the data and its statistical error.

We utilized a different method for the systematic errors, which will be explained in section IV.19.

IV.18 PHYSICS QUANTITIES AND PROPAGATION OF THE STATISTICAL ERRORS

The raw asymmetry is calculated from the count rates:

$$A_{raw}(Q^2, W) = \frac{N^+ - R_{FC}N^-}{N^+ + R_{FC}N^-} \quad (436)$$

where N^+ and N^- are total inclusive counts, for each bin, corresponding to the positive and negative helicity configurations, respectively. The quantity R_{FC} is the normalization factor,

$$R_{FC} = \frac{FC^+}{FC^-} \quad (437)$$

which is the ratio of accumulated Faraday cup charges for these helicity configurations. The statistical error on the raw asymmetry is given by

$$\Delta A_{raw} = \frac{2R_{FC}N^+N^-}{N^+ + R_{FC}N^-} \sqrt{\frac{1}{N^+} + \frac{1}{N^-}} \quad (438)$$

Later, pion and pair symmetric contaminations are determined. Since the pion contamination is small, it is only treated as a systematic error in the final results. The pair symmetric correction is applied to the raw asymmetry,

$$A_{corr} = A_{raw}C_{back} = A_{raw} \frac{1 - RA^{pos}/A_{raw}}{1 - R} = \frac{A_{raw} - RA^{pos}}{1 - R} \quad (439)$$

where R is the e^+/e^- ratio and A^{pos} is the positron raw asymmetry. The error on this quantity propagates as

$$\Delta A_{corr} = \sqrt{\frac{(\Delta A_{raw})^2 + R^2(\Delta A^{pos})^2}{(1 - R)^2}} \quad (440)$$

The next step in the analysis is to determine the dilution factor, F_D , and the beam \times target polarization, P_bP_t . The asymmetry corrected for these effects is

$$A_{\parallel}^{raw} = \frac{A_{corr}}{F_D P_b P_t}. \quad (441)$$

Although extraction of these quantities have their own statistical and systematic uncertainties, they are treated as part of our systematic error calculations. Thus,

their uncertainties do not enter into the statistical error of the final results. The error on the A_{\parallel}^{raw} is written as

$$\Delta A_{\parallel}^{raw} = \frac{\Delta A_{corr}}{F_D P_b P_t}. \quad (442)$$

Then we apply the polarized background corrections,

$$A_{\parallel}^{corr} = C_1 (A_{\parallel}^{raw} - C_2 A_p) \quad (443)$$

where A_p is the un-radiated proton asymmetry. The statistical error becomes

$$\Delta A_{\parallel}^{corr} = C_1 (\Delta A_{\parallel}^{raw} - C_2 \Delta A_p) \quad (444)$$

with the factors C_1 and C_2 described in section IV.14. Finally, radiative corrections are applied in the following form,

$$A_{\parallel}^{Born} = \frac{A_{\parallel}^{corr}}{f_{RC}} + A_{RC}, \quad (445)$$

and the statistical error becomes:

$$\Delta A_{\parallel}^{Born} = \frac{\Delta A_{\parallel}^{corr}}{f_{RC}}. \quad (446)$$

After all corrections described in the preceding sections, the final form of the corrected asymmetry, $A_{\parallel} \equiv A_{\parallel}^{Born}$, can be written as:

$$A_{\parallel} = \frac{C_1}{f_{RC}} \left(\frac{A_{raw}}{F_D P_b P_t} C_{back} - C_2 \right) + A_{RC}. \quad (447)$$

In the next stage, we can calculate the virtual photon asymmetry A_1 :

$$A_1 = \frac{A_{\parallel}}{D} - \eta A_2, \quad (448)$$

where D is the depolarization factor described earlier. The statistical error on the virtual photon asymmetry is calculated as:

$$\Delta A_1 = \frac{\Delta A_{\parallel}}{D}. \quad (449)$$

The spin structure function g_1 is given by

$$g_1 = \frac{F_1}{1 + \gamma^2} \left[\frac{A_{\parallel}}{D} + (\gamma - \eta) A_2 \right]. \quad (450)$$

The statistical error associated with the g_1 is

$$\Delta g_1 = \frac{F_1}{1 + \gamma^2} \left[\frac{\Delta A_{\parallel}}{D} \right]. \quad (451)$$

Finally, we can calculate the moments of the spin structure function. The n^{th} moment is written as,

$$\Gamma_1^n(Q^2) = \int_0^1 g_1(x, Q^2) x^{n-1} dx. \quad (452)$$

The integral can be divided into infinitesimal ranges and expressed as a summation

$$\Gamma_1^n(Q^2) = \sum_{i=0}^N \int_{x_i}^{x_{i+1}} g_1(x, Q^2) x^{n-1} dx. \quad (453)$$

Then the infinitesimal integral can be evaluated by parts

$$\int_{x_i}^{x_{i+1}} g_1(x, Q^2) x^{n-1} dx = g_1(x, Q^2) \left[\frac{x_{i+1}^n - x_i^n}{n} \right] - \frac{x^n}{n} d(g_1(x, Q^2)). \quad (454)$$

Since our bin sizes are small and we have a single g_1 value per bin, hence g_1 is constant within the infinitesimal range of the integration, $d(g_1(x, Q^2)) = 0$. Therefore, the second term in the right hand side vanishes, leaving us with

$$\Gamma_1^n(Q^2) = \sum_{i=0}^N \frac{x_{i+1}^n - x_i^n}{n} g_1(x, Q^2). \quad (455)$$

The small bin sizes we have validates this as a good approximation to a continuous integration. However, our data is in (W, Q^2) bins, so we need to determine the corresponding x for each bin. We used experimentally determined kinematic averages for x_{av} in each (W, Q^2) bin and calculated the n^{th} moment of g_1 as:

$$\Gamma_1^n(Q^2) = \sum_W \frac{x_{high}^n - x_{low}^n}{n} g_1(W, Q^2), \quad (456)$$

with

$$x_{high} = (x_{av[W]} + x_{av[W-1]})/2 \quad (457)$$

$$x_{low} = (x_{av[W]} + x_{av[W+1]})/2 \quad (458)$$

for a constant Q^2 . The statistical error on this quantity is given by

$$\Delta \Gamma_1^n(Q^2) = \left(\sum_W \left[\frac{x_{high}^n - x_{low}^n}{n} \right]^2 \times [\Delta g_1(W, Q^2)]^2 \right)^{1/2}. \quad (459)$$

where $\Delta g_1(W, Q^2)$ is the statistical error on $g_1(W, Q^2)$. The final results on these quantities are presented in chapter V. However, before presenting the final results, we need to estimate the systematic uncertainties on the measurement of these quantities. In the following sections, we will describe how we handled systematic errors.

IV.19 SYSTEMATIC ERROR CALCULATIONS

All applied corrections to the asymmetries and the structure functions as well as the model inputs required to calculate the final results are summarized in Eqs. (447-451). However, each of the correction factors as well as the model inputs for the A_2 , F_1 and D ¹⁹ have their uncertainties. The only way to understand the effects of these uncertainties on the measured quantity is to evaluate that quantity with the standard value of all corrections and model input and with the boundary value (including uncertainties) of every one of these factors. Then the difference between these two measurements can be considered as the systematic error, due to that specific factor, on the quantity of interest. Therefore, the first step in the systematic error calculation is to determine the range of uncertainty for each factor that enters into the calculations. The analysis is first performed by using the standard values, which we can call standard measurement. Then it is repeated again by changing only one of the factors by the amount of its uncertainty while keeping all other quantities at their standard values. Similarly, the full analysis is repeated for each uncertain factor and several different systematic variations are obtained for each measured quantity. For example, if $A_1^{(s)}(W, Q^2)$ is the standard value for a given (W, Q^2) bin and $A_1^{(i)}(W, Q^2)$ is the value obtained by changing a factor i by its uncertainty, the systematic error on $A_1(W, Q^2)$ due to the uncertainty of i is calculated by

$$\delta A_1^{(i)}(W, Q^2) = |A_1^{(s)}(W, Q^2) - A_1^{(i)}(W, Q^2)| \quad (460)$$

The total systematic error $\delta A_1^{(tot)}(W, Q^2)$, is then calculated by adding all the systematic uncertainties in quadrature:

$$\delta A_1^{(tot)}(W, Q^2) = \left(\sum_i [\delta A_1^{(i)}(W, Q^2)]^2 \right)^{1/2} \quad (461)$$

The main factors that enter into the systematic error calculations are:

1. Pion and pair symmetric background
2. Dilution factor
3. Beam \times target polarization
4. Polarized background

¹⁹The depolarization factor D internally depends on the structure function R .

5. Radiative correction
6. Errors on model asymmetries and structure functions

However, it should be noted that, for each item on this list, there may be several sub-parameters varied during the analysis. Overall there are 27 parameters as listed in Table 50. In order to make this procedure quick and automatic, an error index array was used in the analysis program. Each subprocess in the program looks for the status of the index in the array corresponding to its specific correction and decides whether the correction should be applied at the standard value or the boundary value of the parameter. Each index in the array is turned on or off, “on” meaning the systematic change should be applied to that parameter. Then, the whole analysis code is put into a loop over all values of the index array. For each repetition, one element of the index array is turned on to create the systematic results of the analysis. Table 50 lists the elements of the error index array and describes the corresponding variations. In addition, Appendix section C.2 provides detailed tables of systematic errors for individual Q^2 bins as a percentage of the statistical errors. This quantity is calculated as the quadratic mean of the ratio of the systematic error to the statistical error,

$$\sigma_{sys}^{percent}(Q^2) = \sqrt{\frac{1}{N} \sum_W \frac{\sigma_{sys}^2(Q^2, W)}{\sigma_{stat}^2(Q^2, W)}} \times 100 \quad (462)$$

where N is the number of W bins entering into the summation. Tables 70-73 summarize the systematic errors on $A_1 + \eta A_2$ for each data set with different beam energy settings and provides the individual contributions from different sources. Also, Table 74 gives the total systematic errors on A_1 , together with the different sources, and Table 75 provides the systematic errors evaluated in different W regions.

The following sections describe the different systematic variations in more detail. Before continuing to the individual systematic error definitions, it should also be noted that the systematic errors were evaluated independently for standard W bins of 10 MeV and the combined W bins of 40 MeV. While the data and the statistical errors from standard bins were combined within $W = 40$ MeV range as explained in section IV.17.8, the systematic errors cannot be combined in that fashion. Therefore, the full analysis was performed for the combined bins the same way it was done for the standard bin size by running over all systematic variations and adding the systematic differences in quadrature for the combined data.

TABLE 50: Systematic error index and corresponding variations to each index element.

| Error Index | Variation |
|-------------|---------------------------------------|
| 0 | Standard analysis |
| 1 | Pion background correction |
| 2 | Pair symmetric correction varied |
| 3 | Dilution factor varied |
| 4 | Radiative corrections varied |
| 5 - 16 | $P_b P_t$ varied for each beam energy |
| 17 - 22 | Model inputs |
| 23 - 25 | Place holder for further model inputs |
| 26 - 28 | Polarized background corrections |

IV.19.1 Pion and pair-symmetric backgrounds

Most of the pion background was removed by precise identification of electrons and using the geometric-time cuts described in section IV.8. Studies on the remaining pion background revealed a very small amount of pion contamination in the electron sample. The results of that analysis can be seen in section IV.12.1. Since it is very small, the total amount of this contamination was treated as a systematic error. The effect of the remaining pion contamination on the raw asymmetry can be quantified as

$$A_{corr} = \frac{A_{raw} - R_\pi A^\pi}{1 - R_\pi} \quad (463)$$

where $R_\pi = \pi^-/e^-$ ratio and $A^\pi \approx 0$ is the pion asymmetry. The difference between the corrected value and the standard value was used to estimate the systematic error due to the remaining pion contamination.

In order to determine the systematic uncertainty in the pair-symmetric contamination, the average contamination over all θ and momentum bins, weighted by the errors on the fit parameters, were compared for opposing torus polarities for the same beam energy. Half of that difference was added to the e^+/e^- ratio and the asymmetry was corrected by using the new value. In case there were not data for both torus polarities for a particular beam energy, such as the 1.7 and 5.6 GeV data sets, the comparison was made with the closest beam energy. The total systematic error due to the pion and pair symmetric backgrounds is less than 1% of the asymmetry.

IV.19.2 Dilution factor

The dilution factor analysis was performed by R. Fersch, who precisely determined the overall systematic uncertainty on this quantity. The main source of error in determining the dilution factor was the target model parameters, namely, the uncertainties in the physical measurements of the various materials in the target: the lengths and the densities of the carbon, Kapton and aluminum as well as the frozen ammonia target. In order to estimate the systematic error on the dilution factors, these parameters were changed by a reasonable amount [95].

The dilution factor was obtained by two independent methods, first one relying on data and the second one relying on a model, as described in section IV.11. This model used a world data parametrization of unpolarized cross sections. Eventually, the results obtained by using the model were used for the final analysis. However, the systematic errors from the model were not determined. Therefore, in addition to the systematic uncertainties on the target parameters, model uncertainties should also be considered in the systematic error calculation. This was done by comparing the dilution factors obtained from the two different methods. However, the results from the first method had bin to bin statistical fluctuations, so a direct comparison would result in an error dominated by these statistical fluctuations, which are not characteristic for systematic error. Also, that approach would not be possible for some kinematic regions, where we had poor data but the model dependent dilution factors were determined by extrapolation. Therefore, a fit to the dilution factors obtained from the data was generated and a comparison between this fit and the model-based dilution factors were used as part of the systematic error on this quantity. For more detailed information, the reader is encouraged to look at [95].

IV.19.3 Beam and target polarizations

As described in section IV.13, the product of beam and target polarization was extracted using data. The main source of error on this quantity is of a statistical nature. However, the error was not propagated as a statistical error. Instead, the statistical error on $P_b P_t$ was added to the value of the polarization used for the standard analysis, for one data set at a time, keeping others unchanged. The full analysis was repeated 12 times, each corresponding to systematic results due to a change in the polarization of one data set. Then the differences between the standard

analysis and the systematic analysis were added in quadrature to determine the total systematic error due to the uncertainties in the $P_b P_t$ extraction. The $P_b P_t$ extraction was done by using the exclusive method for all data sets except the 1.6 and 1.7 GeV ND₃ sets with negative torus polarity. For these specific data sets, the inclusive method of extraction was used with a 10% error on the value, which is twice and three times larger than the statistical error obtained from the inclusive method, respectively. For the inclusive method, dilution factors were used but because of the overestimated statistical errors on these data sets, the correlation in the systematic errors between the dilution factor and $P_b P_t$ can be safely neglected.

IV.19.4 Polarized background

The correction factors C_1 and C_2 , described in section IV.14, have uncertainties that are not well defined. For the standard correction, the values $C_1 = 1.02$ and $C_2 = -0.03A_p$ were used, where A_p is the proton asymmetry. Then the value of $C_1 = 1.01$ was used for one systematic result and $C_1 = -0.02A_p$ used as another variation. For the ND₃ target, C_1 corrects for ¹⁴N impurities while C_2 corrects for proton and ¹⁵N impurities in the target. The residual ¹⁴N amount is less than 2%, which makes the error on C_1 negligible. C_2 , on the other hand, includes the proton asymmetry and has considerable effect on the measured asymmetry. Its contribution to the total systematic error changes, depending on the kinematics, between 1% to 6% of the statistical error of $A_1 + \eta A_2$.

IV.19.5 Radiative corrections

A proper way to estimate the systematic error on the radiative correction is to run RCSLACPOL for different models and target parameterizations. But, this was not possible at this point. However, it is known from a previous analysis that radiative corrections are reliable within 5%. Therefore, to obtain systematic errors on radiative corrections, the values of A_{RC} and $(1 - f_{RC})$ were increased by 5%. It should be noted that f_{RC} ranges as $0 \leq f_{RC} \leq 1$. The effect of this quantity, and its systematic uncertainty, increases as the value of the f_{RC} decreases. $(1 - f_{RC})$ can be interpreted as the fraction of the contaminating asymmetry while f_{RC} is the fraction of the true asymmetry that contributes to the measured asymmetry. Therefore, the amount of the contamination factor was increased by 5% of its value to estimate the systematic error.

IV.19.6 Systematic errors due to models

Systematic errors due to models are obtained by varying the model choices as well as changing the fit parameters to the world data by a standard deviation.

In the derivation of $A_1 + \eta A_2 = A_{||}/D$, the depolarization factor D includes the structure function ratio R (see Eqs. (29) and (60)). To get the systematic error due to R , one standard deviation was subtracted from the fit parameters for R .

For extraction of A_1 , we had to use modeled values of A_2 . Unfortunately A_2 is not well known due to very limited data. In the DIS region, the standard A_2 model was derived from Eq. (63) by using the *Wandzura-Wilczek* [7] relation for g_2^{WW} , without considering higher twist terms. For systematic errors, the A_2 model varied by taking into account the twist-3 part, g_2^{HT} , in addition to g_2^{WW} . In the resonance region, A_2 was determined by parameterizing the world data for the proton and neutron and combining them with a smearing function that takes care of the nuclear effects because of the Fermi motion of the nucleons and the D-state correction [73]. More detailed information about A_2 in the resonance region is provided in chapter VI. The systematic error from A_2 model was determined by varying the model between the current and old parameterizations.

The structure function F_1 was used in the derivation of g_1 . Its systematic error was determined by varying the fit parameters for F_1 by one standard deviation and using the F_1 with errors added.

CHAPTER V

PHYSICS RESULTS

The results from the analysis are presented in this section by showing comprehensive plots of the physics quantities extracted. The main goal of the analysis is to measure the double spin asymmetry A_{\parallel} with all corrections given in Eq. (447) and extract $A_1 + \eta A_2$, A_1 , g_1 and Γ_1 for the deuteron. It should be noted that the quantities in the following figures are averaged over the final state invariant mass W in 40 MeV bins. The systematic errors for the averaged results were obtained with the usual procedure by independently running the whole analysis on each quantity for each systematic uncertainty.

After measuring A_{\parallel} , $A_1 + \eta A_2$ was calculated according to Eq. (67) by using the model values for D . Figs. 112 and 113 show the results for selected Q^2 bins for various beam energy settings. Fig. 114 explicitly provides the systematic errors on this quantity from different contributing elements. Once $A_1 + \eta A_2$ is calculated, we can extract the virtual photon asymmetry A_1 , by using model inputs for A_2 . Fig. 115 shows this quantity together with different sources of systematic errors. In addition, Figs. 116 and 117 show the final A_1 versus final state invariant W mass for all Q^2 bins in our kinematic coverage. At low Q^2 , the effect of the $\Delta P_{33}(1232)$ resonance is clearly visible which proves that the $A_{3/2}$ transition is dominant in this region as expected, causing the asymmetry to be negative. As we go to higher values of W , the transition $A_{1/2}$ becomes dominant leading to resonances such as $D_{13}(1520)$ and $S_{11}(1535)$.

By using Eq. (450) and taking F_1 and A_2 from models, the spin structure function g_1^d is evaluated for each bin. Figs. 118 and 119 show its behavior with respect to W . In addition, g_1^d versus Bjorken x for each Q^2 bin are also presented in Figs. 120 and 121. The red curve on each plot comes from the our “Models”. g_1 is deeply affected by the resonance structure, again the $\Delta(1232)$ being the most prominent one, making g_1 negative in this region. When we go to higher Q^2 , the effect of the resonances diminishes and g_1 approaches zero toward the quasi-elastic region.

The moments of the structure functions are calculated by integrating the structure functions over the full kinematic region from $x = 0.001$ up to the quasi elastic

threshold x at $W = 1.08$ GeV. By using the relation,

$$W = \sqrt{M^2 + Q^2/x - Q^2} \quad (464)$$

the maximum W values for the kinematic point $x = 0.001$ were determined for each Q^2 bin from $Q^2 = 0.01$ to 10 GeV².

Experimental limitations prevent us from exploring the region where $x \rightarrow 0$ since it would require a very high beam energy. At the limit $x = 0.001$, the invariant mass reaches up to 100 GeV. Moreover, the extrapolation of the integral is not well known below $x = 0.001$. Therefore, this kinematic region was excluded from the integration.

The minimum W value was always kept at 1.08 GeV, which is the quasi-elastic threshold. Convention for the evaluation of the moments generally excludes the quasi-elastic region. The low Q^2 behavior of Γ_1 is more interesting without the elastic contribution since the effect of the Δ resonance becomes more obvious.

The described limits of the integration require model input since the EG1b results do not cover the full kinematic region. Therefore, the model values for g_1 were used where data are not available. The regions for which we use either the data or the model were determined by scanning through the quality of the data for different W regions in each Q^2 bin. Data with large statistical errors were excluded from the integration. The EG1b data for the structure function g_1 starts at $W = 1.15$ GeV, since below that region the radiative effects overwhelm the real data. However, we have a reliable model that can be used for the integration. Above this value, we have data up to $W = 3$ GeV depending on the Q^2 bin. Figs. 120 - 121 show the behavior of g_1 data for all Q^2 bins used in the integration. Also, there are some gaps in our data that correspond to uncovered regions because of discrete beam energies. These gaps appear only for a few Q^2 bins and model values were used for the integration in those regions. Table 76 in Appendix C.3 summarizes the W regions in which the values from the model or the data were used for the integration. An additional constraint can also be put on the data by considering the average kinematic points we have extracted from the data and propagated up to this point. These kinematic variables include ϵ , η and γ for each bin, so that one can calculate a cut parameter y such that,

$$y = \frac{\nu}{E_{beam}} = \frac{\eta(1 - \epsilon)}{\epsilon(\gamma - \eta)}. \quad (465)$$

Then, a requirement $y < 0.80$ can be used to select the regions for which data can be used for the integration. If data with large statistical errors are used in the

integration, these statistical errors will clearly be visible in the relevant Q^2 values of the moments.

With above considerations, the integral can be divided into measured and un-measured regions such that,

$$\begin{aligned} \Gamma_1(Q^2) = & \int_{x=0.001}^{x(W_{data})} g_1(x, Q^2) \quad \text{model} \\ & + \int_{x(W_{data})}^{x(W=1.15)} g_1(x, Q^2) \quad \text{data (or model for gaps)} \\ & + \int_{x(W_{1.15})}^{x(W=1.08)} g_1(x, Q^2) \quad \text{model} \end{aligned} \quad (466)$$

and each integration is performed according to Eqs. (456) and (459). For comparison purposes, the plots of Γ_1^n will usually show the results of the integration using only the data and using the data and model together. Of course the result obtained by only using the data will deviate from the true value since the integral is not complete. However, there are Q^2 regions where the overall model contribution to the integral is very small and the data alone gives a good approximation to the full integral. In those kinematic points, the results obtained from the data alone and from the data + model together come very close to each other. These Q^2 regions that model contribution to the overall integral is minimal can be used to test the model. Figs. 122 - 124 show the Q^2 evolution of the first moment as measured by the EG1b experiment and also the current status of the world data on this quantity. The higher moments Γ_1^3 and Γ_1^5 are also calculated in the same way by using Eq. (456) with appropriate powers $n = 3, 5$. Fig. 125 shows the results for the third moment Γ_1^3 and the fifth moment Γ_1^5 of g_1 as extracted from the EG1b data.

Fig. 126 shows the forward spin polarizability γ_0 for the deuteron, which was calculated according to Eq. (184). Values calculated are also multiplied by 15.134 for unit conversion to $[10^{-4} \text{ fm}^4]$. The figure also shows the integral part of γ_0 without the kinematic factor. Detailed information on γ_0 is provided in section II.4.6. Its calculation heavily depends on the knowledge of the structure function g_2 , as well as g_1 . Indeed, the largest systematic error on γ_0 comes from g_2 as shown in Fig. 126.

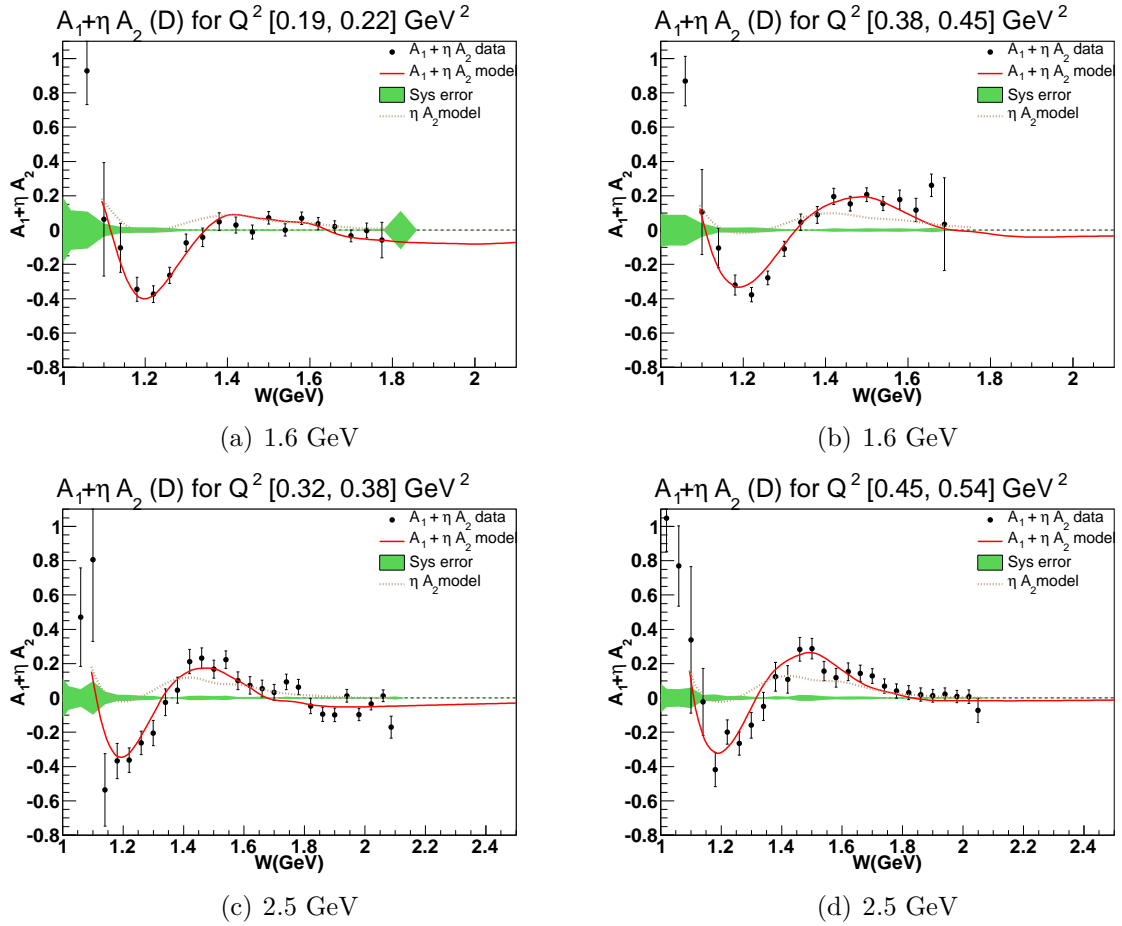


FIG. 112: $A_1 + \eta A_2$ versus final invariant mass W for 1.6 and 2.5 GeV beam energy settings. The Q^2 bin is given at the top of each plot. The red-solid and brown-dotted curves are $A_1 + \eta A_2$ and ηA_2 parameterizations, respectively. The green shade represents the total systematic error on $A_1 + \eta A_2$.

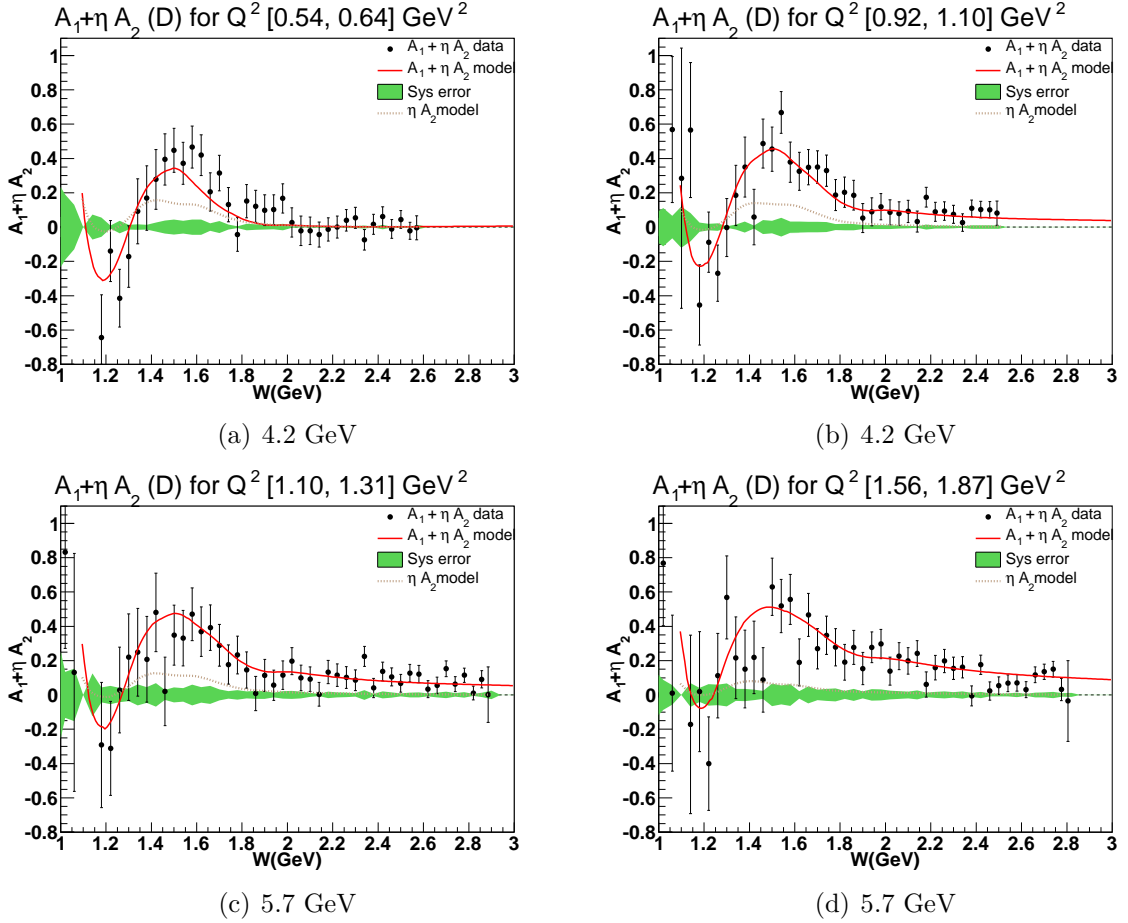


FIG. 113: $A_1 + \eta A_2$ versus final invariant mass W for 4.2 and 5.7 GeV beam energy settings. The Q^2 bin is given at the top of each plot. The red-solid and brown-dotted curves are $A_1 + \eta A_2$ and ηA_2 parameterizations, respectively. The green shade represents the total systematic error on $A_1 + \eta A_2$.

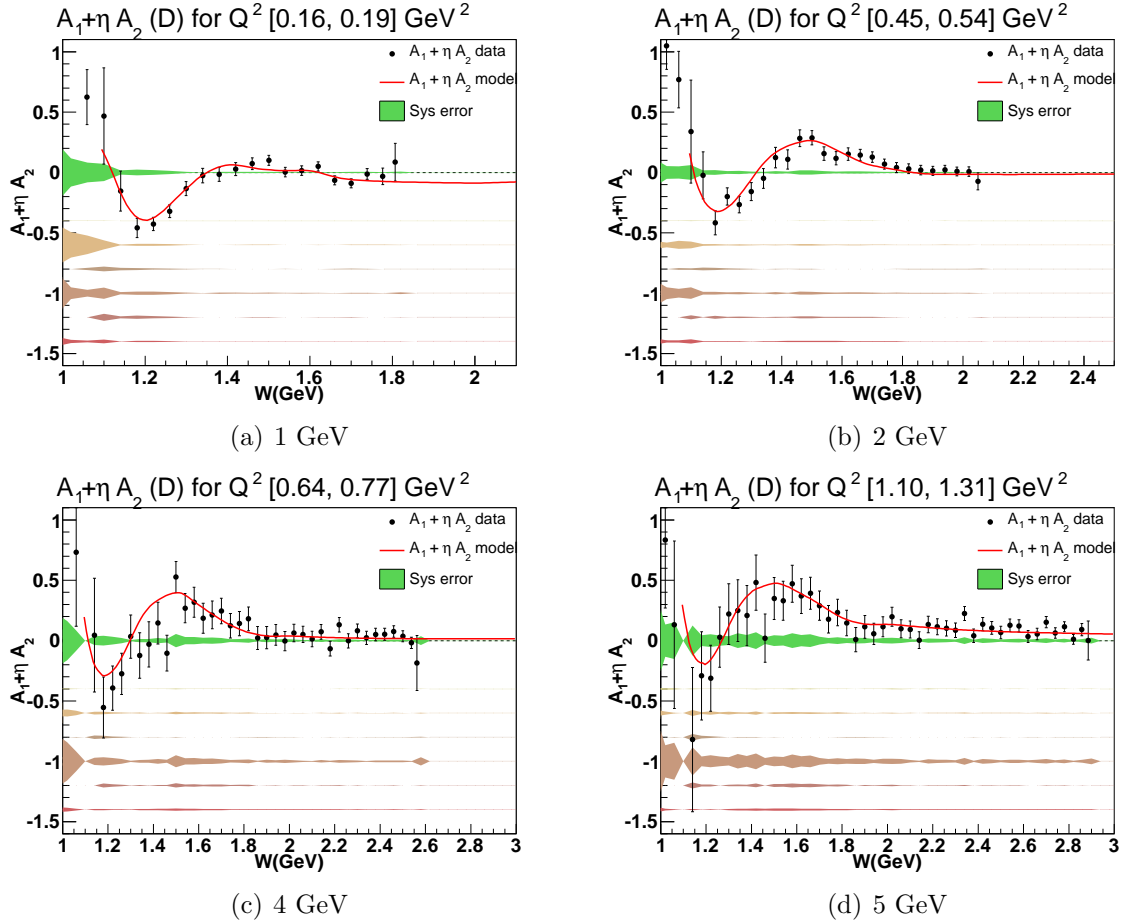


FIG. 114: $A_1 + \eta A_2$ versus W together with different sources of systematic error. The central shade (green) is the total systematic error. The other systematic errors are offset to the following vertical scales, from top to bottom: pion and pair symmetric contamination (-0.4); dilution factor (-0.6); radiative correction (-0.8); $P_b P_t$ (-1.0); models (-1.2); polarized background (-1.4). At this point, the biggest source of our systematic error comes from the $P_b P_t$ extraction.

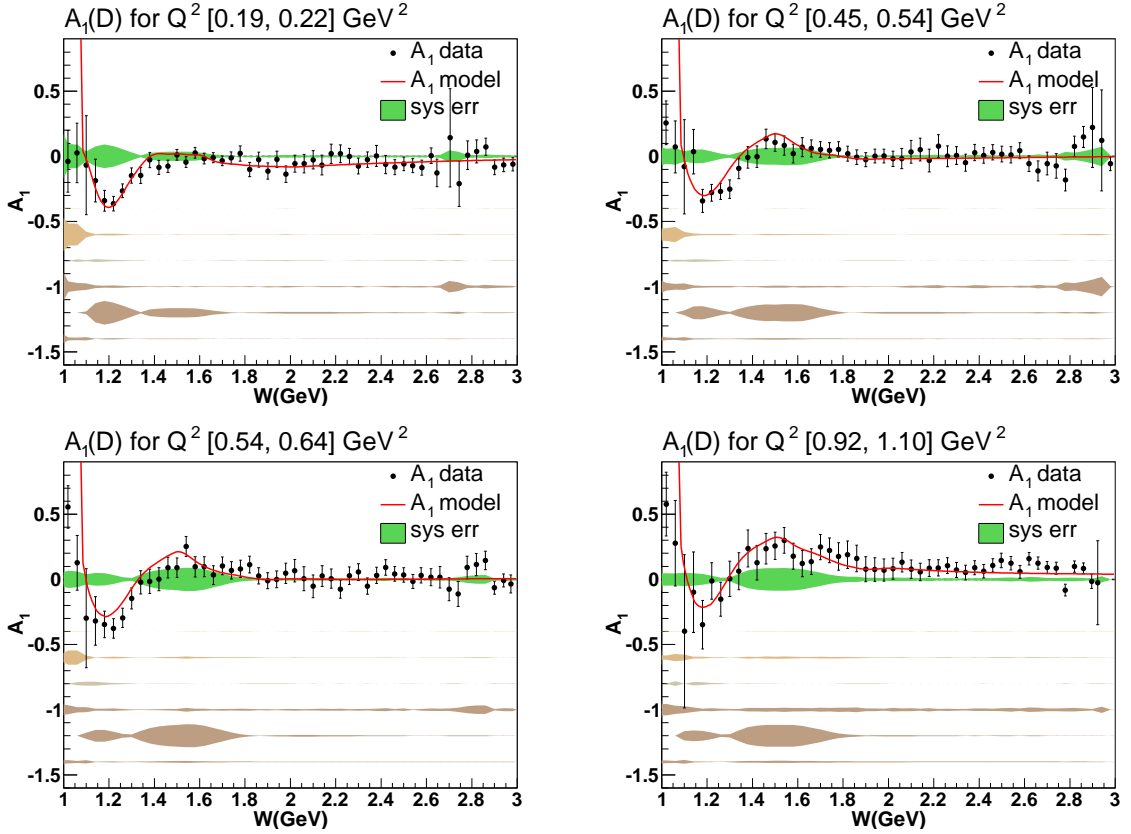


FIG. 115: Virtual photon asymmetry A_1 versus W for a few Q^2 bins are shown together with systematic errors. The central shade is the total systematic error. The other systematic errors are offset to the following vertical scales, from top to bottom: pion and pair symmetric contamination (-0.4); dilution factor (-0.6); radiative correction (-0.8); $P_b P_t$ (-1.0); models (-1.2); polarized background (-1.4). The biggest systematic error for the A_1 extraction comes from the unknown A_2 values. This systematic error can be reduced once we have measurements on A_2 .

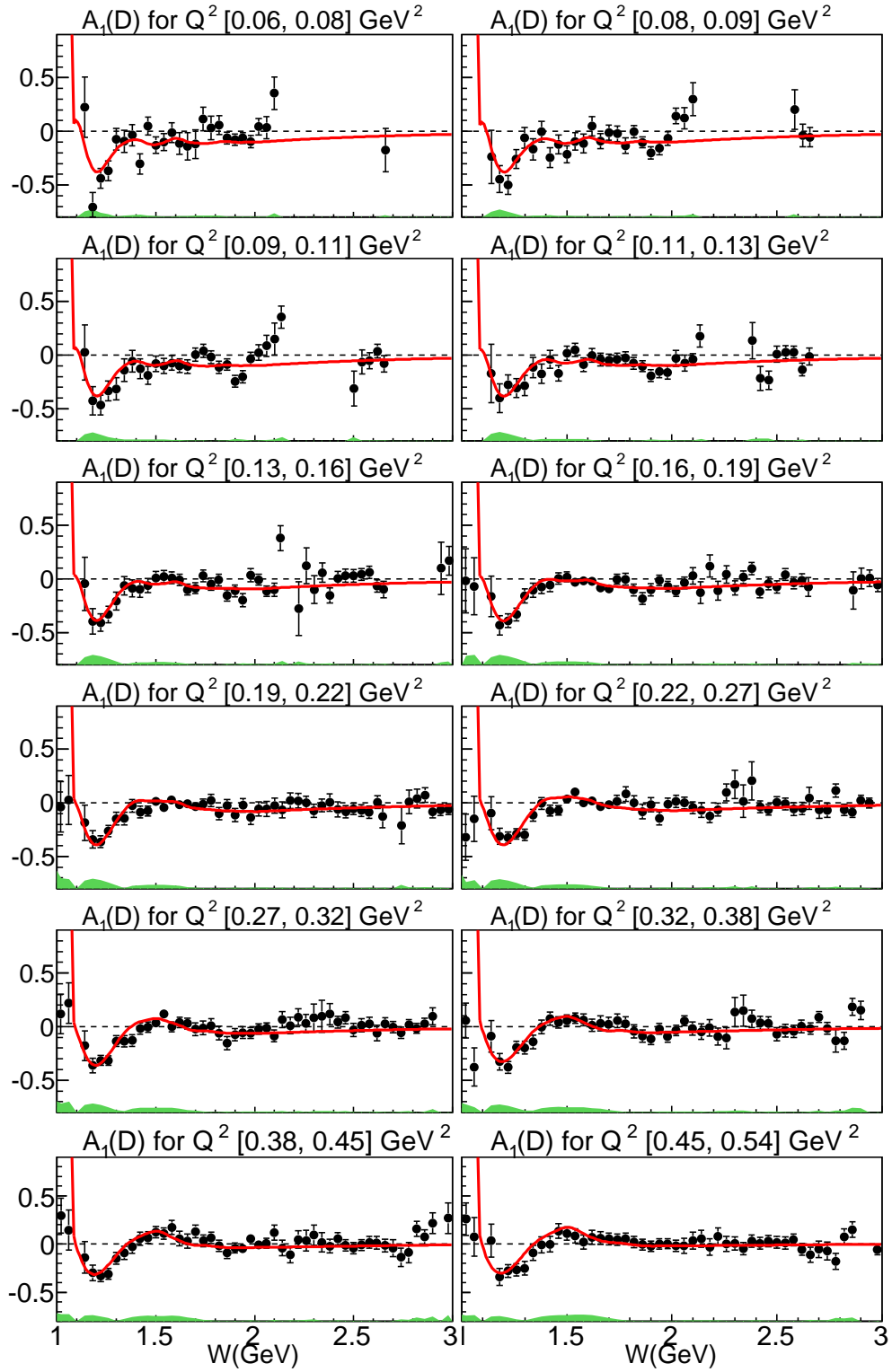


FIG. 116: A_1 for the deuteron versus the final state invariant mass W for various Q^2 bins. Systematic errors are shown as shaded area at the bottom of each plot. Our parametrized model is also shown as a red line on each plot. Only the data points with $\sigma_{stat} < 0.3$ and $\sigma_{sys} < 0.2$ are plotted.

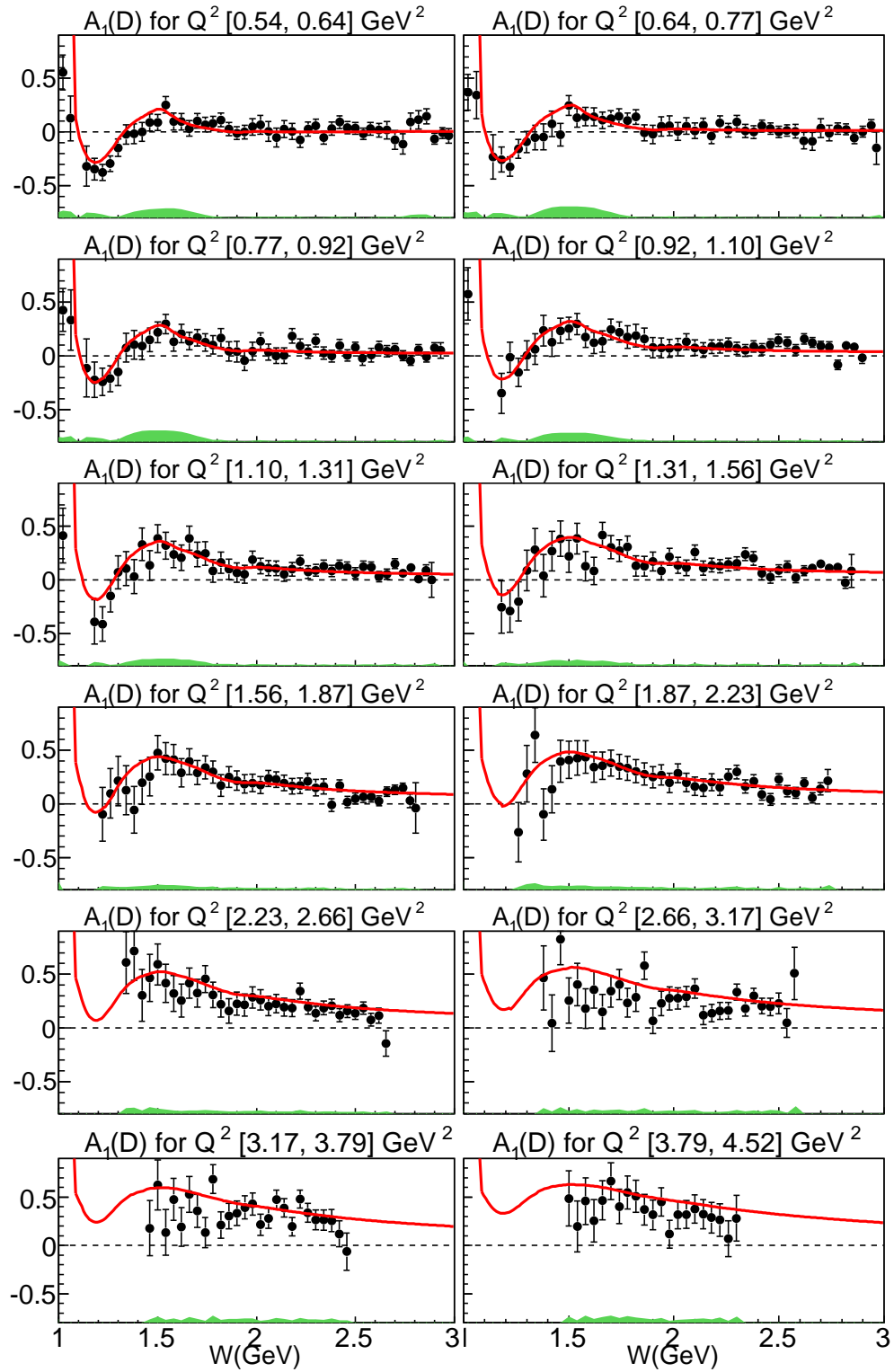


FIG. 117: Continuation of Fig. 116 for remaining Q^2 bins.

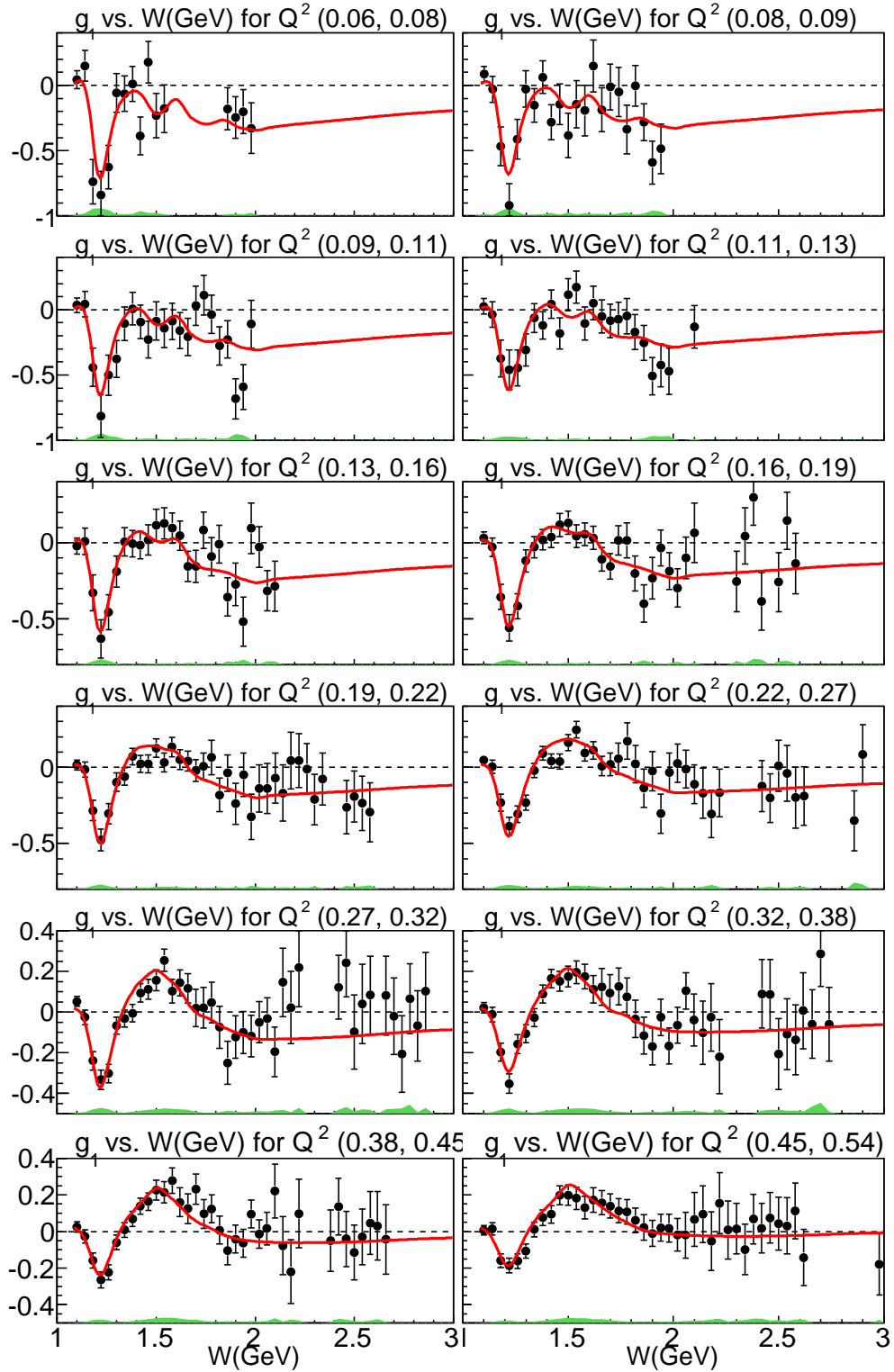


FIG. 118: g_1 for the deuteron with respect to the final state invariant mass W for many Q^2 bins. The shaded area at the bottom of each plot represents the systematic errors. Model for g_1 is shown as a red line on each plot. Only data points with $\sigma_{stat} < 0.2$ are plotted.

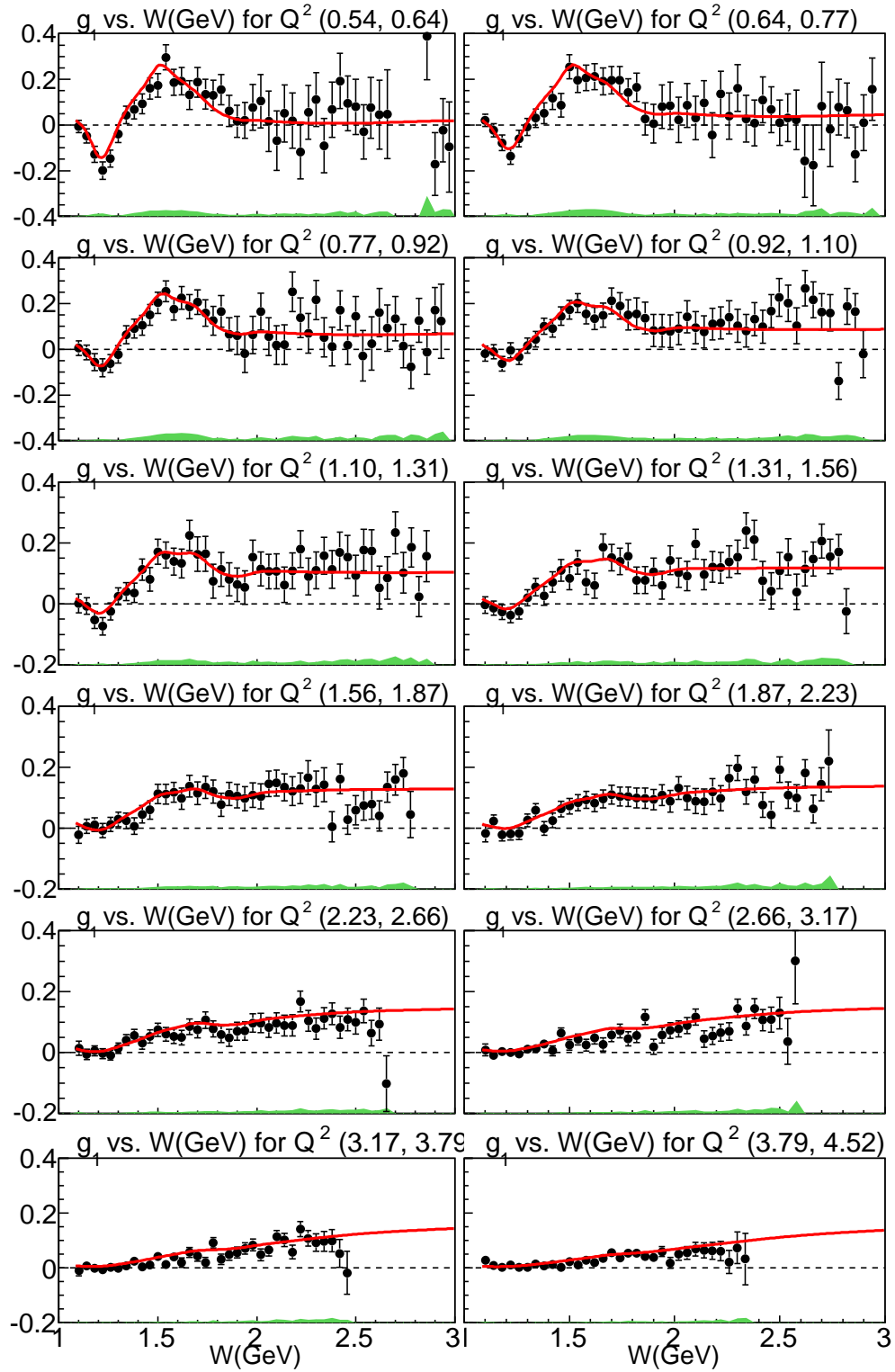


FIG. 119: Continuation of Fig. 118 for remaining Q^2 bins.

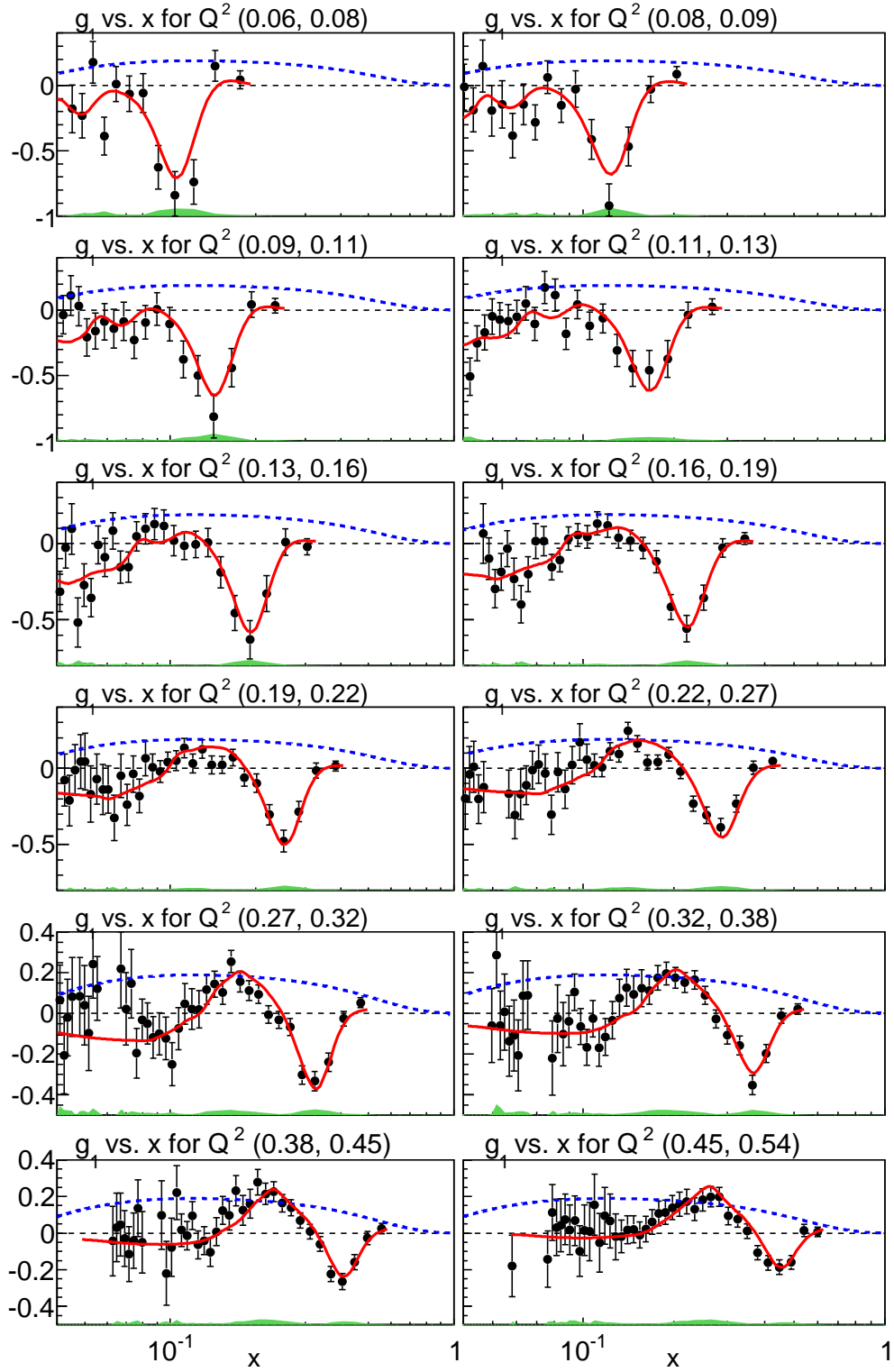


FIG. 120: g_1 with respect to the Bjorken variable x for many Q^2 bins together with model shown as red lines on each plot. The shaded area at the bottom of each plot represents the systematic error. DIS curve for $Q^2 = 10$ GeV is also shown as blue dashed line.

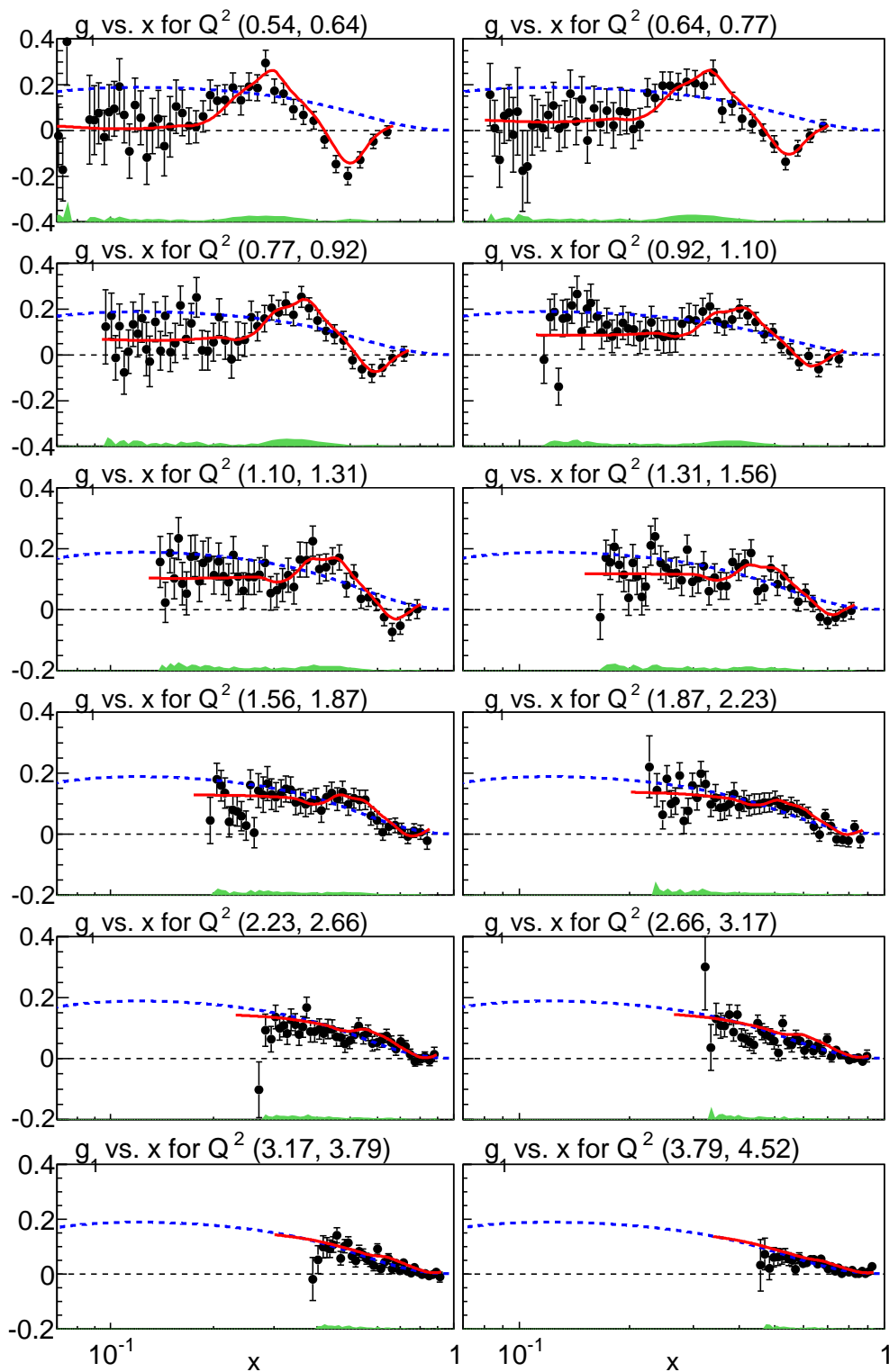


FIG. 121: Continuation of Fig. 120 for remaining Q^2 bins.

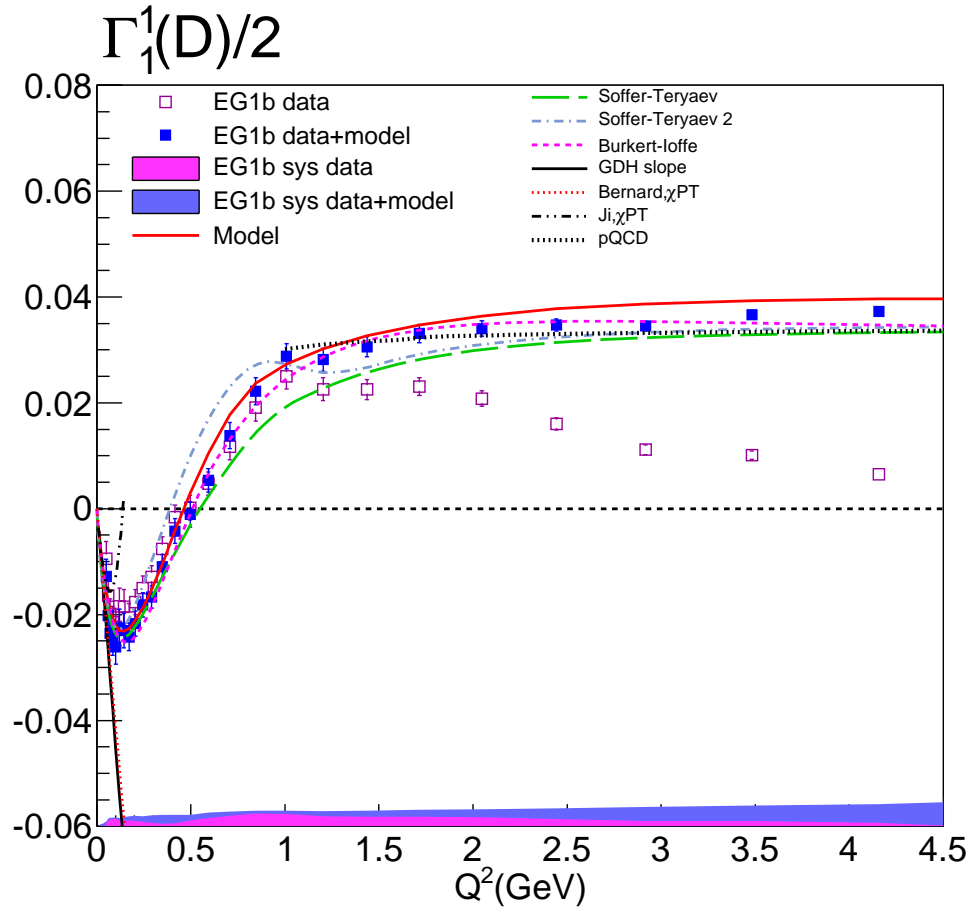


FIG. 122: Γ_1^1 for the deuteron versus Q^2 from data only (hollow-magenta squares) and data+model (full-blue squares), including the extrapolation to the unmeasured kinematics. The red curve is evaluated by only using the model. Also shown are phenomenological calculations from Soffer-Teryaev and Burkert-Ioffe (see section II.4.7), together with the χ PT results from Ji [59] (black dotted dashed line) and Bernard [60] (red dotted line). The GDH slope (black solid line) and pQCD prediction (black dotted line) are also shown on the plots. The systematic errors are shown for only data (magenta shade) and data+model (blue shade) at the bottom of the plot.

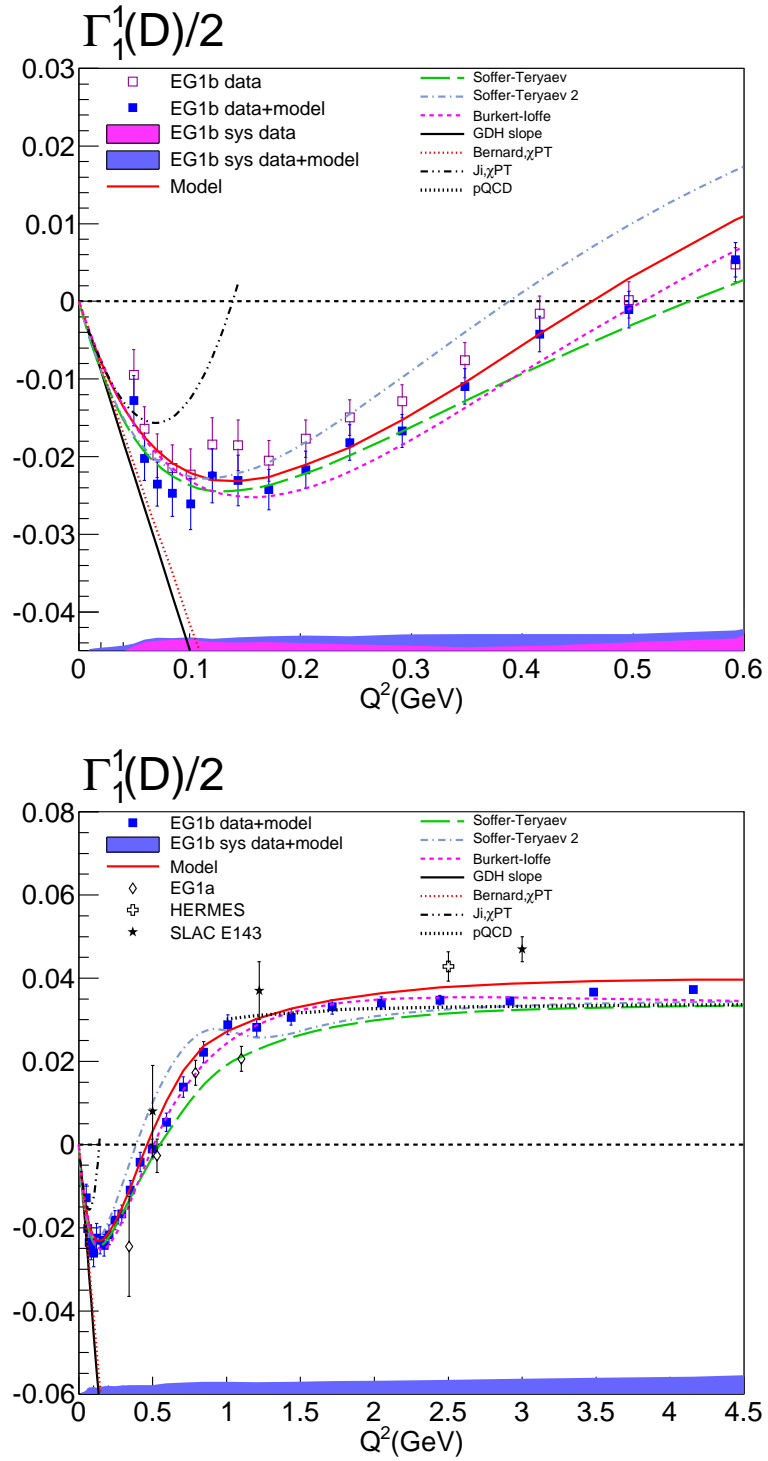


FIG. 123: The top plot is the same as Fig. 122 only zoomed into the low Q^2 region. Results from other experiments are also shown in the bottom plot, including E143 [45], HERMES [48] and EG1a [67].

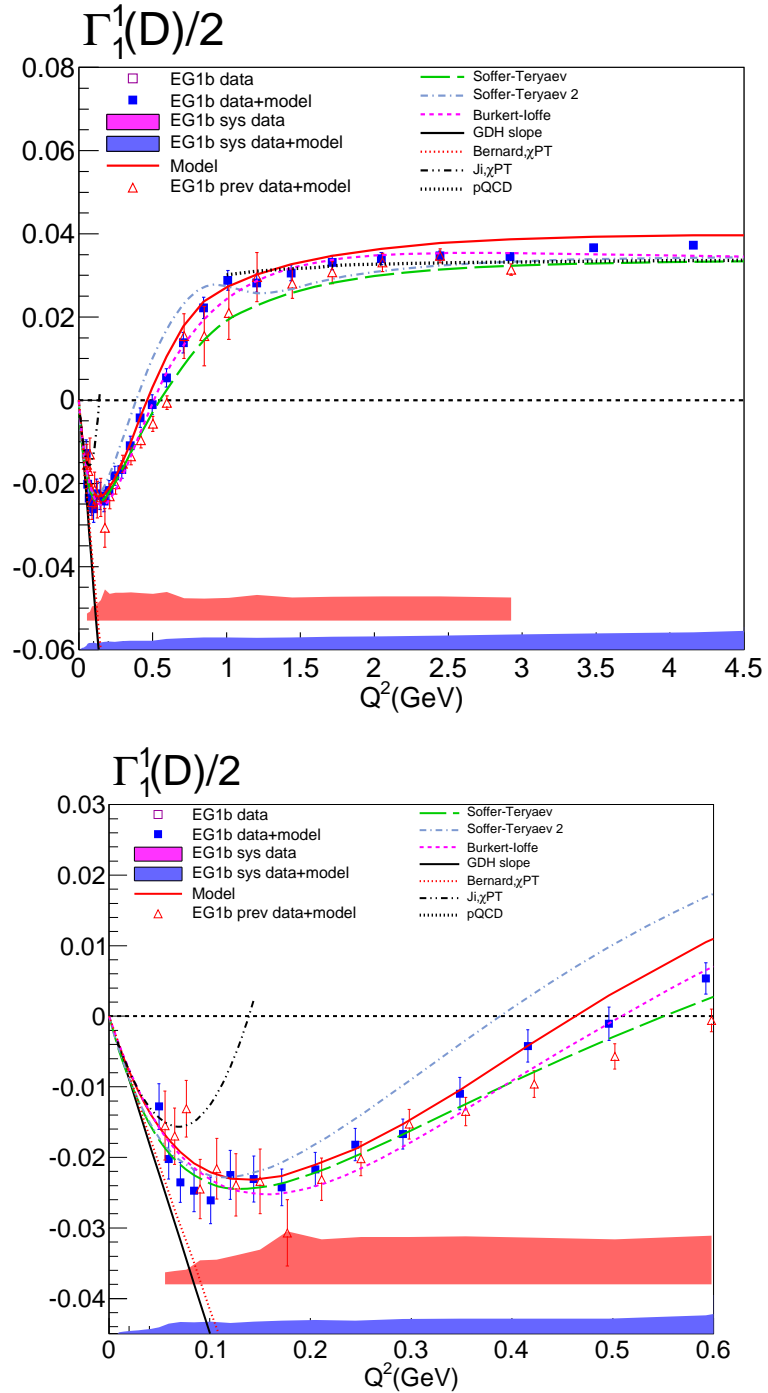


FIG. 124: Comparison of this analysis and the previous one on the Γ_1^1 extraction from EG1b. The red triangles represent the previous analysis, which was done by only using the 1.6 and 5.7 GeV data. For clear visibility, those points are shifted to a slightly higher Q^2 by adding an offset factor. The two independent analysis results complement each other well within statistical errors. Addition of the 2.5 and 4.2 GeV data clearly improves the medium Q^2 region and the overall statistics.

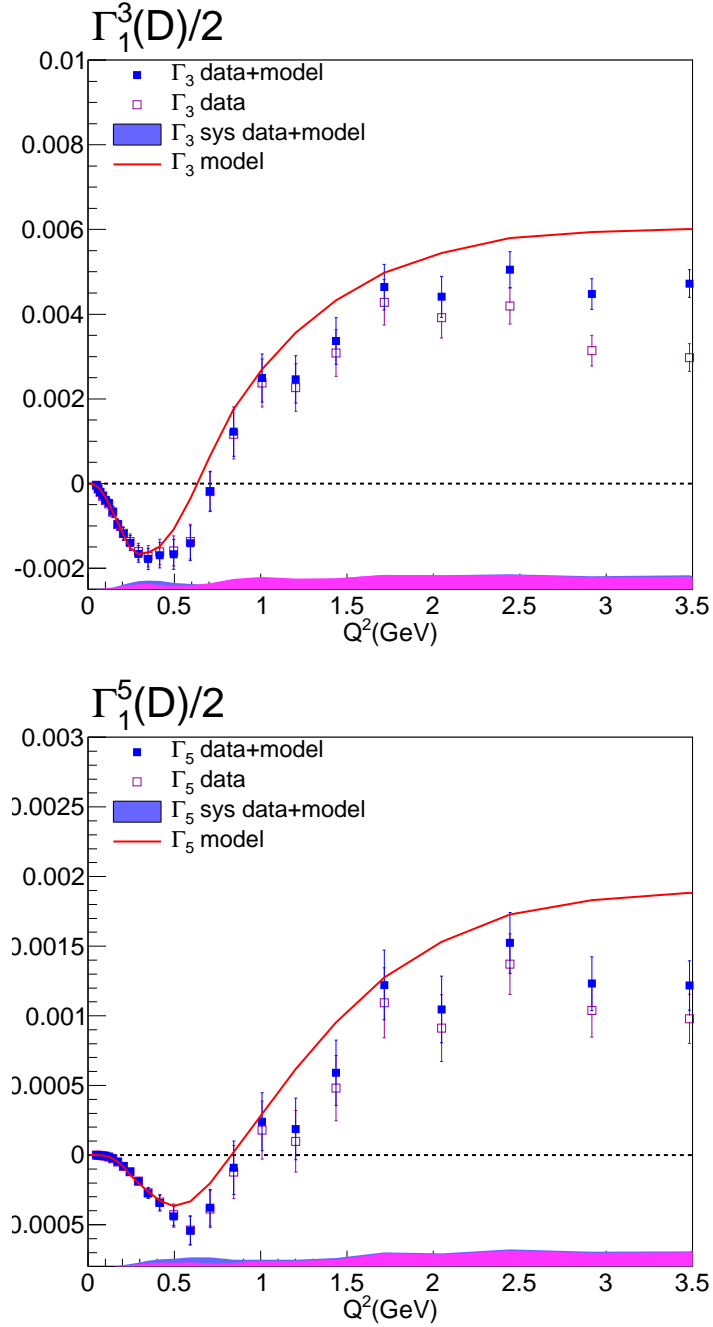


FIG. 125: Higher moments of g_1 extracted from the EG1b data are shown with respect to Q^2 , the third moment Γ_1^3 (top), and the fifth moment Γ_1^5 (bottom). The hollow squares were calculated with no model contribution while the filled squares have model input for the kinematic regions with no available data.

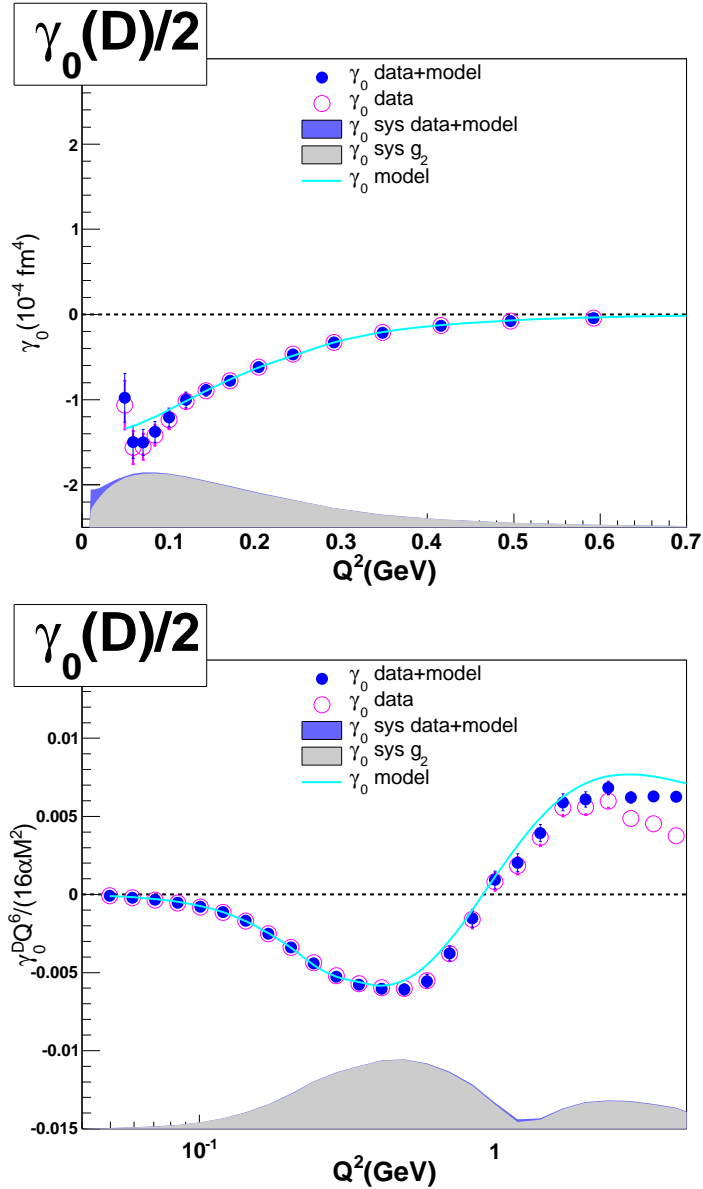


FIG. 126: Forward spin polarizability (γ_0) for the deuteron is shown versus Q^2 . The hollow circles represent the calculation by using only data and the full circles are data + model results. The green shaded area is the total systematic error. The systematic error that comes from g_2 , by taking $g_2 = 0$, is shown with the gray shade overlapped on the total systematic error. The model curve is also shown as a line through data points. The top plot shows values also multiplied by 15.134 for unit conversion to $[10^{-4} \text{ fm}^4]$. The bottom plot is just the integral part, without the kinematic factor taken into account.

CHAPTER VI

MODELING THE WORLD DATA

As new data are generated on the structure functions, our knowledge in different kinematic regions improves, which enables us to upgrade the models on interesting physics quantities such as A_1 and A_2 for the proton, the neutron and the deuteron. This chapter presents the latest efforts for fitting the world data to produce reliable models, specifically for A_1 and A_2 for the proton and neutron. Moreover, since data are rare on the neutron target, existing deuteron and proton data, especially with the help of the EG1b results, provide us a platform to extract information on the neutron spin structure functions.

The behavior of the spin structure functions and the asymmetries in the resonance region is especially interesting because it is the region where theoretical efforts mostly fail. Thus, we don't have a rigorous method to describe this region. Therefore, parametrization of the existing data in the resonance region remains the only reliable option. These parameterizations are needed to extract other physics quantities, study radiative effects and even learn about the effects of nuclear medium on the structure of the nucleon.

The general procedure for the fits includes collection of the world data on the specific quantities and utilization of a least-square fitting routine to determine the optimal parameters that describe the data best by minimizing the χ^2 of the fit, which is defined by

$$\chi^2(Q^2, W) = \sum_n \frac{(A^{data}(Q^2, W) - A^{fit}(Q^2, W))^2}{(\sigma_{A^{data}}(Q^2, W))^2} \quad (467)$$

where the sum is taken over all data points. $A^{data}(Q^2, W)$ is the value of the data for the specific quantity, A_1 or A_2 , and $A^{fit}(Q^2, W)$ is the output of the fit function at the kinematic point of the data. The $\sigma_{A^{data}}(Q^2, W)$ is generally taken as the statistical error of the data point, but for some experiments, statistical and systematic errors were added in quadrature.

Minimization of the χ^2 was performed by using the MINUIT package from CERN [111], which provides various different minimization routines. The most widely used is MIGRAD, which is regarded as “the most efficient and complete single method, recommended for general functions” [111]. We tried MIGRAD as well as MINOS, to evaluate parameter errors. Also, the MINIMIZE scheme uses MIGRAD unless it

gets into trouble, in which case it switches to SIMPLEX, which is another multi-dimensional minimization routine, and then calls MIGRAD again. In the end, we decided to use the MINIMIZE routine. However, we did not observe, in any of the final fits we used, a failure with MIGRAD and a switch to SIMPLEX.

Various parameterizations were tried and compared to each other. The final functional forms are given in the following sections. The parametrized functions, in general, also utilize other existing models such as MAID 2007 [128] as well as an older parameterization of the same kind performed on the more limited data set of the time. MAID is a unitary isobar model for pion photo- and electroproduction on the nucleon. It describes the world data on the $\gamma^*N \rightarrow \Delta$ transition and threshold π^0 production. These existing models provided us a method to extrapolate the fit successfully into the kinematic regions with no available data, which is the case specifically with A_2^p and A_2^n parameterizations..

In the following sections, information is given on the specific parameterizations of the existing world data on the virtual photon asymmetries A_1 and A_2 in the resonance region for the proton and the neutron. We should point out that all data shown in this chapter were averaged over $\Delta W = 40$ MeV for plotting purposes by taking their error weighted averages. However, fitting was performed on the individual data points at their true kinematic values. Once the models for the spin structure functions of the proton and the neutron were created, the deuteron models in the resonance region were obtained by smearing the nucleon structure functions and combining them according to Eq. (205). For this purpose, the smearing procedure developed in Ref. [73] was used.

VI.1 PARAMETRIZATION OF A_1^p

The EG1b experiment measured A_1^p in the resonance region with an unprecedented precision. Therefore, the largest amount of data for this fit comes from the EG1b experiment, in the kinematic region $0.05 \text{ GeV}^2 < Q^2 < 5.0 \text{ GeV}^2$. The next experiment is from MIT BATES [129] and has precision data in the Δ resonance region for $Q^2 = 0.123, 0.175, 0.240$ and 0.312 GeV^2 . Then the RSS experiment [130][131], performed in Hall-C of the Jefferson Lab, provides precision data in the region $1.0 < Q^2 < 1.4 \text{ GeV}^2$ and $1.08 \text{ GeV} < W < 2.0 \text{ GeV}$. We also used the results from the EG1a experiment [68], which measured A_1^p in the Q^2 region from 0.15 to 1.6 GeV^2 .

The fit was performed in two separate steps. The first step employed a 16 parameter fit function. In this function, some of the parameters were used to specifically treat certain W regions to describe the resonant structure better. Also, MAID model and an extrapolation of the DIS model into the resonance region were utilized to ensure the resulting parametrization smoothly continues in the high and low W regions. The resulting parameters from this step were fixed and the function was used as a static quantity in the second step fit. The second step employed a 12 parameter fit function. In this step, we also used an older parametrization and made use of its strength in some kinematic regions. This two-step approach created a good method to treat and fine tune certain kinematic regions and describe the resonant structure better. The fit function for the first step can be written as:

$$\begin{aligned}
E_1 &= P_0 + P_1 \tan^{-1}[(Q^2 - P_2^2) P_3^2] \\
E_2 &= P_4 + P_5 \tan^{-1}[(Q^2 - P_6^2) P_7^2] \\
E_3 &= 1 - E_1 - E_2 \\
E_4 &= P_8 + P_9 \tan^{-1}[(Q^2 - P_{10}^2) P_{11}^2] \\
E_5 &= P_{12} + P_{13} \tan^{-1}[(Q^2 - P_{14}^2) P_{15}^2] \\
C_1 &= 1 - \sin\left(\frac{\pi}{2} \left[\frac{W - 1.08}{2 - 1.08}\right]\right) \\
C_2 &= C_1^2 \\
C_3 &= \cos\left(\frac{\pi}{2} \left[\frac{W - 1.08}{2 - 1.08}\right]\right) \\
C_4 &= \begin{cases} [\sin(\pi \left[\frac{W-1.08}{1.9-1.08}\right])]^2 & W \geq 1.9 \\ 0 & W < 1.9 \end{cases} \\
C_5 &= \begin{cases} \sin(\pi \left[\frac{W-1.08}{1.35-1.08}\right]) & W < 1.35 \\ 0 & W \geq 1.35 \end{cases} \\
\mathcal{M} &= E_1 C_1 + E_2 C_2 + E_3 C_3 + E_4 C_4 + E_5 C_5 \\
A_1^{C[1]} &= \begin{cases} \mathcal{M} A_1^M + (1 - \mathcal{M}) A_1^{DIS} & W \leq 2 \\ A_1^{DIS} & W > 2 \end{cases}
\end{aligned} \tag{468}$$

where P_i represents parameter i , A_1^M is the MAID 2007 model of A_1^p and A_1^{DIS} is the DIS extrapolation. $A_1^{C[1]}$ represents the final calculated fit from the first step.

The final parametrization for $A_1^{C[1]}$ is used in the second step fit function, which is described by

$$\begin{aligned}
Q_{ph}^2 &= \begin{cases} 0 & Q^2 \leq 0.01 \text{ GeV}^2 \\ \frac{1}{3\pi} \left(\frac{\log(Q^2)}{\log(10)} + 2 \right) & 0.01 < Q^2 < 10 \text{ GeV}^2 \\ 1 & Q^2 > 10 \text{ GeV}^2 \end{cases} \\
W_{ph} &= \pi \frac{(W - 1.08)}{(2.04 - 1.08)} \\
D_0 &= P_0 + P_1 \cos(Q_{ph}^2) + P_2 \cos(2Q_{ph}^2) \\
D_1 &= P_3 + P_4 \cos(Q_{ph}^2) + P_5 \cos(2Q_{ph}^2) \\
D_2 &= P_6 + P_7 \cos(Q_{ph}^2) + P_8 \cos(2Q_{ph}^2) \\
D_3 &= P_9 + P_{10} \cos(Q_{ph}^2) + P_{11} \cos(2Q_{ph}^2) \\
\mathcal{B} &= \begin{cases} D_0 \sin(12W_{ph}) + D_1 \sin(W_{ph}) \\ \quad + D_2 \sin(2W_{ph}) + D_3 \sin(4W_{ph}) & W < 2.04 \text{ GeV} \\ 0 & W \leq 2.04 \text{ GeV} \end{cases} \\
A_1^C &= (1 - \mathcal{B}) A_1^{C[1]} + \mathcal{B} A_1^{OM}
\end{aligned} \tag{469}$$

where A_1^{OM} represents an older parametrization and A_1^C is the final parametrized model. The total number of parameters for the whole fit is 28. During each fit step, the minimization was performed iteratively, generally two iterations were used, automatically passing the results of the first iteration as the starting parameters of the second one. In the first iteration, an initial step size of 0.00001 was used on all parameters. After the first evaluation of the χ^2 , MINUIT decides on the step size values based on the first derivatives. In the second iteration, we let MINUIT continue to decide the step sizes internally. We observed that the final step sizes are generally very close to zero, on the order of 10^{-10} . Also, no restrictions were employed on the parameter limits.

Tables 51 and 52 give the initial and final values of the parameters together with estimated errors and the first derivatives. No user defined derivatives were supplied, in which case, MINUIT uses its own method by evaluating the finite differences over the step size. The small step sizes we observe ensures the reliability of these first derivatives, which in turn yields the reliability of the parameter errors. The resulting

first derivatives are generally small or practically zero for some of the parameters. However, the parameter errors were not used to determine the final errors on the actual model. The errors on the model were determined systematically by evaluating the differences between the new fit and various different parameterizations from old fits.

Total number of data points for the A_1^p fit was 4325. For the step 1 fit with 16 parameters, the initial χ^2 value was 22898. After the fit, a χ^2 of 5231.94 was reached. For the second step with 12 parameters, the initial χ^2 was 5331.92 and the final value became 4500.08, which results $\chi^2/n.d.f \approx 1.04$. Figs. 127 and 128 show the resulting fit together with the data and the other models for various Q^2 regions.

TABLE 51: Final parameters for the first step A_1^p fit (version number 20S1 [132]). The fit function is given in Eq. (468). The total number of data points used in the fit was 4325. The final $\chi^2/n.d.f \approx 1.209$ was reached at the end of the fit.

| ParNo | Initial | Final | Error | First Derivatives |
|-------|---------|--------------|-------------|-------------------|
| 1 | 0.4 | -1.01616e-01 | 8.42531e-01 | 2.01952e-03 |
| 2 | 0.1 | -2.97618e+00 | 7.93359e-01 | 2.89470e-03 |
| 3 | 0.5 | -3.23456e-01 | 2.68590e-02 | -7.30760e-03 |
| 4 | 1.0 | 2.74645e+00 | 4.96660e-01 | -2.24628e-03 |
| 5 | 0.4 | 1.21003e+00 | 8.04876e-01 | 2.13005e-03 |
| 6 | 0.1 | 3.10913e+00 | 7.00746e-01 | 2.83534e-03 |
| 7 | 0.5 | 4.56491e-05 | 3.39639e-04 | 4.65342e-03 |
| 8 | 1.0 | 2.17872e+00 | 4.27999e-01 | 2.32311e-03 |
| 9 | 0.1 | 5.08220e-01 | 8.64463e-01 | -6.65403e-03 |
| 10 | 0.1 | -5.99465e-01 | 5.56410e-01 | 1.04521e-02 |
| 11 | 0.5 | -1.09332e+01 | 5.46744e+01 | -6.88992e-14 |
| 12 | 1.0 | -2.03878e+03 | 1.44157e+04 | -1.98474e-12 |
| 13 | 1.0 | 3.42967e-01 | 8.05711e-02 | 1.32518e-02 |
| 14 | 0.1 | 4.38685e-01 | 1.43131e-01 | 5.90950e-03 |
| 15 | 1.0 | 1.28403e-07 | 1.17306e+00 | 1.07202e-06 |
| 16 | 1.0 | 1.01192e+00 | 4.94477e-01 | 2.97119e-03 |

VI.2 PARAMETRIZATION OF A_2^p

A similar method as described in the previous section was used to fit the A_2^p data. Again, there were no restrictions on the parameter limits and the same initial step sizes with two consecutive iterations were employed for MINUIT.

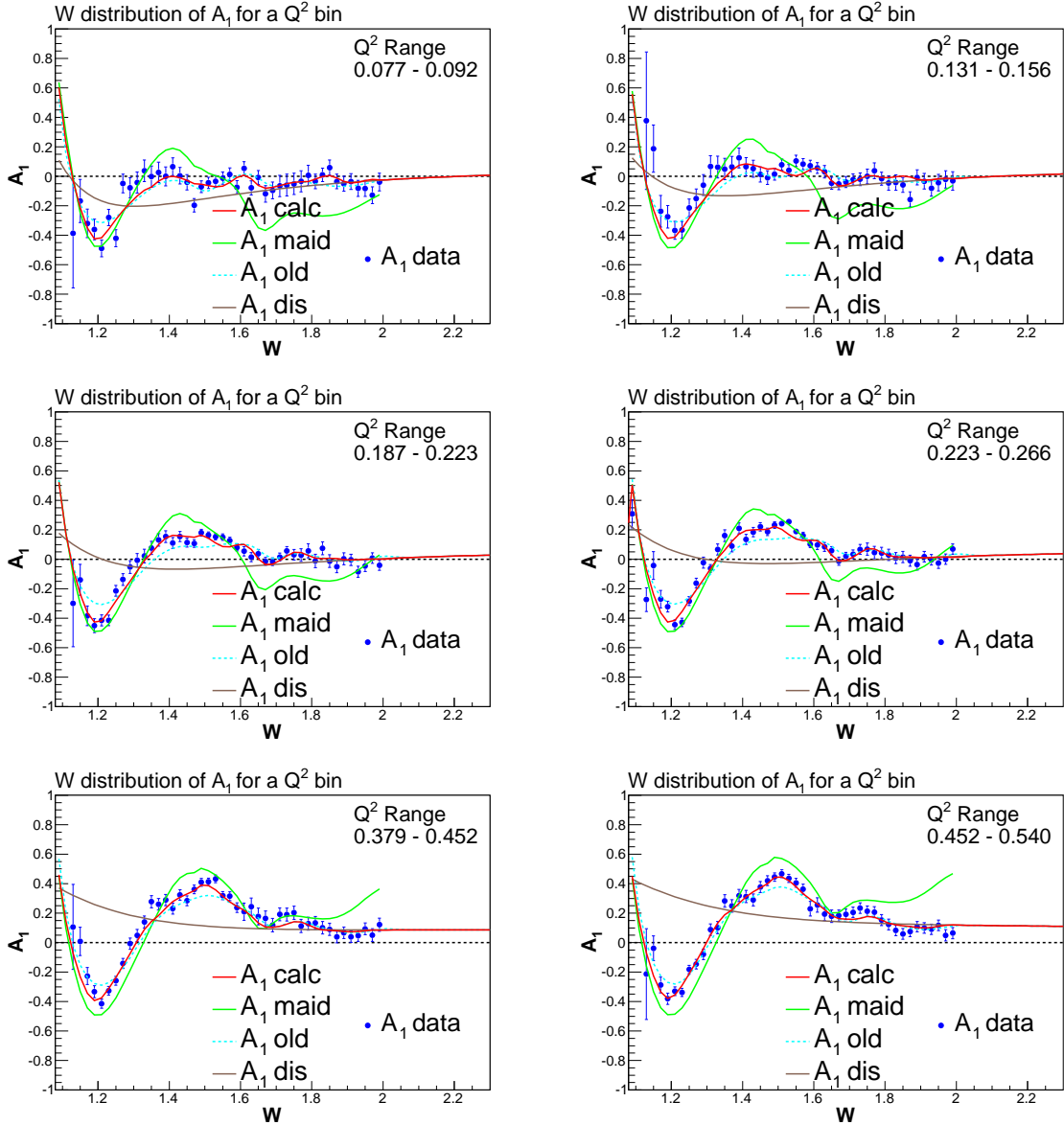


FIG. 127: A_1^p parametrization for various Q^2 bins. The final fit is shown with the red curve. Other curves are MAID 2007, old parametrization and the DIS extrapolation into the resonance region. For only plotting purposes, the data from different contributing experiments were combined over $\Delta W = 40$ MeV, by taking their error weighted averages (fitting was performed on the individual data points at their true kinematic values).

TABLE 52: Final parameters for the second step A_1^p fit (version number 20S2 [132]). The fit function is given in Eq. (469). The total number of data points used in the fit was 4325. The final $\chi^2/n.d.f \approx 1.0405$ was reached at the end of this fit.

| ParNo | Initial | Final | Error | First Derivatives |
|-------|---------|--------------|-------------|-------------------|
| 1 | 0.0 | 2.19052e-01 | 4.25711e-02 | -1.92465e-02 |
| 2 | 0.0 | 1.42339e-01 | 5.77638e-02 | -1.23507e-02 |
| 3 | 0.0 | -1.19772e-01 | 5.96739e-02 | -8.45372e-03 |
| 4 | 0.0 | 4.27655e-01 | 4.96346e-02 | -4.19115e-02 |
| 5 | 0.0 | 1.79650e-01 | 3.12603e-02 | -2.84653e-01 |
| 6 | 0.0 | 3.32088e-03 | 6.51726e-02 | 6.57517e-02 |
| 7 | 0.0 | -7.13901e-02 | 5.61801e-02 | 8.36566e-03 |
| 8 | 0.0 | -2.57325e-01 | 6.96612e-02 | 5.24777e-03 |
| 9 | 0.0 | 2.53712e-01 | 7.17325e-02 | 1.21548e-02 |
| 10 | 0.0 | -1.57327e-01 | 3.74878e-02 | -1.06141e-02 |
| 11 | 0.0 | 1.53637e-01 | 5.66157e-02 | -3.72469e-03 |
| 12 | 0.0 | -2.91941e-01 | 5.66538e-02 | -1.40743e-02 |

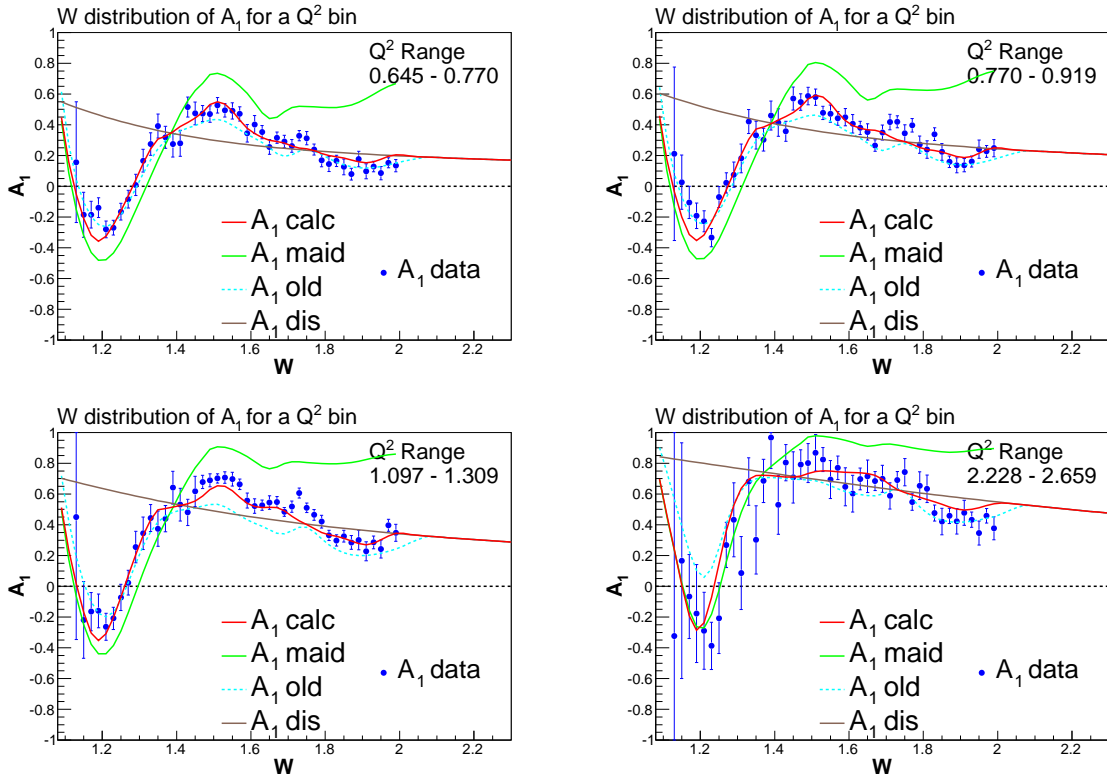


FIG. 128: A_1^p parametrization for various Q^2 bins (continuation of Fig. 127).

Data on A_2^p is sparse, which makes the fit difficult. Mainly, the RSS [133], BATES [129] and the latest EG1b [95] results were used for this fit. The EG1b results were obtained by linear regression between $A_1 + \eta A_2$ values and η from varying beam energies. After various trials with different fit functions, the following form was employed:

$$\begin{aligned}
E_3 &= P_0^2 \left(\frac{\pi}{2} - \tan^{-1} (Q^2 P_1^2 + P_2) \right) \\
E_2 &= \frac{P_3^2 + \tan^{-1} (Q^2 P_4^2 + P_5)}{\frac{\pi}{2} + P_3^2} \\
E_1 &= 1 - E_2 - E_3 \\
E_4 &= \frac{P_6^2}{(\log(Q^2) - P_7)^2 + P_8^2 + 0.0001} \\
C_1 &= 1 - \left[\frac{W - 1.08}{2 - 1.08} \right] \\
C_2 &= \left[1 - \sin \left(\frac{\pi}{2} \left[\frac{W - 1.08}{2 - 1.08} \right] \right) \right]^2 \\
C_3 &= \cos \left(\frac{\pi}{2} \left[\frac{W - 1.08}{2 - 1.08} \right] \right) \\
C_4 &= \begin{cases} \sin \left(\pi \left[\frac{W-1.3}{1.8-1.3} \right] \right) & 1.3 \leq W \leq 1.8 \\ 0 & \text{otherwise} \end{cases} \\
\mathcal{M} &= E_1 C_1 + E_2 C_2 + E_3 C_3 \\
A_2^C &= \begin{cases} \mathcal{M} A_2^M + (1 - \mathcal{M}) A_2^{DIS} + E_4 C_4 & W \leq 2 \\ A_2^{DIS} & W > 2 \end{cases}
\end{aligned} \tag{470}$$

Similar to the previous section, P_i represents parameter i and A_2^C represents the final calculated fit, while A_2^M is the MAID model and A_2^{DIS} is the DIS extrapolation. The Wandzura-Wilczek relation and the Burkhardt-Cottingham Sum Rule [7] were used to estimate the DIS extrapolation of A_2 into the resonance region and were used as a constraint in the fit. A smooth transition between the resonance region and the DIS region was required. In addition, another constraint, the Soffer limit (see Eq. (70)) provided a general estimate and a boundary on the fit results. A penalty was applied to the χ^2 for cases when the calculated fit exceeded the Soffer limit such that:

$$\chi^2(Q^2, W) = \sum_n \frac{(|A^{fit}(Q^2, W)| - A^{soffer}(Q^2, W))^2}{0.005}. \tag{471}$$

The fit was performed in several iterations. In the first iteration, the values of parameters P_6 , P_7 and P_8 were kept constant, and in the second iteration, they were released. The resulting final parameters from these first calculations were used as the starting parameters for the next round and the same fit was repeated twice, again first fixing parameters P_6 , P_7 , P_8 and releasing them after the first 6 parameters reached their optimal values.

The total number of data points for the A_2^p fit was 344. The final χ^2 of the fit was 418.8, resulting in a $\chi^2/n.d.f \approx 1.21$. Table 53 shows the resulting parameter values and Fig. 129 shows the fit results together with the available data for various Q^2 regions.

TABLE 53: Final parameters for the A_2^p fit given in Eq. (470). The final $\chi^2/n.d.f \approx 1.21$ was reached at the end of this fit. The total number of data points used in the fit was 344.

| ParNo | Final | Error | First Derivatives |
|-------|--------------|-------------|-------------------|
| 1 | 5.92348e-01 | 1.97150e-01 | 9.30561e-04 |
| 2 | 1.66989e+02 | 4.89463e-01 | -2.21883e-04 |
| 3 | -2.79601e+04 | 1.62278e+02 | -2.99000e-07 |
| 4 | -1.80099e+00 | 4.56000e-01 | 2.26247e-04 |
| 5 | 3.66274e+00 | 7.98533e+02 | 5.63709e-10 |
| 6 | -7.76211e+04 | 4.47812e+06 | 3.92323e-15 |
| 7 | 2.72528e-01 | 5.91656e-02 | 1.13762e-02 |
| 8 | -1.77948e-01 | 9.76423e-02 | 4.03108e-03 |
| 9 | 4.72596e-01 | 1.06130e-01 | -2.63065e-03 |

VI.3 PARAMETRIZATION OF A_2^n

It is not possible to make a direct measurement on a polarized neutron target to extract the asymmetries and structure functions of the neutron. The best approximates to a polarized neutron target are polarized ^3He and deuterium targets. In both cases, the nuclear effects smear the nucleon structure, making it difficult to isolate the information from a single nucleon. Currently, there are limited data on a transversely polarized deuteron target [130]. However, smearing makes it difficult to extract neutron information for A_2^n from deuteron because proton dominates. In the resonance region, there are also two other experiments that took measurements on a polarized ^3He target. The first experiment was E94-107, which took place in

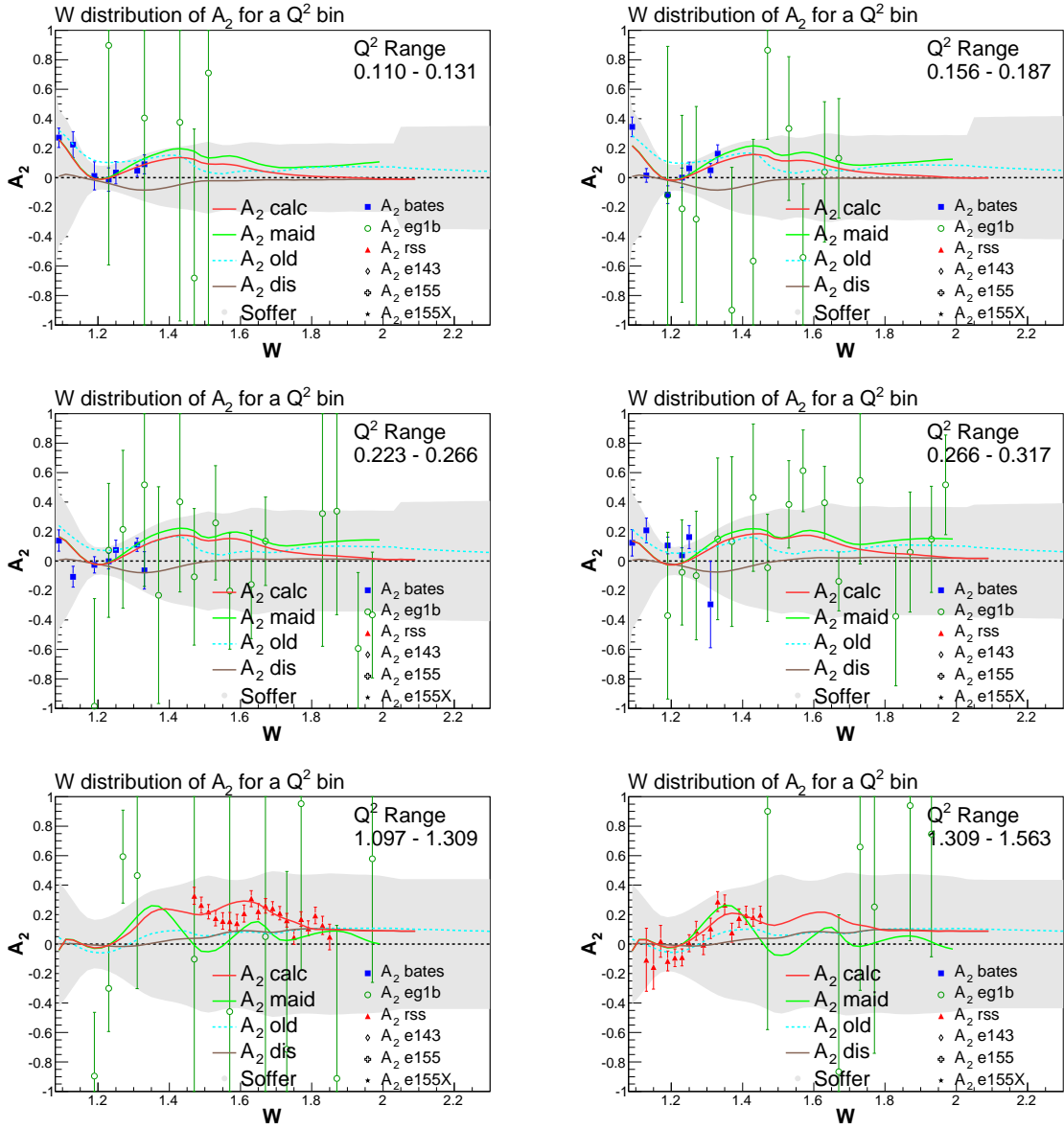


FIG. 129: Final A_2^p parametrization (red line) for various Q^2 bins, for which there are available data, are shown together with other models described in the text. The shaded area represents the Soffer limit. The RSS (red), BATES (blue) and EG1b (green circle) data are also plotted.

Hall-A at Jefferson Lab [134][135]. The experiment measured the spin-dependent cross section for the inclusive scattering of polarized electrons from a polarized ${}^3\text{He}$ target in the quasi-elastic and resonance regions for $0.1 < Q^2 < 0.9 \text{ GeV}^2$. By using both the transverse and longitudinally polarized targets, the experiment extracted the spin structure functions g_1 and g_2 for ${}^3\text{He}$. The second experiment, E01-012, also took place in Hall-A at Jefferson Lab to measure the quark-hadron duality on the neutron by using a polarized ${}^3\text{He}$ target [136][137]. This experiment also extracted the spin structure functions g_1 and g_2 for ${}^3\text{He}$ by measuring the cross section for inclusive electron scattering off longitudinally and transversely polarized targets.

Since we are merely trying to model the general behavior of A_2^n in the resonance region, we decided to use these data on ${}^3\text{He}$ to extract some A_2^n data for our fits. We first applied simple nuclear corrections to get the polarized structure function of the neutron from the ${}^3\text{He}$ data by using our latest model for the proton,

$$g_1^n = \frac{g_1^{\text{He}} + 2.0 \times 0.027 g_1^{p[m]}}{0.87} \quad (472)$$

$$\sigma_{g_1^n} = \frac{\sigma_{g_1^{\text{He}}}}{0.87} \quad (473)$$

$$g_2^n = \frac{g_2^{\text{He}} + 2.0 \times 0.027 g_2^{p[m]}}{0.87} \quad (474)$$

$$\sigma_{g_2^n} = \frac{\sigma_{g_2^{\text{He}}}}{0.87} \quad (475)$$

where the factor 0.87 is for the effective neutron polarization in ${}^3\text{He}$ while 0.027 is that of the proton, with two protons. Then we calculated the corresponding virtual photon asymmetries A_1 and A_2 for the neutron by using these results,

$$A_1 = \frac{g_1 - \gamma^2 g_2}{F_1} \quad (476)$$

$$\sigma_{A_1}^2 = \left(\frac{\sigma_{g_1} - \gamma^2 \sigma_{g_2}}{F_1} \right)^2 \quad (477)$$

$$A_2 = \frac{\gamma}{F_1} (g_1 + g_2) \quad (478)$$

$$\sigma_{A_2}^2 = \left(\frac{\gamma}{F_1} (\sigma_{g_1} + \sigma_{g_2}) \right)^2 \quad (479)$$

where we used the existing models for F_1 , which are described in section IV.16. Once we have the relevant data, we utilized our fit function given in (470), which was also used to fit the proton data on A_2^p . The total number of data points we had for this case was 161. The initial χ^2 of the fit with the starting parameters was 350.55 while

the final χ^2 after the minimization was 190.23, yielding $\chi^2/n.d.f = 1.18$. Table 54 shows the initial and the final parameters of the A_2^n fit. Figs. 130 and 131 show the fit together with the experimental data for various Q^2 values with available data.

TABLE 54: Final parameters for the A_2^n fit given in Eq. 470. The final $\chi^2/n.d.f \approx 1.18$ was reached at the end of this fit. The total number of data points used in the fit was 161.

| ParNo | Initial | Final | Error | First Derivatives |
|-------|---------|--------------|-------------|-------------------|
| 1 | 0.7 | -4.56143e-08 | 5.79134e+00 | -2.72043e-09 |
| 2 | 1.0 | -3.56573e+00 | 1.41421e+00 | 0.00000e+00 |
| 3 | -2.0 | 6.91149e+01 | 1.41421e+00 | 0.00000e+00 |
| 4 | 1.0 | 4.64862e-01 | 9.00620e-02 | 8.86916e-05 |
| 5 | 1.0 | -1.64811e+01 | 3.09743e-02 | 2.48725e-03 |
| 6 | -1.0 | -8.14488e+02 | 3.06294e+00 | -1.08100e-05 |
| 7 | 0.07 | 6.24803e-01 | 2.07558e-02 | -1.21569e-03 |
| 8 | 0.0 | -5.58762e-01 | 1.21758e-01 | 9.07721e-05 |
| 9 | 0.2 | 1.36991e+00 | 5.60160e-02 | 2.78096e-04 |

VI.4 PARAMETRIZATION OF A_1^n BY USING THE DEUTERON DATA

The main ingredients for a fit of A_1 for the neutron are the data on the deuteron spin structure function g_1 and the convolution procedure described in Refs. [73][138] and section II.5. Extraction of the neutron information requires a careful study of the nuclear effects, especially the Fermi motion, which is primarily considered in the convolution procedure. Of course, the D-wave correction was also applied. Moreover, creating the best possible fits to the proton and deuteron data is essential for the best results with this method. Since the EG1b experiment took data on both of these targets, we have a unique opportunity to extract the neutron asymmetries and structure functions by using the final results from EG1b.

The fitting mechanism for this case is quite different than in the previous cases. The fitted data come from the deuteron spin structure function g_1 measurements. The results of the EG1b experiment, described in this thesis, were used as well as the measurements from the RSS [130] and E143 [45] experiments. A fit function was employed to determine A_1^n and the parametrized A_1^n was used in the smearing procedure, together with the final A_1^p parametrization described in section VI.1.

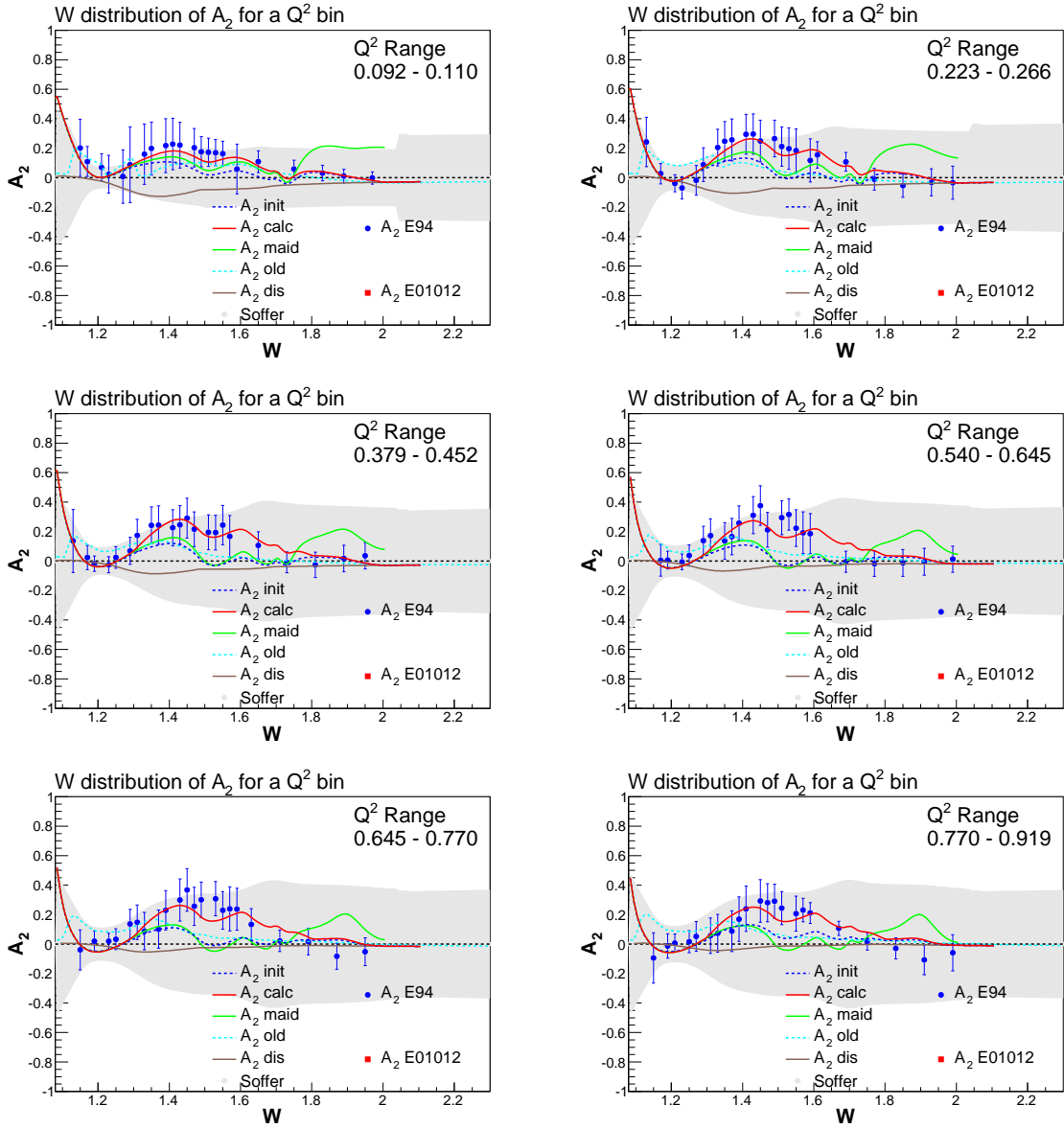


FIG. 130: Final A_2^n parametrization for various Q^2 bins with available data. The red line represents the final fit. Blue data points are from the E94-107 experiment. The MAID model (green), the DIS extrapolation (brown) and older parametrization (cyan) are also plotted. The shaded region is the Soffer limit.

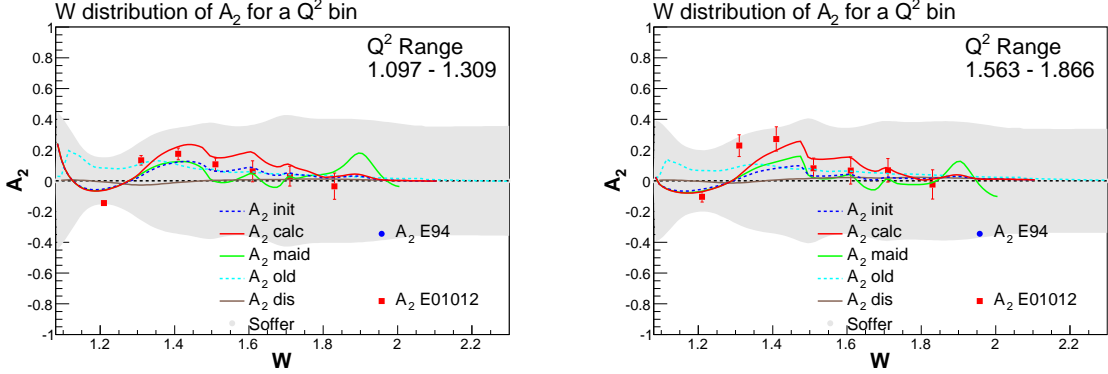


FIG. 131: Final A_2^n parametrization for various Q^2 bins with available data. The red line represents the final fit. The data from E01-012 is also shown (red) together with the MAID model (green), the DIS extrapolation (brown) and an older parametrization (cyan). The shaded region is the Soffer limit.

The smearing function combines the information for the proton and neutron by taking nuclear effects like Fermi motion into account and calculates the deuteron spin structure function g_1^d , which was compared to data to calculate the χ^2 of the fit according to Eq. (467). After the minimization of the χ^2 , the resulting parameters were used in the fit function for the neutron to determine the final parametrized values of A_1^n .

For the fit function, the parameterizations of A_1^p and A_2^p , described in Eqs. (468) and (470), were both tried. Eventually, the A_2^p parametrization in Eq. (470), which was also used for A_2^n , seemed to describe the data best. The total number of data points for this fit was 3175. The final χ^2 was 2503.41, which yields $\chi^2/n.d.f \approx 1.26$. We should point out that this fit will be improved by employing a second step fit as we did for the case of proton. However, the current results describe the data well in most kinematics as can be seen in Fig. 132. The model for A_1^n obtained by using the final parameters is also shown in Fig. 133.

Finally, once we have reliable models for the proton and neutron structure functions, we can determine the deuteron model by properly smearing the proton and neutron. As a result, we have experimental data on deuteron spin structure function g_1 as well as its model obtained by the smearing procedure [73]. We can extract the neutron structure function data by

$$g_1^{n[data]} = \frac{1}{1 - 1.5w_D} (g_1^{d[data]} - g_1^{d[model]}) + g_1^{n[model]} \quad (480)$$

where w_D stands for D-state probability. The statistical and systematic errors propagate as

$$\sigma_{n[data]}^{stat} = \frac{1}{1 - 1.5w_D} \sigma_{d[data]}^{stat} \quad (481)$$

$$\sigma_{n[data]}^{sys} = \frac{1}{1 - 1.5w_D} \sigma_{d[data]}^{sys}. \quad (482)$$

However, since this extraction depends on the model choice, we need to vary both the neutron and deuteron models and add the differences coming from model choices to the total systematic error in quadrature

$$\sigma_{n[data]}^{systot} = \left[(\sigma_{n[data]}^{sys})^2 + \left(\sum_i [g_1^{n[data]} - g_1^{n[i]}] \right)^2 \right]^{1/2}. \quad (483)$$

where summation is over different model choices and $g_1^{n[i]}$ represents the extracted result for model choice i . The results for this extraction are shown in Fig. 134 for a few Q^2 bins.

VI.5 ADDITIONAL COMMENTS

The work on modeling the world data is a continuous and iterative procedure. Some of the results have certain model dependencies. For example, the EG1b results for A_1 have a slight dependence on the A_2 models (see Ref. [95]). By getting a better parametrization for A_2 , the A_1 model can be improved and in turn, the A_2 parametrization can be re-visited to create a better model on this quantity. In addition, the data on these quantities are constantly improving in different kinematic ranges. The efforts will continue as these new data come into existence. In particular, the EG4 experiment [139] will allow us to extend our parameterizations of A_1^p , A_1^n into the lower Q^2 range and give us opportunity to resume our efforts.

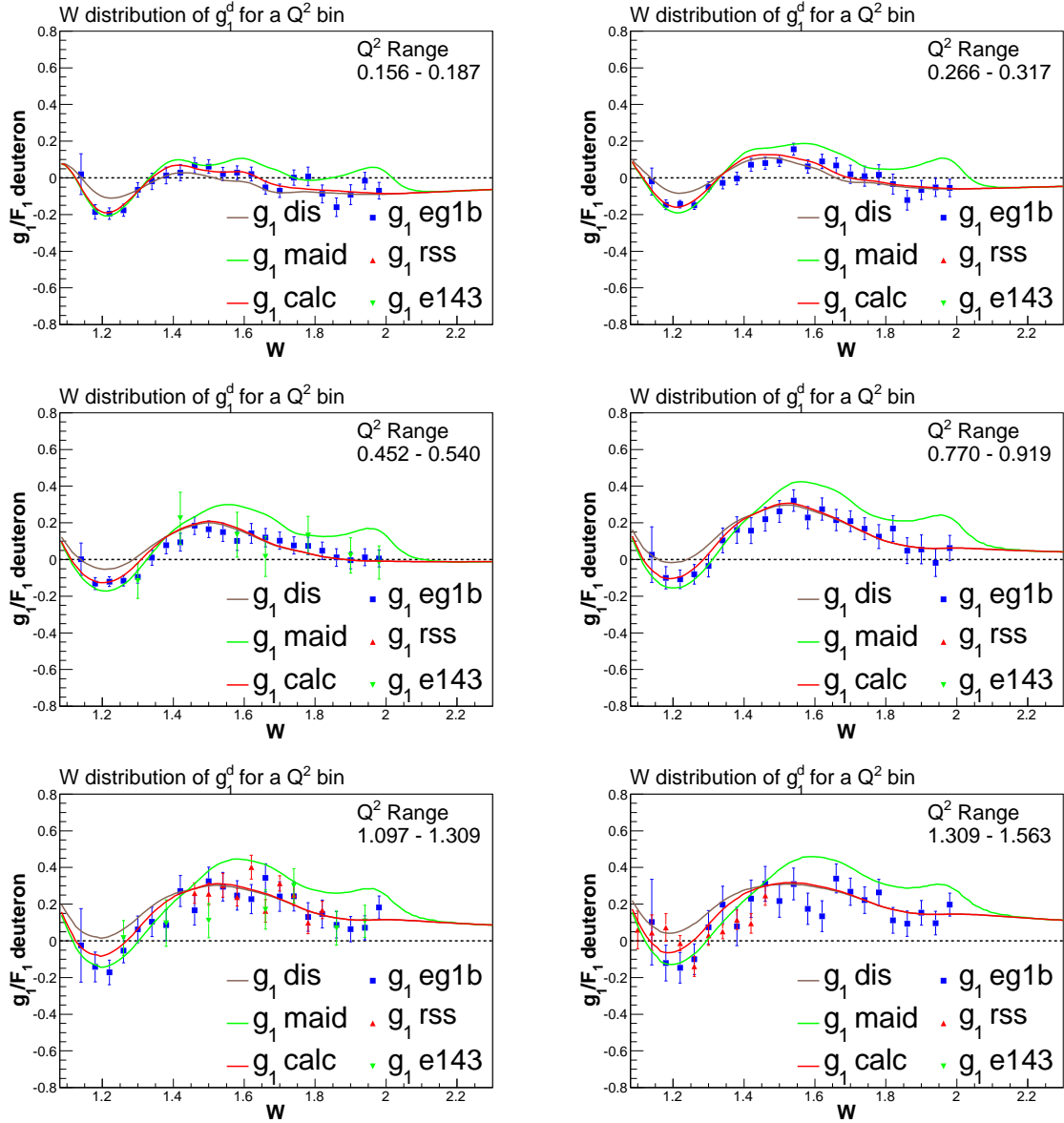


FIG. 132: The model for g_1/F_1 for the deuteron (red solid line), which was calculated from the parametrized A_1^n and A_1^p by applying the smearing procedure, is plotted together with the experimental data points for various Q^2 bins. Together with the EG1b experiment (blue), the RSS (red) and E143 (green) data are also shown. As usual, the green line represents MAID and the brown line is the DIS extrapolation.

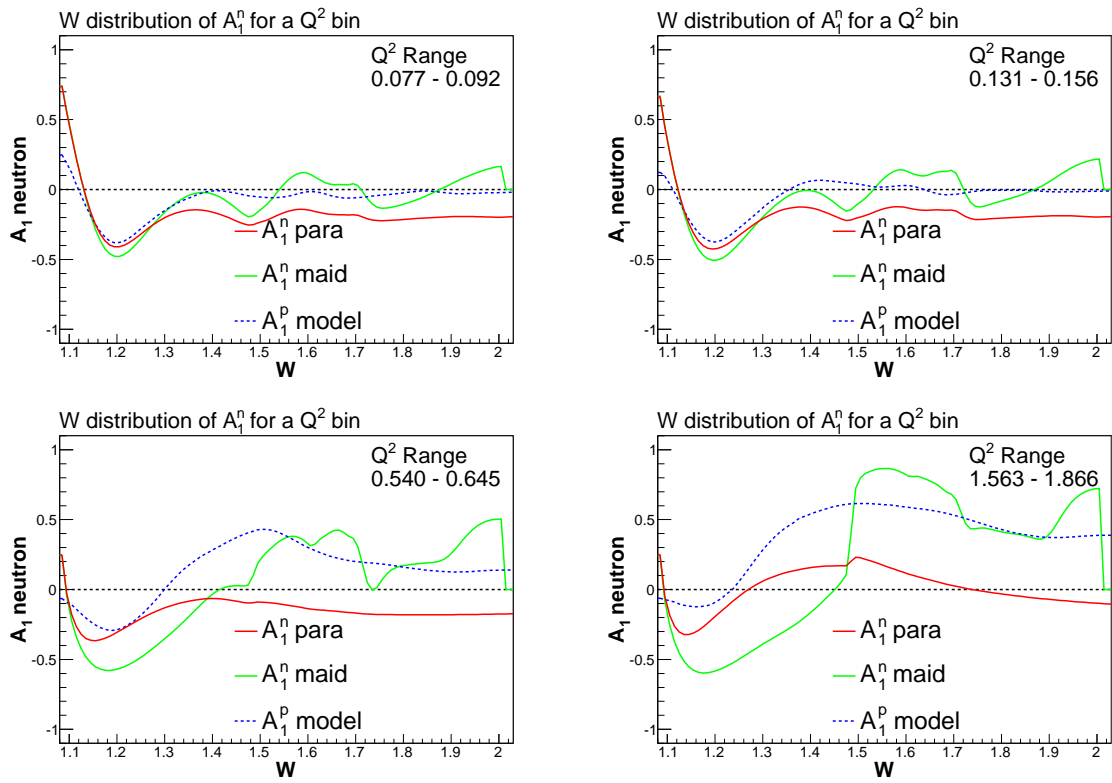


FIG. 133: The parametrized A_1 for the neutron (red curve) is shown for a few Q^2 bins. Also shown are the MAID curve (green) and the model of A_1 proton, for comparison purposes.

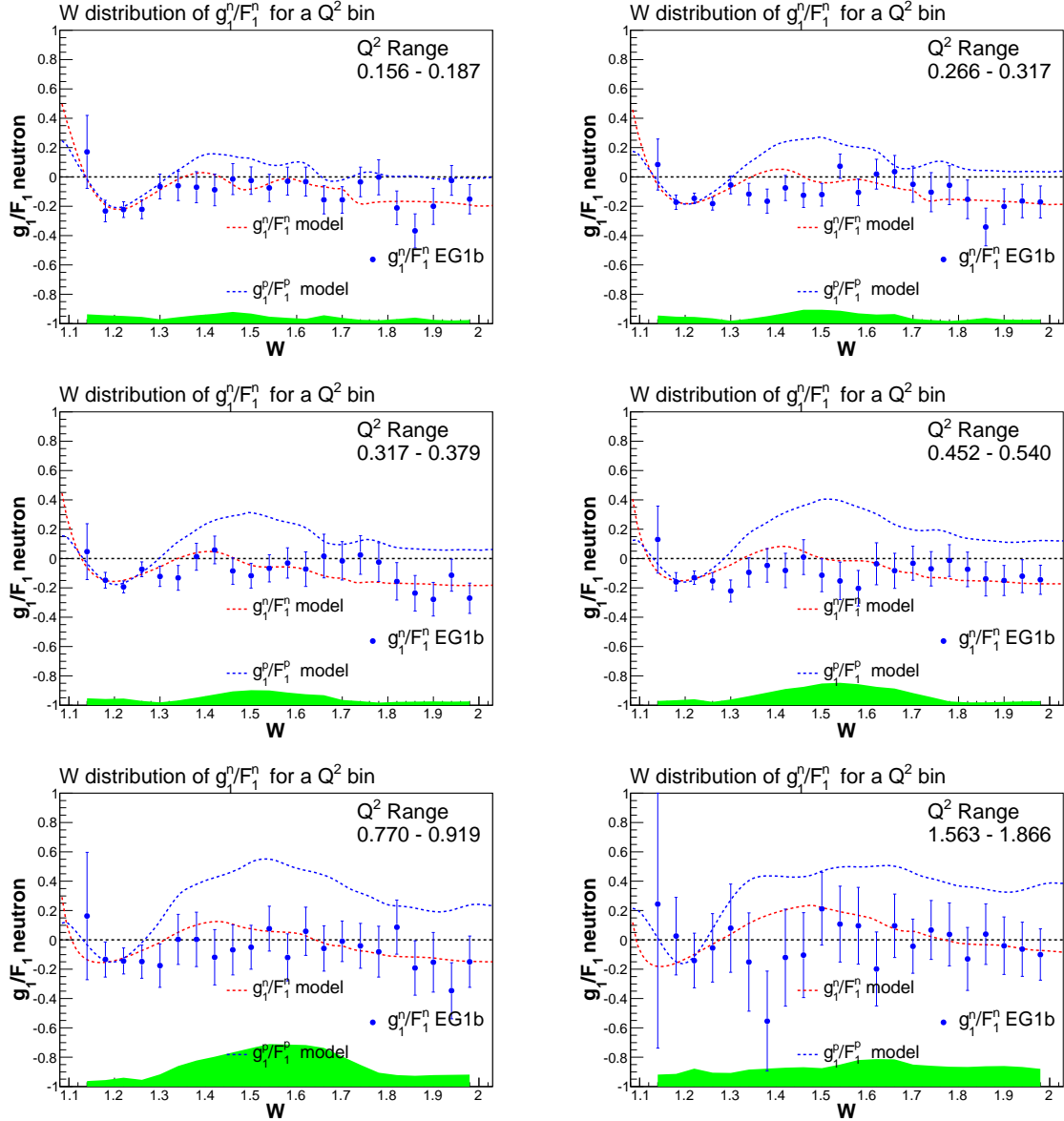


FIG. 134: Parametrized g_1/F_1 (red dashed line) for the neutron is plotted together with g_1/F_1 neutron (blue data points) extracted from the EG1b deuteron data according to Eq. (480). The systematic errors are shown as green shades at the bottom of each plot. The same quantity for proton is also shown for comparison purposes (blue dashed line).

CHAPTER VII

CONCLUSION

The EG1b experiment measured the double spin asymmetry for the deuteron (and the proton) over a large kinematic range that covers the resonance region and the onset of the DIS region. Although the results from the 1.6 and 5.7 GeV data have been available before, these data have been reanalyzed for full statistics by adding the remaining data sets with 2.5 and 4.2 GeV beam energies. This extended the kinematic coverage and reduced the errors on the measured quantities significantly. The measurements from EG1b enabled the extraction of the virtual photon asymmetry A_1 for $0.05 \text{ GeV}^2 < Q^2 < 5.0 \text{ GeV}^2$ with unprecedented precision. The statistical precision of the data enabled us to see clear resonant behavior at low Q^2 . The largest systematic error on A_1 comes from model input for A_2 . The studies on A_2 parametrization is an ongoing process and with its completion, the systematic errors on A_1 , and thus g_1 , will decrease.

At low Q^2 , the structure function g_1^d is also deeply affected by the resonance structure in our kinematic range. As a result, its first moment, Γ_1^1 , as well as the higher moments, have a strong Q^2 dependence. As we go to higher Q^2 , the resonant structure is less explicit and the Q^2 dependence of the first moment slowly diminishes. The experimental data confirm the Q^2 evolution of the first moment envisioned by the phenomenological studies, described in chapter II. At low Q^2 , Γ_1^1 is negative and expected to approach the GDH slope. The data from EG1b do not cover a low enough Q^2 region to put the GDH slope under a robust test. However, the overall tendency in that region obeys the constraints enforced by the GDH slope. The next generation experiments [139] will cover a lower Q^2 range in order to test the GDH slope as well as χ PT theory in this region. Γ_1^1 being negative at low Q^2 is attributed to the $\Delta P_{33}(1232)$ resonance, which is also evident from the g_1 versus x plots that become negative in this region. It should be pointed out that the plots of the moments shown in this analysis all exclude the quasi-elastic peak. Its inclusion would smear out the effects of the resonances. As we go to higher Q^2 , Γ_1^1 for the deuteron experiences its minima around $0.10 < Q^2 < 0.15 \text{ GeV}^2$ and attains a positive slope, then crossing zero around $0.45 < Q^2 < 0.50 \text{ GeV}^2$. As we go above $Q^2 \approx 2 \text{ GeV}^2$, Γ_1^1 becomes almost flat approaching the Bjorken limit. In the intermediate and high Q^2 regions, the data and phenomenological calculations agree well. The data from the EG1b

experiment will create opportunities to test different versions of the generalized GHD integrals and modified Bjorken Sum Rule. Moreover, the results will create a robust ground for studies on duality and calculations of the higher twist coefficients.

Parametrization of the world data on the virtual photon asymmetries is an important basis for calculations of radiative corrections to cross sections. Moreover, these parameterizations are also crucial for the extraction of spin structure functions from future asymmetry measurements as well as providing inputs for phenomenological calculations. In addition, the extraction of the neutron structure functions from the proton and deuteron data by comprehensively taking the nuclear effects into account gives us a more reliable parametrization for the neutron. In addition, this kind of work can provide a different environment to study and test the nuclear effects inside the deuteron.

Although its effect on the final results will be small, the radiative corrections applied to A_{\parallel} still require an update after the completion of the parameterizations on the symmetries. After that, the final official data from this analysis will be available in the CLAS database [140].

APPENDIX A

DST VARIABLES

In the DST tables, the range (R) of a variable is defined in terms of the offset (o), the multiplier (m), the sign (s), that determines whether the variable is signed (1) or not (0), and the number of bits (n) for the variable,

$$R = \left[- \left(\frac{2^n}{m} - o \right) * s ; \left(\frac{2^n}{m} - o \right) \right]. \quad (484)$$

This is the scheme used in the DST libraries to determine the maximum and minimum acceptable values for the variables.

TABLE 55: DST variables: particle ID. SEB is the standard particle ID used in RECSIS, whereas p_id(DST) is the DST equivalent.

| SEB ID | p_id(DST) | particle |
|--------|-----------|----------|
| 11 | 1 | electron |
| 2212 | 2 | proton |
| 2112 | 3 | neutron |
| 211 | 4 | π^+ |
| -211 | 5 | π^- |
| 321 | 6 | K^+ |
| -321 | 7 | K^- |
| 45 | 8 | deuteron |
| 49 | 9 | 3He |
| 47 | 10 | 4He |
| 22 | 11 | photon |
| -11 | 12 | positron |

TABLE 56: DST event headers

| name | offset | multiplier | signed | bits | definition |
|------------|--------|------------|--------|------|-------------------------------------|
| event | 0.0 | 1.0 | 0 | 27 | event number from BOS file |
| n_part | 0.0 | 1.0 | 0 | 5 | number of particles in the event |
| start_time | 0.0 | 100.0 | 1 | 14 | event start_time |
| raster_x | 0.0 | 1.0 | 0 | 16 | x coordinate of the raster position |
| raster_y | 0.0 | 1.0 | 0 | 16 | y coordinate of the raster position |
| trigbits | 0.0 | 1.0 | 0 | 16 | trigger bit |

TABLE 57: DST scaler variables and run information

| name | offset | multiplier | signed | bits | definition |
|--------------|--------|------------|--------|------|-----------------------------------|
| CLOCK_UG | 0.0 | 1.0 | 0 | 31 | live time ungated clock |
| CLOCK_G | 0.0 | 1.0 | 0 | 31 | live time gated clock |
| FC_UG | 0.0 | 1.0 | 0 | 31 | live time ungated faraday cup |
| FC_G | 0.0 | 1.0 | 0 | 31 | live time gated faraday cup |
| EVMIn | 0.0 | 1.0 | 0 | 27 | first event of the helicity state |
| EVmax | 0.0 | 1.0 | 0 | 27 | last event of the helicity state |
| clockug | 0.0 | 1.0 | 0 | 19 | ungated clock |
| clockg | 0.0 | 1.0 | 0 | 19 | gated clock |
| fcupug | 0.0 | 1.0 | 0 | 12 | ungated faraday cup |
| fcupg | 0.0 | 1.0 | 0 | 12 | gated faraday cup |
| synchug | 0.0 | 1.0 | 0 | 16 | ungated SLM |
| synchg | 0.0 | 1.0 | 0 | 16 | gated SLM |
| PMTTop | 0.0 | 1.0 | 0 | 10 | PMT output |
| PMTBottom | 0.0 | 1.0 | 0 | 10 | PMT output |
| PMTBeamRight | 0.0 | 1.0 | 0 | 10 | PMT output |
| PMTBeamLeft | 0.0 | 1.0 | 0 | 10 | PMT output |
| BeamE | 0.0 | 1.0 | 0 | 16 | Beam energy |
| BeamI | 0.0 | 10.0 | 0 | 10 | Beam current |
| TorusI | 0.0 | 1.0 | 1 | 12 | Torus current |
| TargetI | 0.0 | 1.0 | 1 | 12 | Target current |
| BeamPol | 0.0 | 100.0 | 1 | 7 | Beam polarization |
| TargetPol | 0.0 | 100.0 | 1 | 7 | Target polarization |
| BadRun | 0.0 | 1.0 | 0 | 32 | Run flag |
| Target | 0.0 | 1.0 | 0 | 7 | Target type |
| PolPlate | 0.0 | 1.0 | 0 | 2 | Half-wave plate status |

TABLE 58: DST particle variables

| name | offset | multiplier | signed | bits | definition |
|--------------|--------|------------|--------|------|--------------------------------|
| p_id | 0.0 | 1.0 | 0 | 4 | particle identifier |
| p_x | 0.0 | 10000.0 | 1 | 16 | momentum |
| p_y | 0.0 | 10000.0 | 1 | 16 | momentum |
| p_z | 0.0 | 10000.0 | 1 | 17 | momentum |
| v_x | 0.0 | 10.0 | 1 | 9 | vertex coordinates |
| v_y | 0.0 | 10.0 | 1 | 9 | vertex coordinates |
| v_z | -57.0 | 10.0 | 1 | 10 | vertex coordinates |
| q | 0.0 | 1.0 | 1 | 1 | charge |
| beta | 0.0 | 1000.0 | 0 | 11 | beta |
| sector | 0.0 | 1.0 | 0 | 3 | particle sector |
| chi_sqr | 0.0 | 100.0 | 0 | 9 | chi squared of track fit |
| cc_pe | 0.0 | 10.0 | 0 | 10 | number of photoelectrons in CC |
| cc_chi_sqr | 0.0 | 1000.0 | 0 | 9 | not used |
| trl1_theta | 0.0 | 10.0 | 0 | 11 | DC1 angle |
| trl1_phi | 0.0 | 10.0 | 0 | 11 | DC1 angle |
| trl1_x | 0.0 | 1.0 | 0 | 9 | DC1 coordinate |
| trl1_y | 0.0 | 1.0 | 0 | 9 | DC1 coordinate |
| trl1_z | 0.0 | 1.0 | 0 | 9 | DC1 coordinate |
| sc_e | 0.0 | 10.0 | 0 | 10 | energy deposited in SC |
| ec_in | 0.0 | 100.0 | 0 | 8 | EC inner energy |
| ec_out | 0.0 | 100.0 | 0 | 8 | EC outer energy |
| ec_tot | 0.0 | 100.0 | 0 | 8 | EC total energy |
| ec_pos_x | 0.0 | 1.0 | 1 | 10 | hit position in EC |
| ec_pos_y | 0.0 | 1.0 | 1 | 10 | hit position in EC |
| ec_pos_z | 0.0 | 1.0 | 1 | 10 | hit position in EC |
| ec_m2hit | 0.0 | 1.0 | 0 | 11 | m2 of EC shower |
| sc_paddle | 0.0 | 1.0 | 0 | 6 | TOF paddle identifier |
| tdc_time | 0.0 | 100.0 | 0 | 15 | time of flight |
| track_length | 0.0 | 10.0 | 0 | 14 | path length |
| flag | 0.0 | 1.0 | 1 | 16 | status_EVNT+10 |

TABLE 59: DST particle variables (added later to use the geometric and timing cuts).

| name | offset | multiplier | signed | bits | definition |
|-----------|--------|------------|--------|------|---------------------|
| sc_x | 0.0 | 1.0 | 1 | 10 | sc position |
| sc_y | 0.0 | 1.0 | 1 | 10 | sc position |
| sc_z | 0.0 | 1.0 | 1 | 10 | sc position |
| sc_cx | 0.0 | 1000.0 | 1 | 10 | sc direction cosine |
| sc_cy | 0.0 | 1000.0 | 1 | 10 | sc direction cosine |
| sc_cz | 0.0 | 1000.0 | 1 | 10 | sc direction cosine |
| cc_time | 0.0 | 100.0 | 0 | 15 | cc time |
| cc_status | 0.0 | 1.0 | 0 | 15 | cc status flag |
| cc_r | 0.0 | 10.0 | 0 | 15 | cc radial distance |
| cc_sec | 0.0 | 1.0 | 0 | 3 | cc sector |
| sc_time | 0.0 | 100.0 | 0 | 15 | sc time |
| sc_status | 0.0 | 1.0 | 0 | 15 | sc status flag |
| sc_r | 0.0 | 10.0 | 0 | 15 | sc radial distance |
| sc_sec | 0.0 | 1.0 | 0 | 3 | sc sector |

TABLE 60: DST variables: helicity flag

| helicity flag | true helicity | state |
|---------------|---------------|--------------------------|
| 1 | 1 | first state of the pair |
| 2 | 0 | first state of the pair |
| 3 | 1 | second state of the pair |
| 4 | 0 | second state of the pair |
| -1 | 1 | bad helicity flag |
| -2 | 0 | bad helicity flag |

APPENDIX B

FIDUCIAL CUTS

B.1 INBENDING FIDUCIAL CUTS

The fiducial cut limits for ϕ and θ are given by:

$$30^\circ - \Delta\phi < \phi < 30^\circ + \Delta\phi \quad (485)$$

and

$$\theta > \theta_{cut}, \quad (486)$$

where the cut limits $\Delta\phi$ and θ_{cut} are defined by

$$\Delta\phi = A \cdot (\sin(\theta - \theta_{cut}))^{exp} \quad (487)$$

with

$$exp = B \cdot \left(p_{el} \cdot \frac{3375A}{I_{Torus}} \right)^C \quad (488)$$

and

$$\theta_{cut} = D + \frac{E}{(p_{el} + F) \frac{3375A}{I_{Torus}}}. \quad (489)$$

These cuts are used for the part of analysis where backgrounds and contaminations are calculated. They are not used for asymmetry measurements. Instead, loose cuts that remove the direct PMT hits are used in that case. The table of loose fiducial cuts is also included below.

B.2 OUTBENDING FIDUCIAL CUTS

The following cuts are applied to the outbending data when studying backgrounds and contaminations. The parameter values for the fiducial cut are given in the table. No loose fiducial cuts were applied to the outbending data for asymmetry analysis.

$$30^\circ - \Delta\phi < \phi < 30^\circ + \Delta\phi \quad (490)$$

and

$$\theta_{cut} < \theta < \theta_{high}, \quad (491)$$

where

$$\Delta\phi = A \cdot (\sin(\theta - 6.5^\circ))^{exp} \quad (492)$$

$$exp = B \cdot \left(\frac{1}{4}p_{el}\right)^C \quad (493)$$

$$\theta_{cut} = D + E \cdot \left(1 - \frac{1}{4}p_{scale}\right)^F \quad (494)$$

$$\theta_{high} = \min(40^\circ, \theta_{nom}) \quad (495)$$

$$\theta_{nom} = \frac{35^\circ}{(\text{GeV}/c)^{1/3}} \cdot \left[\frac{1}{5} \left(p_{el} \cdot \frac{3375A}{|I_{Torus}|} + 2.5\text{GeV}/c\right)\right]^{1/3} \quad (496)$$

$$p_{scale} = p_{el} \cdot \frac{1500A}{|I_{Torus}|}. \quad (497)$$

TABLE 61: Fiducial cut parameters for the inbending data. Momentum is in GeV and angles are in degrees. These cuts are not used for asymmetry measurements.

| Parameter | $p < 3 \text{ GeV}$ | $p > 3 \text{ GeV}$ |
|--------------|---------------------|---------------------|
| A | 36 | 36 |
| B | 0.28 | 0.25 |
| C | 0.30 | 0.30 |
| D | 10 | 10 |
| E | 16.72 | 16.72 |
| F | 0.06 | 0.06 |
| ϕ_{lim} | 20 | 20 |

TABLE 62: Loose fiducial cut parameters for the inbending data. These cuts remove the direct PMT hits only. They can be applied in case of asymmetry measurements but cannot be applied to any acceptance dependent measurements.

| Parameter | $p < 3 \text{ GeV}$ | $p > 3 \text{ GeV}$ |
|--------------|---------------------|---------------------|
| A | 41 | 41 |
| B | 0.26 | 0.26 |
| C | 0.30 | 0.30 |
| D | 9 | 8 |
| E | 16.72 | 16.72 |
| F | 0.06 | 0.06 |
| ϕ_{lim} | 21.5 | 21.5 |

TABLE 63: Fiducial cut parameters for the outbending data. Momentum is in GeV and angles are in degrees. These cuts are not used for asymmetry measurements but they are used for background analysis.

| Parameter | $p < 3$ GeV (-2250 A) | $p > 3$ GeV (-2250 A) | -1500 A |
|-------------------------|--------------------------|--------------------------|-----------|
| A | 34 | 45 | 34 |
| B | 0.28 | 0.54 | 0.33 |
| C | 0.22 | 0.21 | 0.22 |
| D | 5 | 9.5 | 6.2 |
| E | 3 | -4 | 3 |
| F | 1.46 | 1.2 | 1.46 |
| G_{upper} | 0.15 | 0.3 | 0.15 |
| H_{upper} | -0.09 | 0.1 | -0.09 |
| G_{lower} | 0.15 | 0.3 | 0.15 |
| H_{lower} | -0.09 | 0.1 | -0.09 |
| ϕ_{lim}^{hi} | 21 | 21 | 21 |
| ϕ_{lim}^{lo} | 22 | 22 | 22 |
| offset _{outer} | 1.2 | -0.6 | 1.2 |
| offset _{inner} | 0 | 0 | 0 |

APPENDIX C

ADDITIONAL TABLES

C.1 PION AND PAIR SYMMETRIC CONTAMINATION PARAMETERS

C.2 SYSTEMATIC ERRORS

C.3 KINEMATIC REGIONS FOR MODEL USAGE IN Γ_1^1 INTEGRATION

TABLE 64: Standard π^-/e^- ratio parameters a and b in Eq. (364).

| Target | E | Torus | a | b |
|--------|------|-------|--------------------|--------------------|
| ND3 | 1606 | 1500 | -14.27 ± 2.968 | 0.211 ± 0.092 |
| ND3 | 1606 | -1500 | -11.06 ± 2.600 | 0.217 ± 0.118 |
| NH3 | 1606 | 1500 | -17.27 ± 3.112 | 0.289 ± 0.092 |
| NH3 | 1606 | -1500 | -11.62 ± 3.205 | 0.270 ± 0.146 |
| ND3 | 1723 | -1500 | -11.06 ± 2.600 | 0.217 ± 0.118 |
| NH3 | 1723 | -1500 | -11.62 ± 3.205 | 0.270 ± 0.146 |
| NH3 | 2286 | 1500 | -4.946 ± 1.314 | 0.006 ± 0.042 |
| ND3 | 2561 | 1500 | -5.190 ± 1.229 | 0.022 ± 0.040 |
| ND3 | 2561 | -1500 | -4.250 ± 0.775 | -0.009 ± 0.035 |
| NH3 | 2561 | -1500 | -4.373 ± 0.815 | -0.003 ± 0.037 |
| ND3 | 4238 | 2250 | -4.637 ± 2.096 | 0.036 ± 0.080 |
| ND3 | 4238 | -2250 | -4.192 ± 1.008 | 0.026 ± 0.049 |
| NH3 | 4238 | 2250 | -5.051 ± 1.897 | 0.043 ± 0.073 |
| NH3 | 4238 | -2250 | -4.656 ± 1.266 | 0.045 ± 0.062 |
| ND3 | 5615 | 2250 | -3.791 ± 1.577 | 0.023 ± 0.060 |
| NH3 | 5615 | 2250 | -4.143 ± 2.004 | 0.030 ± 0.076 |
| ND3 | 5725 | 2250 | -2.859 ± 1.584 | -0.005 ± 0.060 |
| ND3 | 5725 | -2250 | -4.322 ± 0.996 | 0.046 ± 0.047 |
| NH3 | 5725 | 2250 | -3.631 ± 1.482 | 0.017 ± 0.057 |
| NH3 | 5725 | -2250 | -4.272 ± 0.872 | 0.042 ± 0.042 |
| ND3 | 5743 | -2250 | -4.695 ± 1.022 | 0.064 ± 0.049 |
| NH3 | 5743 | -2250 | -4.333 ± 0.844 | 0.040 ± 0.040 |

TABLE 65: Standard π^-/e^- ratio parameters c and d in Eq. (364).

| Target | E | Torus | c | d |
|--------|------|-------|--------------------|--------------------|
| ND3 | 1606 | 1500 | 6.417 ± 3.119 | -0.231 ± 0.102 |
| ND3 | 1606 | -1500 | 3.986 ± 2.703 | -0.271 ± 0.126 |
| NH3 | 1606 | 1500 | 9.325 ± 3.013 | -0.297 ± 0.093 |
| NH3 | 1606 | -1500 | 4.386 ± 3.763 | -0.326 ± 0.185 |
| ND3 | 1723 | -1500 | 3.986 ± 2.703 | -0.271 ± 0.126 |
| NH3 | 1723 | -1500 | 4.386 ± 3.763 | -0.326 ± 0.185 |
| NH3 | 2286 | 1500 | 0.218 ± 1.404 | -0.048 ± 0.047 |
| ND3 | 2561 | 1500 | -0.011 ± 1.360 | -0.042 ± 0.045 |
| ND3 | 2561 | -1500 | -0.935 ± 0.828 | -0.005 ± 0.036 |
| NH3 | 2561 | -1500 | -0.727 ± 0.812 | -0.015 ± 0.037 |
| ND3 | 4238 | 2250 | -0.546 ± 1.574 | -0.033 ± 0.060 |
| ND3 | 4238 | -2250 | -0.648 ± 0.785 | -0.030 ± 0.037 |
| NH3 | 4238 | 2250 | 0.010 ± 1.393 | -0.048 ± 0.054 |
| NH3 | 4238 | -2250 | -0.381 ± 0.983 | -0.042 ± 0.046 |
| ND3 | 5615 | 2250 | -0.731 ± 1.130 | -0.022 ± 0.042 |
| NH3 | 5615 | 2250 | -0.483 ± 1.402 | -0.030 ± 0.053 |
| ND3 | 5725 | 2250 | -1.488 ± 1.158 | 0.000 ± 0.044 |
| ND3 | 5725 | -2250 | -0.372 ± 0.749 | -0.034 ± 0.035 |
| NH3 | 5725 | 2250 | -0.713 ± 1.049 | -0.024 ± 0.040 |
| NH3 | 5725 | -2250 | -0.373 ± 0.655 | -0.034 ± 0.030 |
| ND3 | 5743 | -2250 | -0.191 ± 0.775 | -0.045 ± 0.036 |
| NH3 | 5743 | -2250 | -0.342 ± 0.630 | -0.035 ± 0.029 |

TABLE 66: Total π^-/e^- ratio parameters a and b in Eq. (364).

| Target | E | Torus | a | b |
|--------|------|-------|--------------------|-------------------|
| ND3 | 1606 | 1500 | -5.851 ± 1.378 | 0.117 ± 0.042 |
| ND3 | 1606 | -1500 | -2.563 ± 1.299 | 0.015 ± 0.065 |
| NH3 | 1606 | 1500 | -6.057 ± 1.484 | 0.118 ± 0.045 |
| NH3 | 1606 | -1500 | -2.703 ± 1.699 | 0.019 ± 0.086 |
| ND3 | 1723 | -1500 | -2.563 ± 1.299 | 0.015 ± 0.065 |
| NH3 | 1723 | -1500 | -2.703 ± 1.699 | 0.019 ± 0.086 |
| NH3 | 2286 | 1500 | -2.423 ± 0.761 | 0.043 ± 0.023 |
| ND3 | 2561 | 1500 | -2.675 ± 0.663 | 0.055 ± 0.020 |
| ND3 | 2561 | -1500 | -2.728 ± 0.563 | 0.052 ± 0.022 |
| NH3 | 2561 | -1500 | -2.628 ± 0.600 | 0.046 ± 0.023 |
| ND3 | 4238 | 2250 | -0.394 ± 0.914 | 0.039 ± 0.031 |
| ND3 | 4238 | -2250 | -1.112 ± 0.651 | 0.063 ± 0.026 |
| NH3 | 4238 | 2250 | -0.584 ± 0.881 | 0.043 ± 0.029 |
| NH3 | 4238 | -2250 | -1.204 ± 0.711 | 0.063 ± 0.029 |
| ND3 | 5615 | 2250 | 0.087 ± 0.516 | 0.016 ± 0.017 |
| NH3 | 5615 | 2250 | -0.043 ± 0.585 | 0.019 ± 0.020 |
| ND3 | 5725 | 2250 | 0.176 ± 0.516 | 0.014 ± 0.017 |
| ND3 | 5725 | -2250 | -0.907 ± 0.411 | 0.051 ± 0.016 |
| NH3 | 5725 | 2250 | 0.037 ± 0.510 | 0.018 ± 0.017 |
| NH3 | 5725 | -2250 | -0.921 ± 0.404 | 0.050 ± 0.016 |
| ND3 | 5743 | -2250 | -1.012 ± 0.427 | 0.055 ± 0.017 |
| NH3 | 5743 | -2250 | -1.078 ± 0.414 | 0.053 ± 0.016 |

TABLE 67: Total π^-/e^- ratio parameters c and d in Eq. (364).

| Target | E | Torus | c | d |
|--------|------|-------|--------------------|--------------------|
| ND3 | 1606 | 1500 | 0.692 ± 1.889 | -0.106 ± 0.057 |
| ND3 | 1606 | -1500 | -0.334 ± 1.517 | -0.088 ± 0.078 |
| NH3 | 1606 | 1500 | 0.950 ± 2.034 | -0.110 ± 0.062 |
| NH3 | 1606 | -1500 | -0.243 ± 1.995 | -0.092 ± 0.104 |
| ND3 | 1723 | -1500 | -0.334 ± 1.517 | -0.088 ± 0.078 |
| NH3 | 1723 | -1500 | -0.243 ± 1.995 | -0.092 ± 0.104 |
| NH3 | 2286 | 1500 | -1.415 ± 0.947 | -0.026 ± 0.029 |
| ND3 | 2561 | 1500 | -1.281 ± 0.788 | -0.025 ± 0.024 |
| ND3 | 2561 | -1500 | -0.875 ± 0.738 | -0.039 ± 0.027 |
| NH3 | 2561 | -1500 | -0.933 ± 0.789 | -0.037 ± 0.029 |
| ND3 | 4238 | 2250 | -1.846 ± 0.705 | -0.014 ± 0.023 |
| ND3 | 4238 | -2250 | -1.066 ± 0.502 | -0.041 ± 0.019 |
| NH3 | 4238 | 2250 | -1.671 ± 0.678 | -0.019 ± 0.022 |
| NH3 | 4238 | -2250 | -1.013 ± 0.552 | -0.044 ± 0.022 |
| ND3 | 5615 | 2250 | -1.535 ± 0.364 | -0.001 ± 0.012 |
| NH3 | 5615 | 2250 | -1.466 ± 0.418 | -0.004 ± 0.014 |
| ND3 | 5725 | 2250 | -1.558 ± 0.363 | 0.000 ± 0.012 |
| ND3 | 5725 | -2250 | -0.767 ± 0.293 | -0.026 ± 0.011 |
| NH3 | 5725 | 2250 | -1.472 ± 0.360 | -0.003 ± 0.012 |
| NH3 | 5725 | -2250 | -0.783 ± 0.288 | -0.026 ± 0.011 |
| ND3 | 5743 | -2250 | -0.707 ± 0.306 | -0.030 ± 0.012 |
| NH3 | 5743 | -2250 | -0.681 ± 0.294 | -0.030 ± 0.011 |

TABLE 68: e^+/e^- ratio parameters a and b in Eq. (368).

| Target | E | Torus | a | b |
|--------|------|-------|--------------------|--------------------|
| ND3 | 1606 | 1500 | -5.630 ± 0.058 | 0.122 ± 0.001 |
| ND3 | 1606 | -1500 | -0.959 ± 0.015 | 0.004 ± 0.000 |
| NH3 | 1606 | 1500 | -5.962 ± 0.067 | 0.131 ± 0.002 |
| NH3 | 1606 | -1500 | -1.540 ± 0.015 | 0.014 ± 0.000 |
| ND3 | 1723 | -1500 | 0.152 ± 0.015 | -0.017 ± 0.000 |
| NH3 | 1723 | -1500 | 0.079 ± 0.015 | -0.015 ± 0.000 |
| NH3 | 2286 | 1500 | -2.126 ± 0.030 | 0.044 ± 0.000 |
| ND3 | 2561 | 1500 | -2.225 ± 0.027 | 0.056 ± 0.000 |
| ND3 | 2561 | -1500 | -2.596 ± 0.008 | 0.063 ± 0.000 |
| NH3 | 2561 | -1500 | -1.983 ± 0.009 | 0.044 ± 0.000 |
| ND3 | 4238 | 2250 | -1.591 ± 0.050 | 0.084 ± 0.001 |
| ND3 | 4238 | -2250 | -2.419 ± 0.026 | 0.120 ± 0.001 |
| NH3 | 4238 | 2250 | -1.645 ± 0.058 | 0.086 ± 0.002 |
| NH3 | 4238 | -2250 | -2.449 ± 0.024 | 0.118 ± 0.001 |
| ND3 | 5615 | 2250 | -1.181 ± 0.044 | 0.086 ± 0.001 |
| NH3 | 5615 | 2250 | -1.230 ± 0.040 | 0.087 ± 0.001 |
| ND3 | 5725 | 2250 | -0.929 ± 0.044 | 0.076 ± 0.001 |
| ND3 | 5725 | -2250 | -2.299 ± 0.018 | 0.125 ± 0.000 |
| NH3 | 5725 | 2250 | -1.068 ± 0.039 | 0.079 ± 0.001 |
| NH3 | 5725 | -2250 | -2.308 ± 0.017 | 0.123 ± 0.000 |
| ND3 | 5743 | -2250 | -2.453 ± 0.018 | 0.126 ± 0.000 |
| NH3 | 5743 | -2250 | -2.289 ± 0.017 | 0.128 ± 0.000 |

TABLE 69: e^+/e^- ratio parameters c and d in Eq. (368).

| Target | E | Torus | c | d |
|--------|------|-------|--------------------|--------------------|
| ND3 | 1606 | 1500 | -4.707 ± 0.090 | -0.032 ± 0.002 |
| ND3 | 1606 | -1500 | -6.743 ± 0.029 | 0.016 ± 0.001 |
| NH3 | 1606 | 1500 | -4.221 ± 0.104 | -0.046 ± 0.003 |
| NH3 | 1606 | -1500 | -6.397 ± 0.028 | 0.004 ± 0.001 |
| ND3 | 1723 | -1500 | -6.663 ± 0.028 | 0.025 ± 0.001 |
| NH3 | 1723 | -1500 | -6.564 ± 0.027 | 0.021 ± 0.001 |
| NH3 | 2286 | 1500 | -3.952 ± 0.042 | -0.003 ± 0.001 |
| ND3 | 2561 | 1500 | -3.538 ± 0.038 | -0.013 ± 0.001 |
| ND3 | 2561 | -1500 | -3.269 ± 0.013 | -0.025 ± 0.000 |
| NH3 | 2561 | -1500 | -3.908 ± 0.015 | -0.013 ± 0.000 |
| ND3 | 4238 | 2250 | -1.899 ± 0.039 | -0.052 ± 0.001 |
| ND3 | 4238 | -2250 | -1.190 ± 0.022 | -0.084 ± 0.001 |
| NH3 | 4238 | 2250 | -1.885 ± 0.045 | -0.053 ± 0.001 |
| NH3 | 4238 | -2250 | -1.208 ± 0.020 | -0.083 ± 0.000 |
| ND3 | 5615 | 2250 | -1.079 ± 0.033 | -0.065 ± 0.001 |
| NH3 | 5615 | 2250 | -1.025 ± 0.030 | -0.068 ± 0.001 |
| ND3 | 5725 | 2250 | -1.169 ± 0.033 | -0.061 ± 0.001 |
| ND3 | 5725 | -2250 | -0.415 ± 0.015 | -0.090 ± 0.000 |
| NH3 | 5725 | 2250 | -1.097 ± 0.029 | -0.063 ± 0.001 |
| NH3 | 5725 | -2250 | -0.434 ± 0.014 | -0.089 ± 0.000 |
| ND3 | 5743 | -2250 | -0.417 ± 0.015 | -0.089 ± 0.000 |
| NH3 | 5743 | -2250 | -0.438 ± 0.014 | -0.093 ± 0.000 |

TABLE 70: Systematic errors $\sigma_{sys}^{percent}$ for each Q^2 bin as a percentage of statistical errors on $A_1 + \eta A_2$ for the deuteron are listed for 1 GeV data. The percentage values are calculated according to Eq. (462) and evaluated in $1.15 < W < 2.60$ GeV.

| Q^2 bin | Total | Back. | Dilution | Radiative | $P_b P_t$ | Model | Pol. Back. |
|-----------|-------|-------|----------|-----------|-----------|-------|------------|
| 1 | 16 | 0.04 | 3 | 14 | 7 | 1 | 0.8 |
| 2 | 21 | 0.05 | 4 | 18 | 11 | 2 | 1 |
| 3 | 21 | 0.1 | 4 | 16 | 12 | 2 | 1 |
| 4 | 17 | 0.09 | 4 | 13 | 9 | 2 | 1 |
| 5 | 12 | 0.06 | 2 | 7 | 10 | 1 | 1 |
| 6 | 14 | 0.08 | 4 | 9 | 11 | 2 | 1 |
| 7 | 9 | 0.04 | 3 | 5 | 7 | 1 | 0.7 |
| 8 | 11 | 0.05 | 3 | 6 | 9 | 2 | 1 |
| 9 | 12 | 0.06 | 3 | 5 | 9 | 2 | 1 |
| 10 | 15 | 0.09 | 4 | 5 | 13 | 3 | 2 |
| 11 | 18 | 0.1 | 6 | 6 | 15 | 3 | 2 |
| 12 | 21 | 0.1 | 7 | 6 | 18 | 3 | 2 |
| 13 | 18 | 0.1 | 5 | 5 | 16 | 3 | 2 |
| 14 | 17 | 0.1 | 5 | 5 | 15 | 3 | 2 |
| 15 | 13 | 0.07 | 4 | 4 | 11 | 3 | 2 |
| 16 | 15 | 0.08 | 5 | 4 | 12 | 5 | 2 |
| 17 | 15 | 0.1 | 6 | 5 | 10 | 7 | 4 |
| 18 | 15 | 0.2 | 5 | 5 | 10 | 6 | 4 |
| 19 | 17 | 0.1 | 7 | 5 | 12 | 8 | 5 |
| 20 | 19 | 0.2 | 7 | 5 | 12 | 9 | 6 |
| 21 | 18 | 0.2 | 7 | 5 | 12 | 8 | 7 |
| 22 | 20 | 0.3 | 8 | 5 | 14 | 9 | 7 |
| 23 | 17 | 0.2 | 7 | 5 | 11 | 8 | 6 |
| 24 | 15 | 1 | 6 | 5 | 10 | 7 | 5 |
| 25 | 11 | 0.1 | 5 | 5 | 7 | 5 | 3 |
| 26 | 10 | 0.1 | 4 | 4 | 7 | 4 | 2 |

TABLE 71: Systematic errors $\sigma_{sys}^{percent}(Q^2)$ on $A_1 + \eta A_2$ for the deuteron are listed for 2 GeV data. The percentage values are calculated according to Eq. (462) and evaluated in $1.15 < W < 2.60$ GeV.

| Q^2 bin | Total | Back. | Dilution | Radiative | $P_b P_t$ | Model | Pol. Back. |
|-----------|-------|-------|----------|-----------|-----------|-------|------------|
| 1 | 45 | 0.9 | 3 | 44 | 8 | 5 | 1 |
| 2 | 20 | 0.5 | 2 | 20 | 5 | 3 | 0.7 |
| 3 | 25 | 0.7 | 3 | 24 | 7 | 4 | 1 |
| 4 | 25 | 0.8 | 3 | 24 | 7 | 4 | 1 |
| 5 | 13 | 0.5 | 2 | 12 | 5 | 2 | 0.7 |
| 6 | 12 | 0.5 | 2 | 10 | 6 | 2 | 0.8 |
| 7 | 10 | 0.4 | 2 | 7 | 5 | 2 | 0.8 |
| 8 | 15 | 0.7 | 3 | 11 | 9 | 3 | 1 |
| 9 | 8 | 0.4 | 2 | 5 | 5 | 2 | 0.8 |
| 10 | 7 | 0.3 | 2 | 4 | 4 | 2 | 0.7 |
| 11 | 10 | 0.5 | 3 | 5 | 7 | 3 | 1 |
| 12 | 9 | 0.5 | 2 | 4 | 6 | 3 | 1 |
| 13 | 11 | 0.6 | 3 | 5 | 9 | 3 | 1 |
| 14 | 13 | 0.8 | 4 | 6 | 10 | 4 | 2 |
| 15 | 13 | 0.6 | 4 | 4 | 10 | 4 | 2 |
| 16 | 14 | 0.7 | 5 | 5 | 11 | 5 | 2 |
| 17 | 11 | 0.4 | 4 | 4 | 9 | 4 | 2 |
| 18 | 13 | 0.5 | 4 | 4 | 10 | 5 | 2 |
| 19 | 13 | 0.4 | 4 | 3 | 10 | 5 | 3 |
| 20 | 13 | 0.4 | 4 | 4 | 10 | 5 | 3 |
| 21 | 15 | 0.6 | 5 | 4 | 10 | 7 | 4 |
| 22 | 16 | 0.6 | 6 | 4 | 12 | 7 | 5 |
| 23 | 15 | 0.6 | 5 | 4 | 10 | 7 | 6 |
| 24 | 18 | 0.7 | 7 | 4 | 12 | 8 | 7 |
| 25 | 21 | 1 | 7 | 4 | 15 | 9 | 7 |
| 26 | 22 | 1 | 8 | 3 | 16 | 10 | 8 |
| 27 | 19 | 0.8 | 7 | 3 | 14 | 8 | 7 |
| 28 | 16 | 0.7 | 6 | 3 | 13 | 6 | 6 |
| 29 | 14 | 0.5 | 5 | 3 | 11 | 5 | 4 |
| 30 | 7 | 0.2 | 3 | 2 | 6 | 2 | 2 |

TABLE 72: Systematic errors $\sigma_{sys}^{percent}(Q^2)$ on $A_1 + \eta A_2$ for the deuteron are listed for 4 GeV data. The percentage values are calculated according to Eq. (462) and evaluated in $1.15 < W < 2.60$ GeV.

| Q^2 bin | Total | Back. | Dilution | Radiative | $P_b P_t$ | Model | Pol. Back. |
|-----------|-------|-------|----------|-----------|-----------|-------|------------|
| 7 | 15 | 0.7 | 2 | 11 | 10 | 5 | 0.9 |
| 8 | 11 | 0.5 | 1 | 7 | 8 | 4 | 0.8 |
| 9 | 19 | 0.9 | 3 | 10 | 14 | 8 | 1 |
| 10 | 11 | 0.5 | 1 | 5 | 8 | 4 | 0.8 |
| 11 | 12 | 0.5 | 2 | 4 | 10 | 6 | 1 |
| 12 | 13 | 0.4 | 2 | 3 | 10 | 6 | 1 |
| 13 | 13 | 0.6 | 2 | 3 | 11 | 5 | 1 |
| 14 | 9 | 0.4 | 1 | 2 | 7 | 4 | 0.8 |
| 15 | 11 | 0.5 | 2 | 2 | 10 | 5 | 1 |
| 16 | 15 | 0.6 | 3 | 2 | 13 | 6 | 1 |
| 17 | 11 | 0.5 | 2 | 2 | 10 | 4 | 1 |
| 18 | 9 | 0.4 | 2 | 2 | 8 | 3 | 0.9 |
| 19 | 12 | 0.4 | 2 | 2 | 11 | 4 | 1 |
| 20 | 13 | 0.7 | 2 | 1 | 12 | 5 | 2 |
| 21 | 12 | 0.4 | 2 | 2 | 11 | 5 | 2 |
| 22 | 16 | 0.6 | 3 | 1 | 14 | 5 | 2 |
| 23 | 12 | 0.5 | 2 | 2 | 11 | 4 | 2 |
| 24 | 18 | 0.7 | 3 | 2 | 17 | 6 | 3 |
| 25 | 17 | 0.6 | 3 | 2 | 15 | 5 | 4 |
| 26 | 19 | 0.7 | 4 | 1 | 17 | 7 | 4 |
| 27 | 21 | 0.8 | 5 | 2 | 19 | 7 | 5 |
| 28 | 23 | 0.9 | 6 | 2 | 21 | 7 | 5 |
| 29 | 23 | 0.9 | 6 | 1 | 20 | 7 | 5 |
| 30 | 23 | 0.8 | 6 | 0.9 | 21 | 6 | 5 |
| 31 | 24 | 0.7 | 6 | 1 | 22 | 7 | 5 |
| 32 | 20 | 0.5 | 5 | 0.9 | 18 | 5 | 4 |
| 33 | 16 | 0.6 | 4 | 0.7 | 14 | 3 | 3 |
| 34 | 13 | 0.3 | 3 | 0.7 | 12 | 2 | 2 |
| 35 | 9 | 0.2 | 3 | 0.3 | 8 | 2 | 1 |

TABLE 73: Systematic errors $\sigma_{sys}^{percent}(Q^2)$ on $A_1 + \eta A_2$ for the deuteron are listed for 5 GeV data. The percentage values are calculated according to Eq. (462) and evaluated in $1.15 < W < 2.60$ GeV.

| Q^2 bin | Total | Back. | Dilution | Radiative | $P_b P_t$ | Model | Pol. Back. |
|-----------|-------|-------|----------|-----------|-----------|-------|------------|
| 16 | 13 | 0.8 | 1 | 0.9 | 12 | 3 | 0.6 |
| 17 | 14 | 0.5 | 0.6 | 0.4 | 14 | 2 | 0.4 |
| 18 | 23 | 3 | 2 | 1 | 22 | 5 | 1 |
| 19 | 20 | 2 | 2 | 0.7 | 19 | 5 | 1 |
| 20 | 23 | 2 | 2 | 0.6 | 21 | 8 | 1 |
| 21 | 17 | 2 | 1 | 0.7 | 15 | 6 | 1 |
| 22 | 20 | 1 | 2 | 0.8 | 20 | 4 | 1 |
| 23 | 19 | 1 | 2 | 0.7 | 18 | 3 | 1 |
| 24 | 24 | 2 | 3 | 0.7 | 23 | 4 | 2 |
| 25 | 24 | 1 | 3 | 0.9 | 23 | 4 | 3 |
| 26 | 25 | 1 | 3 | 1 | 24 | 4 | 3 |
| 27 | 25 | 2 | 4 | 0.9 | 24 | 4 | 4 |
| 28 | 25 | 1 | 4 | 1 | 24 | 5 | 5 |
| 29 | 28 | 2 | 5 | 1 | 26 | 6 | 5 |
| 30 | 27 | 2 | 5 | 1 | 25 | 7 | 6 |
| 31 | 30 | 2 | 6 | 1 | 28 | 6 | 6 |
| 32 | 30 | 2 | 6 | 1 | 28 | 6 | 6 |
| 33 | 29 | 2 | 5 | 0.8 | 27 | 5 | 6 |
| 34 | 29 | 1 | 5 | 0.6 | 27 | 4 | 5 |
| 35 | 24 | 0.9 | 4 | 0.5 | 23 | 3 | 4 |
| 36 | 21 | 0.6 | 4 | 0.4 | 21 | 2 | 3 |
| 37 | 18 | 0.3 | 5 | 0.5 | 17 | 2 | 1 |

TABLE 74: Systematic errors on A_1 deuteron for each Q^2 bin as a percentage of the statistical errors, as given in Eq. (462). The percentage values are evaluated in $1.15 < W < 2.60$ GeV.

| Q^2 bin | Total | Back. | Dilution | Radiative | $P_b P_t$ | Model | Pol. Back. |
|-----------|-------|-------|----------|-----------|-----------|-------|------------|
| 1 | 26 | 0.4 | 3 | 25 | 7 | 3 | 0.9 |
| 2 | 21 | 0.3 | 3 | 18 | 9 | 2 | 1 |
| 3 | 22 | 0.4 | 4 | 19 | 11 | 3 | 1 |
| 4 | 21 | 0.5 | 4 | 18 | 9 | 3 | 1 |
| 5 | 13 | 0.3 | 2 | 9 | 8 | 2 | 0.9 |
| 6 | 13 | 0.3 | 3 | 9 | 9 | 2 | 1 |
| 7 | 11 | 0.4 | 2 | 7 | 7 | 2 | 0.8 |
| 8 | 14 | 0.5 | 3 | 10 | 9 | 3 | 1 |
| 9 | 13 | 0.4 | 3 | 7 | 10 | 5 | 1 |
| 10 | 14 | 0.4 | 3 | 6 | 10 | 7 | 1 |
| 11 | 16 | 0.5 | 4 | 6 | 11 | 9 | 2 |
| 12 | 18 | 0.4 | 3 | 5 | 12 | 12 | 2 |
| 13 | 20 | 0.6 | 4 | 5 | 12 | 15 | 2 |
| 14 | 22 | 0.7 | 4 | 5 | 12 | 17 | 2 |
| 15 | 25 | 0.5 | 3 | 4 | 10 | 22 | 2 |
| 16 | 33 | 0.7 | 4 | 4 | 11 | 30 | 2 |
| 17 | 43 | 0.4 | 4 | 4 | 9 | 41 | 2 |
| 18 | 50 | 0.3 | 4 | 3 | 7 | 49 | 3 |
| 19 | 55 | 0.3 | 4 | 3 | 9 | 54 | 3 |
| 20 | 56 | 0.3 | 4 | 3 | 9 | 55 | 4 |
| 21 | 51 | 0.4 | 4 | 3 | 8 | 50 | 3 |
| 22 | 47 | 0.7 | 4 | 3 | 9 | 45 | 4 |
| 23 | 45 | 0.5 | 3 | 3 | 8 | 44 | 4 |
| 24 | 51 | 0.7 | 4 | 3 | 10 | 50 | 4 |
| 25 | 53 | 0.8 | 4 | 2 | 11 | 51 | 4 |
| 26 | 51 | 1 | 4 | 2 | 12 | 49 | 5 |
| 27 | 39 | 1 | 4 | 2 | 14 | 36 | 5 |
| 28 | 29 | 1 | 4 | 2 | 16 | 23 | 5 |
| 29 | 25 | 1 | 5 | 1 | 18 | 16 | 5 |
| 30 | 23 | 1 | 5 | 1 | 19 | 11 | 6 |
| 31 | 26 | 1 | 6 | 1 | 23 | 8 | 6 |
| 32 | 25 | 1 | 5 | 1 | 23 | 6 | 6 |
| 33 | 27 | 1 | 5 | 0.8 | 25 | 5 | 6 |
| 34 | 28 | 1 | 5 | 0.6 | 26 | 5 | 5 |
| 35 | 24 | 0.8 | 4 | 0.5 | 23 | 3 | 4 |
| 36 | 21 | 0.6 | 4 | 0.4 | 21 | 2 | 3 |
| 37 | 18 | 0.3 | 5 | 0.5 | 17 | 2 | 1 |

TABLE 75: Systematic errors on A_1 deuteron for Q^2 bins, as a percentage of statistical errors, calculated according to Eq. (462). The percentage values are evaluated in three different regions: Total ($1.15 < W < 2.60$ GeV); Region1 ($1.15 < W < 1.25$ GeV); Region2 ($1.25 < W < 1.80$ GeV); Region3 ($1.80 < W < 2.60$ GeV).

| Q^2 bin | Total | Region1 | Region2 | Region3 |
|-----------|-------|---------|---------|---------|
| 1 | 26 | 0.0052 | 18 | 38 |
| 2 | 21 | 0 | 22 | 19 |
| 3 | 22 | 23 | 21 | 24 |
| 4 | 21 | 7 | 19 | 25 |
| 5 | 13 | 8 | 12 | 15 |
| 6 | 13 | 11 | 16 | 10 |
| 7 | 11 | 5 | 10 | 12 |
| 8 | 14 | 6 | 13 | 16 |
| 9 | 13 | 10 | 13 | 13 |
| 10 | 14 | 24 | 12 | 13 |
| 11 | 16 | 37 | 14 | 14 |
| 12 | 18 | 50 | 16 | 13 |
| 13 | 20 | 59 | 16 | 15 |
| 14 | 22 | 63 | 19 | 15 |
| 15 | 25 | 68 | 25 | 15 |
| 16 | 33 | 89 | 36 | 17 |
| 17 | 43 | 117 | 50 | 14 |
| 18 | 50 | 130 | 61 | 11 |
| 19 | 55 | 134 | 71 | 13 |
| 20 | 56 | 135 | 72 | 13 |
| 21 | 51 | 108 | 69 | 13 |
| 22 | 47 | 84 | 66 | 13 |
| 23 | 45 | 59 | 67 | 12 |
| 24 | 51 | 46 | 79 | 12 |
| 25 | 53 | 38 | 82 | 13 |
| 26 | 51 | 26 | 80 | 15 |
| 27 | 39 | 22 | 59 | 18 |
| 28 | 29 | 18 | 39 | 20 |
| 29 | 25 | 13 | 30 | 22 |
| 30 | 23 | 13 | 24 | 22 |
| 31 | 26 | 13 | 22 | 29 |
| 32 | 25 | 12 | 21 | 29 |
| 33 | 27 | 13 | 18 | 32 |
| 34 | 28 | 11 | 22 | 33 |
| 35 | 24 | 18 | 24 | 23 |
| 36 | 21 | 9 | 22 | 22 |
| 37 | 18 | 26 | 17 | 0.04 |

TABLE 76: W regions (in GeV) used for Γ_1 calculation. Model was used where data is not available.

| bin | Q^2 | model | data | model | data | model |
|-----|-------|-------------|-------------|-------------|-------------|--------------|
| 10 | 0.049 | 1.08 - 1.14 | 1.15 - 1.59 | 1.60 - 2.99 | - | 3.00 - 7.10 |
| 11 | 0.059 | 1.08 - 1.14 | 1.15 - 1.59 | 1.60 - 2.99 | - | 3.00 - 7.74 |
| 12 | 0.070 | 1.08 - 1.14 | 1.15 - 1.59 | 1.60 - 1.84 | 1.85 - 1.99 | 2.00 - 8.45 |
| 13 | 0.084 | 1.08 - 1.14 | 1.15 - 1.79 | 1.80 - 2.99 | - | 3.00 - 9.23 |
| 14 | 0.101 | 1.08 - 1.14 | 1.15 - 1.79 | 1.80 - 2.99 | - | 3.00 - 10.10 |
| 15 | 0.120 | 1.08 - 1.14 | 1.15 - 1.83 | 1.84 - 2.99 | - | 3.00 - 11.00 |
| 16 | 0.144 | 1.08 - 1.14 | 1.15 - 1.83 | 1.84 - 2.99 | - | 3.00 - 12.00 |
| 17 | 0.171 | 1.08 - 1.14 | 1.15 - 2.19 | 2.20 - 2.99 | - | 3.00 - 13.10 |
| 18 | 0.205 | 1.08 - 1.14 | 1.15 - 2.19 | 2.20 - 2.99 | - | 3.00 - 14.30 |
| 19 | 0.244 | 1.08 - 1.14 | 1.15 - 2.19 | 2.20 - 2.39 | 2.40 - 2.59 | 2.60 - 15.60 |
| 20 | 0.292 | 1.08 - 1.14 | 1.15 - 2.19 | 2.20 - 2.99 | - | 3.00 - 17.10 |
| 21 | 0.348 | 1.08 - 1.14 | 1.15 - 2.24 | 2.25 - 2.99 | - | 3.00 - 18.70 |
| 22 | 0.416 | 1.08 - 1.14 | 1.15 - 2.59 | 2.60 - 2.99 | - | 3.00 - 20.40 |
| 23 | 0.496 | 1.08 - 1.14 | 1.15 - 2.59 | 2.60 - 2.99 | - | 3.00 - 22.30 |
| 24 | 0.592 | 1.08 - 1.14 | 1.15 - 2.59 | 2.60 - 2.99 | - | 3.00 - 24.30 |
| 25 | 0.707 | 1.08 - 1.14 | 1.15 - 2.79 | 2.80 - 2.99 | - | 3.00 - 26.60 |
| 26 | 0.844 | 1.08 - 1.14 | 1.15 - 2.89 | 2.90 - 2.99 | - | 3.00 - 29.00 |
| 27 | 1.01 | 1.08 - 1.14 | 1.15 - 2.89 | 2.90 - 2.99 | - | 3.00 - 31.80 |
| 28 | 1.2 | 1.08 - 1.14 | 1.15 - 2.89 | 2.90 - 2.99 | - | 3.00 - 34.60 |
| 29 | 1.44 | 1.08 - 1.14 | 1.15 - 2.89 | 2.90 - 2.99 | - | 3.00 - 37.90 |
| 30 | 1.71 | 1.08 - 1.14 | 1.15 - 2.89 | 2.90 - 2.99 | - | 3.00 - 41.30 |
| 31 | 2.05 | 1.08 - 1.14 | 1.15 - 2.79 | 2.80 - 2.99 | - | 3.00 - 45.30 |
| 32 | 2.44 | 1.08 - 1.14 | 1.15 - 2.59 | 2.60 - 2.99 | - | 3.00 - 49.40 |
| 33 | 2.92 | 1.08 - 1.14 | 1.15 - 2.59 | 2.60 - 2.99 | - | 3.00 - 54.00 |
| 34 | 3.48 | 1.08 - 1.14 | 1.15 - 2.49 | 2.50 - 2.99 | - | 3.00 - 59.00 |
| 35 | 4.16 | 1.08 - 1.14 | 1.15 - 2.29 | 2.30 - 2.99 | - | 3.00 - 64.50 |
| 36 | 4.96 | 1.08 - 1.14 | 1.15 - 1.99 | 2.00 - 2.99 | - | 3.00 - 70.40 |
| 37 | 5.92 | 1.08 - 1.14 | 1.15 - 1.59 | 1.60 - 2.99 | - | 3.00 - 76.90 |

BIBLIOGRAPHY

- [1] S.E. Kuhn. “Nucleon Structure Functions: Experiments and Models,” Lecture notes from HUGS (Hampton University Graduate Studies at JLab) lectures (1997).
- [2] H. Fritzsche and G. Eldahoumi, “Constituent Quarks and the Spin of the Proton,” arXiv:hep-ph/0906.1139 (2009).
- [3] R. P. Feynman, “Proceedings of the 3rd Topical Conference on High Energy Collision of Hadrons,” Stony Brook, N. Y. (1969).
- [4] J. D. Bjorken and E. A. Paschos, “Inelastic Electron-Proton and γ -Proton Scattering and the Structure of the Nucleon,” Phys. Rev. **185**, 1975 (1969).
- [5] J. D. Bjorken, “Asymptotic Sum Rules at Infinite Momentum,” Phys. Rev. **179**, 1547 (1969).
- [6] J.J. Aubert *et al.*, Phys. Lett. B 123, **275** (1983).
- [7] S. E. Kuhn, J. P. Chen and E. Leader, “Spin Structure of the Nucleon - Status and Recent Results,” Prog. Part. Nucl. Phys. **63**, 1 (2009) [arXiv:hep-ph/0812.3535].
- [8] F. Halzen and A. D. Martin, *Quarks and Leptons*, New York: John Wiley & Sons (1979).
- [9] E. Leader and E. Predazzi, *An introduction to gauge theories and the “new physics”*, Cambridge university Press (1982).
- [10] T. Pussieux and R. Windmolders, *A collection of formulas for spin dependent deep inelastic scattering*, (Unpublished).
- [11] J. Soffer and O. V. Teryaev, hep-ph/9906455.
- [12] M. Osipenko *et al.* [CLAS Collaboration], “The deuteron structure function F2 with CLAS”, arXiv:hep-ex/0507098 (2005).
- [13] C.S. Armstrong, *et al.*, Phys. Rev. D **63** 094008 (2001). [hep-ph/0104055].
- [14] P. Hoodbhoy, R. L. Jaffe and A. Manohar, Nucl. Phys. B **312**, 571 (1989).

- [15] A. Airapetian *et al.*, Phys. Rev. Lett. **95** 242001 (2005) [arXiv:hep-ex/0506018]
- [16] F. E. Close, *An Introduction to Quarks and Partons*, London: Academic Press (1984). [ISBN 0-12-175150-3]
- [17] Y. Prok, “Measurement of the Spin Structure Function $g_1(x, Q^2)$ of the Proton Measured in the Resonance Region,” Ph.D. diss., University of Virginia, 2004.
- [18] V. N. Gribov and L.N. Lipatov, Sov. J. Nucl. Phys. **15**, 138 (1972); Y.L. Dokahitzer, Sov. Phys. JETP. **16**, 161, (1977); G. Altarelli and G. Parisi, Nucl. Phys. B **126**, 298 (1977).
- [19] B. W. Filippone and X. Ji, Adv. Nucl. Phys. **26**, 1 (2001).
- [20] E. Leader, *Spin in particle physics*, Cambridge Monogr. Part. Phys. Nucl. Phys. Cosmol. 15 (2001).
- [21] W. Melnitchouk and W. Weise, arXiv:hep-ph/0006170 (2000).
- [22] B. Lampe and E. Reya, “Spin physics and polarized structure functions,” Phys. Rep. **332** 1 (2000).
- [23] K. Wilson, Phys. Rev. **179**, 1499 (1969); R. A. Brandt and G. Preparata, Nucl. Phys. B **27**, 541 (1971); O. Nachtmann, Nucl. Phys. B **63**, 237 (1973).
- [24] Z.E. Meziani, arXiv:hep-ph/0404066 (2004).
- [25] M. Osipenko, arXiv:hep-ph/0404195 (2004).
- [26] A. Deur, “Higher-twist analysis of moments of spin structure function,” arXiv:nucl-ex/0508022 (2005).
- [27] X. Ji and P. Unrau, Phys. Lett. B **333**, 228 (1994).
- [28] C. E. Carlson and N. C. Mukhopadhyay, Phys. Rev. D **58**, 094029 (1998).
- [29] J. Edelman, G. Piller, N. Kaiser and W. Weise, Nucl. Phys. A **665**, 125 (2000).
- [30] A. Thomas and W. Weise, *The structure of the nucleon*, Wiley-VCH, Berlin (2001).

- [31] E.D. Bloom and F.J. Gilman, “Scaling, Duality, and the Behavior of Resonances in Inelastic electron-Proton Scattering,” *Phys. Rev. Lett.* **25** 1140 (1970).
- [32] W. Melnitchouk, R. Ent, and C. Keppel, *Phys. Rep.* **406**, 127 (2005).
- [33] F.E. Close and W. Melnitchouk, “Symmetry breaking and quark-hadron duality in structure functions,” *Phys. Rev. C* **68** 035210 (2003).
- [34] J. Blmllein and A. Tkabladze, *Nucl. Phys. B* **553**, 427 (1999).
- [35] I. Niculescu *et al.*, *Phys. Rev. Lett.* **85**, 1186 (2000).
- [36] P.E. Bosted *et al.*, “Quark-hadron duality in spin structure functions g_1^p and g_1^d ,” *Phys. Rev. C* **75**, 035203 (2007).
- [37] T.A. Forest, GDH 2004 Proceedings, p84, World Scientific (2004).
- [38] De Rujula, H. Georgi and H.D. Politzer, *Ann. Phys.* **103**, 315 (1977).
- [39] F. E. Close and N. Isgur, *Phys. Lett. B* **509**, 81 (2001).
- [40] Z. Dziembowski and J. Franklin, *Nucl. Part. Phys.* **17** **213**, (1991).
- [41] David Griffiths, *Introduction to Elementary Particles*, New York: John Wiley & Sons (1987).
- [42] M. Anselmino, A. Efremov, E. Leader, CERN Reports TH/7216/94 (1994).
- [43] P. L. Anthony *et al.*, E142 Collaboration, *Phys. Rev. D* **54**, 6620 (1996).
- [44] B. Adeva *et al.*, Spin Muon Collaboration, *Phys. Rev. D* **58**, 112001 (1998).
- [45] K. Abe *et al.*, E143 Collaboration, *Phys. Rev. D* **58**, 112003 (1998) [arXiv:hep-ph/9802357].
- [46] K. Abe *et al.*, E154 Collaboration, *Phys. Lett. B* **405**, 180 (1997).
- [47] P. L. Anthony *et al.*, E155 Collaboration, *Phys. Lett. B* **493**, 19 (2000); arXiv:hep-ex/9904002.
- [48] A. Airapetian *et al.*, HERMES Collaboration, *Phys. Rev. D* **75**, 012007 (2007); *Phys. Lett. B* **404**, 383 (1997).

- [49] V. Y. Alexakhin *et al.*, COMPASS Collaboration, Phys. Lett. B **647**, 8 (2007).
- [50] K. V. Dharmawardane *et al.* [CLAS Collaboration], Phys. Lett. B **641**, 11 (2006) [arXiv:nucl-ex/0605028].
- [51] S. L. Adler, Phys. Rev. **177**, 2426 (1969).
- [52] R. D. Carlitz, J. C. Collins and A. H. Mueller, Phys. Lett. B **214**, 229 (1988).
- [53] S.B. Gerasimov, Sov. J. of Nucl. Phys. **2**, 430 (1966).
- [54] S.D. Drell and A.C. Hearn, Phys. Rev. Lett. **16**, 908 (1966).
- [55] K. Helbing, “The Gerasimov-Drell-Hearn sum rule,” Prog. Part. Nucl. Phys. **57**, 405 (2006) [arXiv:nucl-ex/0603021].
- [56] D. Drechsel, B. Pasquini, and M. Vanderhaeghen, Phys. Rep. **378**, 99 (2003).
- [57] H. Arenhovel *et al.*, GDH 2004 Proceedings, p294, World Scientific (2004).
- [58] X. Ji and J. Osborne, J. Phys. G **27**, 127 (2001) [arXiv:hep-ph/9905410].
- [59] X. Ji, C. Kao, and J. Osborne, Phys. Lett. B **472**, 1 (2000).
- [60] V. Bernard, T.R. Hemmert, and U.G. Meisner, Phys. Lett. B **545**, 105 (2002).
- [61] Drechsel, D., S. S. Kamalov, and L. Tiator, Phys. Rev. D **63**, 114010 (2001).
- [62] M. Anselmino, B.L. Ioffe and E. Leader, Sov. J. Nucl. Phys. **49**, 136 (1989).
- [63] V. D. Burkert and B. L. Ioffe and E. Leader, Phys. Lett. B **296**, 223 (1992).
- [64] J. J. Sakurai, *Currents and Mesons*, University of Chicago Press, Chicago (1969).
- [65] J. Soffer and O. V. Teryaev, Phys. Rev. D **51**, 25 (1995); J. Soffer and O. V. Teryaev, Phys. Rev. D **56**, 7458 (1997).
- [66] H. Burkhardt and W.N. Cottingham, Ann. Phys. (NY) **56**, 453 (1970).
- [67] J. Yun *et al.*, Phys. Rev. C **67**, 055204 (2003).
- [68] R. Fatemi *et al.*, “Measurement of the Proton Spin Structure Function $g_1(x, Q^2)$ for Q^2 from 0.15 to 1.6 GeV² with CLAS,” Phys. Rev. Lett. **91**, 2220022 (2003).

- [69] O.A. Rondon, Phys. Rev. C **60**, 035201 (1999).
- [70] X. Zheng, GDH 2004 Proceedings, p73, World Scientific (2004); X. Zheng *et al.*, Phys. Rev. Lett. **92**, 012004 (2004).
- [71] C. Ciofi degli Atti, L. P. Kaptari, S. Scopetta and A. Y. Umnikov, “The Neutron Spin Structure Function from the Deuteron Data in the Resonance Region,” Phys. Lett. B **376**, 309 (1996) [arXiv:nucl-th/9601045].
- [72] W. Melnitchouk, Nucl. Phys. A **631**, 296C (1997) [arXiv:hep-ph/9708484].
- [73] Y. Kahn, W. Melnitchouk and S. A. Kulagin, “New method for extracting neutron structure functions from nuclear data,” Phys. Rev. C **79**, 035205 (2009) [arXiv:nucl-th/0809.4308].
- [74] D. F. Geesaman, K. Saito and A.W. Thomas, Annu. Rev. Nucl. Part. Sci. **45** 337 (1995).
- [75] W. Bentz, I. C. Cloet and A. W. Thomas, “The polarized EMC effect,” AIP Conf. Proc. **892**, 248 (2007).
- [76] B. A. Mecking, *et al.*, “The CEBAF large acceptance spectrometer (CLAS),” Nucl. Instr. Meth. A **503**, 513 (2003).
- [77] V. Dharmawardane, “Spin Structure Functions of the Deuteron Measured with CLAS In and Above the Resonance Region,” Ph.D. diss., Old Dominion University (2004).
- [78] M. D. Mestayer *et al.*, Nucl. Instr. and Meth. A **449**, 81 (2000).
- [79] L. Qin *et al.*, CLAS-NOTE **1996-018** JLAB (1996).
- [80] E. S. Smith *et al.*, Nucl. Instr. and Meth. A **432**, 265 (1999).
- [81] G. Adams *et al.*, Nucl. Instr. and Meth. A **465**, 414 (2001).
- [82] M. Amarian *et al.*, Nucl. Instr. and Meth. A **460**, 239 (2001).
- [83] C. D. Keith *et al.*, “A polarized target for the CLAS detector,” Nucl. Instr. and Meth. A **501**, 327 (2003).
- [84] S. Stepanyan, “Simple Event Builder (SEB) in the framework of RECSIS,”

http://www.jlab.org/~stepanya/seb_man.html

- [85] Jefferson Lab Computing,

https://wiki.jlab.org/cc/external/wiki/index.php/Scientific_Computing

- [86] Harut Avagyan, *et al.*, “The CLAS Calibration Database,” CLAS-NOTE **2001-003** JLAB (2001).

- [87] E.S. Smith *et al.*, “The time-of-flight system for CLAS,” Nucl. Instr. Meth. **A 432**, 265 (1999).

- [88] E.S. Smith, V.Dharmawardane, *et al.*, “Calibration of the CLAS TOF System,” CLAS-NOTE **1999-011** JLAB (1999). (Updated in 2001).

- [89] C. Smith, EC Energy Calibration,

http://www.jlab.org/~lcsmith/EC_Energy_Calibration.html

- [90] L.M. Qin *et al.*, “Prototype studies and design considerations for the CLAS Region 2 drift chambers,” Nucl. Instr. Meth. **A 411**, 265 (1998).

- [91] Dieter Cords *et al.*, “CLAS Event Format with BOS,” CLAS-NOTE **1994-005** JLAB (1994).

- [92] “HELicity Physics analysis for EG1b,”

<http://www.jlab.org/~claseg1/analysis/eg1b/He1P.html>

- [93] S. Kuhn and N. Guler, “False Asymmetry Studies for EG1b Experiment,” CLAS-NOTE **2005-005** JLAB (2005).

- [94] W.M. Yao *et al.*, (Particle Data Group), “The Review of Particle Physics,” J. Phys. **G33**, 1 (2007).

- [95] Robert Fersch, “Measurement of Inclusive Proton Double-Spin Asymmetries and Polarized Structure Functions in the CLAS EG1B Experiment,” Ph.D. diss., The College of William and Marry (2008).

- [96] “Quality Checks for the EG1b 4.2 and 2.5 GeV data sets,”

http://www.jlab.org/Hall-B/secure/eg1/EG2000/nevzat/QUALITY_CHECKS/

- [97] “Quality Checks for the EG1b experiment,”

http://www.jlab.org/Hall-B/secure/eg1/EG2000/fersch/QUALITY_CHECKS/

- [98] M. Osipenko, A. Vlassov and M. Taiuti, “Matching between the electron candidate track and the Cherenkov counter hit,” CLAS-NOTE **2004-020** JLAB (2004).

- [99] “Geometric and Timing Cuts for EG1b,”

http://www.jlab.org/Hall-B/secure/eg1/EG2000/nevzat/GEOM_CC_CUTS/

- [100] A. Vlassov, “CLAS Cherekov Counter study,”

<http://www.jlab.org/~vlassov/cc/index.html>

- [101] Peter Posted, S. Kuhn, Y. Prok, “Raster Corrections for EG1B,” CLAS-NOTE **2003-008** JLAB (2003).

- [102] M. Bellis, “Reliability and Limitations of GSIM,” CLAS-NOTE **2002-016** JLAB (2002).

- [103] P. Bosted and H. Avakian, “Multiple Scattering and Stray Magnetic Field Corrections for Tracking in the Presence of Target Field,” CLAS-NOTE **2006-006** JLAB (2006). (The magnetic field correction is updated later.)

- [104] H. Avakian, personal correspondence.

- [105] “Hall A Absolute Beam Energy Measurements,”

http://hallaweb.jlab.org/equipment/beam/energy/absolute_beam_energy.html

- [106] Glenn F. Knoll, *Radiation Detection and Measurement*, New York: John Wiley & Sons (2000).

- [107] W.M. Yao *et al.*, (Particle Data Group), “The Review of Particle Physics,” J. Phys. **G33**, 1 (2007).

- [108] William R. Leo, *Techniques for Nuclear and Particle Physics Experiments*, Berlin: Springer-Verlag (1994)
- [109] S.E. Kuhn, A.V. Klimenko, “Momentum corrections for E6,” CLAS-NOTE **2003-005** JLAB (2003).
- [110] CEBAF Hall B Conceptual Design Report (1990).
- [111] F. James, “MINUIT Function Minimization and Error Analysis Reference Manual,”
<http://wwwasdoc.web.cern.ch/wwwasdoc/minuit/minmain.html>
- [112] P. Bosted and R. Fersch *et al.*, “Ratios of $^{15}\text{N}/^{12}\text{C}$ and $^4\text{He}/^{12}\text{C}$ inclusive electroproduction cross-sections in the nucleon resonance region,” *Phys. Rev. C* **78** 015202 (2008) [arXiv:nucl-ex/0712.2438v3].
- [113] S. Kuhn, “Data Analysis for EG1” (analysis document),
<http://www.jlab.org/Hall-B/secure/eg1/AnalysisDoc/EG2000DataAnalysis.pdf>
- [114] D.R. Lide, ed. *CRC Handbook of Chemistry and Physics, 78th Ed.* Boca Raton, FL: CRC Press (1997).
- [115] Peter Posted, “Pair Symmetric and Pion Backgrounds for EG1B,” CLAS-NOTE **2004-005** JLAB (2004).
- [116] J. Arrington, “Implications of the discrepancy between proton form factor measurements,” *Phys. Rev. C* **69**, 022201 (2004).
- [117] “ $P_b P_t$ studies for EG1b,”
<http://www.jlab.org/Hall-B/secure/eg1/EG2000/nevzat/PBPT/Comparisons>
- [118] K. Abe *et al.*, *Phys. Rev. D* **58**, 112003 (1998).
- [119] T.V. Kuchto and N.M. Shumeiko, “Radiative Effects in Deep Inelastic Scattering of Polarized Leptons by Polarized Nucleons,” *Nucl. Phys.* **B219**, 412 (1983).
- [120] L.W. Mo and Y.S. Tsai, “Radiative Corrections to Elastic and Inelastic ep and μp Scattering,” *Rev. Mod. Phys.* **41**, 205 (1969).

- [121] F.R. Wesselmann, “Precision Measurement of the Spin Structure of the Proton and the Deuteron in the.” Ph.D. diss., Old Dominion University (2000).
- [122] P.E. Bosted and M.E. Christy, “Empirical Fit to Inelastic Electron-Deuteron and Electron-Neutron Resonance Region Transverse Cross Sections,” *Phys. Rev. C* **77**, 065206 (2008).
- [123] M.E. Christy and P.E. Bosted, “Empirical Fit to Precision Inclusive Electron-Proton Cross Sections in the Resonance Region,” arXiv:0712.3731 (2007).
- [124] M. Arneodo *et al.*, *Phys. Lett. B* **364**, 107 (1995).
- [125] H. Dutz *et al.*, *Phys. Rev. Lett.* **91**, 192001 (2003).
- [126] H. Dutz *et al.*, *Phys. Rev. Lett.* **94**, 162001 (2005).
- [127] H. Dutz *et al.*, *Phys. Rev. Lett.* **93**, 032003 (2004)
- [128] <http://wwwkph.kph.uni-mainz.de/MAID//maid2007/>
- [129] Octavian Florin Filoti, Ph.D. diss., pages 190-194, University of New Hampshire (2007).
- [130] K. Slifer *et al.* [Resonance Spin Structure Collaboration], “Spin Structure Moments of the Proton and Deuteron,” arXiv:0812.0031 [nucl-ex].
- [131] O. A. Rondon, *AIP Conf. Proc.* **842**, 395 (2006).
- [132] <http://www.jlab.org/Hall-B/secure/eg1/EG2000/nevzat/MODELS/>
- [133] Oscar A. Rondon and Karl Slifer, personal correspondence.
- [134] M. Amarian *et al.*, “The Q² Evolution of the Neutron Spin Structure Moments using a ³He Target”, *Phys. Rev. Lett.* **92** 022301 (2004).
- [135] K. Slifer *et al.*, (The Jefferson Lab E94-010 Collaboration), “He-3 Spin-Dependent Cross Sections and Sum Rules”, *Phys. Rev. Lett.* **101**, 022303 (2008) [arXiv:nucl-ex/0803.2267].
- [136] P. Solvignon *et al.* [Jefferson Lab E01-012 Collaboration], *Phys. Rev. Lett.* **101**, 182502 (2008) [arXiv:nucl-ex/0803.3845].

- [137] Patricia Solvignon, “Measurement of the ^3He Spin Structure Functions in the Resonance Region: A Test of Quark-Hadron Duality on the Neutron,” Ph.D. diss., Temple University (2006).
- [138] S. A. Kulagin and W. Melnitchouk, *Phys. Rev. C* **77**, 015210 (2008) [arXiv:nucl-th/0710.1101].
- [139] M. Anghinolfi *et al.* “The GDH Sum Rule with Nearly-Real Photons and the Proton g_1 Structure Function at Low Momentum Transfer,” CLAS Proposal PR-03-006 (2003).
- [140] <http://clasweb.jlab.org/physicsdb/>
- [141] K. Abe *et al.*, “Measurements of $R = \sigma_L/\sigma_T$ for $0.03 < x < 0.1$ and fit to world data.” *Phys. Lett.* **B452** 194 (1999).
- [142] S. Kuhn, “Model for the Asymmetry A_2 .” Technical note (2001).

<http://www.jlab.org/Hall-B/secure/eg1/Models/A2technote.ps>
- [143] G. Adams *et al.*, “CLAS detector”, Preprint submitted to Elsevier Science, July 15, (2002).
- [144] R.M Gibbons, D.I Nathan, “Thermodynamic Data of Helium-3”, Tech. Report AFML-TR-67-175, Air Force Materials Laboratory, October 1967, Reproduced by U.S. Department of Commerce.
- [145] D. Lawrence, M.D. Mestayer, “CLAS Drift Chamber Calibration Procedures,” CLAS-NOTE **1999-011** JLAB (1999).
- [146] A.V. Klimenko “Electron Scattering from a High Momentum Neutron in Deuterium,” Ph.D. diss., Old Dominion University (2004)
- [147] J.M. Musolf *et al.*, *Phys. Rep.* **239**, 1 (1994).
- [148] Peter Renton, *Electroweak Interactions: An Introduction to the Physics of Quarks and Leptons* Cambridge University Press, 1990.

VITA

Nevzat Guler

Department of Physics

Old Dominion University

Norfolk, VA 23529

EDUCATION:

- Ph.D. Physics, Old Dominion University, Norfolk, Virginia anticipated 2009, “Spin Structure of the Deuteron and the Neutron”, advised by Sebastian Kuhn.
- M.Sc. Physics, University of Texas at Arlington, Arlington, Texas, 2002, “Development and Test of Silicon Microstip Detector Package for pp2pp experiment at RHIC at BNL”, advised by Kaushik De.
- B.Sc. Physics, Midle East Technical University, Ankara, Turkey, 1998, “Neutrino Oscillations”, advised by Perihan Tolun.

EXPERIENCE:

- 2002 - Present: Research Assistant, Old Dominion University, Norfolk, VA
- 2000 - 2002: User Scientist, Brookhaven National Laboratory, Upton, NY
- 1999 - 2002: Research Assistant, Univ. of Texas at Arlington, Arlington, TX
- 1999 Summer: Summer Student, CERN, Geneva, Switzerland
- 1998 - 1999: Teaching Assistant, Midle East Technical Univ., Ankara, Turkey